Nonlinear Control and Synchronization of Multiple Lagrangian Systems with Application to Tethered Formation Flight Spacecraft

by

Soon-Jo Chung

B.S., Korea Advanced Institute of Science and Technology (1998)
S.M., Massachusetts Institute of Technology (2002)

Submitted to the Department of Aeronautics and Astronautics
in partial fulfillment of the requirements for the degree of

Doctor of Science in Estimation and Control

at the

MASSACHUSETTS INSTITUTE OF TECHNOLOGY

June 2007

Author .....
Department of Aeronautics and Astronautics
February 23, 2007

Certified by .....
David W. Miller
Professor of Aeronautics and Astronautics
Thesis Supervisor

Certified by .....
Jean-Jacques E. Slotine
Professor of Mechanical Engineering and Information Sciences
Professor of Brain and Cognitive Sciences
Thesis co-advisor

Certified by .....
Enrico Lorenzini
Professor of Aerospace Engineering, University of Padova, Italy
Research Associate, Harvard-Smithsonian Center for Astrophysics

Certified by .....
Edmund M.-C. Kong
Senior Principal Engineer, Orbital Science Corporation

Accepted by .....
Jaime Peraire
Chairman, Department Committee on Graduate Students

Nonlinear Control and Synchronization of Multiple Lagrangian Systems with Application to Tethered Formation Flight Spacecraft

by

Soon-Jo Chung

Submitted to the Department of Aeronautics and Astronautics
on February 23, 2007, in partial fulfillment of the
requirements for the degree of
Doctor of Science in Estimation and Control

Abstract

This dissertation focuses on the synchronization of multiple dynamical systems using contraction theory, with applications to cooperative control of multi-agent systems and synchronization of interconnected dynamics such as tethered formation flight. Inspired by stable combinations of biological systems, contraction nonlinear stability theory provides a systematic method to reduce arbitrarily complex systems into simpler elements. One application of oscillation synchronization is a fully decentralized nonlinear control law, which eliminates the need for any inter-satellite communications. We use contraction theory to prove that a nonlinear control law stabilizing a single-tethered spacecraft can also stabilize arbitrarily large circular arrays of tethered spacecraft, as well as a three-spacecraft inline configuration. The convergence result is global and exponential due to the nature of contraction analysis. The proposed decentralized control strategy is further extended to robust adaptive control in order to account for model uncertainties. Numerical simulations and experimental results validate the exponential stability of the tethered formation arrays by implementing a tracking control law derived from the reduced dynamics.

This thesis also presents a new synchronization framework that can be directly applied to cooperative control of autonomous aerospace vehicles and oscillation synchronization in robotic manipulation and locomotion. We construct a dynamical network of multiple Lagrangian systems by adding diffusive couplings to otherwise freely moving or flying vehicles. The proposed tracking control law synchronizes an arbitrary number of robots into a common trajectory with global exponential convergence. The proposed control law is much simpler than earlier work in terms of both the computational load and the required signals. Furthermore, in contrast with earlier work which used simple double integrator models, the proposed method permits highly nonlinear systems and is further extended to adaptive synchronization, partial-joint coupling, and concurrent synchronization.

Another contribution of the dissertation is a novel nonlinear control approach for underactuated tethered formation flight spacecraft. This is motivated by a controllability analysis that indicates that both array resizing and spin-up are fully controllable by the reaction wheels and the tether motor. This work reports the first propellant-free underactuated control results for tethered formation flight. We also fulfill the potential of the proposed strategy by providing a new momentum dumping method.

This dissertation work has evolved based on the research philosophy of balancing theoretical work with practicality, aiming at physically intuitive algorithms that can be directly implemented in real systems. In order to validate the effectiveness of the decentralized control and estimation framework, a new suite of hardware has been designed and added to the SPHERES (Synchronize Position Hold Engage and Reorient Experimental Satellite) testbed. Such recent improvements described in this dissertation include a new tether reel mechanism, a force-torque sensor and an air-bearing carriage with a reaction wheel. This thesis also introduces a novel relative attitude estimator, in which a series of Kalman filters incorporate the gyro, force-torque sensor and ultrasound ranging measurements. The closed-loop control experiments can be viewed at *http://ssl.mit.edu/spheres/videos.html*.

Thesis supervisor: David W. Miller
Title: Professor of Aeronautics and Astronautics

Acknowledgments

The author would like to gratefully acknowledge the NASA Goddard Space Flight Center (Contract Monitor: Dr. David Leisawitz) for both financial and technical support for the MIT-SSL and Payload Systems (PSI) SPHERES Tether program.

Personal Acknowledgements:

I am extremely grateful to my advisor, Prof. David Miller for his inspiration, guidance and financial support throughout my study at MIT (September 2000- March 2007). In particular, his practical mind and ingenuity in experimentation have enlightened me as to the importance of control experiments. I take great pride in the influence of Dave's research philosophy, evidenced by the two excellent spacecraft testbeds (ARGOS and SPHERES) that I have worked on.

Meeting with Prof. Jean-Jacques Slotine, my co-advisor, was another turning point in my life. His encouragement and inspiration have continuously motivated me into the field of nonlinear control theory. Through countless discussions with him in which his mathematics and control prowess were clearly visible, I was able to establish the theoretical aspect of this dissertation.

I wish to thank my doctoral committee members, Prof. Enrico Lorenzini and Dr. Edmund Kong. I was fortunate to get advice from Prof. Lorenzini, the leading authority in space tethers. His inspiration has been essential to my research. Edmund has been a great friend and mentor during my years at MIT. I also express my sincere gratitude to my thesis readers: Dr. Raymond Sedwick, Prof. Emilio Frazzoli and Prof. Jonathan How. I also appreciate the advice from my minor advisor, Prof. George Barbastathis. Additionally, my precious chance to share my first office at MIT with Prof. Olivier de Weck has nurtured my MIT life in many ways.

I gratefully acknowledge technical discussions and support from the MIT SSL SPHERES team including Alvar Saenz-Otero, Simon Nolet, Danielle Adams, Christophe Mandy, Hiraku Sakamoto, Nicholas Hoff, Swati Mohan, Thomas Coffee, and Amer Fejzic.

I have also learned a lot from my former and current colleagues at the MIT Space Systems Lab (SSL) including Carl Blaurock, Scott Uebelhart, Cyrus Jilla, Alice Liu, Becky Masterson, Julie Wertz, Allen Chen, David Lobosco, Laila Elias, Daniel Kwon, Umair Ahsun, Deborah Howell, Seung Chung, Thomas McGuire, Mark Hilstad, Julien-Alexandre Lamamy, Sangil Lee, and Ryan Lim.

The other SSL faculty and staff have been very helpful too. I greatly thank Paul Bauer, Col. John Keesee, Marilyn Good, Sharon-Leah Brown and Peggy Edwards. The administrative staff at the Aero/Astro department has been instrumental- I am deeply grateful to Marie Stuppard and Barbara Lechner.

I express enormous gratitude to Payload Systems, Inc. for their technical support and friendship. I would like to thank Joe Parrish, Javier de Luis, John Merk, Steve Sell, Chris Krebs, Edison Guerra and Joanne Vinning.

I also enjoyed stimulating technical discussions and fun days with my Korean friends at MIT and the church. I appreciate the friendship with Kyungyeol Song, Sanghyuk Park, Jinwook Lee, Hanlim Choi, Kitae Nam, Dogkun Lee, Hyunjin In, Jaemyung Ahn, Sunghoon Kang, Eunseok Suh, Ilyong Kim, Euiheon Chung and Chulmin Joo.

My parents have been a constant source of inspiration and encouragement. A Space Shuttle toy they bought me 25 years ago eventually led me to the field of spacecraft controls. I cannot thank my parents enough since I owe everything I have ever achieved to them. I am also enormously thankful to my parent-in-laws for their emotional support and love.

Last and foremost, I wish to express my affectionate gratitude to my wife, SunHee. She has been patiently there, standing by me through the hardships. She also made my last two years at MIT by far more rewarding, enjoyable and happy. She is a much more talented yet more considerate person than I am, but she has sacrificed everything for me.

Contents

1 Introduction **17**
- 1.1 Preface . . . 17
- 1.2 Motivation . . . 17
  - 1.2.1 Formation Flying in Space: Stellar Interferometry . . . 17
  - 1.2.2 Motivation for Tethered Formation Flight . . . 18
  - 1.2.3 Why Nonlinear Control? . . . 20
  - 1.2.4 Rationale Behind Decentralized Control Architecture . . . 20
  - 1.2.5 Motivation for Underactuated Tethered System . . . 21
  - 1.2.6 Criticality of Control Experiments . . . 22
- 1.3 Problem statement . . . 22
- 1.4 Goal and Objectives . . . 23
- 1.5 Research Approach and Contributions . . . 24
  - 1.5.1 Nonlinear Model Reduction and Decentralized Control by Synchronization (OBJ1: Chapter 4) . . . 24
  - 1.5.2 Dynamics Modeling With Focus on the Compound Pendulum Mode (OBJ2: Chapter 3) . . . 26
  - 1.5.3 Underactuated Linear and Nonlinear Control (OBJ3: Chapter 6) . . . 27
  - 1.5.4 Development of Tethered Formation Flying Testbed and Experimental Validation (OBJ4: Chapter 7) . . . 27
  - 1.5.5 Extension of Synchronization to Robot Cooperative Control and Formation Flying (OBJ5: Chapter 5) . . . 28
- 1.6 Literature Review . . . 29
  - 1.6.1 Dynamics of Spacecraft and Tethered Spacecraft . . . 29
  - 1.6.2 Previous Experimental Work on Tethered Satellite Formation Flight . . . 30
  - 1.6.3 Nonlinear Model Reduction . . . 30
  - 1.6.4 Networked Arrays and Coupled Dynamics . . . 31
  - 1.6.5 Synchronization of Dynamical Systems . . . 31
  - 1.6.6 Control of Underactuated Mechanical Systems . . . 32

2 Challenges of Nonlinear Dynamics and Control **35**
- 2.1 Chapter Objective . . . 35
- 2.2 Lagrangian Systems . . . 35
  - 2.2.1 Euler-Lagrangian Equations . . . 35
  - 2.2.2 Lagrangian on Riemannian Manifolds . . . 36
  - 2.2.3 Symmetry . . . 37
  - 2.2.4 Legendre Transformation and Hamiltonian . . . 38
  - 2.2.5 Zero Riemann Curvature and Flat Mechanical Systems . . . 39
  - 2.2.6 Nonholonomic Systems and Underactuated Dynamics . . . 40
  - 2.2.7 Passivity . . . 41
- 2.3 Examples of Nonlinear Dynamics . . . 42
  - 2.3.1 Two-Link Manipulator . . . 42
  - 2.3.2 Walking Robot: Compass-Gait . . . 44

2.3.3 Spherical Pendulum . . . 44
2.3.4 Robotic Arm on a Cart . . . 45
2.3.5 Attitude Dynamics of Rigid Spacecraft . . . 46
2.4 Previous Work on Nonlinear Stability . . . 48
2.4.1 Lyapunov-Based Method . . . 48
2.4.2 Extension of Lyapunov Function to Time-Varying Systems . . . 49
2.4.3 Exponential Stability [178, 92] . . . 50
2.5 Nonlinear Stability by Contraction Analysis . . . 50
2.5.1 Fundamentals . . . 51
2.5.2 Contraction of Combined and Coupled Systems . . . 54
2.5.3 Partial Contraction and Synchronization . . . 55
2.5.4 High-Order Contraction Theory . . . 56
2.5.5 Tracking Control of Robots and Aerospace Vehicles . . . 58
2.5.6 Tracking Control of Hamiltonian . . . 59
2.6 Review of Nonlinear Control Methods . . . 60
2.6.1 Linear Optimal Control . . . 60
2.6.2 Feedback Linearization and Inverse Dynamics . . . 60
2.6.3 Control Lyapunov Function . . . 61
2.6.4 Backstepping Design . . . 61
2.6.5 Robust Nonlinear Control . . . 62
2.6.6 Adaptive Nonlinear Control . . . 62
2.7 Concluding Remarks . . . 63

3 Dynamics of Tethered Formation Flight for NASA's SPECS Mission 65
3.1 Chapter Objective . . . 65
3.2 Reduction of 3D Dynamics to Planar Motion . . . 65
3.2.1 Three-Dimensional Attitude Dynamics . . . 65
3.3 Single-Tethered System with Ideal Tether . . . 67
3.3.1 Importance of Compound Pendulum Mode . . . 67
3.3.2 Assumptions . . . 67
3.3.3 Newton-Euler Formulation . . . 68
3.3.4 Euler-Lagrangian Formulation . . . 70
3.3.5 Nonlinear Phase Portrait and Relative Equilibria . . . 71
3.3.6 Linearization and Pendulum Mode Frequency . . . 71
3.3.7 Controllability Test . . . 73
3.3.8 Effect of Varying Tether Length . . . 74
3.4 Two-Spacecraft Dynamics . . . 76
3.5 Triangular Array and Multiple Circular Arrays . . . 79
3.6 Three Inline Configuration . . . 81
3.7 Flexible Tethers . . . 87
3.7.1 Dynamics Modeling . . . 87
3.8 Transverse Vibration of a Tether with Distributed Mass . . . 89
3.8.1 Dynamics Modeling . . . 89
3.8.2 Impedance Matching Control . . . 90

4 Nonlinear Model Reduction and Decentralized Control by Synchronization 93
4.1 Chapter Objective . . . 93
4.2 Dynamics Modeling and Contraction Theory . . . 93
4.2.1 Reduction of Two Spacecraft Dynamics . . . 94
4.3 Stability of a Decentralized Control Law . . . 95
4.3.1 Diagonalization of Linearized System . . . 95
4.3.2 Nonlinear Model Reduction by Contraction Theory . . . 97
4.4 Application to Nonlinear Robust Adaptive Control . . . 99
4.4.1 Decentralized Robust Sliding Control . . . 100

4.4.2 Decentralized Adaptive Control . . . 101
4.4.3 Decentralized Robust Adaptive Control . . . 103
4.5 Multiple Tether Arrays . . . 104
4.5.1 Spinning Triangular Array and Multiple Circular Arrays . . . 104
4.5.2 Three Inline Array . . . 105
4.6 Simulations . . . 108
4.6.1 Spin-Up Maneuver of Three Inline Spacecraft . . . 108
4.6.2 Simulation Results for Decentralized Nonlinear Adaptive Control . . . 108
4.7 Conclusion . . . 111

5 Cooperative Robot Control and Synchronization of Multiple Lagrangian Systems 113
5.1 Chapter Objective . . . 113
5.2 Introduction . . . 113
5.2.1 Organization . . . 115
5.3 Modeling of Multi-Robot Network . . . 115
5.4 A New Approach to Synchronization Tracking Control . . . 116
5.4.1 Proposed Synchronization Control Strategy . . . 116
5.4.2 Proof of Exponential Tracking . . . 119
5.5 Proof of Exponential Synchronization . . . 120
5.5.1 Challenges Associated with Nonlinear Inertia Matrix . . . 120
5.5.2 Existence of Flow-Invariant Submanifold . . . 121
5.5.3 Contraction with Two Time-Scales . . . 121
5.5.4 Generalization . . . 126
5.5.5 A Perspective on Model Reduction by Synchronization . . . 128
5.6 Extensions and Examples . . . 128
5.6.1 Synchronization of Non-Identical Robots . . . 128
5.6.2 Cooperative Control of Robot Manipulators . . . 129
5.6.3 Tracking Synchronization of Four Robots . . . 133
5.6.4 Synchronization of Multiple Formation Flying Spacecraft . . . 136
5.6.5 Synchronization with Uni-Directional Coupling . . . 136
5.6.6 Synchronization with Partial Degrees-of-Freedom Coupling . . . 137
5.7 Effects of Transmission Delays and External Disturbances . . . 139
5.7.1 Synchronization with Time Delays . . . 139
5.7.2 Effect of Bounded Disturbances . . . 140
5.8 Adaptive Synchronization . . . 141
5.9 PD Synchronization of Robots . . . 142
5.9.1 Velocity Coupling, $\mathbf{\Lambda} = 0$ . . . 143
5.10 Concurrent Synchronization . . . 143
5.11 Conclusions . . . 144

6 Nonlinear Control of Underactuated Tethered Systems 145
6.1 Chapter Objective . . . 145
6.2 Fundamentals of Underactuated Systems . . . 145
6.2.1 Challenges of Nonlinear Underactuated Systems . . . 146
6.2.2 Normal Forms for Underactuated Systems . . . 147
6.3 Gain-Scheduled LQR Approach . . . 148
6.4 Partial Feedback Linearization . . . 150
6.4.1 Collocated Linearization . . . 150
6.4.2 Analysis of Zero-Dynamics . . . 151
6.5 Momentum Decoupling and Feedback Linearization of Reduced Models . . . 151
6.6 Tracking Control by Backstepping and Contraction Analysis . . . 154
6.6.1 Review of Integrator Backstepping [100] . . . 154
6.6.2 Nonlinear Control by Backstepping . . . 154
6.7 Decentralized Control For Multi-Vehicle Systems . . . 156

6.8 Simulation Results . . . 158
6.8.1 Comparison with LQR Control . . . 158
6.8.2 Two-Spacecraft System . . . 158
6.8.3 Three-Spacecraft Inline Configuration . . . 159
6.9 New Momentum Dumping Method for Saturated Wheels . . . 163
6.10 Conclusions . . . 164

7 Testbed Development and Experimental Validation 167
7.1 Chapter Objective . . . 167
7.2 Tethered-SPHERES Testbed . . . 167
7.2.1 Overview of SPHERES Satellite . . . 167
7.2.2 Flight Quality Tether Reel with Force-Torque Sensor . . . 170
7.2.3 Tether Data Interface Module using FPGA . . . 173
7.3 Reaction Wheel Air-Carriage . . . 175
7.3.1 Sizing the Wheel Using Observation Strategies from SPECS . . . 176
7.3.2 Local Control of Reaction Wheel Motor . . . 178
7.4 Relative Sensing and Decentralized Estimation . . . 180
7.4.1 Rationale for Decentralized Relative Sensing . . . 180
7.4.2 Functional Requirements . . . 181
7.4.3 Previous Method using Ultrasonic Metrology System . . . 181
7.4.4 Problems with the Ultrasonic Measurement System . . . 183
7.4.5 New Bearing Angle Measurement Method . . . 184
7.5 Experimental Results . . . 186
7.5.1 Objective of Experimental Validation . . . 186
7.5.2 Validation of Dynamics Modeling and Estimator . . . 187
7.5.3 Overview of Control Experiments . . . 189
7.5.4 Decentralized Gain-Scheduled LQR Control . . . 190
7.5.5 Further Analyses . . . 193
7.5.6 Decentralized Nonlinear Control . . . 193
7.5.7 Decentralized Nonlinear Adaptive Control . . . 196
7.6 Conclusions . . . 197

8 Conclusions and Recommendations 199
8.1 Thesis Summary and Contributions . . . 199
8.2 Recommended Future Work . . . 201
8.2.1 Further Theoretical Work . . . 201
8.2.2 Suggested Improvements for Tethered SPHERES . . . 202

A Analytical Solution of Torsional Vibrations of Tapered Tether 203
A.1 Introduction . . . 203
A.2 Solution By Numerical Method . . . 203
A.3 Exact Analytical Solution . . . 205
A.3.1 General Solution of Differential Equation . . . 205
A.3.2 Eigenvalues by Boundary Value Problem . . . 206
A.4 Numerical Validation and Conclusion . . . 207

B Orbital Dynamics of Tethered Array 209

C Mathematica Codes 211
C.1 Involutivity Test for Section 6.2.1 . . . 211
C.2 Controllability Test . . . 212
C.2.1 Controllability Test for a Single Tethered Spacecraft . . . 212
C.2.2 Controllability Test for a Two-Spacecraft Array . . . 213
C.3 Diagonalization Transformation in Chapter 4 . . . 214

List of Figures

1-1 Motivation for Tethered Formation Flying. A Tethered Spacecraft Interferometer represents a good balance between a Separated Spacecraft Interferometer and a Structurally Connected Interferometer. 18
1-2 Deployment and operational maneuvers of tethered formation flight spacecraft. . . . 19
1-3 Rationale behind the decentralized control architecture 21
1-4 Outline of the dissertation. Tethered Formation Flight and Synchronization represent the two central themes of this dissertation. 24
1-5 Biological inspiration for synchronization control 25
1-6 Experiments using the SPHERES testbed at the NASA MSFC, September 2006. . . 28
1-7 Examples of robot cooperative control. The arrows indicate the coupling control law. 29

2-1 Two-link manipulator robot 42
2-2 Compass gait 43
2-3 Spherical pendulum 44
2-4 Two-link manipulator on a moving cart. Rotational angles are measured clockwise. . 45
2-5 Rigid spacecraft attitude representation. Picture courtesy: NASA JPL/Caltech . . . 47
2-6 Contraction of a volume 51
2-7 Exponential convergence to a single trajectory 52
2-8 Lorenz attractor 53

3-1 Decoupling of the in-plane rotational motions from the out-of-plane motions justifies our approach to reduce a 3-D attitude dynamics to a 2-D case. 66
3-2 Free-body diagram of a revolving tether problem 68
3-3 Phase portrait of (3.20). The dots indicate the relative equilibria. Units in rad (ϕ) and rad/s ($\dot{\phi}$). 72
3-4 Contour plots of the pendulum mode frequency. 73
3-5 Condition number of the controllability matrix for the tethered SPHERE. 74
3-6 Poles of ϕ with -0.5m/s $< \dot{\ell} <$ 0.5m/s, ℓ=1m, ω=0.3rad/s. 75
3-7 Free-body diagram of two tethered satellites. 76
3-8 Triangular Configuration. The ϕ angles are measured between the attachment of the pseudo-tether and the CM of each spacecraft. 79
3-9 Reduction of circular and star arrays of tethered spacecraft into multiple single-tethered systems 81
3-10 Free-body diagram with θ_1 and θ_2 defined as relative angles 82
3-11 Three-spacecraft array θ_1 and θ_2 defined from the center reference frame 84
3-12 Three inline configuration's mode shapes and natural frequencies. The rigid body mode is not shown. 86
3-13 Bode plot of the linear system for the input u_o to the output ψ, based on the linearized three-inline dynamics. A small amount of damping has been added to each joint angle. 87
3-14 Free-body diagram of single and two spacecraft systems with a flexible tether 88
3-15 Modeling of the transverse vibration 90
3-16 Two methods of stabilizing the tether transverse vibration 91

4-1 Synchronization of motions: human locomotion (bottom left), three tethered spacecraft (top), and Huygens's pendulum clock [17] (bottom right) 94
4-2 Poles of two tethered spacecraft and single spacecraft ($\dot{\ell} = 0$) with linear control. . . 97
4-3 Reduction of circular and star tethered arrays into multiple single-tethered systems . 106
4-4 Three-spacecraft array decoupled into three sub-systems. 107
4-5 Spin-up control of three-inline configuration 109
4-6 Spin-up control of two-spacecraft array using the decentralized adaptive control . . . 110

5-1 Possible applications of synchronization of multiple agents. 114
5-2 Multi-agent networks of identical or nonidentical robots using local couplings. They are on balanced bi-directional graphs. 117
5-3 A network of three identical (left) and non-identical (right) robots 118
5-4 Multiple timescales of synchronization (faster) and tracking (slower). The dashed line indicates the desired trajectory. Arrows indicate increasing time. 122
5-5 Examples of cooperative control. The arrows indicate the coupling control law . . . 129
5-6 Synchronization of two robots with **stable** tracking 131
5-7 Synchronization of two robots with **unstable** tracking 132
5-8 Synchronization of a four-robot network. The arrows indicate the coupling control law.133
5-9 Simulation results of the four-robot network 134
5-10 Four identical robots: time history of the states 135
5-11 Synchronization of a free-flying, uncoupled network of two spacecraft 136
5-12 One-way (uni-directional) coupling of identical robots 137
5-13 Two identical two-link robots with only one-joint coupling. The arrows indicate the coupling control law 137
5-14 Synchronization of two identical robots with partial joint coupling 138
5-15 Synchronization of two identical robots with transmission delays 139
5-16 Concurrent synchronization between two different groups. The desired trajectory inputs are denoted by the dashed-lines whereas the solid lines indicate mutual diffusive couplings. The independent leader sends the same desired trajectory input to the first network group. 143

6-1 Three representative cases of underactuated two-link mechanical systems 146
6-2 LQR gains scheduled for a range of $\dot{\theta}$ and ℓ 149
6-3 Plot of $\gamma(\phi)$ using ℓ=(0.3m, 0.6m, 0.9m) and the physical parameters Section 7.5.2 . 153
6-4 Two-spacecraft tethered system with a reaction wheel, depicted on the rotation plane. The ϕ_1 and ϕ_2 angles indicate the compound pendulum modes. 156
6-5 Nonlinear tracking control using the feedback linearization of the reduced variable (NLFL) in Section 6.5 and the LQR control 160
6-6 Nonlinear tracking control using backstepping (NLBS) in Section 6.6 and the LQR control 161
6-7 Simulation result of a decentralize control for Figure 6-4 162
6-8 Simulation result of a decentralize control for a three-inline configuration 162
6-9 Two-spacecraft tethered system equipped with a high-bandwidth linear actuator on the tether (P), a reaction wheel (u), and a tangential thruster (F, not shown) in each spacecraft. 163
6-10 Momentum dumping operation with stabilization 165

7-1 Three operational environments of SPHERES. ISS (a), KC 135 reduced-gravity flight (b), NASA MSFC flat floor (c,d) 168
7-2 SPHERES nano-satellites 169
7-3 A SPHERES satellite on the new air-bearing carriage with a reaction wheel and its block diagram of signal and data transfer. A schematic of the FPGA board is expanded in Figure 7-8 and the motor control loop is detailed in Figure 7-11. 170
7-4 Space flight version of tether reel mechanism, courtesy: Payload Systems 171

7-5 Exploded view of the tether guide, courtesy Payload Systems Incorporated. 172
7-6 Exploded view of the reel head, courtesy Payload Systems Incorporated. 172
7-7 FPGA avionics board and its key components with a tether reel mechanism removed (left), A side view of the SPHERES Expansion port face (right). The FPGA board sits between the tether reel mechanism and the expansion port. 173
7-8 Schematic of FPGA avionics board showing a flow of signals between different components. The gray blocks indicate the external hardware connected to the FPGA board. The power lines from the expansion port are omitted. The RWA controller contains a DAC smoothing filter 174
7-9 RWA motor controller and reaction wheel mounted on the air-carriage 176
7-10 Comparison of UV plots with the same initial velocities 177
7-11 Schematic of the control loop of the RWA servo 178
7-12 Performance of the reaction wheel motor controller 180
7-13 Two different methods for measuring bearing angle 181
7-14 New bearing angle ϕ metrology system using a Force-Torque sensor (ϕ in the negative direction). 184
7-15 Forces on the F/T sensor of the tether reel, where the z axis indicates the vertical direction to the tether spool in Figure 7-14 185
7-16 A spinning single-tethered SPHERES 187
7-17 Free-rotation of single-tethered system. Experiment and Simulation 188
7-18 Test configurations at NASA MSFC, September 2006. The two-body formation is shown in Figure 7-22. 189
7-19 Control of three-triangular array 190
7-20 State estimates and commands from SPHERE #1 during spin-up and deployment of the two-satellite tethered formation using gain-scheduled LQR 191
7-21 State estimates and commands from SPHERE #2 during spin-up and deployment of the two-satellite tethered formation using gain-scheduled LQR 192
7-22 Two-SPHERES spin-up maneuver 192
7-23 Gain-Scheduled LQR control on the MIT glass table 194
7-24 nonlinear controller with varying tether length in a two-body array, 1st SPHERES . 195
7-25 Nonlinear controller with varying tether length in a two-body array, 2nd SPHERES 196
7-26 Experimental result using the adaptive control on the single-tethered system 197

A-1 Linearly Tapered Torsional Rod Clamped at One End 204
A-2 First Four Mode Shapes of a=1 208

List of Tables

5.1 Physical parameters of the robots shown in Figures 5-5. 129
5.2 Physical parameters of the robots shown in Figures 5-8. 133
5.3 Physical parameters of the robots shown in Figures 5-8. 133

7.1 SPHERES Properties 169
7.2 Key components of the FPGA board and F/T Sensor 174
7.3 Physical and electrical parameters of the reaction wheel motor 179
7.4 Functional Requirements 181
7.5 Three approaches for measuring pendulum mode angle. AA filter denotes anti-aliasing filter. 183

A.1 Comparison of the natural frequencies 207

Chapter 1

Introduction

Simplicity is the ultimate sophistication.
-Leonardo da Vinci

1.1 Preface

The dynamics of tethered satellite formation flight tend to be very complex mostly due to their multidisciplinary nature and dimensionality. This dissertation seeks a systematic method of reducing the complexity in designing nonlinear control of multi-agent systems. In particular, we show that dynamical network systems like tethered formation flight or a swarm of robots can be synchronized within a cluster to achieve the same goal. Once synchronized, they look and behave as a whole. Simplicity is achieved without sacrificing efficiency.

Dissertation Keywords:

nonlinear control, tethered formation flight, space tethers, formation flying, nonlinear robust and adaptive control, decentralized nonlinear control, relative estimation, nonlinear model reduction, nonlinear stability theory, Lagrangian dynamics, multi-body rigid dynamics, underactuated mechanical systems, synchronization of dynamical systems, cooperative control, robotics, robot swarms, geometric control, backstepping, Kalman filtering, control experiments.

1.2 Motivation

NASA's SPECS (Submillimeter Probe of the Evolution of Cosmic Structure) mission [77, 118, 61] is proposed as a tethered formation flight interferometer that detects submillimeter-wavelength light from the early universe. In this dissertation, the inherent complexity and cross-coupling of the multi-vehicle dynamics is identified as one of the technological gaps to be bridged for the success of the SPECS mission. To deal with such difficulties associated with the multi-vehicle dynamics, this dissertation presents a new model reduction and decentralization strategy using synchronization. Additionally, we leverage the synchronization strategy for tethered formation flight towards other forms of dynamical networks such as multi-robot coordination and formation flying of aerospace vehicles.

1.2.1 Formation Flying in Space: Stellar Interferometry

The quest for unprecedented image resolution in astronomy inevitably leads to a huge aperture, since angular resolution is proportional to the wavelength divided by the telescope diameter (recall the Rayleigh criterion: $\theta_r = 1.22\lambda/D$ where θ_r, λ, D denote the angular resolution in radians, the wavelength of light, and the diameter of the aperture, respectively). The Hubble Space Telescope

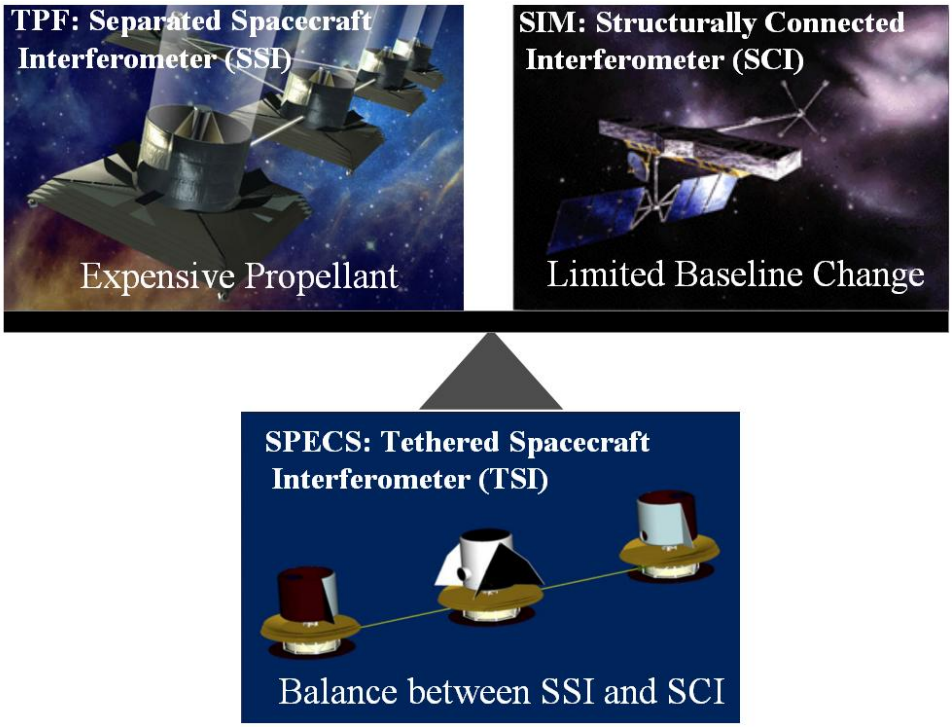

Figure 1-1: Motivation for Tethered Formation Flying. A Tethered Spacecraft Interferometer represents a good balance between a Separated Spacecraft Interferometer and a Structurally Connected Interferometer.

(HST) is currently the largest spaceborne observatory having a diameter of 2.4 m. Most current launch vehicles have fairing diameters between 3 and 5 meters, limiting the feasible size of a telescope aperture. SPECS aims at an angular resolution similar to that of HST, about 50 milliarcseconds. In the Far-Infrared/Submillimeter (FIR/SMM) wavelengths [123], this translates to a telescope diameter requirement on the order of 1 kilometer [118]. Such a telescope could not be launched fully deployed. In addition, the fabrication cost of a large monolithic aperture is prohibitively expensive according to Meinel's scaling laws of manufacturing costs [42]. To overcome these difficulties, stellar interferometry is currently being developed for space applications by NASA. Through interferometry, multiple apertures in a large formation combine light coherently to achieve a fine angular resolution comparable to a filled aperture. The current stellar interferometry missions include NASA's Terrestrial Planet Finder (TPF) mission (top left in Figure 1-1), and the Stellar Interferometry Mission (SIM) (top right, Figure 1-1).

1.2.2 Motivation for Tethered Formation Flight

The possible architectures of spaceborne interferometers include a Structurally Connected Interferometer (SCI), which allows for very limited baseline changes, and a Separated Spacecraft Interferometer (SSI) where the usage of propellant can be prohibitively expensive. A tethered spacecraft interferometer (TSI) represents a good balance between SCI and SSI (see Figure 1-1). The SPECS mission will use tethered formation flight to achieve its large baseline requirements. The kinds of stellar objects that will be observed will contain information at many spatial frequencies, thus the ability of interferometers to observe at multiple baselines will be key. Tethered formation flight enables interferometric baseline changes with minimal fuel consumption; without tethers, a massive amount of fuel would be required to power the thrusters to change the baseline, as in the SSI architecture. In addition, multi-directional force measurements can be used to determine the relative

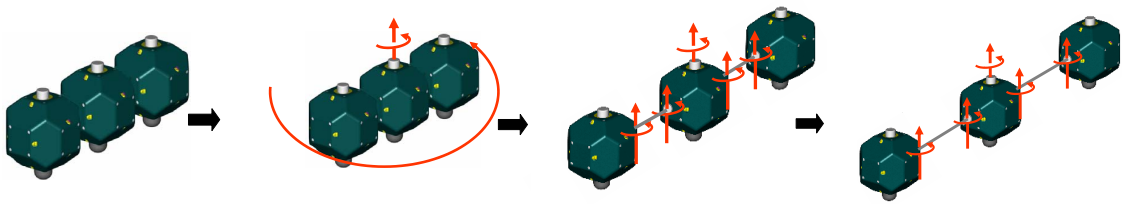

(a) Pre-launch configuration. Just released from the mother spacecraft.

(b) Initial spin-up.

(c) Tether deployment.

(d) Operation at various tether lengths.

Figure 1-2: Deployment and operational maneuvers of tethered formation flight spacecraft.

attitude (see the estimator design using a force-torque sensor in Chapter 7). The basic observational strategy can be easily achieved by reeling out the tethers and rotating the array in the plane of the tether. Compared to free-flying separated formation flight, tethered formation flight is a more efficient way to both know their relative positions and to control the spacecraft.

Overview of the SPECS mission

The current architecture anticipated for SPECS calls for a two-aperture Michelson interferometer [77]. The two 4-meter-diameter apertures and a beam combiner would be arranged in a line connected by two tethers, with the combiner in the center (see Figure 1-1). The tethers could be reeled in and out to achieve baselines between the two apertures of up to one kilometer. The telescope will observe light in the range between 40 and 640 μm, using cryogenically cooled detectors. By observing light at the FIR/SMM wavelengths, the SPECS mission aims to address questions about the synthesis of the first heavy elements, the formation of galaxies through the merger of smaller galaxies, and the dynamics of protostars and gaseous debris disks [77]. The proposed orbit for the observatory is at the Earth-Sun Lagrangian L2 point, which offers numerous advantages. For instance, this allows the tethered flight to be relatively undisturbed by gravity gradients avoiding significant wobbling of a spinning array. In addition, the L2 point provides a relatively unobstructed view of the sky and a lower thermal radiation background than a low-Earth orbit, which facilitates cryo-cooling. The basic observation scenario is to reel the tethers out or in gradually while rotating the array in a plane perpendicular to the target being observed. According to initial studies, each observation cycle performed in this way will take approximately twenty four hours to achieve full UV plane coverage [118]. Figure 1-2 illustrates a potential mission scenario of the deployment and retrieval operation. A completely docked, tethered-spacecraft array is released from a mother spaceship (see Figure 1-2(a)). The docked spacecraft are initially at zero speed, and spun to reach some target angular rate (see Figure 1-2(b)). Then, the tether is deployed at a pre-defined speed to meet the UV coverage requirement (see Figure 1-2(c,d)). Once a tethered array spun by reaction wheels reaches its maximum size, a momentum dumping method in Chapter 6 can be used to extend the size beyond this limit or the tether is retrieved to fill smaller spatial UV frequencies. Such a maneuver is experimentally validated in Section 7.5.4.

Several decisions are yet to be confirmed with respect to the SPECS architecture including the number of apertures and their configuration [77, 118]. At the time of writing, the leading option is to have two light collectors at the ends of a tether with a beam combiner in the middle (see Figure 1-1). Another option is to have three light collectors at the vertices of an equilateral-triangle and to have the beam combiner at some central location. Given an equilateral-triangular configuration, there is the question of whether to use counterweights to avoid unwanted spin-up when the tether length changes (e.g. the Tetra-Stat configuration [61]). The second open issue is the method of spacecraft attitude actuation in order to control the spin rate of the array as well as relative motions of each spacecraft. One proposal is to use electric thrusters [118]. This dissertation analyzes the potential of actuation for in-plane (aperture pupil plane) rotation with only reaction wheels. This would significantly save the mass required for fuel to control the rotation rate of the array. The third open

issue is the observation strategy. Given the basic goal of spiraling out and reaching some given level of UV plane coverage (i.e., more UV filling with smaller gaps in Modulation Transfer Function), there are several available strategies: constant angular momentum, constant angular velocity, and constant linear velocity operations. These observation strategies are detailed in Section 7.3.

1.2.3 Why Nonlinear Control?

Tethered formation flight spacecraft exhibit inherently coupled nonlinear dynamics. One simple intuitive approach to stabilize highly nonlinear systems is to apply linearization approximation around some nominal points, and schedule the linear control gains according to the slowly varying parameters. This so-called gain-scheduling [165] appears attractive since it permits the use of a wealth of mature linear control techniques to address nonlinear systems. However, only a local stability result can be assured under the assumption that the nonlinear system varies slowly around nominal points. In other words, linear control based on the linearization approximation is not guaranteed to work with a nonlinear system undergoing large dynamic changes. Tethered formation flying spacecraft are subject to large-angle maneuvers and are required to follow a desired trajectory precisely to achieve coherent interferometric beam combination.

Furthermore, coming up with a satisfactory controller schedule can consume far more human resources and efforts than a nonlinear control design. Even though classical linear methods such as pole-zero analysis, root-locus, and bode plots are not applicable to nonlinear systems, a wealth of nonlinear analysis and control design tools have been developed to justify the direct nonlinear approach, which takes advantage of inherent nonlinear dynamics.

This dissertation utilizes contraction theory and nonlinear control methodologies to derive exact global stability results for the nonlinear dynamics. Global stability, as opposed to local stability of linear control, indicates that the system tends to a desired equilibrium or trajectory regardless of initial conditions. Another motivation to justify the use of nonlinear control in lieu of a linear control framework has do with high-performance tracking. Simple linear control cannot be expected to handle the dynamic demands of efficiently following trajectories. Specifically, achieving exponential convergence ensures more effective tracking performance than asymptotic convergence by linear Proportional and Derivative (PD) control. In general, ensuring exponential stability for nonlinear systems is made possible only through nonlinear control.

1.2.4 Rationale Behind Decentralized Control Architecture

As stated earlier, the inherent complexity due to the nonlinearity, dimensionality and cross-coupling of tethered formation flight, is identified as one of the technological hurdles to be crossed for the success of the future tether missions. In order to deal with such difficulties related with the multi-body dynamics, we investigate the feasibility and practicality of decentralized control and estimation algorithms for the tethered system eliminating the need for satellite communications. *Decentralized* means that each control or estimation process must not involve exchange of information with adjacent satellites. *Relative* means that the measured quantity is formulated with respect to the local frame of the individual satellite. The decentralized controller along with the decentralized estimator will enable the simple independent control of each satellite by eliminating the need for exchanging individual state information. This will significantly simplify both the control algorithm and hardware implementation with a lesser degree of complication as well as eliminating a possibility of performance degradation due to noisy and delayed communications.

Figure 1-3 compares decentralized control with centralized control (see also the discussion in [63]). In the centralized architecture, the master satellite receives all the state information from the subordinate satellites and then sends the control inputs back to them. This has an advantage in that the subordinate cluster members do not require great computational capabilities for determining actuation commands. The central architecture requires intensive communication, and is expected to achieve the best performance if the communication links are perfect.

In reality, communication between members of a spacecraft formation may be limited for a variety of reasons. For example, [13] states as follows. *Various forms of interference, such as solar radiation*

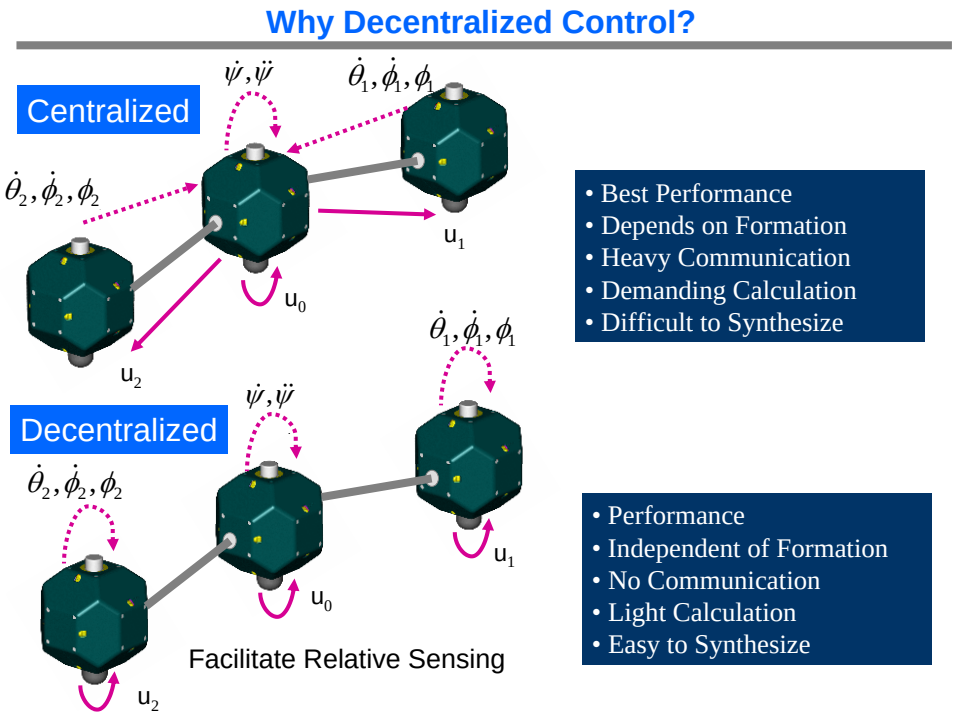

Figure 1-3: Rationale behind the decentralized control architecture

or RF interference from a satellite's thrusters, may cause errors in communication or prevent it altogether. Communication between satellites may also be delayed if channels normally used for such communication are being used for other purposes, such as exchange of command or scientific data with a ground station. Also, communication may be delayed if the data to be transmitted is temporarily unavailable. For example, if a satellite is thrusting it may not be able to acquire reliable measurement data. Another fatal flaw of a centralized control system is the following: if the central satellite malfunctions or stops operation, the whole formation could be lost resulting in a failure of the entire mission.

A decentralized control approach overcomes such drawbacks. In a separated formation flying architecture, a malfunctioning satellite can be replaced or discarded. The same logic can also be applied to tethered formation flight even though the configuration should be changed after the loss of one malfunctioning member. In addition, using decentralized control based on relative metrology means that the amount of communication required between spacecraft is reduced or eliminated. This reduced communication leads to reduced power and mass requirements for the overall system.

1.2.5 Motivation for Underactuated Tethered System

This dissertation also investigates the feasibility of controlling the array spin rate and relative attitude without thrusters. There are several advantages to the proposed underactuated control strategy. First, using reaction wheels instead of thrusters implies that power will be supplied via conversion of solar energy instead of carrying expensive propellant. We still envision using thrusters for out-of-plane motions (see Chapter 3), but the life span of the mission would be greatly increased by using reaction wheels for controlling the array spin-rate. Second, the optics will risk less contamination by exhaust from the thrusters. The main application of tethered formation flight is stellar interferometry, and optics contamination should be avoided by all means.

1.2.6 Criticality of Control Experiments

Any vision without implementation is irresponsible. This dissertation work has evolved based on the author's research philosophy: balancing theoretical excellence with practicality, aiming at physically intuitive algorithms that can be directly implemented in real systems. Miller [127] offers an interesting analog. The majority of Nobel laureates in physics are experimentalists. Any theory that could not be experimentally validated is rejected. The same principle should be applied to control theory. In [127], the following key areas are identified where control experimentation is crucial in the research and development cycle.

1. *Demonstration and Validation*: Demonstrating a research result on a physical system, in its operational environment, often provides the only acceptable information to a person who needs to make a go/no-go decision but who may not be fluent in the details of the technology.

2. *Repeatability and Reliability*: To develop the necessary heritage for critical applications, a control technology must demonstrate reliable and repeatable behavior in its interactions with other foreseeable subsystems. It must work more than once.

3. *Determination of Simulation Accuracy*: The results of control experiments can be compared with simulations, thereby providing credibility in control system simulation techniques and measuring the simulation accuracy.

4. *Identification of Performance Limitations*: Tests provide insights into, and prioritization of, the various physical constraints that limit a control system's performance.

5. *Operational Drivers*: Systems issues such as sensor-actuator resolution, saturation, nonlinearity, power consumption, roll-off dynamics, degradation, drift, and mounting techniques are most often constraints rather than design variables. Experiments uncover their inter-relations.

6. *Investigation of New Physical Phenomena*: New physical phenomena can be discovered and modeled through observation of physical systems (e.g. thermal snap as a disturbance source for a spacecraft)

In particular, the control engineer needs to address implementation and hardware issues such as A/D, D/A conversion, sampling rate, sensor noise, and computational load, which cannot easily be quantified in theory and simulation. Furthermore, developing a system testbed provides a critical opportunity to investigate interactions and relations among subsystems. For example, designing a space-based stellar interferometer, which requires tight tolerances on pointing and alignment for its apertures, presents unique multidisciplinary challenges in the areas of structural dynamics, controls, and active optics for multi-aperture phasing [42]. A control testbed provides an efficient means of examining multidisciplinary issues.

1.3 Problem statement

Many significant technical challenges must be overcome before the formation flying interferometer can be realized. For example, the tethered spacecraft architecture requires extensive technology development for precise attitude and position maintenance of formation flying spacecraft. None of these technologies are identified as insurmountable problems, but the largest area of technical risk for the stellar interferometer is in the operation of the various elements as a complete system [12]. The problem statements for this dissertation can be broken into the following categories.

1. **[PROB1]** In this thesis, the inherent nonlinearity and dimensionality of the multi-vehicle dynamics are identified as one of the technological bridges to be crossed for the success of the future Tethered Spacecraft Interferometer (TSI) missions.

2. **[PROB2]** TSI also presents its own challenges. It is expected that vibratory motion, consisting of compound pendulum modes of the satellite and tether vibration modes, will be observed,

affecting coherent interferometric beam combination. In addition, instability occurs when the tether retracts, which cannot be avoided due to the observation requirement (see the discussion in Section 1.2.2).

3. **[PROB3]** Accomplishing the goal of spiraling out and reaching some given level of UV plane coverage using traditional thrusters leads to prohibitively high propellant usage for the spin-up and attitude control of tethered spacecraft.

4. **[PROB4]** Because no previous space science mission has used a tethered formation flight architecture, many technological advances should be demonstrated. Control experimentation of tethered formation flight spacecraft is indispensable to validate control/estimation algorithms, to verify simulation results, and to capture un-modeled physical phenomena.

It should be noted that the control of tethered spacecraft will be responsible only for a fraction of the required precision. As a rule of thumb, controlling the locations of the apertures to within 10 cm is sufficient while the fine staged optical control [103] maintains the Optical Path-length Difference (OPD) between individual apertures within a tenth of the operating wavelength [42]. A longer wavelength of the FIR/SMM range makes SPECS even more technologically feasible– compare SPECS's wavelength range of 40-640 μm to 10-17 μm of the TPF-Interferometer (TPF-I) mission.

1.4 Goal and Objectives

In response to the problem statements described above, this dissertation focuses on the issues of nonlinear model reduction and decentralized control, on the actuation method, and on the demonstration of controlled tethered formation flight. In addition, the synchronization of multi-agent systems is explored. The main objectives are presented as the following.

1. **[OBJ1] Decentralized nonlinear control by model reduction**:
   develop decentralized control strategies that do not require centralized and absolute knowledge of each spacecraft's position and orientation. Relative metrology is utilized and each spacecraft is controlled independently using only the information about relative distance and attitude from the adjacent spacecraft. In particular, an emphasis is placed on nonlinear control, which takes full advantage of nonlinear dynamics. This objective directly addresses **[PROB1]**.

2. **[OBJ2] Modeling of attitude dynamics facilitating control law development**:
   develop and illuminate the dynamics modeling, and analyze stability and controllability issues, which facilitate the development of decentralized control and relative sensing. This objective is associated with **[PROB1]** and **[PROB2]**.

3. **[OBJ3] Exploiting tether-coupling to derive a fuel-efficient attitude control strategy**:
   demonstrate that an array of tethered spacecraft can be controlled with only reaction wheels for actuating array spin rate and relative attitude between satellites. This objective presents a solution to **[PROB3]**.

4. **[OBJ4] Development of a tethered satellite formation flight testbed**:
   experimentally implement and validate the proposed decentralized control and estimation strategies. In addition, conduct closed-loop control experiments which permit the verification of a system-level integration of the subsystems including actuators, sensors and control algorithms. This objective directly responds to **[PROB4]** by providing an experimental research platform.

5. **[OBJ5] Unified treatment of synchronization for multiple dynamical networks**:
   leverage the synchronization strategy for tethered formation flight towards dynamical networks consisting of highly nonlinear systems; establish a unified synchronization framework, which can be utilized for cooperative control of multi-robot systems or formation flight aerospace vehicles.

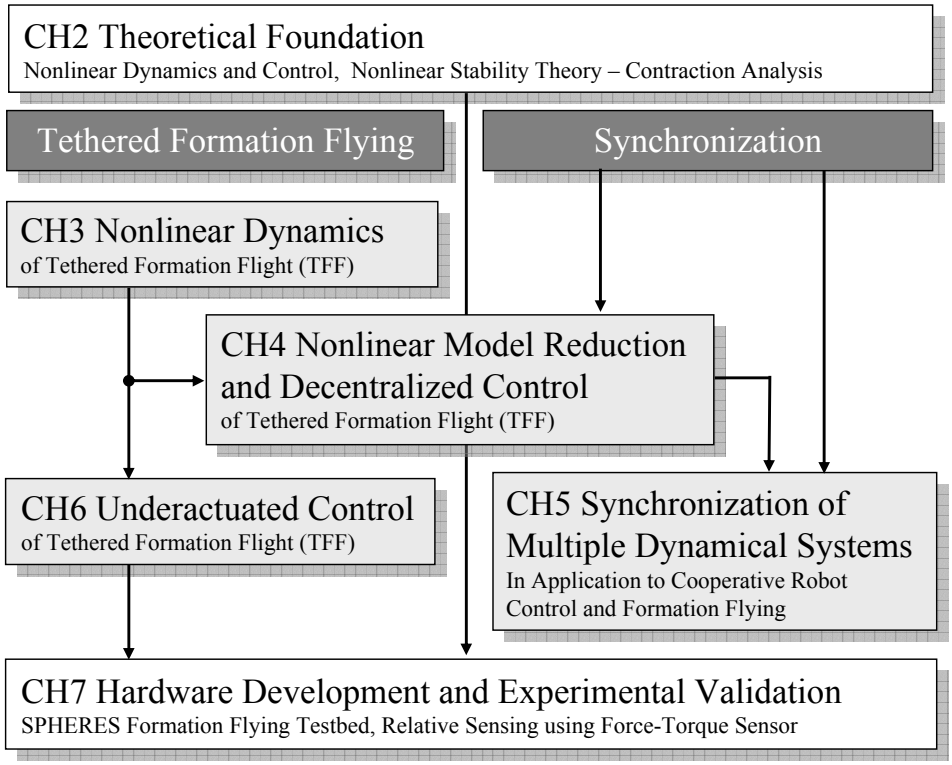

Figure 1-4: Outline of the dissertation. Tethered Formation Flight and Synchronization represent the two central themes of this dissertation.

The following section summarizes the unique contributions of this dissertation, which directly accomplish the above objectives.

1.5 Research Approach and Contributions

The outline of the dissertation is illustrated in Figure 1-4. Dynamics and control of tethered formation flight and synchronization of multi-agent systems represent the two central themes of this thesis. Specifically, the following unique contributions are identified, and expanded in order of the corresponding objectives from Section 1.4. Namely, nonlinear decentralized control using oscillation synchronization (Chapter 4); modeling of relative attitude dynamics with focus on the compound pendulum mode (Chapter 3); underactuated control of tethered formation flight (Chapter 6); experimental validation of tethered formation flying maneuvers, and development of a relative sensing mechanism using a force-torque sensor (Chapter 7); and nonlinear tracking control framework for synchronization of Lagrangian systems (Chapter 5).

1.5.1 Nonlinear Model Reduction and Decentralized Control by Synchronization (OBJ1: Chapter 4)

Control of distributed and multi-agent mechanical systems such as formation flying spacecraft has become a popular area of research, where distributed computation and decentralized control schemes, as well as information flows between elements, are explored. In spite of the popularity of these modular architectures, it is rare to find work on modular stability analysis for such systems exhibiting coupled dynamics.

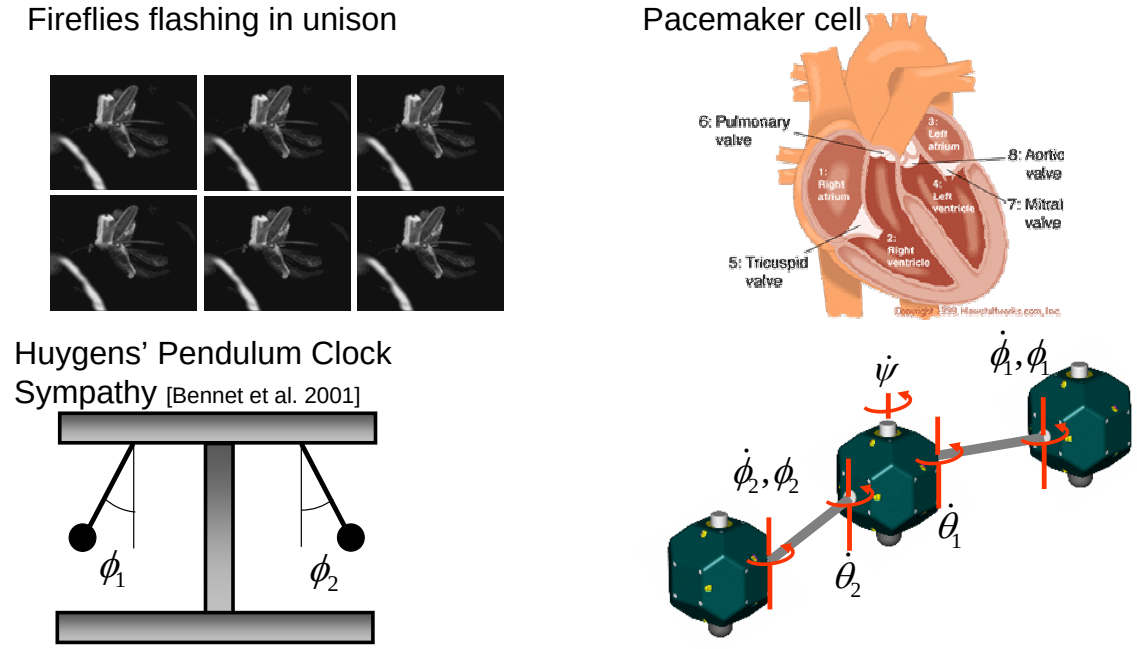

Figure 1-5: Biological inspiration for synchronization control

This dissertation introduces a fully decentralized nonlinear control law for spinning tethered formation flight spacecraft, based on exploiting geometric symmetries to reduce the original nonlinear dynamics into simpler stable dynamics. Motivated by oscillation synchronization in biological systems, we use contraction theory to prove that a control law stabilizing a single-tethered spacecraft can also stabilize arbitrarily large circular arrays of spacecraft, as well as a three inline configuration. The proposed decentralized control strategy is also applied to robust sliding control and nonlinear adaptive control to account for model uncertainties.

Biological and Physical Inspiration

In dealing with such coupled dynamics, an attempt is made to learn from distributed computation in biological systems. Figure 1-5 shows synchronous fireflies flashing in perfect unison. The fireflies found in the Great Smoky Mountains of Tennessee send out five to eight flashes in unison, stop for a quarter of a minute, and then repeat. No matter when and where they start, they end up flashing in sync by adjusting their internal clock in response to other fireflies' flashing. In the context of control theory, the convergence of synchronous fireflies is independent of initial conditions (global stability), and the internal clock mechanism corresponds to diffusive coupling. In this dissertation, contraction theory yielding exponential and global convergence is exploited. There is no apparent leader in the synchronous fireflies, which is by far more a robust design than centralized control. The motivation of synchronous fireflies also sheds light on the objective of cooperative control: by flashing in synchrony, the males create a brighter light that has a better chance of getting the female's attention. Even though they are eventually in competition, they cooperate to accomplish the common goal. Other examples abound. Any biological object, specifically the brain, is the result of evolution, and evolution proceeds by accumulation and combination of stable intermediate

states [176]. The heart's pacemaker shown in Figure 1-5 is also a marvel of evolution, perhaps the most impressive oscillator ever created: a cluster of about 10,000 cardiac pacemaker cells is synchronized to set the pace [191].

This dissertation introduces reduction of the original dynamics by oscillation synchronization, as observed in the Huygens' clocks [191, 17] in Figure 1-5. The pendulum clocks in Figure 1-5 swung with exactly the same frequency and 180 degrees out of phase, regardless of the initial conditions. When the pendulums were perturbed, the anti-phase state was restored within half an hour and persisted indefinitely. As Huygens surmised, the study in [17] shows that damping effects of the pendulum platform favor anti-phase motion, since in-phase oscillations induce additional counter-motion of the frame. And while the clock escapements can transfer energy into the in-phase mode, it is never enough to overcome this frictional disadvantage [17]. Similarly, we pay particular attention to oscillations of the compound pendulum mode of tethered satellite formation flight. In Chapter 4, the center satellite of a three inline configuration in Figure 1-5 is shown to play a crucial role, similarly to the common platform of the pendulum clock, in inducing stabilization and synchronization of the satellites.

Modular Stability Analysis By Contraction Theory

In control theory, Popov's passivity [178] was originally motivated by similar concerns. However, combinations and accumulations of stable elements do not necessarily result in stable dynamics [176]. This dissertation uses contraction theory [176, 112, 202, 114] to analyze the nonlinear stability of a decentralized control of tethered satellite formation flight (Chapter 4), and also to establish a unified synchronization framework (Chapter 5). Contraction theory, introduced in Chapter 2, takes a slightly different notion of stability– a system is stable in some region if initial conditions or temporary disturbances are somehow forgotten [112]. Lyapunov's linearization method indicates that the local stability of the nonlinear system can be analyzed using its differential approximation. What is new in contraction theory is that a differential stability analysis can be made exact, thereby yielding **global and exponential convergence** results in nonlinear systems. Contraction theory provides a systematic method to build arbitrarily complex nonlinear systems (e.g. a tethered formation array) out of simpler elements (e.g. a single-tethered spacecraft). Combinations validated by contraction theory, such as hierarchical combinations, parallel combinations, and synchronized coupled oscillations, are explored to simplify the nonlinear dynamics of multiple dynamical systems.

Decentralized Nonlinear Control and Estimation

This dissertation proposes reduction of the original dynamics by oscillation synchronization. Our approach to nonlinear model reduction is unique in the sense that we use oscillation synchronization to simplify the coupled dynamics into the simplest form for which combined stability can be analyzed systematically. The importance of this approach lies in the fact that we can employ a fully decentralized control law (or estimation algorithm) from the reduced single-tether system to control a more complex multiple-spacecraft array, reducing the complexity of both hardware and software. The decentralized controller will enable simple independent control of each satellite without the need for exchanging individual state information. This will significantly simplify both the control algorithm and hardware implementation as well as eliminating the possibility of performance degradation due to noisy and delayed communications.

1.5.2 Dynamics Modeling With Focus on the Compound Pendulum Mode (OBJ2: Chapter 3)

The dynamics modeling using the Euler-Lagrangian formulation is preferred throughout the entire thesis due to its simplicity. For example, we show that the dynamics of a two-link manipulator robot can be reduced to the dynamics of a single-tethered spinning satellite. This single-tethered system is used to construct a more complex array consisting of multiple spacecraft. One benefit of this simplified modeling is that it readily offers many engineering insights. For example, the positive definite inertia matrix and symmetry play a critical role in the stability analysis and control synthesis

in this dissertation. Such work cannot easily be conducted using the general N-body formulation of multi-body tethered systems (e.g. [90, 144]).

We pay particular attention to control of oscillations of the compound pendulum mode of tethered formation flight satellites. Previously, the instability of the tether retrieval was usually discussed in the context of two spacecraft connected by a single tether [101]. The representative work on tethered formation flight [55, 94, 26, 27, 132, 144] does not include the compound pendulum mode, by assuming that the spacecraft can be regarded as a point mass with a long tether. However, it is indispensable to examine this mode because of the instability occurring while retracting the tether in spinning arrays.

Chapter 3 introduces the dynamics equations of planar motion of the tethered formation flying spacecraft considered in the entire thesis. The rationale behind the reduced dynamics modeling on the two-dimensional plane is that the symmetry of a spinning array can be exploited to decouple the in-plane rotational motions (aperture pupil plane) from the out-of-plane motions. In particular, the stability and controllability analyses, in conjunction with the compound pendulum modes of the tethered arrays, constitute the main contributions of this chapter. In addition, the dynamics modeling in this chapter facilitates nonlinear spatial decoupling of multiple-spacecraft coupled arrays; the dynamics modeling in this thesis permits a relative and decentralized sensing mechanism for deep space formation flight. In deep space, absolute attitude might be available via star-trackers but the availability of absolute positions, like those provided by the Global Positioning System (GPS), is very limited.

1.5.3 Underactuated Linear and Nonlinear Control (OBJ3: Chapter 6)

The previous chapters are based upon the assumption that the tethered system is fully actuated. Motivated by the controllability analysis in Chapter 3, indicating that both array resizing and spin-up are fully controllable by the reaction wheels and the tether motor, the aim of Chapter 6 is to introduce some new nonlinear control techniques for spinning tethered arrays without thrusters. To our knowledge, this work reports the first propellant-free underactuated control results for tethered formation flying spacecraft, and fulfills the potential of the proposed strategy by providing a new momentum dumping method for saturated wheels without relying on torque-generating thrusters. For satellites in orbit, a pair of thrusters is conventionally used to dump the angular momentum of the saturated momentum wheel. The proposed new method deals with the issue of maintaining the zero compound pendulum mode and desired array spin-rate during the momentum dumping operation without relying on torque-generating thrusters. Maintaining the zero compound pendulum mode without diagonal thrusters poses a challenge since the reaction wheel, which directly controls the pendulum mode, is decelerated continuously in one direction. In the proposed method, all relevant degrees of freedom are stabilized using only the linear thruster and translational actuator on the tether during the momentum dumping operation.

Such a tethered spacecraft array without thrusters is called an *underactuated* mechanical system since it has fewer inputs than configuration variables. In contrast with linear systems in which an underactuated control law can be synthesized easily, designing a nonlinear controller for nonlinear underactuated systems poses a challenge, mainly due to lack of full state feedback linearizability. We exploit gain-scheduling linear control (Section 6.3), partial feedback linearization (Section 6.4), feedback linearization via momentum decoupling (Section 6.5), and backstepping (Section 6.6). We shall consider only the case of the fixed tether length, focusing on the spin-up attitude control problem on the assumption that the tether length is controllable separately.

1.5.4 Development of Tethered Formation Flying Testbed and Experimental Validation (OBJ4: Chapter 7)

This dissertation elucidates the hardware experiments that were carried out to validate the effectiveness of the decentralized nonlinear control framework introduced in Chapter 4 for spinning tethered formation flying arrays. The experiments also evaluate the performance of the proposed decentralized and relative estimator. Specifically, we are using the SPHERES (Synchronize Position Hold

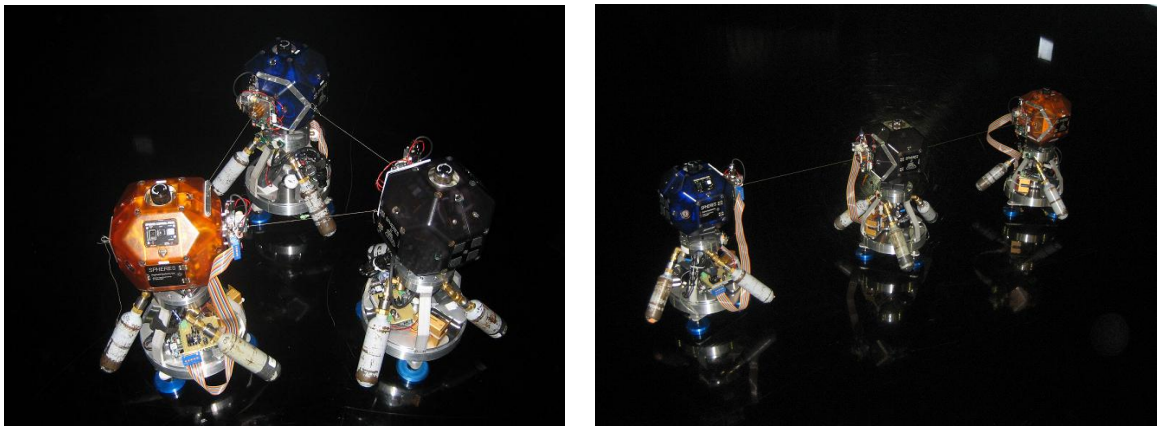

(a) Three triangular configuration

(b) Three-inline configuration

Figure 1-6: Experiments using the SPHERES testbed at the NASA MSFC, September 2006.

Engage and Reorient Experimental Satellite) formation flight testbed to perform experiments in controlling tethered spacecraft arrays. An operational mode representative of real-world spacecraft like SPHERES permits the verification of a system-level integration of various subsystems. A new suite of hardware has been designed and added to the SPHERES testbed to support tethered formation flight. Such recent improvements to SPHERES include a new tether reel mechanism, a force-torque sensor, and an air-bearing carriage with a reaction wheel. This dissertation also introduces a novel decentralized estimator, in which a series of Extended Kalman filters incorporate the gyro, force-torque sensor and ultrasound ranging measurements. To our knowledge, the experiments performed at NASA MSFC (see Figure 1-6) are the first experimental validation of tethered satellite formation flight using

- Nonlinear/linear decentralized control and estimation.
- Control of three-satellite-inline configuration.
- Development of force sensor-based attitude estimator using a series of Kalman filters.
- Reaction-wheel-only attitude control for all configurations (two-inline, three-inline, three-triangular).
- Decentralized fault-tolerant adaptive control under sensor failures.

1.5.5 Extension of Synchronization to Robot Cooperative Control and Formation Flying (OBJ5: Chapter 5)

The main application of this dissertation is tethered formation flight, which exhibits inherent nonlinear couplings between spacecraft due to the physical connections of the tethers. In particular, Chapter 4 presents a novel decentralized control strategy, by oscillation synchronization, which eliminates the need for any inter-satellite communications. Beyond this, we extend a synchronization framework to inherently physically *uncoupled* multi-agent systems (see Figure 1-7). In other words, we construct a network of multiple dynamical systems by adding communication couplings to otherwise freely moving or flying vehicles. It should be noted that the global exponential convergence of contraction analysis plays a central role in treating the synchronization of multiple nonlinear dynamics. An exponentially stabilizing nonlinear control law that can synchronize an arbitrary number of robots into a common trajectory is introduced in Chapter 5. In this dissertation, synchronization is defined as a complete match of all configuration variables of each dynamical systems such that $\mathbf{x}_1 = \mathbf{x}_2 = \cdots = \mathbf{x}_p$ and p denotes the number of sub-systems in the network. The proposed controller is much simpler than earlier work, such as the synchronization law in [164], in terms of both

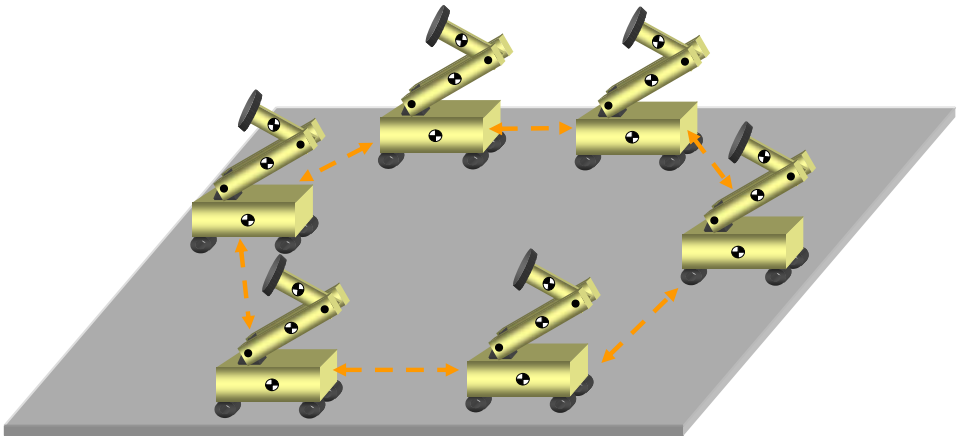

Figure 1-7: Examples of robot cooperative control. The arrows indicate the coupling control law.

the computational load and the required signals. In addition, the convergence result is stronger: global and exponential.

The main contributions of Chapter 5 can be stated as follows. First, the proposed strategy is developed for general nonlinear dynamics derived from the Lagrangian formulation whereas prior work consensus problems on graphs are mainly restricted to simple linear dynamics [146]. As shall be seen in Chapter 5, the proof of synchronization for linear systems is a lot simpler than that of nonlinear systems. In addition, the proposed control laws are of a decentralized form requiring only local velocity/position coupling feedback for global exponential convergence, thereby facilitating implementation in real systems. As opposed to some previous work requiring all-to-all coupling [164], this will significantly reduce communication burdens. The theory is generalized and extended to multi-robot systems with partial joint coupling and uni-directional coupling. Since the main nonlinear stability tool is contraction analysis [112, 176, 202], we derive exact and global results with exponential convergence. Discussions on time-delayed communications and external disturbances are provided to emphasize the robust properties of the proposed control law.

1.6 Literature Review

Since Chapter 2 lays a foundation for the dynamics modeling, the main stability theorems (contraction analysis) and the nonlinear control techniques used in the entire thesis, such topics are not expanded here. We refer the readers to Chapter 2 and the references therein for further details.

1.6.1 Dynamics of Spacecraft and Tethered Spacecraft

Three dimensional attitude control problems for a class of rigid spacecraft have gained considerable attention, in particular, in the context of adaptive control [60, 177], rigid body dynamics [208, 207], and geometric control theory [53, 24, 166]. Prior work on multiple free-flying spacecraft can be found in [201, 104, 195, 126, 182] and the references therein. Of particular interest is work on electromagnetic formation flight [2]. There are numerous technical papers on the dynamics of tethers in space [14, 97, 96]. Some papers discuss the elasticity and vibration of tethers [97, 68]. A mass-distributed tether is described by a system of partial differential equations [213]. Compared to the early literature focused on the two-body dynamics for tether retrieval and momentum exchange purposes (see the review paper [133]), recent research efforts investigate the dynamics of a three-body inline configuration [26, 132] and a triangular configuration [55, 102, 94, 138, 144, 196, 160]. A counterweight can be added to produce a more-slowly varying angular speed (e.g. Tetra-Star configuration [61]). A recent study [27] investigated the feasibility of spinning tethered formation

flight of constant angular momentum for space-based interferometry applications in an Earth trailing, heliocentric orbit. The general N-body formulation of multi-body tethered systems is found in [90]. The coupling of tether lateral vibration and satellite attitude motions is discussed in [18]. A nonlinear control method is proposed to stabilize the librational motion of a tethered satellite [96]. The study in [209] proposes utilizing the distributed Lorentz forces in an electromagnetic tether as a control actuator for the tether motion. An active control of the transverse vibration of the tether using impedance matching [128, 129, 130] is discussed in [68, 69]. Another impedance matching strategy using an electromagnetic damper is being considered for SPECS [118]. In [211], the dynamics of a wheel-spoke configuration, in the vicinity of the L2 Lagrangian point of the Earth-Sun system, is examined. More literature can be found in a very recent review paper on non-electrodynamic tethered satellite systems [101]. Some recent papers investigated dynamics and control of tethered formation flying, particularly tailored towards the SPECS mission [156, 61, 77, 107, 118, 94].

This dissertation introduces reduction of the original dynamics by oscillation synchronization, as observed in the Huygens' pendulum clocks [191, 17]. The pendulum clocks in Figure 4-1 swung with exactly the same frequency and 180 degrees out of phase, regardless of the initial conditions. Similarly, we systematically attempt to synchronize oscillations of the compound pendulum mode of tethered satellite formation flight. The representative work on tethered formation flight [94, 26, 27, 132, 144, 196] does not include this mode, by assuming that the spacecraft can be regarded as a point mass with a longer tether. However, it is indispensable to examine this mode because of the instability occurring while retracting the tether for spinning arrays.

1.6.2 Previous Experimental Work on Tethered Satellite Formation Flight

Several space missions have already been flown to verify Tethered Satellite Systems (TSS). These important milestones include NASA and Italian Space Agency's retrival of tether in space (TSS-1 in 1992, TSS-1R in 1996); NASA's Small Expendable Deployer System (SEDS-1 in 1993, SEDS-2 in 1994); and the U.S. Naval Research Laboratory's tether physics and survivability (TiPS in 1996). Descriptions of these missions are found in [49]. The recent review paper [101] also introduces some ground-based experimental results of the out-of-plane libration control scheme with the equivalent tension control law with tether length and length rate as feedback [75], and active control of the in-plane pendulum oscillations and tether bobbling of the TSS by boom rotation [15].

To our knowledge, there exist only three closed-loop control experiments on tethered formation flight: work done by the Stanford University Aerospace Robotics Laboratory [210, 167, 95], the three-spacecraft simulator by the Japanese group [138, 139], and the SPHERES testbed introduced in this dissertation. A notable previous experiment using two-inline satellites is done by [210]. The experimental hardware consists of two spacecraft modules that float on gas bearings on a granite table. A potentiometer was employed to measure the relative angles between the spacecraft (see Chapter 7 for the comparison with the force/torque sensor used in the present dissertation). A recent paper also describes the tethered-satellites testbed with a triangular configuration [138]. The satellites in [138] rely on a global metrology system using the CCD camera overlooking the array. The Synchronized Position Hold Engage and Reorient Experimental Satellites (SPHERES) testbed, presented in this dissertation, is the first satellite testbed fully exploiting the dynamics of tethered satellites under various formation flight configurations including a two-inline, a three-inline and a triangular configuration. It is also a fully 3-D operational satellite with sophisticated sensors and actuators permitting replication of an operational mode representative of real world spacecraft. In other words, it could control in 3-D.

1.6.3 Nonlinear Model Reduction

The model reduction theory for linear systems is very mature and rich (e.g. the balanced realization model reduction algorithm [216, 217]). In contrast, a unified theory of model reduction for nonlinear systems is relatively rare. Model reduction means a procedure to reduce control design for the original system to control of a lower-order system with minimum loss of fidelity [145]. Popov's passivity [178] was originally motivated by similar concerns. The center manifold theorem [200, 172] offers a rigorous

mathematical formulation to reduce the dimensionality of the nonlinear systems whose linearized dynamics have zero eigenvalues. On the other hand, the singular perturbation theory [92] can be viewed as an approximate model reduction method, which analyzes the responses of the two different time scales separately. Nonlinear model reduction theory using controlled Lagrangians (or Hamiltonians) is an area of intense research, especially in the sense of geometric control theory [37, 35]. The study in [33, 34] introduces kinematic reductions for mechanical systems and studies their controllability properties. In [145], the kinetic symmetry is exploited as a means of reducing the complexity of control of high-order underactuated mechanical systems.

We seek various forms of model reduction techniques in this thesis. For example, we exploit spatial symmetry to decouple the attitude dynamics of the tethered array (see Section 3.2.1) and also to reduce the coupled nonlinear dynamics of the tethered array to the singled-tethered spacecraft (see Chapter 4). Spatial reduction of linear systems with input-output symmetry can be traced back to the use of circulant matrices [131]. This dissertation's approach to nonlinear model reduction is unique in the sense that oscillation synchronization is used to simplify the coupled dynamics into the simplest form that still permits combined stability to be analyzed systematically. The kinetic symmetry is also exploited for control of underactuated tethered systems (see Chapter 6).

1.6.4 Networked Arrays and Coupled Dynamics

Networked arrays of coupled dynamics abound in biological systems. For example, the motion control architecture in vertebrates involves combinations of simple motor primitives [20, 19, 91], and synchronous fireflies [191] and animal gaits [48, 91] might shed some light on the stability of coupled arrays. Some recent work on multi-agent robots [86], aircraft formation flight [173, 63], and robotics [99], also deal with coupled oscillations. In control theory, Popov's passivity [178] was originally motivated by similar concerns. However, combinations and accumulations of stable elements do not necessarily result in stable dynamics [176]. This dissertation uses contraction theory [112, 176, 202, 114, 180] to analyze the nonlinear stability of a decentralized control of tethered satellite formation flight. Contraction theory provides a systematic method to build arbitrarily complex systems (e.g. a tethered formation array) out of simpler elements (e.g. a single-tethered spacecraft). Combinations validated by contraction theory, such as hierarchical combinations and synchronized coupled oscillations, are explored to simplify the nonlinear dynamics of multiple tethered spacecraft.

1.6.5 Synchronization of Dynamical Systems

Distributed and decentralized synchronization phenomena are the subjects of intense research. Group synchronization and cooperative control are topics that are currently receiving a lot of interest in a variety of research communities, including biology [73, 70], artificial intelligence [7, 30] and neuroscience [54, 91], robotics [62, 164, 85], communications and sensor networks [146, 175], spacecraft formation flight [45, 201, 195, 126, 182], ship replenishment [28] and formation control [84], automatic control of multiple mobile robots [86, 111, 147] and distributed systems [8, 115]. Other potential applications of synchronization include oscillation synchronization of robotic locomotion [85, 154], and tele-manipulation of robots [143, 81, 4, 105, 40].

The consensus problems on graph [146] and the coordination of multi-agent systems [86, 111, 147, 148] are closely related with the synchronization problem. In particular, the use of graph theory and Laplacian yielded many interesting results [106, 86, 111, 126, 146]. The main drawback of the aforementioned work is that they mainly deal with very simple dynamic models such as linear systems and single or double-integrator models with a constant inertia (mass) matrix. Hence, much of earlier work on multi-agent coordination cannot be used for highly nonlinear systems (e.g. helicopters, attitude dynamics of spacecraft, walking robots and manipulator robots). As shall be seen in Chapter 5, the proof of the synchronization for network systems that possess a nonlinear inertia matrix is much more involved and difficult. This dissertation focuses on such issues associated with nonlinear dynamics.

One recent representative work on synchronization of multi-link robots with highly nonlinear

dynamics is [164]. This study proposes a nonlinear tracking control law to synchronize multiple robots to track a common desired trajectory. The following difficulties of [164] can be identified. The number of variables to be estimated increases with the number of robots to be synchronized, which imposes a significant communication burden. Thus, a method to eliminate the all-to-all coupling is explored in Chapter 5. Finally, the feedback of estimated acceleration errors requires unnecessary information and complexity. In another example, [193] studied the synchronization of mechanical networks consisting of underactuated dynamics using the controlled Lagrangians.

Another notable approach to synchronization of robot networks is to exploit the passivity of the input-output dynamics [105, 40]. Its property of robustness to time-delays is particularly attractive. However, robot dynamics are passive only with velocity outputs unless composite variables are employed. In addition, the mutual synchronization problem, which not only synchronizes the submembers but also enforces them to follow a stable desired trajectory, is not addressed. Another recent work using the passive decomposition [104, 106] is interesting in the sense that it shares the same philosophy of the mutual synchronization problem as in [164]. The passive decomposition describes a strategy of decoupling into two dynamics: the same system representing the internal group formation shape, and the locked system describing the total group maneuver. One drawback of [104] is its dependency on a centralized control architecture; the decoupling is not generally ensured under the decentralized control. Additionally, [106] only considers a linear double integrator model, which can degenerate into a trivial problem. The approach introduced in this dissertation has a clear advantage in its broad applications to a larger class of identical or nonidentical nonlinear systems. The proposed approach is even able to deal with time-delays, non-passive input-output, and complex coupling geometry including uni-directional coupling and partial degrees-of-freedom coupling, while ensuring a simple decentralized coupling control law.

1.6.6 Control of Underactuated Mechanical Systems

Underactuated mechanical systems are characterized by fewer actuators than degrees of freedom (DOF) or configuration variables, and encountered in a wide range of applications such as walking robots [194, 206], aerospace vehicles [67, 145], and nonholonomic systems [22]. Control of underactuated mechanical systems is an active area of research [22, 35, 145, 161]. In particular, Spong [187] developed the partial feedback linearization technique for the swing up maneuver of the acrobot. One drawback of the partial feedback linearization method is that it does not automatically guarantee stable zero dynamics after applying the change of control. The zero dynamics is defined to be the internal dynamics of the system when the system output is kept at zero by the input [178]. By analogy with linear systems, a nonlinear system with the stable zero dynamics corresponds to a minimum phase system. Olfati-Saber [145] developed cascade normal forms for underactuated mechanical systems, based upon mechanical symmetry. Normal forms can be further classified into triangular normal forms and nontriangular forms. Both strict-feedback and strict-feedforward systems are called "triangular" by analogy with linear systems. In particular, a strict-feedback system permits a systematic nonlinear control design called backstepping [100]. In addition, recent work examines the sliding-mode control [205], intelligent control [31], and hybrid switching control [214] for underactuated nonlinear systems. In the context of geometric control theory, two energy-based methods can be considered for underactuated nonlinear systems. First, an oscillatory control based on averaging [22, 35] can be developed, which requires a high-frequency control input. The second geometric control approach is the method of controlled Lagrangians via the so-called matching process [22]. In essence, the control design involves shaping the system's total or kinetic energy with the additional parameters and the matching process. One recent work also combines techniques of potential shaping with those of kinetic shaping [23]. One drawback is that generic physical damping makes the control-modified energy rate indefinite, thus invalidating the nonlinear stability argument of the controlled Lagrangian method [212]. In some cases, a linear control law using gain-scheduling can be designed. One merit of the linearization is that it permits the use of mature and well-established linear control techniques to address nonlinear problems. However, stability can be assured only locally and in a "slow-variation" setting [165]. In [124], an alternative method to gain-scheduling is presented for control of nonlinear systems.

Control of underactuated spacecraft has also been a popular subject. Of particular interest is work by Tsiotras [197, 198, 199] showing that a nonsmooth time-invariant feedback control law can be used to rotate an axis-symmetric rigid spacecraft to the zero equilibrium using only two control torques.

Most aforementioned work is restricted to a single-body dynamics problem. In Chapter 6, the decentralized control strategy from Chapter 4 is extended to the underactuated control of multi-vehicle tethered formation flying. To our knowledge, this work presents the first nonlinear underactuated control results of tethered formation flying systems.

Chapter 2

Challenges of Nonlinear Dynamics and Control

2.1 Chapter Objective

This chapter elucidates some principal nonlinear dynamics analysis tools and control strategies used in this dissertation as well as some new insightful examples. The theorems and definitions offered in the present chapter will be frequently used in the entire thesis. In particular, contraction analysis is introduced as our main nonlinear stability tool, and compared with the classical Lyapunov method. This chapter is intended to make this thesis sufficiently self-contained. Readers are encouraged to refer to the references cited in this chapter for further details.

2.2 Lagrangian Systems

This dissertation is devoted to the use of the Lagrangian formulation to derive most nonlinear dynamics including tethered formation flying arrays. The aim of Section 2.2 is to present a unified treatment of the underlying characteristics of the particular forms of Lagrangian systems offered in this thesis. For example, the positive definite inertia matrix and symmetry of the nonlinear systems play a central role in our stability analysis and control synthesis.

2.2.1 Euler-Lagrangian Equations

To derive nonlinear equations of motion for generalized coordinates, $\mathbf{q} \in \mathbb{R}^n$, a method employing the Euler-Lagrangian equations of motion [22, 35, 188] is preferred throughout the thesis for its simplicity in dealing with complex systems involving multiple dynamics. Another advantage of the Lagrangian approach [146] is its invariance with respect to coordinate changes.

Let us define Q as a smooth (C^∞) **n-dimensional** configuration manifold of a mechanical system with generalized coordinates $\mathbf{q} \in Q$. Its tangent bundle, TQ is the union of every tangent space $TQ_{\mathbf{q}}$ on $\mathbf{q}$. The cotangent bundle of Q is defined as $T^\star Q$. Let $\delta\mathbf{q}$ be the virtual displacement corresponding to the variation of $\mathbf{q}$. In the presence of external forces (e.g. control action by actuators or external disturbances), the Lagrange-D'Alembert principle indicates that

$$\delta \int_a^b L(\mathbf{q}, \dot{\mathbf{q}})dt + \int_a^b F(\delta\mathbf{q})dt = 0 \tag{2.1}$$

where a Lagrangian $L : TQ \to \mathbb{R}$ is defined as

$$L(\mathbf{q}, \dot{\mathbf{q}}) = K(\mathbf{q}, \dot{\mathbf{q}}) - V(\mathbf{q}) = \frac{1}{2}\dot{\mathbf{q}}^T\mathbf{M}(\mathbf{q})\dot{\mathbf{q}} - V(\mathbf{q}) \tag{2.2}$$

Notice that the potential energy, $V(\mathbf{q}) : Q \to \mathbb{R}$ is independent of $\dot{\mathbf{q}}$ whereas the kinetic energy can often be represented in a quadratic form, $K = \frac{1}{2}\dot{\mathbf{q}}^T\mathbf{M}(\mathbf{q})\dot{\mathbf{q}}$.

From (2.1), the following Euler-Lagrange equations of motion for a mechanical system with a configuration manifold Q can be derived:

$$\frac{d}{dt}\frac{\partial L(\mathbf{q},\dot{\mathbf{q}})}{\partial \dot{\mathbf{q}}} - \frac{\partial L(\mathbf{q},\dot{\mathbf{q}})}{\partial \mathbf{q}} = \mathbf{F} \tag{2.3}$$

where $\mathbf{F} : \mathbb{R} \times TQ \to T^\star Q$ is an m-dimensional generalized force or torque vector ($\mathbf{F} \in \mathbb{R}^m$) acting on the system. The dependency on time ($t \in \mathbb{R}$) usually originates from a time-varying desired trajectory. Otherwise, a map of $\mathbf{F}$ is defined by $TQ \to T^\star Q$. If $m = n$ with $\mathbf{q} \in \mathbb{R}^n$, the system is a fully actuated system. However, if $m < n$, the system is an underactuated mechanical system, which is extensively treated in Chapter 6.

Sometimes, it is convenient to introduce dissipative nonconservative forces such as mechanical friction and aerodynamic drag:

$$\frac{d}{dt}\frac{\partial L(\mathbf{q},\dot{\mathbf{q}})}{\partial \dot{\mathbf{q}}} - \frac{\partial L(\mathbf{q},\dot{\mathbf{q}})}{\partial \mathbf{q}} = \mathbf{F} + \mathbf{B}(\mathbf{q},\dot{\mathbf{q}}) \tag{2.4}$$

where $\mathbf{B}(\mathbf{q},\dot{\mathbf{q}})$ denotes a generalized nonconservative force or torque vector.

Sometimes, when some subsystems are quasi-continuous, this dissipation force term depends only on the rate such that the quadratic Rayleigh dissipation function can be defined as follows:

$$\mathcal{D} = \frac{1}{2}\sum_{r=1}^{n}\sum_{s=1}^{n} d_{rs}\dot{q}_r\dot{q}_s = \dot{\mathbf{q}}^T D\dot{\mathbf{q}} \tag{2.5}$$

where D is generally symmetric positive definite.

Then, $\mathbf{B}(\mathbf{q},\dot{\mathbf{q}})$ in (2.4) is obtained by

$$\mathbf{B}(\mathbf{q},\dot{\mathbf{q}}) = -\frac{\partial \mathcal{D}}{\partial \dot{\mathbf{q}}} \tag{2.6}$$

For example, one of the dissipation forces considered in this thesis is a friction term of the air-bearing carriages, which is characterized as a viscous damping force. Such friction forces have been considered in the experiments using the SPHERES testbed in Chapter 7.

2.2.2 Lagrangian on Riemannian Manifolds

The representation of the kinetic energy in a quadratic form in (2.2) warrants a further discussion. Recalling

$$K(\mathbf{q},\dot{\mathbf{q}}) = \frac{1}{2}\dot{\mathbf{q}}^T\mathbf{M}(\mathbf{q})\dot{\mathbf{q}}, \tag{2.7}$$

we can construct a mass/inertia matrix, $\mathbf{M}(\mathbf{q}) \in \mathbb{R}^{n\times n}$ from the kinetic energy, $K(\mathbf{q},\dot{\mathbf{q}})$. In a large class of nonlinear systems, the matrix $\mathbf{M}(\mathbf{q})$ is symmetric positive definite, which permits the following definition from geometric control theory [1, 22, 35].

Definition 2.1 Riemannian Manifolds
A differentiable manifold with a positive definite symmetric quadratic form $\langle\cdot,\cdot\rangle$ on every tangent space $TQ_{\mathbf{q}}$ of the configuration variable, $\mathbf{q}$ is called a Riemannian manifold. The quadratic form $\langle\cdot,\cdot\rangle$ is often called a Riemannian metric.

As shall be seen later, this Riemannian metric and its matrix representation, $\mathbf{M}(\mathbf{q})$ constructed from the kinetic energy of a nonlinear mechanical system, play a central role in the nonlinear control design and stability analysis offered in this thesis. Plugging (2.2) into (2.3), Euler-Lagrange equations on a Riemannian manifold are obtained:

$$\mathbf{M}(\mathbf{q})\ddot{\mathbf{q}} + \dot{\mathbf{q}}^T\boldsymbol{\Gamma}(\mathbf{q},\dot{\mathbf{q}})\dot{\mathbf{q}} + \mathbf{g}(\mathbf{q}) = \mathbf{F} \tag{2.8}$$

where $\mathbf{g}(\mathbf{q})$ contains a gravity term of a rigid body such that $\frac{\partial \mathbf{V}(\mathbf{q})}{\partial \mathbf{q}} = \mathbf{g}(\mathbf{q})$, and the elements of the $\boldsymbol{\Gamma}$ matrix are Christoffel symbols [188, 178]:

$$\Gamma_{ijk} = \frac{1}{2}\left(\frac{\partial M_{ij}}{\partial q_k} + \frac{\partial M_{ik}}{\partial q_j} - \frac{\partial M_{jk}}{\partial q_i}\right) \tag{2.9}$$

The quadratic term $\dot{\mathbf{q}}^T\boldsymbol{\Gamma}(\mathbf{q},\dot{\mathbf{q}})\dot{\mathbf{q}}$ can be classified into two different types. The terms involving q_iq_j with $i \neq j$ represent the Coriolis force (torque) whereas the other terms involving ${q_i}^2$ correspond to the centrifugal force (torque). It should be emphasized that the definition in (2.9) is one of many possible choices of $\boldsymbol{\Gamma}$ from the Euler-Lagrangian equations in (2.3). To show the reason behind this choice, we proceed to illustrate the significance of the relationship between the Riemannian metric and Christoffel symbols. Let us represent an equivalent form to (2.8):

$$\mathbf{M}(\mathbf{q})\ddot{\mathbf{q}} + \mathbf{C}(\mathbf{q},\dot{\mathbf{q}})\dot{\mathbf{q}} + \mathbf{g}(\mathbf{q}) = \mathbf{F} \tag{2.10}$$

where the $\mathbf{C}$ matrix is defined as

$$c_{ij} = \frac{1}{2}\sum_{k=1}^{n}\frac{\partial M_{ij}}{\partial q_k}\dot{q_k} + \frac{1}{2}\sum_{k=1}^{n}\left(\frac{\partial M_{ik}}{\partial q_j} - \frac{\partial M_{jk}}{\partial q_i}\right)\dot{q_k} \tag{2.11}$$

Then, it is straightforward to show that $(\dot{\mathbf{M}} - 2\mathbf{C})$ is skew-symmetric [178] resulting in $\mathbf{x}^T(\dot{\mathbf{M}} - 2\mathbf{C})\mathbf{x} = 0$ for arbitrary $\mathbf{x} \in \mathbb{R}^n$. This skew-symmetric property can be viewed as a matrix expression of energy conservation [178], which is explained in the context of the passivity formalism in Section 2.2.7. In addition, since $\mathbf{M}(\mathbf{q})$ is symmetric, one can find that

$$\dot{\mathbf{M}}(\mathbf{q}) = \mathbf{C}(\mathbf{q},\dot{\mathbf{q}})^T + \mathbf{C}(\mathbf{q},\dot{\mathbf{q}}). \tag{2.12}$$

The property in (2.12) is widely exploited for stability analysis and control synthesis in the remainder of this dissertation. Furthermore, one can derive the Euler-Lagrangian equations in (2.10) using $\dot{\mathbf{M}} = \mathbf{C}^T + \mathbf{C}$ without solving (2.11) to derive the $\mathbf{C}$ matrix.

We make extensive use of (2.10) in this thesis as our primary nonlinear differential equations of a mechanical system.

2.2.3 Symmetry

When the subsystems in a coupled dynamical system are assumed to be identical, the overall system exhibits symmetries. We take an example of multiple spacecraft connected by equally spaced tethers (See Chapters 3 and 4). This kind of system has a geometrical symmetry, where the coordinates are invariant under angle rotational transformations such as $\mathbf{y} = \mathbf{R}\mathbf{x}$.

In this section, we pay attention to a different notion of symmetry, so-called mechanical symmetry, which makes a connection with the conservation laws. Most mechanical systems, despite being non-symmetric in geometry, possess some symmetry properties. In the context of geometric control theory, mechanical symmetries lead to to reduction of the model complexity [37, 145]. We start with the definition of mechanical symmetry.

Definition 2.2 Symmetry in Mechanics
The Lagrangian $L(\mathbf{q},\dot{\mathbf{q}}) = K(\mathbf{q},\dot{\mathbf{q}}) - V(\mathbf{q})$ is symmetric with respect to the configuration variable q_i if and only if

$$\frac{\partial L(\mathbf{q},\dot{\mathbf{q}})}{\partial q_i} = 0 \tag{2.13}$$

where q_i is the i-th ($i \in \{1,\ldots,n\}$) configuration variable in the vector $\mathbf{q}$.

Definition 2.2 states that the system is symmetric when its Lagrangian is invariant under the group action of q_i.

We define the i-th generalized momentum, p_i as

$$p_i = \frac{\partial L(\mathbf{q}, \dot{\mathbf{q}})}{\partial \dot{q}_i} \tag{2.14}$$

Then, the unforced Euler-Lagrange equation from (2.3) reduces to

$$\frac{d}{dt} p_i - \frac{\partial L}{\partial q_i} = 0 \tag{2.15}$$

Consequently, symmetry of a Lagrangian system, $\frac{\partial L}{\partial q_i} = 0$, leads to $\frac{d}{dt} p_i = 0$. In other words, the i-th generalized momentum is conserved, when the system is symmetric with respect to q_i. Most mechanical systems possess a relaxed form of symmetry as follows.

Definition 2.3 Kinetic Symmetry
A Lagrangian system is kinetically symmetric with respect to a joint variable vector, $\mathbf{q}$ if

$$\frac{\partial K}{\partial q_i} = 0. \tag{2.16}$$

The kinetic symmetry leads to symmetry in mechanics in Definition 2.2 in the absence of a potential field, i.e. $V(\mathbf{q}) = 0$, which in turn corresponds to the conservation of the momentum of an unforced system.

Note that the two-link manipulator robot in Figure 2-1 is kinetic symmetric with respect to the first joint angle θ_1, thereby resulting in an inertia matrix independent of θ_1. This independent variable is often called an *external variable [145] or cyclic [22]*. A dependent variable (θ_2) of a two-link manipulator is called a *shape variable*. Reduction theory for controlled Lagrangian and controlled Hamiltonian systems with symmetry is an active area of research [37]. For example, a nonlinear control design using a control Lagrangian makes extensive use of the conservation law derived by symmetry. In another example, Olfati-Saber [145] developed cascade normal forms for underactuated mechanical systems, based upon the mechanical symmetry introduced in this section. A similar approach is introduced to control an underactuated spinning tethered array in Chapter 6.

2.2.4 Legendre Transformation and Hamiltonian

The generalized momentum $\mathbf{p}$ is defined as

$$\mathbf{p} = \frac{\partial L}{\partial \dot{\mathbf{q}}} = \mathbf{M}(\mathbf{q})\dot{\mathbf{q}} \tag{2.17}$$

This coordinate transformation is referred to as the Legendre transformation [145, 22].

We can re-write (2.10) using the Legendre transformation in (2.17):

$$\begin{aligned} \dot{\mathbf{q}} &= \mathbf{M}^{-1}(\mathbf{q})\mathbf{p} \\ \dot{\mathbf{p}} &= \mathbf{C}\left(\mathbf{q}, \mathbf{M}^{-1}(\mathbf{q})\mathbf{p}\right)^T \mathbf{M}^{-1}(\mathbf{q})\mathbf{p} - \mathbf{g}(\mathbf{q}) + \mathbf{F} \end{aligned} \tag{2.18}$$

where we used $\dot{\mathbf{M}} = \mathbf{C} + \mathbf{C}^T$ from the skew-symmetric property of $\dot{\mathbf{M}} - 2\mathbf{C}$. The second-order differential equation in (2.10) is now in the first-order differential form, which has an advantage in contraction analysis, as shall be seen in the subsequent sections.

We can easily verify that (2.18) corresponds to Hamilton's equations by introducing the Hamil-

tonian, $H(\mathbf{q}, \mathbf{p})$:

$$\begin{aligned} H(\mathbf{q}, \mathbf{p}) = \dot{\mathbf{q}}^T \mathbf{p} - L(\mathbf{q}, \dot{\mathbf{q}}) = \frac{1}{2} \mathbf{p}^T \mathbf{M}^{-1}(\mathbf{q}) \mathbf{p} + V(\mathbf{q}) \\ \dot{\mathbf{q}} = \frac{\partial H(\mathbf{q}, \mathbf{p})}{\partial \mathbf{p}}, \\ \dot{\mathbf{p}} = -\frac{\partial H(\mathbf{q}, \mathbf{p})}{\partial \mathbf{q}} + \mathbf{F} \end{aligned} \tag{2.19}$$

Since the kinetic energy, K can be written as

$$K = \frac{1}{2} \dot{\mathbf{q}}^T \mathbf{M}(\mathbf{q}) \dot{\mathbf{q}} = \frac{1}{2} \mathbf{p}^T \mathbf{M}^{-1}(\mathbf{q}) \mathbf{p}, \tag{2.20}$$

the Hamiltonian represents the total energy of the system, i.e. $H = K + V$, as opposed to the Lagrangian, $L = K - V$.

In this dissertation, we will often encounter the closed loop dynamics of the following form:

$$\mathbf{M}(\mathbf{q}) \dot{\mathbf{s}} + \mathbf{C}(\mathbf{q}, \dot{\mathbf{q}}) \mathbf{s} + \mathbf{K} \mathbf{s} = \mathbf{u}(t) \tag{2.21}$$

where $\mathbf{s}(t)$ is the composite variable [178], often introduced in the sliding control literature such that

$$\mathbf{s} = \dot{\mathbf{q}} - \dot{\mathbf{q}}_d + \mathbf{\Lambda}(\mathbf{q} - \mathbf{q}_d) \tag{2.22}$$

where $\mathbf{q}_d$ represents the desired reference trajectory.

For the system in (2.21), we can employ the following transformation by redefining $\mathbf{p}$:

$$\mathbf{p} = \mathbf{M}(\mathbf{q}) \mathbf{s} \tag{2.23}$$

Hence, (2.21) reduces to the following first-order canonical form:

$$\begin{aligned} \dot{\mathbf{q}} &= -\mathbf{\Lambda} \mathbf{q} + \mathbf{M}^{-1}(\mathbf{q}) \mathbf{p} + (\dot{\mathbf{q}}_d + \mathbf{\Lambda} \mathbf{q}_d) \\ \dot{\mathbf{p}} &= \Big[\mathbf{C} \left(\mathbf{q}, \mathbf{M}^{-1}(\mathbf{q}) \mathbf{p} \right)^T - \mathbf{K} \Big] \mathbf{M}^{-1}(\mathbf{q}) \mathbf{p} + \mathbf{u}(t) \end{aligned} \tag{2.24}$$

A nice thing about the equations, (2.18) and (2.24), is that the external control input vector, $\mathbf{F}$ is intact via the transformation, thereby facilitating the control design and controllability analysis.

2.2.5 Zero Riemann Curvature and Flat Mechanical Systems

If the inertia matrix, $\mathbf{M}(\mathbf{q})$ can be factored as $\mathbf{N}(\mathbf{q})^T \mathbf{N}(\mathbf{q})$, we can derive a transformation that significantly simplifies the robot dynamics. Such a transformation is called a linearizing point transformation [10] and all point transformations are also canonical transformations [186]. In the absence of the potential term V (or canceled by a feedforward term), suppose the inertia matrix $\mathbf{M}(\mathbf{q})$ can be factored into

$$\mathbf{M}(\mathbf{q}) = \mathbf{N}^T(\mathbf{q}) \mathbf{N}(\mathbf{q}) \tag{2.25}$$

where $\mathbf{N}(\mathbf{q})$ is integrable.

Also consider a canonical transformation by $Q(\mathbf{p}, \mathbf{q})$ and $P(\mathbf{p}, \mathbf{q})$ by which a system preserves the Hamiltonian structure of the system in (2.18).

$$dQ = \frac{\partial Q}{\partial \mathbf{q}} d\mathbf{q} = \mathbf{N}(\mathbf{q}) d\mathbf{q} \tag{2.26}$$

$$P = \mathbf{N}(\mathbf{q}) \dot{\mathbf{q}} \tag{2.27}$$

This transformation yields the following Hamiltonian

$$H = \frac{1}{2}\dot{\mathbf{q}}^T\mathbf{M}(\mathbf{q})\dot{\mathbf{q}} = \frac{1}{2}\dot{\mathbf{q}}^T\mathbf{N}^T(\mathbf{q})\mathbf{N}(\mathbf{q})\dot{\mathbf{q}} = \frac{1}{2}P^TP \tag{2.28}$$

which is independent of Q.

This simplification leads to the following double integrator system

$$\begin{aligned} \dot{Q} &= P \\ P &= \mathbf{N}(\mathbf{q})^{-T}\mathbf{F} \end{aligned} \tag{2.29}$$

This significantly simplifies the computation of a controller compared to the original feedback linearization (computed torque) control law since it only requires a computation of $\mathbf{N}(\mathbf{q})$. Then, a natural question arises as to the existence of such a decomposition in (2.25). It turns out that there is a sufficient and necessary condition to the existence which relates a Riemannian manifold with a Euclidean manifold.

Theorem 2.2.1 *A linearizing point transformation exists if and only if all elements of the Riemann curvature tensor, R_{ijkl} are identically zero. (See [186] and [10] for the exact definition of R_{ijkl}). Such a Riemannian manifold is called a "locally flat" manifold.*

One trivial example of a "zero Riemann curvature tensor" is a system with a constant inertia matrix, thereby eliminating the Christoffel symbols in (2.9) automatically. This in turn makes $\mathbf{C}(\mathbf{q}, \dot{\mathbf{q}})$ vanish as well.

Definition 2.4 Flat Mechanical System [145]
Mechanical systems with a constant inertia matrix $\mathbf{M}$ are called *Flat Mechanical Systems.*

This definition of flatness should not be confused with another notion of flatness of a mechanical system– "*differential flatness.*" [146, 136, 159] Roughly speaking, a control system is differentially flat if we can find a set of outputs equal in number to the inputs such that all states and inputs can be determined from these outputs without integration. One can inevitably infer that this differential flatness is particularly useful for motion planning. There are many examples of differentially flat mechanical systems including fully actuated nonlinear systems with feedback linearizability.

2.2.6 Nonholonomic Systems and Underactuated Dynamics

Consider a mechanical system of $\mathbf{q} \in \mathbb{R}^n$, subject to the following p constraint equations, linear in the velocity field:

$$\sum_{k=1}^{n} a_k^j(q_i)\dot{q}_k = 0, \quad j = 1, \ldots, p. \quad \text{Equivalently, } \mathbf{A}(\mathbf{q})\dot{\mathbf{q}} = \mathbf{0} \tag{2.30}$$

where $\mathbf{A}(\mathbf{q}) \in \mathbb{R}^{p\times n}$ and $p < n$.

Definition 2.5 Nonholonomic Constraints [22]
The constraints in (2.30) are ***holonomic*** or ***integrable*** if there is a real-valued vector function $\mathbf{h}(\mathbf{q}) \in \mathbb{R}^p$ such that the constraint can be written as $\mathbf{h}(\mathbf{q})$ =constant, or in differentiated form, $(\frac{\partial h_i}{\partial q_i}\dot{q}_i = 0)$. Thus the configuration of the system is actually constrained to be on a submanifold of the configuration manifold. We can then write Lagrange's equations using coordinates on this submanifold and thus get a system of equations with fewer variables.

If no such function $\mathbf{h}$ exists, the constraints are said to be ***nonintegrable*** or ***nonholonomic***.

For example, the length constraint on a pendulum is a holonomic constraint. We actually use a holonomic constraint of a tether in Chapter 3 to reduce a tethered system to fewer relative variables. On the other hand, a constraint of rolling without slipping is nonholonomic. In addition, constraints

that are independent of time are called ***scleronomic***, whereas ***rheonomic*** indicates constraints depending on time.

Using the Lagrange-d'Alembert principle given in (2.1) together with the nonholonomic velocity constraints of the form in (2.30), we can derive the following equations of motion:

$$\begin{aligned} \mathbf{M}(\mathbf{q})\ddot{\mathbf{q}} + \mathbf{C}(\mathbf{q},\dot{\mathbf{q}})\dot{\mathbf{q}} + \mathbf{g}(\mathbf{q}) &= \mathbf{A}(\mathbf{q})^T\lambda + \mathbf{F} \\ \mathbf{A}(\mathbf{q})\dot{\mathbf{q}} &= \mathbf{0} \end{aligned} \tag{2.31}$$

where $\lambda \in \mathbb{R}^p$ is a vector of Lagrange multipliers. Notice that we now have $2n$ first-order differential equations and m constraint equations for $2n+m$ variables $(\mathbf{q}, \dot{\mathbf{q}}, \lambda)$.

The above constraints are first-order nonholonomic constraints. In this dissertation, we shall focus on the second-order nonholonomic constraints arising from underactuated control inputs.

Definition 2.6 Underactuated Mechanical Systems
A Lagrangian system in (2.10), which has a fewer number of inputs ($\mathbf{F} \in \mathbb{R}^m$) than the number of degrees-of-freedom, n ($\mathbf{q} \in \mathbb{R}^n$) such that $m < n$, is called an ***Underactuated*** Lagrangian system.

Hence, we can derive a second-order nonholonomic constraint from the unactuated coordinates. For example, if the first coordinate variable q_1 out of $\mathbf{q} = \begin{pmatrix} q_1 & q_2 & \cdots & q_n \end{pmatrix}^T$ is not actuated, the following acceleration constraint equation is obtained:

$$m_{11}(\mathbf{q})\ddot{q}_1 + m_{12}(\mathbf{q})\ddot{q}_2 + \cdots + m_{1n}(\mathbf{q})\ddot{q}_n + h_1(\mathbf{q},\dot{\mathbf{q}}) = 0, \tag{2.32}$$

which is not integrable.

Control of underactuated mechanical systems is an active area of research [22, 35, 145, 187]. In this dissertation, we introduce some underactuated control strategies for the spinning tethered formation flying problem in Chapter 6.

2.2.7 Passivity

A passive system is one where the energy output of the system is not greater than the energy injected into the system from external sources. Hence, the passivity property makes an essential connection with the energy conservation law. Before we introduce Lyapunov functions to generalize the notion of energy in a dynamical system, particulary in the context of stability theory, we briefly characterize a passive mechanical system in this section.

Consider a control affine, smooth nonlinear system with an output $\mathbf{y} \in \mathbb{R}^m$,

$$\begin{aligned} \dot{\mathbf{x}}(t) &= \mathbf{f}(\mathbf{x}(t),t) + \mathbf{g}(\mathbf{x}(t),t)\mathbf{u} \\ \mathbf{y} &= \mathbf{h}(\mathbf{x}) \end{aligned} \tag{2.33}$$

where $\mathbf{x} \in \mathbb{R}^n$, $\mathbf{u} \in \mathbb{R}^m$, and $\mathbf{f}, \mathbf{g}$ and $\mathbf{h}$ are continuous in t and smooth in $\mathbf{x}$ with $\mathbf{f}(\mathbf{0},t) = \mathbf{0}$ and $\mathbf{h}(\mathbf{0},t) = \mathbf{0}$ for all $t \geq 0$.

Definition 2.7 Passivity
The nonlinear system in (2.33) is said to be passive if there exists a $\mathcal{C}^1$ storage function $V(\mathbf{x},t) \geq 0$, $V(\mathbf{0},t) = 0, \forall t \geq 0$ and a function $S(\mathbf{x}) \geq 0$ such that for $\forall t \geq t_0 \geq 0$

$$V(\mathbf{x}(t),t) - V(x(t_0),t_0) = \int_{t_0}^{t} \mathbf{u}^T(s)\mathbf{y}(s)ds - \int_{t_0}^{t} S(\mathbf{x}(s))ds \tag{2.34}$$

The system in (2.33) is strictly passive for $S(\mathbf{x}) > 0$ and lossless for $S(\mathbf{x}) = 0$.

Notice that the external power input term is written as $\mathbf{u}^T\mathbf{y}$. We can easily show that a combination of two passive systems is passive, which leads to the "additive" property of Lyapunov functions [178].

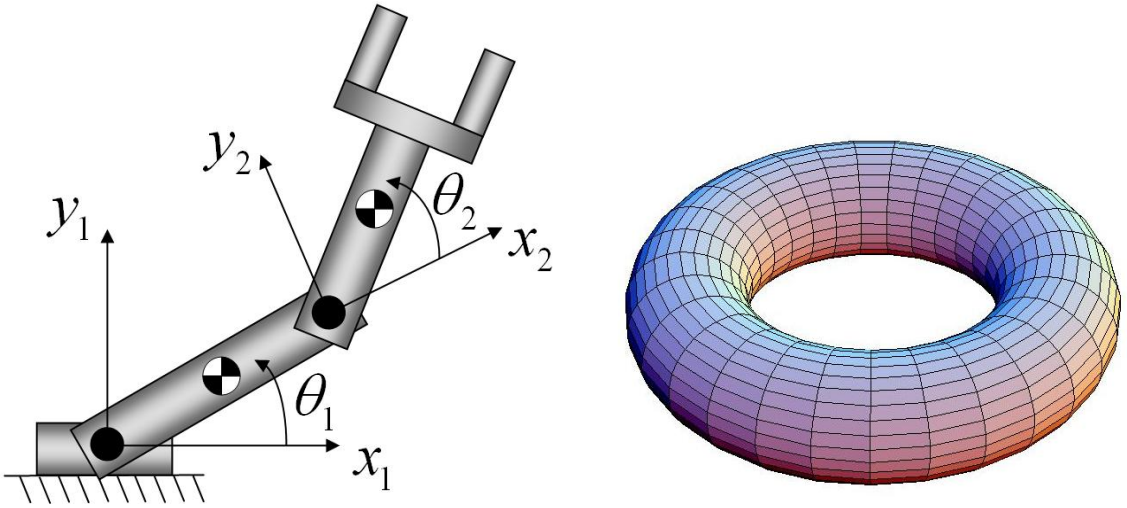

(a) Joint angles are measured counterclockwise. (b) Configuration manifold of two-link manipulator.

Figure 2-1: Two-link manipulator robot

Let us take an example of a mechanical system such as a robotic manipulator in (2.10):

$$\mathbf{M}(\mathbf{q})\ddot{\mathbf{q}} + \mathbf{C}(\mathbf{q}, \dot{\mathbf{q}})\dot{\mathbf{q}} + \mathbf{g}(\mathbf{q}) = \tau \tag{2.35}$$

In the presence of external gravity torques $\mathbf{g}(\mathbf{q})$, the energy conservation law can be written as

$$\dot{\mathbf{q}}^T(\tau - \mathbf{g}(\mathbf{q})) = \frac{1}{2}\frac{d}{dt}(\dot{\mathbf{q}}^T\mathbf{M}(\mathbf{q})\dot{\mathbf{q}}) \tag{2.36}$$

which implies that the mapping $\tau - \mathbf{g} \rightarrow \dot{\mathbf{q}}$ is passive. By expanding the right-hand side, we can prove that $\dot{\mathbf{q}}^T(\dot{\mathbf{M}} - 2\mathbf{C})\dot{\mathbf{q}}$. In conclusion, a robot's dynamics are passive only with a velocity vector $\dot{\mathbf{q}}$ unless a composite variable structure [178] is employed.

Passivity is a subject of intense research, with applications to robotics [178], spacecraft control [60], and more recently, teleoperation [105] and network synchronization [40].

2.3 Examples of Nonlinear Dynamics

The following nonlinear dynamics are encountered in this dissertation, either as a basic set of dynamics which establishes a more complex system, or as a subsystem comprising a multi-agent network.

2.3.1 Two-Link Manipulator

A two-link planar robot manipulator in Figure 2-1 has been selected as a representative example in nonlinear control theory and the robotics research communities. This example has also formed a basic dynamics model for a spinning single-tethered spacecraft in Chapter 3.

This system has two degrees-of-freedom and the configuration manifold $Q = \mathbb{S}^1 \times \mathbb{S}^1$ is specified by $\mathbf{q} = (\theta_1, \theta_2)^T$. It is well known that its configuration space is identified to a torus consisting of the union of two circles ($\mathbb{S}^1 \times \mathbb{S}^1$) as shown in Figure 2-1(b).

The moment of inertia about the center of mass of each manipulator is given as I_1 and I_2. The lengths of each manipulator are ℓ_1 and ℓ_2 while ℓ_{c1} and ℓ_{c2} denote the distance from the previous joint to the center of mass of the next link. Also, m_1 and m_2 denote the mass of each manipulator link, respectively. The gravitational pull is acting uniformly in the vertical direction.

We find the following Euler-Lagrangian equations of motion by constructing the kinetic energy

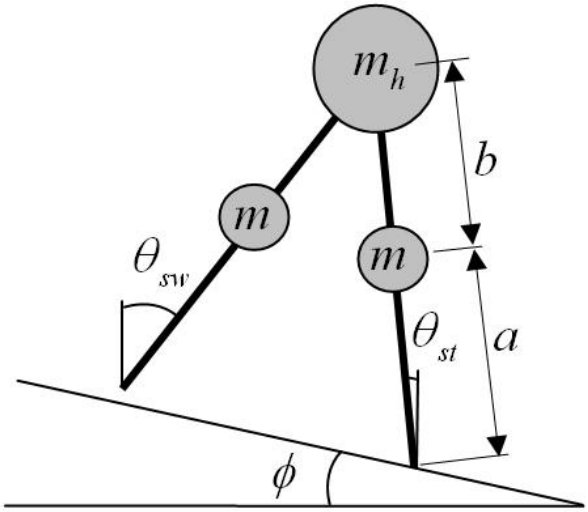

Figure 2-2: Compass gait

$K = \frac{1}{2}\dot{\mathbf{q}}^T\mathbf{M}(\mathbf{q})\dot{\mathbf{q}}$:

$$\mathbf{M}(\mathbf{q})\ddot{\mathbf{q}} + \mathbf{C}(\mathbf{q},\dot{\mathbf{q}})\dot{\mathbf{q}} + \mathbf{g}(\mathbf{q}) = \tau. \tag{2.37}$$

where the inertial matrix is defined as

$$\mathbf{M}(\mathbf{q}) = \begin{bmatrix} I_1 + I_2 + m_1{\ell_{c1}}^2 + m_2({\ell_1}^2 + {\ell_{c2}}^2 + 2\ell_1\ell_{c2}\cos\theta_2) & I_2 + m_2({\ell_{c2}}^2 + \ell_1\ell_{c2}\cos\theta_2) \\ I_2 + m_2({\ell_{c2}}^2 + \ell_1\ell_{c2}\cos\theta_2) & I_2 + m_2{\ell_{c2}}^2 \end{bmatrix}. \tag{2.38}$$

From (2.11) or (2.12), the $\mathbf{C}$ matrix is obtained as

$$\mathbf{C}(\mathbf{q},\dot{\mathbf{q}}) = \begin{bmatrix} h\dot{\theta_2} & h(\dot{\theta_1} + \dot{\theta_2}) \\ -h\dot{\theta_1} & 0 \end{bmatrix} \tag{2.39}$$

where $h = -m_2\ell_1\ell_{c2}\sin\theta_2$.

The potential term is obtained as

$$g_1(\mathbf{q}) = \frac{\partial V}{\partial\theta_1} = (m_1\ell_{c1} + m_2\ell_1)g\cos\theta_1 + m_2\ell_{c2}g\cos(\theta_1 + \theta_2) \tag{2.40}$$

$$g_2(\mathbf{q}) = \frac{\partial V}{\partial\theta_2} = m_2\ell_{c2}g\cos(\theta_1 + \theta_2) \tag{2.41}$$

We can also derive equations of motion when θ_2 is not a joint variable but defined with respect to the horizontal axis. This will simplify the dynamics by eliminating the corresponding Coriolis force terms. In such a case, the inertia matrix is given as

$$\mathbf{M}(\mathbf{q}) = \begin{pmatrix} I_1 + m_1{\ell_{c1}}^2 + m_2{\ell_1}^2 & m_2\ell_1\ell_{c2}\cos(\theta_2 - \theta_1) \\ m_2\ell_1\ell_{c2}\cos(\theta_2 - \theta_1) & I_2 + m_2{\ell_{c2}}^2 \end{pmatrix}. \tag{2.42}$$

The $\mathbf{C}$ matrix and the gravity terms can be similarly obtained. Such generalized coordinates are employed in a three-spacecraft inline configuration of a spinning tethered array in Chapters 3 and 4, which not only simplify the equations of motion but also make a model reduction technique in Chapter 4 more intuitive.

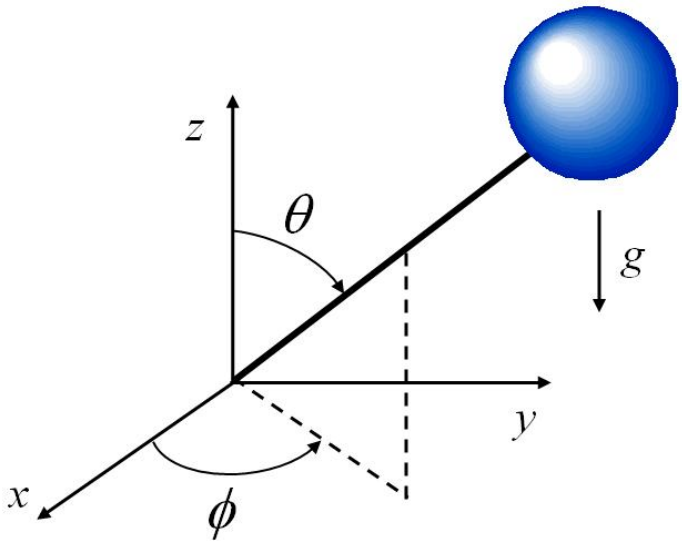

Figure 2-3: Spherical pendulum

2.3.2 Walking Robot: Compass-Gait

Considerable effort is being made to understand the physics of biological and human locomotion, with an aim to build more robust and energy efficient [194] walking robots [157, 206, 189].

A compass gait in Figure 2-2 is a simple but representative dynamic model of bipedal walking, first reported in [71]:

$$\mathbf{M}(\mathbf{q}) = \begin{bmatrix} mb^2 & -m\ell b\cos(\theta_{st}-\theta_{sw}) \\ -m\ell b\cos(\theta_{st}-\theta_{sw}) & (m_h+m)\ell^2+ma^2 \end{bmatrix} \tag{2.43}$$

where $\mathbf{q} = (\theta_{sw}, \theta_{st})^T$ and $\ell = a + b$.

$$\mathbf{C}(\mathbf{q}, \dot{\mathbf{q}}) = \begin{bmatrix} 0 & m\ell b\sin(\theta_{st}-\theta_{sw})\dot{\theta}_{st} \\ m\ell b\sin(\theta_{st}-\theta_{sw})\dot{\theta}_{sw} & 0 \end{bmatrix} \tag{2.44}$$

and

$$\mathbf{g}(\mathbf{q}) = \begin{pmatrix} mbg\sin\theta_{sw} \\ -(m_h\ell+ma+m\ell)g\sin\theta_{st} \end{pmatrix}. \tag{2.45}$$

The compass gait consists of two legs with point feet: the swinging leg (θ_{sw}) and the stance leg (θ_{st}). On heelstrike, an inelastic collision occurs under which angular momentum is conserved. Immediately after the collision, the model switches its swing and stance legs, and forms the limit cycle. One potential application of the compass gait dynamics is extending the synchronization strategy in this dissertation to the coupled linkages and joints of walking robots. It is assumed that synchronization between coupled dynamical systems provides a powerful adaptive mechanism to receive, encode, and store external events into a system's internal dynamics [154].

2.3.3 Spherical Pendulum

As shall be seen in Chapter 3, we derive the planar rotational dynamics of tethered formation flight, based on the compound pendulum motion of the rigid body. A spherical pendulum, which has two degrees of rotational freedom, is considered in Figure 2-3.

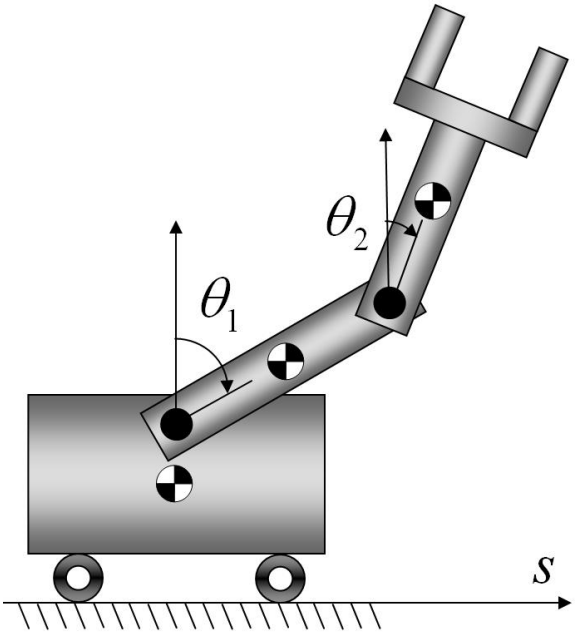

Figure 2-4: Two-link manipulator on a moving cart. Rotational angles are measured clockwise.

The Lagrangian is

$$L = \frac{1}{2}m\left(\ell^2\dot{\theta}^2 + \ell^2\sin^2\theta\dot{\phi}^2\right) + mg\ell\cos\theta. \tag{2.46}$$

The Euler-Lagrange equations give

$$\mathbf{M}(\mathbf{q})\ddot{\mathbf{q}} + \mathbf{C}(\mathbf{q},\dot{\mathbf{q}})\dot{\mathbf{q}} + \mathbf{g}(\mathbf{q}) = \tau \tag{2.47}$$

where

$$\begin{aligned}
\mathbf{M}(\mathbf{q}) &= \begin{bmatrix} m\ell^2 & 0 \\ 0 & m\ell^2\sin^2\theta \end{bmatrix} \\
\mathbf{C}(\mathbf{q},\dot{\mathbf{q}}) &= \begin{bmatrix} 0 & -m\ell^2\sin\theta\cos\theta\dot{\phi} \\ m\ell^2\sin\theta\cos\theta\dot{\phi} & m\ell^2\sin\theta\cos\theta\dot{\theta} \end{bmatrix} \\
\mathbf{g}(\mathbf{q}) &= \begin{pmatrix} mg\ell\sin\theta \\ 0 \end{pmatrix}, \quad \mathbf{q} = \begin{pmatrix} \theta \\ \phi \end{pmatrix}
\end{aligned} \tag{2.48}$$

It should be noted that the above Euler-Lagrangian formulation is much simpler than the Newton-Euler formulation of the spherical pendulum problem introduced in [207].

2.3.4 Robotic Arm on a Cart

We can envision a mobile robot equipped with robotic manipulators for special applications such as a robotic arm on a spacecraft for EVA tasks and a mobile humanoid robot platform for eliminating human involvement in the hazardous situations. Such robotic research platforms actually exist– e.g., the Stanford Assistant Mobile Manipulator (SAMM) [93] and NASA's astronaut robot a.k.a. robonaut [3]. Figure 2-4 depicts such an example of mobile manipulators. This is actually a two degree-of-freedom manipulator moving on a cart and often called a double inverted pendulum on a cart. Like its simpler counterpart- a cart-pole system [22], much attention has been recently devoted to this more complex inverted pendulum system [215, 25].

For simplicity, the two joint variables are defined with respect to the inertial vertical frames. All

the physical parameters are the same as those of a two-link robot in Section 2.3.1. In addition, the mass of the moving cart is M and its translation coordinate is defined as s. From the kinetic energy, we can find the following inertia matrix for $\mathbf{q} = (s, \theta_1, \theta_2)^T$:

$$\mathbf{M}(\mathbf{q}) = \begin{bmatrix} M + m_1 + m_2 & (m_1\ell_{c1} + m_2\ell_1)\cos\theta_1 & m_2\ell_{c2}\cos\theta_2 \\ (m_1\ell_{c1} + m_2\ell_1)\cos\theta_1 & I_1 + m_1{\ell_{c1}}^2 + m_2{\ell_1}^2 & m_2\ell_1\ell_{c2}\cos(\theta_1 - \theta_2) \\ m_2\ell_{c2}\cos\theta_2 & m_2\ell_1\ell_{c2}\cos(\theta_1 - \theta_2) & I_2 + m_2{\ell_{c2}}^2 \end{bmatrix}. \tag{2.49}$$

We can recognize that the sub-matrix formed by rows (2,3) and columns (2,3) is the same as the inertia matrix of the two-link manipulator in (2.42).

It is straightforward to calculate the $\mathbf{C}$ matrix as

$$\mathbf{C}(\mathbf{q}, \dot{\mathbf{q}}) = \begin{bmatrix} 0 & -(m_1\ell_{c1} + m_2\ell_1)\sin\theta_1\dot{\theta}_1 & -m_2\ell_{c2}\sin\theta_2\dot{\theta}_2 \\ 0 & 0 & m_2\ell_1\ell_{c2}\sin(\theta_1 - \theta_2)\dot{\theta}_2 \\ 0 & -m_2\ell_1\ell_{c2}\sin(\theta_1 - \theta_2)\dot{\theta}_1 & 0 \end{bmatrix} \tag{2.50}$$

The gravity term $\mathbf{g}(\mathbf{q}) = \frac{\partial V}{\partial \mathbf{q}}$ is given as

$$\mathbf{g}(\mathbf{q}) = \begin{pmatrix} 0 \\ -(m_1\ell_{c1} + m_2\ell_1)g\sin\theta_1 \\ -m_2\ell_{c2}g\sin\theta_2 \end{pmatrix} \tag{2.51}$$

The above dynamic model is used in Chapter 5 to construct an example network comprised of highly nonlinear systems.

2.3.5 Attitude Dynamics of Rigid Spacecraft

Three dimensional attitude control problems for a class of rigid spacecraft have gained considerable attention, in particular, in the context of adaptive control [60, 177], rigid body dynamics [208, 207], and geometric control theory [53, 24, 166]. Following [177], we show in this section that we can establish a Lagrangian dynamics form in (2.10) from the rotational attitude dynamics.

Using the Euler rotational equations of motion, the following equation describes the angular velocity vector $\vec{\omega}$ of the spacecraft in its body axes in Figure 2-5.

$$\mathbf{H}\dot{\vec{\omega}} = \mathbf{p} \times \vec{\omega} + \tau \tag{2.52}$$

where $\mathbf{p}$ is the total spacecraft angular momentum in its body frame.

The inertia matrix $\mathbf{H}$ is symmetric positive definite and can be decomposed into

$$\mathbf{H} = \mathbf{H}_{s/c} - \mathbf{H}_{wheel} \tag{2.53}$$

where all are expressed in the body frame.

The attitude of the spacecraft has the following relation:

$$\dot{\mathbf{x}} = \mathbf{J}(\mathbf{x})\vec{\omega} \tag{2.54}$$

where $\mathbf{x}$ and $\mathbf{J}(\mathbf{x})$ can be either the Euler angle representation ($\mathbf{x} = \gamma$) or the representation using Gibbs parameters ($\mathbf{x} = \xi$).

In the classical Euler angle representation, the attitude of the spacecraft is described using the successive angular clockwise rotations of roll (ϕ), pitch (θ), and yaw (ψ). In this case, Equation (2.54) becomes [53]

$$\dot{\gamma} = \mathbf{R}(\gamma)\vec{\omega} \tag{2.55}$$

where $\mathbf{R}(\gamma) = \begin{bmatrix} 1 & \sin\phi\tan\theta & \cos\phi\tan\theta \\ 0 & \cos\phi & -\sin\phi \\ 0 & \sin\phi\sec\theta & \cos\phi\sec\theta \end{bmatrix}$ for $-\pi/2 < \theta < \pi/2$.

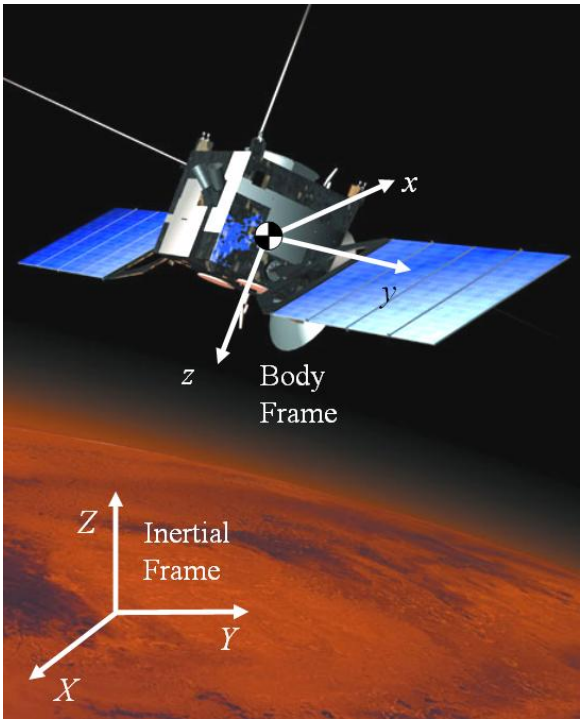

Figure 2-5: Rigid spacecraft attitude representation. Picture courtesy: NASA JPL/Caltech

One drawback of the Euler angular representation is its singularity. To avoid this singularity problem, it is often preferred to use quaternions to represent an angular orientation between two different coordinate frames:

$$q_1 = e_1 \sin\frac{\theta}{2}, \quad q_2 = e_2 \sin\frac{\theta}{2}, \quad q_3 = e_3 \sin\frac{\theta}{2}, \quad q_4 = \cos\frac{\theta}{2} \tag{2.56}$$

where $\mathbf{e} = (e_1, e_2, e_3)^T$ is the Euler axis of rotation expressed in the body frame (see Figure 2-5) and θ is the rotation angle about $\mathbf{e}$.

Gibbs parameters (or commonly referred to as Rodrigues parameters) can be defined from quaternions as follows.

$$\xi = \begin{pmatrix} \xi_1 \\ \xi_2 \\ \xi_3 \end{pmatrix} = \begin{pmatrix} q_1/q_4 \\ q_2/q_4 \\ q_3/q_4 \end{pmatrix} = \mathbf{e} \tan\frac{\theta}{2} \tag{2.57}$$

In this case, Equation (2.54) becomes [208, 177]

$$\dot{\xi} = \mathbf{Z}(\xi)\vec{\omega} \tag{2.58}$$

where

$$\mathbf{Z}(\xi) = \frac{1}{2}\left(\mathbf{I} + \xi\xi^T + \mathbf{S}(\xi)\right) = \frac{1}{2}\begin{bmatrix} 1+{\xi_1}^2 & \xi_1\xi_2 - \xi_3 & \xi_1\xi_3 + \xi_2 \\ \xi_2\xi_1 + \xi_3 & 1+{\xi_2}^2 & \xi_2\xi_3 - \xi_1 \\ \xi_3\xi_1 - \xi_2 & \xi_3\xi_2 + \xi_1 & 1+{\xi_3}^2 \end{bmatrix}, \tag{2.59}$$

and the skew-symmetric matrix function, $\mathbf{S}(\mathbf{x})$ is defined as

$$\mathbf{S}(\mathbf{x}) = \begin{bmatrix} 0 & -x_3 & x_2 \\ x_3 & 0 & -x_1 \\ -x_2 & x_1 & 0 \end{bmatrix} \tag{2.60}$$

We can also express the angular momentum in the body axes ($\mathbf{p}$ in (2.52)) as a function of ξ:

$$\mathbf{p} = \mathbf{P}(\xi)\mathbf{p}^{\mathbf{I}} \tag{2.61}$$

where $\mathbf{p}^{\mathbf{I}}$ is the inertial angular momentum and is constant by the conservation of angular momentum. In addition,

$$\mathbf{P}(\xi) = 2(1+\xi^T\xi)^{-1}\left[\mathbf{I} + \xi\xi^T - \mathbf{S}(\xi)\right] - \mathbf{I} \tag{2.62}$$

By combining (2.52) and (2.54), the following equations of motion are obtained with respect to $\mathbf{x}$:

$$\mathbf{M}(\mathbf{x})\ddot{\mathbf{x}} + \mathbf{C}(\mathbf{x},\dot{\mathbf{x}})\dot{\mathbf{x}} = \mathbf{F} \tag{2.63}$$

where

$$\begin{aligned}
\tau &= \mathbf{J}^T(\mathbf{x})\mathbf{F} \\
\mathbf{M}(\mathbf{x}) &= \mathbf{J}^{-T}(\mathbf{x})\mathbf{H}(\mathbf{x})\mathbf{J}^{-1}(\mathbf{x}) \\
\mathbf{C}(\mathbf{x},\dot{\mathbf{x}}) &= -\mathbf{J}^{-T}\mathbf{H}\mathbf{J}^{-1}\dot{\mathbf{J}}\mathbf{J}^{-1} - \mathbf{J}^{-T}\mathbf{S}(\mathbf{p})\mathbf{J}^{-1}.
\end{aligned}$$

In essence, we established a Lagrangian formulation for the attitude dynamics of rigid spacecraft. This allows us to apply a wealth of control laws that were originally developed for robot dynamics to spacecraft. As discussed in (2.12), the most important feature of (2.63) is to have a skew-symmetric $\dot{\mathbf{M}} - 2\mathbf{C}$ due to energy conservation. Indeed, we can verify that

$$\dot{\mathbf{M}} - 2\mathbf{C} = \frac{d\mathbf{J}^{-T}}{dt}\mathbf{H}\mathbf{J}^{-1} - \mathbf{J}^{-T}\mathbf{H}\frac{d\mathbf{J}^{-1}}{dt} + 2\mathbf{J}^{-T}\mathbf{S}(\mathbf{p})\mathbf{J}^{-1} \tag{2.64}$$

Note that $\mathbf{x}$ in (2.63) represents the inertial coordinates.

2.4 Previous Work on Nonlinear Stability

This section is intended to be a brief introduction to Lyapunov stability theorems for the purpose of comparison with our main stability tool, contraction theory in Section 2.5. A wealth of literature exists for the further treatment of Lyapunov methods (see Khalil [92], Sastry [172], Slotine [178], Vidyasagar [200]).

2.4.1 Lyapunov-Based Method

Consider a smooth autonomous nonlinear system of $\mathbf{x} \in \mathbb{R}^n$

$$\dot{\mathbf{x}} = \mathbf{f}(\mathbf{x}) \tag{2.65}$$

In the sense of Lyapunov, the system in (2.65) is stable if the system trajectory can be kept arbitrarily close to the origin. A stronger form of stability is defined as asymptotically stable where the states that started from some initial conditions actually converge to the equilibrium points. If the convergence rate is determined by an exponential function, then the system is exponentially stable. When the domain of attraction is all the configuration space in $\mathbb{R}^n$, the system is globally stable.

One easy way of checking the local stability of an equilibrium point $\mathbf{x}_\star$ of (2.65) is to check the eigenvalues of the Jacobian of (2.65).

Theorem 2.4.1 ***Lyapunov Indirect Method***
Consider the Jacobian

$$\mathbf{A} = \frac{\partial \mathbf{f}}{\partial \mathbf{x}} \text{ at } x_\star. \tag{2.66}$$

If $\mathbf{A}$ *is Hurwitz (not Hurwitz) then the equilibrium point* $x_\star$ *is asymptotically stable (unstable). If A is marginally stable, then no conclusion of the stability can be drawn.*

A fundamental approach of the Lyapunov function is to find a scalar representation of the energy contained in a system. Hence, if one can find that the associated Lyapunov function is decreasing over time, then one can inevitably conclude that the system is stable.

Theorem 2.4.2 ***Lyapunov Direct Method***
Let $V(\mathbf{x}) : \mathbb{R}^n \to \mathbb{R}_+$ be a continuously differentiable ***positive*** *scalar function such that the following is true in the neighborhood of an equilibrium point*

$$\dot{V} = \frac{\partial V}{\partial \mathbf{x}} \mathbf{f}(\mathbf{x}) < 0 \tag{2.67}$$

Then, the system is locally asymptotically stable. If $V(\mathbf{x})$ is radially unbounded such that $V \to \infty$ as $\|x\| \to \infty$, then the equilibrium is globally asymptotically stable.

Such a function, V is called a Lyapunov function.

If we replace the inequality condition with "$\leq$", the equilibrium is just stable without asymptotic convergence. In practice, this inequality condition is a stringent requirement for most mechanical systems. For a time-invariant nonlinear system, LaSalle's invariant lemma is exploited to derive asymptotic convergence with a negative semi-definite rate of V.

Theorem 2.4.3 ***LaSalle's Invariant Set Theorem*** *[178]*
Consider an autonomous system in (2.65). Assume that the region $\mathbf{\Omega}_l$ defined by $V(\mathbf{x}) < l$ is bounded, and $\dot{V}(\mathbf{x}) \leq 0$ on $\mathbf{\Omega}_l$. Let $\mathbf{R}$ be the set of all points within $\mathbf{\Omega}_l$ where $\dot{V}(\mathbf{x}) = 0$, and $\mathbf{M}$ be the largest invariant set in $\mathbf{R}$. Then, every solution $\mathbf{x}(t)$ originating in $\mathbf{\Omega}_l$ tends to $\mathbf{M}$ as $t \to \infty$.

This invariant set theorem can be conveniently used for a system with a negative semi-definite $\dot{V}$ to prove its asymptotic stability, however this is restricted to a time-invariant (autonomous) system. A more generalized theory on stability of nonautonomous systems is introduced in the subsequent section.

2.4.2 Extension of Lyapunov Function to Time-Varying Systems

Consider a smooth nonlinear time-varying system

$$\dot{\mathbf{x}}(t) = \mathbf{f}(\mathbf{x}(t), t) \tag{2.68}$$

where $\mathbf{x}(t) \in \mathbb{R}^n$, and $\mathbf{f} : \mathbb{R}^n \times \mathbb{R}_+ \to \mathbb{R}^n$

The Lyapunov's direct method in Theorem 2.4.2 still holds for a nonautonomous system in 2.68, with the additional condition that V is decrescent [178]. This condition means that $V(x, t)$ is upper-bounded by a time-invariant positive definite function.

In order to weaken the inequality requirement for asymptotic stability, the following lemma can be used:

Theorem 2.4.4 *Barbalat's Lemma*
If the differentiable function, $V(t)$ tends to a finite limit as $t \to \infty$, and if $\dot{V}(t)$ is uniformly continuous, then

$$\lim_{t \to \infty} \dot{V}(t) = 0 \tag{2.69}$$

Note that the uniform continuity of $\dot{V}(t)$ is sufficiently met if $\ddot{V}(t)$ exists and is bounded.

The Lyapunov theorem along with Barbalat's lemma leads to the following powerful theorem:

Theorem 2.4.5 *LaSalle-Yoshizawa [100]*
Let $\mathbf{x} = 0$ be an equilibrium point of (2.68) and suppose $\mathbf{f}$ is locally Lipschitz in $\mathbf{x}$ uniformly in t. Let $V : \mathbb{R}^n \times \mathbb{R}_+ \to \mathbb{R}_+$ be a continuously differentiable function such that

$$\dot{V} = \frac{\partial V}{\partial t} + \frac{\partial V}{\partial \mathbf{x}} \mathbf{f}(\mathbf{x}, t) \leq -W(\mathbf{x}) \leq 0 \tag{2.70}$$

$$\gamma_1(\|\mathbf{x}\|) \leq V(\mathbf{x},t) \leq \gamma_2(\|\mathbf{x}\|) \tag{2.71}$$

$\forall t \geq 0$, $\forall \mathbf{x} \in \mathbb{R}^n$, where γ_1 and γ_2 are strictly increasing class $\mathcal{K}$ functions and W is a continuous function. Then, all solutions of (2.68) are globally uniformly bounded and satisfy

$$\lim_{t\to\infty} W(\mathbf{x}(t)) = 0 \tag{2.72}$$

In addition, if $W(\mathbf{x})$ is positive definite, then the equilibrium $\mathbf{x} = 0$ is globally uniformly asymptotically stable.

Often times, the asymptotic convergence of $W(\mathbf{x}(t))$ and $\dot{V}$ to zero is sufficient to prove the convergence of tracking errors even though the system per se might not be asymptotically stable.

2.4.3 Exponential Stability [178, 92]

In linear systems, asymptotic stability automatically means global exponential convergence. For a time-varying nonlinear system such as (2.68), some additional conditions are required:

Theorem 2.4.6 *Exponential Stability*
Let $\mathbf{x} = 0$ be an equilibrium point of (2.68) and suppose $\mathbf{f}$ is locally Lipschitz in $\mathbf{x}$ uniformly in t. Let $V : \mathbb{R}^n \times \mathbb{R}_+ \to \mathbb{R}_+$ be a continuously differentiable function such that

$$c_1\|\mathbf{x}\|^2 \leq V(\mathbf{x},t) \leq c_2\|\mathbf{x}\|^2 \tag{2.73}$$

$$\dot{V} = \frac{\partial V}{\partial t} + \frac{\partial V}{\partial \mathbf{x}}\mathbf{f}(\mathbf{x},t) \leq -c_3\|\mathbf{x}\|^2 \tag{2.74}$$

$$\|\frac{\partial V}{\partial \mathbf{x}}\| \leq c_4\|\mathbf{x}\| \tag{2.75}$$

where c_1, c_2, c_3, and c_4 are strictly positive and $\forall t \geq 0$.

Then, the equilibrium $\mathbf{x} = 0$ is exponentially stable. If the above conditions hold globally, then it is globally exponentially stable.

Exponential convergence offers numerous advantages. For instance, it provides a stronger form of stability, resulting in more efficient performance than the asymptotic convergence of PD control, particularly for tracking demanding trajectories. In addition, exponential stability is robust with respect to a class of perturbations [92], as seen in perturbation theories.

In the next section, we introduce contraction theory, which can be efficiently used to prove global exponential stability of nonlinear systems.

2.5 Nonlinear Stability by Contraction Analysis

Contraction analysis is introduced herein as our main nonlinear stability tool for the entire thesis. Contraction theory provides a systematic method to build arbitrarily complex systems (e.g. a tethered formation array) out of simpler elements (e.g. a single-tethered spacecraft). We also exploit contraction and partial contraction theory [202] to prove the stability of multiple coupled nonlinear dynamics.

Lyapunov's linearization method indicates that the local stability of the nonlinear system can be analyzed using its differential approximation. What is new in contraction theory is that a differential stability analysis can be made exact, thereby yielding **global and exponential convergence** results in nonlinear systems. A brief review of the results from [112, 176, 202] along with the author's own intepretation is presented in this section. Readers are referred to these references for detailed descriptions and proofs on the following theorems. Note that contraction theory is a generalization of the classical Krasovskii's theorem [178], and that approaches closely related to contraction, although not based on differential analysis, can be traced back to [78, 56] and even to [109]. A recent work by Rantzer [158] also independently derived a similar result on the use of the monotonicity of singulary weighted volumes.

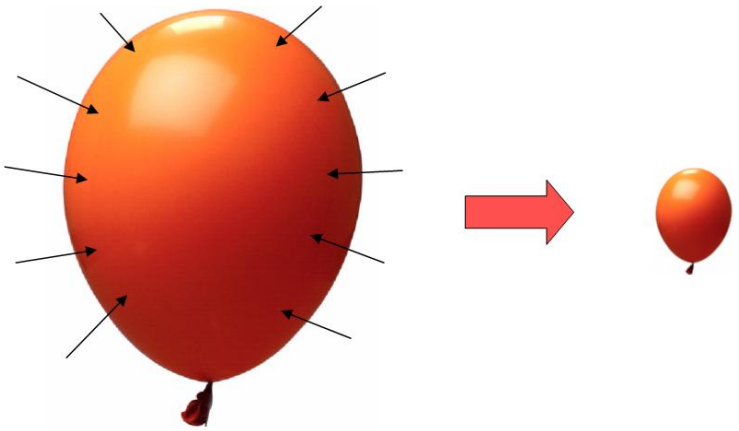

Figure 2-6: Contraction of a volume

Before we move onto the details, the key advantages of contraction analysis are summarized as below.

- Contraction theory is a differential-based analysis. Therefore, it is much easier to combine multiple systems.
- Contraction theory is more generalized. For instance, all examples and theorems in [158] are for autonomous systems whereas contraction theory can be easily applied to general time-varying systems including systems with time-varying desired trajectories.
- Convergence of contraction theory is stronger: exponential and global. Asymptotic convergence of a PD controller is not enough for tracking demanding time-varying reference inputs of nonlinear systems.
- The proof is intuitive and much simpler. This truly sets contraction analysis aside from other methodologies. For example, one can recall the proof of global and time-varying version of Krasovskii's theorem.
- Contraction theory also permits a non-constant metric and a pure differential coordinate change, which is not explicit in [158]. This generalization of the metric (generalized Jacobian, not just $\frac{df}{dx}$) is one of the differences with other methodologies.

2.5.1 Fundamentals

Contraction theory takes a slightly different notion of stability - a system is stable in some region if initial conditions or temporary disturbances are somehow forgotten [112]. Suppose that one can construct a virtual volume out of the given dynamics. Rather than finding a decreasing scalar function by the Lyapunov method, a contracting volume indicates the system is contracting, thereby stable, as illustrated in Figure 2-6. How can we quantify the contraction rate of the virtual volume constructed from the dynamical system? By computing contraction of two neighboring trajectories in the flow field.

Consider a smooth nonlinear system

$$\dot{\mathbf{x}}(t) = \mathbf{f}(\mathbf{x}(t), \mathbf{u}(\mathbf{x}, t), t) \tag{2.76}$$

where $\mathbf{x}(t) \in \mathbb{R}^n$, and $\mathbf{f} : \mathbb{R}^n \times \mathbb{R}^m \times \mathbb{R}_+ \to \mathbb{R}^n$. A virtual displacement, $\delta\mathbf{x}$ is defined as an infinitesimal displacement at a fixed time– a common supposition in the calculus of variations.

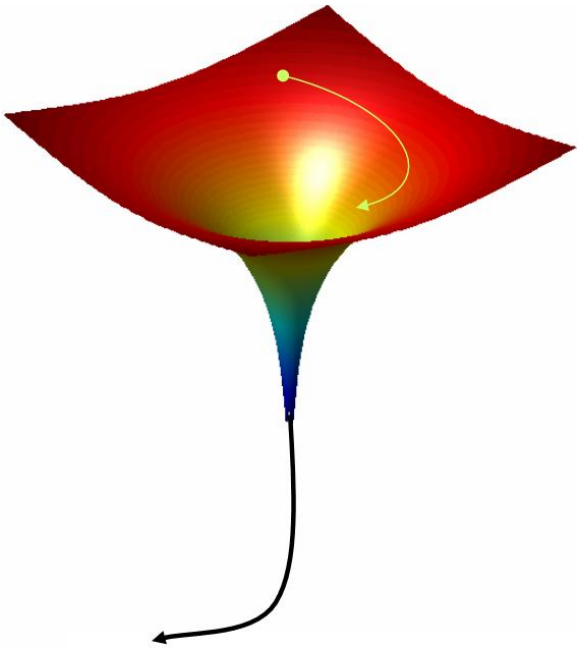

Figure 2-7: Exponential convergence to a single trajectory

Theorem 2.5.1 *For the system in (2.76), if there exists a uniformly positive definite metric,*

$$\mathbf{M}(\mathbf{x},t) = \mathbf{\Theta}(\mathbf{x},t)^T\mathbf{\Theta}(\mathbf{x},t) \tag{2.77}$$

where $\mathbf{\Theta}$ *is some smooth coordinate transformation of the virtual displacement,* $\delta\mathbf{z} = \mathbf{\Theta}\delta\mathbf{x}$*, such that the associated generalized Jacobian* $\mathbf{F}$ *is uniformly negative definite, i.e.,* $\exists\lambda > 0$ *such that*

$$\mathbf{F} = \left(\dot{\mathbf{\Theta}}(\mathbf{x},t) + \mathbf{\Theta}(\mathbf{x},t)\frac{\partial\mathbf{f}}{\partial\mathbf{x}}\right)\mathbf{\Theta}(\mathbf{x},t)^{-1} \leq -\lambda\mathbf{I}, \tag{2.78}$$

then all system trajectories converge globally to a single trajectory exponentially fast regardless of the initial conditions, with a global exponential convergence rate of the largest eigenvalues of the symmetric part of $\mathbf{F}$*.*

Such a system is said to be contracting.

Proof The proof is given in [112]. Briefly, the dynamics of $\delta\mathbf{z} = \mathbf{\Theta}\delta\mathbf{x}$ are computed as

$$\frac{d}{dt}\delta\mathbf{z} = \dot{\mathbf{\Theta}}\delta\mathbf{x} + \mathbf{\Theta}\delta\dot{\mathbf{x}} = \mathbf{F}\delta\mathbf{z} \tag{2.79}$$

Hence, the rate of change of squared length, which quantifies the contraction rate of the volume, is represented as

$$\frac{d}{dt}(\delta\mathbf{z}^T\delta\mathbf{z}) = 2\delta\mathbf{z}^T\frac{d}{dt}\delta\mathbf{z} = 2\delta\mathbf{z}^T\mathbf{F}\delta\mathbf{z} \tag{2.80}$$

∎

In the context of fluid dynamics, we can recall Gauss' divergence theorem [121]. Indeed, the divergence of the virtual length vector field, $\text{div}(\frac{d}{dt}\delta\mathbf{z})$ is the trace of $\mathbf{F}$ [112].

Exponential convergence to a single trajectory, regardless of the initial conditions, is graphically illustrated in Figure 2-7. No matter where the initial states start in the configuration manifold, they

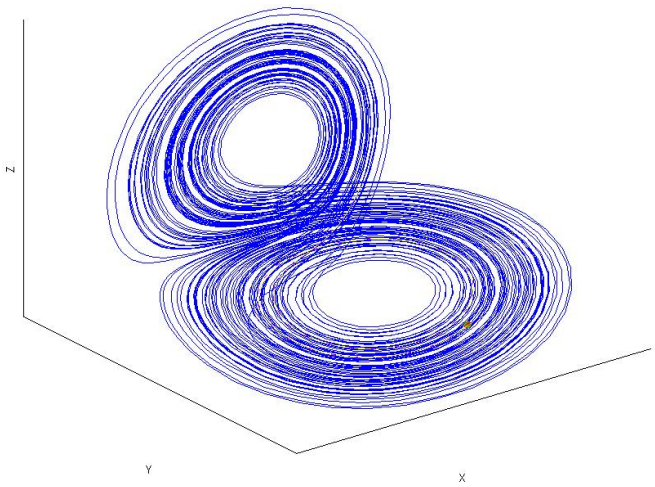

Figure 2-8: Lorenz attractor

converge into a single trajectory with global and exponential convergence. This convergence result epitomizes the significance of contraction analysis.

Corollary 2.5.2 *Equivalently, the system is contracting if* $\exists \lambda > 0$ *such that*

$$\dot{\mathbf{M}} + \left(\frac{\partial \mathbf{f}}{\partial \mathbf{x}}\right)^T \mathbf{M} + \mathbf{M}\frac{\partial \mathbf{f}}{\partial \mathbf{x}} \leq -2\lambda \mathbf{M} \tag{2.81}$$

Proof We can easily find

$$\frac{d}{dt}\left(\delta \mathbf{x}^T \mathbf{M} \delta \mathbf{x}\right) = \delta \mathbf{x}^T \Big(\dot{\mathbf{M}} + (\frac{\partial \mathbf{f}}{\partial \mathbf{x}})^T \mathbf{M} + \mathbf{M}\frac{\partial \mathbf{f}}{\partial \mathbf{x}}\Big)\delta \mathbf{x} \tag{2.82}$$

Hence, we can conclude that the condition in (2.81) leads to exponential convergence of $\delta \mathbf{x}$ to zero. ∎

Corollary 2.5.2 is extensively used in the entire thesis, in particular in Chapters 4 and 5. The symmetric and positive definite Riemann metric [22, 35], from the Lagrangian representation of dynamical systems, facilitates the use of such a metric in contraction analysis.

It can also be shown that for a contracting autonomous system, of the form $\dot{\mathbf{x}} = \mathbf{f}(\mathbf{x}, \mathbf{u}(\mathbf{x}))$, all trajectories converge to an equilibrium point exponentially fast. In essence, contraction analysis implies that stability of nonlinear systems can be analyzed more simply by checking the negative definiteness of a proper matrix, rather than finding some implicit motion integral as in Lyapunov theory.

Example Chaotic synchronization [176]

Much attention has been devoted to synchronization in chaotic systems. A central characateristic of a chaotic system like the Lorenz Attractor [117] in Figure 2-8 is that its long-term behavior is often impossible to predict but its short-term behavior is relatively easy to anticipate, so its immediate propagation can be controlled. In particular, Pecora et al. [151] reported that this phenomenon can be used for communications by means of chaotic synchronization. Recently, Argyris [5, 6] implemented the fist long-distance demonstration of chaotic synchronization using a pair of laser diodes, amplifiers, a mirror and more than 120 kilometers of underground fiber.

Consider the Lorenz system

$$\dot{x} \;=\; \sigma\,(y - x)$$

$$\dot{y} \;=\; \rho\, x \;-\; y \;-\; x\, z$$
$$\dot{z} \;=\; -\,\beta\, z \;+\; x\, y$$

with strictly positive constants σ, ρ, β, and, as in [151], a reduced-order identity observer for this system based on an available measurement of the variable x,

$$\dot{\hat{y}} \;=\; \rho\, x \;-\; \hat{y} \;-\; x\, \hat{z}$$
$$\dot{\hat{z}} \;=\; -\,\beta\, \hat{z} \;+\; x\, \hat{y}$$

The symmetric part of the observer's Jacobian is $-\operatorname{diag}(1, \beta)$, and thus the observer is contracting with an identity metric. Since by construction $(\hat{y}, \hat{z}) = (y, z)$ is a particular solution, the estimated state converges exponentially to the actual state. This can also be described as an active-passive decomposition [150].

2.5.2 Contraction of Combined and Coupled Systems

The following theorems are used to derive stability and synchronization of coupled dynamics systems.

Theorem 2.5.3 ***parallel combination***
Consider two time-varying nonlinear systems, contracting in the same metric function which does not explicitly depend on time such that $\mathbf{M}(\mathbf{x}) = \mathbf{\Theta}(\mathbf{x})^T \mathbf{\Theta}(\mathbf{x})$ *and* $\dot{\mathbf{\Theta}} = \frac{\partial \mathbf{\Theta}}{\partial \mathbf{x}} \dot{\mathbf{x}}$*:*

$$\dot{\mathbf{x}} = \mathbf{f}_i(\mathbf{x}, t) \qquad i = 1, 2 \tag{2.83}$$

Then, any positive superposition with $\alpha_i > 0$

$$\dot{\mathbf{x}} = \alpha_1 \mathbf{f}_1(\mathbf{x}, t) + \alpha_2 \mathbf{f}_2(\mathbf{x}, t) \tag{2.84}$$

is contracting in the same metric. By recursion, this parallel combination can be extended to any number of systems.

Proof Since the original dynamics are contracting with a time-independent metric, the generalized Jacobian, $\mathbf{F}$ in (2.78) becomes

$$\mathbf{F} = \left(\dot{\mathbf{\Theta}}(\mathbf{x}) + \mathbf{\Theta}(\mathbf{x}) \frac{\partial \mathbf{f}_i}{\partial \mathbf{x}} \right) \mathbf{\Theta}(\mathbf{x})^{-1} = \left(\frac{\partial \mathbf{\Theta}(\mathbf{x})}{\partial \mathbf{x}} \mathbf{f}_i + \mathbf{\Theta}(\mathbf{x}) \frac{\partial \mathbf{f}_i}{\partial \mathbf{x}} \right) \mathbf{\Theta}(\mathbf{x})^{-1} \tag{2.85}$$

Since the individual systems are contracting,

$$\frac{d}{dt}(\delta \mathbf{z}^T \delta \mathbf{z}) = \delta \mathbf{z}^T \left(\frac{\partial \mathbf{\Theta}}{\partial \mathbf{x}} \mathbf{f}_i + \mathbf{\Theta} \frac{\partial \mathbf{f}_i}{\partial \mathbf{x}} \right) \mathbf{\Theta}^{-1} \delta \mathbf{z} \leq -2\lambda_i \delta \mathbf{z}^T \delta \mathbf{z}, \qquad i = 1, 2 \tag{2.86}$$

Hence, the $\delta \mathbf{z}$ dynamics of the combined system result in

$$\begin{aligned} \frac{d}{dt}(\delta \mathbf{z}^T \delta \mathbf{z}) &= \delta \mathbf{z}^T \left(\frac{\partial \mathbf{\Theta}}{\partial \mathbf{x}} (\alpha_1 \mathbf{f}_1 + \alpha_2 \mathbf{f}_2) + \mathbf{\Theta} (\alpha_1 \frac{\partial \mathbf{f}_1}{\partial \mathbf{x}} + \alpha_2 \frac{\partial \mathbf{f}_2}{\partial \mathbf{x}}) \right) \mathbf{\Theta}^{-1} \delta \mathbf{z} \\ &= \alpha_1 \delta \mathbf{z}^T \left(\frac{\partial \mathbf{\Theta}}{\partial \mathbf{x}} \mathbf{f}_1 + \mathbf{\Theta} \frac{\partial \mathbf{f}_1}{\partial \mathbf{x}} \right) \mathbf{\Theta}^{-1} \delta \mathbf{z} + \alpha_2 \delta \mathbf{z}^T \left(\frac{\partial \mathbf{\Theta}}{\partial \mathbf{x}} \mathbf{f}_2 + \mathbf{\Theta} \frac{\partial \mathbf{f}_2}{\partial \mathbf{x}} \right) \mathbf{\Theta}^{-1} \delta \mathbf{z} \\ &\leq -2(\alpha_1 \lambda_1 + \alpha_2 \lambda_2) \delta \mathbf{z}^T \delta \mathbf{z} \end{aligned} \tag{2.87}$$

∎

This parallel combination is extremely important if the system possesses a certain geometrical symmetry. For example, the $\mathbf{M}$ and $\mathbf{C}$ matrices from the Lagrangian equation might satisfy $\mathbf{M_2} = \mathbf{M}_{\phi_1} + \mathbf{M}_{\phi_2}$ and $\mathbf{C_2} = \mathbf{C}_{\phi_1} + \mathbf{C}_{\phi_2}$. This property is extensively exploited in Chapter 4.

Theorem 2.5.4 ***Hierarchical combination*** *[180, 176]*
Consider two contracting systems, of possibly different dimensions and metrics, and connect them

in series, leading to a smooth virtual dynamics of the form

$$\frac{d}{dt}\begin{pmatrix}\delta\mathbf{z}_1\\ \delta\mathbf{z}_2\end{pmatrix}=\begin{pmatrix}\mathbf{F}_{11} & \mathbf{0}\\ \mathbf{F}_{21} & \mathbf{F}_{22}\end{pmatrix}\begin{pmatrix}\delta\mathbf{z}_1\\ \delta\mathbf{z}_2\end{pmatrix} \tag{2.88}$$

Then the combined system is contracting if $\mathbf{F_{21}}$ *is bounded.*

Proof Intuitively, since $\delta\mathbf{z}_1$ tends to zero, $\delta\mathbf{z}_2$ tends to zero as well for a bounded $\mathbf{F}_{21}$. By using a smooth transformation $\mathbf{\Theta}$:

$$\mathbf{\Theta}=\begin{pmatrix}\mathbf{I} & \mathbf{0}\\ \mathbf{0} & \epsilon\mathbf{I}\end{pmatrix} \tag{2.89}$$

Then, the new transformed Jacobian matrix is given as

$$\mathbf{\Theta F \Theta}^{-1}=\begin{pmatrix}\mathbf{F}_{11} & \mathbf{0}\\ \epsilon\mathbf{F}_{21} & \mathbf{F}_{22}\end{pmatrix}, \tag{2.90}$$

which is negative definite for a sufficiently small $\epsilon > 0$. ∎

Composite variables, $\mathbf{s}=\dot{\mathbf{q}}-\dot{\mathbf{q}}_d+\mathbf{\Lambda}(\mathbf{q}-\mathbf{q}_d)$ are an excellent example of a hierarchical combination. Its usage for nonlinear tracking control and robust sliding control shall be discussed in the subsequent sections.

Another interesting combination that occurs in the nonlinear control synthesis is feedback combination.

Theorem 2.5.5 ***Feedback combination*** *[202]*

The overall dynamics of the generalized virtual displacements might be represented as

$$\frac{d}{dt}\begin{pmatrix}\delta\mathbf{z}_1\\ \delta\mathbf{z}_2\end{pmatrix}=\mathbf{F}\begin{pmatrix}\delta\mathbf{z}_1\\ \delta\mathbf{z}_2\end{pmatrix}=\begin{pmatrix}\mathbf{F_1} & \mathbf{G}^T\\ \mathbf{G} & \mathbf{F_2}\end{pmatrix}\begin{pmatrix}\delta\mathbf{z}_1\\ \delta\mathbf{z}_2\end{pmatrix} \tag{2.91}$$

where $\mathbf{F}_1$ *and* $\mathbf{F}_2$ *are symmetric negative definite matrices.*

In order to prove contraction of the combined system, one needs to check if $\mathbf{F}$ *is negative definite. From the standard linear algebra [82],* $\mathbf{F}$ *is uniformly negative definite if and only if*

$$\mathbf{F}_2 < \mathbf{G}^T{\mathbf{F}_1}^{-1}\mathbf{G} \tag{2.92}$$

A sufficient condition for the above inequality can be given as

$$\lambda(\mathbf{F}_1)\lambda(\mathbf{F}_2) > \sigma^2(\mathbf{G}) \tag{2.93}$$

where $\lambda(\cdot)$ *is the contraction rate, which is the absolute value of the largest eigenvalue (least negative) of the contracting system.* $\sigma(\cdot)$ *denotes the largest singular value.*

It should be noted that the overall contraction rate is no greater than the individual contraction rate of $\mathbf{F}_1$ and $\mathbf{F}_2$ by the eigenvalue interlacing theorem [82]. Indeed, one can find the explicit lower bound of the contraction rate as [176]

$$\lambda(\mathbf{F})=\frac{\lambda(\mathbf{F}_1)+\lambda(\mathbf{F}_2)}{2}-\sqrt{\left(\frac{\lambda(\mathbf{F}_1)-\lambda(\mathbf{F}_2)}{2}\right)^2+\sigma^2(\mathbf{G})} \tag{2.94}$$

2.5.3 Partial Contraction and Synchronization

Theorem 2.5.6 ***Partial contraction*** *[202]*
Consider a nonlinear system of the form $\dot{\mathbf{x}}=\mathbf{f}(\mathbf{x},\mathbf{x},t)$ *and assume that the auxiliary system* $\dot{\mathbf{y}}=\mathbf{f}(\mathbf{y},\mathbf{x},t)$ *is contracting with respect to* $\mathbf{y}$*. If a particular solution of the auxiliary* $\mathbf{y}$*-system*

verifies a specific smooth property, then all trajectories of the original x-system verify this property exponentially. The original system is said to be partially contracting.

Proof If a particular solution of the auxiliary contracting system of $\mathbf{y}$ given as $\dot{\mathbf{y}} = \mathbf{f}(\mathbf{y}, \mathbf{x}, t)$, verifies a smooth specific property, then all trajectories of the original $\dot{\mathbf{x}} = \mathbf{f}(\mathbf{x}, \mathbf{x}, t)$ system verify this property exponentially. $\mathbf{y} = \mathbf{x}$ is another solution of the auxiliary system. Consequently, $\mathbf{x}$ verifies this property exponentially fast. ∎

This partial contraction theory can be regarded as a further generalization of contraction theory in Theorem 2.5.1. This theorem is particularly useful to derive synchronization with an input symmetry.

Theorem 2.5.7 ***Synchronization*** *[202]*
Consider two coupled systems. If the dynamics equations satisfy

$$\dot{\mathbf{x}}_1 - \mathbf{f}(\mathbf{x}_1, t) = \dot{\mathbf{x}}_2 - \mathbf{f}(\mathbf{x}_2, t) \tag{2.95}$$

where the function $\mathbf{f}(\mathbf{x}, t)$ is contracting in an input-independent metric, then $\mathbf{x}_1$ and $\mathbf{x}_2$ will converge to each other exponentially, regardless of the initial conditions. Mathematically, stable concurrent synchronization corresponds to convergence to a flow-invariant linear subspace of the global state space[152].

Proof Let us define the common input, $\mathbf{g}(\mathbf{x}_1, \mathbf{x}_2, t)$, enforcing the equality of two dynamics equations such that

$$\begin{aligned} \dot{\mathbf{x}}_1 - \mathbf{f}(\mathbf{x}_1, t) &= \mathbf{g}(\mathbf{x}_1, \mathbf{x}_2, t) \\ \dot{\mathbf{x}}_2 - \mathbf{f}(\mathbf{x}_2, t) &= \mathbf{g}(\mathbf{x}_1, \mathbf{x}_2, t) \end{aligned} \tag{2.96}$$

Construct a virtual system of $\mathbf{y}$:

$$\dot{\mathbf{y}} - \mathbf{f}(\mathbf{y}, t) = \mathbf{g}(\mathbf{x}_1, \mathbf{x}_2, t) \tag{2.97}$$

which has two particular solutions, $\mathbf{x}_1$ and $\mathbf{x}_2$.

If the virtual system is contracting, all solutions of $\mathbf{y}$ converge to each other exponentially. As a result, $\mathbf{x}_1$ tends to $\mathbf{x}_2$ exponentially fast. ∎

Notice that the original dynamics per se, with the input $\mathbf{g}(\mathbf{x}_1, \mathbf{x}_2, t)$ might not be contracting. Nevertheless, the system is partially contracting, thereby achieving synchronization.

Based upon the results from Theorems 2.5.6 and 2.5.7, the following examples are illustrated in the subsequent sections to shed some light on potential applications of synchronization to nonlinear control.

2.5.4 High-Order Contraction Theory

This thesis presents a new theorem that can be conveniently used to prove contraction of a second-order nonlinear system. Consider the following second-order time-varying nonlinear differential equation

$$\ddot{x} + a_1(x)\dot{x} + a_2(x, t) = u(t) \tag{2.98}$$

where $a_1(x)$ is a smooth function of x, and $a_2(x, t)$ is a smooth function of x and t.

Proving contraction of (2.98) is difficult, since the original contraction analysis is originally stated for first-order systems. Finding some smooth coordinate transformation of the virtual displacement, $\delta\mathbf{z} = \mathbf{\Theta}\delta\mathbf{x}$, is key such that the generalized Jacobian $\mathbf{F}$ associated with the augmented system of $(x, \dot{x})^T$ is uniformly negative definite. In general, finding such a transformation, $\mathbf{\Theta}$ is not trivial. Even without the use of contraction theory, proving exponential and global stability of a general time-varying nonlinear second-order system can be a very difficult problem.

We present the main theorem of this section, which provides a sufficient condition for contraction of (2.98)

Theorem 2.5.8 *The nonlinear system in (2.98) is contracting (all solutions converge to a single trajectory exponentially fast from any initial conditions), if*

$$a_1(x) > 0, \qquad \forall x \tag{2.99}$$

and if

$$\frac{\partial a_2(x,t)}{\partial x} > 0, \quad \frac{d}{dt}\left(\frac{\partial a_2(x,t)}{\partial x}\right) > 0 \qquad \forall t \tag{2.100}$$

Proof The virtual displacement equation of (2.98) is

$$\delta\ddot{x} + a_1(x)\delta\dot{x} + \left[\dot{a}_1 + \frac{\partial a_2(x,t)}{\partial x}\right]\delta x = 0 \tag{2.101}$$

Equation (2.101) can be written as a first-order differential equation by defining the vector state $\mathbf{x} = (x, \dot{x})^T$:

$$\begin{aligned} \delta\dot{\mathbf{x}} &= \frac{\partial \mathbf{f}}{\partial \mathbf{x}}\delta\mathbf{x} \\ \frac{d}{dt}\begin{pmatrix}\delta x \\ \delta\dot{x}\end{pmatrix} &= \begin{bmatrix} 0 & 1 \\ -\left(\dot{a}_1 + \frac{\partial a_2}{\partial x}\right) & -a_1 \end{bmatrix}\begin{pmatrix}\delta x \\ \delta\dot{x}\end{pmatrix} \end{aligned} \tag{2.102}$$

Let us take the following transformation matrix

$$\mathbf{\Theta}(\mathbf{x},t) = \begin{pmatrix} 1 & 0 \\ a_1/\sqrt{\frac{\partial a_2}{\partial x}} & 1/\sqrt{\frac{\partial a_2}{\partial x}} \end{pmatrix} \tag{2.103}$$

It is straightforward to calculate the associated Jacobian as

$$\begin{aligned} \mathbf{F} &= \left(\dot{\mathbf{\Theta}}(\mathbf{x},t) + \mathbf{\Theta}(\mathbf{x},t)\frac{\partial \mathbf{f}}{\partial \mathbf{x}}\right)\mathbf{\Theta}(\mathbf{x},t)^{-1} \\ &= \begin{bmatrix} -a_1(x) & \sqrt{\frac{\partial a_2}{\partial x}} \\ -\sqrt{\frac{\partial a_2}{\partial x}} & -\frac{d}{dt}\left(\frac{\partial a_2}{\partial x}\right)/\left(2\frac{\partial a_2}{\partial x}\right) \end{bmatrix} \end{aligned} \tag{2.104}$$

From the contraction theory, (2.98) is contracting if the symmetric part of $\mathbf{F}$ is uniformly negative definite, which corresponds to the conditions in Theorem 2.5.8 ∎.

We illustrate the use of this theorem in a few examples.

Example Driven damped Van der Pol oscillator
Consider the following second-order system

$$\ddot{x} + (\beta + \alpha x^2)\dot{x} + \omega^2 x = u(t) \tag{2.105}$$

The first condition in Theorem 2.5.8 holds if $a_1(x) = (\beta + \alpha x^2) > 0$ uniformly (i.e. α and β are strictly positive). Also, note that $\frac{\partial a_2}{\partial x} = \omega^2$. This is a semi-contracting system. Indeed, the generalized Jacobian in (2.104) yields the same $\mathbf{F}$ as in [202].

Example Extension
Suppose that ω in (2.105) is now time-varying such that

$$\ddot{x} + a_1(x)\dot{x} + K_1 e^{K_2 t}x = u(t) \tag{2.106}$$

where $a_1(x) > 0$, $K_1 > 0$, and $K_2 > 0$.

The above dynamics is contracting since $\frac{d}{dt}\left(\frac{\partial a_2(x,t)}{\partial x}\right) = K_1 K_2 e^{K_2 t} > 0$.

2.5.5 Tracking Control of Robots and Aerospace Vehicles

The dynamics of a robot are given from (2.10)

$$\mathbf{M}(\mathbf{q})\ddot{\mathbf{q}} + \mathbf{C}(\mathbf{q},\dot{\mathbf{q}})\dot{\mathbf{q}} + \mathbf{g}(\mathbf{q}) = \tau \tag{2.107}$$

One may consider the following tracking control law [178, 181] to follow the desired trajectory $\mathbf{q}_d(t)$

$$\tau = \mathbf{M}(\mathbf{q})\ddot{\mathbf{q}}_r + \mathbf{C}(\mathbf{q},\dot{\mathbf{q}})\dot{\mathbf{q}}_r + \mathbf{g}(\mathbf{q}) - \mathbf{K}(\dot{\mathbf{q}} - \dot{\mathbf{q}}_r) \tag{2.108}$$

where $\dot{\mathbf{q}}_r = \dot{\mathbf{q}}_d - \mathbf{\Lambda}\widetilde{\mathbf{q}} = \dot{\mathbf{q}}_d - \mathbf{\Lambda}(\mathbf{q} - \mathbf{q}_d)$.

We can then introduce the dynamics of $\mathbf{y}$ such as

$$\tau = \mathbf{M}(\mathbf{q})\dot{\mathbf{y}} + \mathbf{C}(\mathbf{q},\dot{\mathbf{q}})\mathbf{y} + \mathbf{g}(\mathbf{q}) - \mathbf{K}(\dot{\mathbf{q}} - \mathbf{y}) \tag{2.109}$$

This virtual dynamics has two particular solutions, $\dot{\mathbf{q}}$ and $\dot{\mathbf{q}}_r$ since both solutions satisfy (2.110). The virtual displacement equation becomes

$$\mathbf{M}(\mathbf{q})\delta\dot{\mathbf{y}} + \mathbf{C}(\mathbf{q},\dot{\mathbf{q}})\delta\mathbf{y} + \mathbf{K}\delta\mathbf{y} = \mathbf{0} \tag{2.110}$$

It is straightforward to find that $\mathbf{K} > 0$ needs to hold true for exponential convergence to the desired trajectory. The skew-symmetry of $(\dot{\mathbf{M}} - 2\mathbf{C})$ results in the following differential length analysis

$$\begin{aligned}\frac{d}{dt}(\delta\mathbf{y}^T\mathbf{M}(\mathbf{q})\delta\mathbf{y}) &= 2\delta\mathbf{y}^T\mathbf{M}(\mathbf{q})\delta\dot{\mathbf{y}} + \delta\mathbf{y}^T\dot{\mathbf{M}}(\mathbf{q})\delta\mathbf{y} \\ &= -2\delta\mathbf{y}^T\Big(\mathbf{C}(\mathbf{q},\dot{\mathbf{q}})\delta\mathbf{y} + \mathbf{K}\delta\mathbf{y}\Big) + \delta\mathbf{y}^T\dot{\mathbf{M}}(\mathbf{q})\delta\mathbf{y} \\ &= -2\delta\mathbf{y}^T\mathbf{K}\delta\mathbf{y}\end{aligned} \tag{2.111}$$

which indicates that the $\mathbf{y}$-system is contracting with $\mathbf{K} > 0$. This implies exponential convergence of $\dot{\mathbf{q}}$ to $\dot{\mathbf{q}}_r$. This in turn indicates exponential convergence of $\mathbf{q}$ to $\mathbf{q}_d$ since

$$\dot{\mathbf{q}} - \dot{\mathbf{q}}_r = \dot{\mathbf{q}} - \dot{\mathbf{q}}_d + \mathbf{\Lambda}(\mathbf{q} - \mathbf{q}_d) = \mathbf{0} \tag{2.112}$$

is contracting with $\mathbf{\Lambda} > 0$.

This is a hierarchical combination due to reduction of the system order via introduction of the composite variable, $\mathbf{s}$ in (2.22). Recalling Theorem 2.5.4, contraction with the proposed tracking control law in (2.108) can be proven using the following hierarchical virtual system of $\mathbf{y}_1$ and $\mathbf{y}_2$:

$$\begin{bmatrix}\mathbf{M}(\mathbf{q}) & \mathbf{0}\\ \mathbf{0} & \mathbf{I}\end{bmatrix}\begin{pmatrix}\dot{\mathbf{y}}_1\\ \dot{\mathbf{y}}_2\end{pmatrix} + \begin{bmatrix}\mathbf{C}(\mathbf{q},\dot{\mathbf{q}}) + \mathbf{K} & \mathbf{0}\\ -\mathbf{I} & \mathbf{\Lambda}\end{bmatrix}\begin{pmatrix}\mathbf{y}_1\\ \mathbf{y}_2\end{pmatrix} = \begin{pmatrix}\mathbf{0}\\ \mathbf{0}\end{pmatrix} \tag{2.113}$$

It is straightforward to verify that (2.113) has two particular solutions:

$$\begin{pmatrix}\mathbf{y}_1 = \mathbf{s}\\ \mathbf{y}_2 = \mathbf{q} - \mathbf{q}_d\end{pmatrix}, \qquad \begin{pmatrix}\mathbf{y}_1 = \mathbf{0}\\ \mathbf{y}_2 = \mathbf{0}\end{pmatrix} \tag{2.114}$$

Similarly, the differential length analysis with respect to the uniformly positive definite metric,

$$\begin{bmatrix}\mathbf{M}(\mathbf{q}) & \mathbf{0}\\ \mathbf{0} & \alpha\mathbf{I}\end{bmatrix}, \quad \exists\alpha > 0 \tag{2.115}$$

yields

$$\begin{aligned}
&\frac{d}{dt}\begin{pmatrix}\delta\mathbf{y}_1\\ \delta\mathbf{y}_2\end{pmatrix}^T\begin{bmatrix}\mathbf{M}(\mathbf{q}) & \mathbf{0}\\ \mathbf{0} & \alpha\mathbf{I}\end{bmatrix}\begin{pmatrix}\delta\mathbf{y}_1\\ \delta\mathbf{y}_2\end{pmatrix}\\
&\quad=\begin{pmatrix}\delta\mathbf{y}_1\\ \delta\mathbf{y}_2\end{pmatrix}^T\begin{bmatrix}\dot{\mathbf{M}}(\mathbf{q}) & \mathbf{0}\\ \mathbf{0} & \mathbf{0}\end{bmatrix}\begin{pmatrix}\delta\mathbf{y}_1\\ \delta\mathbf{y}_2\end{pmatrix}+2\begin{pmatrix}\delta\mathbf{y}_1\\ \delta\mathbf{y}_2\end{pmatrix}^T\begin{bmatrix}\mathbf{M}(\mathbf{q}) & \mathbf{0}\\ \mathbf{0} & \alpha\mathbf{I}\end{bmatrix}\begin{pmatrix}\delta\dot{\mathbf{y}}_1\\ \delta\dot{\mathbf{y}}_2\end{pmatrix}\\
&\quad=\begin{pmatrix}\delta\mathbf{y}_1\\ \delta\mathbf{y}_2\end{pmatrix}^T\begin{bmatrix}\dot{\mathbf{M}}(\mathbf{q}) & \mathbf{0}\\ \mathbf{0} & \mathbf{0}\end{bmatrix}\begin{pmatrix}\delta\mathbf{y}_1\\ \delta\mathbf{y}_2\end{pmatrix}+2\begin{pmatrix}\delta\mathbf{y}_1\\ \delta\mathbf{y}_2\end{pmatrix}^T\begin{bmatrix}-\mathbf{C}(\mathbf{q},\dot{\mathbf{q}})-\mathbf{K} & \mathbf{0}\\ \alpha\mathbf{I} & -\alpha\mathbf{\Lambda}\end{bmatrix}\begin{pmatrix}\delta\mathbf{y}_1\\ \delta\mathbf{y}_2\end{pmatrix}\\
&\quad=\begin{pmatrix}\delta\mathbf{y}_1\\ \delta\mathbf{y}_2\end{pmatrix}^T\begin{bmatrix}-2\mathbf{K} & \mathbf{0}\\ 2\alpha\mathbf{I} & -2\alpha\mathbf{\Lambda}\end{bmatrix}\begin{pmatrix}\delta\mathbf{y}_1\\ \delta\mathbf{y}_2\end{pmatrix}
\end{aligned}\tag{2.116}$$

Let us define the matrix $\mathbf{B}$ as

$$\mathbf{B}=\begin{bmatrix}-2\mathbf{K} & \mathbf{0}\\ 2\alpha\mathbf{I} & -2\alpha\mathbf{\Lambda}\end{bmatrix}\tag{2.117}$$

The symmetric part of $\mathbf{B}$ is

$$\mathbf{B}_s=\frac{1}{2}(\mathbf{B}+\mathbf{B}^T)=\begin{bmatrix}-2\mathbf{K} & \alpha\mathbf{I}\\ \alpha\mathbf{I} & -2\alpha\mathbf{\Lambda}\end{bmatrix}\tag{2.118}$$

According to Theorem 2.5.1, (2.113) is contracting if the symmetric matrix $\mathbf{B}_s$ is uniformly negative definite. It is straightforward to show that $\mathbf{B}_s$ is negative definite if and only if

$$\begin{gathered}\alpha\mathbf{I}<4\mathbf{K}\mathbf{\Lambda},\ \text{equivalently, } \alpha<4\lambda_{min}(\mathbf{K}\mathbf{\Lambda})\\ \text{and } \mathbf{K}>0,\ \mathbf{\Lambda}>0\end{gathered}\tag{2.119}$$

Accordingly, all solutions of (2.113) converge to each exponentially fast, resulting in synchronization of $\mathbf{q}$ with $\mathbf{q}_d$.

Note that the tracking control law in (2.108) is extensively used in Chapter 4 and Chapter 5. It was first introduced by Li and Slotine [179] for the new adaptive control law. Compared to the feedback linearized control law (computed torque control), the equation in (2.108) does not cancel the robot dynamics, but it still guarantees exponential tracking convergence at the same rate as an exact cancelation of the feedback linearized control (see the discussion in [178]).

2.5.6 Tracking Control of Hamiltonian

We show an equivalent result from the previous section, using the first order canonical form obtained by the transformation, $\mathbf{p}=\mathbf{M}(\mathbf{q})\mathbf{s}$ in Section 2.2.4.

The closed-loop system with the tracking control law in (2.108) is obtained as

$$\mathbf{M}(\mathbf{q})\dot{\mathbf{s}}+\mathbf{C}(\mathbf{q},\dot{\mathbf{q}})\mathbf{s}+\mathbf{K}\mathbf{s}=\mathbf{0}\tag{2.120}$$

where $\mathbf{s}$ is defined in (2.22).
Equation (2.120) reduces to the following first-order canonical form:

$$\begin{aligned}\dot{\mathbf{p}}&=\left[\mathbf{C}\left(\mathbf{q},\mathbf{M}^{-1}(\mathbf{q})\mathbf{p}\right)^T-\mathbf{K}\right]\mathbf{M}^{-1}(\mathbf{q})\mathbf{p}\\ \dot{\mathbf{q}}&=-\mathbf{\Lambda}\mathbf{q}+\mathbf{M}^{-1}(\mathbf{q})\mathbf{p}+(\dot{\mathbf{q}}_d+\mathbf{\Lambda}\mathbf{q}_d)\end{aligned}\tag{2.121}$$

Consider a virtual system, having $\mathbf{y}_1=\mathbf{p},\mathbf{y}_2=\mathbf{q}$ and $\mathbf{y}_1=\mathbf{0},\mathbf{y}_2=\mathbf{q}_d$ as its particular solutions:

$$\begin{aligned}\dot{\mathbf{y}}_1&=\left[\mathbf{C}\left(\mathbf{q},\mathbf{M}^{-1}(\mathbf{q})\mathbf{p}\right)^T-\mathbf{K}\right]\mathbf{M}^{-1}(\mathbf{q})\mathbf{y}_1\\ \dot{\mathbf{y}}_2&=-\mathbf{\Lambda}\mathbf{y}_2+\mathbf{M}^{-1}(\mathbf{q})\mathbf{y}_1+(\dot{\mathbf{q}}_d+\mathbf{\Lambda}\mathbf{q}_d)\end{aligned}\tag{2.122}$$

which is also a hierarchical combination.

This virtual system can be easily shown to be contracting. Similarly to the previous section, the virtual length analysis with respect to the metric, $\mathbf{M}^{-1}(\mathbf{q}) > 0$ yields

$$\begin{aligned}
&\frac{d}{dt}(\delta\mathbf{y}_1{}^T\mathbf{M}^{-1}(\mathbf{q})\delta\mathbf{y}_1) = 2\delta\mathbf{y}_1{}^T\mathbf{M}^{-1}(\mathbf{q})\delta\dot{\mathbf{y}}_1 + \mathbf{y}_1{}^T\mathbf{M}^{-1}(\mathbf{q})(-\dot{\mathbf{M}}(\mathbf{q}))\mathbf{M}^{-1}(\mathbf{q})\delta\mathbf{y}_1 \\
&= \delta\mathbf{y}_1{}^T\mathbf{M}^{-1}(\mathbf{q})\Big(\mathbf{C} + \mathbf{C}^T - 2\mathbf{K}\Big)\mathbf{M}^{-1}(\mathbf{q})\delta\mathbf{y}_1 - \delta\mathbf{y}_1{}^T\mathbf{M}^{-1}(\mathbf{q})\dot{\mathbf{M}}(\mathbf{q})\mathbf{M}^{-1}(\mathbf{q})\delta\mathbf{y}_1 \\
&= -2\delta\mathbf{y}_1{}^T\mathbf{M}^{-1}(\mathbf{q})\mathbf{K}\mathbf{M}^{-1}(\mathbf{q})\delta\mathbf{y}_1
\end{aligned} \tag{2.123}$$

where we used

$$\frac{d}{dt}\mathbf{M}^{-1}(\mathbf{q}) = -\mathbf{M}^{-1}(\mathbf{q})\dot{\mathbf{M}}(\mathbf{q})\mathbf{M}^{-1}(\mathbf{q}) \tag{2.124}$$

This shows that $\mathbf{y}_1$ is contracting with $\mathbf{K} > 0$, which in turn corresponds to contraction of $\mathbf{y}_2$ due to the hierarchy. Therefore, all solutions of $\mathbf{y}_1$ and $\mathbf{y}_2$ tend to each other resulting in $\mathbf{q} \to \mathbf{q}_d$.

2.6 Review of Nonlinear Control Methods

We briefly review the nonlinear control techniques used in this dissertation. Specifically, we are more focused on achieving guaranteed stability of the nonlinear decentralized control strategy and synchronization of dynamics networks designed from the established nonlinear control techniques, rather than developing completely new control techniques. It is emphasized again that combinations and accumulations of stable dynamics have no reason to be stable– further analysis is required, which is the focus of this dissertation.

2.6.1 Linear Optimal Control

One simple intuitive approach to stabilize highly nonlinear systems is to apply linearization approximation around equilibrium points. One advantage of such linearization is that it permits the use of mature and well-established linear control techniques to address nonlinear problems. In addition, controllability analysis is much more straightforward. However, stability can be assured only locally and in a "slow-variation" setting [165]. In other words, only nonlinear control techniques can ensure global and exponential convergence of nonlinear systems. As introduced in Section 2.5, contraction analysis is explored to analyze the nonlinear stability of the proposed control architectures in the remainder of this thesis. Nonetheless, linearization allows us to apply numerous mature linear control techniques, which can be an alternative means to nonlinear control in some cases. Linear Quadratic Regulator (LQR) and Linear Quadratic Gaussian (LQG) controllers are classical optimal control methodologies [29, 64, 216, 217, 72]. As in most state-feedback control laws, the LQR control often involves a full-state feedback, which sometimes poses a challenge. The LQG control overcomes such a difficulty by combining a steady-state Kalman filter [32, 52, 64]. In this dissertation, the use of LQR control with a time-varying optimal Kalman filter is preferred (see Chapter 7). Nowadays, another optimal control methodology is enjoying popularity in a wide variety of applications. Model Predictive Control (MPC) or Receding Horizontal Control (RHC) [86, 162] computes each control action by solving an optimal control problem on-line based on the current estimated state of the plant. The MPC scheme is a natural choice to deal with input and state constraints and dynamic environments.

2.6.2 Feedback Linearization and Inverse Dynamics

The most popular technique for stabilization of fully actuated systems involves transforming a system to a linear system via a change of coordinates as well as a transformation of control input. The key idea in feedback linearization is straightforward. By canceling the nonlinear effects in the original dynamics by a feedforward control law, we can enforce the transformed dynamics to appear linear. Such linearization facilitates a design of an exponentially stabilizing control law. Compared to

asymptotic convergence of a linear PD control, exponential convergence via this exact feedback linearization offers superior tracking performance. For example, for the robot dynamics given in (2.10), the following controller

$$\mathbf{F} = \mathbf{M}(\mathbf{q})(\ddot{\mathbf{q}}_\mathbf{d} - 2\mathbf{\Lambda}\dot{\tilde{\mathbf{q}}} - \mathbf{\Lambda}^2\tilde{\mathbf{q}}) + \mathbf{C}(\mathbf{q}, \dot{\mathbf{q}})\dot{\mathbf{q}} + \mathbf{g}(\mathbf{q}) \tag{2.125}$$

exponentially stabilizes the tracking errors.

In Section 6.2.1, two explicit conditions are given for input-state feedback linearizability: the condition corresponding to a controllability test and the condition for involutivity [178, 92]. In the context of biological inspiration, a human neural control system always consists of sensory feedback control plus feedforward anticipatory control. Therefore, the exact canceling dynamics (e.g. $\mathbf{C}(\mathbf{q}, \dot{\mathbf{q}})\dot{\mathbf{q}} + \mathbf{g}(\mathbf{q})$ in the above control law) can be interpreted as feedforward anticipatory action. In this dissertation, an alternative form of a nonlinear tracking controller is extensively used, which was introduced in Section 2.5.5.

$$\mathbf{F} = \mathbf{M}(\mathbf{q})\ddot{\mathbf{q}}_r + \mathbf{C}(\mathbf{q}, \dot{\mathbf{q}})\dot{\mathbf{q}}_r + \mathbf{g}(\mathbf{q}) - \mathbf{K}(\dot{\mathbf{q}} - \dot{\mathbf{q}}_r) \tag{2.126}$$

where $\dot{\mathbf{q}}_r = \dot{\mathbf{q}}_d - \mathbf{\Lambda}\tilde{\mathbf{q}} = \dot{\mathbf{q}}_d - \mathbf{\Lambda}(\mathbf{q} - \mathbf{q}_d)$.

In the limiting case, both controls can be shown to be equivalent, even though the control in Section 2.5.5 avoids canceling the $\mathbf{C}(\mathbf{q}, \dot{\mathbf{q}})\dot{\mathbf{q}}$ term. For underactuated mechanical systems, full-state feedback linearization is not generally permitted. Instead, partial feedback linearization [187] can be applied with respect to a reduced set of variables (see the discussions in Chapter 6).

2.6.3 Control Lyapunov Function

The Control Lyapunov Function (CLF) is essentially a nonlinear control design that extends the Lyapunov's second (direct) method in Theorem 2.4.2 to a nonlinear system with the control input u. The method of using CLFs for nonlinear control lays a theoretical foundation for a large class of nonlinear control methodologies such as backstepping and Lyapunov redesign. In essence, first proposed by Sontag [184, 185], CLF refers to a closed-loop Lyapunov function using the control input u to ensure that the rate of a positive scalar function V is negative definite:

$$\dot{V} = \frac{\partial V}{\partial \mathbf{x}}[\mathbf{f}(\mathbf{x}) + \mathbf{g}(\mathbf{x})u] < 0 \tag{2.127}$$

In general, finding such a CLF is difficult. It can be shown that the existence of a CLF is equivalent to global asymptotic stabilizability [100].

2.6.4 Backstepping Design

Feedback linearization in Section 2.6.2 often leads to cancellations of useful nonlinearities. The recursive control design method called Backstepping [100] interlaces CLFs with the design of feedback control. One main advantage of backstepping lies in the fact that it avoids cancellations of useful nonlinearities. Moreover, the design flexibility of backstepping allows for additional nonlinear terms as a means of improving transient performance. In addition, its robust properties can easily be discussed along with a straightforward extension to adaptive backstepping [100]. Chapter 6 presents a backstepping nonlinear control design for the underactuated single tethered system, based upon the strict-feedback cascade normal form obtained by a particular nonlinear change of coordinates. The backstepping method is limited by the required triangular structure. Both strict-feedback and strict-feedforward systems are called "triangular" by analogy with linear systems. For example, in some incarnations of backstepping, the triangular structure arises from an assumption that the system is feedback linearizable [35].

2.6.5 Robust Nonlinear Control

The challenge of nonlinear control design is much more aggravated in the presence of uncertainties. The sliding control [178] is one popular nonlinear control methodology dealing with unstructured but bounded uncertainties such as disturbances and modeling imperfections. For structured uncertainties, it is preferred to use adaptive control in the next section. The following sliding controller can be defined for a system (2.10)

$$\tau = \hat{\mathbf{M}}\ddot{\mathbf{q}}_\mathbf{r} + \hat{\mathbf{C}}\dot{\mathbf{q}}_\mathbf{r} + \hat{\mathbf{g}} - \mathbf{K}\text{sgn}(\mathbf{s}) \tag{2.128}$$

where $\mathbf{K}$ is a positive diagonal matrix, and selected to be larger than the bounded uncertainty. Also, $\text{sgn}(\cdot)$ denotes a signum function. In Chapter 4, a decentralized sliding controller is introduced. The stability analysis, in conjunction with the modular nature of tethered spacecraft arrays, is presented.

Another robust control approach is Lyapunov redesign [92]. This method uses a Lyapunov function of a nominal system to design an additional control component that makes the design robust to matched uncertainties.

2.6.6 Adaptive Nonlinear Control

Robust control and adaptive control are two different approaches to the problem of inherent uncertainty in the nonlinear system: robust control attempts to design a fixed parameter controller that successfully performs in the presence of the worst-case errors in the model, while adaptive control dynamically adjusts its parameters to compensate for the initial model uncertainty or very slowly varying parameters. Hence, adaptive control [178, 169, 140, 141] is a natural choice when only parametric uncertainty exits. However, adaptive controllers do not have long term memory and hence do not "remember" the optimal control parameters corresponding to different configurations of the plant [140].

In this dissertation, the nonlinear adaptive controller was designed such that it can overcome model uncertainties including: tether length change, mass and inertia changes due to lack of precise modeling and inherent mass change due to thruster firing (see Section 4.4.2). The proposed nonlinear adaptive controller was able to adjust its control output by adapting to the reasonably slow tether length changes as well. More importantly, through its online tuning it was able to efficiently adapt to the rough and irregular surface of the NASA MSFC flat-floor (see the addition of the friction coefficients in the adaptive scheme in Chapter 7).

We consider the following adaptive control law for a Lagrangian system from (2.10):

$$\mathbf{F} = \mathbf{Y}\hat{\mathbf{a}} - \mathbf{K}\mathbf{s} = \hat{\mathbf{M}}(\mathbf{q})\ddot{\mathbf{q}}_\mathbf{r} + \hat{\mathbf{C}}(\mathbf{q},\dot{\mathbf{q}})\dot{\mathbf{q}}_\mathbf{r} + \hat{\mathbf{g}}(\mathbf{q}) - \mathbf{K}\mathbf{s} \tag{2.129}$$

where $\mathbf{s}$ denotes the composite variable $\mathbf{s} = \dot{\mathbf{q}} - \dot{\mathbf{q}}_r$.

The asymptotic convergence of the tracking error and parameter estimates can be proven using contraction analysis. Consider the closed-loop system with the parameter estimates update law $\dot{\hat{a}} = -\mathbf{\Gamma}\mathbf{Y}^T\mathbf{s}$:

$$\begin{bmatrix} \mathbf{M}(\mathbf{q}) & \mathbf{0} \\ \mathbf{0} & \mathbf{\Gamma}^{-1} \end{bmatrix} \begin{pmatrix} \dot{\mathbf{s}} \\ \dot{\tilde{\mathbf{a}}} \end{pmatrix} + \begin{bmatrix} \mathbf{C}(\mathbf{q},\dot{\mathbf{q}}) + \mathbf{K} & -\mathbf{Y} \\ \mathbf{Y}^T & \mathbf{0} \end{bmatrix} \begin{pmatrix} \mathbf{s} \\ \tilde{\mathbf{a}} \end{pmatrix} = \begin{pmatrix} \mathbf{0} \\ \mathbf{0} \end{pmatrix} \tag{2.130}$$

where $\hat{\mathbf{a}}$ denotes an estimate, and $\tilde{\mathbf{a}}$ denotes an error of the estimate such that $\tilde{\mathbf{a}} = \hat{\mathbf{a}} - \mathbf{a}$, while $\mathbf{a}$ is a constant vector of the true parameter values.

As shall be seen in Section 4.4.2, the above system has a positive semi-definite generalized Jacobian with $\mathbf{K} > 0$, thereby resulting in a semi-contracting system [112, 113]. Using Barbalat's lemma, the asymptotic convergence of $\mathbf{s}$ and $\tilde{\mathbf{a}}$ can be proven. It should be noted that the open loop dynamics of a multi-link robot are only passive for $\mathbf{F} - \mathbf{g}$ and the joint velocity $\dot{\mathbf{q}}$. To the contrary, the above adaptation law modifies the closed-loop dynamics such that the mapping $\mathbf{Y}^T\mathbf{s} \rightarrow \tilde{\mathbf{a}}$ is passive.

2.7 Concluding Remarks

This chapter has reviewed some principal nonlinear dynamics tools and control strategies used in the entire dissertation. In particular, we presented a unified treatment of the underlying characteristics of the particular forms of Lagrangians systems. For example, the nonlinear dynamics, with the positive definite inertia matrix, lead to a simplified stability result using contraction analysis. Our main nonlinear stability tool, contraction theory, provides a systematic method to reduce arbitrarily complex systems into simpler elements in the context of nonlinear control. It should be noted that combinations and accumulations of stable elements do not necessarily result in stable dynamics– further analysis is required, which is the focus of this dissertation.

Chapter 3

Dynamics of Tethered Formation Flight for NASA's SPECS Mission

3.1 Chapter Objective

The aim of the present chapter is to introduce the dynamics equations of planar motion of the tethered formation flying spacecraft considered in the entire thesis. The rationale behind the reduced dynamics modeling is that the symmetry of a spinning array can be exploited to decouple the in-plane rotational motions (aperture pupil plane) from the out-of-plane motions. In particular, the stability and controllability analyses, in conjunction with the compound pendulum modes of the tethered array, constitute the main contributions of this chapter.

This chapter is organized as follows: modeling of a single-tethered spacecraft that possesses an ideal tether is presented in Section 3.3 along with the key modeling assumptions. The same approach is extended to two-spacecraft systems in Section 3.4, and to arbitrarily large circular arrays of tethered spacecraft in Section 3.5. Section 3.6 expands the modeling of a three inline configuration. The dynamic models with flexible tethers are discussed in Section 3.7. This chapter also introduces modeling methods and control strategies for tethers with distributed mass in Section 3.8.

3.2 Reduction of 3D Dynamics to Planar Motion

This section briefly justifies our approach, which focuses on the spinning planar motions, by showing that the three-dimensional attitude dynamics of tethered formation flight can be decoupled into in-plane motions and out-of-plane motions.

3.2.1 Three-Dimensional Attitude Dynamics

Recall that the equations of the angular velocity vector $\vec{\omega}$ of a spacecraft in its body axes in (2.52) is:

$$\mathbf{H}\dot{\vec{\omega}} + \mathbf{H}\vec{\omega} \times \vec{\omega} = \tau, \tag{3.1}$$

which can be simplified assuming the body axes are along the principal axes of inertia of the rigid body. Figure 3-1 shows a three-spacecraft tethered array in the inline configuration. The simplified equations of the three identical spacecraft array at the center of mass of the spacecraft formation become:

$$\begin{bmatrix} J_1 & 0 & 0 \\ 0 & J_2 & 0 \\ 0 & 0 & J_3 \end{bmatrix} \begin{pmatrix} \dot{\omega}_1 \\ \dot{\omega}_2 \\ \dot{\omega}_3 \end{pmatrix} + \begin{bmatrix} 0 & -\omega_3 & \omega_2 \\ \omega_3 & 0 & -\omega_1 \\ -\omega_2 & \omega_1 & 0 \end{bmatrix} \begin{bmatrix} J_1 & 0 & 0 \\ 0 & J_2 & 0 \\ 0 & 0 & J_3 \end{bmatrix} \begin{pmatrix} \omega_1 \\ \omega_2 \\ \omega_3 \end{pmatrix} = \begin{pmatrix} \tau_1 \\ \tau_2 \\ \tau_3 \end{pmatrix} \tag{3.2}$$

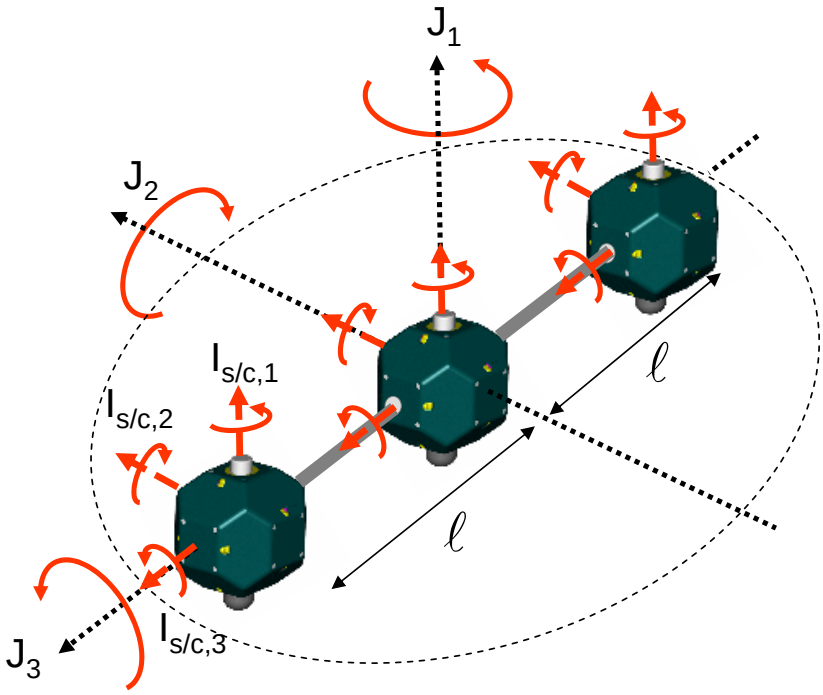

Figure 3-1: Decoupling of the in-plane rotational motions from the out-of-plane motions justifies our approach to reduce a 3-D attitude dynamics to a 2-D case.

where J_i with $i = 1, 2, 3$ is the moment of inertia of the tethered spacecraft array in Figure 3-1. This implies that $J_1 = I_{s/c,1} + 2(I_{s/c,1} + m\ell^2)$ for the vertical axis (axis 1), where $I_{s/c,1}$ denotes the moment of inertia of an individual spacecraft in the body frame, and ℓ is the radius of the array. For the second axis, J_2 is similarly defined as $J_2 = 3I_{s/c,2} + 2m\ell^2$.

For simplicity, let us assume that all relative angles between spacecraft are small (i.e., perfectly aligned). The first axis is perpendicular to the plane of rotation, defined by the second and third axes. Rotations about the second axis would characterize out-of-plane motions whereas the third axis lies along the tethers. If the individual spacecraft are axisymmetric, such that $I_{s/c,1} = I_{s/c,2}$, then the spacecraft array is also axisymmetric about the tether line (axis 3), resulting in

$$J_1 = J_2 = J = 3I_{s/c,1} + 2m\ell^2 = 3I_{s/c,2} + 2m\ell^2 \tag{3.3}$$

Hence, (3.2) reduces to

$$\begin{aligned} J\dot{\omega}_1 - (J - J_3)\omega_3\omega_2 &= \tau_1 \\ J\dot{\omega}_2 - (J - J_3)\omega_3\omega_1 &= \tau_2 \\ J_3\dot{\omega}_3 &= \tau_3 \end{aligned} \tag{3.4}$$

which indicates that the dynamics of a torsional rate ω_3 is completely decoupled from the other axes.

We can implement a simple control law τ_3 to regulate ω_3 and $\dot{\omega}_3$ to zero at all times. This further reduces the dynamics to

$$\begin{aligned} J\dot{\omega}_1 &= \tau_1 \\ J\dot{\omega}_2 &= \tau_2 \end{aligned} \tag{3.5}$$

which in turn corresponds to decoupling of the in-plane rotational dynamics (axis 1) from the out-

of-plane motions (axis 2).

Note that a similar reduction can be carried out for arbitrarily large circular arrays of tethered spacecraft. As a result, out-of-plane motions can be separately controlled by out-of-plane thruster firings without affecting the rotational dynamics of the array. This result agrees with the previous result [101] in the sense that out-of-plane libration motion of the tethered array is generally small and has less effect on the rotational motion than the in-plane motion. In the remainder of this chapter, we develop nonlinear equations of motion on this two-dimensional rotational plane (see Figure 3-1).

3.3 Single-Tethered System with Ideal Tether

The equations of motion of the single-tethered system shown in Figure 3-2 are presented here. A single-tethered system in this dissertation refers to a single-tethered spacecraft rotating with respect to some inertial frame. As shall be seen in the remainder of the thesis, the key motivation behind this modeling is to construct the dynamic model of a complex multiple tethered spacecraft system out of a simpler element- a single-tethered spacecraft model.

3.3.1 Importance of Compound Pendulum Mode

We pay particular attention to control of oscillations of the compound pendulum mode of tethered formation flight satellites. The representative work on tethered formation flight [94, 26, 27, 132, 144] does not include this mode, by assuming that the spacecraft can be regarded as a point mass with a long tether. However, it is indispensable to examine this mode because of the instability occurring while retracting the tether for spinning arrays. In other words, it is shown in Section 3.3.8 that the system goes unstable when the tether motor reels in ($\dot{\ell} < 0$).

The stability and controllability analyses, in conjunction with the compound pendulum modes of the tethered arrays, constitute the main contribution of this chapter. In addition, the dynamic modeling in this chapter facilitates the nonlinear spatial decoupling of multiple-spacecraft arrays; a decentralized control can be designed from the simple single-tether dynamics. The dynamics modeling also permits a relative and decentralized sensing mechanism for deep space formation flight.

3.3.2 Assumptions

1. The tether is assumed to be ideal– i.e., massless and inextensible.
   Hence, neither longitudinal nor transverse vibrations of the tether are allowed until otherwise noted in Sections 3.7 and 3.8. The zero mass assumption can be realized by rather strong thin material like Kevlar [14] to avoid a detrimental phenomenon such as the coupling between in-plane and out-plane oscillations of a more massive tether and the spacecraft attitude [18]. At this point, the tether of SPECS consists of four tether lines, each with an oblate flattened cross section [118]. It is estimated that the total mass of the 1-km-long ribbon tether will be less than 30 kg.

2. The array is assumed to always rotate at a certain angular rate.
   As a result, the tether is taut and straight at all times. A nonzero angular rotation [102] is a realistic assumption since tethered interferometers will attempt to provide a complete u-v coverage [42] by rotation.

3. For simplicity, the tether reels in and out only at constant speed.
   The speed of the tether motor can be easily pre-defined in the control code and does not constitute one of the system states. This tether velocity control has been successfully validated with the SPHERES testbed, as shown in Chapter 7.

4. The gravity term $V(\mathbf{q})$ is neglected under the assumption that a tethered formation array such as SPECS will operate in a very weak gravity field - e.g. the second Lagrangian point

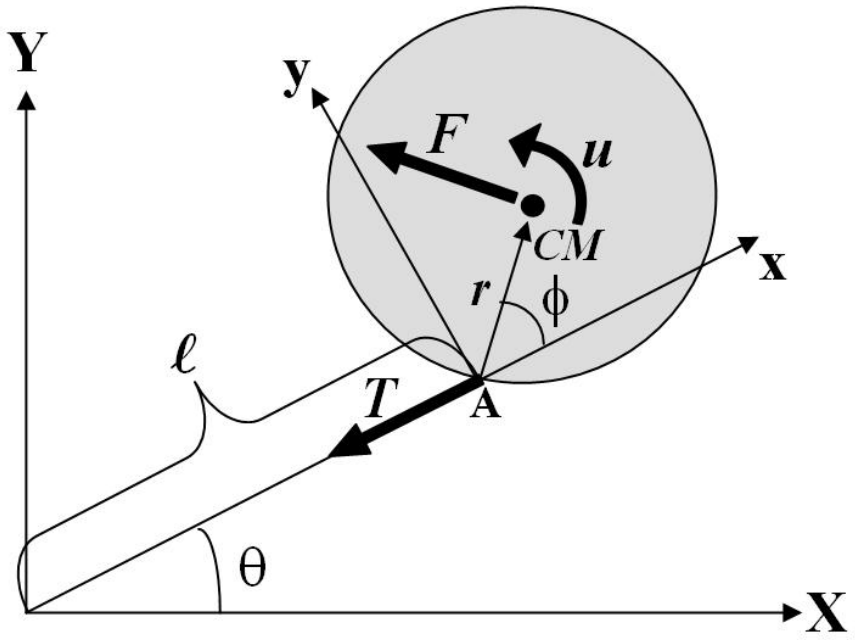

Figure 3-2: Free-body diagram of a revolving tether problem

L2 of the Earth-Sun system. The operation of tethered formation arrays in any kind of Earth orbit is not plausible due to expensive fuel consumption and unsatisfactory photon yield [94]. Operating at L2 also offers other advantages. For instance, this allows the tethered flight to be relatively undisturbed by gravity gradients avoiding significant wobbling of a spinning array. In addition, the L2 point provides a relatively unobstructed view of the sky and a lower thermal radiation background than low-Earth orbit, which facilitates cryo-cooling. More importantly, the thermal environment is less variable with the Sun remaining fixed with respect to the spacecraft. The L2 point is unstable on a time scale of approximately 23 days, which requires satellites parked at these positions to undergo regular course and attitude corrections. Control-wise, any additional un-modeled gravity is regarded as a low-frequency disturbance to the system.

5. The out-of-plane motion is eliminated because it can simply be decoupled from the in-plane dynamics (see Section 3.2.1). The out-of-plane is directly controllable by out-of-plane thruster firings. The out-of-plane libration motion of the tethered spacecraft is generally small and has less effect on the in-plane motion because the velocity it produces is orthogonal to the in-plane rotation velocity.

3.3.3 Newton-Euler Formulation

Figure 3-2 shows a single satellite revolving about the center of the fixed inertial axes X-Y. The body-fixed axes, x-y are chosen such that the y direction always coincides with the direction of increasing θ while the x direction is aligned with the tether. The notation T is the tension force in the tether, F is the force due to thruster firing, and u is the torque exerted on the CM by a Reaction Wheel Assembly (RWA).
The velocity and acceleration terms are expressed in the small x-y rotating frame with the corresponding unit directional vectors: e_x and e_y.

The velocity of the CM of the spacecraft is characterized as

$$v_B = [\dot{\ell} - r\sin\phi(\dot{\theta}+\dot{\phi})]e_x + [r\cos\phi(\dot{\theta}+\dot{\phi}) + \ell\dot{\theta}]e_y \tag{3.6}$$

The relationship between the absolute and relative acceleration is obtained by differentiating the relative velocity equation to get

$$a_B = a_A + \ddot{\theta} e_z \times r_{B/A} + \dot{\theta} e_z \times (\dot{\theta} e_z \times r_{B/A}) + 2\dot{\theta} e_z \times v_{B/A} + a_{B/A} \tag{3.7}$$

where A denotes the tether attachment point in Figure 3-2 (origin of the body axes).

Since the satellite is rotating in the x-y frame that is revolving around the center of the fixed inertial X-Y frame, we are observing the coriolis term ($2\dot{\theta} e_z \times v_{B/A}$) as well as the centrifugal acceleration ($\dot{\theta} e_z \times (\dot{\theta} e_z \times r_{B/A})$).

Each term in (3.7) is computed as

$$\begin{aligned}
a_A &= (-l\dot{\theta}^2 + \ddot{\ell})ex + (\ell\ddot{\theta} + 2\dot{\ell}\dot{\theta})e_y \\
\ddot{\theta} e_z \times r_{B/A} &= -r\sin\phi\ddot{\theta} e_x + r\cos\phi\ddot{\theta} e_y \\
\dot{\theta} e_z \times (\dot{\theta} e_z \times r_{B/A}) &= -r\cos\phi\dot{\theta}^2 e_x - r\sin\phi\dot{\theta}^2 e_y \\
2\dot{\theta} e_z \times v_{B/A} &= -2r\cos\phi\dot{\theta}\dot{\phi} e_x - 2r\sin\phi\dot{\theta}\dot{\phi} e_y \\
a_{B/A} &= (-r\ddot{\phi}\sin\phi - r\dot{\phi}^2\cos\phi)e_x + (r\ddot{\phi}\cos\phi - r\dot{\phi}^2\sin\phi)e_y
\end{aligned} \tag{3.8}$$

Let us assume for now that the tether length is fixed. This means that $a_A = (-\ell\dot{\theta}^2 + \ddot{\ell})e_x + (\ell\ddot{\theta} + 2\dot{\ell}\dot{\theta})e_y$ is reduced to $a_A = (-\ell\dot{\theta}^2)e_x + (\ell\ddot{\theta})e_y$.

Then, (3.7) becomes

$$\begin{aligned}
a_B = e_x[&-\ell\dot{\theta}^2 - r\sin\phi\ddot{\theta} - r\cos\phi\dot{\theta}^2 - 2r\cos\phi\dot{\theta}\dot{\phi} - r\ddot{\phi}\sin\phi - r\dot{\phi}^2\cos\phi] \\
+e_y[&(\ell + r\cos\phi)\ddot{\theta} - r\sin\phi\dot{\theta}^2 - 2r\sin\phi\dot{\theta}\dot{\phi} + r\ddot{\phi}\cos\phi - r\dot{\phi}^2\sin\phi]
\end{aligned} \tag{3.9}$$

The equations of the tethered system are derived using (3.9):

$$\begin{aligned}
\sum F_{e_x} &= -F_x - T = -F\sin\phi - T = ma_x \\
\sum F_{e_y} &= F_y = F\cos\phi = ma_y \\
\sum M_G &= -Tr\sin\phi + u = I_G(\ddot{\theta} + \ddot{\phi})
\end{aligned} \tag{3.10}$$

where M_G is the moment around CM and I_G denotes the moment of inertia around CM. In addition, a_x and a_y are the x and y acceleration components of (3.9), respectively.

Eliminating T results in the following differential equation:

$$[M(\phi)]\begin{pmatrix} \ddot{\theta} \\ \ddot{\phi} \end{pmatrix} + \left[C(\phi, \dot{\theta}, \dot{\phi})\right] = \begin{pmatrix} F\cos\phi \\ Fr + u \end{pmatrix} \tag{3.11}$$

where

$$\begin{aligned}
[M(\phi)] &= \begin{bmatrix} m\ell + mr\cos\phi & mr\cos\phi \\ I_G + mr^2 + mr\ell\cos\phi & I_G + mr^2 \end{bmatrix} \\
\left[C(\phi, \dot{\theta}, \dot{\phi})\right] &= \begin{bmatrix} -2mr\sin\phi\dot{\theta}\dot{\phi} - mr\sin\phi\dot{\theta}^2 - mr\sin\phi\dot{\phi}^2 \\ mr\ell\sin\phi\dot{\theta}^2 \end{bmatrix} = \begin{bmatrix} -mr\sin\phi(\dot{\theta} + \dot{\phi})^2 \\ mr\ell\sin\phi\dot{\theta}^2 \end{bmatrix}
\end{aligned} \tag{3.12}$$

When the tether motor reels in or out at a constant speed ($\dot{\ell}$ =constant), the force term in (3.11) becomes:

$$\begin{pmatrix} F \\ u \end{pmatrix} \Rightarrow \begin{pmatrix} F - 2m\dot{\ell}\dot{\theta} \\ u \end{pmatrix} \tag{3.13}$$

which can be used to investigate the effect of $\dot{\ell}$.

3.3.4 Euler-Lagrangian Formulation

The equations of motion with a constant tether length ($\dot{\ell} = 0$), can be derived by exploiting the Euler-Lagrange equations in (2.3):

$$\mathbf{M_1}(\phi)\begin{pmatrix}\ddot{\theta}\\ \ddot{\phi}\end{pmatrix} + \mathbf{C_1}(\phi,\dot{\theta},\dot{\phi})\begin{pmatrix}\dot{\theta}\\ \dot{\phi}\end{pmatrix} = \begin{pmatrix}\tau_\theta\\ \tau_\phi\end{pmatrix} \tag{3.14}$$

where

$$\begin{aligned}\mathbf{M_1}(\phi) &= \begin{bmatrix}m_{11}(\phi) & m_{12}(\phi)\\ m_{12}(\phi) & m_{22}\end{bmatrix} = \begin{bmatrix}I_r + m\ell^2 + 2mr\ell\cos\phi & I_r + mr\ell\cos\phi\\ I_r + mr\ell\cos\phi & I_r\end{bmatrix},\\ \mathbf{C_1}(\phi,\dot{\theta},\dot{\phi}) &= \begin{bmatrix}c_{11}(\phi,\dot{\phi}) & c_{12}(\phi,\dot{\theta},\dot{\phi})\\ c_{21}(\phi,\dot{\theta}) & c_{22}\end{bmatrix} = \begin{bmatrix}-mr\ell\sin\phi\dot{\phi} & -mr\ell\sin\phi(\dot{\theta}+\dot{\phi})\\ +mr\ell\sin\phi\dot{\theta} & 0\end{bmatrix}\end{aligned} \tag{3.15}$$

In the equations above, r, ℓ, and I_G denote the satellite's radius, tether length, and moment of inertia. Note that I_r is the moment of inertia about the tether attachment point A such that $I_r = I_G + mr^2$. Additionally, τ_θ and τ_ϕ denote a resultant torque about each angle ,θ and ϕ respectively, exerted by the control actuators (F and u).

Note that we can derive the same equation from the two-link manipulator dynamics in Section 2.3.1, by assuming the mass and moment of inertia of the first link are zero and gravity is absent. Compared to (3.11), Equation (3.14) has a simpler form of $\mathbf{C}(\phi,\dot{\theta},\dot{\phi})$, and the inertia matrix, $\mathbf{M_1}(\phi)$ is now symmetric.

It can be shown that Equations (3.11) and (3.14) are essentially the same since the first row of (3.11) times ℓ plus the second row of (3.11) is equal to the first row of (3.14). Hence, the external force and torque terms can be matched as follows:

$$\begin{pmatrix}\tau_\theta\\ \tau_\phi\end{pmatrix} = \begin{bmatrix}r + \ell\cos\phi & 1\\ r & 1\end{bmatrix}\begin{pmatrix}F\\ u\end{pmatrix} \tag{3.16}$$

where F is the linear force due to thruster firing, and u is the torque exerted on the CM of the satellite.

For the purpose of feedback control, the corresponding force and torque can be calculated from the inverse of (3.16):

$$\begin{pmatrix}F\\ u\end{pmatrix} = \frac{1}{\cos\phi}\begin{bmatrix}1 & -1\\ -r & r + \ell\cos\phi\end{bmatrix}\begin{pmatrix}\tau_\theta\\ \tau_\phi\end{pmatrix} \tag{3.17}$$

Now, as opposed to (3.14), let us assume that the tether reels in and out at constant speed such that $\dot{\ell}$=constant. We can exploit the relationship in (3.13) or reduce the full-order differential equation of (θ,ϕ,ℓ) in (3.63), using $\dot{\ell} = 0, \ddot{\ell} = 0$ Then, the governing equations of motion on the array rotational plane (aperture pupil plane) become

$$\mathbf{M_1}(\phi)\begin{pmatrix}\ddot{\theta}\\ \ddot{\phi}\end{pmatrix} + \mathbf{C_1}(\phi,\dot{\theta},\dot{\phi})\begin{pmatrix}\dot{\theta}\\ \dot{\phi}\end{pmatrix} + \begin{pmatrix}2m(r\cos\phi + \ell)\dot{\theta}\dot{\ell}\\ 2mr\cos\phi\dot{\theta}\dot{\ell}\end{pmatrix} = \begin{pmatrix}\tau_\theta\\ \tau_\phi\end{pmatrix} \tag{3.18}$$

where $\mathbf{M_1}(\phi)$ and $\mathbf{C_1}(\phi,\dot{\theta},\dot{\phi})$ are defined in (3.14).

It should be noted that we use the following particular definition of the $\mathbf{C_1}$ matrix [178] in both (3.14) and (3.18):

$$c_{ij} = \frac{1}{2}\sum_{k=1}^{n}\frac{\partial M_{ij}}{\partial q_k}\dot{q_k} + \frac{1}{2}\sum_{k=1}^{n}\left(\frac{\partial M_{ik}}{\partial q_j} - \frac{\partial M_{jk}}{\partial q_i}\right)\dot{q_k} \tag{3.19}$$

This implies that that $(\dot{\mathbf{M}}_\mathbf{1} - 2\mathbf{C_1})$ is skew-symmetric.

3.3.5 Nonlinear Phase Portrait and Relative Equilibria

In this section, we study graphically the nonlinear trajectories of (3.11) by plotting a phase portrait (also commonly called a phase plane). By looking at a phase portrait, stability and trajectory information from various initial conditions $(\phi(0), \dot{\phi}(0))$ are obtained. As shall be seen in the linearized model (Section 3.3.6) as well, the nonzero rotational rate, $\dot{\theta}$, adds a potential term to the dynamics, even in the absence of gravity. This artificial potential energy induced by array rotation makes the system controllable and stable [43]. This is especially true for large classes of underactuated systems (e.g. tethered systems with $F = 0$), which are neither controllable in the absence of potential energy nor fully feedback linearizable [145].

We can multiply (3.14) by the inverse of the inertia matrix, $\mathbf{M}$ to get the equation for $\ddot{\phi}$. We assume that the system rotates at a constant angular velocity ($\dot{\theta} = \omega$). Then, the homogeneous equation of ϕ results in the following second-order differential equation:

$$\frac{d}{dt}\begin{pmatrix}\phi\\ \dot{\phi}\end{pmatrix} = \begin{pmatrix}\dot{\phi}\\ -\frac{r\sin\phi}{\ell(I_G+mr^2(\sin^2\hat{\phi}))}\left[(I_r+mr\ell\cos\phi)(\dot{\theta}+\dot{\phi})^2+mr\ell\dot{\theta}^2\cos\phi+m\ell^2\dot{\theta}^2\right]\end{pmatrix} \tag{3.20}$$

Figure 3-3(a) shows a phase portrait of the nonlinear compound pendulum motion when the single tethered satellite revolves around the center of the inertial frame at a constant angular speed ($\dot{\theta} = \omega$). The following physical parameters are used: I_G=0.0213 kgm^2, m=4.5 kg; r=0.125 m; ω=0.3 rad/s; and ℓ=0.5 m. It correctly predicts a pendulum libration mode. When $\dot{\phi}$ is small enough, it oscillates in a closed circle or ellipse, which is a periodic orbit of the libration motion. However, a larger $\dot{\phi}$ results in the rotation of ϕ greater than 180 degrees. In reality, it will hit the tether when ϕ crosses π rad. Since ω is positive (counterclockwise) rotation, the maximum allowable value of $\dot{\phi}$, in order to remain in a closed orbit, is greater when $\dot{\phi}$ is positive (see Figure 3-3(a)).

To investigate the effect of different tether lengths and angular rotation speeds, several phase plots are constructed. Figure 3-3(b) shows a phase portrait with an increased angular velocity (ω=1.0 rad/s). We can see the region of a periodic orbit has been greatly expanded. A circular orbit becomes more elliptical toward the vertical $\dot{\phi}$ axis. A similar trend is observed when we increase the tether length ℓ, in Figures 3-3 (c) and (d).

There exist three equilibrium points in those phase portraits. Only $\phi = 0, \dot{\phi} = 0$ is a stable equilibrium. Along with the nominal array rotational rate, ω, the equilibria of (3.20) define the relative [35] equilibria of the spinning tethered array. Relative equilibria are commonly found in spinning rigid bodies with symmetries. For the case of the three-dimensional free rigid body, the body is in relative equilibrium if and only if its angular velocity and angular momentum align, that is, if the body rotates about one of its principal axes [79].

3.3.6 Linearization and Pendulum Mode Frequency

We linearize (3.14) about the relative equilibrium point with $\dot{\theta} = \omega$, $\phi = 0$, and $\dot{\phi} = 0$ where ω denotes a nominal angular rate. Each term can be linearized as follows:

$$mrl\sin(\phi)\dot{\theta}^2 \approx mrl\omega^2\phi, \quad mrl\sin(\phi)\dot{\phi}^2 \approx 0, \quad mrl\sin(\phi)\dot{\theta}\dot{\phi} \approx 0, \quad \cos\phi \approx 1 \tag{3.21}$$

The linearized equation of the motion is

$$\begin{bmatrix} I_G+m(r+\ell)^2 & I_G+mr(r+\ell)\\ I_G+mr(r+\ell) & I_G+mr^2\end{bmatrix}\begin{pmatrix}\ddot{\theta}\\ \ddot{\phi}\end{pmatrix}+\begin{bmatrix}0 & 0\\ 0 & mr\ell\omega^2\end{bmatrix}\begin{pmatrix}\theta\\ \phi\end{pmatrix}=\begin{pmatrix}\tau_\theta\\ \tau_\phi\end{pmatrix} \tag{3.22}$$

Similarly, we can linearize (3.11), and transformation between the two system equations is easily performed using (3.16).

It is observed that the nonzero rotational rate, ω adds a potential term to the dynamics even though there is no gravitational term in the model. This nonzero artificial potential energy, induced by the centripetal force associated with array rotation, plays a crucial role in making the system controllable and stable. This is especially true for underactuated systems with $F = 0$.

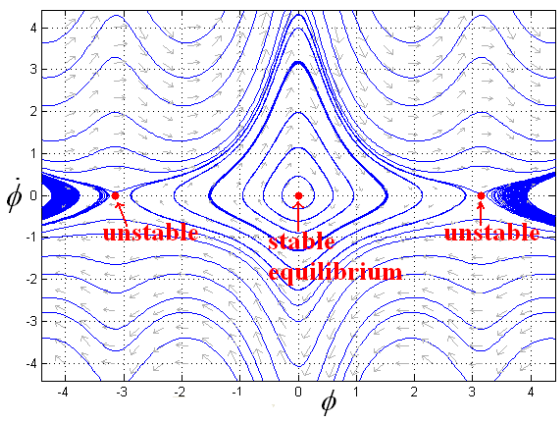

(a) ω=0.3 rad/s and ℓ=0.5 m

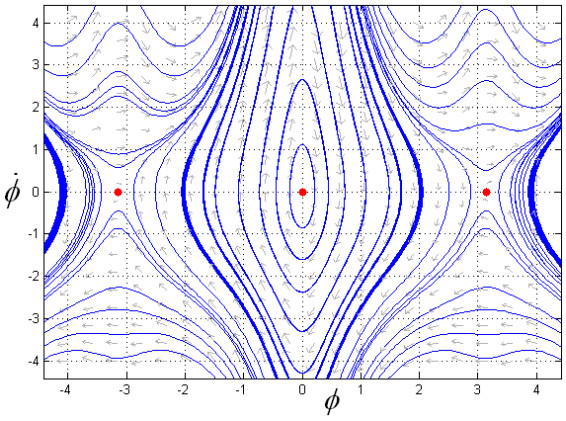

(b) ω=1.0 rad/s and ℓ=0.5 m

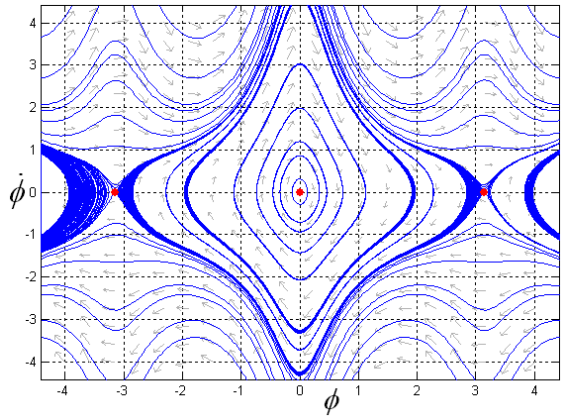

(c) ω=0.3 rad/s and ℓ=2.0 m

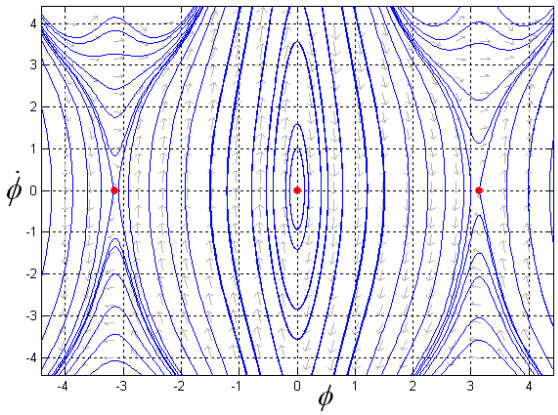

(d) ω=1.0 rad/s and ℓ=2.0 m

Figure 3-3: Phase portrait of (3.20). The dots indicate the relative equilibria. Units in rad (ϕ) and rad/s ($\dot{\phi}$).

A nice property about this linearized equation (3.22) is that we can decouple the equation for ϕ from that for θ. The first equation is merely the dynamics of a rigid body mode for θ.
Since the linearized inertia matrix $\mathbf{M_1}$ is invertible, we multiply both sides of (3.22) by the inverse of the $\mathbf{M_1}$ matrix and use the linearized relationship of (3.16):

$$\begin{pmatrix} \ddot{\theta} \\ \ddot{\phi} \end{pmatrix} + \begin{bmatrix} 0 & -\frac{r\omega^2\left(I_G+mr(r+\ell)\right)}{\ell I_G} \\ 0 & \frac{r\omega^2\left(I_G+m(r+\ell)^2\right)}{\ell I_G} \end{bmatrix} \begin{pmatrix} \theta \\ \phi \end{pmatrix} = \begin{bmatrix} \frac{1}{m\ell} & -\frac{r}{I_G\ell} \\ -\frac{1}{m\ell} & \frac{r+\ell}{I_G\ell} \end{bmatrix} \begin{pmatrix} F \\ u \end{pmatrix} \tag{3.23}$$

The second-order nonlinear equation of motion of ϕ from the second line of (3.23) becomes:

$$\ddot{\phi} + {\omega_\phi}^2 \phi = -\frac{1}{m\ell}F + \frac{r+\ell}{I_G\ell}u \tag{3.24}$$

where ω_ϕ is the frequency of the pendular libration mode:

$$\omega_\phi = \sqrt{\frac{r(I_G+m(r+\ell)^2)}{\ell I_G}}\omega = \sqrt{\frac{r(I_r+m\ell(2r+\ell))}{\ell I_G}}\omega \quad \text{[rad/s]} \tag{3.25}$$

Figures 3-4 (a) and (b) plot ω_ϕ as a function of ℓ and ω. Overall, the faster the array spins, the

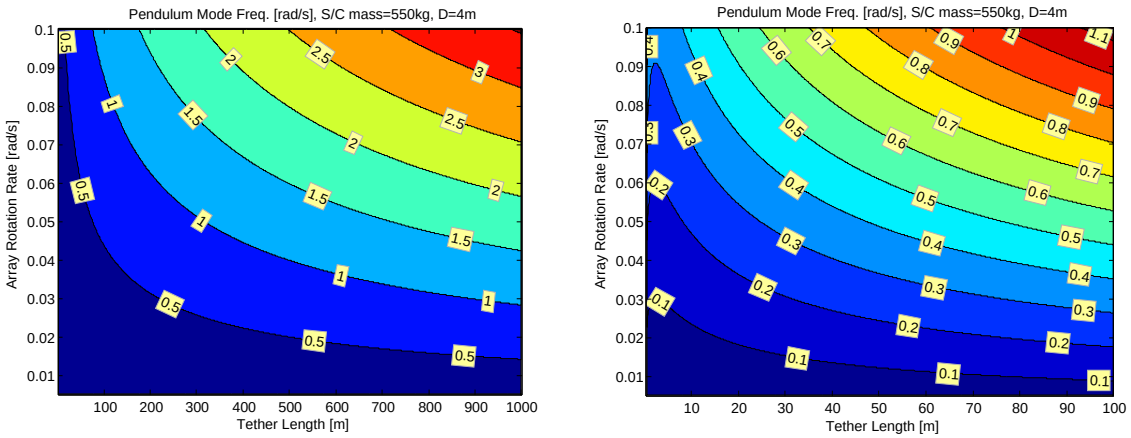

(a) natural frequency

(b) natural frequency

Figure 3-4: Contour plots of the pendulum mode frequency.

higher the pendulum mode frequency becomes. The tether length ℓ also increases the pendulum mode frequency past the minimum point (e.g., see the contour line of ω_ϕ=0.3 rad/s in Figure 3-4(b)).

3.3.7 Controllability Test

The linearized system for a single-tethered spacecraft, rotating at a constant rate $\dot{\theta} = \omega$, is derived from (3.23) in state-space form ($\dot{\vec{x}} = A\vec{x} + B\vec{u}$) as

$$\frac{d}{dt}\begin{pmatrix} \theta \\ \phi \\ \dot{\theta} \\ \dot{\phi} \end{pmatrix} = \begin{bmatrix} 0 & 0 & 1 & 0 \\ 0 & 0 & 0 & 1 \\ 0 & \frac{r\omega^2\left(I_G+mr(r+\ell)\right)}{\ell I_G} & 0 & 0 \\ 0 & -\frac{r\omega^2\left(I_G+m(r+\ell)^2\right)}{\ell I_G} & 0 & 0 \end{bmatrix} \begin{pmatrix} \theta \\ \phi \\ \dot{\theta} \\ \dot{\phi} \end{pmatrix} + \begin{bmatrix} 0 & 0 \\ 0 & 0 \\ \frac{1}{m\ell} & -\frac{r}{I_G\ell} \\ -\frac{1}{m\ell} & \frac{r+\ell}{I_G\ell} \end{bmatrix} \begin{pmatrix} F \\ u \end{pmatrix} \tag{3.26}$$

where the first matrix of the righthand side is the 4×4 system matrix A and the second is the 4×2 input matrix B. Note that θ is easily eliminated by removing the first column and the first row of the A matrix, thereby reducing the dimension to three.

We can check if the system is really controllable around the nominal points by computing the controllability matrix:

$$\mathcal{C} = \begin{bmatrix} B & AB & A^2B & A^3B \end{bmatrix} = \begin{bmatrix} 0 & 0 & \frac{1}{m\ell} & -\frac{r}{I_G\ell} \\ 0 & 0 & -\frac{1}{m\ell} & \frac{r+\ell}{I_G\ell} \\ \frac{1}{m\ell} & -\frac{r}{I_G\ell} & 0 & 0 \\ -\frac{1}{m\ell} & \frac{r+\ell}{I_G\ell} & 0 & 0 \end{bmatrix} \tag{3.27}$$

This matrix has full rank ($n = 4$). Hence, the system is fully controllable with u and F. In fact, all the states (θ,ϕ,$\dot{\theta}$,$\dot{\phi}$) are still controllable when only the torque generating actuator u is available

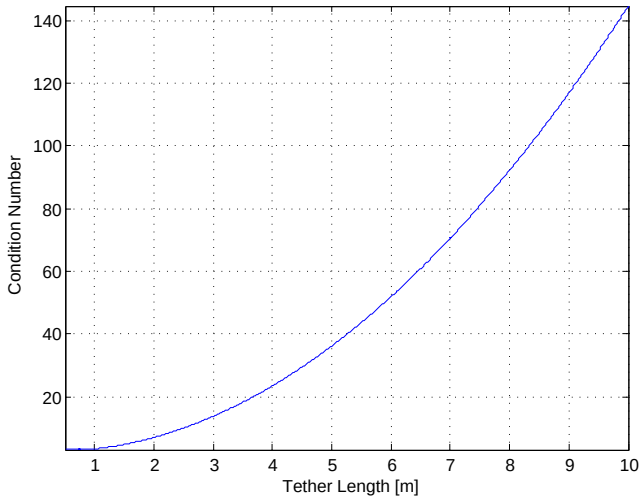

Figure 3-5: Condition number of the controllability matrix for the tethered SPHERE.

(e.g. RWA). The controllability matrix using the second column of B matrix in (3.26) becomes

$$\mathcal{C} = \begin{bmatrix} B_2 & AB_2 & A^2B_2 & A^3B_2 \end{bmatrix} \tag{3.28}$$
$$= \begin{bmatrix} 0 & -\frac{r}{I_G\ell} & 0 & \frac{r(r+\ell)\omega^2\left(I_G+mr(r+\ell)\right)}{\ell^2{I_G}^2} \\ 0 & \frac{r+\ell}{I_G\ell} & 0 & -\frac{r(r+\ell)\omega^2\left(I_G+m(r+\ell)^2\right)}{l^2{I_G}^2} \\ -\frac{r}{I_G\ell} & 0 & \frac{r(r+\ell)\omega^2\left(I_G+mr(r+\ell)\right)}{\ell^2{I_G}^2} & 0 \\ \frac{r+l}{I_G\ell} & 0 & -\frac{r(r+\ell)\omega^2\left(I_G+m(r+\ell)^2\right)}{\ell^2{I_G}^2} & 0 \end{bmatrix}$$

This is also a full rank ($n = 4$) matrix for any nonzero ω and tether length, ℓ. If its linear approximations in a closed connected region U are all controllable, then, under some mild smoothness assumptions, the nonlinear system can be driven from any point in U to any point in U [178]. Its implication to the control of tethered systems is significant: the tethered satellite systems are able to spin up and re-size the array without the use of propellant when operating around the relative equilibrium of a nominal array angular rate, $\dot{\theta} = \omega$. The underactuated controllers, introduced in Chapter 6, take advantage of this observation. It should be noted that the controllability matrix $\mathcal{C}$ tends to a singular matrix as the tether length ℓ tends to infinity. For example, Figure 3-5 plots the condition number of the controllability matrix using the physical parameters of the SPHERES testbed (see Chapter 7). This result implies that the underactuated system using only torque input becomes less controllable as the tether length increases.

3.3.8 Effect of Varying Tether Length

In the previous sections, the length of the tether is assumed to be invariant ($\dot{\ell} = 0$). The dynamics of the varying tether length with a constant motor reel-in/out speed ($\dot{\ell}$ =constant), is investigated in this section.

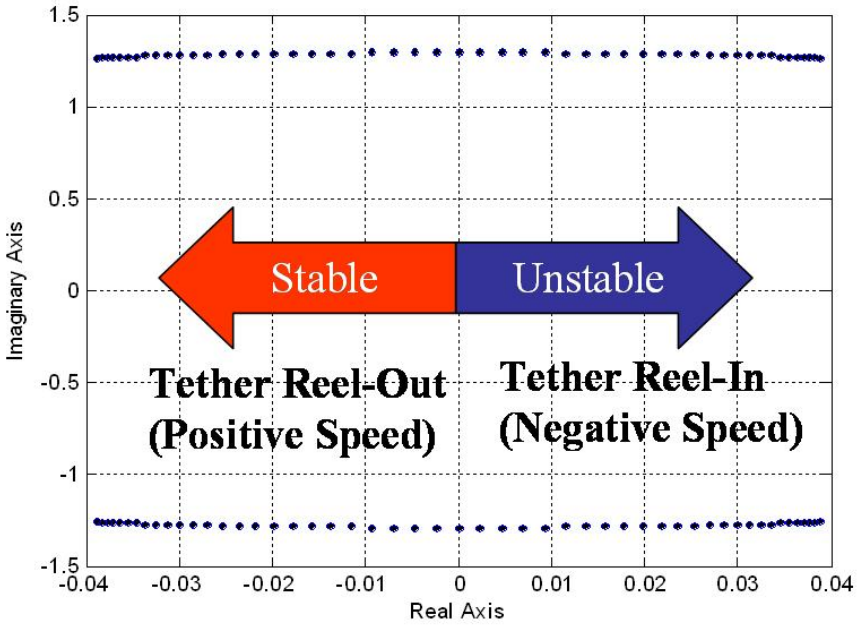

Figure 3-6: Poles of ϕ with -0.5m/s $< \dot{\ell} <$ 0.5m/s, ℓ=1m, ω=0.3rad/s.

Similar to Section 3.3.6, we linearize (3.18) for an array rotational rate, $\dot{\theta} = \omega$ as follows:

$$\begin{pmatrix} \ddot{\theta} \\ \ddot{\phi} \end{pmatrix} + \begin{bmatrix} 2\frac{\dot{\ell}}{\ell} & 0 \\ -2\frac{\dot{\ell}}{\ell} & 0 \end{bmatrix} \begin{pmatrix} \dot{\theta} \\ \dot{\phi} \end{pmatrix} + \begin{bmatrix} 0 & -\frac{r\omega^2\left(I_G+mr(r+\ell)\right)}{\ell I_G} \\ 0 & \frac{r\omega^2\left(I_G+m(r+\ell)^2\right)}{\ell I_G} \end{bmatrix} \begin{pmatrix} \theta \\ \phi \end{pmatrix} = \begin{bmatrix} \frac{1}{m\ell} & -\frac{r}{I_G\ell} \\ -\frac{1}{m\ell} & \frac{r+\ell}{I_G\ell} \end{bmatrix} \begin{pmatrix} F \\ u \end{pmatrix} \tag{3.29}$$

Hence, the following linearized equation (3.26) is obtained:

$$\frac{d}{dt}\begin{pmatrix} \theta \\ \phi \\ \dot{\theta} \\ \dot{\phi} \end{pmatrix} = \begin{bmatrix} 0 & 0 & 1 & 0 \\ 0 & 0 & 0 & 1 \\ 0 & \frac{r\omega^2\left(I_G+mr(r+\ell)\right)}{\ell I_G} & -2\frac{\dot{\ell}}{\ell} & 0 \\ 0 & -\frac{r\omega^2\left(I_G+m(r+\ell)^2\right)}{\ell I_G} & 2\frac{\dot{\ell}}{\ell} & 0 \end{bmatrix} \begin{pmatrix} \theta \\ \phi \\ \dot{\theta} \\ \dot{\phi} \end{pmatrix} + \begin{bmatrix} 0 & 0 \\ 0 & 0 \\ \frac{1}{m\ell} & -\frac{r}{I_G\ell} \\ -\frac{1}{m\ell} & \frac{r+\ell}{I_G\ell} \end{bmatrix} \begin{pmatrix} F \\ u \end{pmatrix} \tag{3.30}$$

Instead of showing the analytic solutions of the eigenvalues of (3.30) with zero F and u, a real-imaginary axis plot is presented as shown in Figure 3-6. It is noted that the system is stable when the motor reels out. In other words, a positive tether speed ($\dot{\ell} > 0$) results in damping of both $\dot{\theta}$ and pendulum motion of ϕ. However, we will see unstable states for a negative tether speed ($\dot{\ell} < 0$). In essence, we need a stabilizing controller (F,u) for the system with the tether length decreasing. It should be noted that the deployment operation ($\dot{\ell} > 0$) may also lead to system instability in the presence of orbital dynamics (gravity). For example, Kumar [101] found that the critical minimum value of spin rate in a gravity field is found to be 0.58 times the orbital rate. This indicates that the array spin rate should be fast enough to overcome the gravity effect in the deployment operation. Nonetheless, the retrieval motion is always unstable regardless of gravity.

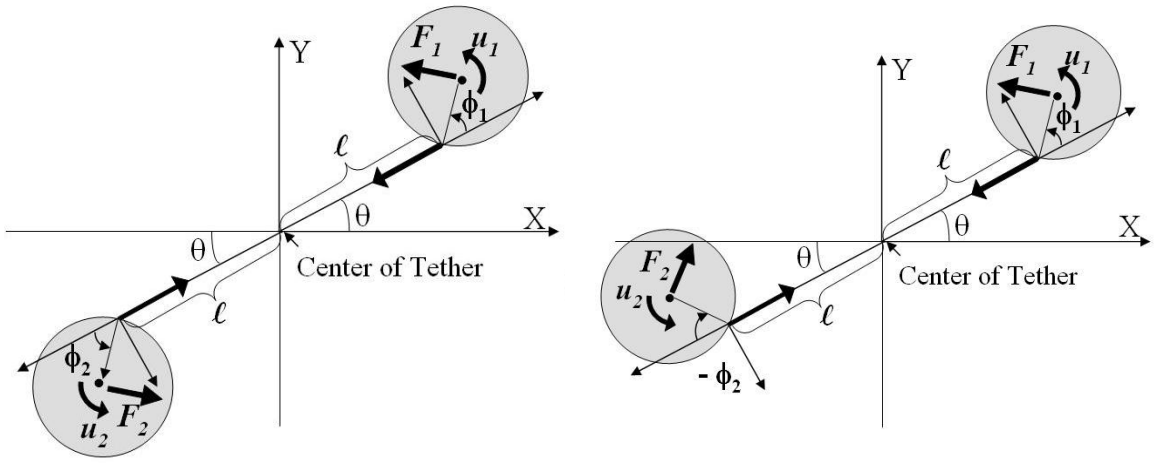

(a) Synchrony (b) Asynchrony

Figure 3-7: Free-body diagram of two tethered satellites.

Instability Proof by Lyapunov Function

The above linearization presents a conclusive result which is sufficient to determine the stability of the nonlinear tethered-array dynamics. However, we can also intuitively determine the nonlinear stability by inspecting the nonlinear dynamics in (3.18) and invoking the Lyapunov stability theorem.

The instability of $\dot{\theta}$ with $\dot{\ell} < 0$ is easily interpreted by the conservation of angular momentum. In other words, as the size of the array decreases, the angular rate of the array rotation increases. The term that is multiplied by $\dot{\theta}\dot{\ell}$ in (3.18) can be interpreted as the Coriolis torque in a rotating object, which exerts a force sideways, thereby exciting the pendulum mode and making the system unstable. Hence, $\dot{\ell} < 0$ adds negative damping, driving the system unstable. This can be proven by the instability theorem [178] which can be derived by the Lyapunov direct method in Chapter 2.

Consider the following positive Lyapunov function from (3.18),

$$V = \dot{\mathbf{q}}^T \mathbf{M_1}(\mathbf{q})\dot{\mathbf{q}} \qquad \text{with} \quad \mathbf{q} = \begin{pmatrix} \theta \\ \phi \end{pmatrix} \tag{3.31}$$

The rate of change of V for an unforced system can be found utilizing the skew symmetry of $\dot{\mathbf{M}}_\mathbf{1} - \mathbf{C_1}$:

$$\dot{V} = \dot{\mathbf{q}}^T \begin{pmatrix} -2m(r\cos\phi + \ell)\dot{\ell} & 0 \\ -2mr\cos\phi\dot{\ell} & 0 \end{pmatrix} \dot{\mathbf{q}} \tag{3.32}$$

which is positive definite around a sufficiently small $\dot{\phi} \approx 0$ and a nonzero $\dot{\theta} = \omega$ since

$$\dot{V} = 2m(r\cos\phi + \ell)(-\dot{\ell})\omega^2 > 0 \tag{3.33}$$

for $\dot{\ell} < 0$. Hence, the system goes unstable with $\dot{V} > 0$.

3.4 Two-Spacecraft Dynamics

The dynamics of two tethered satellites in the plane of rotation, shown in Figure 3-7, are derived using the Euler-Lagrangian equations. While the absolute position of the origin of the X-Y axes might translate in the 2-D plane, we will focus on the relative dynamics. Note that the origin coincides with the CM of the array when ϕ angles are in synchrony (in phase), as seen in Figure 3-7(a), and the CM of the array is controlled by a separate controller. The positive direction of both ϕ angles is defined as counterclockwise. The assumption that all spacecraft have identical size, mass

and inertia properties allows us to develop the following equations of motion:

$$\frac{d}{dt}\frac{\partial L(\mathbf{q},\dot{\mathbf{q}})}{\partial \dot{\mathbf{q}}} - \frac{\partial L(\mathbf{q},\dot{\mathbf{q}})}{\partial \mathbf{q}} = \tau \tag{3.34}$$

where the kinetic energy K is equal to the Lagrangian L in the absence of the potential energy V, and is defined as

$$\begin{aligned} K = &\frac{1}{2}m\left([r\sin\phi_1(\dot{\theta}+\dot{\phi}_1)]^2 + [r\cos\phi_1(\dot{\theta}+\dot{\phi}_1)+\ell\dot{\theta}]^2\right) \\ &+ \frac{1}{2}m\left([r\sin\phi_1(\dot{\theta}+\dot{\phi}_2)]^2 + [r\cos\phi_2(\dot{\theta}+\dot{\phi}_2)+\ell\dot{\theta}]^2\right) + \frac{1}{2}I_G(\dot{\theta}+\dot{\phi}_1)^2 + \frac{1}{2}I_G(\dot{\theta}+\dot{\phi}_2)^2. \end{aligned} \tag{3.35}$$

The equations of motion become

$$\mathbf{M_2}(\phi_1,\phi_2)\begin{pmatrix}\ddot{\theta}\\ \ddot{\phi}_1\\ \ddot{\phi}_2\end{pmatrix} + \mathbf{C_2}(\phi_1,\phi_2,\dot{\theta},\dot{\phi}_1,\dot{\phi}_2)\begin{pmatrix}\dot{\theta}\\ \dot{\phi}_1\\ \dot{\phi}_2\end{pmatrix} = \begin{pmatrix}\tau_{\theta,1}+\tau_{\theta,2}\\ \tau_{\phi,1}\\ \tau_{\phi,2}\end{pmatrix} \tag{3.36}$$

where

$$\begin{aligned} \mathbf{M_2} &= \begin{bmatrix} 2I_r + 2m\ell^2 + 2mr\ell\cos\phi_1 + 2mr\ell\cos\phi_2 & I_r + mr\ell\cos\phi_1 & I_r + mr\ell\cos\phi_2 \\ I_r + mr\ell\cos\phi_1 & I_r & 0 \\ I_r + mr\ell\cos\phi_2 & 0 & I_r \end{bmatrix}, \\ \mathbf{C_2}(\phi_1,\phi_2,\dot{\theta},\dot{\phi}_1,\dot{\phi}_2) &= \begin{bmatrix} c_{11}(\phi_1,\dot{\phi}_1) + c_{11}(\phi_2,\dot{\phi}_2) & c_{12}(\phi_1,\dot{\theta},\dot{\phi}_1) & c_{12}(\phi_2,\dot{\theta},\dot{\phi}_2) \\ c_{21}(\phi_1,\dot{\theta}) & c_{22} & 0 \\ c_{21}(\phi_2,\dot{\theta}) & 0 & c_{22} \end{bmatrix}, \\ \begin{pmatrix}\tau_{\theta,i}\\ \tau_{\phi,i}\end{pmatrix} &= \begin{bmatrix} r+\ell\cos\phi_i & 1 \\ r & 1 \end{bmatrix}\begin{pmatrix}F_i\\ u_i\end{pmatrix} \quad \text{for} \quad i=1,2 \end{aligned} \tag{3.37}$$

Also, c_{ij} is given in (3.14). Note that I_r is again defined as $I_r = I_G + mr^2$.

Similar to the single-tethered system, the following dynamics account for the Coriolis force due to the varying tether length ($\dot{\ell}$=constant).

$$\begin{aligned} &\mathbf{M_2}(\phi_1,\phi_2)\begin{pmatrix}\ddot{\theta}\\ \ddot{\phi}_1\\ \ddot{\phi}_2\end{pmatrix} + \mathbf{C_2}(\phi_1,\phi_2,\dot{\theta},\dot{\phi}_1,\dot{\phi}_2)\begin{pmatrix}\dot{\theta}\\ \dot{\phi}_1\\ \dot{\phi}_2\end{pmatrix} \\ &\qquad + \begin{pmatrix}2m(r\cos\phi_1 + r\cos\phi_2 + 2\ell)\dot{\theta}\dot{\ell}\\ 2mr\cos\phi_1\dot{\theta}\dot{\ell}\\ 2mr\cos\phi_2\dot{\theta}\dot{\ell}\end{pmatrix} = \begin{pmatrix}\tau_{\theta,1}+\tau_{\theta,2}\\ \tau_{\phi,1}\\ \tau_{\phi,2}\end{pmatrix} \end{aligned} \tag{3.38}$$

Since, ℓ is defined as the length of the tether from the origin to the spacecraft attachment point, the total tether length is now 2ℓ and $\dot{\ell}$ is half the rate of change of the total tether length. The array angular rate $\dot{\theta}$ is assumed to be the same for both satellites. This is especially true when the tether is in tension. Furthermore, the mass and inertia properties are assumed to be roughly the same. These geometric symmetry properties are pervasive in stellar interferometers where sub-telescopes must be identical for interferometric beam combining. This Lagrangian system is also kinetically symmetric with respect to θ since $\frac{\partial K}{\partial \theta} = 0$. In fact, the kinetic symmetry leads to the symmetry in mechanics [35] in the absence of a potential field, i.e. $\frac{\partial L}{\partial \theta} = 0$, which in turn corresponds to the conservation of the momentum ($\frac{\partial L}{\partial \dot{\theta}}$=constant) for an unforced system. Note that both the single and two spacecraft systems are symmetric in mechanics with respect to θ, thereby resulting in an inertia matrix that is independent of θ. This independent variable is often called an external variable [145].

Linearization and Controllability Analysis

We can also linearize the two-body dynamics in (3.36) with respect to the relative equilibrium, $\dot{\theta} = \omega$, $\phi_1 = 0$, $\dot{\phi}_1 = 0$, $\phi_2 = 0$, and $\dot{\phi}_2 = 0$:

$$\begin{pmatrix} \dot{\theta} \\ \dot{\phi}_1 \\ \dot{\phi}_2 \\ \ddot{\theta} \\ \ddot{\phi}_1 \\ \ddot{\phi}_2 \end{pmatrix} = \begin{bmatrix} 0 & 0 & 0 & 1 & 0 & 0 \\ 0 & 0 & 0 & 0 & 1 & 0 \\ 0 & 0 & 0 & 0 & 0 & 1 \\ 0 & \frac{r(I_r+mr\ell)\omega^2}{2I_G\ell} & \frac{r(I_r+mr\ell)\omega^2}{2I_G\ell} & 0 & 0 & 0 \\ 0 & -\frac{r\left((I_r+mr\ell)^2+2I_Gm\ell^2\right)\omega^2}{2I_GI_r\ell} & -\frac{r(I_r+mr\ell)^2\omega^2}{2I_GI_r\ell} & 0 & 0 & 0 \\ 0 & -\frac{r(I_r+mr\ell)^2\omega^2}{2I_GI_r\ell} & -\frac{r\left((I_r+mr\ell)^2+2I_Gm\ell^2\right)\omega^2}{2I_GI_r\ell} & 0 & 0 & 0 \end{bmatrix} \begin{pmatrix} \theta \\ \phi_1 \\ \phi_2 \\ \dot{\theta} \\ \dot{\phi}_1 \\ \dot{\phi}_2 \end{pmatrix} + \begin{bmatrix} 0 & 0 \\ 0 & 0 \\ 0 & 0 \\ -\frac{r}{2I_G\ell} & -\frac{r}{2I_G\ell} \\ \frac{1}{2}\left(\frac{r+\ell}{I_G\ell}+\frac{1}{I_r}\right) & \frac{r(I_r+mr\ell)}{2I_G\ell I_r} \\ \frac{r(I_r+mr\ell)}{2I_G\ell I_r} & \frac{1}{2}\left(\frac{r+\ell}{I_G\ell}+\frac{1}{I_r}\right) \end{bmatrix} \begin{pmatrix} u_1 \\ u_2 \end{pmatrix} \tag{3.39}$$

where only torque actuation (u_1, u_2) is shown.

It can also be shown that the controllability matrix yields a full rank of six, justifying the underactuated control approach that uses only reaction wheels. This result can also be extended to the case of $\dot{\ell}$=constant.

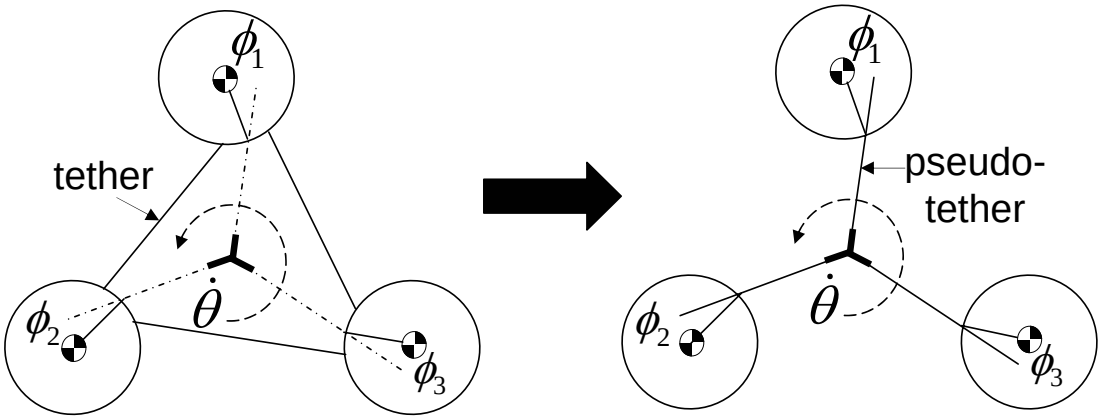

Figure 3-8: Triangular Configuration. The ϕ angles are measured between the attachment of the pseudo-tether and the CM of each spacecraft.

3.5 Triangular Array and Multiple Circular Arrays

The equations of motion of a three-spacecraft triangular configuration are derived in this section. Three imaginary pseudo-tethers [138], connecting each satellite to the CM of the array, are assumed to exist, replacing the three actual tether lines (see Figure 3-8). When the tethers are taut and straight in a rotating array, a small ϕ (angle of the compound pendulum mode) is approximated as a perturbed angle that the satellites make with respect to the corresponding pseudo-tether. Here, ℓ is defined as the length of the pseudo-tether; the actual tether length is then $L = \sqrt{3}(\ell + r) - 2r$. The original six degrees of freedom (ϕ and θ for each satellite) are reduced to four with addition of two rheonomic constraints,

$$\begin{aligned} L_{13} &= \sqrt{(x_{1a} - x_{3b})^2 + (y_{1a} - y_{3b})^2} \\ L_{12} &= \sqrt{(x_{1b} - x_{2a})^2 + (y_{1b} - y_{2a})^2} \end{aligned} \tag{3.40}$$

where

$$\begin{aligned} x_{ia} &= \ell \cos\theta_i + 2r \sin 15^\circ \cos(\theta_i - 75^\circ + \phi_i) \\ y_{ia} &= \ell \sin\theta_i + 2r \sin 15^\circ \sin(\theta_i - 75^\circ + \phi_i) \\ x_{jb} &= \ell \cos\theta_j + 2r \sin 15^\circ \cos(\theta_j + 75^\circ + \phi_j) \\ y_{jb} &= \ell \sin\theta_j + 2r \sin 15^\circ \sin(\theta_j + 75^\circ + \phi_j) \end{aligned} \tag{3.41}$$

for each i and j. In addition, x_{ia} and x_{jb} are x-coordinates of the tether attachment points, and y_{ia} and y_{jb} are similarly defined. The equations of motion of a three-spacecraft triangular array, approximated by the pseudo-tethers, are given as

$$\mathbf{M_3}(\mathbf{q}) \begin{pmatrix} \ddot{\theta} \\ \ddot{\phi}_1 \\ \ddot{\phi}_2 \\ \ddot{\phi}_3 \end{pmatrix} + \mathbf{C_3} \begin{pmatrix} \dot{\theta} \\ \dot{\phi}_1 \\ \dot{\phi}_2 \\ \dot{\phi}_3 \end{pmatrix} + \begin{pmatrix} 2m(\sum_{k=1}^{n} r\cos\phi_k + \ell)\dot{\theta}\dot{\ell} \\ 2mr\cos\phi_1\dot{\theta}\dot{\ell} \\ 2mr\cos\phi_2\dot{\theta}\dot{\ell} \\ 2mr\cos\phi_3\dot{\theta}\dot{\ell} \end{pmatrix} = \begin{pmatrix} \sum_{k=1}^{n=3} \tau_{\theta,k} \\ \tau_{\phi,1} \\ \tau_{\phi,2} \\ \tau_{\phi,3} \end{pmatrix} \tag{3.42}$$

where

$$\mathbf{M_3} = \begin{bmatrix} \sum_{k=1}^{n=3} m_{11}(\phi_k) & m_{12}(\phi_1) & m_{12}(\phi_2) & m_{12}(\phi_3) \\ m_{12}(\phi_1) & m_{22} & 0 & 0 \\ m_{12}(\phi_2) & 0 & m_{22} & 0 \\ m_{12}(\phi_3) & 0 & 0 & m_{22} \end{bmatrix}, \tag{3.43}$$

$$\mathbf{C_3} = \begin{bmatrix} \sum_{k=1}^{n=3} c_{11}(\phi_k, \dot{\phi_k}) & c_{12}(\phi_1, \dot{\theta}, \dot{\phi_1}) & c_{12}(\phi_2, \dot{\theta}, \dot{\phi_2}) & c_{12}(\phi_n, \dot{\theta}, \dot{\phi_n}) \\ c_{21}(\phi_1, \dot{\theta}) & c_{22} & 0 & 0 \\ c_{21}(\phi_2, \dot{\theta}) & 0 & c_{22} & 0 \\ c_{21}(\phi_3, \dot{\theta}) & 0 & 0 & c_{22} \end{bmatrix}$$

When linearized, the system has four eigenvalues, two of which are anti-synchrony modes. Eigenvalues for the triangular array ($n = 3$) are

$$0, \quad \sqrt{\frac{r(I_r + m\ell(2r+\ell))}{lI_G}}\omega \ , \quad \sqrt{\frac{mr\ell}{I_r}}\omega, \quad \sqrt{\frac{mr\ell}{I_r}}\omega \tag{3.44}$$

.

We can generalize (3.42) for a spinning array consisting of an arbitrary number of spacecraft whose circumferential spacing is uniform:

$$\mathbf{M_n(q)} \begin{pmatrix} \ddot{\theta} \\ \ddot{\phi_1} \\ \ddot{\phi_2} \\ \vdots \\ \ddot{\phi_n} \end{pmatrix} + \mathbf{C_n} \begin{pmatrix} \dot{\theta} \\ \dot{\phi_1} \\ \dot{\phi_2} \\ \vdots \\ \dot{\phi_n} \end{pmatrix} + \begin{pmatrix} 2m(\sum_{k=1}^{n} r\cos\phi_k + \ell)\dot{\theta}\dot{\ell} \\ 2mr\cos\phi_1\dot{\theta}\dot{\ell} \\ 2mr\cos\phi_2\dot{\theta}\dot{\ell} \\ \vdots \\ 2mr\cos\phi_n\dot{\theta}\dot{\ell} \end{pmatrix} = \begin{pmatrix} \sum_{k=1}^{n} \tau_{\theta,k} \\ \tau_{\phi,1} \\ \tau_{\phi,2} \\ \vdots \\ \tau_{\phi,n} \end{pmatrix} \tag{3.45}$$

where

$$\mathbf{M_n} = \begin{bmatrix} \sum_{k=1}^{n} m_{11}(\phi_k) & m_{12}(\phi_1) & m_{12}(\phi_2) & \dots & m_{12}(\phi_n) \\ m_{12}(\phi_1) & m_{22} & 0 & \dots & 0 \\ m_{12}(\phi_2) & 0 & m_{22} & \dots & 0 \\ \vdots & 0 & 0 & \ddots & 0 \\ m_{12}(\phi_n) & 0 & 0 & 0 & m_{22} \end{bmatrix}, \tag{3.46}$$

$$\mathbf{C_n} = \begin{bmatrix} \sum_{k=1}^{n} c_{11}(\phi_k, \dot{\phi_k}) & c_{12}(\phi_1, \dot{\theta}, \dot{\phi_1}) & c_{12}(\phi_2, \dot{\theta}, \dot{\phi_2}) & \dots & c_{12}(\phi_n, \dot{\theta}, \dot{\phi_n}) \\ c_{21}(\phi_1, \dot{\theta}) & c_{22} & 0 & \dots & 0 \\ c_{21}(\phi_2, \dot{\theta}) & 0 & c_{22} & \dots & 0 \\ \vdots & 0 & 0 & \ddots & 0 \\ c_{21}(\phi_n, \dot{\theta}) & 0 & 0 & 0 & c_{22} \end{bmatrix}$$

Equation (3.45) originally represents the dynamics of arbitrarily large star arrays (hub-spoke configurations) with the radius ℓ as shown in the second row of Figure 3-9. Hence, the same controller designed from the single-tethered system will stabilize a star network. This method can be extended to an arbitrarily large circular array of tethered spacecraft if the dynamics equation can be represented as the form in (3.45). This is automatically true for $n = 3$. However, we need more constraints for (3.45) to approximate a circular array of $n \geq 4$ since the lengths of the pseudo-tethers (ℓ) or diagonal distances can be different. For spinning tethered arrays, thruster firings in the radial direction can control the diagonal distances to keep the pseudo tether length ℓ the same. In the absence of such control, we can add more diagonal tethers, as seen in the hexagonal array in Figure 3-9. The circular geometry, in a non-hub-spoke connectivity, is not the minimum energy (maximum inertia)

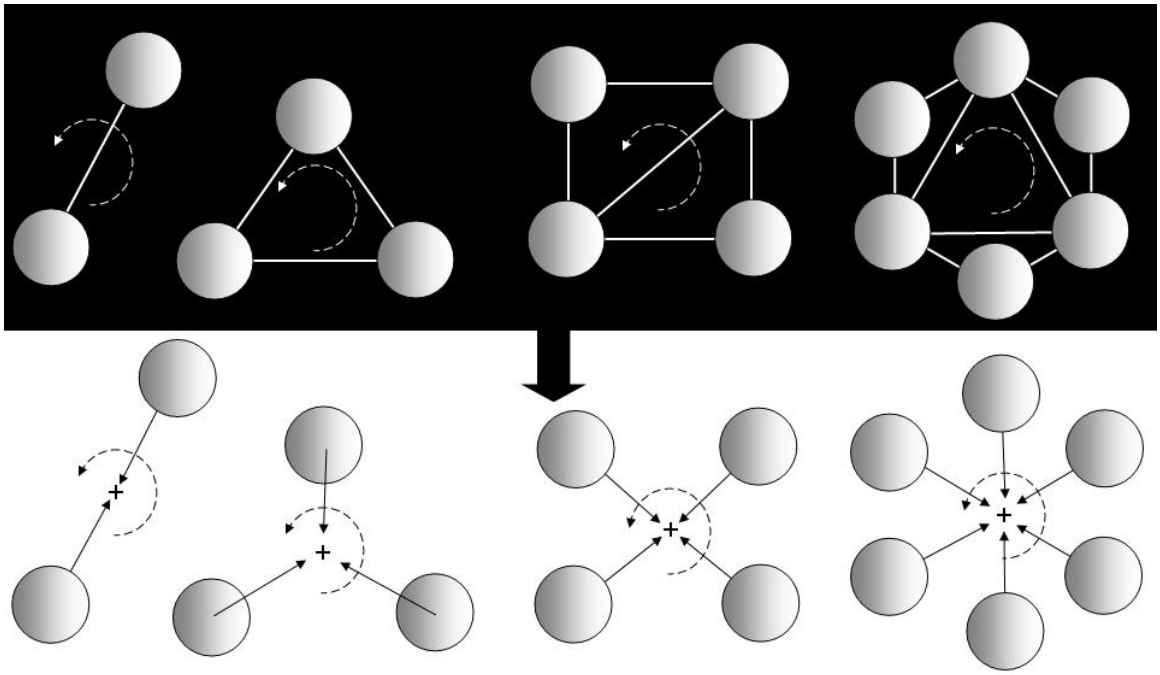

Figure 3-9: Reduction of circular and star arrays of tethered spacecraft into multiple single-tethered systems

geometry. The number of additional tethers required for an array with n spacecraft is

$$\begin{aligned} \mathbf{3n}(=\text{DOF}) - \mathbf{n}(=\text{number of tethers}) - \mathbf{2}(\text{CM x,y}) \\ -(\mathbf{n}+\mathbf{1})(=\text{No. of variables}) \\ = \mathbf{n}-\mathbf{3} \end{aligned} \tag{3.47}$$

As shall be seen in Chapter 4, under the reasonable assumption of the taut and equal-length pseudo-tether, a controller designed from a single-tethered system will synchronize both array spin rate and oscillations of each spacecraft, thereby reducing the original dynamics to those of a single-tethered spacecraft, as seen in Figure 3-9.

3.6 Three Inline Configuration

The equations of motion of the three-spacecraft inline configuration in Figure 3-10 are developed using the Euler-Lagrange equations of motion. We show herein that the definition of the generalized coordinates, θ_1 and θ_2, largely affects the complexity of the dynamic equations. We first begin with the more complex form. One might define θ_1 and θ_2 with respect to ψ as relative angles (see Figure 3-10). For simplicity, we assume the tether length is fixed. We can later add the fully coupled dynamics of the tether ℓ, as discussed in Section 3.7. Alternatively, ℓ dynamics can be eliminated by assuming $\dot{\ell}$ is constant (the tether is changing its length at a constant speed) as in the previous sections.

Since we assume that the gravity term is negligible, the Lagrangian is defined as

$$L(\mathbf{q},\dot{\mathbf{q}}) = K(\mathbf{q},\dot{\mathbf{q}}) - V(\mathbf{q}) = K(\mathbf{q},\dot{\mathbf{q}}) = \frac{1}{2}\dot{\mathbf{q}}^T\mathbf{M}(\mathbf{q})\dot{\mathbf{q}} \tag{3.48}$$

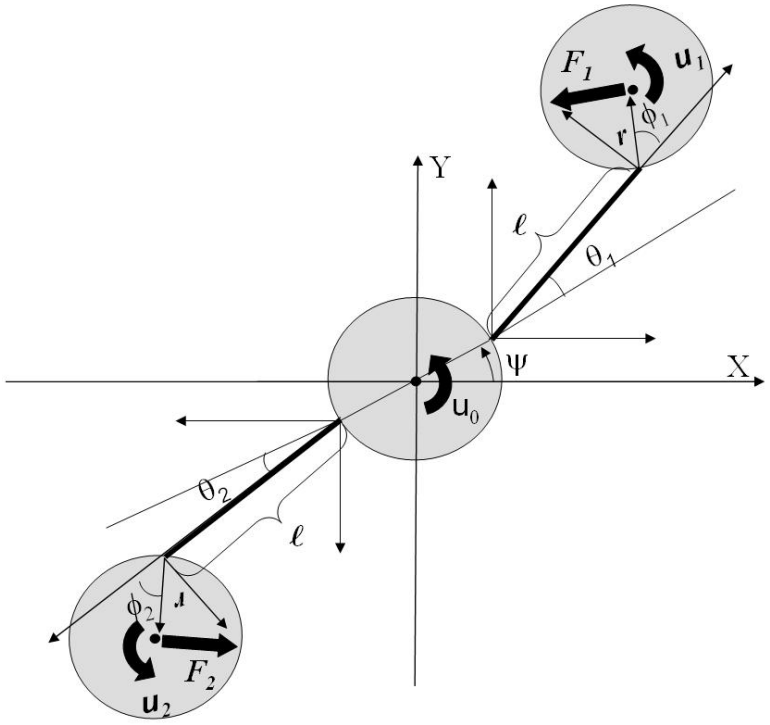

Figure 3-10: Free-body diagram with θ_1 and θ_2 defined as relative angles

where $\mathbf{q} = (\psi \quad \theta_1 \quad \phi_1 \quad \theta_2 \quad \phi_2)^T$ and K is defined as the summation of the kinetic energy of the three spacecraft:

$$K(\mathbf{q}, \dot{\mathbf{q}}) = K_1 + K_2 + \frac{1}{2} I_G \dot{\psi}^2 \tag{3.49}$$

with

$$\begin{aligned} K_1 = \frac{1}{2} I_G (\dot{\psi} + \dot{\theta}_1 + \dot{\phi}_1)^2 + \frac{1}{2} m \Big(r\dot{\psi} + \ell \cos\theta_1 (\dot{\theta}_1 + \dot{\psi}) + r \cos(\theta_1 + \phi_1)(\dot{\theta}_1 + \dot{\psi} + \dot{\phi}_1) \Big)^2 \\ + \frac{1}{2} m \Big(-\ell \sin\theta_1 (\dot{\theta}_1 + \dot{\psi}) - r \sin(\theta_1 + \psi_1)(\dot{\theta}_1 + \dot{\psi} + \dot{\phi}_1) \Big)^2 \\ K_2 = \frac{1}{2} I_G (\dot{\psi} + \dot{\theta}_2 + \dot{\phi}_2)^2 + \frac{1}{2} m \Big(r\dot{\psi} + \ell \cos\theta_2 (\dot{\theta}_2 + \dot{\psi}) + r \cos(\theta_2 + \phi_2)(\dot{\theta}_2 + \dot{\psi} + \dot{\phi}_2) \Big)^2 \\ + \frac{1}{2} m \Big(-\ell \sin\theta_2 (\dot{\theta}_2 + \dot{\psi}) - r \sin(\theta_2 + \psi_2)(\dot{\theta}_2 + \dot{\psi} + \dot{\phi}_2) \Big)^2. \end{aligned} \tag{3.50}$$

Alternatively, using the inertia matrix, $L = K$ is represented as

$$K(\mathbf{q}, \dot{\mathbf{q}}) = \frac{1}{2} \begin{pmatrix} \dot{\psi} \\ \dot{\theta}_1 \\ \dot{\phi}_1 \\ \dot{\theta}_2 \\ \dot{\phi}_2 \end{pmatrix}^T \begin{bmatrix} M_{11} & M_{12} & M_{13} & M_{14} & M_{15} \\ M_{12} & & & 0 & 0 \\ M_{13} & & \mathbf{M_1}(\phi_1) & 0 & 0 \\ M_{14} & 0 & 0 & & \\ M_{15} & 0 & 0 & \mathbf{M_1}(\phi_2) & \end{bmatrix} \begin{pmatrix} \dot{\psi} \\ \dot{\theta}_1 \\ \dot{\phi}_1 \\ \dot{\theta}_2 \\ \dot{\phi}_2 \end{pmatrix} \tag{3.51}$$

where the 2×2 matrix, $\mathbf{M_1}(\phi_1)$, is from the single-tethered dynamics in Figure 3-2 and (3.14):

$$\mathbf{M_1}(\phi) = \begin{bmatrix} m_{11}(\phi) & m_{12}(\phi) \\ m_{12}(\phi) & m_{22} \end{bmatrix} = \begin{bmatrix} I_r + m\ell^2 + 2mr\ell\cos\phi & I_r + mr\ell\cos\phi \\ I_r + mr\ell\cos\phi & I_r \end{bmatrix}$$

In addition,

$$
\begin{aligned}
M_{11} &= 3I_G + 2m\ell^2 + 4mr^2 + 2mr\ell(\cos\theta_1 + \cos\theta_2 + \cos\phi_1 + \cos\phi_2) \\
&\quad + 2mr^2\left(\cos\left(\theta_1+\phi_1\right) + \cos\left(\theta_2+\phi_2\right)\right), \\
M_{12} &= I_G + m\ell^2 + mr^2 + mr^2\cos\left(\theta_1+\phi_1\right) + mr\ell(\cos\theta_1 + 2\cos\phi_1), \\
M_{13} &= I_G + mr^2 + mr\ell\cos\phi_1 + mr^2\cos\left(\theta_1+\phi_1\right), \\
M_{14} &= I_G + m\ell^2 + mr^2 + 2mr\ell\cos\phi_2 + mr\ell\cos\theta_2 + mr^2\cos\left(\theta_2+\phi_2\right), \\
M_{15} &= I_G + mr^2 + mr\ell\cos\phi_2 + mr^2\cos\left(\theta_2+\phi_2\right) \\
I_r &= I_G + mr^2.
\end{aligned}
$$

Using the Euler-Lagrange equations, we can find that

$$
\frac{d}{dt}\frac{\partial L(\mathbf{q},\dot{\mathbf{q}})}{\partial\dot{\mathbf{q}}} - \frac{\partial L(\mathbf{q},\dot{\mathbf{q}})}{\partial\mathbf{q}} = \tau \tag{3.52}
$$

which results in the following equations of motion.

$$
\begin{bmatrix}
M_{11} & M_{12} & M_{13} & M_{14} & M_{15} \\
M_{12} & \multicolumn{2}{c}{\multirow{3}{*}{$\mathbf{M_1}(\phi_1)$}} & 0 & 0 \\
M_{13} & & & 0 & 0 \\
M_{14} & 0 & 0 & \multicolumn{2}{c}{\multirow{2}{*}{$\mathbf{M_1}(\phi_2)$}} \\
M_{15} & 0 & 0 & &
\end{bmatrix}
\begin{pmatrix} \ddot{\psi} \\ \ddot{\theta}_1 \\ \ddot{\phi}_1 \\ \ddot{\theta}_2 \\ \ddot{\phi}_2 \end{pmatrix} +
$$

$$
\begin{bmatrix}
C_{11} & C_{12} & C_{13} & C_{14} & C_{15} \\
C_{21} & \multicolumn{2}{c}{\multirow{3}{*}{$\mathbf{C_1}(\phi_1,\dot{\theta}_1,\dot{\phi}_1)$}} & 0 & 0 \\
C_{31} & & & 0 & 0 \\
C_{41} & 0 & 0 & \multicolumn{2}{c}{\multirow{2}{*}{$\mathbf{C_1}(\phi_2,\dot{\theta}_2,\dot{\phi}_2)$}} \\
C_{51} & 0 & 0 & &
\end{bmatrix}
\begin{pmatrix} \dot{\psi} \\ \dot{\theta}_1 \\ \dot{\phi}_1 \\ \dot{\theta}_2 \\ \dot{\phi}_2 \end{pmatrix} =
\begin{pmatrix} \tau_\psi \\ \tau_{\theta_1} \\ \tau_{\phi_1} \\ \tau_{\theta_2} \\ \tau_{\phi_2} \end{pmatrix} \tag{3.53}
$$

where $\mathbf{C_1}(\phi,\theta,\dot{\phi})$ is from the single-tethered dynamics in Figure 3-2 and (3.14):

$$
\mathbf{C_1}(\phi,\dot{\theta},\dot{\phi}) = \begin{bmatrix} c_{11}(\phi,\dot{\phi}) & c_{12}(\phi,\dot{\theta},\dot{\phi}) \\ c_{21}(\phi,\dot{\theta}) & c_{22} \end{bmatrix} = \begin{bmatrix} -mr\ell\sin\phi\dot{\phi} & -mr\ell\sin\phi(\dot{\theta}+\dot{\phi}) \\ +mr\ell\sin\phi\dot{\theta} & 0 \end{bmatrix}. \tag{3.54}
$$

Recalling $\dot{\mathbf{M}}(\mathbf{q}) = \mathbf{C}(\mathbf{q},\dot{\mathbf{q}}) + \mathbf{C}(\mathbf{q},\dot{\mathbf{q}})^T$ due to the symmetry of $\mathbf{M}(\mathbf{q})$ and skew-symmetry of $\mathbf{M}(\mathbf{q}) - 2\mathbf{C}(\mathbf{q},\dot{\mathbf{q}})$, we can easily calculate C_{ij} such that

$$
\dot{M}_{11} = 2C_{11},\ \dot{M}_{12} = C_{12}+C_{21},\ \dot{M}_{13} = C_{13}+C_{31},\ \dot{M}_{14} = C_{14}+C_{41},\ \text{and}\ \dot{M}_{15} = C_{15}+C_{51}. \tag{3.55}
$$

We show that these equations can be greatly simplified by a different coordinate definition of θ, e.g., θ defined with respect to the rotating frame of the center spacecraft ($\theta \to \theta + \psi$) as shown in Figure 3-11. Moreover, this definition of the generalized coordinates enables decoupling of the dynamics of the outlying spacecraft from the center spacecraft. As shall be seen in Chapter 4, the dynamics of the three-spacecraft inline configuration in Figure 3-11 can be decoupled into two independent dynamics of the single-tethered system with the tether length ℓ and the rotational dynamics of the center spacecraft.

The equations of motion of the inline array dynamics in Figure 3-11 are developed using the Euler-Lagrange equations of motion. The Lagrangian $L = K$ in the absence of the potential energy

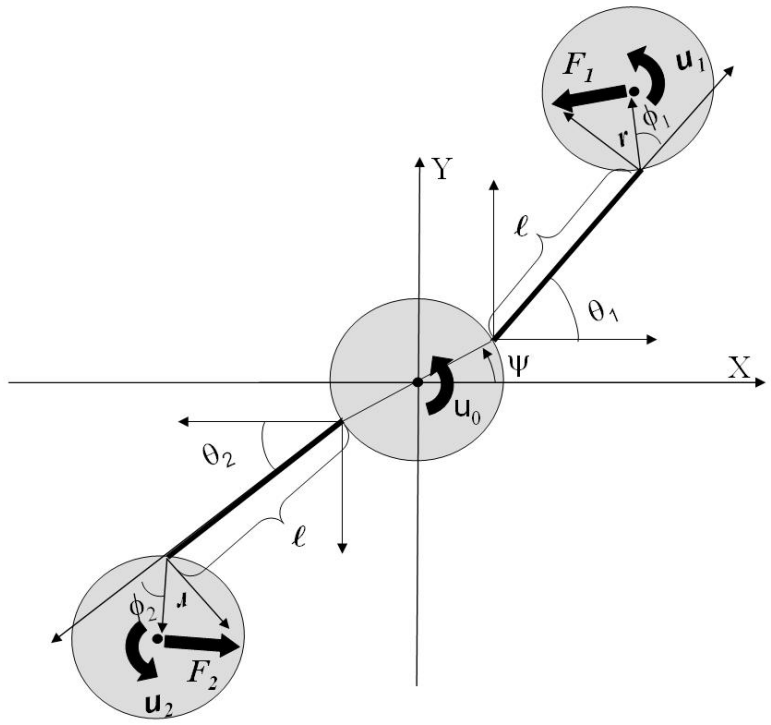

Figure 3-11: Three-spacecraft array θ_1 and θ_2 defined from the center reference frame

is defined as

$$K(\mathbf{q},\dot{\mathbf{q}}) = \frac{1}{2}\begin{pmatrix}\dot{\psi}\\ \dot{\theta}_1\\ \dot{\phi}_1\\ \dot{\theta}_2\\ \dot{\phi}_2\end{pmatrix}^T \begin{bmatrix} M_{11} & M_{12} & M_{13} & M_{14} & M_{15}\\ M_{12} & \multicolumn{2}{c}{\multirow{2}{*}{$\mathbf{M_1}(\phi_1)$}} & 0 & 0\\ M_{13} & & & 0 & 0\\ M_{14} & 0 & 0 & \multicolumn{2}{c}{\multirow{2}{*}{$\mathbf{M_1}(\phi_2)$}}\\ M_{15} & 0 & 0 & & \end{bmatrix} \begin{pmatrix}\dot{\psi}\\ \dot{\theta}_1\\ \dot{\phi}_1\\ \dot{\theta}_2\\ \dot{\phi}_2\end{pmatrix} \tag{3.56}$$

where the 2×2 matrix, $\mathbf{M_1}(\phi_1)$ is from the single-tethered dynamics in Figure 3-2 and (3.14):

$$\mathbf{M_1}(\phi) = \begin{bmatrix} m_{11}(\phi) & m_{12}(\phi)\\ m_{12}(\phi) & m_{22}\end{bmatrix} = \begin{bmatrix} I_r + m\ell^2 + 2mr\ell\cos\phi & I_r + mr\ell\cos\phi\\ I_r + mr\ell\cos\phi & I_r\end{bmatrix}.$$

In addition, notice that the other terms are much simpler:

$$\begin{aligned} M_{11} &= I_G + 2mr^2\\ M_{12} &= mr\ell\cos(\theta_1-\psi) + mr^2\cos(\theta_1+\phi_1-\psi)\\ M_{13} &= mr^2\cos(\theta_1+\phi_1-\psi)\\ M_{14} &= mr\ell\cos(\theta_2-\psi) + mr^2\cos(\theta_2+\phi_2-\psi)\\ M_{15} &= mr^2\cos(\theta_2+\phi_2-\psi)\end{aligned} \tag{3.57}$$

The equations of motion are given as

$$\begin{bmatrix} M_{11} & M_{12} & M_{13} & M_{14} & M_{15} \\ M_{12} & \multicolumn{2}{c}{\multirow{2}{*}{$\mathbf{M_1}(\phi_1)$}} & 0 & 0 \\ M_{13} & & & 0 & 0 \\ M_{14} & 0 & 0 & \multicolumn{2}{c}{\multirow{2}{*}{$\mathbf{M_1}(\phi_2)$}} \\ M_{15} & 0 & 0 & & \end{bmatrix} \begin{pmatrix} \ddot{\psi} \\ \ddot{\theta}_1 \\ \ddot{\phi}_1 \\ \ddot{\theta}_2 \\ \ddot{\phi}_2 \end{pmatrix} + \\ \begin{bmatrix} 0 & C_{12} & C_{13} & C_{14} & C_{15} \\ C_{21} & \multicolumn{2}{c}{\multirow{2}{*}{$\mathbf{C_1}(\phi_1, \dot{\theta}_1, \dot{\phi}_1)$}} & 0 & 0 \\ C_{31} & & & 0 & 0 \\ C_{41} & 0 & 0 & \multicolumn{2}{c}{\multirow{2}{*}{$\mathbf{C_1}(\phi_2, \dot{\theta}_2, \dot{\phi}_2)$}} \\ C_{51} & 0 & 0 & & \end{bmatrix} \begin{pmatrix} \dot{\psi} \\ \dot{\theta}_1 \\ \dot{\phi}_1 \\ \dot{\theta}_2 \\ \dot{\phi}_2 \end{pmatrix} = \begin{pmatrix} u_0 \\ \tau_{\theta,1} \\ \tau_{\phi,1} \\ \tau_{\theta,2} \\ \tau_{\phi,2} \end{pmatrix} \tag{3.58}$$

where the 2×2 matrices, $\mathbf{M_1}(\phi_1)$ and $\mathbf{C_1}(\phi, \theta, \dot{\phi})$ are from the single-tethered dynamics in Figure 3-2 and (3.14)

$$\begin{aligned} \mathbf{M_1}(\phi) &= \begin{bmatrix} m_{11}(\phi) & m_{12}(\phi) \\ m_{12}(\phi) & m_{22} \end{bmatrix} = \begin{bmatrix} I_r + m\ell^2 + 2mr\ell\cos\phi & I_r + mr\ell\cos\phi \\ I_r + mr\ell\cos\phi & I_r \end{bmatrix} \\ \mathbf{C_1}(\phi, \dot{\theta}, \dot{\phi}) &= \begin{bmatrix} c_{11}(\phi, \dot{\phi}) & c_{12}(\phi, \dot{\theta}, \dot{\phi}) \\ c_{21}(\phi, \dot{\theta}) & c_{22} \end{bmatrix} = \begin{bmatrix} -mr\ell\sin\phi\dot{\phi} & -mr\ell\sin\phi(\dot{\theta} + \dot{\phi}) \\ +mr\ell\sin\phi\dot{\theta} & 0 \end{bmatrix} \\ \begin{pmatrix} \tau_{\theta,i} \\ \tau_{\phi,i} \end{pmatrix} &= \begin{bmatrix} r + \ell\cos\phi_i & 1 \\ r & 1 \end{bmatrix} \begin{pmatrix} F_i \\ u_i \end{pmatrix} \text{ for } i = 1, 2. \end{aligned} \tag{3.59}$$

In addition,

$$\begin{aligned} C_{12} &= -mr\ell\sin(\theta_1 - \psi)\dot{\theta}_1 - mr^2\sin(\theta_1 + \phi_1 - \psi)(\dot{\theta}_1 + \dot{\phi}_1) \\ C_{13} &= -mr^2\sin(\theta_1 + \phi_1 - \psi)(\dot{\theta}_1 + \dot{\phi}_1) \\ C_{14} &= -mr\ell\sin(\theta_2 - \psi)\dot{\theta}_2 - mr^2\sin(\theta_2 + \phi_2 - \psi)(\dot{\theta}_2 + \dot{\phi}_2) \\ C_{15} &= -mr^2\sin(\theta_2 + \phi_2 - \psi)(\dot{\theta}_2 + \dot{\phi}_2) \\ C_{21} &= mr\ell\sin(\theta_1 - \psi)\dot{\psi} + mr^2\sin(\theta_1 + \phi_1 - \psi)\dot{\psi} \\ C_{31} &= mr^2\sin(\theta_1 + \phi_1 - \psi)\dot{\psi} \\ C_{41} &= mr\ell\sin(\theta_2 - \psi)\dot{\psi} + mr^2\sin(\theta_2 + \phi_2 - \psi)\dot{\psi} \\ C_{51} &= mr^2\sin(\theta_2 + \phi_2 - \psi)\dot{\psi} \end{aligned} \tag{3.60}$$

Note that the equations in (3.58) are simpler than those with a different coordinate definition of θ in (3.53). This is because θ now captures more complex behaviors than just the relative angles between the center spacecraft and the tether. It is straightforward to show that the two equations are identical by setting $\theta_1 = \psi - \theta_1$ and $\theta_2 = \psi - \theta_2$ in (3.58).

Using (3.58), a nonlinear decentralized control strategy is presented in Chapter 4. As will be shown, a controller designed from the single-tethered dynamics in (3.18) can stabilize the coupled dynamics of the three inline configuration as long as the center spacecraft is also stabilized by a simple rotation control law. This validates a fully decentralized control scheme without any inter-spacecraft communications (see the discussion in Chapter 4).

Equation (3.58) can also be linearized about a nominal rotational rate, $\dot{\psi}, \dot{\theta}_1, \dot{\theta}_2 \approx \omega$ while other relative angles and their rates are sufficiently close to zero such that $\theta_1 - \psi, \theta_2 - \psi \approx 0$ and $\phi_1, \dot{\phi}_1, \phi_2, \dot{\phi}_2 \approx 0$:

$$[\mathbf{M}]\ddot{\mathbf{q}} + [\mathbf{K}]\mathbf{q} = (\tau) \tag{3.61}$$

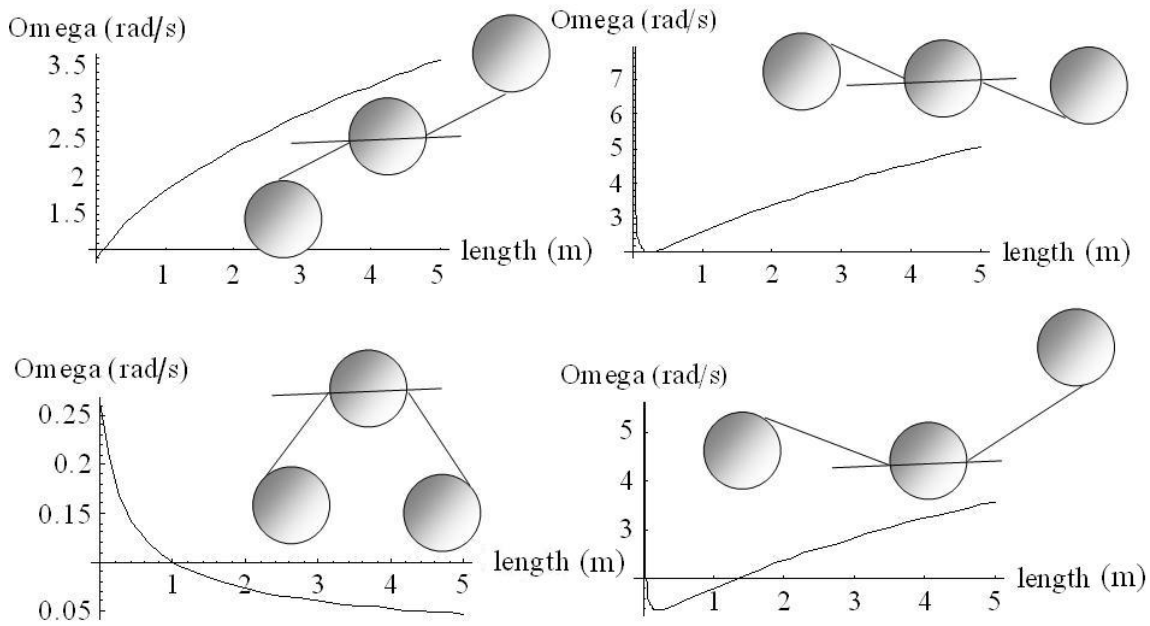

Figure 3-12: Three inline configuration's mode shapes and natural frequencies. The rigid body mode is not shown.

where

$$[\mathbf{M}] = \begin{bmatrix} I_G + 2mr^2 & mr(\ell+r) & mr^2 & mr(\ell+r) & mr^2 \\ mr(\ell+r) & I_G + m(\ell+r)^2 & I_G + mr(\ell+r) & 0 & 0 \\ mr^2 & I_G + mr(\ell+r) & I_G + mr^2 & 0 & 0 \\ mr(\ell+r) & 0 & 0 & I_G + m(\ell+r)^2 & I_G + mr(\ell+r) \\ mr^2 & 0 & 0 & I_G + mr(\ell+r) & I_G + mr^2 \end{bmatrix}$$

$$[\mathbf{K}] = \begin{bmatrix} 2mr(\ell+r)\omega^2 & -mr(\ell+r)\omega^2 & -mr^2\omega^2 & -mr(\ell+r)\omega^2 & -mr^2\omega^2 \\ -mr(\ell+r)\omega^2 & mr(\ell+r)\omega^2 & mr^2\omega^2 & 0 & 0 \\ -mr^2\omega^2 & mr^2\omega^2 & mr(\ell+r)\omega^2 & 0 & 0 \\ -mr(\ell+r)\omega^2 & 0 & 0 & mr(\ell+r)\omega^2 & mr^2\omega^2 \\ -mr^2\omega^2 & 0 & 0 & mr^2\omega^2 & mr(\ell+r)\omega^2 \end{bmatrix} \tag{3.62}$$

$$(\tau) = \begin{pmatrix} u_0 \\ (r+\ell)F_1 + u_1 \\ rF_1 + u_1 \\ (r+\ell)F_2 + u_2 \\ rF_2 + u_2 \end{pmatrix}, \quad \text{and} \quad \mathbf{q} = \begin{pmatrix} \psi \\ \theta_1 \\ \phi_1 \\ \theta_2 \\ \phi_2 \end{pmatrix}$$

Using the linearized equations, we can calculate the natural frequencies and mode shapes of the three inline configuration with the rigid tether. Figure 3-12 shows the mode shapes of four compound pendulum modes and their natural frequencies (y-axis) as a function of the tether length for a three-satellite inline array rotating with $m = 4$kg, $I_G = 0.0213$kgm^2, and $\omega = 0.3$rad/s. It has also one rigid body rotation mode.

Figure 3-13 depicts a bode plot of the ψ angle perturbed by a torque (u_o) on the center spacecraft. It is indispensable to investigate potential interactions of other vibratory motions with those pendulum modes, by examining such a frequency domain plot. In particular, the interactions between the compound pendulum mode and the tether vibrations would be detrimental and should be avoided by all means.

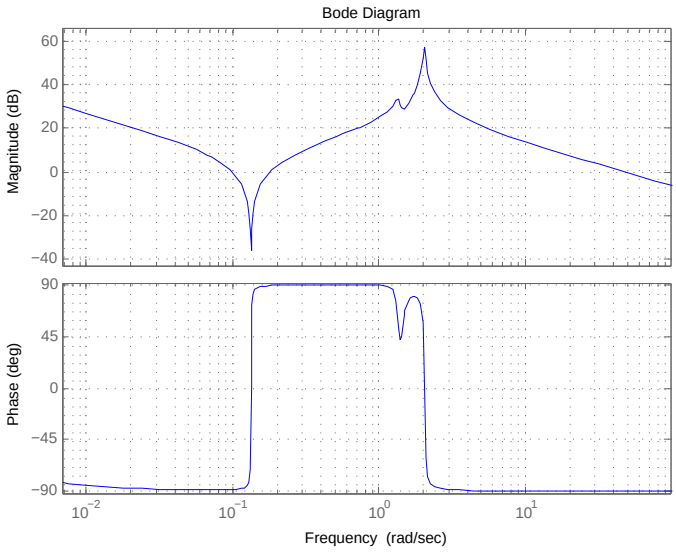

Figure 3-13: Bode plot of the linear system for the input u_o to the output ψ, based on the linearized three-inline dynamics. A small amount of damping has been added to each joint angle.

3.7 Flexible Tethers

The equations of motion of a single-tethered system with a flexible tether (Figure 3-14) are presented in this section. The tether is now assumed to be extensible along its length.

3.7.1 Dynamics Modeling

The tether is assumed to be massless. Therefore, no transverse vibrations of tether (violin mode) are allowed. The difference from the previous model in Section 3.3 is that the tether is now extensible along its length, as depicted Figure 3-14. For simplification, this flexible tether can be regarded as a rigid tether connected in series with an elastic spring. Using the Euler-Lagrange equations, the following equations of motion in the rotational plane (a plane normal to the aperture line-of-sight) are developed:

$$\mathbf{M_1}(\phi)\begin{pmatrix}\ddot{\theta}\\ \ddot{\phi}\\ \ddot{\ell}\end{pmatrix} + \mathbf{C_1}(\phi,\dot{\theta},\dot{\phi})\begin{pmatrix}\dot{\theta}\\ \dot{\phi}\\ \dot{\ell}\end{pmatrix} + \begin{pmatrix}0\\ 0\\ c\dot{\ell}+k\Delta\ell\end{pmatrix} = \begin{bmatrix}r+\ell\cos\phi & 1 & 0\\ r & 1 & 0\\ 0 & 0 & 1\end{bmatrix}\begin{pmatrix}F\\ u\\ P\end{pmatrix} \tag{3.63}$$

where

$$\begin{aligned}\mathbf{M_1}(\phi) &= \begin{bmatrix}I_r+m\ell^2+2mr\ell\cos\phi & I_r+mr\ell\cos\phi & -mr\sin\phi\\ I_r+mr\ell\cos\phi & I_r & -mr\sin\phi\\ -mr\sin\phi & -mr\sin\phi & m\end{bmatrix}\\ \mathbf{C_1}(\phi,\dot{\theta},\dot{\phi},\dot{\ell}) &= \begin{bmatrix}-mr\ell\sin\phi\dot{\phi}+m(r\cos\phi+\ell)\dot{\ell} & -mr\ell\sin\phi(\dot{\theta}+\dot{\phi}) & m(r\cos\phi+\ell)\dot{\theta}\\ +mr\ell\sin\phi\dot{\theta}+mr\cos\phi\dot{\ell} & 0 & mr\cos\phi\dot{\theta}\\ -m(r\cos\phi+\ell)\dot{\theta}-mr\cos\phi\dot{\phi} & -mr\cos\phi(\dot{\theta}+\dot{\phi}) & 0\end{bmatrix}\end{aligned} \tag{3.64}$$

In the equations above, r, ℓ, and I_G denote the satellite's radius, tether length, and moment of inertia. Again, I_r is the moment of inertia about the tether attachment point ($I_r = I_G + mr^2$). The tether has both elasticity and damping modeled as a spring k and a dashpot c. Also, F is the linear

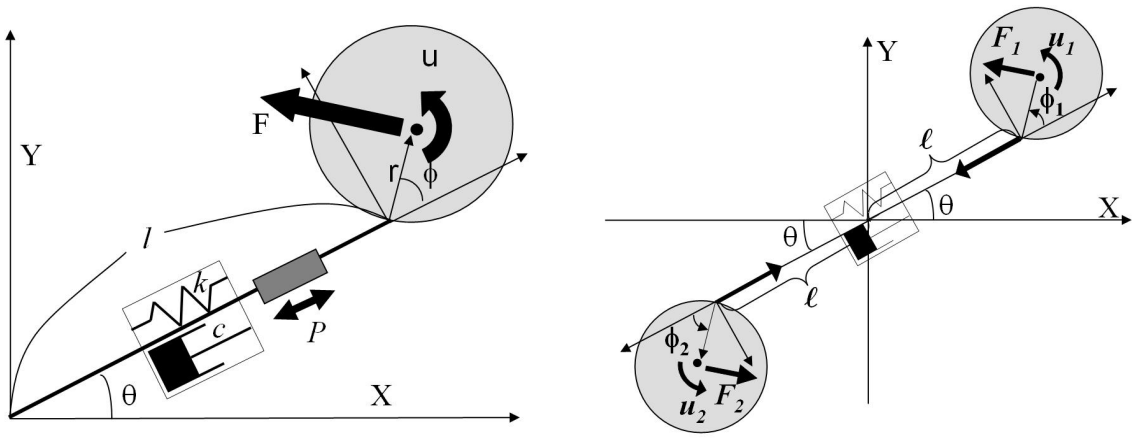

(a) Single tethered system

(b) Two spacecraft systems with two possible pendulum oscillations

Figure 3-14: Free-body diagram of single and two spacecraft systems with a flexible tether

force due to thruster firing, and u is the torque exerted on the CM of the satellite, and P is the linear force actuated by both the low-bandwidth tether motor and the high-bandwidth translational actuator.

Note that this system reduces to the rigid-tether single-spacecraft system introduced in Section 3.3 if we assume that tether is not flexible and ℓ varies only at constant speed ($\ddot{\ell} = 0$), thereby eliminating the third equation in (3.63).

This system has a rigid body mode for θ and an undamped natural frequency for the compound pendulum mode of

$$\omega_\phi = \sqrt{\frac{r(I_r + m\ell(2r+\ell))}{\ell I_G}}\omega \quad [rad/s] \tag{3.65}$$

when it is linearized about nominal velocities $\dot{\theta} = \omega$, $\dot{\ell} = v$ and $\dot{\phi}$, $\phi = 0$. It can be shown that the system goes unstable when the tether motor reels in by checking the eigenvalues of the following linear system,

$$\begin{aligned}\frac{d}{dt}\begin{pmatrix}\theta\\ \phi\\ \ell\\ \dot{\theta}\\ \dot{\phi}\\ \dot{\ell}\end{pmatrix} &= \begin{bmatrix}0 & 0 & 0 & 1 & 0 & 0\\ 0 & 0 & 0 & 0 & 1 & 0\\ 0 & 0 & 0 & 0 & 0 & 1\\ 0 & \frac{r\omega^2\left(I_r+mr\ell\right)}{\ell I_G} & 0 & -2\frac{v}{\ell} & 0 & -2\frac{\omega}{\ell}\\ 0 & -\frac{r\omega^2\left(I_r+m\ell(2r+\ell)\right)}{\ell I_G} & 0 & 2\frac{v}{\ell} & 0 & 2\frac{\omega}{\ell}\\ 0 & 0 & -\frac{k\Delta\ell}{m\ell} & 2(r+\ell)\omega & 2r\omega & -\frac{c}{m}\end{bmatrix}\begin{pmatrix}\theta\\ \phi\\ \ell\\ \dot{\theta}\\ \dot{\phi}\\ \dot{\ell}\end{pmatrix}\\ &+ \begin{pmatrix}0 & 0 & 0\\ 0 & 0 & 0\\ 0 & 0 & 0\\ \frac{1}{m\ell} & -\frac{r}{I_G\ell} & 0\\ -\frac{1}{m\ell} & \frac{r+\ell}{I_G\ell} & 0\\ 0 & 0 & \frac{1}{m}\end{pmatrix}\begin{pmatrix}F\\ u\\ P\end{pmatrix}\end{aligned} \tag{3.66}$$

In other words, a positive reel-out speed ($\dot{\ell} > 0$) results in damping of both $\dot{\theta}$ and the pendulum motion of ϕ whereas we will see unstable dynamics for a negative reel-in speed ($\dot{\ell} < 0$). Hence, it is indispensable to investigate this mode even for a large baseline length. It is also easy to verify that the system attitude states $(\dot{\theta}, \phi, \dot{\phi})$, with a nonzero ω, are fully controllable even when only using u. In addition, ℓ is directly controllable by P. Consequently, the system in (3.66) is fully controllable

by u and P (without the need for F):

$$\begin{bmatrix} B_{23} & AB_{23} & A^2B_{23} & \cdots \end{bmatrix} = \begin{bmatrix} 0 & 0 & -\frac{r}{I_G\ell} & 0 & \frac{2rv}{I_G\ell^2} & -\frac{2\omega}{\ell m} \\ 0 & 0 & \frac{\ell+r}{I_G\ell} & 0 & -\frac{2rv}{I_G\ell^2} & \frac{2\omega}{\ell m} \\ 0 & 0 & 0 & \frac{1}{m} & 0 & 0 \\ -\frac{r}{I_G\ell} & 0 & \frac{2rv}{I_G\ell^2} & -\frac{2\omega}{\ell m} & \frac{r(\ell mr(\ell+r)^2\omega^2+I_G(-4v^2+\ell(\ell+r)\omega^2))}{{I_G}^2\ell^3} & \frac{4v\omega}{l^2m} \\ \frac{\ell+r}{I_G\ell} & 0 & -\frac{2rv}{I_G\ell^2} & \frac{2\omega}{\ell m} & -\frac{r(\ell m(\ell+r)^3\omega^2+I_G(-4v^2+\ell(\ell+r)\omega^2))}{{I_G}^2\ell^3} & -\frac{4v\omega}{\ell^2m} \\ 0 & \frac{1}{m} & 0 & 0 & \frac{4rv\omega}{I_G\ell} & -\frac{4\omega^2}{m} \end{bmatrix} \tag{3.67}$$

has a full rank of six. Note that

$$B_{23} = \begin{pmatrix} 0 & 0 \\ 0 & 0 \\ 0 & 0 \\ -\frac{r}{I_G\ell} & 0 \\ \frac{r+\ell}{I_G\ell} & 0 \\ 0 & \frac{1}{m} \end{pmatrix}, \tag{3.68}$$

which corresponds to the control B matrix for u and P. This controllability analysis justifies our control approach to control the tethered array without using thrusters.

The nonzero rotational rate, ω, adds an artificial potential term to the dynamics. This nonzero artificial potential energy induced by the centrifugal force associated with array rotation, plays a crucial role in making the system controllable and stable. The equilibrium relationship between a perturbed tether length ($\Delta\ell$) and ω can easily be found as

$$\omega = \sqrt{\frac{k\Delta\ell}{2m(r+\ell)}} \tag{3.69}$$

which can be used to determine the required strength of the tether.

3.8 Transverse Vibration of a Tether with Distributed Mass

This section briefly reviews the modeling of the transverse vibration of a tether which has non-negligible mass.

3.8.1 Dynamics Modeling

Consider the spinning single-tethered system shown in Figure 3-15(a). We make the following assumptions: the material of the tether follows Hooke's Law; the angle inclination of the displaced string with respect to the horizontal axis (x in Figure 3-15(a)) is small; and the tether vibrates only in the transverse direction as a result of the wave disturbance. Newton's second law in the vertical direction yields:

$$\left[T(x) + \frac{\partial T(x)}{\partial x}dx\right]\left[\frac{\partial y(x,t)}{\partial x} + \frac{\partial^2 y(x,t)}{\partial x^2}\right] - T(x)\frac{\partial y(x,t)}{\partial x} + f(x,t)dx = \rho(x)dx\frac{\partial^2 y(x,t)}{\partial t^2} \tag{3.70}$$

where $T(x)$ is the tension along the tether length x; $\rho(x)$ is the linear density of the tether; and $y(x,t)$ denotes the transverse deflection. In addition, $f(x,t)$ is the external distributed force. Ignoring the second order terms results in

$$\frac{\partial}{\partial x}\left[T(x)\frac{\partial y(x,t)}{\partial x}\right] + f(x,t) = \rho(x)\frac{\partial^2 y(x,t)}{\partial t^2} \tag{3.71}$$

If the tension $T(x)$, and the density $\rho(x)$ are constant, and $f(x,t)$ is zero, (3.71) reduces to the

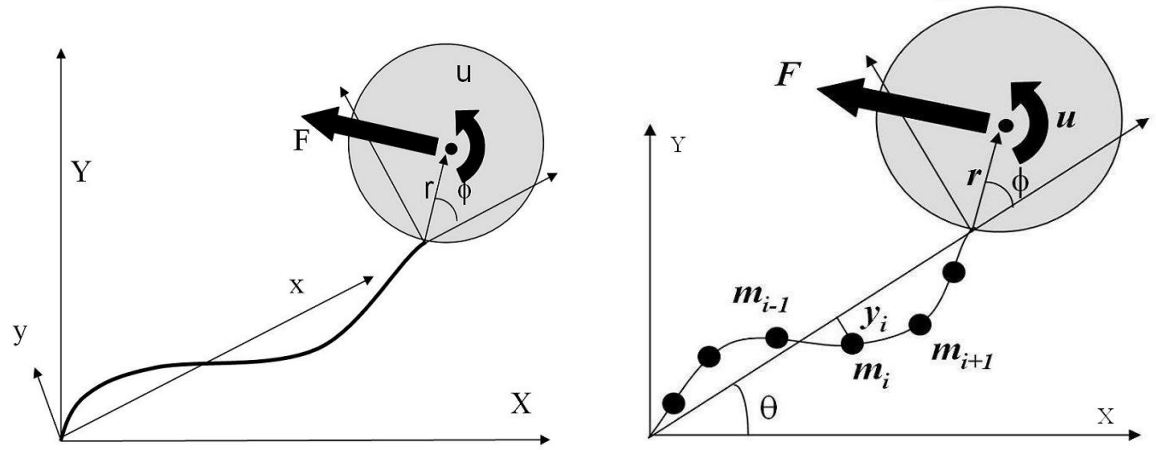

(a) Continuous model of a massive tether

(b) Discretized model of a massive tether

Figure 3-15: Modeling of the transverse vibration

well-known wave equation:

$$\frac{\partial^2 y(x,t)}{\partial x^2} = \frac{1}{c^2}\frac{\partial^2 y(x,t)}{\partial t^2} = \frac{\rho}{T}\frac{\partial^2 y(x,t)}{\partial t^2} \tag{3.72}$$

The above partial differential equation can be solved using two boundary conditions at $x = 0$ and $x = \ell$. The study in [18] derived the exact analytical solution of the natural frequencies of the tether vibration under this configuration.

$$\tan\lambda = \frac{3\rho\ell n^2(\ell+r)}{T^2\lambda}\frac{\left[(I_G + mr^2)T\lambda^2/\rho\ell^2 - 3mn^2r(\ell+r)\right]}{I_G\lambda^2/\rho\ell^2 - r} \tag{3.73}$$

where ρ is the linear density of the tether, and r, ℓ, and I_G denote the satellite's radius, tether length, and moment of inertia. Also, n is the rotational velocity, which can be the nominal spinning rate of the array (ω) in order to be consistent with this thesis.

The non-dimensional frequency, λ is solved from the above equation and is a function of ω

$$\lambda^2 = \frac{\rho\ell^2}{T}\omega^2 \tag{3.74}$$

The above equations are used to examine the coupling between tether string vibrations and the compound pendulum modes of a tethered satellite. Alternatively, we can discretize the tether as a lumped mass model consisting of N divided masses, and develop the equations of motion for N plus two (θ and ϕ) variables (see Figure 3-15). Special care should be practiced in the tether retrieval and deployment problem, since the number of the tether elements varies over time.

3.8.2 Impedance Matching Control

The mass of the tether is not negligible in this section. Especially in the case of the maximum tether deployment, up to 1 km, a violin mode (transverse vibration of the tether) is expected as discussed earlier. Its interaction with other oscillatory modes, such as the compound pendulum modes, would be detrimental. In order to actively control this violin mode, we investigate an impedance matching [128, 129, 130] control technique with a sliding tether boundary condition and a re-actuated transverse force shown in Figure 3-16(a). Tether vibration is fundamentally governed by the wave behavior of a string under tension, as given in (3.72). For each tether, motion can be decomposed into incoming (w_i) and outgoing propagating waves (w_o) resulting in $y = w_i + w_o$. A

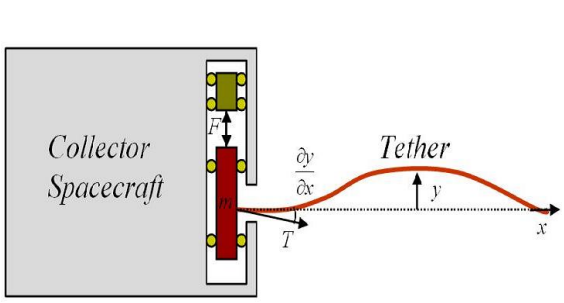

(a) Impedance matched tether termination. Courtesy: Prof. David W. Miller

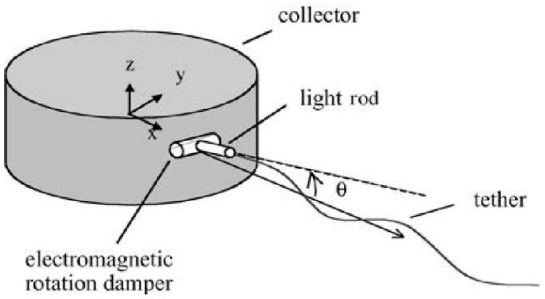

(b) Electromagnetic rotation damper on the tether attachment point [118]

Figure 3-16: Two methods of stabilizing the tether transverse vibration

transformation between physical and wave states in the tether can be derived as

$$\begin{pmatrix} y \\ \frac{\partial y}{\partial x} \end{pmatrix} = \begin{bmatrix} 1 & 1 \\ ik & -ik \end{bmatrix} \begin{pmatrix} w_i \\ w_o \end{pmatrix} \tag{3.75}$$

The free-body diagram in Figure (3-16)(a) yields the force relation at the tether attachment point,

$$m\frac{\partial^2 y}{\partial t^2} = T\frac{\partial y}{\partial x} - F. \tag{3.76}$$

The boundary Ordinary Differential Equation (ODE), when transformed to wave coordinates with the wave number k, gives the following input-output condition.

$$F = \begin{bmatrix} m\omega^2 & T \end{bmatrix} \begin{bmatrix} 1 & 1 \\ ik & -ik \end{bmatrix} \begin{pmatrix} w_i \\ w_o \end{pmatrix} \tag{3.77}$$

which can be rewritten as

$$w_o = -\frac{m\omega^2 + ikT}{m\omega^2 - ikT} w_i + \frac{1}{m\omega^2 - ikT} F \tag{3.78}$$

where the first term is the scattering (refection) coefficient and the second term is the product of the wave generation coefficient and force actuator.

Setting the outgoing wave to zero gives the force in terms of the incoming wave resulting in

$$F = (m\omega^2 + ikT)w_i \tag{3.79}$$

Transforming back to the physical coordinates gives the feedback law as the following,

$$F = \frac{i\omega}{c_o} Ty - mc_o(i\omega)\frac{\partial y}{\partial x} = \frac{T}{c_o}\frac{\partial y}{\partial t} - mc_o(i\omega)\frac{\partial^2 y}{\partial x \partial t} \tag{3.80}$$

where

$$c_o = \sqrt{\frac{T}{\rho A}} \tag{3.81}$$

An alternative way of damping the tether transverse motions is to utilize a mass-spring-dashpot system mounted at each tether attachment point to the spacecraft (see Figure 3-16(b)). Currently, the SPECS mission is equipped with electromagnetic devices in which the rotational stiffness and damping can be adjusted [118]. The transfer of energy carried by the waves from the tether to the passive damper is maximized when the tether wave impedance is matched to the damper impedance [130]. An impedance matching damping coefficient, depending on the wave propagation velocity, can be developed similar to (3.80). We are currently investigating the coupling motions [18] of this tether

violin mode with the spacecraft's attitude motion, in particular, the compound pendulum mode $(\phi, \dot{\phi})$ in Figure 3-2. Even though the current SPHERES testbed is not equipped with this kind of impedance matching actuator, future work will investigate the effectiveness of such a controller. The essential measurement of the tether slope $\frac{\partial y}{\partial x}$ can be realized by using a force-torque sensor, described in Chapter 7.

Chapter 4

Nonlinear Model Reduction and Decentralized Control by Synchronization

4.1 Chapter Objective

This chapter describes a fully decentralized nonlinear control law for spinning tethered formation flight, based on exploiting geometric symmetries to reduce the original nonlinear dynamics into simpler stable dynamics. In dealing with such coupled dynamics, an attempt is made to learn from distributed computation in biological systems. Figure 4-1 shows a picture of a human running by synchronizing oscillations of his leg joints; a three-spacecraft tethered formation can also be viewed as a multiple-joint system. Motivated by oscillation synchronization in biological systems, we use contraction theory to prove that a control law stabilizing a single-tethered spacecraft can also stabilize arbitrarily large circular arrays of spacecraft, as well as a three inline configuration. The convergence result is global and exponential. The decentralized control strategy is also extended to robust adaptive control in order to account for model uncertainties. In particular, the convenience of the differential analysis in combining multiple contracting systems is demonstrated. Numerical simulations and experimental results in Chapter 7, using the SPHERES testbed, validate the exponential stability of the tethered formation arrays by implementing a tracking control law derived from the reduced dynamics. The nonlinear stability of the decentralized control architecture in Section 4.3.2 constitutes the main contribution of this chapter.

The organization of this chapter is as follows: Modeling of single and double spacecraft systems is reviewed in Section 4.2. The stability of the decentralized control law is proven in the local and global convergence sense in Section 4.3. The results are extended to multiple-spacecraft arrays in Section 4.5. Simulation results are detailed in Section 4.6. It should be noted that the nonlinear decentralized control methodology introduced in the present chapter is experimentally validated in Chapter 7. We refer the readers to Chapter 1 for the motivation behind the proposed approach as well as related previous work on nonlinear model reduction.

4.2 Dynamics Modeling and Contraction Theory

We show herein that the dynamics of the two-spacecraft tethered system in Figure 3-7 is the superposition of two independent single-tethered systems. The main nonlinear stability tool, contraction analysis, exploits this observation to derive a decentralized control law.

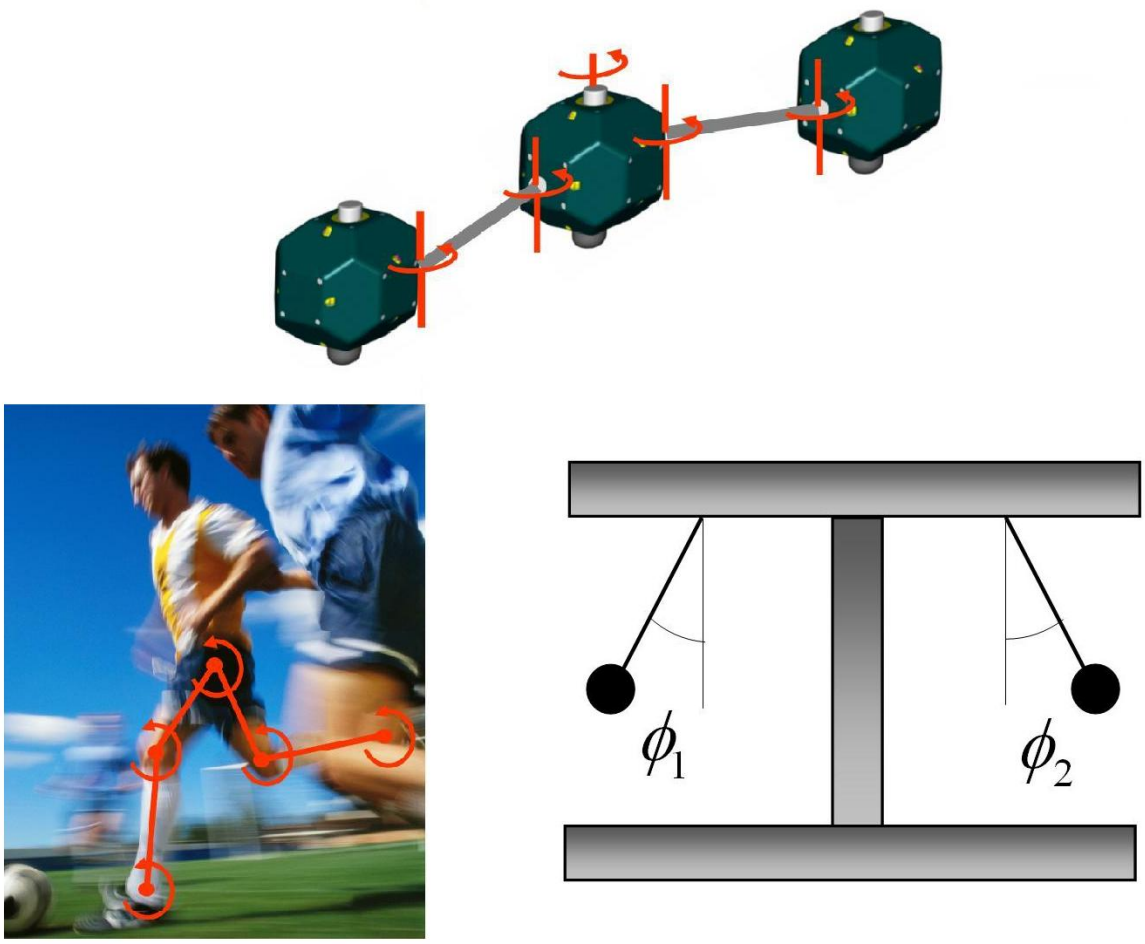

Figure 4-1: Synchronization of motions: human locomotion (bottom left), three tethered spacecraft (top), and Huygens's pendulum clock [17] (bottom right)

4.2.1 Reduction of Two Spacecraft Dynamics

In Chapter 3, the dynamics of two tethered satellites in the plane of rotation, shown in Figure 3-7, were derived using the Lagrangian equations (see (3.38)). It can be inferred by inspecting (3.38) that the first row of the equation contains the only term that couples ϕ_1 and ϕ_2, which is the sum of the first rows of two independent single-tethered systems of the form in (3.18):

$$\mathbf{M_1}(\phi_1)\begin{pmatrix}\ddot{\theta}\\ \ddot{\phi}_1\end{pmatrix} + \mathbf{C_1}(\phi_1,\dot{\theta},\dot{\phi}_1)\begin{pmatrix}\dot{\theta}\\ \dot{\phi}_1\end{pmatrix} + \begin{pmatrix}2m(r\cos\phi_1+\ell)\dot{\theta}\dot{\ell}\\ 2mr\cos\phi_1\dot{\theta}\dot{\ell}\end{pmatrix} = \begin{pmatrix}\tau_{\theta,1}\\ \tau_{\phi,1}\end{pmatrix} = \tau_{\mathbf{1}} \tag{4.1}$$

$$\mathbf{M_1}(\phi_2)\begin{pmatrix}\ddot{\theta}\\ \ddot{\phi}_2\end{pmatrix} + \mathbf{C_1}(\phi_2,\dot{\theta},\dot{\phi}_2)\begin{pmatrix}\dot{\theta}\\ \dot{\phi}_2\end{pmatrix} + \begin{pmatrix}2m(r\cos\phi_2+\ell)\dot{\theta}\dot{\ell}\\ 2mr\cos\phi_2\dot{\theta}\dot{\ell}\end{pmatrix} = \begin{pmatrix}\tau_{\theta,2}\\ \tau_{\phi,2}\end{pmatrix} = \tau_{\mathbf{2}} \tag{4.2}$$

where $\mathbf{M_1}(\phi)$, $\mathbf{C_1}(\phi,\dot{\theta},\dot{\phi})$ are given in (3.18).

It is easily verified that (3.38) reduces to Eqs. (4.1-4.2) if ϕ_1 and ϕ_2 can somehow be driven to oscillate in synchrony. In other words, we can decouple the dynamics of the first satellite from the other resulting in the same equation as (3.18) if the controller u_1 and u_2 make ϕ_1 and ϕ_2 converge towards each other exponentially fast. This important finding leads to the following definition.

Definition 4.1: Decentralized Control Law
Assume that for a two-spacecraft tethered system, some control function $\mathbf{u}$ is decentralized, in the sense that it does not require state information from the other satellite, and that

$$\tau_{\mathbf{1}} = \mathbf{u}(\phi_1, \dot{\theta}, \dot{\phi_1}) \text{ and } \tau_{\mathbf{2}} = \mathbf{u}(\phi_2, \dot{\theta}, \dot{\phi_2}) \text{ where } \mathbf{u} \text{ is the same control function}$$

Assume further that the strictly stabilizing control laws, $\tau_{\mathbf{1}}$ and $\tau_{\mathbf{2}}$, designed based on the single tethered systems in (4.1) and (4.2) respectively, also strictly stabilize the combined system in (3.38). Then a decentralized control law, $\tau_{\mathbf{i}} = u(\phi_i, \dot{\theta}, \dot{\phi_i})$, i=1,2 can be designed from a single-tethered system given in Eqs. (4.1-4.2) in lieu of the two body dynamics in (3.38). In addition, this control law $\mathbf{u}$ makes ϕ_1 and ϕ_2 converge to each other.

This decentralized control law will significantly simplify both the control algorithm and satellite hardware with few complications in terms of dimensionality and no communication burden. Basically, the fixed center of the rotation for a single-tethered system will be replaced with the center of the tether of the two satellites (see Figure 3-7). Subsequent sections demonstrate the existence of such controller as defined in **Definition 4.1** in two ways: locally through a linear diagonalizing transformation (Section 4.3.1) and globally by contraction theory (Section 4.3.2).

4.3 Stability of a Decentralized Control Law

4.3.1 Diagonalization of Linearized System

The two-spacecraft equation (3.38) with the tether length fixed ($\dot{\ell} = 0$) can also be linearized about $\dot{\theta} = \omega$, and $\dot{\phi}$, $\phi = 0$ with $F_1 = 0, F_2 = 0$ (torque actuation only):

$$\begin{bmatrix} 2I_r + 2m\ell(2r+\ell) & I_r + mr\ell & I_r + mr\ell \\ I_r + mr\ell & I_r & 0 \\ I_r + mr\ell & 0 & I_r \end{bmatrix} \begin{pmatrix} \ddot{\theta} \\ \ddot{\phi_1} \\ \ddot{\phi_2} \end{pmatrix} + \begin{bmatrix} 0 & 0 & 0 \\ 0 & mr\ell\omega^2 & 0 \\ 0 & 0 & mr\ell\omega^2 \end{bmatrix} \begin{pmatrix} \theta \\ \phi_1 \\ \phi_2 \end{pmatrix} = \begin{pmatrix} u_1 + u_2 \\ u_1 \\ u_2 \end{pmatrix} \tag{4.3}$$

It is observed that the nonzero rotation rate, ω, adds an artificial potential term to the dynamics even though there is no gravitational force in the model. As stated in Chapter 3, this nonzero artificial potential energy induced by the centripetal force of array rotation, plays a crucial role in making the system controllable and stable [43]. This is especially true for large classes of underactuated systems (e.g. tethered systems with $F = 0$), which are neither controllable in the absence of potential energy nor fully feedback linearizable [145].

The natural frequencies of this LTI system are computed as

$$\begin{pmatrix} \omega_\theta \\ \omega_\phi \\ \omega_o \end{pmatrix} = \begin{pmatrix} 0 \\ \sqrt{\frac{r(I_r + m\ell(2r+\ell))}{lI_G}}\omega \\ \sqrt{\frac{mr\ell}{I_r}}\omega \end{pmatrix} \tag{4.4}$$

Note that ω_ϕ is the same compound pendulum mode frequency as in the single spacecraft case, and ω_θ represents the same rigid body mode of θ and $\dot{\theta}$ as in the single-tethered system, whereas ω_o is the natural frequency of the anti-synchronization (out-of-phase) mode depicted in Figure 3-7. It can be shown that ω_o is always smaller than ω_ϕ.

We can diagonalize the system in (4.3) using normalized eigenvectors [43]. Then, with a linear decentralized control law of the form:

$$u_i = -K_1\phi_i - K_2\dot{\theta} - K_3\dot{\phi_i} \; i\text{=}1,2 \tag{4.5}$$

Equation (4.3) becomes

$$\begin{aligned}
&[V]^T [M] [V] \begin{pmatrix} \ddot{z}_1 \\ \ddot{z}_2 \\ \ddot{z}_3 \end{pmatrix} + [V]^T [K] [V] \\
&= [V]^T \begin{bmatrix} 0 & K_1 & K_1 \\ 0 & K_1 & 0 \\ 0 & 0 & K_1 \end{bmatrix} [V] \begin{pmatrix} z_1 \\ z_2 \\ z_3 \end{pmatrix} + [V]^T \begin{bmatrix} 2K_2 & K_3 & K_3 \\ K_2 & K_3 & 0 \\ K_2 & 0 & K_3 \end{bmatrix} [V] \begin{pmatrix} \dot{z}_1 \\ \dot{z}_2 \\ \dot{z}_3 \end{pmatrix}
\end{aligned} \tag{4.6}$$

where constant matrices $[M]$ and $[K]$ are from (4.3), and $[V]$ denotes a matrix of normalized eigenvectors sorted in the same order as (4.4):

$$[V] = \begin{bmatrix} \frac{1}{\sqrt{2I_G+2m(r+\ell)^2}} & -\frac{I_G+m(r+\ell)}{\sqrt{2I_G\ell^2m}\sqrt{I_G+m(r+\ell)^2}} & 0 \\ 0 & \frac{\sqrt{I_G+m(r+\ell)^2}}{\sqrt{2I_G\ell^2m}} & -\frac{1}{\sqrt{2I_G+2mr^2}} \\ 0 & \frac{\sqrt{I_G+m(r+\ell)^2}}{\sqrt{2I_G\ell^2m}} & \frac{1}{\sqrt{2I_G+2mr^2}} \end{bmatrix} \tag{4.7}$$

Since $[V]^T [M] [V] = I_{3\times3}$ and $[V]^T [K] [V] = \text{diag}(0, {\omega_\phi}^2, {\omega_o}^2)$, Equation (4.6) becomes:

$$\begin{aligned}
\ddot{z}_1 &= s_1\dot{z}_1 + s_2\dot{z}_2 + p_1 z_2 \\
\ddot{z}_2 + {\omega_\phi}^2 z_2 &= s_3\dot{z}_1 + s_4\dot{z}_2 + p_2 z_2 \\
\ddot{z}_3 + \frac{K_3}{I_r}\dot{z}_3 + ({\omega_o}^2 + \frac{K_1}{I_r}) z_3 &= 0
\end{aligned} \tag{4.8}$$

where

$$\begin{aligned}
&s_1 = \frac{-K_2}{I_r + m\ell(2r+\ell)}, \quad s_2 = \frac{I_G(K_2-K_3) + m(r+\ell)(rK_2 - K_3(r+\ell))}{\sqrt{I_G\ell^2m}(I_r + m\ell(2r+\ell))}, \\
&s_3 = \frac{m\ell(r+\ell)}{\sqrt{I_G\ell^2m}} s_1, \quad s_4 = (r+\ell)\sqrt{\frac{m}{I_G}} s_2, \quad p_1 = \frac{-K_1}{\sqrt{I_G\ell^2m}}, \quad p_2 = \frac{-K_1(r+\ell)}{I_G\ell}
\end{aligned} \tag{4.9}$$

By inspecting the eigenvectors given in (4.7), it is clear that z_1 represents θ and z_2 is the dynamics of the synchronized compound pendulum mode $(\phi_1 + \phi_2)$ in Figure 3-7 with the same natural frequency ω_ϕ as in the single-tethered case. The additional mode is the compound pendulum mode associated with anti-synchrony, which is $z_3 \propto \phi_1 - \phi_2$.

Likewise, diagonalizing the linearized single spacecraft system in (3.18) yields the same normalized equations of motion for z_1 and z_2 in (4.8). Thus, the stabilizing controller u_i from the single-tethered system will stabilize θ and the synchronized compound pendulum mode z_2. Now satisfying **Definition 4.1** comes down to finding conditions in which the anti-synchronized mode z_3 is stabilized.

The global stability condition of K_1 and K_3 for the linear z_3 dynamics in (4.8) can be found as $K_3 > 0$ and ${\omega_o}^2 + K_1/I_r > 0$.
Similarly, it can be shown that any controller satisfying $rK_2 < (r+\ell)K_3$, $K_1 > 0$, and $K_2 > 0$ can stabilize z_1 and z_2. Note that $K_3 > 0$ and ${\omega_o}^2 + K_1/I_r > 0$ are automatically satisfied by this condition, thereby stabilizing the coupled two-body system in (4.3). This proves the existence of controller as defined in **Definition 4.1**.

This result is graphically illustrated in Figure 4-2. Since $(r+\ell)/r = (0.125m + 1m)/0.125m = 9$, the system is strictly stable until K_2 reaches $9K_3 = 1.8$ as shown in Figure 4-2(a). It is also shown that the anti-synchrony mode (mode z_3) is independent of K_2. Moreover, the poles of the controlled single tethered system are the poles of modes z_1 and z_2 in (4.8).

Theorem 4.3.1 ***Effect of nonzero speed of the tether*** $(\dot{\ell} \neq 0)$

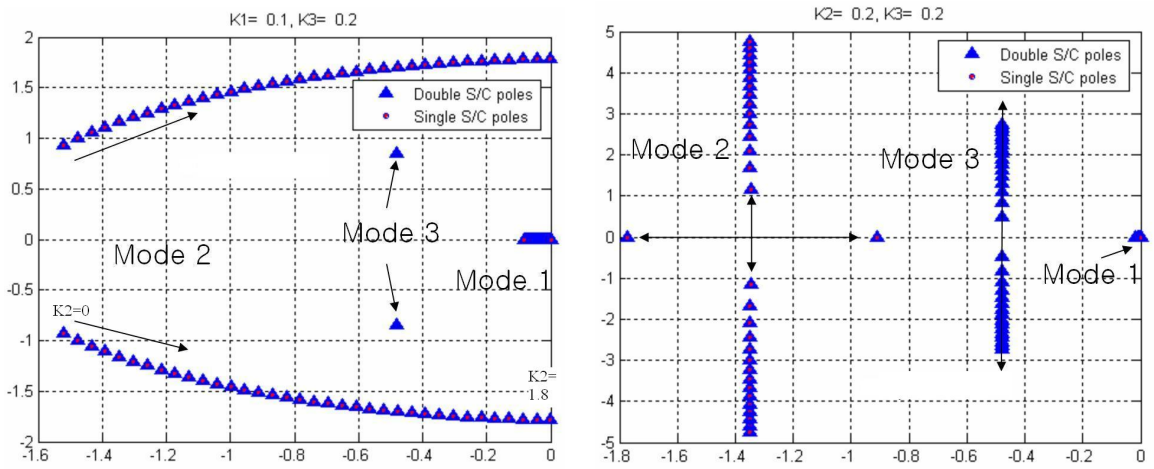

(a) K_1=0.1,K_2 is changing from 0 to 1.8, and K_3=0.2.

(b) K_1 is changing from 0 to 1.5, K_2=0.2, and K_3=0.2.

Figure 4-2: Poles of two tethered spacecraft and single spacecraft ($\dot{\ell} = 0$) with linear control.

When the tether motors reel in or out, $\dot{\ell}$ is a nonzero term. It can be shown that $\dot{\ell}$ does not affect the anti-synchronizing mode z_3; therefore a controller stabilizing a single-tethered system with a constant $\dot{\ell} \neq 0$, can be used to stabilize a two-spacecraft system.

4.3.2 Nonlinear Model Reduction by Contraction Theory

This section constitutes the main contribution of the present chapter. The stability of the anti-synchronizing compound pendulum mode z_3 in (4.8) can be verified more easily using contraction theory, specifically **Theorems 2.5.4 and 2.5.7**. From the second and third row of (4.3),

$$\begin{aligned}(I_r + mr\ell)\ddot{\theta} + I_r\ddot{\phi}_1 + mr\ell\omega^2\phi_1 &= -K_1\phi_1 - K_3\dot{\phi}_1 - K_2\dot{\theta} \\ (I_r + mr\ell)\ddot{\theta} + I_r\ddot{\phi}_2 + mr\ell\omega^2\phi_2 &= -K_1\phi_2 - K_3\dot{\phi}_2 - K_2\dot{\theta}\end{aligned} \tag{4.10}$$

Subtracting the first line from the second in (4.10) results in:

$$I_r\ddot{\phi}_1 + mr\ell\omega^2\phi_1 + K_1\phi_1 + K_3\dot{\phi}_1 = I_r\ddot{\phi}_2 + mr\ell\omega^2\phi_2 + K_1\phi_2 + K_3\dot{\phi}_2$$

According to **Theorem 2.5.7**, if the z_3 dynamics in (4.8) are exponentially stable, then ϕ_1 converges to ϕ_2 exponentially fast. Then, the stability of the original system depends on the stability of the reduced single-tethered system. Furthermore, $(I_r + mr\ell)\ddot{\theta}$ can be regarded as an auxiliary input to the partially contracting dynamics of z_3. Therefore, stable closed-loop single-tethered dynamics guarantees that the z_3 dynamics are stable.

The previous analysis is limited to the linear Proportional and Derivative (PD) controller given in (4.5). This is a local stability result based on the linearized dynamics. On the other hand, contraction theory exploits a differential analysis to derive a global stability result for the nonlinear dynamics. In addition, the simple PD control cannot be expected to handle the demands of efficiently tracking dynamic trajectories [178]. Thus, an exponentially stable nonlinear controller is proposed, and contraction analysis is used to check whether the combination of exponentially stable single-tethered systems leads to exponential stability.

Consider a single-tethered system in (4.1) with the tether length fixed ($\dot{\ell} = 0$),

$$\mathbf{M_1}(\mathbf{q_1})\ddot{\mathbf{q}}_\mathbf{1} + \mathbf{C_1}(\mathbf{q_1}, \dot{\mathbf{q}}_\mathbf{1})\dot{\mathbf{q}}_\mathbf{1} = \tau_\mathbf{1} \tag{4.11}$$

where $\mathbf{M_1}$, $\mathbf{C_1}$, and $\tau_\mathbf{1}$ are given in (3.18). In addition, $\mathbf{q_1}$ is defined as $\begin{pmatrix}\theta & \phi_1\end{pmatrix}^T$.

The following tracking control law is proposed in Section 2.5.5:

$$\tau_{\mathbf{1}} = \mathbf{M_1}(\mathbf{q_1})\ddot{\mathbf{q}}_{\mathbf{1r}} + \mathbf{C_1}(\mathbf{q_1}, \dot{\mathbf{q}}_{\mathbf{1}})\dot{\mathbf{q}}_{\mathbf{1r}} - \mathbf{K}(\dot{\mathbf{q}}_{\mathbf{1}} - \dot{\mathbf{q}}_{\mathbf{1r}}) \tag{4.12}$$

The reference velocity vector, $\dot{\mathbf{q}}_{\mathbf{1r}}$ is given by shifting the desired velocity $\dot{\mathbf{q}}_{\mathbf{1d}}$ with the position error:

$$\dot{\mathbf{q}}_{\mathbf{1r}} = \dot{\mathbf{q}}_{\mathbf{1d}} - \mathbf{\Lambda}\tilde{\mathbf{q}}_{\mathbf{1}} = \dot{\mathbf{q}}_{\mathbf{1d}} - \mathbf{\Lambda}(\mathbf{q_1} - \mathbf{q_{1d}}) \tag{4.13}$$

where $\mathbf{\Lambda}$ is a symmetric positive definite matrix.

From (4.11) and (4.12), consider the following virtual system,

$$\mathbf{M_1}(\mathbf{q_1})\dot{\mathbf{y}} + \mathbf{C_1}(\mathbf{q_1}, \dot{\mathbf{q}}_{\mathbf{1}})\mathbf{y} - \mathbf{K}(\dot{\mathbf{q}}_{\mathbf{1}} - \mathbf{y}) = \tau_{\mathbf{1}} \tag{4.14}$$

where $\dot{\mathbf{q}}_{\mathbf{1}}$ and $\dot{\mathbf{q}}_{\mathbf{1r}}$ are two particular solutions of these virtual dynamics, which is obvious by substituting for $\mathbf{y}$.

For system (4.14), we select the inertia matrix $\mathbf{M_1}(\mathbf{q_1})$ as a metric in (2.77), which is uniformly positive definite. Then, the squared length of the corresponding $\delta\mathbf{z}$ can be written as $\delta\mathbf{z}^T\delta\mathbf{z} = \delta\mathbf{y}^T\mathbf{M_1}(\mathbf{q_1})\delta\mathbf{y}$, and its derivative can be computed directly from (4.14),

$$\begin{aligned} \frac{d}{dt}(\delta\mathbf{y}^T\mathbf{M_1}(\mathbf{q_1})\delta\mathbf{y}) \;&=\; 2\;\delta\mathbf{y}^T\mathbf{M_1}(\mathbf{q_1})\delta\dot{\mathbf{y}} + \delta\mathbf{y}^T\dot{\mathbf{M}}_{\mathbf{1}}(\mathbf{q_1})\delta\mathbf{y} \\ &=\; -\;2\;\delta\mathbf{y}^T(\mathbf{C_1}(\mathbf{q_1}, \dot{\mathbf{q}}_{\mathbf{1}})\delta\mathbf{y} + \mathbf{K}\delta\mathbf{y}) + \delta\mathbf{y}^T\dot{\mathbf{M}}_{\mathbf{1}}(\mathbf{q_1})\delta\mathbf{y} \;=\; -\;2\;\delta\mathbf{y}^T\mathbf{K}\delta\mathbf{y} \end{aligned} \tag{4.15}$$

where we used the skew symmetric property, $\mathbf{y}^T(\dot{\mathbf{M}}_{\mathbf{1}} - 2\mathbf{C_1})\mathbf{y} = 0$.

The virtual system of $\mathbf{y}$ is shown to be contracting with a uniformly positive definite $\mathbf{K}$ with respect to θ and ϕ_1 using contraction analysis, introduced in Chapter 2. Then, the two particular solutions, $\dot{\mathbf{q}}_{\mathbf{1}}$ and $\dot{\mathbf{q}}_{\mathbf{1r}}$ converge to each other exponentially fast using **Theorem 2.5.7**.

Equation (4.13) implies that $\mathbf{q_1} \to \mathbf{q_{1d}}$ exponentially fast according to the hierarchical combination of contracting systems (**Theorem 2.5.4**)

$$\dot{\tilde{\mathbf{q}}}_{\mathbf{1}} = (\dot{\mathbf{q}}_{\mathbf{1}} - \dot{\mathbf{q}}_{\mathbf{1r}}) - \mathbf{\Lambda}\tilde{\mathbf{q}}_{\mathbf{1}} \tag{4.16}$$

One choice of $\mathbf{K}$ is

$$\mathbf{K} = \begin{bmatrix} k_{11} & k_{12} \\ k_{12} & k_{22} \end{bmatrix} \qquad \text{where} \quad k_{11} > 0 \text{ and } k_{22} - \frac{{k_{12}}^2}{k_{11}} > 0 \tag{4.17}$$

Similarly, we can construct an exponentially stabilizing tracking controller for the second spacecraft with $\mathbf{q_2} = \begin{pmatrix} \theta & \phi_2 \end{pmatrix}^T$.

$$\tau_{\mathbf{2}} = \mathbf{M_1}(\mathbf{q_2})\ddot{\mathbf{q}}_{\mathbf{2r}} + \mathbf{C_1}(\mathbf{q_2}, \dot{\mathbf{q}}_{\mathbf{2}})\dot{\mathbf{q}}_{\mathbf{2r}} - \mathbf{K}(\dot{\mathbf{q}}_{\mathbf{2}} - \dot{\mathbf{q}}_{\mathbf{2r}}) \tag{4.18}$$

This controller can be shown to exponentially stabilize the second spacecraft dynamics in (4.2) with the same $\mathbf{K}$ as in (4.17).

Let us now check whether these controllers from the single-tethered systems can exponentially stabilize the two-spacecraft tethered system in (3.38). For the first spacecraft given in (4.11), we augment the states, θ, ϕ with an auxiliary coordinate ϕ_2 such that

$$\mathbf{M}_{\phi_1}(\mathbf{q})\ddot{\mathbf{q}} + \mathbf{C}_{\phi_1}(\mathbf{q}, \dot{\mathbf{q}})\dot{\mathbf{q}} = \tau_{\mathbf{a}} \tag{4.19}$$

$$\tau_{\mathbf{a}} = \mathbf{M}_{\phi_1}(\mathbf{q})\ddot{\mathbf{q}}_{\mathbf{r}} + \mathbf{C}_{\phi_1}(\mathbf{q}, \dot{\mathbf{q}})\dot{\mathbf{q}}_{\mathbf{r}} - \mathbf{K_{D1}}(\dot{\mathbf{q}} - \dot{\mathbf{q}}_{\mathbf{r}}) \tag{4.20}$$

where

$$\mathbf{M}_{\phi_1} = \begin{bmatrix} m_{11}(\phi) & m_{12}(\phi) & 0 \\ m_{12}(\phi) & m_{22} & 0 \\ 0 & 0 & 0 \end{bmatrix}_{\phi=\phi_1}, \quad \mathbf{C}_{\phi_1} = \begin{bmatrix} c_{11}(\phi,\dot{\phi}) & c_{12}(\phi,\dot{\theta},\dot{\phi}) & 0 \\ c_{21}(\phi,\dot{\theta}) & c_{22} & 0 \\ 0 & 0 & 0 \end{bmatrix}_{\substack{\phi=\phi_1 \\ \dot{\phi}=\dot{\phi}_1}},$$

$$\tau_{\mathbf{a}} = \begin{pmatrix} \tau_{\theta,1} \\ \tau_{\phi,1} \\ 0 \end{pmatrix}, \quad \mathbf{K_{D1}} = \begin{bmatrix} k_{11} & k_{12} & 0 \\ k_{12} & k_{22} & 0 \\ 0 & 0 & 0 \end{bmatrix}, \quad \text{and} \quad \mathbf{q} = \begin{pmatrix} \theta \\ \phi_1 \\ \phi_2 \end{pmatrix}.$$

Equation (4.19) is the equation of motion of θ and ϕ_1; ϕ_2 is added just as a dummy variable to facilitate the proof in this section.
Similarly, we can augment the dynamics equations of the second spacecraft as

$$\mathbf{M}_{\phi_2}(\mathbf{q})\ddot{\mathbf{q}} + \mathbf{C}_{\phi_2}(\mathbf{q},\dot{\mathbf{q}})\dot{\mathbf{q}} = \tau_{\mathbf{b}} \tag{4.21}$$

$$\tau_{\mathbf{b}} = \mathbf{M}_{\phi_2}(\mathbf{q})\ddot{\mathbf{q}}_{\mathbf{r}} + \mathbf{C}_{\phi_2}(\mathbf{q},\dot{\mathbf{q}})\dot{\mathbf{q}}_{\mathbf{r}} - \mathbf{K_{D2}}(\dot{\mathbf{q}} - \dot{\mathbf{q}}_{\mathbf{r}}) \tag{4.22}$$

where

$$\mathbf{M}_{\phi_2} = \begin{bmatrix} m_{11}(\phi) & 0 & m_{12}(\phi) \\ 0 & 0 & 0 \\ m_{12}(\phi) & 0 & m_{22} \end{bmatrix}_{\phi=\phi_2}, \quad \mathbf{C}_{\phi_2} = \begin{bmatrix} c_{11}(\phi,\dot{\phi}) & 0 & c_{12}(\phi,\dot{\theta},\dot{\phi}) \\ 0 & 0 & 0 \\ c_{21}(\phi,\dot{\theta}) & 0 & c_{22} \end{bmatrix}_{\substack{\phi=\phi_2 \\ \dot{\phi}=\dot{\phi}_2}},$$

$$\tau_{\mathbf{b}} = \begin{pmatrix} \tau_{\theta,2} \\ 0 \\ \tau_{\phi,2} \end{pmatrix}, \quad \text{and} \quad \mathbf{K_{D2}} = \begin{bmatrix} k_{11} & 0 & k_{12} \\ 0 & 0 & 0 \\ k_{12} & 0 & k_{22} \end{bmatrix}.$$

Since τ in (3.38) is the *sum* of two tracking control laws individually designed from the single-tethered systems, $\tau = \tau_{\mathbf{a}} + \tau_{\mathbf{b}}$ in (4.20) and (4.22), the virtual dynamics of the two spacecraft system becomes,

$$\mathbf{M_2}(\mathbf{q})\dot{\mathbf{y}} + \mathbf{C_2}(\mathbf{q},\dot{\mathbf{q}})\mathbf{y} - (\mathbf{K_{D1}} + \mathbf{K_{D2}})(\dot{\mathbf{q}} - \mathbf{y}) = \tau, \tag{4.23}$$

which still has two particular solutions, $\dot{\mathbf{q}}$ and $\dot{\mathbf{q}}_{\mathbf{r}}$. The symmetry property discussed in Section 4.2.1 enforces $\mathbf{M_2} = \mathbf{M}_{\phi_1} + \mathbf{M}_{\phi_2}$ and $\mathbf{C_2} = \mathbf{C}_{\phi_1} + \mathbf{C}_{\phi_2}$.

The same squared-length analysis used earlier, now with respect to the uniformly positive definite metric $\mathbf{M_2}(\mathbf{q})$, results in

$$\frac{d}{dt}(\delta\mathbf{y}^T\mathbf{M_2}(\mathbf{q})\delta\mathbf{y}) \;=\; -\,2\;\delta\mathbf{y}^T(\mathbf{K_{D1}} + \mathbf{K_{D2}})\delta\mathbf{y}$$

This system is contracting, since

$$\mathbf{K_{D1}} + \mathbf{K_{D2}} = \begin{bmatrix} 2k_{11} & k_{12} & k_{12} \\ k_{12} & k_{22} & 0 \\ k_{12} & 0 & k_{22} \end{bmatrix} \tag{4.24}$$

is uniformly positive definite. This proves the existence of such controller as defined in **Definition 4.1** for exponentially stabilizing nonlinear controllers. The global convergence of contraction analysis strengthens the local convergence result of the linear approximation of the previous section.

4.4 Application to Nonlinear Robust Adaptive Control

The proposed decentralized technique is shown to be more powerful and practical by addressing its robustness properties. This section shows that the spatial symmetry of a tethered array yields the same stability result for the decentralized robust sliding control, decentralized adaptive control, and

the combination of both techniques.

4.4.1 Decentralized Robust Sliding Control

We show herein that the main result in the previous section can easily be extended to construction of nonlinear robust sliding controllers [178] to account for tether slack dynamics and modeling uncertainties, including lack of modeling of external disturbances. In particular, slackness of the tether affects the inertia matrix $\mathbf{M}$ and specifically the $\mathbf{C}$ matrix, removing the coupling terms because the energy transfer along the tether line is instantaneously disrupted. It can be shown that a sliding controller designed from the single-tethered system will exponentially stabilize the combined system using the previous analysis and the triangle inequality.

In order to proceed to prove the combined stability of a decentralized sliding control, let us consider again the augmented dynamics of the individual spacecraft for the two-spacecraft array:

$$\begin{aligned} \mathbf{M}_{\phi_1}(\mathbf{q})\ddot{\mathbf{q}} + \mathbf{C}_{\phi_1}(\mathbf{q},\dot{\mathbf{q}})\dot{\mathbf{q}} &= \tau_{\mathbf{a}} \\ \mathbf{M}_{\phi_2}(\mathbf{q})\ddot{\mathbf{q}} + \mathbf{C}_{\phi_2}(\mathbf{q},\dot{\mathbf{q}})\dot{\mathbf{q}} &= \tau_{\mathbf{b}} \end{aligned} \tag{4.25}$$

where the superposition of the two dynamics results in the two-spacecraft dynamics in (3.38) such that $\mathbf{M_2} = \mathbf{M}_{\phi_1} + \mathbf{M}_{\phi_2}$, $\mathbf{C_2} = \mathbf{C}_{\phi_1} + \mathbf{C}_{\phi_2}$, $\tau = \tau_{\mathbf{a}} + \tau_{\mathbf{b}}$, and $\mathbf{q} = \begin{pmatrix} \theta \\ \phi_1 \\ \phi_2 \end{pmatrix}$.

We can define the sliding mode control law [178] for the individual single-tethered spacecraft in (4.25)

$$\begin{aligned} \tau_{\mathbf{a}} &= \hat{\mathbf{M}}_{\phi_1}\ddot{\mathbf{q}}_{\mathbf{r}} + \hat{\mathbf{C}}_{\phi_1}\dot{\mathbf{q}}_{\mathbf{r}} - \mathbf{K}^{(\mathbf{1})}\mathrm{sgn}(\mathbf{s}) \\ \tau_{\mathbf{b}} &= \hat{\mathbf{M}}_{\phi_2}\ddot{\mathbf{q}}_{\mathbf{r}} + \hat{\mathbf{C}}_{\phi_2}\dot{\mathbf{q}}_{\mathbf{r}} - \mathbf{K}^{(\mathbf{2})}\mathrm{sgn}(\mathbf{s}) \end{aligned} \tag{4.26}$$

where $\hat{\mathbf{M}}$, and $\hat{\mathbf{C}}$ denote the estimated models from (3.18):

$$\hat{\mathbf{M}}_{\phi_1} = \begin{bmatrix} \hat{m}_{11}(\phi) & \hat{m}_{12}(\phi) & 0 \\ \hat{m}_{12}(\phi) & \hat{m}_{22} & 0 \\ 0 & 0 & 0 \end{bmatrix}_{\phi=\phi_1}, \hat{\mathbf{C}}_{\phi_1} = \begin{bmatrix} c_{11}(\phi,\dot{\phi}) & c_{12}(\phi,\dot{\theta},\dot{\phi}) & 0 \\ c_{21}(\phi,\dot{\theta}) & c_{22} & 0 \\ 0 & 0 & 0 \end{bmatrix}_{\left(\begin{smallmatrix}\phi=\phi_1 \\ \dot{\phi}=\dot{\phi}_1\end{smallmatrix}\right)},$$

$$\hat{\mathbf{M}}_{\phi_2} = \begin{bmatrix} \hat{m}_{11}(\phi) & 0 & \hat{m}_{12}(\phi) \\ 0 & 0 & 0 \\ \hat{m}_{12}(\phi) & 0 & \hat{m}_{22} \end{bmatrix}_{\phi=\phi_2}, \hat{\mathbf{C}}_{\phi_2} = \begin{bmatrix} c_{11}(\phi,\dot{\phi}) & 0 & c_{12}(\phi,\dot{\theta},\dot{\phi}) \\ 0 & 0 & 0 \\ c_{21}(\phi,\dot{\theta}) & 0 & c_{22} \end{bmatrix}_{\left(\begin{smallmatrix}\phi=\phi_2 \\ \dot{\phi}=\dot{\phi}_2\end{smallmatrix}\right)}$$

.

In addition,

$$\mathbf{K}^{(\mathbf{1})} = \begin{bmatrix} k_1 & 0 & 0 \\ 0 & k_2 & 0 \\ 0 & 0 & 0 \end{bmatrix} \text{ and } \mathbf{K}^{(\mathbf{2})} = \begin{bmatrix} k_1 & 0 & 0 \\ 0 & 0 & 0 \\ 0 & 0 & k_2 \end{bmatrix} \tag{4.27}$$

are constructed from the positive diagonal matrix

$$\begin{bmatrix} k_1 & 0 \\ 0 & k_2 \end{bmatrix} \tag{4.28}$$

It can be shown that these controllers can achieve robust performance in the presence of modelling imperfections for a two-spacecraft system in (3.38). Choosing the components k_i of the vector $\mathbf{K}^{(\mathbf{1})}, \mathbf{K}^{(\mathbf{2})}$ such that

$$\begin{aligned} k_i^{(1)} &\geq \left|[\tilde{\mathbf{M}}_{\phi_1}\ddot{\mathbf{q}}_{\mathbf{r}} + \tilde{\mathbf{C}}_{\phi_1}\dot{\mathbf{q}}_{\mathbf{r}}]_i\right| + \eta_i = \left|[\tilde{\mathbf{M}}_{\mathbf{1}}(\mathbf{q_1})\ddot{\mathbf{q}}_{\mathbf{1r}} + \tilde{\mathbf{C}}_{\mathbf{1}}(\mathbf{q_1},\dot{\mathbf{q}}_{\mathbf{1}})\dot{\mathbf{q}}_{\mathbf{1r}}]_i\right| + \eta_i \\ k_i^{(2)} &\geq \left|[\tilde{\mathbf{M}}_{\phi_2}\ddot{\mathbf{q}}_{\mathbf{r}} + \tilde{\mathbf{C}}_{\phi_2}\dot{\mathbf{q}}_{\mathbf{r}}]_i\right| + \eta_i = \left|[\tilde{\mathbf{M}}_{\mathbf{1}}(\mathbf{q_2})\ddot{\mathbf{q}}_{\mathbf{2r}} + \tilde{\mathbf{C}}_{\mathbf{1}}(\mathbf{q_2},\dot{\mathbf{q}}_{\mathbf{2}})\dot{\mathbf{q}}_{\mathbf{2r}}]_i\right| + \eta_i \end{aligned} \tag{4.29}$$

(with $\eta_i > 0$) will ensure the sliding condition,

$$\frac{d}{2dt}\mathbf{s}^T\mathbf{M}_1\mathbf{s} < -\sum_{i=1}^{n}\eta_i|s_i| \tag{4.30}$$

is satisfied for each spacecraft. This sliding controller, based upon the single-tethered dynamics, will also exponentially stabilize the coupled two-spacecraft system since

$$\begin{aligned} k_i^{(1)} \geq \left|[\tilde{\mathbf{M}}_{\phi_\mathbf{1}}\ddot{\mathbf{q}}_\mathbf{r} + \tilde{\mathbf{C}}_{\phi_\mathbf{1}}\dot{\mathbf{q}}_\mathbf{r}]_i\right| + \eta_i, \text{ and } k_i^{(2)} \geq \left|[\tilde{\mathbf{M}}_{\phi_\mathbf{2}}\ddot{\mathbf{q}}_\mathbf{r} + \tilde{\mathbf{C}}_{\phi_\mathbf{2}}\dot{\mathbf{q}}_\mathbf{r}]_i\right| + \eta_i \longrightarrow \\ k_i^{(1)} + k_i^{(2)} \geq \left|[\tilde{\mathbf{M}}_{\phi_\mathbf{1}}\ddot{\mathbf{q}}_\mathbf{r} + \tilde{\mathbf{C}}_{\phi_\mathbf{1}}\dot{\mathbf{q}}_\mathbf{r}]_i\right| + \left|[\tilde{\mathbf{M}}_{\phi_\mathbf{2}}\ddot{\mathbf{q}}_\mathbf{r} + \tilde{\mathbf{C}}_{\phi_\mathbf{2}}\dot{\mathbf{q}}_\mathbf{r}]_i\right| + 2\eta_i \\ \geq \left|[\tilde{\mathbf{M}}_\mathbf{2}\ddot{\mathbf{q}}_\mathbf{r} + \tilde{\mathbf{C}}_\mathbf{2}\dot{\mathbf{q}}_\mathbf{r}]_i\right| + 2\eta_i > 0 \end{aligned} \tag{4.31}$$

where we used the triangle inequality, $|x| + |y| \geq |x + y|$, and $\tilde{\mathbf{M}}$, $\tilde{\mathbf{C}}$ denote modeling errors, i.e. $\tilde{\mathbf{M}} = \hat{\mathbf{M}} - \mathbf{M}$ and $\tilde{\mathbf{C}} = \hat{\mathbf{C}} - \mathbf{C}$.

This ensures that the sliding condition

$$\frac{d}{2dt}\mathbf{s}^T\mathbf{M}_2(\mathbf{q})\mathbf{s} < -\sum_{i=1}^{n}2\eta_i|s_i| \tag{4.32}$$

is satisfied for the two-spacecraft tethered array. To mitigate the high-frequency chattering of the proposed sliding control law, we can replace the $\text{sgn}(\mathbf{s})$ function with the saturation function $\text{sat}(\mathbf{s}/\phi)$. This concludes the proof of the stability of the decentralized sliding control law.

4.4.2 Decentralized Adaptive Control

In this section, the decentralized adaptive control designed from the single-tethered system is shown to asymptotically stabilize the coupled two-spacecraft tethered array. Previously, Narendra [142] and a few others reported work on decentralized adaptive control. Nonetheless, the decentralized nonlinear adaptive control in this section offers a fresh and unique perspective of modular stability using contraction analysis. In particular, the convenience of the differential analysis in combining multiple contracting systems is clearly demonstrated. Furthermore, this work reports the first application of adaptive control to tethered formation flying spacecraft.

Before we proceed to the proof for the coupled spacecraft array, let us first prove the asymptotic stability of the adaptive control law for each decoupled spacecraft using contraction analysis. As in the previous section, $\hat{(\cdot)}$ denotes an estimate, and $\tilde{(\cdot)}$ denotes an error of the estimate such that $\tilde{(\cdot)} = \hat{(\cdot)} - (\cdot)$. Consider the following adaptive control [178] for the single-tethered spacecraft in (4.11) with $\mathbf{q_1} = \begin{pmatrix}\theta & \phi_1\end{pmatrix}^T$:

$$\tau_\mathbf{1} = \mathbf{Y_1}\hat{\mathbf{a}} - \mathbf{K}\mathbf{s_1} = \hat{\mathbf{M}}_\mathbf{1}(\mathbf{q_1})\ddot{\mathbf{q}}_\mathbf{1r} + \hat{\mathbf{C}}_\mathbf{1}(\mathbf{q_1}, \dot{\mathbf{q}}_\mathbf{1})\dot{\mathbf{q}}_\mathbf{1r} - \mathbf{K}\mathbf{s_1} \tag{4.33}$$

where $\mathbf{s_1}$ denotes the composite variable $\mathbf{s_1} = \dot{\mathbf{q}}_\mathbf{1} - \dot{\mathbf{q}}_\mathbf{1r}$, and the parameter estimate $\hat{\mathbf{a}}$ is updated by the correlation integral:

$$\dot{\hat{\mathbf{a}}}_\mathbf{1} = -\mathbf{\Gamma}{\mathbf{Y}_\mathbf{1}}^T\mathbf{s_1} \tag{4.34}$$

with a symmetric positive definite matrix $\mathbf{\Gamma}$, and $\mathbf{Y_1} = \mathbf{Y}(\mathbf{q_1}, \dot{\mathbf{q}}_\mathbf{1}, \dot{\mathbf{q}}_\mathbf{1r}, \ddot{\mathbf{q}}_\mathbf{1r})$. The function $\mathbf{Y}$ is derived from the linear relationship with the unknown parameters $\mathbf{a}$:

$$\mathbf{Y} = \begin{bmatrix} \ddot{\theta}_r & \ddot{\phi}_r & 2\cos\phi\ddot{\theta}_r + \cos\phi\ddot{\phi}_r - \sin\phi\dot{\phi}\dot{\theta}_r - \sin\phi(\dot{\phi}+\dot{\theta})\dot{\phi}_r \\ 0 & \ddot{\theta}_r + \ddot{\phi} & \sin\phi\dot{\theta}\dot{\theta}_r \end{bmatrix} \tag{4.35}$$

In addition, there are three unknown physical parameters that the above adaptive control updates in real-time: I_G, m, and ℓ. The unknown true values are represented by a constant vector, $\mathbf{a}$ such

that

$$\mathbf{a} = \begin{pmatrix} a_1 \\ a_2 \\ a_3 \end{pmatrix} = \begin{pmatrix} I_G + mr^2 + m\ell^2 \\ I_G + mr^2 \\ mr\ell \end{pmatrix}. \tag{4.36}$$

The asymptotic convergence of the tracking error and parameter estimates can be proven using contraction analysis. Consider the closed-loop system using (4.33) with the parameter estimate update law $\dot{\hat{\mathbf{a}}}_\mathbf{1} = -\boldsymbol{\Gamma}\mathbf{Y_1}^T\mathbf{s_1}$:

$$\begin{bmatrix} \mathbf{M_1}(\mathbf{q_1}) & \mathbf{0} \\ \mathbf{0} & \boldsymbol{\Gamma}^{-1} \end{bmatrix} \begin{pmatrix} \dot{\mathbf{s}}_\mathbf{1} \\ \dot{\tilde{\mathbf{a}}}_\mathbf{1} \end{pmatrix} + \begin{bmatrix} \mathbf{C_1}(\mathbf{q_1}, \dot{\mathbf{q}}_\mathbf{1}) + \mathbf{K} & -\mathbf{Y_1} \\ \mathbf{Y_1}^T & \mathbf{0} \end{bmatrix} \begin{pmatrix} \mathbf{s_1} \\ \tilde{\mathbf{a}}_\mathbf{1} \end{pmatrix} = \begin{pmatrix} \mathbf{0} \\ \mathbf{0} \end{pmatrix} \tag{4.37}$$

where we used $\dot{\tilde{\mathbf{a}}}_\mathbf{1} = \dot{\hat{\mathbf{a}}}_\mathbf{1}$.
Consider the virtual system of $\mathbf{y}_1$ and $\mathbf{y}_2$

$$\begin{bmatrix} \mathbf{M_1}(\mathbf{q_1}) & \mathbf{0} \\ \mathbf{0} & \boldsymbol{\Gamma}^{-1} \end{bmatrix} \begin{pmatrix} \dot{\mathbf{y}}_1 \\ \dot{\mathbf{y}}_2 \end{pmatrix} + \begin{bmatrix} \mathbf{C_1}(\mathbf{q_1}, \dot{\mathbf{q}}_\mathbf{1}) + \mathbf{K} & -\mathbf{Y_1} \\ \mathbf{Y_1}^T & \mathbf{0} \end{bmatrix} \begin{pmatrix} \mathbf{y}_1 \\ \mathbf{y}_2 \end{pmatrix} = \begin{pmatrix} \mathbf{0} \\ \mathbf{0} \end{pmatrix} \tag{4.38}$$

which has two particular solutions: $\begin{pmatrix} \mathbf{y}_1 = \mathbf{s_1} \\ \mathbf{y}_2 = \tilde{\mathbf{a}}_\mathbf{1} \end{pmatrix}$ and $\begin{pmatrix} \mathbf{y}_1 = \mathbf{0} \\ \mathbf{y}_2 = \mathbf{0} \end{pmatrix}$.
The squared-length analysis using the positive definite metric

$$\begin{bmatrix} \mathbf{M_1}(\mathbf{q_1}) & \mathbf{0} \\ \mathbf{0} & \boldsymbol{\Gamma}^{-1} \end{bmatrix} \tag{4.39}$$

yields

$$\dot{V} = \frac{d}{dt} \begin{pmatrix} \delta\mathbf{y}_1 \\ \delta\mathbf{y}_2 \end{pmatrix}^T \begin{bmatrix} \mathbf{M_1}(\mathbf{q_1}) & \mathbf{0} \\ \mathbf{0} & \boldsymbol{\Gamma}^{-1} \end{bmatrix} \begin{pmatrix} \delta\mathbf{y}_1 \\ \delta\mathbf{y}_2 \end{pmatrix} = -2 \begin{pmatrix} \delta\mathbf{y}_1 \\ \delta\mathbf{y}_2 \end{pmatrix}^T \begin{bmatrix} \mathbf{K} & -\mathbf{Y_1} \\ \mathbf{Y_1}^T & \mathbf{0} \end{bmatrix} \begin{pmatrix} \delta\mathbf{y}_1 \\ \delta\mathbf{y}_2 \end{pmatrix} \tag{4.40}$$

where the symmetric part of the generalized Jacobian

$$\begin{bmatrix} -2\mathbf{K} & \mathbf{0} \\ \mathbf{0} & \mathbf{0} \end{bmatrix} \tag{4.41}$$

is negative semi-definite with $\mathbf{K} > 0$. Hence, the system is semi-contracting [112, 113].

The rate of the virtual length ($\dot{V}$) is uniformly continuous since bounded $\delta\dot{\mathbf{y}}_1$ and $\delta\dot{\mathbf{y}}_2$ from (4.38) lead to bounded $\ddot{V}$. Due to $\dot{V} \leq 0$, the use of Barbalat's lemma (see Theorem 2.4.4) verifies that $\dot{V} \to 0$ as $t \to \infty$. This implies that $\delta\mathbf{y}_1$ and $\delta\mathbf{y}_2$ tends to zero asymptotically. Therefore, all solutions of (4.37) tend to each other yielding $\mathbf{s_1} \to \mathbf{0}$ and $\hat{\mathbf{a}}_\mathbf{1} \to \mathbf{a}$. This concludes the proof showing that the adaptive controller tracks the desired trajectory asymptotically while the error of the parameter estimate tends to zero as well.

The objective of this section is to show that such a nonlinear adaptive controller, independently implemented in each spacecraft in the decentralized fashion, can stabilize a tethered coupled array, thereby extending the main result of this chapter. Similar to the previous section, let us consider again the augmented dynamics of the individual spacecraft for the two-spacecraft array:

$$\begin{aligned} \mathbf{M}_{\phi_\mathbf{1}}(\mathbf{q})\ddot{\mathbf{q}} + \mathbf{C}_{\phi_\mathbf{1}}(\mathbf{q}, \dot{\mathbf{q}})\dot{\mathbf{q}} &= \tau_\mathbf{a} \\ \mathbf{M}_{\phi_\mathbf{2}}(\mathbf{q})\ddot{\mathbf{q}} + \mathbf{C}_{\phi_\mathbf{2}}(\mathbf{q}, \dot{\mathbf{q}})\dot{\mathbf{q}} &= \tau_\mathbf{b} \end{aligned} \tag{4.42}$$

where $\mathbf{q} = \begin{pmatrix} \theta & \phi_1 & \phi_2 \end{pmatrix}^T$, and $\mathbf{s} = \dot{\mathbf{q}} - \dot{\mathbf{q}}_\mathbf{r}$.

Then, the decentralized adaptive control law for each spacecraft is given as

$$\begin{aligned} \tau_\mathbf{a} &= \mathbf{Y_a}\hat{\mathbf{a}}_1 - \mathbf{K_{D1}}\mathbf{s} = \hat{\mathbf{M}}_{\phi_\mathbf{1}}\ddot{\mathbf{q}}_\mathbf{r} + \hat{\mathbf{C}}_{\phi_\mathbf{1}}\dot{\mathbf{q}}_\mathbf{r} - \mathbf{K_{D1}}\mathbf{s} \\ \tau_\mathbf{b} &= \mathbf{Y_b}\hat{\mathbf{a}}_2 - \mathbf{K_{D2}}\mathbf{s} = \hat{\mathbf{M}}_{\phi_\mathbf{2}}\ddot{\mathbf{q}}_\mathbf{r} + \hat{\mathbf{C}}_{\phi_\mathbf{2}}\dot{\mathbf{q}}_\mathbf{r} - \mathbf{K_{D2}}\mathbf{s} \end{aligned} \tag{4.43}$$

where the matrices $\mathbf{K_{D1}}$ and $\mathbf{K_{D2}}$ are defined in Equations (4.19) and (4.21). In addition, the augmented $\mathbf{Y_a}$ and $\mathbf{Y_b}$ are defined as

$$\begin{aligned}
\mathbf{Y_a} &= \begin{bmatrix} \ddot{\theta}_r & \ddot{\phi}_r & 2\cos\phi\ddot{\theta}_r + \cos\phi\ddot{\phi}_r - \sin\phi\dot{\phi}\dot{\theta}_r - \sin\phi(\dot{\phi}+\dot{\theta})\dot{\phi}_r \\ 0 & \ddot{\theta}_r + \ddot{\phi} & \sin\phi\dot{\theta}\dot{\theta}_r \\ 0 & 0 & 0 \end{bmatrix}_{\left(\begin{smallmatrix}\phi=\phi_1\\ \dot{\phi}=\dot{\phi}_1\end{smallmatrix}\right)} \\
\mathbf{Y_b} &= \begin{bmatrix} \ddot{\theta}_r & \ddot{\phi}_r & 2\cos\phi\ddot{\theta}_r + \cos\phi\ddot{\phi}_r - \sin\phi\dot{\phi}\dot{\theta}_r - \sin\phi(\dot{\phi}+\dot{\theta})\dot{\phi}_r \\ 0 & 0 & 0 \\ 0 & \ddot{\theta}_r + \ddot{\phi} & \sin\phi\dot{\theta}\dot{\theta}_r \end{bmatrix}_{\left(\begin{smallmatrix}\phi=\phi_2\\ \dot{\phi}=\dot{\phi}_2\end{smallmatrix}\right)}.
\end{aligned} \tag{4.44}$$

The parameter estimates $\hat{\mathbf{a}}_1$ and $\hat{\mathbf{a}}_2$ are updated according to the correlation integrals

$$\begin{aligned}
\dot{\hat{\mathbf{a}}}_\mathbf{1} &= -\mathbf{\Gamma Y_a}^T\mathbf{s} \\
\dot{\hat{\mathbf{a}}}_\mathbf{2} &= -\mathbf{\Gamma Y_b}^T\mathbf{s}
\end{aligned} \tag{4.45}$$

Since the $\mathbf{a}$ vector is linear with the $\mathbf{Y}$ matrix, we can easily verify that $\mathbf{Y_a} + \mathbf{Y_b} = \mathbf{Y_{2s}}$ such that

$$\mathbf{Y_{2s}a} = \mathbf{M_2(q)}\ddot{\mathbf{q}}_\mathbf{r} + \mathbf{C_2(q,\dot{q})}\dot{\mathbf{q}}_\mathbf{r} \tag{4.46}$$

In addition, the symmetry property discussed in Section 4.2.1 enforces $\mathbf{M_2} = \mathbf{M}_{\phi_1} + \mathbf{M}_{\phi_2}$, $\mathbf{C_2} = \mathbf{C}_{\phi_1} + \mathbf{C}_{\phi_2}$, and $\tau = \tau_\mathbf{a} + \tau_\mathbf{b}$.

The closed-loop system for the two-spacecraft system in (3.38) verifies

$$\begin{bmatrix} \mathbf{M_2(q)} & \mathbf{0} & \mathbf{0} \\ \mathbf{0} & \mathbf{\Gamma}^{-1} & \mathbf{0} \\ \mathbf{0} & \mathbf{0} & \mathbf{\Gamma}^{-1} \end{bmatrix} \begin{pmatrix} \dot{\mathbf{s}} \\ \dot{\tilde{\mathbf{a}}}_\mathbf{1} \\ \dot{\tilde{\mathbf{a}}}_\mathbf{2} \end{pmatrix} + \begin{bmatrix} \mathbf{C_2(q,\dot{q})} + \mathbf{K_{D1}} + \mathbf{K_{D2}} & -\mathbf{Y_a} & -\mathbf{Y_b} \\ \mathbf{Y_a}^T & \mathbf{0} & \mathbf{0} \\ \mathbf{Y_b}^T & \mathbf{0} & \mathbf{0} \end{bmatrix} \begin{pmatrix} \mathbf{s} \\ \tilde{\mathbf{a}}_\mathbf{1} \\ \tilde{\mathbf{a}}_\mathbf{2} \end{pmatrix} = \begin{pmatrix} \mathbf{0} \\ \mathbf{0} \\ \mathbf{0} \end{pmatrix} \tag{4.47}$$

which can be shown to be semi-contracting similar to (4.37). Therefore, applying Barbalat's lemma results in asymptotic convergence of $\begin{pmatrix} \mathbf{s} & \tilde{\mathbf{a}}_\mathbf{1} & \tilde{\mathbf{a}}_\mathbf{2} \end{pmatrix}^T$ to zero. This result ensures that the decentralized adaptive control law globally and asymptotically stabilizes the two-spacecraft tethered array.

4.4.3 Decentralized Robust Adaptive Control

Combining the robust sliding control and the adaptive control introduced above, we can derive a robust adaptive control law as follows:

$$\begin{aligned}
\tau_\mathbf{1} &= \mathbf{Y_1}\hat{\mathbf{a}}_\mathbf{1} - \mathbf{K}\text{sat}(\mathbf{s_1}/\phi) = \hat{\mathbf{M}}_\mathbf{1}(\mathbf{q_1})\ddot{\mathbf{q}}_\mathbf{1r} + \hat{\mathbf{C}}_\mathbf{1}(\mathbf{q_1},\dot{\mathbf{q}}_\mathbf{1})\dot{\mathbf{q}}_\mathbf{1r} - \mathbf{K}\text{sat}(\mathbf{s_1}/\phi) \\
\tau_\mathbf{2} &= \mathbf{Y_2}\hat{\mathbf{a}}_\mathbf{2} - \mathbf{K}\text{sat}(\mathbf{s_2}/\phi) = \hat{\mathbf{M}}_\mathbf{1}(\mathbf{q_2})\ddot{\mathbf{q}}_\mathbf{2r} + \hat{\mathbf{C}}_\mathbf{1}(\mathbf{q_2},\dot{\mathbf{q}}_\mathbf{2})\dot{\mathbf{q}}_\mathbf{2r} - \mathbf{K}\text{sat}(\mathbf{s_2}/\phi)
\end{aligned} \tag{4.48}$$

where $\mathbf{Y_1} = \mathbf{Y}(\mathbf{q_1},\dot{\mathbf{q}}_\mathbf{1},\dot{\mathbf{q}}_\mathbf{1r},\ddot{\mathbf{q}}_\mathbf{1r})$ and $\mathbf{Y_2} = \mathbf{Y}(\mathbf{q_2},\dot{\mathbf{q}}_\mathbf{2},\dot{\mathbf{q}}_\mathbf{2r},\ddot{\mathbf{q}}_\mathbf{2r})$. Also, we show that a saturation function sat$(\cdot)$ can be used in lieu of a signum function in order to avoid chattering.

The parameter estimates $\hat{\mathbf{a}}_\mathbf{1}$ and $\hat{\mathbf{a}}_\mathbf{2}$ are updated according to the same correlation integrals

$$\begin{aligned}
\dot{\hat{\mathbf{a}}}_\mathbf{1} &= -\mathbf{\Gamma Y}_1^T\mathbf{s}_1 \\
\dot{\hat{\mathbf{a}}}_\mathbf{2} &= -\mathbf{\Gamma Y}_2^T\mathbf{s}_2
\end{aligned} \tag{4.49}$$

This adaptive decentralized control law yields bounded tracking errors with asymptotic convergence for bounded disturbances. The proof is straightforward combining the results in the previous sections.

4.5 Multiple Tether Arrays

This section extends the previous result for decentralized control for two-spacecraft systems to an arbitrary number of circularly connected arrays, including a triangular configuration and a three-spacecraft inline configuration.

4.5.1 Spinning Triangular Array and Multiple Circular Arrays

Motivated by successful decoupling of the two-spacecraft case, three imaginary pseudo-tethers [138] connecting each satellite to the CM of the array are assumed to exist, replacing the three actual tether lines (see Figure 4-3). The equations of motion for a three-spacecraft triangular array are given in (3.42) while the equations for an arbitrarily large circular array of tethered spacecraft are given in (3.45).

It is straightforward to show that a stabilizing controller for a single-tethered spacecraft will stabilize a three-spacecraft triangular array using the same methods as described in Section 4.3. For example, we can construct an exponentially stabilizing controller from (4.12) by introducing dummy variables to each individual spacecraft of a three-spacecraft triangular array:

$$\begin{aligned}
&\mathbf{M}_{\phi_1}(\mathbf{q})\ddot{\mathbf{q}} + \mathbf{C}_{\phi_1}(\mathbf{q},\dot{\mathbf{q}})\dot{\mathbf{q}} = \tau_{\mathbf{a}} \\
&\tau_{\mathbf{a}} = \mathbf{M}_{\phi_1}(\mathbf{q})\ddot{\mathbf{q}}_{\mathbf{r}} + \mathbf{C}_{\phi_1}(\mathbf{q},\dot{\mathbf{q}})\dot{\mathbf{q}}_{\mathbf{r}} - \mathbf{K_{D1}}(\dot{\mathbf{q}} - \dot{\mathbf{q}}_{\mathbf{r}}) \\
&\mathbf{M}_{\phi_2}(\mathbf{q})\ddot{\mathbf{q}} + \mathbf{C}_{\phi_2}(\mathbf{q},\dot{\mathbf{q}})\dot{\mathbf{q}} = \tau_{\mathbf{b}} \\
&\tau_{\mathbf{b}} = \mathbf{M}_{\phi_2}(\mathbf{q})\ddot{\mathbf{q}}_{\mathbf{r}} + \mathbf{C}_{\phi_2}(\mathbf{q},\dot{\mathbf{q}})\dot{\mathbf{q}}_{\mathbf{r}} - \mathbf{K_{D2}}(\dot{\mathbf{q}} - \dot{\mathbf{q}}_{\mathbf{r}}) \\
&\mathbf{M}_{\phi_3}(\mathbf{q})\ddot{\mathbf{q}} + \mathbf{C}_{\phi_3}(\mathbf{q},\dot{\mathbf{q}})\dot{\mathbf{q}} = \tau_{\mathbf{c}} \\
&\tau_{\mathbf{c}} = \mathbf{M}_{\phi_3}(\mathbf{q})\ddot{\mathbf{q}}_{\mathbf{r}} + \mathbf{C}_{\phi_3}(\mathbf{q},\dot{\mathbf{q}})\dot{\mathbf{q}}_{\mathbf{r}} - \mathbf{K_{D3}}(\dot{\mathbf{q}} - \dot{\mathbf{q}}_{\mathbf{r}})
\end{aligned} \tag{4.50}$$

where

$$\mathbf{M}_{\phi_1} = \begin{bmatrix} m_{11}(\phi_1) & m_{12}(\phi_1) & 0 & 0 \\ m_{12}(\phi_1) & m_{22} & 0 & 0 \\ 0 & 0 & 0 & 0 \\ 0 & 0 & 0 & 0 \end{bmatrix}, \quad \mathbf{C}_{\phi_1} = \begin{bmatrix} c_{11}(\phi_1,\dot{\phi_1}) & c_{12}(\phi_1,\dot{\theta},\dot{\phi_1}) & 0 & 0 \\ c_{21}(\phi_1,\dot{\theta}) & c_{22} & 0 & 0 \\ 0 & 0 & 0 & 0 \\ 0 & 0 & 0 & 0 \end{bmatrix}$$

$$\mathbf{M}_{\phi_2} = \begin{bmatrix} m_{11}(\phi_2) & 0 & m_{12}(\phi_2) & 0 \\ 0 & 0 & 0 & 0 \\ m_{12}(\phi_2) & 0 & m_{22} & 0 \\ 0 & 0 & 0 & 0 \end{bmatrix}, \quad \mathbf{C}_{\phi_2} = \begin{bmatrix} c_{11}(\phi_2,\dot{\phi_2}) & 0 & c_{12}(\phi_2,\dot{\theta},\dot{\phi_2}) & 0 \\ 0 & 0 & 0 & 0 \\ c_{21}(\phi_2,\dot{\theta}) & 0 & c_{22} & 0 \\ 0 & 0 & 0 & 0 \end{bmatrix},$$

$$\mathbf{M}_{\phi_3} = \begin{bmatrix} m_{11}(\phi_3) & 0 & 0 & m_{12}(\phi_3) \\ 0 & 0 & 0 & 0 \\ 0 & 0 & 0 & 0 \\ m_{12}(\phi_3) & 0 & 0 & m_{22} \end{bmatrix}, \quad \mathbf{C}_{\phi_3} = \begin{bmatrix} c_{11}(\phi_3,\dot{\phi_3}) & 0 & 0 & c_{12}(\phi_3,\dot{\theta},\dot{\phi_3}) \\ 0 & 0 & 0 & 0 \\ 0 & 0 & 0 & 0 \\ c_{21}(\phi_3,\dot{\theta}) & 0 & 0 & c_{22} \end{bmatrix}.$$

In addition,

$$\tau_{\mathbf{a}} = \begin{pmatrix} \tau_{\theta,1} \\ \tau_{\phi,1} \\ 0 \\ 0 \end{pmatrix}, \quad \mathbf{K_{D1}} = \begin{bmatrix} k_{11} & k_{12} & 0 & 0 \\ k_{12} & k_{22} & 0 & 0 \\ 0 & 0 & 0 & 0 \\ 0 & 0 & 0 & 0 \end{bmatrix}, \quad \tau_{\mathbf{b}} = \begin{pmatrix} \tau_{\theta,2} \\ 0 \\ \tau_{\phi,2} \\ 0 \end{pmatrix}, \quad \mathbf{K_{D2}} = \begin{bmatrix} k_{11} & 0 & k_{12} & 0 \\ 0 & 0 & 0 & 0 \\ k_{12} & 0 & k_{22} & 0 \\ 0 & 0 & 0 & 0 \end{bmatrix},$$

$$\tau_{\mathbf{c}} = \begin{pmatrix} \tau_{\theta,3} \\ 0 \\ 0 \\ \tau_{\phi,3} \end{pmatrix}, \quad \mathbf{K_{D3}} = \begin{bmatrix} k_{11} & 0 & 0 & k_{12} \\ 0 & 0 & 0 & 0 \\ 0 & 0 & 0 & 0 \\ k_{12} & 0 & 0 & k_{22} \end{bmatrix}, \quad \mathbf{q} = \begin{pmatrix} \theta \\ \phi_1 \\ \phi_2 \\ \phi_3 \end{pmatrix}$$

where k_{11} and k_{12} meet the condition in (4.17). The symmetry property discussed earlier leads to

$$\mathbf{M_3} = \mathbf{M}_{\phi_1} + \mathbf{M}_{\phi_2} + \mathbf{M}_{\phi_3} \quad \text{and} \quad \mathbf{C_3} = \mathbf{C}_{\phi_1} + \mathbf{C}_{\phi_2} + \mathbf{C}_{\phi_3}.$$

We can easily find that the combined gain matrix,

$$\mathbf{K_{D1}} + \mathbf{K_{D2}} + \mathbf{K_{D3}} = \begin{bmatrix} 3k_{11} & k_{12} & k_{12} & k_{12} \\ k_{12} & k_{22} & 0 & 0 \\ k_{12} & 0 & k_{22} & 0 \\ k_{12} & 0 & 0 & k_{22} \end{bmatrix} \tag{4.51}$$

is uniformly positive definite, which in turn leads to contraction of the combined system.

In summary, under the reasonable assumption of the taut and equal-length pseudo-tether, a controller designed from a single-tethered system will synchronize both array spin rate and oscillations of each spacecraft, thereby reducing the original dynamics to those of a single-tethered spacecraft, as seen in Figure 4-3. The result in this section was predicted in Ref. [202], in the sense that for a star network with an arbitrary number of satellites, the minimum coupling strength to guarantee synchronization is independent of the number of satellites.

4.5.2 Three Inline Array

Similarly, the dynamics of the three-spacecraft inline configuration in Figure 4-4 can be decoupled into two independent dynamics of the single-tethered system with the tether length ℓ and rotational dynamics of the center spacecraft. The equations of motion of the inline array dynamics have been presented in Section 3.6. Equation (3.58), where θ is defined from the fixed center inertial frame, is simpler than (3.53) with a different coordinate definition of θ, e.g., θ defined with respect to the rotating frame of the center spacecraft ($\theta \to \theta + \psi$), as discussed in Section 3.6. Moreover, this definition of coordinates enables decoupling of the dynamics of the outlying spacecraft from the center spacecraft, as seen in the figure.

The dynamics of the spacecraft at the tips of the array are

$$\begin{aligned} \begin{pmatrix} M_{12} \\ M_{13} \end{pmatrix} \ddot{\psi} + \begin{pmatrix} C_{21} \\ C_{31} \end{pmatrix} \dot{\psi} + \mathbf{M_1}(\phi_1) \begin{pmatrix} \ddot{\theta}_1 \\ \ddot{\phi}_1 \end{pmatrix} + \mathbf{C_1}(\phi_1, \dot{\theta}_1, \dot{\phi}_1) \begin{pmatrix} \dot{\theta}_1 \\ \dot{\phi}_1 \end{pmatrix} = \begin{pmatrix} \tau_{\theta,1} \\ \tau_{\phi,1} \end{pmatrix} \\ \begin{pmatrix} M_{14} \\ M_{15} \end{pmatrix} \ddot{\psi} + \begin{pmatrix} C_{41} \\ C_{51} \end{pmatrix} \dot{\psi} + \mathbf{M_1}(\phi_2) \begin{pmatrix} \ddot{\theta}_2 \\ \ddot{\phi}_2 \end{pmatrix} + \mathbf{C_1}(\phi_2, \dot{\theta}_2, \dot{\phi}_2) \begin{pmatrix} \dot{\theta}_2 \\ \dot{\phi}_2 \end{pmatrix} = \begin{pmatrix} \tau_{\theta,2} \\ \tau_{\phi,2} \end{pmatrix} \end{aligned} \tag{4.52}$$

This is a hierarchical combination, as introduced in **Theorem 2.5.4** since the dynamics reduce to those of the single-tethered system when the dynamics of ψ vanish. It is easy to implement an exponentially stabilizing controller for ψ, in particular with measurement of tether tensions [43]. Then, the dynamics of the center spacecraft and its feedback linearized control law are given as

$$I_G \ddot{\psi} = T_1 r \sin(\theta_1 - \psi) + T_2 r \sin(\theta_2 - \psi) + u_0 \tag{4.53}$$

where T_1 and T_2 are the tension measurements. Also, note that the bearing angles $(\theta_1 - \psi, \theta_2 - \psi)$ are easily measured by the force-sensor-based measurement system presented in Chapter 7. Then, its feedback linearized controller is given as

$$u_0 = I_G \ddot{\psi}_d - K(\dot{\psi} - \dot{\psi}_d) - T_1 r \sin(\theta_1 - \psi) - T_2 r \sin(\theta_2 - \psi) \tag{4.54}$$

which exponentially stabilizes $\dot{\psi}$ with $K > 0$.

Therefore, as long as $\ddot{\psi} \to 0$, $\psi \approx \theta_i$, and $\phi_i \to 0$ (or $\ddot{\psi}, \dot{\psi} \to 0$), the same controller stabilizing the single-tethered system in the previous sections will also stabilize the combined system. Equation

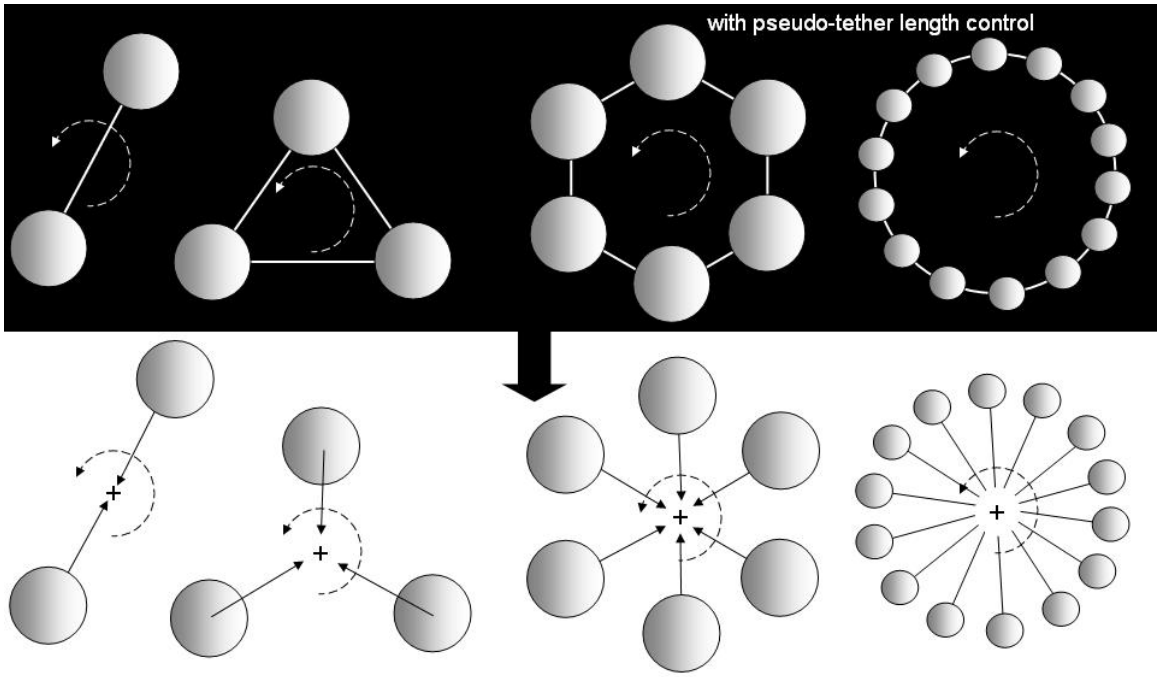

(a) With control of the pseudo-tether lengths

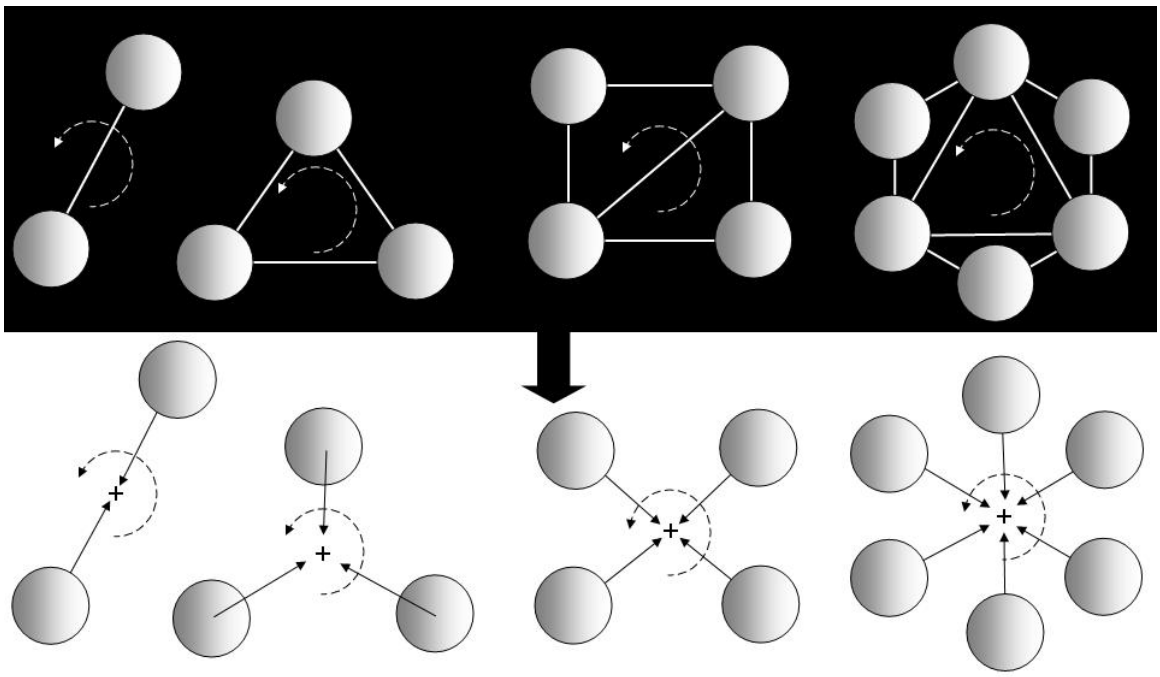

(b) With diagonal-tether constraints

Figure 4-3: Reduction of circular and star tethered arrays into multiple single-tethered systems

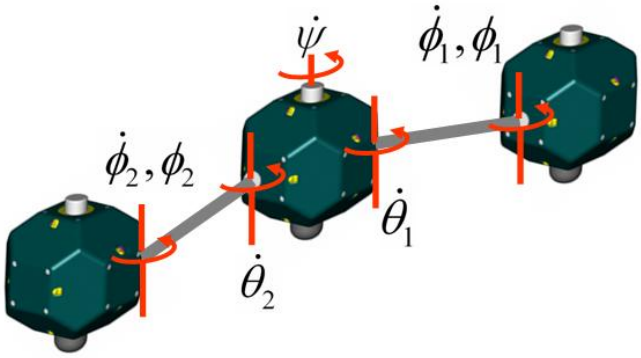

(a) Three inline configuration with a hierarchical combination

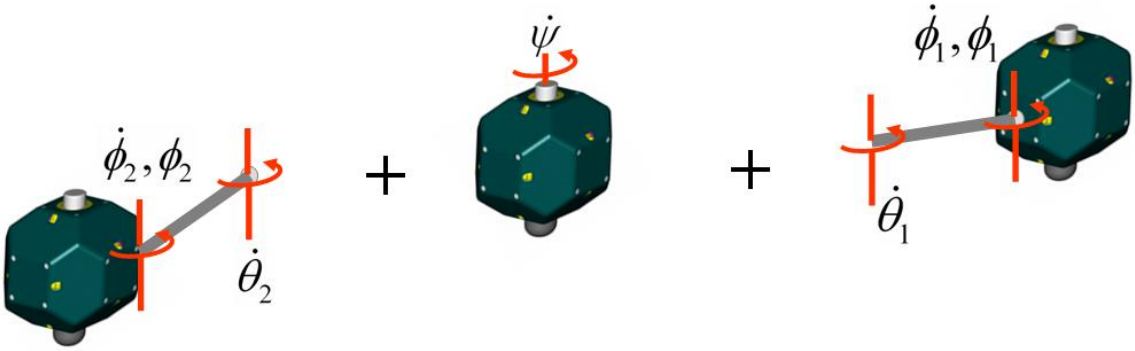

(b) Decoupled into two independent single-tethered systems and a center spacecraft

Figure 4-4: Three-spacecraft array decoupled into three sub-systems.

(4.52) then satisfies the following,

$$\mathbf{M_1}(\phi_1)\begin{pmatrix}\ddot{\theta_1}\\ \ddot{\phi_1}\end{pmatrix}+\mathbf{C_1}(\phi_1,\dot{\theta_1},\dot{\phi_1})\begin{pmatrix}\dot{\theta_1}\\ \dot{\phi_1}\end{pmatrix}-\tau_{\mathbf{1}}=\mathbf{M_1}(\phi_2)\begin{pmatrix}\ddot{\theta_2}\\ \ddot{\phi_2}\end{pmatrix}+\mathbf{C_1}(\phi_2,\dot{\theta_2},\dot{\phi_2})\begin{pmatrix}\dot{\theta_2}\\ \dot{\phi_2}\end{pmatrix}-\tau_{\mathbf{2}} \tag{4.55}$$

According to the synchronization theorem (**Theorem 2.5.7**), θ_1 and ϕ_1 exponentially converge to θ_2 and ϕ_2, respectively, as long as the decentralized controllers, $\tau_{\mathbf{1}}$ and $\tau_{\mathbf{2}}$, make each single-tethered system contracting. In other words, contraction analysis shows that implementing a control law based upon the single-tethered dynamics ensures the stability of the rotation rate and the relative motions in an inline three-spacecraft array. The exact proof of the synchronization of the compound pendulum modes can be given, similar to the method in Chapter 5.

4.6 Simulations

A few representative simulation results are presented in order to verify the proposed decentralized nonlinear control approach.

4.6.1 Spin-Up Maneuver of Three Inline Spacecraft

The control law introduced in (4.12) is used to spin up the two spacecraft at the tip of the inline three-spacecraft array in Figure 4-4 while a simple control law, $u_0 = K(\omega - \dot{\psi})$ spins the center spacecraft. The desired spin rates, $\dot{\theta}_{1d}, \dot{\theta}_{2d}, \dot{\psi}_d$, are ω=0.3 rad/s with no motion of the compound pendulum mode. The initial rotation rates ($\dot{\theta}_{10}$, $\dot{\theta}_{20}$, $\dot{\psi}_0$), are 0.2, 0.22, 0.2 rad/s with the following compound pendulum mode initial conditions, $\phi_1, \dot{\phi}_1, \phi_2, \dot{\phi}_2 = 0$. The radius of SPHERES, r is 0.125 m, the tether length, ℓ is 1 m, the mass of a SPHERES satellite with the air-bearing carriage is 8.6 kg, and the moment of inertia, I is 0.074 kgm^2. Figure 4-5 shows that a controller from the single spacecraft dynamics successfully performs a spin-up of the array to the desired rate. During the spin-up maneuver, Figure 4-5(b) indicates that the compound pendulum modes of the two outlying spacecraft remained close to zero while synchronizing with each other.

4.6.2 Simulation Results for Decentralized Nonlinear Adaptive Control

In this section, the tracking performance of the decentralized nonlinear adaptive control law introduced in Section 4.4.2 is simulated to stabilize a two-spacecraft coupled array. The objective of the control is to spin up the interferometric array to the target angular rate ω, while minimizing the compound pendulum mode. Then, the desired trajectory is defined as follows:

$$\dot{\theta}_d = (\omega - \dot{\theta}_0)(1 - e^{-\tau t}) + \dot{\theta}_0, \quad \ddot{\theta}_d = (\omega - \dot{\theta}_0)\tau e^{-\tau t}, \tag{4.56}$$

$$\ddot{\phi}_d = 0, \quad \dot{\phi}_d = 0, \quad \phi_d = 0. \tag{4.57}$$

where $\dot{\theta}_0$= 0.1 rad/s, ω= 0.2 rad/s. The initial conditions are defined as $\dot{\theta}_0$=0.1 rad/s, ϕ_0= −0.1 rad, and $\dot{\phi}_0$= 0.1 rad/s for the first spacecraft, and ϕ_0= −0.1 rad, and $\dot{\phi}_0$= 0.05 rad/s for the second spacecraft. The physical parameters used in the simulations are selected from the actual values of the SPHERES testbed on the new air-bearing carriage described in Chapter 7. The radius of SPHERES, r is 0.15 m, the mass of SPHERES with the air-bearing carriage, m is 20.346 kg, and the moment of inertia, I is 0.178 kgm^2. The tether length ℓ is either 0.5 m or 1 m.

Recalling the decentralized adaptive control in (4.33), the tracking gain $\mathbf{K}$ is selected such that the tracking of $\dot{\theta}_d$ is weighted more heavily than the minimization of the compound pendulum mode:

$$\mathbf{K} = \begin{bmatrix}5 & 0\\ 0 & 1\end{bmatrix} \tag{4.58}$$

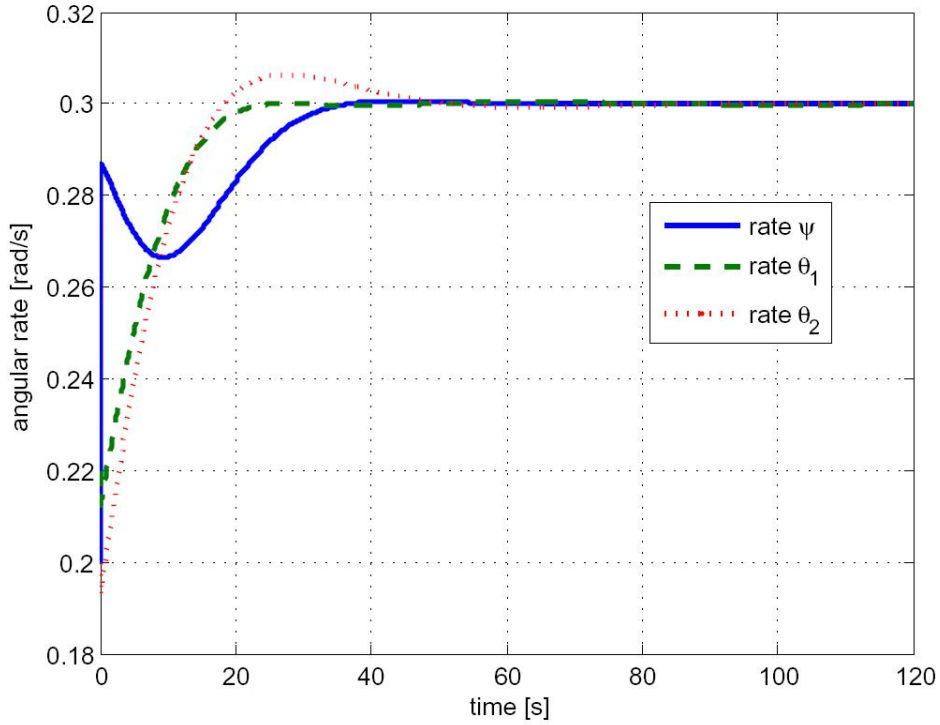

(a) Array angular rate

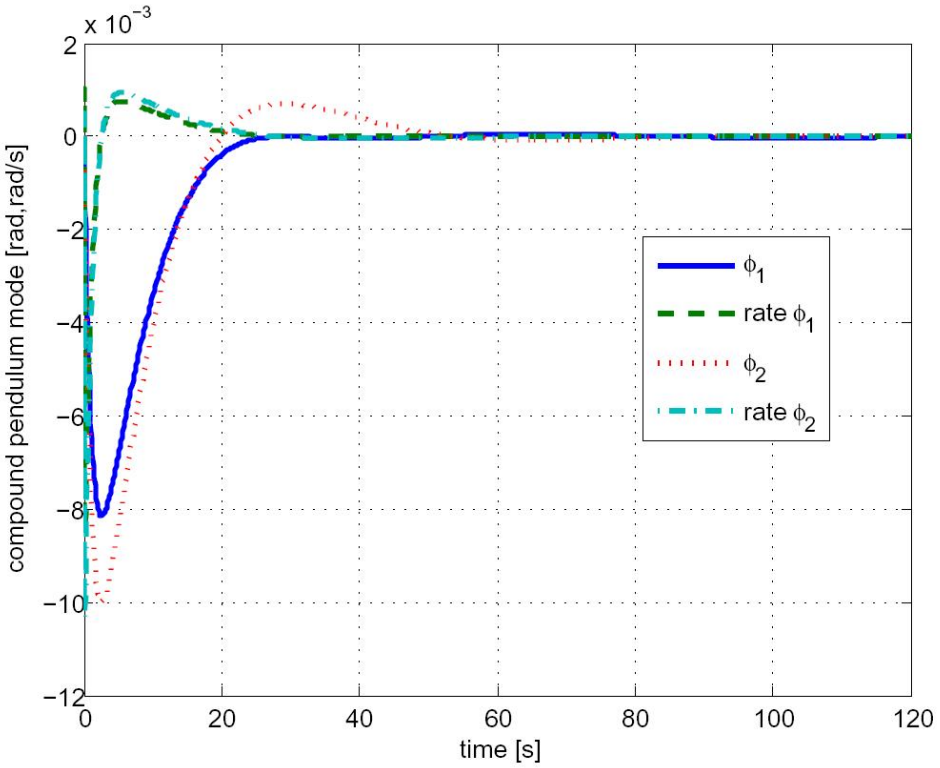

(b) Compound pendulum mode

Figure 4-5: Spin-up control of three-inline configuration

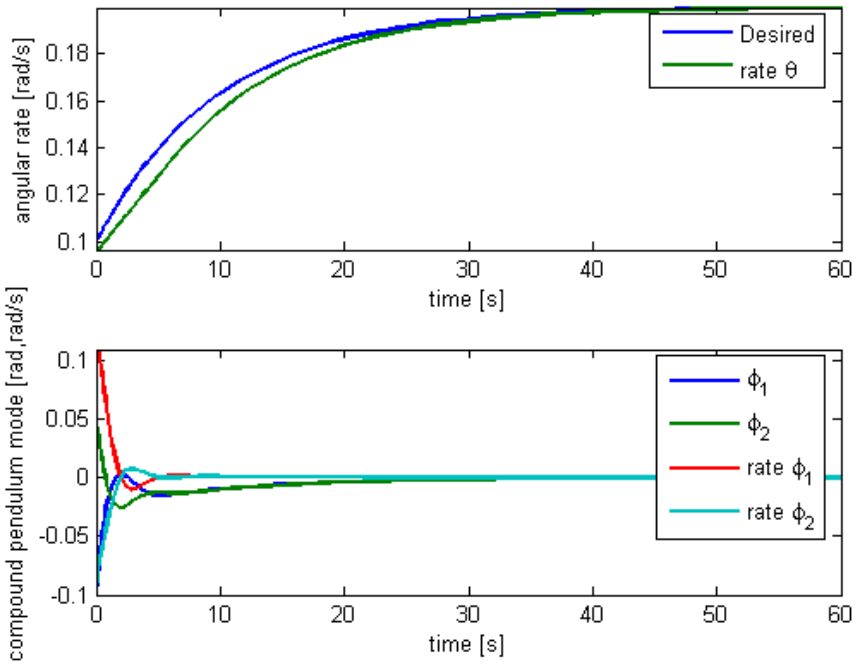

(a) Tracking performance

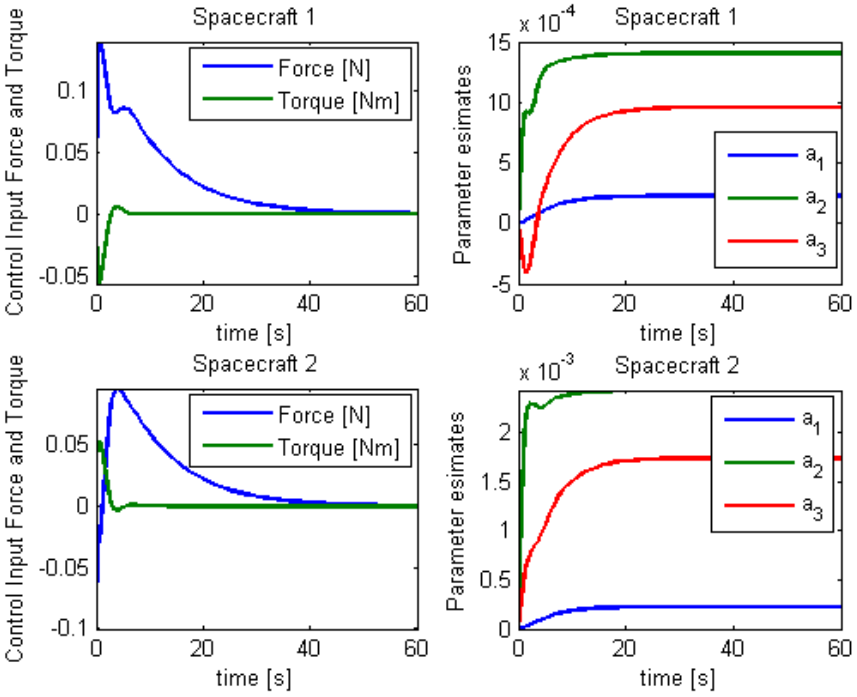

(b) Control input and parameter estimates

Figure 4-6: Spin-up control of two-spacecraft array using the decentralized adaptive control

and $\mathbf{\Lambda} = \mathbf{I}$. In addition, the vector of parameter estimate update uses

$$\mathbf{\Gamma} = \begin{bmatrix} 0.3 & 0 & 0 \\ 0 & 0.5 & 0 \\ 0 & 0 & 1 \end{bmatrix} \tag{4.59}$$

and the initial condition $\hat{\mathbf{a}}(0) = \mathbf{0}$.

The simulation results are presented in Figure 4-6. Without the need for inter-satellite communications, the decentralized adaptive control law successfully performs tracking without any a-priori knowledge of the physical parameters. Figure 4-6(b) shows that the parameter estimates tend to the steady-state values. As typical of adaptive control, the decentralized approach in this section does not necessarily estimate the unknown parameters exactly, but simply generates values that allow the desired task to be achieved [178]. Figure 4-6(a) also depicts the synchronization of ϕ_1 and ϕ_2 while they tend to zero simultaneously.

4.7 Conclusion

We introduced a decentralized control technique by reducing the original dynamics to simpler stable closed-loop dynamics exploiting oscillation synchronization. Contraction theory proves that a decentralized control law can be designed based on a single-tethered system in lieu of the coupled dynamics of multiple spacecraft, reducing the computation and communication burdens. Furthermore, the stability of the combined system is global and exponential. The technique is extended to the three-spacecraft inline configuration and the triangular configuration, both of which are being studied for NASA's SPECS mission. The proposed decentralized control strategy is further extended to robust adaptive control to account for model uncertainties. Results of numerical simulations show the effectiveness of the proposed control strategy.

Chapter 5

Cooperative Robot Control and Synchronization of Multiple Lagrangian Systems

5.1 Chapter Objective

The main application of this dissertation has been tethered formation flight, which exhibits inherent nonlinear couplings between spacecraft due to the physical connections of the tethers. In particular, Chapter 4 presented a novel decentralized control strategy, by oscillation synchronization, which eliminates the need for any inter-satellite communications. In this chapter, we extend a synchronization framework to inherently physically *uncoupled* multi-agent systems. The main contributions of this chapter have been stated in Section 1.5.5.

5.2 Introduction

In this dissertation, synchronization is defined as a complete match of all configuration variables of each dynamical system such that $\mathbf{x}_1 = \mathbf{x}_2 = \cdots = \mathbf{x}_p$ and p denotes the number of sub-systems in the network. While such a definition directly concerns the attitude tracking problem, this chapter further addresses synchronization of biased variables with application to the position coordination problem. In the latter case, synchronization corresponds to $\mathbf{y}_1 = \mathbf{y}_2 = \cdots = \mathbf{y}_p$ where $\mathbf{y}_i$, $1 \leq i \leq p$ connotes a vector of biased variables constructed from the configuration vector $\mathbf{x}_i$ such that $\mathbf{x}_i(t) = \mathbf{y}_i(t) + \mathbf{b}_i(t)$ and the separation vector $\mathbf{b}_i(t)$ is independent of the dynamics.

The objective of this chapter is to introduce a unified synchronization framework that can be directly applied to cooperative control of multi-robot systems or formation flying aerospace vehicles to achieve a common goal. For example, a large swarm of robots can first synchronize their attitudes and positions to form a certain formation pattern, then track the common trajectory to accomplish the given mission (see Figure 5-1(a)). In production processes, such as manufacturing and automotive applications, where high flexibility, manipulability, and maneuverability cannot be achieved by a single system [164], there has been widespread interest in cooperative schemes for multiple robot manipulators (Figure 5-1(b)). A stellar formation flight interferometer is another example where precision control of relative spacecraft motions is indispensable (Figure 5-1(c)). The proposed synchronization tracking control law can be implemented for such purposes, thereby achieving more efficient and robust performance through local interactions. Other potential applications include oscillation synchronization of robotic locomotion [85, 154], and tele-manipulation of robots [143, 81, 4, 105, 40].

Another benefit of synchronization is its implication for model reduction. The exponential synchronization of multiple nonlinear dynamics allows us to reduce the dimensionality of the stability analysis of a large network. The model reduction aspect of synchronization, also introduced for spa-

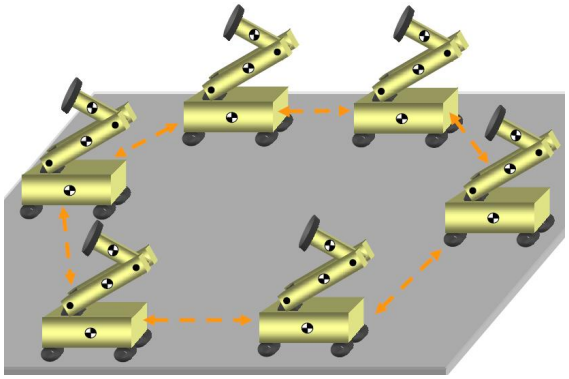

(a) Dynamic network of robots

(b) Robot cooperation, courtesy: KAIST RSlab, http://rslab.kaist.ac.kr

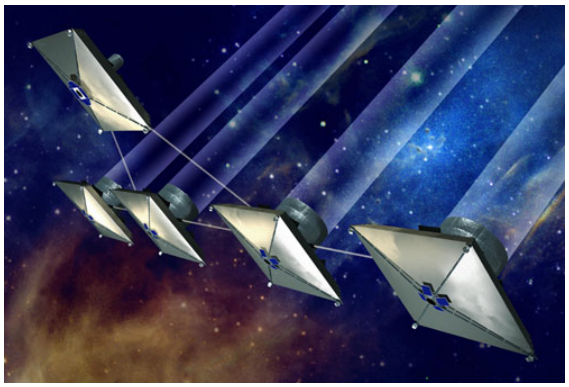

(c) NASA formation flying interferometer TPF, courtesy: NASA, http://planetquest.jpl.nasa.gov

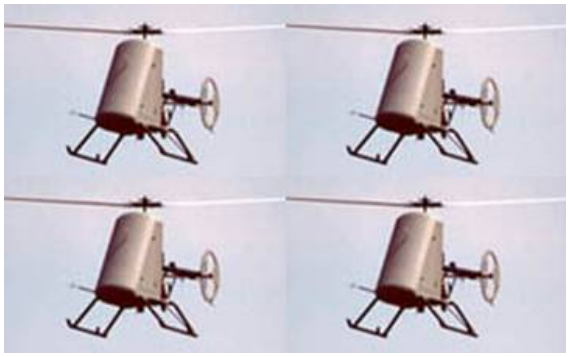

(d) Formation flying UAVs

Figure 5-1: Possible applications of synchronization of multiple agents.

tially inter-connected systems in Chapter 4, is further generalized and strengthened in this chapter. This implies that once the network is proven to synchronize, we can regard a network as a single synchronized set of dynamics, which simplifies any additional stability analysis.

The main contributions of this chapter can be stated as follows.

- In contrast with prior work on consensus and flocking problems using graphs, the proposed strategy primarily deals with dynamical networks consisting of highly nonlinear time-varying dynamics. Proving stability of nonlinear dynamic network systems is a much more difficult problem.

- The proposed control laws are of a decentralized form requiring only local velocity/position coupling feedback for global exponential convergence, thereby facilitating implementation in real systems. As opposed to some previous work requiring all-to-all coupling [164], this will significantly reduce communication burdens.

- The theory is generalized and extended to multi-robot systems with non-identical dynamics, partial joint coupling, uni-directional coupling, and adaptive control.

- Since the main nonlinear stability tool is contraction analysis [112, 176, 202], we derive exact and global results with exponential convergence.

- Time-delayed communications and robustness properties are also discussed.

5.2.1 Organization

In Section 1.6.5, prior work on the multi-agent synchronization has been discussed and compared with the approach proposed in this chapter. The organization of this chapter is as follows: modeling of robots based on the Lagrangian formulation is described in Section 5.3. Section 5.4 summarizes the main theorems of this chapter; the new tracking control law, which synchronizes each robot to track the same desired trajectory, is proposed. While the tracking stability is proven in Section 5.4.2, the proof of exponential synchronization is more involved and treated separately in Section 5.5. The remainder of the chapter further highlights the unique contributions of this chapter. A few examples of dynamics networks are given in Section 5.6, validating the effectiveness of the proposed synchronization framework. The same section also introduces the partial joint couplings and uni-directional couplings. Additionally, the properties of robustness to transmission delays and disturbances are discussed in Section 5.7. An adaptive control version of the proposed synchronization strategy is presented in Section 5.8. The main idea of this chapter is extended to networks with Proportional-Derivative (PD) coupling in Section 5.9. Section 5.10 offers a potential application of the proposed scheme to the concurrent synchronization and leader-follower problem.

5.3 Modeling of Multi-Robot Network

An exponentially stabilizing nonlinear control law that can synchronize an arbitrary number of robots to track a common trajectory is introduced in this chapter. The proposed controller is much simpler than earlier work, such as the synchronization law in [164], in terms both of the computational load and the required signals. The equations of motion for a robot with multiple joints ($\mathbf{q}_i \in \mathbb{R}^n$) can be derived by exploiting the Euler-Lagrange equations:

$$\begin{aligned}
\mathbf{M}_1(\mathbf{q}_1)\ddot{\mathbf{q}}_1 + \mathbf{C}_1(\mathbf{q}_1, \dot{\mathbf{q}}_1)\dot{\mathbf{q}}_1 + \mathbf{g}_1(\mathbf{q}_1) &= \tau_1 \\
\mathbf{M}_2(\mathbf{q}_2)\ddot{\mathbf{q}}_2 + \mathbf{C}_2(\mathbf{q}_2, \dot{\mathbf{q}}_2)\dot{\mathbf{q}}_2 + \mathbf{g}_2(\mathbf{q}_2) &= \tau_2 \\
&\cdots \\
\mathbf{M}_i(\mathbf{q}_i)\ddot{\mathbf{q}}_i + \mathbf{C}_i(\mathbf{q}_i, \dot{\mathbf{q}}_i)\dot{\mathbf{q}}_i + \mathbf{g}_i(\mathbf{q}_i) &= \tau_i \\
&\cdots \\
\mathbf{M}_p(\mathbf{q}_p)\ddot{\mathbf{q}}_p + \mathbf{C}_p(\mathbf{q}_p, \dot{\mathbf{q}}_p)\dot{\mathbf{q}}_p + \mathbf{g}_p(\mathbf{q}_p) &= \tau_p
\end{aligned} \tag{5.1}$$

where i, $(1 \leq i \leq p)$ denotes the index of robots or dynamical systems comprising a network, and p is the total number of the individual elements. Also, $\mathbf{g}_i(\mathbf{q}_i) = \frac{\partial V}{\mathbf{q}_i}$, and, τ_i is a generalized force or torque acting on the i-th robot.

Note that we define $\mathbf{C}_i(\mathbf{q}_i, \dot{\mathbf{q}}_i)$ such that $(\dot{\mathbf{M}}_i - 2\mathbf{C}_i)$ is skew-symmetric. It is emphasized that this property plays a central role in the stability analysis of this chapter.

The following key assumptions are used throughout this chapter. The robot system in (5.1) is fully actuated. In other words, the number of control inputs is equal to the dimension of their configuration manifold ($= n$). The mass-inertia matrix $\mathbf{M}$ is assumed to be uniformly positive definite, for all positions $\mathbf{q}$ in the robot workspace [178]. Such an inertia matrix is called a Riemannian metric (see the discussion in Chapter 2). Furthermore, the matrix is bounded– i.e. $\exists \alpha, \beta > 0$ such that

$$\alpha\mathbf{I} \leq \mathbf{M}(\mathbf{q}) \leq \beta\mathbf{I}, \text{ and } \frac{1}{\beta}\mathbf{I} \leq \mathbf{M}^{-1}(\mathbf{q}) \leq \frac{1}{\alpha}\mathbf{I} \tag{5.2}$$

The $\mathbf{C}$ matrix in (5.1) can be decomposed as follows [51, 164]:

$$\mathbf{C}(\mathbf{q}, \dot{\mathbf{q}}) = \begin{bmatrix} \dot{\mathbf{q}}^T C_1(\mathbf{q}) \\ \dot{\mathbf{q}}^T C_2(\mathbf{q}) \\ \cdots \\ \dot{\mathbf{q}}^T C_n(\mathbf{q}) \end{bmatrix}, \text{ and } \|C_j(\mathbf{q})\| \leq c_{max} \tag{5.3}$$

where $C_j(\mathbf{q}) \in \mathbb{R}^{n \times n}$ with $j = 1, 2, \cdots, n$ is a symmetric matrix and $c_{max} > 0$.

The inequality in (5.3) also implies

$$\|\mathbf{C}(\mathbf{q},\dot{\mathbf{q}})\| \leq C_{max}\|\dot{\mathbf{q}}\|, \quad C_{max} > 0 \tag{5.4}$$

5.4 A New Approach to Synchronization Tracking Control

We consider the synchronization of multiple robots following a common time-varying trajectory. A tracking controller introduced in this section achieves not only global and exponential synchronization of the configuration variables, but also global exponential convergence to the desired trajectory.

5.4.1 Proposed Synchronization Control Strategy

We introduce a simple alternative control law for the mutual synchronization problem of multiple robots, as seen in [164]. The following tracking control law with two-way-ring symmetry is proposed for the i-th robot in the network consisting of p identical robots:

$$\begin{aligned}\tau_i = \mathbf{M}(\mathbf{q}_i)\ddot{\mathbf{q}}_{ir} + \mathbf{C}(\mathbf{q}_i,\dot{\mathbf{q}}_i)\dot{\mathbf{q}}_{ir} + \mathbf{g}(\mathbf{q}_i) \\ - \mathbf{K}_1(\dot{\mathbf{q}}_i - \dot{\mathbf{q}}_{ir}) + \mathbf{K}_2(\dot{\mathbf{q}}_{i-1} - \dot{\mathbf{q}}_{i-1,r}) + \mathbf{K}_2(\dot{\mathbf{q}}_{i+1} - \dot{\mathbf{q}}_{i+1,r})\end{aligned} \tag{5.5}$$

where a positive-definite matrix $\mathbf{K}_1 \in \mathbb{R}^{n\times n}$ is a feedback gain for the i-th robot, and another positive-definite matrix $\mathbf{K}_2 \in \mathbb{R}^{n\times n}$ is a coupling gain with the adjacent members ($i-1$ and $i+1$). The above control law can also be applied to a network consisting of p non-identical robots, as shall be seen in Section 5.6.1 (see Figure 5-2 for network structures permitted here) The reference velocity vector, $\dot{\mathbf{q}}_{ir}$ is given by shifting the common desired velocity $\dot{\mathbf{q}}_\mathbf{d}$ with the position error:

$$\dot{\mathbf{q}}_{ir} = \dot{\mathbf{q}}_d - \mathbf{\Lambda}\widetilde{\mathbf{q}}_i = \dot{\mathbf{q}}_d - \mathbf{\Lambda}(\mathbf{q}_i - \mathbf{q}_d) \tag{5.6}$$

where $\mathbf{\Lambda}$ is a positive diagonal matrix.
In contrast with [164], the proposed control law requires only the coupling feedback of the most adjacent robots ($i-1$ and $i+1$) for exponential convergence (see Figure 5-2). Note that the last (p-th) robot is connected with the first robot to form a ring network as suggested in [202]. Moreover, estimates of $\ddot{\mathbf{q}}$ are no longer required.

The closed-loop dynamics using (5.1) and (5.5) become

$$\mathbf{M}(\mathbf{q}_i)\dot{\mathbf{s}}_i + \mathbf{C}(\mathbf{q}_i,\dot{\mathbf{q}}_i)\mathbf{s}_i + \mathbf{K}_1\mathbf{s}_i - \mathbf{K}_2\mathbf{s}_{i-1} - \mathbf{K}_2\mathbf{s}_{i+1} = \mathbf{0} \tag{5.7}$$

where $\mathbf{s}_i$ denotes the composite variable $\mathbf{s}_i = \dot{\mathbf{q}}_i - \dot{\mathbf{q}}_{ir}$.
This system is equivalent to

$$\mathbf{M}(\mathbf{q}_i)\dot{\mathbf{s}}_i + \mathbf{C}(\mathbf{q}_i,\dot{\mathbf{q}}_i)\mathbf{s}_i + \mathbf{K}_1\mathbf{s}_i - \mathbf{K}_2(\mathbf{s}_{i-1} + \mathbf{s}_{i+1}) + \mathbf{K}_2\sum_{j=1}^{p}\mathbf{s}_j = \mathbf{K}_2\sum_{j=1}^{p}\mathbf{s}_j \tag{5.8}$$

Hence, the closed-loop dynamics of each robot have the same excitation input $\mathbf{u}(t) = \mathbf{K}_2\sum_{j=1}^{p}\mathbf{s}_j$, which facilitates the use of contraction analysis.

Let us define the following $p \times p$ square matrices:

$$[\mathbf{L}^p_{\mathbf{A},\mathbf{B}}] = \begin{bmatrix} \mathbf{A} & \mathbf{B} & \mathbf{0} & \mathbf{0} & \cdots & \mathbf{B} \\ \mathbf{B} & \mathbf{A} & \mathbf{B} & \mathbf{0} & \cdots & \mathbf{0} \\ \vdots & \ddots & \ddots & \ddots & & \vdots \\ \mathbf{0} & & \mathbf{B} & \mathbf{A} & \mathbf{B} & \mathbf{0} \\ \mathbf{B} & \cdots & \mathbf{0} & \mathbf{0} & \mathbf{B} & \mathbf{A} \end{bmatrix}_{p\times p}, \quad [\mathbf{U}^p_{\mathbf{A}}] = \begin{bmatrix} \mathbf{A} & \mathbf{A} & \cdots & \mathbf{A} \\ \mathbf{A} & \mathbf{A} & \cdots & \mathbf{A} \\ \vdots & \vdots & \ddots & \vdots \\ \mathbf{A} & \mathbf{A} & \cdots & \mathbf{A} \end{bmatrix}_{p\times p} \tag{5.9}$$

By the definition of the controller in (5.5), $[\mathbf{L}^p_{\mathbf{A},\mathbf{B}}]$ has only three nonzero matrix elements in each row (i.e., $\mathbf{A}, \mathbf{B}, \mathbf{B}$).

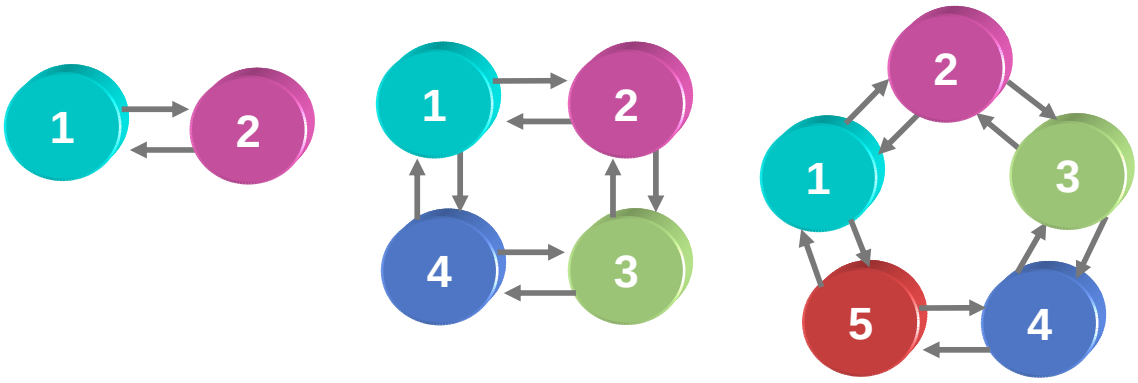

(a) identical robots

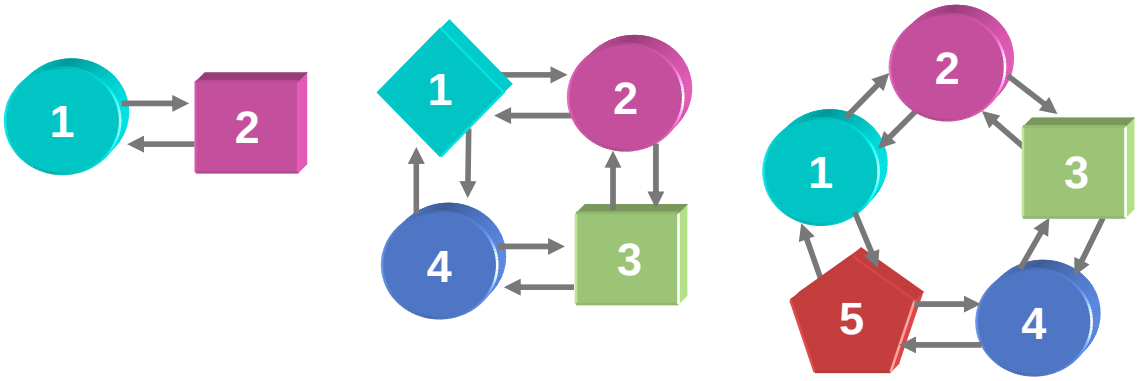

(b) non-identical robots

Figure 5-2: Multi-agent networks of identical or nonidentical robots using local couplings. They are on balanced bi-directional graphs.

Then, we can write the closed-loop dynamics in (5.8) in a block matrix form

$$[\mathbf{M}]\dot{\mathbf{x}} + [\mathbf{C}]\mathbf{x} + \left([\mathbf{L}^p_{\mathbf{K}_1,-\mathbf{K}_2}] + [\mathbf{U}^p_{\mathbf{K}_2}]\right)\mathbf{x} = [\mathbf{U}^p_{\mathbf{K}_2}]\mathbf{x} \tag{5.10}$$

where

$$[\mathbf{M}] = \begin{bmatrix} \mathbf{M}(\mathbf{q}_1) & \cdots & \mathbf{0} \\ \vdots & \ddots & \vdots \\ \mathbf{0} & \cdots & \mathbf{M}(\mathbf{q}_p) \end{bmatrix}, \quad [\mathbf{C}] = \begin{bmatrix} \mathbf{C}(\mathbf{q}_1, \dot{\mathbf{q}}_1) & \cdots & \mathbf{0} \\ \vdots & \ddots & \vdots \\ \mathbf{0} & \cdots & \mathbf{C}(\mathbf{q}_p, \dot{\mathbf{q}}_p) \end{bmatrix}, \quad \mathbf{x} = \begin{pmatrix} \mathbf{s}_1 \\ \vdots \\ \mathbf{s}_p \end{pmatrix} \tag{5.11}$$

Note that $[\mathbf{L}^p_{\mathbf{K}_1,-\mathbf{K}_2}]$ can be viewed as the weighted Laplacian of the network in the context of graph theory. In other words, $[\mathbf{L}^p_{\mathbf{K}_1,-\mathbf{K}_2}]$ indicates the connectivity with adjacent systems as well as the strength of the coupling by $\mathbf{K}_2$. Note that there are only three nonzero elements in each row of the matrix, which implies that there exist diffusive couplings only between adjacent members. The network graphs illustrated in Figure 5-2 are *balanced* due to bi-directional coupling [146]. However, it should be noted that the matrix $[\mathbf{L}^p_{\mathbf{K}_1,-\mathbf{K}_2}]$ is different from the standard Laplacian found in [146]. By definition, every row sum of the Laplacian matrix is zero. Hence, the Laplacian matrix always has a zero eigenvalue corresponding to a right eigenvector, $\mathbf{1} = (1, 1, \cdots, 1)^T$ [146]. In contrast, a strictly positive definite $[\mathbf{L}^p_{\mathbf{K}_1,-\mathbf{K}_2}]$ is required for exponential convergence for the proposed control law in this chapter. In other words, unless otherwise noted, $[\mathbf{L}^p_{\mathbf{K}_1,-\mathbf{K}_2}]$ is assumed to have no zero eigenvalue.

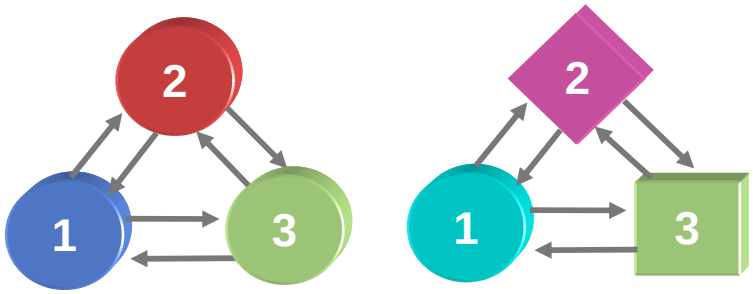

Figure 5-3: A network of three identical (left) and non-identical (right) robots

The closed-loop dynamics using (5.1) and (5.5) for three identical robots ($p = 3$) become

$$\begin{aligned} \mathbf{M}(\mathbf{q}_1)\dot{\mathbf{s}}_1 + \mathbf{C}(\mathbf{q}_1, \dot{\mathbf{q}}_1)\mathbf{s}_1 + (\mathbf{K}_1 + \mathbf{K}_2)\mathbf{s}_1 &= \mathbf{u}(t) \\ \mathbf{M}(\mathbf{q}_2)\dot{\mathbf{s}}_2 + \mathbf{C}(\mathbf{q}_2, \dot{\mathbf{q}}_2)\mathbf{s}_2 + (\mathbf{K}_1 + \mathbf{K}_2)\mathbf{s}_2 &= \mathbf{u}(t) \\ \mathbf{M}(\mathbf{q}_3)\dot{\mathbf{s}}_3 + \mathbf{C}(\mathbf{q}_3, \dot{\mathbf{q}}_3)\mathbf{s}_3 + (\mathbf{K}_1 + \mathbf{K}_2)\mathbf{s}_3 &= \mathbf{u}(t) \\ \mathbf{u}(t) &= \mathbf{K}_2(\mathbf{s}_1 + \mathbf{s}_2 + \mathbf{s}_3) \end{aligned} \tag{5.12}$$

which is equivalent to

$$[\mathbf{M}]\dot{\mathbf{x}} + [\mathbf{C}]\mathbf{x} + \left([\mathbf{L}^3_{\mathbf{K}_1,-\mathbf{K}_2}] + [\mathbf{U}^3_{\mathbf{K}_2}]\right)\mathbf{x} = [\mathbf{U}^3_{\mathbf{K}_2}]\mathbf{x} \tag{5.13}$$

where

$$\begin{gathered} [\mathbf{M}] = \begin{bmatrix} \mathbf{M}(\mathbf{q}_1) & \mathbf{0} & \mathbf{0} \\ \mathbf{0} & \mathbf{M}(\mathbf{q}_2) & \mathbf{0} \\ \mathbf{0} & \mathbf{0} & \mathbf{M}(\mathbf{q}_3) \end{bmatrix}, \quad [\mathbf{C}] = \begin{bmatrix} \mathbf{C}(\mathbf{q}_1, \dot{\mathbf{q}}_1) & \mathbf{0} & \mathbf{0} \\ \mathbf{0} & \mathbf{C}(\mathbf{q}_2, \dot{\mathbf{q}}_2) & \mathbf{0} \\ \mathbf{0} & \mathbf{0} & \mathbf{C}(\mathbf{q}_3, \dot{\mathbf{q}}_3) \end{bmatrix}, \\ [\mathbf{L}^3_{\mathbf{K}_1,-\mathbf{K}_2}] = \begin{bmatrix} +\mathbf{K}_1 & -\mathbf{K}_2 & -\mathbf{K}_2 \\ -\mathbf{K}_2 & +\mathbf{K}_1 & -\mathbf{K}_2 \\ -\mathbf{K}_2 & -\mathbf{K}_2 & +\mathbf{K}_1 \end{bmatrix}, \quad [\mathbf{U}^3_{\mathbf{K}_2}] = \begin{bmatrix} \mathbf{K}_2 & \mathbf{K}_2 & \mathbf{K}_2 \\ \mathbf{K}_2 & \mathbf{K}_2 & \mathbf{K}_2 \\ \mathbf{K}_2 & \mathbf{K}_2 & \mathbf{K}_2 \end{bmatrix} \end{gathered} \tag{5.14}$$

and $\mathbf{x} = \begin{pmatrix} \mathbf{s}_1 & \mathbf{s}_2 & \mathbf{s}_3 \end{pmatrix}^T$. Notice that $[\mathbf{L}^3_{\mathbf{K}_1,-\mathbf{K}_2}]$ is positive definite with $\mathbf{K}_1 - 2\mathbf{K}_2 > 0$.

In the case of a robot network consisting of four robots ($p = 4$), the block matrix $[\mathbf{L}^4_{\mathbf{K}_1,-\mathbf{K}_2}]$ becomes

$$[\mathbf{L}^4_{\mathbf{K}_1,-\mathbf{K}_2}] = \begin{bmatrix} +\mathbf{K}_1 & -\mathbf{K}_2 & \mathbf{0} & -\mathbf{K}_2 \\ -\mathbf{K}_2 & +\mathbf{K}_1 & -\mathbf{K}_2 & \mathbf{0} \\ \mathbf{0} & -\mathbf{K}_2 & +\mathbf{K}_1 & -\mathbf{K}_2 \\ -\mathbf{K}_2 & \mathbf{0} & -\mathbf{K}_2 & +\mathbf{K}_1 \end{bmatrix} \tag{5.15}$$

which is also positive definite with $\mathbf{K}_1 - 2\mathbf{K}_2 > 0$. For a two-robot network, it is straightforward to verify

$$[\mathbf{L}^2_{\mathbf{K}_1,-\mathbf{K}_2}] = \begin{bmatrix} +\mathbf{K}_1 & -\mathbf{K}_2 \\ -\mathbf{K}_2 & +\mathbf{K}_1 \end{bmatrix} \tag{5.16}$$

requiring the condition $\mathbf{K}_1 - \mathbf{K}_2 > 0$ for positive definite $[\mathbf{L}^2_{\mathbf{K}_1,-\mathbf{K}_2}]$.

We are well poised to introduce the main theorems of the present chapter. The following condition should be true for exponential convergence to the common desired trajectory $\mathbf{q}_d$.

Theorem 5.4.1 ***Global Exponential Convergence to the Desired Trajectory***
If $[\mathbf{L}^p_{\mathbf{K}_1,-\mathbf{K}_2}]$ *is positive definite, then every member of the network follows the desired trajectory* $\mathbf{q}_d$ *exponentially fast regardless of initial conditions.*

$$[\mathbf{L}^p_{\mathbf{K}_1,-\mathbf{K}_2}] > 0$$

In other words, if $\mathbf{K}_1 - 2\mathbf{K}_2 > 0$*, then* $\mathbf{q}_i$*, (*$i = 1, 2, \cdots, p$*,* $p \geq 3$*) converges to* $\mathbf{q}_d$ *with global and exponential convergence. For two-robot systems (*$p = 2$*),* $\mathbf{K}_1 - \mathbf{K}_2 > 0$ *needs to be true instead.*

It is straightforward to prove this theorem by checking the positive-definiteness of $[\mathbf{L}^p_{\mathbf{K}_1,-\mathbf{K}_2}]$ in the closed-loop equations (5.10). The elaborate proof is expanded in Section 5.4.2.

The next question to be addressed is how to guarantee the synchronization of the individual dynamics.

Theorem 5.4.2 ***Synchronization of Multiple Robots***
Suppose the conditions in Theorem 5.4.1 are true, thus the individual dynamics are exponentially tracking the common desired trajectory. A swarm of p robots synchronize exponentially from any initial conditions if $\exists$ *diagonal matrices* $\mathbf{K}_1 > 0$*,* $\mathbf{K}_2 > 0$ *such that*

$$[\mathbf{L}^p_{\mathbf{K}_1,-\mathbf{K}_2}] + [\mathbf{U}^p_{\mathbf{K}_2}] > 0$$

In addition, $\mathbf{\Lambda}$ *is a positive diagonal matrix defining a stable composite variable* $\mathbf{s}_i = \dot{\widetilde{\mathbf{q}}}_i + \mathbf{\Lambda}\widetilde{\mathbf{q}}_i$*.*

This theorem corresponds to synchronization with stable tracking. The proof is expanded in Section 5.5 by separating the two different time scales of the closed-loop dynamics. As shall be seen in Section 5.6.1, multiple dynamics need not be identical to achieve stable synchronization.

It is useful to note that the above condition corresponds to $\mathbf{K}_1 + \mathbf{K}_2 > 0$ for two-robot and three-robot networks ($p = 2, 3$). A four-robot network ($p = 4$) would require $\mathbf{K}_1 + 2\mathbf{K}_2 > 0$. We can also construct a network of multiple robots that can synchronize even with unstable tracking. In this case, the follow lemma can be used.

Lemma 5.4.3 ***Synchronization of Identical Robots with Unstable Tracking***
Suppose the conditions in Theorem 5.4.1 are not *true, thus the individual systems are exponentially* unstable *or* indifferent*. Nevertheless, a swarm of p* identical *robots synchronize exponentially fast from any initial conditions if* $\exists$ *diagonal matrices* $\mathbf{K}_1 > 0$*,* $\mathbf{K}_2$ *such that*

$$[\mathbf{L}^p_{\mathbf{K}_1,-\mathbf{K}_2}] + [\mathbf{U}^p_{\mathbf{K}_2}] > 0$$

In this case, $\mathbf{\Lambda}$ *should be sufficiently large such that* $\|\mathbf{\Lambda}\| \gg \frac{\|\mathbf{K}_1 - \mathbf{K}_2\|}{\underline{\sigma}(\mathbf{M}(\mathbf{q}))}$ *for* $p = 2$ *or* $\|\mathbf{\Lambda}\| \gg \frac{\|\mathbf{K}_1 - 2\mathbf{K}_2\|}{\underline{\sigma}(\mathbf{M}(\mathbf{q}))}$ *for* $p \geq 3$*, where* $\underline{\sigma}(\cdot)$ *denotes the smallest singular value. In contrast with Theorem 5.4.2, the individual dynamics must be identical in the unstable tracking case.*

This lemma describes the synchronization with unstable tracking ($\mathbf{K}_1 - \mathbf{K}_2 < 0$) or indifferent dynamics ($\mathbf{K}_1 - \mathbf{K}_2 = 0$) for $p = 2$; unstable ($\mathbf{K}_1 - 2\mathbf{K}_2 < 0$) or indifferent ($\mathbf{K}_1 - 2\mathbf{K}_2 = 0$) for $p \geq 3$. The proof is more involved than Theorem 5.4.2 since the synchronized system becomes unstable while individual members synchronize. Section 5.5 provides a unified treatment of both stable tracking (Theorem 5.4.2) and unstable tracking (Lemma 5.4.3). As opposed to stable tracking, the synchronization with unstable tracking requires identical dynamics.

Note that we can render the system synchronized first, then follow the common trajectory by tuning the gains properly. For an example of a two-robot network, $\mathbf{K}_2 > 0$ ensures that the two robots synchronize faster than they follow the common desired trajectory, since $\mathbf{K}_1 + \mathbf{K}_2 > \mathbf{K}_1 - \mathbf{K}_2$ for $\forall\ \mathbf{K}_2 > 0$. This indicates that there exist two different time-scales in the closed-loop systems constructed with the proposed controllers. For two-robot systems, the convergence of exponential tracking is proportional to $\mathbf{K}_1 - \mathbf{K}_2$ whereas the synchronization has a convergence rate of $\mathbf{K}_1 + \mathbf{K}_2$. This multi-time-scale behavior will be exploited in the subsequent sections.

Let us first consider the condition of exponentially stable tracking.

5.4.2 Proof of Exponential Tracking

We present the proof of Theorem 5.4.1 in this section. Consider the closed-loop systems given in (5.10)

$$[\mathbf{M}]\dot{\mathbf{x}} + [\mathbf{C}]\mathbf{x} + \left([\mathbf{L}^p_{\mathbf{K}_1,-\mathbf{K}_2}] + [\mathbf{U}^p_{\mathbf{K}_2}]\right)\mathbf{x} = [\mathbf{U}^p_{\mathbf{K}_2}]\mathbf{x} \tag{5.17}$$

We can cancel out the $[\mathbf{U}^p_{\mathbf{K}_2}]$ matrix term to obtain

$$[\mathbf{M}]\dot{\mathbf{x}} + [\mathbf{C}]\mathbf{x} + [\mathbf{L}^p_{\mathbf{K}_1,-\mathbf{K}_2}]\mathbf{x} = \mathbf{0} \tag{5.18}$$

This equation corresponds to a conventional tracking problem, as shown in the examples in Chapter 2. Hence, we can show that $\mathbf{x}$ tends to zero exponentially with $[\mathbf{L}^p_{\mathbf{K}_1,-\mathbf{K}_2}] > 0$.

For example, consider the virtual system of $\mathbf{y}$ obtained by replacing $\mathbf{x}$ with $\mathbf{y}$ in (5.18).

$$[\mathbf{M}]\dot{\mathbf{y}} + [\mathbf{C}]\mathbf{y} + [\mathbf{L}^p_{\mathbf{K}_1,-\mathbf{K}_2}]\mathbf{y} = \mathbf{0} \tag{5.19}$$

This virtual system has two particular solutions: $\mathbf{x} = (\mathbf{s}_1, \cdots, \mathbf{s}_p)^T$ and $\mathbf{0}$.
The squared-length analysis yields

$$\begin{aligned}
&\frac{d}{dt}\left(\delta\mathbf{y}^T[\mathbf{M}]\delta\mathbf{y}\right) = 2\delta\mathbf{y}^T[\mathbf{M}]\delta\dot{\mathbf{y}} + \delta\mathbf{y}^T[\dot{\mathbf{M}}]\delta\mathbf{y} \\
&= -2\delta\mathbf{y}^T\left([\mathbf{C}]\delta\mathbf{y} + [\mathbf{L}^p_{\mathbf{K}_1,-\mathbf{K}_2}]\delta\mathbf{y}\right) + \delta\mathbf{y}^T[\dot{\mathbf{M}}]\delta\mathbf{y} \\
&= -2\delta\mathbf{y}^T[\mathbf{L}^p_{\mathbf{K}_1,-\mathbf{K}_2}]\delta\mathbf{y}
\end{aligned} \tag{5.20}$$

where we used the skew-symmetric property of $[\dot{\mathbf{M}}] - 2[\mathbf{C}]$.

Accordingly, $[\mathbf{L}^p_{\mathbf{K}_1,-\mathbf{K}_2}] > 0$ will make the system contracting, thus all solutions of $\mathbf{y}$ converge to a single trajectory exponentially fast. This in turn indicates that the composite variable of each robot tends to zero exponentially ($\mathbf{s} \to \mathbf{0}$). By the definition of $\mathbf{s}_i = \dot{\mathbf{q}} - \dot{\mathbf{q}}_d + \mathbf{\Lambda}(\mathbf{q}_i - \mathbf{q}_d)$, the exponential convergence of $\mathbf{q}_i$ to the common reference trajectory $\mathbf{q}_d$ is proven. The positive-definiteness of $[\mathbf{L}^p_{\mathbf{K}_1,-\mathbf{K}_2}]$ corresponds to $\mathbf{K}_1 - \mathbf{K}_2 > 0$ for two-robot systems ($p = 2$). For a network consisting of more than two robots ($p \geq 3$), it can be shown that $\mathbf{K}_1 - 2\mathbf{K}_2$ is a sufficient condition of the positive-definiteness of $[\mathbf{L}^p_{\mathbf{K}_1,-\mathbf{K}_2}]$ given $\mathbf{K}_1 > 0, \mathbf{K}_2 > 0$.

5.5 Proof of Exponential Synchronization

We prove Theorem 5.4.2 and Lemma 5.4.3 for the exponential synchronization of multiple nonlinear dynamics in this section. First, we demonstrate the difficulties inherent in proving the synchronization of highly nonlinear systems in Section 5.5.1. We then focus on the two-robot synchronization problem in Section 5.5.3. The main result is generalized for an arbitrary number of robots in Section 5.5.4.

5.5.1 Challenges Associated with Nonlinear Inertia Matrix

The difficulties associated with nonlinear time-varying inertia matrices can be easily demonstrated with the following two-robot example. The closed-loop dynamics of two identical robots from (5.8) becomes

$$\begin{aligned}
\mathbf{M}(\mathbf{q}_1)\dot{\mathbf{s}}_1 + \mathbf{C}(\mathbf{q}_1, \dot{\mathbf{q}}_1)\mathbf{s}_1 + (\mathbf{K}_1 + \mathbf{K}_2)\mathbf{s}_1 &= \mathbf{u}(t) \\
\mathbf{M}(\mathbf{q}_2)\dot{\mathbf{s}}_2 + \mathbf{C}(\mathbf{q}_2, \dot{\mathbf{q}}_2)\mathbf{s}_2 + (\mathbf{K}_1 + \mathbf{K}_2)\mathbf{s}_2 &= \mathbf{u}(t) \\
\mathbf{u}(t) &= \mathbf{K}_2(\mathbf{s}_1 + \mathbf{s}_2)
\end{aligned} \tag{5.21}$$

which is equivalent to

$$[\mathbf{M_2}]\{\dot{\mathbf{s}}\} + [\mathbf{C_2}]\{\mathbf{s}\} + [\mathbf{K}]\{\mathbf{s}\} = [\mathbf{U}^2_{\mathbf{K}_2}]\{\mathbf{s}\} \tag{5.22}$$

where

$$\begin{aligned}
[\mathbf{M_2}] = \begin{bmatrix} \mathbf{M}(\mathbf{q}_1) & \mathbf{0} \\ \mathbf{0} & \mathbf{M}(\mathbf{q}_2) \end{bmatrix}, \quad [\mathbf{C_2}] = \begin{bmatrix} \mathbf{C}(\mathbf{q}_1, \dot{\mathbf{q}}_1) & \mathbf{0} \\ \mathbf{0} & \mathbf{C}(\mathbf{q}_2, \dot{\mathbf{q}}_2) \end{bmatrix}, \\
[\mathbf{K}] = [\mathbf{H}^2_{\mathbf{K}_1,-\mathbf{K}_2}] + [\mathbf{U}^2_{\mathbf{K}_2}] = \begin{bmatrix} \mathbf{K}_1 + \mathbf{K}_2 & \mathbf{0} \\ \mathbf{0} & \mathbf{K}_1 + \mathbf{K}_2 \end{bmatrix}, \quad [\mathbf{U}^2_{\mathbf{K}_2}] = \begin{bmatrix} \mathbf{K}_2 & \mathbf{K}_2 \\ \mathbf{K}_2 & \mathbf{K}_2 \end{bmatrix}, \quad \{\mathbf{s}\} = \begin{pmatrix} \mathbf{s}_1 \\ \mathbf{s}_2 \end{pmatrix}
\end{aligned} \tag{5.23}$$

Note that $\mathbf{s}_1$ and $\mathbf{s}_2$ are the composite variables defined in (5.7):

$$\begin{aligned}\mathbf{s}_1 &= \dot{\mathbf{q}}_1 - \dot{\mathbf{q}}_{1r} = \dot{\mathbf{q}}_1 + \mathbf{\Lambda}\mathbf{q}_1 - (\dot{\mathbf{q}}_d + \mathbf{\Lambda}\mathbf{q}_d) \\ \mathbf{s}_2 &= \dot{\mathbf{q}}_2 - \dot{\mathbf{q}}_{2r} = \dot{\mathbf{q}}_2 + \mathbf{\Lambda}\mathbf{q}_2 - (\dot{\mathbf{q}}_d + \mathbf{\Lambda}\mathbf{q}_d)\end{aligned} \tag{5.24}$$

Direct application of synchronization (Theorem 2.5.7) appears elusive because the original dynamics in (5.1) with the control law (5.5) is in general not contracting. Since (5.1) is a second-order differential equation, this can also be viewed as a high-order contraction problem [116]. If we transform the dynamics into a first-order canonical form, we have to prove that they are contracting in the same metric while preserving the input symmetry [152]. For example, multiplying (5.21) by $\mathbf{M}^{-1}$ breaks the input symmetry: i.e., $\mathbf{M}^{-1}(\mathbf{q}_1)\mathbf{u}(t) \neq \mathbf{M}^{-1}(\mathbf{q}_2)\mathbf{u}(t)$. In essence, $\mathbf{M}(\mathbf{q}_1) \neq \mathbf{M}(\mathbf{q}_2)$ makes this problem intractable in general.

Instead, suppose that $\mathbf{M}(\mathbf{q})$ remains constant, thereby making $\mathbf{C}(\mathbf{q}, \dot{\mathbf{q}})$ zero. Then, we can easily prove $\mathbf{s}_1$ and $\mathbf{s}_2$ tend to each other from

$$\begin{aligned}\mathbf{M}\dot{\mathbf{s}}_1 + (\mathbf{K}_1 + \mathbf{K}_2)\mathbf{s}_1 &= \mathbf{K}_2(\mathbf{s}_1 + \mathbf{s}_2) \\ \mathbf{M}\dot{\mathbf{s}}_2 + (\mathbf{K}_1 + \mathbf{K}_2)\mathbf{s}_2 &= \mathbf{K}_2(\mathbf{s}_1 + \mathbf{s}_2)\end{aligned} \tag{5.25}$$

Since the virtual system with the common input $\mathbf{u}(t) = \mathbf{K}_2(\mathbf{s}_1 + \mathbf{s}_2)$

$$\mathbf{M}\dot{\mathbf{y}} + (\mathbf{K}_1 + \mathbf{K}_2)\mathbf{y} = \mathbf{u}(t) \tag{5.26}$$

is contracting with $\mathbf{K}_1 + \mathbf{K}_2 > 0$. Hence, its particular solutions $\mathbf{s}_1$ and $\mathbf{s}_2$ tend to each other exponentially fast according to the synchronization theorem 2.5.7. Without loss of generality, this result can easily be extended to arbitrarily large networks. The synchronization of a large network with a constant metric is already discussed in [202] using contraction analysis.

We now turn to a much more difficult problem focused on the synchronization of two robots with non-constant nonlinear metrics ($\mathbf{M}(\mathbf{q}_1) \neq \mathbf{M}(\mathbf{q}_2)$).

5.5.2 Existence of Flow-Invariant Submanifold

We define and prove the existence of a flow-invariant manifold for any system given in (5.21), regardless of $[\mathbf{K}]$, prior to finding the condition of $[\mathbf{K}]$ for exponential synchronization. Let us start with the definition of flow-invariant manifold.
Consider a flow-invariant differentiable submanifold of the configuration space,

$$\mathcal{M}_{\mathbf{q}} = \left\{ (\mathbf{q}_1; \dot{\mathbf{q}}_1; \mathbf{q}_2; \dot{\mathbf{q}}_2) | \begin{bmatrix}\mathbf{I} & -\mathbf{I}\end{bmatrix} \begin{pmatrix}\mathbf{q}_1 \\ \mathbf{q}_2\end{pmatrix} = \mathbf{0}, \begin{bmatrix}\mathbf{I} & -\mathbf{I}\end{bmatrix} \begin{pmatrix}\dot{\mathbf{q}}_1 \\ \dot{\mathbf{q}}_2\end{pmatrix} = \mathbf{0} \right\} \tag{5.27}$$

Note that $\mathcal{M}_{\mathbf{q}}$ ia a flow-invariant submanifold for the closed-loop system (5.21). This follows from the fact that the initial condition, $\mathbf{q}_1(t_0) = \mathbf{q}_2(t_0), \dot{\mathbf{q}}_1(t_0) = \dot{\mathbf{q}}_2(t_0)$ for an arbitrary $t_0 \in \mathbb{R}_+$ yields $\ddot{\mathbf{q}}_1(\cdot) = \ddot{\mathbf{q}}_2(\cdot)$, which implies that any trajectory starting in $\mathcal{M}_{\mathbf{q}}$ remains in $\mathcal{M}_{\mathbf{q}}$. The flow-invariant manifold, $\mathcal{M}_{\mathbf{q}}$ corresponds to the synchronization of the two dynamical systems.

5.5.3 Contraction with Two Time-Scales

For simplicity, we focus on the proof of a two-robot network ($p = 2$) until we generalize the proof in Section 5.5.4. As shown earlier, the convergence rate of exponential tracking to the desired trajectory is proportional to $\mathbf{K}_1 - \mathbf{K}_2$ whereas the synchronization counterpart has the faster convergence of $\mathbf{K}_1 + \mathbf{K}_2$.

$$\mathbf{K}_1 + \mathbf{K}_2 > \mathbf{K}_1 - \mathbf{K}_2, \ \forall \ \mathbf{K}_2 > 0 \tag{5.28}$$

This multi timescale behavior is graphically illustrated in Figure 5-4. The figure[1] depicts that $\mathbf{s}_1$

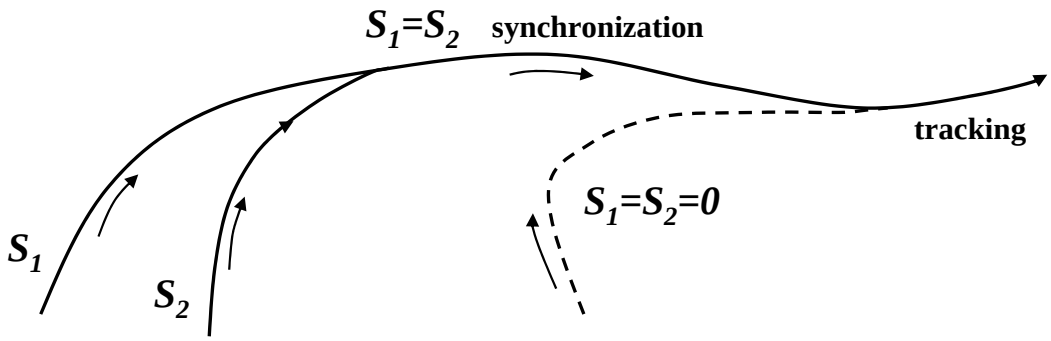

Figure 5-4: Multiple timescales of synchronization (faster) and tracking (slower). The dashed line indicates the desired trajectory. Arrows indicate increasing time.

and $\mathbf{s}_2$ synchronize first, then they converge to the desired trajectory while staying together. This observation motivates separation of the two different time scales, namely $\mathbf{K}_1 + \mathbf{K}_2$ and $\mathbf{K}_1 - \mathbf{K}_2$.

Recall the closed-loop dynamics of the two-robot network,

$$\begin{aligned} \mathbf{M}(\mathbf{q}_1)\dot{\mathbf{s}}_1 + \mathbf{C}(\mathbf{q}_1, \dot{\mathbf{q}}_1)\mathbf{s}_1 + (\mathbf{K}_1 + \mathbf{K}_2)\mathbf{s}_1 &= \mathbf{u}(t) \\ \mathbf{M}(\mathbf{q}_2)\dot{\mathbf{s}}_2 + \mathbf{C}(\mathbf{q}_2, \dot{\mathbf{q}}_2)\mathbf{s}_2 + (\mathbf{K}_1 + \mathbf{K}_2)\mathbf{s}_2 &= \mathbf{u}(t) \\ \mathbf{u}(t) &= \mathbf{K}_2(\mathbf{s}_1 + \mathbf{s}_2) \end{aligned} \tag{5.29}$$

Consider two linearly transformed variables $\mathbf{s}_p$ and $\mathbf{s}_m$ such that

$$\begin{pmatrix} \mathbf{s}_p \\ \mathbf{s}_m \end{pmatrix} = \begin{bmatrix} \mathbf{I} & \mathbf{I} \\ \mathbf{I} & -\mathbf{I} \end{bmatrix} \begin{pmatrix} \mathbf{s}_1 \\ \mathbf{s}_2 \end{pmatrix} \text{ and } \begin{pmatrix} \mathbf{s}_1 \\ \mathbf{s}_2 \end{pmatrix} = \begin{bmatrix} \frac{1}{2}\mathbf{I} & \frac{1}{2}\mathbf{I} \\ \frac{1}{2}\mathbf{I} & -\frac{1}{2}\mathbf{I} \end{bmatrix} \begin{pmatrix} \mathbf{s}_p \\ \mathbf{s}_m \end{pmatrix} \tag{5.30}$$

We take the sum and difference between the two equations in (5.29) to obtain

$$\begin{aligned} \mathbf{M}(\mathbf{q}_1)\dot{\mathbf{s}}_1 + \mathbf{M}(\mathbf{q}_2)\dot{\mathbf{s}}_2 + \mathbf{C}(\mathbf{q}_1, \dot{\mathbf{q}}_1)\mathbf{s}_1 + \mathbf{C}(\mathbf{q}_2, \dot{\mathbf{q}}_2)\mathbf{s}_2 + (\mathbf{K}_1 - \mathbf{K}_2)(\mathbf{s}_1 + \mathbf{s}_2) &= \mathbf{0} \\ \mathbf{M}(\mathbf{q}_1)\dot{\mathbf{s}}_1 - \mathbf{M}(\mathbf{q}_2)\dot{\mathbf{s}}_2 + \mathbf{C}(\mathbf{q}_1, \dot{\mathbf{q}}_1)\mathbf{s}_1 - \mathbf{C}(\mathbf{q}_2, \dot{\mathbf{q}}_2)\mathbf{s}_2 + (\mathbf{K}_1 + \mathbf{K}_2)(\mathbf{s}_1 - \mathbf{s}_2) &= \mathbf{0} \end{aligned} \tag{5.31}$$

Substituting $\mathbf{s}_p$ and $\mathbf{s}_m$ for $\mathbf{s}_1$ and $\mathbf{s}_2$ into (5.31) results in

$$\begin{bmatrix} \frac{\mathbf{M}_1+\mathbf{M}_2}{2} & \frac{\mathbf{M}_1-\mathbf{M}_2}{2} \\ \frac{\mathbf{M}_1-\mathbf{M}_2}{2} & \frac{\mathbf{M}_1+\mathbf{M}_2}{2} \end{bmatrix} \begin{pmatrix} \dot{\mathbf{s}}_p \\ \dot{\mathbf{s}}_m \end{pmatrix} + \begin{bmatrix} \frac{\mathbf{C}_1+\mathbf{C}_2}{2} & \frac{\mathbf{C}_1-\mathbf{C}_2}{2} \\ \frac{\mathbf{C}_1-\mathbf{C}_2}{2} & \frac{\mathbf{C}_1+\mathbf{C}_2}{2} \end{bmatrix} \begin{pmatrix} \mathbf{s}_p \\ \mathbf{s}_m \end{pmatrix} + \begin{bmatrix} \mathbf{K}_1 - \mathbf{K}_2 & \mathbf{0} \\ \mathbf{0} & \mathbf{K}_1 + \mathbf{K}_2 \end{bmatrix} \begin{pmatrix} \mathbf{s}_p \\ \mathbf{s}_m \end{pmatrix} = \begin{pmatrix} \mathbf{0} \\ \mathbf{0} \end{pmatrix} \tag{5.32}$$

where we simplified the notations as follows: $\mathbf{M}_1 = \mathbf{M}(\mathbf{q}_1)$, $\mathbf{M}_2 = \mathbf{M}(\mathbf{q}_2)$, $\mathbf{C}_1 = \mathbf{C}(\mathbf{q}_1, \dot{\mathbf{q}}_1)$, and $\mathbf{C}_2 = \mathbf{C}(\mathbf{q}_2, \dot{\mathbf{q}}_2)$. Intuitively, for sufficiently small $\mathbf{M}_1 - \mathbf{M}_2$, the above equation indicates that $\mathbf{s}_p$ has the convergence rate proportional to $\lambda(\mathbf{K}_1 - \mathbf{K}_2)$ whereas $\mathbf{s}_m$ has $\lambda(\mathbf{K}_1 + \mathbf{K}_2)$.

Consider the virtual system of $\mathbf{y}_1$ and $\mathbf{y}_2$:

$$\begin{bmatrix} \frac{\mathbf{M}_1+\mathbf{M}_2}{2} & \frac{\mathbf{M}_1-\mathbf{M}_2}{2} \\ \frac{\mathbf{M}_1-\mathbf{M}_2}{2} & \frac{\mathbf{M}_1+\mathbf{M}_2}{2} \end{bmatrix} \begin{pmatrix} \dot{\mathbf{y}}_1 \\ \dot{\mathbf{y}}_2 \end{pmatrix} + \begin{bmatrix} \frac{\mathbf{C}_1+\mathbf{C}_2}{2} & \frac{\mathbf{C}_1-\mathbf{C}_2}{2} \\ \frac{\mathbf{C}_1-\mathbf{C}_2}{2} & \frac{\mathbf{C}_1+\mathbf{C}_2}{2} \end{bmatrix} \begin{pmatrix} \mathbf{y}_1 \\ \mathbf{y}_2 \end{pmatrix} + \begin{bmatrix} \mathbf{K}_1 - \mathbf{K}_2 & \mathbf{0} \\ \mathbf{0} & \mathbf{K}_1 + \mathbf{K}_2 \end{bmatrix} \begin{pmatrix} \mathbf{y}_1 \\ \mathbf{y}_2 \end{pmatrix} = \begin{pmatrix} \mathbf{0} \\ \mathbf{0} \end{pmatrix} \tag{5.33}$$

that has the following two particular solutions:

$$\begin{pmatrix} \mathbf{y}_1 = \mathbf{s}_p \\ \mathbf{y}_2 = \mathbf{s}_m \end{pmatrix}, \qquad \begin{pmatrix} \mathbf{y}_1 = \mathbf{0} \\ \mathbf{y}_2 = \mathbf{0} \end{pmatrix} \tag{5.34}$$

[1]The picture is slightly exaggerated because $\mathbf{s}_1$ and $\mathbf{s}_2$ appear overlapped when they synchronize. Strictly speaking, their difference is decreasing exponentially to zero but they will never be the same unless time tends to infinity.

For $\mathbf{K}_2 > 0$ and $\mathbf{K}_1 - \mathbf{K}_2 > 0$, which also lead to $\mathbf{K}_1 + \mathbf{K}_2 > \mathbf{K}_1 - \mathbf{K}_2$, we can show that the above virtual system is contracting. We take the symmetric block matrix

$$\begin{bmatrix} \frac{\mathbf{M}(\mathbf{q}_1)+\mathbf{M}(\mathbf{q}_2)}{2} & \frac{\mathbf{M}(\mathbf{q}_1)-\mathbf{M}(\mathbf{q}_2)}{2} \\ \frac{\mathbf{M}(\mathbf{q}_1)-\mathbf{M}(\mathbf{q}_2)}{2} & \frac{\mathbf{M}(\mathbf{q}_1)+\mathbf{M}(\mathbf{q}_2)}{2} \end{bmatrix} \tag{5.35}$$

as our contraction metric. This metric is uniformly positive definite since a diagonal transformation using its orthonormal eigenvectors

$$\mathbf{V} = \begin{bmatrix} \frac{1}{\sqrt{2}}\mathbf{I} & \frac{1}{\sqrt{2}}\mathbf{I} \\ \frac{1}{\sqrt{2}}\mathbf{I} & -\frac{1}{\sqrt{2}}\mathbf{I} \end{bmatrix} \tag{5.36}$$

results in

$$\begin{bmatrix} \frac{\mathbf{M}(\mathbf{q}_1)+\mathbf{M}(\mathbf{q}_2)}{2} & \frac{\mathbf{M}(\mathbf{q}_1)-\mathbf{M}(\mathbf{q}_2)}{2} \\ \frac{\mathbf{M}(\mathbf{q}_1)-\mathbf{M}(\mathbf{q}_2)}{2} & \frac{\mathbf{M}(\mathbf{q}_1)+\mathbf{M}(\mathbf{q}_2)}{2} \end{bmatrix} = \mathbf{V} \begin{bmatrix} \mathbf{M}(\mathbf{q}_1) & \mathbf{0} \\ \mathbf{0} & \mathbf{M}(\mathbf{q}_2) \end{bmatrix} \mathbf{V}^T \tag{5.37}$$

Note that the block diagonal matrix

$$\begin{bmatrix} \mathbf{M}(\mathbf{q}_1) & \mathbf{0} \\ \mathbf{0} & \mathbf{M}(\mathbf{q}_2) \end{bmatrix} \tag{5.38}$$

is positive definite since $\forall \mathbf{q} \in \mathbb{R}^n, \mathbf{M}(\mathbf{q}) > 0$. This leads to the positive definiteness of

$$\begin{bmatrix} \frac{\mathbf{M}(\mathbf{q}_1)+\mathbf{M}(\mathbf{q}_2)}{2} & \frac{\mathbf{M}(\mathbf{q}_1)-\mathbf{M}(\mathbf{q}_2)}{2} \\ \frac{\mathbf{M}(\mathbf{q}_1)-\mathbf{M}(\mathbf{q}_2)}{2} & \frac{\mathbf{M}(\mathbf{q}_1)+\mathbf{M}(\mathbf{q}_2)}{2} \end{bmatrix} \tag{5.39}$$

(see [190]). The usage of such a transformation is generalized for an arbitrarily large network in Section 5.5.4.

Performing the squared-length analysis with respect to this metric yields

$$\begin{aligned} &\frac{d}{dt} \begin{pmatrix} \delta\mathbf{y}_1 \\ \delta\mathbf{y}_2 \end{pmatrix}^T \begin{bmatrix} \frac{\mathbf{M}_1+\mathbf{M}_2}{2} & \frac{\mathbf{M}_1-\mathbf{M}_2}{2} \\ \frac{\mathbf{M}_1-\mathbf{M}_2}{2} & \frac{\mathbf{M}_1+\mathbf{M}_2}{2} \end{bmatrix} \begin{pmatrix} \delta\mathbf{y}_1 \\ \delta\mathbf{y}_2 \end{pmatrix} \\ &= 2 \begin{pmatrix} \delta\mathbf{y}_1 \\ \delta\mathbf{y}_2 \end{pmatrix}^T \begin{bmatrix} \frac{\mathbf{M}_1+\mathbf{M}_2}{2} & \frac{\mathbf{M}_1-\mathbf{M}_2}{2} \\ \frac{\mathbf{M}_1-\mathbf{M}_2}{2} & \frac{\mathbf{M}_1+\mathbf{M}_2}{2} \end{bmatrix} \begin{pmatrix} \delta\dot{\mathbf{y}}_1 \\ \delta\dot{\mathbf{y}}_2 \end{pmatrix} + \begin{pmatrix} \delta\mathbf{y}_1 \\ \delta\mathbf{y}_2 \end{pmatrix}^T \begin{bmatrix} \frac{\dot{\mathbf{M}}_1+\dot{\mathbf{M}}_2}{2} & \frac{\dot{\mathbf{M}}_1-\dot{\mathbf{M}}_2}{2} \\ \frac{\dot{\mathbf{M}}_1-\dot{\mathbf{M}}_2}{2} & \frac{\dot{\mathbf{M}}_1+\dot{\mathbf{M}}_2}{2} \end{bmatrix} \begin{pmatrix} \delta\mathbf{y}_1 \\ \delta\mathbf{y}_2 \end{pmatrix} \\ &= -2 \begin{pmatrix} \delta\mathbf{y}_1 \\ \delta\mathbf{y}_2 \end{pmatrix}^T \Big(\begin{bmatrix} \frac{\mathbf{C}_1+\mathbf{C}_2}{2} & \frac{\mathbf{C}_1-\mathbf{C}_2}{2} \\ \frac{\mathbf{C}_1-\mathbf{C}_2}{2} & \frac{\mathbf{C}_1+\mathbf{C}_2}{2} \end{bmatrix} + \begin{bmatrix} \mathbf{K}_1 - \mathbf{K}_2 & \mathbf{0} \\ \mathbf{0} & \mathbf{K}_1 + \mathbf{K}_2 \end{bmatrix} + \begin{bmatrix} \frac{\dot{\mathbf{M}}_1+\dot{\mathbf{M}}_2}{2} & \frac{\dot{\mathbf{M}}_1-\dot{\mathbf{M}}_2}{2} \\ \frac{\dot{\mathbf{M}}_1-\dot{\mathbf{M}}_2}{2} & \frac{\dot{\mathbf{M}}_1+\dot{\mathbf{M}}_2}{2} \end{bmatrix} \Big) \begin{pmatrix} \delta\mathbf{y}_1 \\ \delta\mathbf{y}_2 \end{pmatrix} \\ &= -2 \begin{pmatrix} \delta\mathbf{y}_1 \\ \delta\mathbf{y}_2 \end{pmatrix}^T \begin{bmatrix} \mathbf{K}_1 - \mathbf{K}_2 & \mathbf{0} \\ \mathbf{0} & \mathbf{K}_1 + \mathbf{K}_2 \end{bmatrix} \begin{pmatrix} \delta\mathbf{y}_1 \\ \delta\mathbf{y}_2 \end{pmatrix} \end{aligned} \tag{5.40}$$

where we used the skew-symmetric property of $\dot{\mathbf{M}} - 2\mathbf{C}$.

We can recall the stability analysis of the trajectory tracking, depending on the sign of $\mathbf{K}_1 - \mathbf{K}_2$ in Section 5.4.2. In the following, three possible cases are classified by the sign of $\mathbf{K}_1 - \mathbf{K}_2$, and discussed respectively. Namely, stable tracking with $\mathbf{K}_1 - \mathbf{K}_2 > 0$; indifferent tracking with $\mathbf{K}_1 - \mathbf{K}_2 = \mathbf{0}$; unstable tracking with $\mathbf{K}_1 - \mathbf{K}_2 < 0$.

Case I: $\mathbf{K}_1 - \mathbf{K}_2 > 0$

If $\mathbf{K}_1 + \mathbf{K}_2 > \mathbf{K}_1 - \mathbf{K}_2 > 0$, the rate of the virtual length in (5.40) is uniformly negative definite:

$$\frac{d}{dt} \begin{pmatrix} \delta\mathbf{y}_1 \\ \delta\mathbf{y}_2 \end{pmatrix}^T \begin{bmatrix} \frac{\mathbf{M}(\mathbf{q}_1)+\mathbf{M}(\mathbf{q}_2)}{2} & \frac{\mathbf{M}(\mathbf{q}_1)-\mathbf{M}(\mathbf{q}_2)}{2} \\ \frac{\mathbf{M}(\mathbf{q}_1)-\mathbf{M}(\mathbf{q}_2)}{2} & \frac{\mathbf{M}(\mathbf{q}_1)+\mathbf{M}(\mathbf{q}_2)}{2} \end{bmatrix} \begin{pmatrix} \delta\mathbf{y}_1 \\ \delta\mathbf{y}_2 \end{pmatrix} = -2 \begin{pmatrix} \delta\mathbf{y}_1 \\ \delta\mathbf{y}_2 \end{pmatrix}^T \begin{bmatrix} \mathbf{K}_1 - \mathbf{K}_2 & \mathbf{0} \\ \mathbf{0} & \mathbf{K}_1 + \mathbf{K}_2 \end{bmatrix} \begin{pmatrix} \delta\mathbf{y}_1 \\ \delta\mathbf{y}_2 \end{pmatrix} < 0 \tag{5.41}$$

for nonzero $\delta\mathbf{y}_1, \delta\mathbf{y}_2$.

Consequently, the combined virtual system in (5.33) is contracting. In other words, $\delta\mathbf{y}_1, \delta\mathbf{y}_2 \to \mathbf{0}$ exponentially fast. This in turn implies all solutions of $\mathbf{y}_1$ and $\mathbf{y}_2$ tend to the single trajectory. As a result, $\mathbf{s}_p = \mathbf{s}_1 + \mathbf{s}_2$ and $\mathbf{s}_m = \mathbf{s}_1 - \mathbf{s}_2$ tend to zero exponentially. It is straightforward to show that $\mathbf{s}_m \to 0$ also hierarchically makes $\mathbf{q}_1$ tend to $\mathbf{q}_2$ exponentially.
From the definition of the composite variables in (5.24), we can find the following contracting dynamics,

$$(\dot{\mathbf{q}}_1 - \dot{\mathbf{q}}_2) + \mathbf{\Lambda}(\mathbf{q}_1 - \mathbf{q}_2) = \mathbf{s}_m \tag{5.42}$$

Note that $\dot{\mathbf{y}} + \mathbf{\Lambda}\mathbf{y} = 0$ is contracting with $\mathbf{\Lambda} > 0$. Consequently, $\mathbf{\Lambda} > 0$ and $\mathbf{s}_m \to \mathbf{0}$ make $\mathbf{q}_1 \to \mathbf{q}_2$ exponentially fast. This also implies that the diagonal terms of the metric, $\frac{\mathbf{M}(\mathbf{q}_1)-\mathbf{M}(\mathbf{q}_2)}{2}$ tend to zero exponentially, thereby eliminating the coupling of the inertia term.

$$\begin{bmatrix} \frac{\mathbf{M}(\mathbf{q}_1)+\mathbf{M}(\mathbf{q}_2)}{2} & \frac{\mathbf{M}(\mathbf{q}_1)-\mathbf{M}(\mathbf{q}_2)}{2} \\ \frac{\mathbf{M}(\mathbf{q}_1)-\mathbf{M}(\mathbf{q}_2)}{2} & \frac{\mathbf{M}(\mathbf{q}_1)+\mathbf{M}(\mathbf{q}_2)}{2} \end{bmatrix} \longrightarrow \begin{bmatrix} \frac{\mathbf{M}(\mathbf{q}_1)+\mathbf{M}(\mathbf{q}_2)}{2} & \mathbf{0} \\ \mathbf{0} & \frac{\mathbf{M}(\mathbf{q}_1)+\mathbf{M}(\mathbf{q}_2)}{2} \end{bmatrix} \tag{5.43}$$

Once the inertia matrix is sufficiently close to the diagonal matrix in (5.43), the squared-length analysis in (5.40) reduces to

$$\begin{aligned} \frac{d}{dt}\delta\mathbf{y}_1{}^T \left[\frac{\mathbf{M}(\mathbf{q}_1) + \mathbf{M}(\mathbf{q}_2)}{2}\right] \delta\mathbf{y}_1 &= -2\delta\mathbf{y}_1{}^T \left[\mathbf{K}_1 - \mathbf{K}_2\right] \delta\mathbf{y}_1 \\ \frac{d}{dt}\delta\mathbf{y}_2{}^T \left[\frac{\mathbf{M}(\mathbf{q}_1) + \mathbf{M}(\mathbf{q}_2)}{2}\right] \delta\mathbf{y}_2 &= -2\delta\mathbf{y}_2{}^T \left[\mathbf{K}_1 + \mathbf{K}_2\right] \delta\mathbf{y}_2 \end{aligned} \tag{5.44}$$

This in turn implies that the convergence rate of tracking, $(\delta\mathbf{y}_1)$ is proportional to $\mathbf{K}_1 - \mathbf{K}_2$ while the synchronization, $(\delta\mathbf{y}_2)$ occurs at a faster convergence rate, $\mathbf{K}_1 + \mathbf{K}_2$. This completes the proof of Theorem 5.4.2.

Case II: $\mathbf{K}_1 - \mathbf{K}_2 = \mathbf{0}$

We can also consider a case with $\mathbf{K}_1 - \mathbf{K}_2 = \mathbf{0}$, which fails the exponential stability condition in Theorem 5.4.1. The combined virtual system per se is then semi-contracting [112, 113] since the squared-length analysis in (5.40) yields the negative semi-definite matrix:

$$\frac{d}{dt}\begin{pmatrix}\delta\mathbf{y}_1 \\ \delta\mathbf{y}_2\end{pmatrix}^T \begin{bmatrix} \frac{\mathbf{M}(\mathbf{q}_1)+\mathbf{M}(\mathbf{q}_2)}{2} & \frac{\mathbf{M}(\mathbf{q}_1)-\mathbf{M}(\mathbf{q}_2)}{2} \\ \frac{\mathbf{M}(\mathbf{q}_1)-\mathbf{M}(\mathbf{q}_2)}{2} & \frac{\mathbf{M}(\mathbf{q}_1)+\mathbf{M}(\mathbf{q}_2)}{2} \end{bmatrix} \begin{pmatrix}\delta\mathbf{y}_1 \\ \delta\mathbf{y}_2\end{pmatrix} = \begin{pmatrix}\delta\mathbf{y}_1 \\ \delta\mathbf{y}_2\end{pmatrix}^T \begin{bmatrix} \mathbf{0} & \mathbf{0} \\ \mathbf{0} & -2(\mathbf{K}_1 + \mathbf{K}_2) \end{bmatrix} \begin{pmatrix}\delta\mathbf{y}_1 \\ \delta\mathbf{y}_2\end{pmatrix} \leq 0 \tag{5.45}$$

While $\delta\mathbf{y}_1$, representing the tracking dynamics, remains in a finite ball due to $\mathbf{K}_1 - \mathbf{K}_2 = 0$, $\delta\mathbf{y}_2$ tends to zero exponentially due to $-2(\mathbf{K}_1 + \mathbf{K}_2) < 0$. This result can be proven as follows. The rate $\dot{V}$ is uniformly continuous since a bounded $\delta\dot{\mathbf{y}}_2$ from (5.33) leads to a bounded $\ddot{V}$ from

$$\ddot{V} = -4\delta\mathbf{y}_2^T(\mathbf{K}_1 + \mathbf{K}_2)\delta\dot{\mathbf{y}}_2. \tag{5.46}$$

Due to $\dot{V} \leq 0$, the use of Barbalat's lemma [178] verifies that $\dot{V} \to 0$ as $t \to \infty$. This implies that $\delta\mathbf{y}_2$ tends to zero asymptotically fast.

We introduce the third virtual variable $\mathbf{y}_3$ to verify a hierarchical combination of $\mathbf{s}_m$ and $\mathbf{q}_1 - \mathbf{q}_2$, stated in (5.42):

$$\delta\dot{\mathbf{y}}_3 + \mathbf{\Lambda}\delta\mathbf{y}_3 = \delta\mathbf{y}_2 \tag{5.47}$$

where $\mathbf{y}_3$ has two particular solutions: $\mathbf{y}_3 = \mathbf{q}_1 - \mathbf{q}_2$ when $\mathbf{y}_2 = \mathbf{s}_1 - \mathbf{s}_2$, and $\mathbf{y}_3 = \mathbf{0}$ when $\mathbf{y}_2 = \mathbf{0}$. Since $\delta\mathbf{y}_2 \to \mathbf{0}$ asymptotically by Barbalat's lemma, $\delta\mathbf{y}_3$ tends to zero with a positive $\mathbf{\Lambda} > 0$. Consequently, $\delta\mathbf{y}_3 \to \mathbf{0}$ indicates $\mathbf{q}_1 \to \mathbf{q}_2$. This will eventually decouple the metric matrix with $\mathbf{\Lambda} > 0$, as seen in (5.43), since $\mathbf{M}(\mathbf{q}_1) - \mathbf{M}(\mathbf{q}_2)$ tends to zero simultaneously as $\mathbf{q}_1 \to \mathbf{q}_2$. As a result, when $\mathbf{M}(\mathbf{q}_1) - \mathbf{M}(\mathbf{q}_2)$ is sufficiently close to zero, the convergence of $\delta\mathbf{y}_2 \to 0$ turns exponential.

We can conclude that $\mathbf{q}_1$ and $\mathbf{q}_2$ synchronize even with $\mathbf{K}_1 - \mathbf{K}_2 = \mathbf{0}$. Furthermore, using (5.32), we can prove synchronization in the presence of tracking instability ($\mathbf{K}_1 - \mathbf{K}_2 < 0$) with sufficiently

small $\|\mathbf{K}_1 - \mathbf{K}_2\|$ by decoupling the unstable dynamics from the stable synchronization dynamics as follows.

Case III: $\mathbf{K}_1 - \mathbf{K}_2 < 0$

Consider a case when the individual tracking system is unstable with $\mathbf{K}_1 - \mathbf{K}_2 < 0$. This case warrants further discussion. In essence, we will show herein that the synchronization can occur fast enough to overcome the tracking instability. In the context of singular perturbation theory [92], the fast dynamics of synchronization represent transient boundary layer dynamics while the tracking dynamics represents slow dynamics.

For the sake of simplicity, the gain matrices are assumed to be diagonal such that $\mathbf{K}_1 = k_1\mathbf{I}$ and $\mathbf{K}_2 = k_2\mathbf{I}$ where $k_1, k_2 \in \mathbb{R}_+$, and $\mathbf{I}$ is the $n \times n$ identity matrix. In order to freeze the slow dynamics of tracking, relative to the fast dynamics, we let $\frac{1}{|k_1-k_2|}$ be the time unit.

We introduce the new time variable $t_r = |k_1 - k_2|t$ such that

$$\frac{d\mathbf{s}}{dt} = |k_1 - k_2|\frac{d\mathbf{s}}{dt_r}. \tag{5.48}$$

Notice that we consider the absolute value of $k_1 - k_2$ since it can be negative. Then, (5.32) becomes

$$\begin{aligned}\begin{bmatrix} \frac{\mathbf{M}_1+\mathbf{M}_2}{2} & \frac{\mathbf{M}_1-\mathbf{M}_2}{2} \\ \frac{\mathbf{M}_1-\mathbf{M}_2}{2} & \frac{\mathbf{M}_1+\mathbf{M}_2}{2} \end{bmatrix} \begin{pmatrix} \frac{d\mathbf{s}_p}{dt_r} \\ \frac{d\mathbf{s}_m}{dt_r} \end{pmatrix} + \begin{bmatrix} \frac{\mathbf{C}_1+\mathbf{C}_2}{2|k_1-k_2|} & \frac{\mathbf{C}_1-\mathbf{C}_2}{2|k_1-k_2|} \\ \frac{\mathbf{C}_1-\mathbf{C}_2}{2|k_1-k_2|} & \frac{\mathbf{C}_1+\mathbf{C}_2}{2|k_1-k_2|} \end{bmatrix} \begin{pmatrix} \mathbf{s}_p \\ \mathbf{s}_m \end{pmatrix} \\ + \begin{bmatrix} \mathrm{sgn}(k_1 - k_2)\mathbf{I} & \mathbf{0} \\ \mathbf{0} & \frac{k_1+k_2}{|k_1-k_2|}\mathbf{I} \end{bmatrix} \begin{pmatrix} \mathbf{s}_p \\ \mathbf{s}_m \end{pmatrix} = \begin{pmatrix} \mathbf{0} \\ \mathbf{0} \end{pmatrix}\end{aligned} \tag{5.49}$$

where we simplified the notations as follows: $\mathbf{M}_i = \mathbf{M}(\mathbf{q}_i)$ and $\mathbf{C}_i = \mathbf{C}(\mathbf{q}_i, \dot{\mathbf{q}}_i)$ for i=1,2. In addition, $\mathrm{sgn}(x)$ indicates the signum function such that

$$\mathrm{sgn}(x) = \begin{pmatrix} 1, & x > 0 \\ 0, & x = 0 \\ -1, & x < 0 \end{pmatrix} \tag{5.50}$$

Equation (5.49) can be further transformed into a standard singular perturbation model by multiplying $\epsilon = \frac{|k_1-k_2|}{k_1+k_2}$ and assuming $\mathbf{K}_1 - \mathbf{K}_2 < 0$.

$$\epsilon \begin{bmatrix} \frac{\mathbf{M}_1+\mathbf{M}_2}{2} & \frac{\mathbf{M}_1-\mathbf{M}_2}{2} \\ \frac{\mathbf{M}_1-\mathbf{M}_2}{2} & \frac{\mathbf{M}_1+\mathbf{M}_2}{2} \end{bmatrix} \begin{pmatrix} \frac{d\mathbf{s}_p}{dt_r} \\ \frac{d\mathbf{s}_m}{dt_r} \end{pmatrix} + \begin{bmatrix} \frac{\mathbf{C}_1+\mathbf{C}_2}{2k_1+2k_2} & \frac{\mathbf{C}_1-\mathbf{C}_2}{2k_1+2k_2} \\ \frac{\mathbf{C}_1-\mathbf{C}_2}{2k_1+2k_2} & \frac{\mathbf{C}_1+\mathbf{C}_2}{2k_1+2k_2} \end{bmatrix} \begin{pmatrix} \mathbf{s}_p \\ \mathbf{s}_m \end{pmatrix} + \begin{bmatrix} -\epsilon\mathbf{I} & \mathbf{0} \\ \mathbf{0} & \mathbf{I} \end{bmatrix} \begin{pmatrix} \mathbf{s}_p \\ \mathbf{s}_m \end{pmatrix} = \begin{pmatrix} \mathbf{0} \\ \mathbf{0} \end{pmatrix} \tag{5.51}$$

If ϵ tends to zero, then $\frac{d\mathbf{s}_m}{dt_r}$ tends to infinity even for a very small t whereas the change in $\mathbf{s}_p$ is relatively small. The same reasoning can be used to prove why the system synchronizes even when the combined system becomes unstable with $\mathbf{K}_1 - \mathbf{K}_2 < 0$.

We can develop the squared-length analysis with respect to the new time variable t_r,

$$\frac{d}{dt_r}\begin{pmatrix} \delta\mathbf{y}_1 \\ \delta\mathbf{y}_2 \end{pmatrix}^T \begin{bmatrix} \frac{\mathbf{M}(\mathbf{q}_1)+\mathbf{M}(\mathbf{q}_2)}{2} & \frac{\mathbf{M}(\mathbf{q}_1)-\mathbf{M}(\mathbf{q}_2)}{2} \\ \frac{\mathbf{M}(\mathbf{q}_1)-\mathbf{M}(\mathbf{q}_2)}{2} & \frac{\mathbf{M}(\mathbf{q}_1)+\mathbf{M}(\mathbf{q}_2)}{2} \end{bmatrix} \begin{pmatrix} \delta\mathbf{y}_1 \\ \delta\mathbf{y}_2 \end{pmatrix} = 2\begin{pmatrix} \delta\mathbf{y}_1 \\ \delta\mathbf{y}_2 \end{pmatrix}^T \begin{bmatrix} \mathbf{I} & \mathbf{0} \\ \mathbf{0} & -\frac{1}{\epsilon}\mathbf{I} \end{bmatrix} \begin{pmatrix} \delta\mathbf{y}_1 \\ \delta\mathbf{y}_2 \end{pmatrix} \tag{5.52}$$

where we used $\frac{d\mathbf{M}(\mathbf{q})}{dt_r} = \frac{1}{\epsilon(k_1+k_2)}\Big(\mathbf{C}(\mathbf{q}, \dot{\mathbf{q}})^T + \mathbf{C}(\mathbf{q}, \dot{\mathbf{q}})\Big)$.

This implies the contraction of $\mathbf{s}_m \to \mathbf{0}$ while $\delta\mathbf{y}_1$ (thus, $\mathbf{s}_p$) is relatively frozen with small ϵ, regardless of the sign of $k_1 - k_2$. It follows from (5.42) that $\mathbf{s}_m \to \mathbf{0}$ implies $\mathbf{q}_1 \to \mathbf{q}_2$. Since $\epsilon \ll 1$, we can expect that the convergence to the flow invariant manifold, $\mathcal{M}_q$ exponentially decouples the metric

matrix such that

$$\begin{bmatrix} \frac{\mathbf{M}(\mathbf{q}_1)+\mathbf{M}(\mathbf{q}_2)}{2} & \frac{\mathbf{M}(\mathbf{q}_1)-\mathbf{M}(\mathbf{q}_2)}{2} \\ \frac{\mathbf{M}(\mathbf{q}_1)-\mathbf{M}(\mathbf{q}_2)}{2} & \frac{\mathbf{M}(\mathbf{q}_1)+\mathbf{M}(\mathbf{q}_2)}{2} \end{bmatrix} \longrightarrow \begin{bmatrix} \frac{\mathbf{M}(\mathbf{q}_1)+\mathbf{M}(\mathbf{q}_2)}{2} & \mathbf{0} \\ \mathbf{0} & \frac{\mathbf{M}(\mathbf{q}_1)+\mathbf{M}(\mathbf{q}_2)}{2} \end{bmatrix} \tag{5.53}$$

In the case of stable tracking (Case I), $\mathbf{\Lambda} = 0$ still leads to the synchronization of the velocities. In contrast, $\mathbf{\Lambda}$ cannot be zero for Case III. This is because the off-diagonal terms of the augmented mass matrix should vanish exponentially as $\mathbf{q}_1 \to \mathbf{q}_2$, in order to prevent the unstable tracking dynamics from affecting the stable synchronization dynamics.

Then, a natural question arises as to how small $\mathbf{\Lambda}$ can be, given $\epsilon = \frac{|k_1-k_2|}{k_1+k_2}$. Conversely, one might ask how large ϵ can be relative to $\mathbf{\Lambda}$ in order to make the system synchronize in spite of the unstable tracking due to $k_1 - k_2 < 0$.

Perform the following virtual squared-length analysis for $\delta\mathbf{y}_2$ (thus, $\mathbf{s}_m$) using (5.51)

$$\begin{aligned} \frac{d}{dt}\delta\mathbf{y}_2^T \left(\frac{\mathbf{M}_1+\mathbf{M}_2}{2}\right)\delta\mathbf{y}_2 &= -2\delta\mathbf{y}_2^T(\mathbf{K}_1+\mathbf{K}_2)\delta\mathbf{y}_2 - 2\delta\mathbf{y}_2^T\left(\frac{\mathbf{M}_1-\mathbf{M}_2}{2}\delta\dot{\mathbf{y}}_1 + \frac{\mathbf{C}_1-\mathbf{C}_2}{2}\delta\mathbf{y}_1\right) \\ &\leq -2k\delta\mathbf{y}_2^T\delta\mathbf{y}_2 + 2\|\delta\mathbf{y}_2\|\left(\|\mathbf{M}_{12}\|\|\delta\dot{\mathbf{y}}_1\| + \|\mathbf{C}_{12}\|\|\delta\mathbf{y}_1\|\right) \\ &\leq -2k\delta\mathbf{y}_2^T\delta\mathbf{y}_2 + 2\|\delta\mathbf{y}_2\|\left(m_{12}a + c_{12}\right)\|\delta\mathbf{y}_1\|\|\delta\mathbf{y}_3\| \end{aligned} \tag{5.54}$$

where $k = k_1 + k_2$ and a is some bounded constant such that $\|\delta\dot{\mathbf{y}}_1\| \leq a\|\delta\mathbf{y}_1\|$. Additionally, using the inequalities bounding the $\mathbf{M}$ and $\mathbf{C}$ matrices, given in (5.2) and (5.3), we can verify that

$$\begin{aligned} \|\mathbf{M}_{12}\| &= \left\|\frac{\mathbf{M}(\mathbf{q}_1)-\mathbf{M}(\mathbf{q}_2)}{2}\right\| \leq m_{12}\|\delta\mathbf{y}_3\| \\ \|\mathbf{C}_{12}\| &= \left\|\frac{\mathbf{C}(\mathbf{q}_1,\dot{\mathbf{q}}_1)-\mathbf{C}(\mathbf{q}_2,\dot{\mathbf{q}}_2)}{2}\right\| \leq c_{12}\|\delta\mathbf{y}_3\| \end{aligned}$$

where m_{12} and c_{12} are some positive constants.

From (5.47), one can find that the solution of $\|\delta\mathbf{y}_1\|\|\delta\mathbf{y}_3\|$ is bounded by

$$\|\delta\mathbf{y}_3\|\|\delta\mathbf{y}_1\| \leq e^{-\mathbf{\Lambda}(t-t_0)}\|\delta\mathbf{y}_1(t)\|\|\delta\mathbf{y}_3(t_0)\| + \int_{t_0}^{t} e^{-\mathbf{\Lambda}(t-\tau)}\|\delta\mathbf{y}_1(t)\|\|\delta\mathbf{y}_2(\tau)\|d\tau \tag{5.55}$$

By comparing the convergence rate of unstable $\delta\mathbf{y}_1$ and stable $\delta\mathbf{y}_3$, the following condition should hold in order to make $(\|\delta\mathbf{y}_1\|\|\delta\mathbf{y}_3\|)$ tend to zero exponentially,

$$\|\mathbf{\Lambda}\| \gg \frac{|k_1-k_2|}{\underline{\sigma}(\mathbf{M}(\mathbf{q}))} \tag{5.56}$$

where $\underline{\sigma}(\cdot)$ denotes the smallest singular value. For a general p-robot network with $p \geq 3$, $k_1 - k_2$ is replaced by $k_1 - 2k_2$. Under such conditions, $\|\delta\mathbf{y}_1\|\|\delta\mathbf{y}_3\|$ tends to zero exponentially even with the unstable tracking gain ($k_1 - k_2 < 0$ for $p = 2$ or $k_1 - 2k_2 < 0$ for $p \geq 3$), thereby making $\delta\mathbf{y}_2$ tend to zero exponentially. Note that $\delta\mathbf{y}_2$ in turn implies $\mathbf{q}_1 \to \mathbf{q}_2$ exponentially fast.

In conclusion, we proved Theorem 5.4.2 and Lemma 5.4.3 indicating that the synchronization occurs at a faster rate than the trajectory tracking. The gains can be selected such that the individual members of the network synchronize even if they are individually unstable (see the simulation results in Section 5.6.2).

5.5.4 Generalization

The substitution of $\mathbf{s}_p$ and $\mathbf{s}_m$, and the manipulation of the close-loop dynamics, actually represent the transformation using the eigenvectors of $[\mathbf{L}^p_{\mathbf{K}_1,-\mathbf{K}_2}]$.

Recall the closed-loop dynamics given in (5.10)

$$[\mathbf{M}]\dot{\mathbf{x}} + [\mathbf{C}]\mathbf{x} + [\mathbf{L}^p_{\mathbf{K}_1,-\mathbf{K}_2}]\mathbf{x} = \mathbf{0} \tag{5.57}$$

Since $[\mathbf{L}^p_{\mathbf{K}_1,-\mathbf{K}_2}]$ is a real symmetric matrix, we can perform the spectral decomposition, as in spectral graph theory [41],

$$\begin{aligned} [\mathbf{L}^p_{\mathbf{K}_1,-\mathbf{K}_2}] &= \mathbf{V}\mathbf{D}\mathbf{V}^T \\ \mathbf{V}^T[\mathbf{L}^p_{\mathbf{K}_1,-\mathbf{K}_2}]\mathbf{V} &= \mathbf{D} \end{aligned} \tag{5.58}$$

where $\mathbf{D}$ is a block diagonal matrix and $\mathbf{V}^T\mathbf{V} = \mathbf{V}\mathbf{V}^T = \mathbf{I}$. Symmetry of a matrix gives rise to real eigenvalues and perpendicular eigenvectors [190].

Pre-multiplying (5.57) by $\mathbf{V}^T$ and setting $\mathbf{x} = \mathbf{V}\mathbf{V}^T\mathbf{x}$ result in

$$\left(\mathbf{V}^T[\mathbf{M}]\mathbf{V}\right)\mathbf{V}^T\dot{\mathbf{x}} + \left(\mathbf{V}^T[\mathbf{C}]\mathbf{V}\right)\mathbf{V}^T\mathbf{x} + \left(\mathbf{V}^T[\mathbf{L}^p_{\mathbf{K}_1,-\mathbf{K}_2}]\mathbf{V}\right)\mathbf{V}^T\mathbf{x} = \mathbf{0} \tag{5.59}$$

By setting $\mathbf{V}^T\mathbf{x} = \mathbf{z}$, (5.59) becomes

$$\left(\mathbf{V}^T[\mathbf{M}]\mathbf{V}\right)\dot{\mathbf{z}} + \left(\mathbf{V}^T[\mathbf{C}]\mathbf{V}\right)\mathbf{z} + \mathbf{D}\mathbf{z} = \mathbf{0} \tag{5.60}$$

Then, we can develop the squared-length analysis similar to the previous section. Notice that $\left(\mathbf{V}^T[\mathbf{M}]\mathbf{V}\right)$ is always symmetric and positive definite since $[\mathbf{M}]$ is symmetric positive definite. For the case of a two-agent network, we can easily verify that

$$\mathbf{V}^T[\mathbf{M}]\mathbf{V} = \begin{bmatrix} \frac{\mathbf{M}_1+\mathbf{M}_2}{2} & \frac{\mathbf{M}_1-\mathbf{M}_2}{2} \\ \frac{\mathbf{M}_1-\mathbf{M}_2}{2} & \frac{\mathbf{M}_1+\mathbf{M}_2}{2} \end{bmatrix}, \quad \mathbf{D} = \begin{bmatrix} \mathbf{K}_1-\mathbf{K}_2 & \mathbf{0} \\ \mathbf{0} & \mathbf{K}_1+\mathbf{K}_2 \end{bmatrix}, \quad \mathbf{V} = \begin{bmatrix} \frac{1}{\sqrt{2}}\mathbf{I} & \frac{1}{\sqrt{2}}\mathbf{I} \\ \frac{1}{\sqrt{2}}\mathbf{I} & -\frac{1}{\sqrt{2}}\mathbf{I} \end{bmatrix}. \tag{5.61}$$

This produces the same results as the transformation in Section 5.5.3.

We can extend the method in this section to arbitrarily large networks. For example, a network of three robots has the following $\mathbf{V}$ whose columns are orthonormal eigenvectors of $[\mathbf{L}^{p=3}_{\mathbf{K}_1,-\mathbf{K}_2}]$:

$$\mathbf{V} = \begin{bmatrix} -\frac{1}{\sqrt{3}}\mathbf{I} & -\frac{2}{\sqrt{6}}\mathbf{I} & \mathbf{0} \\ -\frac{1}{\sqrt{3}}\mathbf{I} & \frac{1}{\sqrt{6}}\mathbf{I} & -\frac{1}{\sqrt{2}}\mathbf{I} \\ -\frac{1}{\sqrt{3}}\mathbf{I} & \frac{1}{\sqrt{6}}\mathbf{I} & \frac{1}{\sqrt{2}}\mathbf{I} \end{bmatrix} \tag{5.62}$$

which is a unitary matrix such that $\mathbf{V}^T\mathbf{V} = \mathbf{V}\mathbf{V}^T = \mathbf{I}$.

The new transformed inertia matrix, $\mathbf{V}^T[\mathbf{M}]\mathbf{V}$ is written as

$$\begin{bmatrix} \frac{1}{3}\mathbf{M}_1 + \frac{1}{3}\mathbf{M}_2 + \frac{1}{3}\mathbf{M}_3 & \frac{\sqrt{2}}{3}\mathbf{M}_1 - \frac{1}{3\sqrt{2}}\mathbf{M}_2 - \frac{1}{3\sqrt{2}}\mathbf{M}_3 & \frac{1}{\sqrt{6}}\mathbf{M}_2 - \frac{1}{\sqrt{6}}\mathbf{M}_3 \\ \frac{\sqrt{2}}{3}\mathbf{M}_1 - \frac{1}{3\sqrt{2}}\mathbf{M}_2 - \frac{1}{3\sqrt{2}}\mathbf{M}_3 & \frac{2}{3}\mathbf{M}_1 + \frac{1}{6}\mathbf{M}_2 + \frac{1}{6}\mathbf{M}_3 & -\frac{1}{2\sqrt{3}}\mathbf{M}_2 + \frac{1}{2\sqrt{3}}\mathbf{M}_3 \\ \frac{1}{\sqrt{6}}\mathbf{M}_2 - \frac{1}{\sqrt{6}}\mathbf{M}_3 & -\frac{1}{2\sqrt{3}}\mathbf{M}_2 + \frac{1}{2\sqrt{3}}\mathbf{M}_3 & \frac{1}{2}\mathbf{M}_2 + \frac{1}{2}\mathbf{M}_3 \end{bmatrix} \tag{5.63}$$

where $\mathbf{M}_1 = \mathbf{M}(\mathbf{q}_1)$, $\mathbf{M}_2 = \mathbf{M}(\mathbf{q}_2)$, and $\mathbf{M}_3 = \mathbf{M}(\mathbf{q}_3)$.

This matrix is symmetric and positive definite. Also notice that its off-diagonal terms vanish as $\mathbf{q}_1 \to \mathbf{q}_2, \mathbf{q}_2 \to \mathbf{q}_3$:

$$\mathbf{V}^T[\mathbf{M}]\mathbf{V} \longrightarrow \begin{bmatrix} \mathbf{M}(\mathbf{q}) & \mathbf{0} & \mathbf{0} \\ \mathbf{0} & \mathbf{M}(\mathbf{q}) & \mathbf{0} \\ \mathbf{0} & \mathbf{0} & \mathbf{M}(\mathbf{q}) \end{bmatrix} \tag{5.64}$$

where $\mathbf{q} = \mathbf{q}_1 = \mathbf{q}_2 = \mathbf{q}_3$.

The diagonal matrix $\mathbf{D}$ is also computed as

$$\begin{bmatrix} \mathbf{K}_1 - 2\mathbf{K}_2 & \mathbf{0} & \mathbf{0} \\ \mathbf{0} & \mathbf{K}_1 + \mathbf{K}_2 & \mathbf{0} \\ \mathbf{0} & \mathbf{0} & \mathbf{K}_1 + \mathbf{K}_2 \end{bmatrix} \tag{5.65}$$

For a four-robot network $p = 4$, $\mathbf{D}$ is given as

$$\begin{bmatrix} \mathbf{K}_1 - 2\mathbf{K}_2 & \mathbf{0} & \mathbf{0} & \mathbf{0} \\ \mathbf{0} & \mathbf{K}_1 + 2\mathbf{K}_2 & \mathbf{0} & \mathbf{0} \\ \mathbf{0} & \mathbf{0} & \mathbf{K}_1 & \mathbf{0} \\ \mathbf{0} & \mathbf{0} & \mathbf{0} & \mathbf{K}_1 \end{bmatrix} \tag{5.66}$$

5.5.5 A Perspective on Model Reduction by Synchronization

It is emphasized that the exponential synchronization of multiple nonlinear dynamics allows us to reduce the dimensionality of the stability analysis of a large network. As noted earlier, the convergence rate $(\mathbf{K}_1 + \mathbf{K}_2)$ is faster than the tracking rate $(\mathbf{K}_1 - \mathbf{K}_2)$. Assuming that the dynamics are synchronized, the augmented dynamics in (5.18) reduces to

$$\mathbf{M}(\mathbf{q})\dot{\mathbf{s}} + \mathbf{C}(\mathbf{q}, \dot{\mathbf{q}})\mathbf{s} + (\mathbf{K}_1 - \mathbf{K}_2)\mathbf{s} = \mathbf{0} \tag{5.67}$$

where $\mathbf{q} = \mathbf{q}_1 = \cdots = \mathbf{q}_p$.
This implies that once the network is proven to synchronize, we can regard a network as a single set of synchronized dynamics, which simplifies any additional stability analysis.

5.6 Extensions and Examples

Let us examine the effectiveness of the proposed control law in a variety of nonlinear dynamics networks.

5.6.1 Synchronization of Non-Identical Robots

Notice that the proposed tracking and synchronization control law in (5.5) can easily be applied to a network consisting of heterogenous robots in (5.1), if the stable tracking condition in Theorem 5.4.2 is true:

$$\begin{aligned} \tau_i = \mathbf{M}_i(\mathbf{q}_i)\ddot{\mathbf{q}}_{ir} + \mathbf{C}_i(\mathbf{q}_i, \dot{\mathbf{q}}_i)\dot{\mathbf{q}}_{ir} + \mathbf{g}_i(\mathbf{q}_i) \\ -\mathbf{K}_1(\dot{\mathbf{q}}_i - \dot{\mathbf{q}}_{ir}) + \mathbf{K}_2(\dot{\mathbf{q}}_{i-1} - \dot{\mathbf{q}}_{i-1,r}) + \mathbf{K}_2(\dot{\mathbf{q}}_{i+1} - \dot{\mathbf{q}}_{i+1,r}) \end{aligned} \tag{5.68}$$

where $\mathbf{M}_i$, $\mathbf{C}_i$, and $\mathbf{g}_i(\mathbf{q}_i)$ represent the i-th robot dynamics, which can be different from robot to robot. Each robot has the same number of configuration variables ($q_i \in \mathbb{R}^n$).
For example, the $\mathbf{M}_1$, $\mathbf{M}_2$, $\mathbf{C}_1$, and $\mathbf{C}_2$ notations used in the previous sections can be interpreted as $\mathbf{M}_1 = \mathbf{M}_1(\mathbf{q}_1)$ and $\mathbf{M}_2 = \mathbf{M}_2(\mathbf{q}_2)$ with $\mathbf{M}_1(\cdot) \neq \mathbf{M}_2(\cdot)$ (the same for the $\mathbf{C}$ matrices). Hence, the assumption of non-identical dynamics does not alter the proof of exponential tracking in Section 5.4.2 and stable synchronization in Section 5.5. However, the synchronization with unstable tracking (Lemma 5.4.3) is no longer true for the case of non-identical robots since $\mathbf{q}_1 = \mathbf{q}_2$ does not cancel $\mathbf{M}_1 - \mathbf{M}_2$ in the metric matrix

$$\begin{bmatrix} \frac{\mathbf{M}_1 + \mathbf{M}_2}{2} & \frac{\mathbf{M}_1 - \mathbf{M}_2}{2} \\ \frac{\mathbf{M}_1 - \mathbf{M}_2}{2} & \frac{\mathbf{M}_1 + \mathbf{M}_2}{2} \end{bmatrix}. \tag{5.69}$$

The above discussion is summarized in the following lemma.

Lemma 5.6.1 ***Synchronization of Multiple Non-Identical Robots***
If $[\mathbf{L}^p_{\mathbf{K}_1, -\mathbf{K}_2}]$ *is positive definite, then every member of the network follows the desired trajectory* $\mathbf{q}_d$

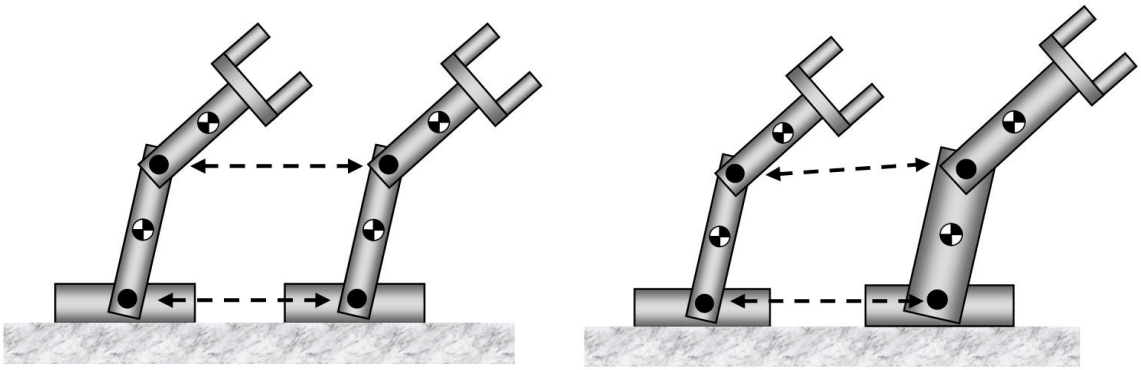

(a) Two identical two-link robots

(b) Two different two-link robots

Figure 5-5: Examples of cooperative control. The arrows indicate the coupling control law

exponentially fast.

$$[\mathbf{L}^p_{\mathbf{K}_1,-\mathbf{K}_2}] > 0 \tag{5.70}$$

In addition, a swarm of p non-identical robots synchronize exponentially from any initial conditions if $\exists$ *diagonal matrices* $\mathbf{K}_1 > 0$, $\mathbf{K}_2 > 0$ *such that*

$$[\mathbf{L}^p_{\mathbf{K}_1,-\mathbf{K}_2}] + [\mathbf{U}^p_{\mathbf{K}_2}] > 0$$

where the closed-loop dynamics in (5.10) can be rewritten to account for the non-identical dynamics of each robot.

$$[\mathbf{M}]\dot{\mathbf{x}} + [\mathbf{C}]\mathbf{x} + \left([\mathbf{L}^p_{\mathbf{K}_1,-\mathbf{K}_2}] + [\mathbf{U}^p_{\mathbf{K}_2}]\right)\mathbf{x} = [\mathbf{U}^p_{\mathbf{K}_2}]\mathbf{x} \tag{5.71}$$

where

$$[\mathbf{M}] = \begin{bmatrix} \mathbf{M}_1(\mathbf{q}_1) & \cdots & \mathbf{0} \\ \vdots & \ddots & \vdots \\ \mathbf{0} & \cdots & \mathbf{M}_p(\mathbf{q}_p) \end{bmatrix}, \quad [\mathbf{C}] = \begin{bmatrix} \mathbf{C}_1(\mathbf{q}_1, \dot{\mathbf{q}}_1) & \cdots & \mathbf{0} \\ \vdots & \ddots & \vdots \\ \mathbf{0} & \cdots & \mathbf{C}_p(\mathbf{q}_p, \dot{\mathbf{q}}_p) \end{bmatrix}, \quad \mathbf{x} = \begin{pmatrix} \mathbf{s}_1 \\ \vdots \\ \mathbf{s}_p \end{pmatrix}. \tag{5.72}$$

5.6.2 Cooperative Control of Robot Manipulators

The proposed control law in (5.5) is simulated for two identical two-link robots shown in Figure 5-5(a). The physical parameters of the robot are taken from the page 396 of [178] (see Table 5.1). In order to compare with the performance of the controller for a network consisting of non-identical robots, consider the two different robots in Figure 5-5(b). The first robot has the same physical parameters as in Figure 5-5(a), and the second robot's parameters are given in Table 5.1.

Table 5.1: Physical parameters of the robots shown in Figures 5-5.

Physical Parameters	m_1	ℓ_1	m_e	I_1	ℓ_{c1}	I_e	ℓ_{ce}
Robots in Fig. 5-5(a)	1 kg	1 m	2 kg	0.12 kgm^2	0.5 m	0.25 kgm^2	0.6 m
Left robot in Fig. 5-5(b)	2 kg	1.2 m	2.5 kg	0.25 kgm^2	0.6 m	0.4 kgm^2	0.7 m
Right robot in Fig. 5-5(b)	2 kg	1.2 m	2.5 kg	0.25 kgm^2	0.6 m	0.4 kgm^2	0.7 m

The simulation result is presented in Figure 5-6. The control gains are defined as $\mathbf{K}_1 = 5\mathbf{I}$, $\mathbf{K}_2 = 1.5\mathbf{I}$, and $\mathbf{\Lambda} = 5\mathbf{I}$. The desired trajectory is $\mathbf{q}_d = \begin{pmatrix} 0.3(1-\cos 2\pi t) \\ 0.5(1-e^{-t}) \end{pmatrix}$. The lower joints are initially at 0.3 rad with 1 rad/s (first robot) and 1.0 rad at rest (second robot). The upper joint of the first robot is initially at 0.4 rad. The rest of the initial conditions are zero. The same

initial conditions are used for both the robots in Figures 5-5 (a) and (b). The synchronization gain of $\mathbf{s}_1$ and $\mathbf{s}_2$ corresponds to $\mathbf{K}_1 + \mathbf{K}_2 = 6.5\mathbf{I}$, which is larger than the tracking convergence gain $\mathbf{K}_1 - \mathbf{K}_2 = 3.5\mathbf{I}$. As a result, we can see in Figure 5-6 that the first and second robots exponentially synchronize first. Then, they exponentially converge together to the desired trajectory.
Let us now investigate the synchronization under the instability condition. For example, the control gains are re-defined as $\mathbf{K}_1 = 5\mathbf{I}$, $\mathbf{K}_2 = 5.3\mathbf{I}$, and $\mathbf{\Lambda} = \mathbf{I}$. Now the tracking gain, $\mathbf{K}_1 - \mathbf{K}_2 = -0.3\mathbf{I}$ is negative, thus instability occurs. Figures 5-7 shows the simulation result with the instability. For the network with two identical robots, both robots synchronize exponentially fast even though the synchronized trajectory becomes unstable. In contrast, the exponential synchronization of the two different robots is no longer guaranteed in the presence of tracking instability, as seen in Figure 5-7(b).

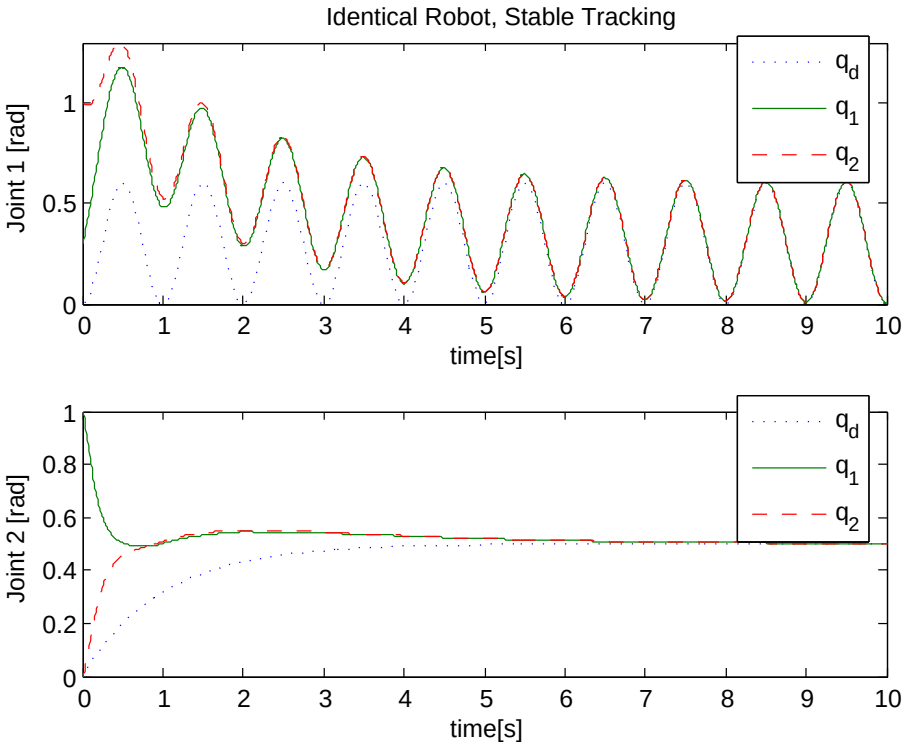

(a) Identical robots

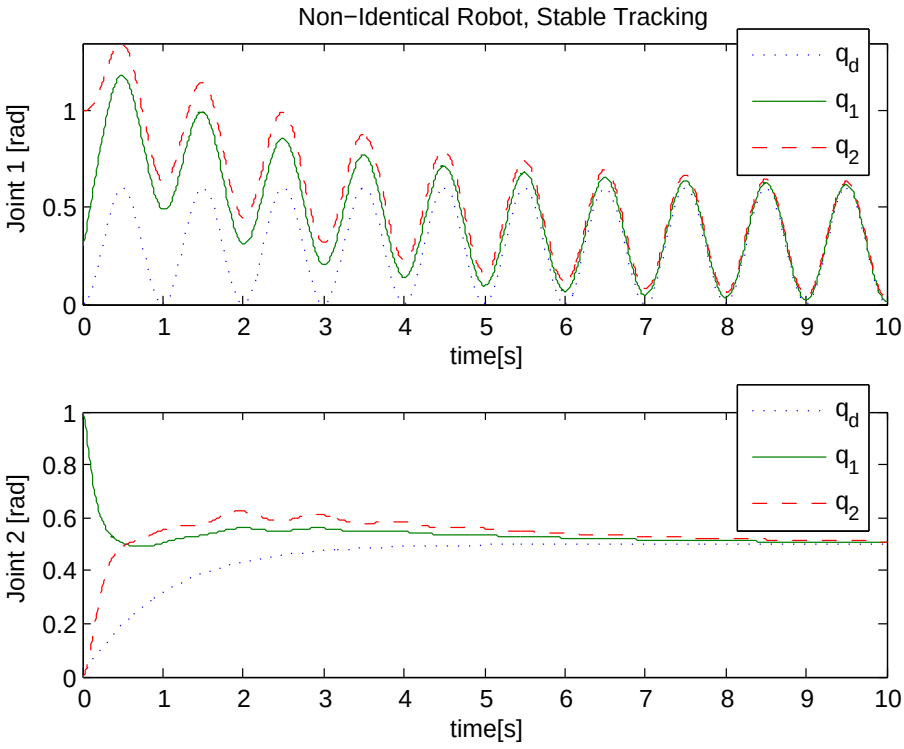

(b) Non-identical robots

Figure 5-6: Synchronization of two robots with **stable** tracking

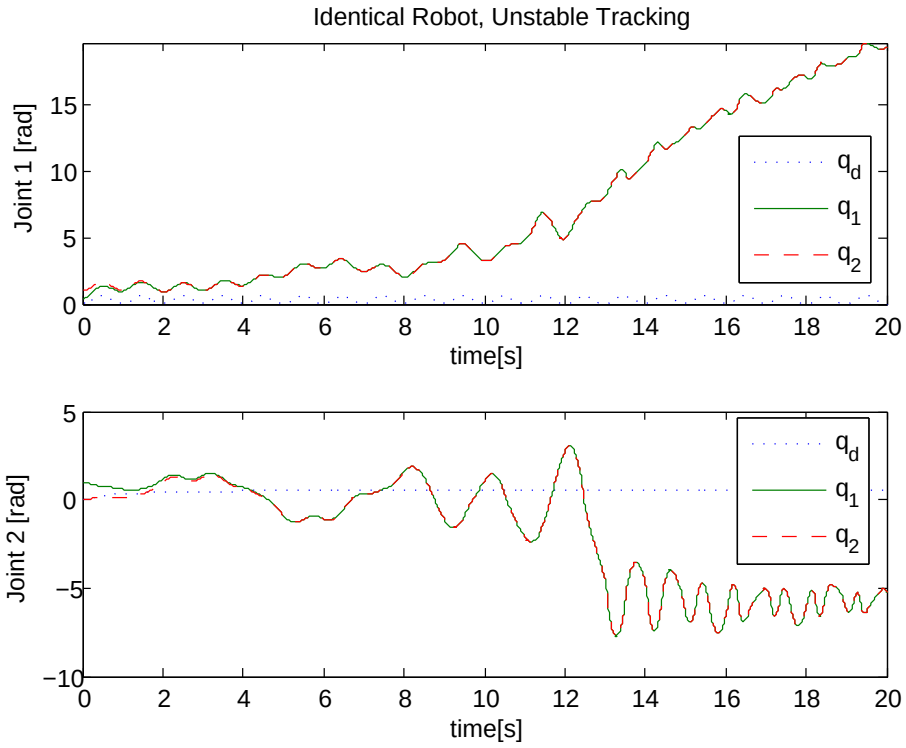

(a) Identical robots

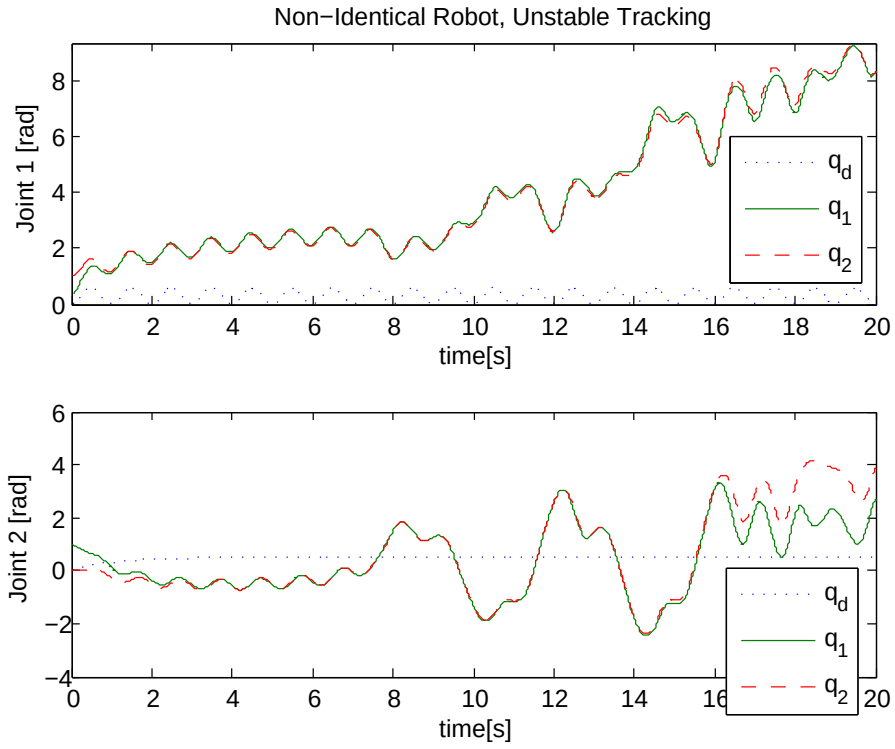

(b) Non-identical robots

Figure 5-7: Synchronization of two robots with **unstable** tracking

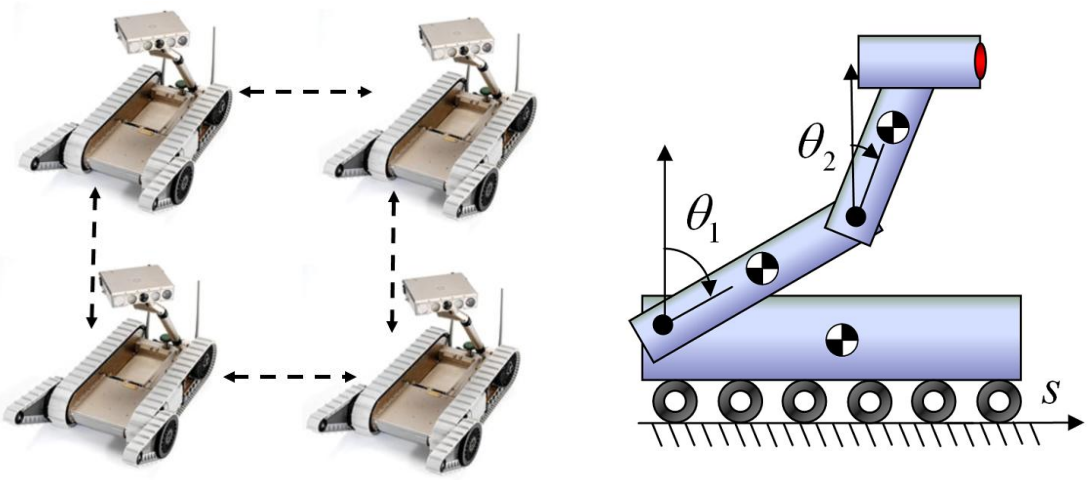

(a) A network of four Packbot robots (picture courtesy: iRobot)

(b) Modeling of the Packbot as a manipulator robot on a cart in Section 2.3.4

Figure 5-8: Synchronization of a four-robot network. The arrows indicate the coupling control law.

5.6.3 Tracking Synchronization of Four Robots

Even though the local coupling structure of the proposed control law in (5.5) has been emphasized, the difference from all-to-all coupling is not evident in a network consisting of less than four members ($p \leq 3$). To illustrate the effectiveness of the proposed scheme for a dynamical network consisting of highly nonlinear systems with $p \geq 4$, a network of four identical 3-DOF robots is considered here (see Figure 5-8). Each joint is assumed to be frictionless, and the dynamics modeling of the 3DOF robot is based upon the double inverted pendulum robot on a cart. The equations of motion are given in Section 2.3.4.

The physical parameters of each robot are given in Table 5.2.

Table 5.2: Physical parameters of the robots shown in Figures 5-8.

Physical Parameters	M	m_1	ℓ_1	I_1	ℓ_{c1}	m_2	I_2	ℓ_{c2}
Values	4 kg	1 kg	1 m	0.12 kgm^2	0.5 m	2 kg	0.25 kgm^2	0.6 m

The initial conditions are defined as in Table 5.3.

Table 5.3: Physical parameters of the robots shown in Figures 5-8.

Variable [unit]	s [m]	$\dot{s}$ [m/s]	θ_1 [rad]	$\dot{\theta}_1$ [rad/s]	θ_2 [rad]	$\dot{\theta}_2$ [rad/s]
Robot 1	-0.5	1	0.3	0	-0.3	0
Robot 2	-0.2	-0.5	1	0	0	0
Robot 3	0.4	1	-0.7	0.4	2	0
Robot 4	-0.3	0	-0.5	0	1.2	0.5

The simulation result is presented in Figure 5-9. The four identical robots, initially at the

conditions in Table 5.3, are driven to synchronize as well as to track the following desired trajectory:

$$
\begin{aligned}
&s_d = 0.2t, \quad \dot{s}_d = 0.2, \quad \ddot{s}_d = 0 \\
&\theta_1 = \cos(0.02\pi t), \quad \dot{\theta}_1 = -\sin(0.02\pi t)(0.02\pi), \quad \ddot{\theta}_1 = -\cos(0.02\pi t)(0.02\pi)^2 \\
&\theta_2 = \frac{\pi}{4}(1-\cos(0.08\pi t)), \quad \dot{\theta}_2 = \frac{\pi}{4}\sin(0.08\pi t)(0.08\pi), \quad \ddot{\theta}_2 = \frac{\pi}{4}\cos(0.08\pi t)(0.08\pi)^2
\end{aligned}
\tag{5.73}
$$

Note that this simulation fully considers the nonlinear rotational dynamics of the robots, as opposed to some earlier work on multi-agent coordination [146, 147].

Figure 5-10 represents a time history plot of Figure 5-9. For the control gains in the control law (5.5), we used $\mathbf{K}_1 = \mathbf{I}$, $\mathbf{K}_2 = 0.4\mathbf{I}$, and $\mathbf{\Lambda} = \mathbf{I}$. According to Theorems 5.4.1 and 5.4.2, the corresponding tracking gain $\mathbf{K}_1 - 2\mathbf{K}_2 = 0.2$ is smaller than the corresponding synchronization gain $\mathbf{K}_1 + 2\mathbf{K}_2$. Figure 5-10 shows that the system states synchronize exponentially fast and the synchronized states converge to the desired trajectory together.

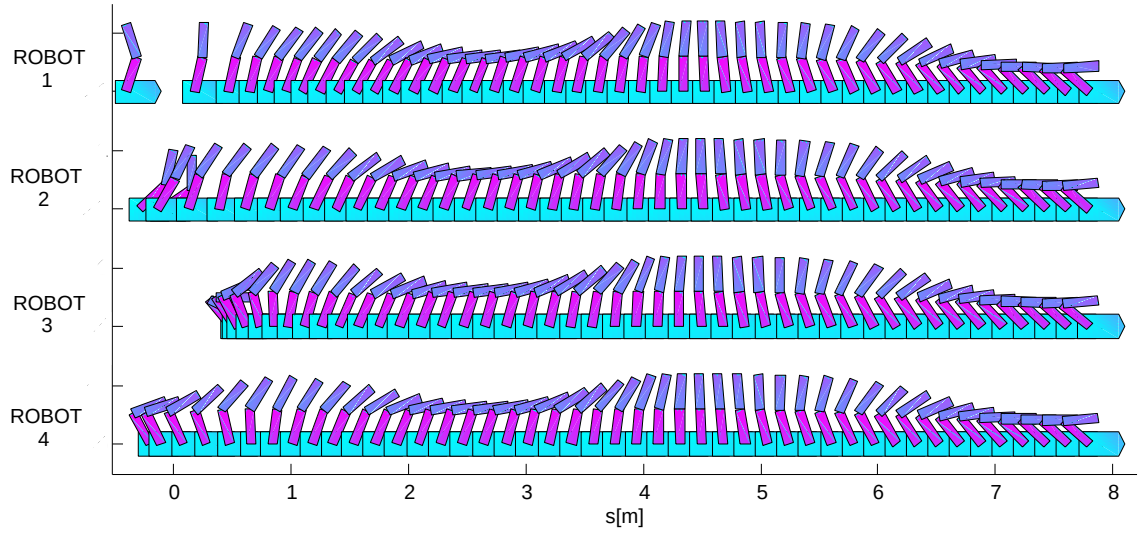

Figure 5-9: Simulation results of the four-robot network

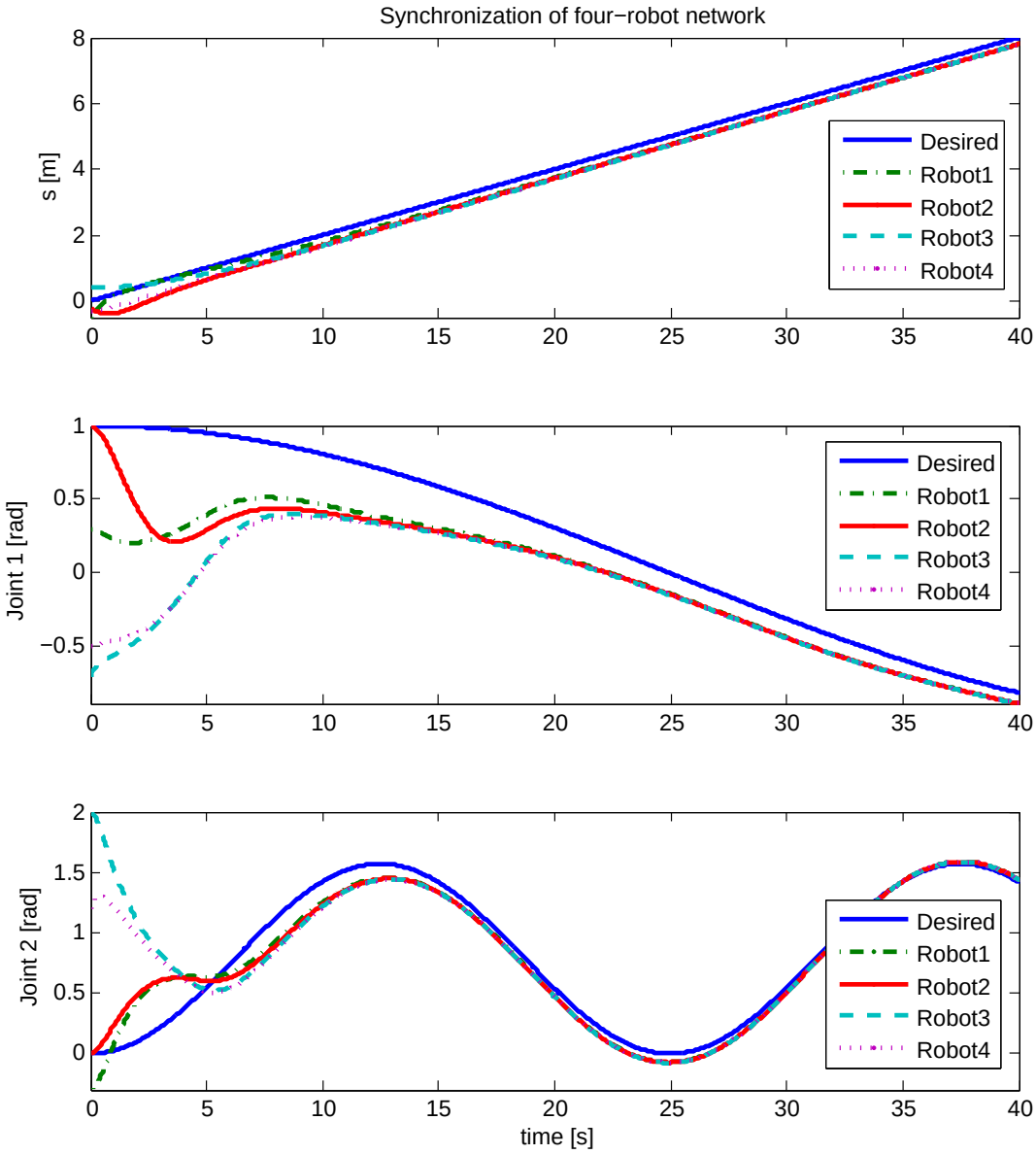

Figure 5-10: Four identical robots: time history of the states

5.6.4 Synchronization of Multiple Formation Flying Spacecraft

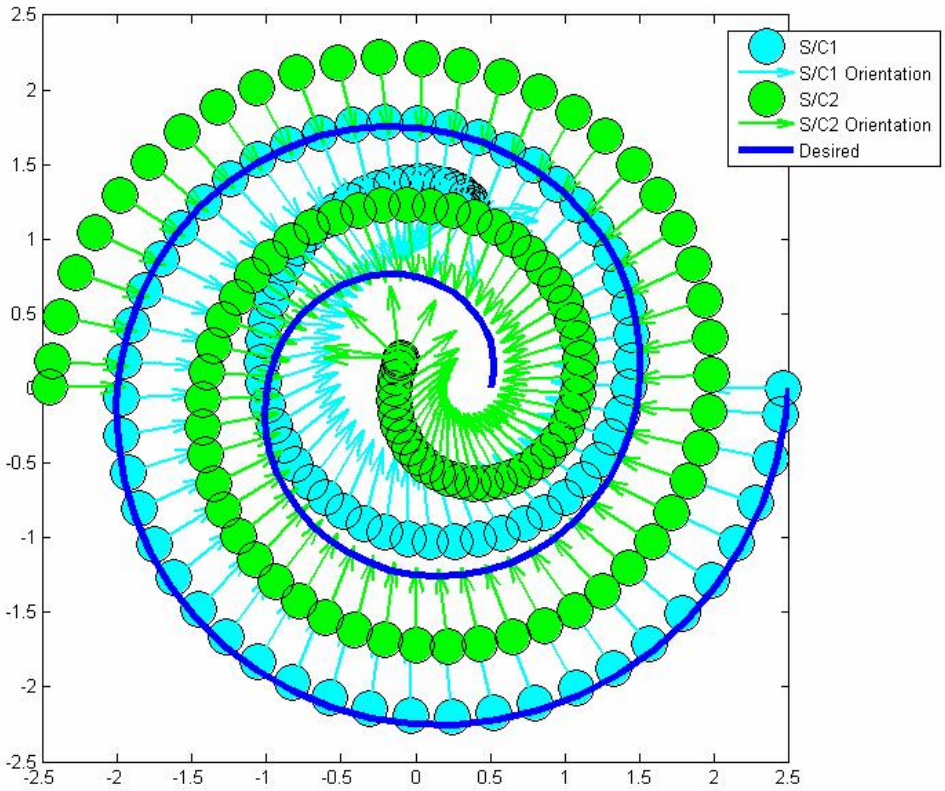

Figure 5-11: Synchronization of a free-flying, uncoupled network of two spacecraft

Formation flight of spacecraft has be an subject of intense research [201, 104]. In this section, the synchronization strategy in this chapter is applied to formation flight attitude control of free flying vehicles. Note that this kind of free flying system is inherently uncoupled, as opposed to tethered formation flight array studied in this thesis. Figure 5-11 shows a simulation result where two spacecraft synchronize their positions and attitude exponentially fast from arbitrary initial conditions. We can add bias to maintain the separation between the spacecraft. In this case, the synchronized position is defined as $\mathbf{x}_1(t) = \mathbf{x}_2(t) + \mathbf{b}(t)$ with $b(t)$ is the displacement vector representing a desired baseline length.

5.6.5 Synchronization with Uni-Directional Coupling

It is straightforward to extend the two-way coupling introduced in this section to one-way coupling (uni-directional coupling) control laws introduced in [202]. For example, Figure 5-12 depicts a dynamical system network with one-way coupling. The control law can be given for a two-agent system as

$$\begin{aligned}\tau_1 &= \mathbf{M}(\mathbf{q}_1)\ddot{\mathbf{q}}_{1r} + \mathbf{C}(\mathbf{q}_1, \dot{\mathbf{q}}_1)\dot{\mathbf{q}}_{1r} + \mathbf{g}(\mathbf{q}_1) \\ \tau_2 &= \mathbf{M}(\mathbf{q}_2)\ddot{\mathbf{q}}_{2r} + \mathbf{C}(\mathbf{q}_2, \dot{\mathbf{q}}_2)\dot{\mathbf{q}}_{2r} + \mathbf{g}(\mathbf{q}_2) - \mathbf{K}(\dot{\mathbf{q}}_2 - \dot{\mathbf{q}}_{2r}) + \mathbf{K}(\dot{\mathbf{q}}_1 - \dot{\mathbf{q}}_{1r})\end{aligned} \tag{5.74}$$

This can easily be converted to two closed-loop dynamics driven by the same input $\mathbf{u}(t) = \mathbf{K}\mathbf{s}_1$. Therefore, the similar analysis as in Section 5.5 leads to the proof of the following theorem:

Theorem 5.6.2 ***One-way, Uni-Directional Coupling Law***

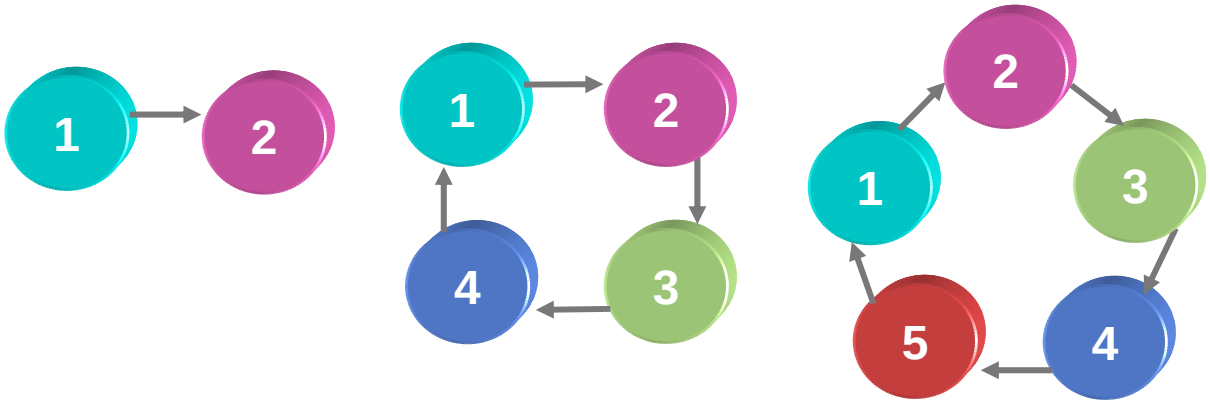

Figure 5-12: One-way (uni-directional) coupling of identical robots

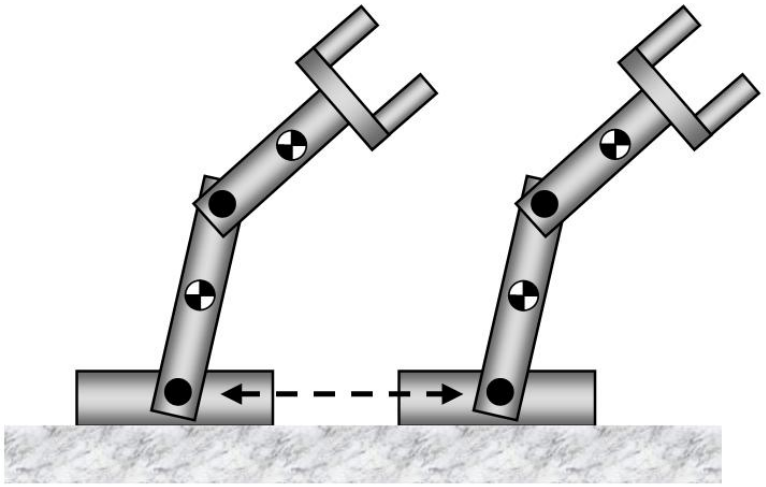

Figure 5-13: Two identical two-link robots with only one-joint coupling. The arrows indicate the coupling control law

If $\mathbf{K}$ *in (5.74) is uniformly positive definite, then such a one-way coupling law in (5.74) synchronizes the individual dynamics of a two-robot network exponentially fast.*

Note that directional couplings yield unbalanced Laplacians.

5.6.6 Synchronization with Partial Degrees-of-Freedom Coupling

We now consider multiple dynamics with partially coupled joints (or partially coupled variables). As shown in Figure 5-13, we can assume that only the lower joint is coupled in a two-robot system having two joint variables–$\mathbf{q} = \begin{pmatrix} x_1 & x_2 \end{pmatrix}^T$:

$$\begin{aligned} \tau_1 &= \mathbf{M}(\mathbf{q}_1)\ddot{\mathbf{q}}_{1r} + \mathbf{C}(\mathbf{q}_1, \dot{\mathbf{q}}_1)\dot{\mathbf{q}}_{1r} + \mathbf{g}(\mathbf{q}_1) - \mathbf{K}_1\mathbf{s}_1 + \mathbf{K}_2 \begin{pmatrix} \dot{\widetilde{x}}_1 \\ 0 \end{pmatrix}_{\mathbf{q}_2} + \mathbf{K}_2\mathbf{\Lambda} \begin{pmatrix} \widetilde{x}_1 \\ 0 \end{pmatrix}_{\mathbf{q}_2} \\ \tau_2 &= \mathbf{M}(\mathbf{q}_2)\ddot{\mathbf{q}}_{2r} + \mathbf{C}(\mathbf{q}_2, \dot{\mathbf{q}}_2)\dot{\mathbf{q}}_{2r} + \mathbf{g}(\mathbf{q}_2) - \mathbf{K}_1\mathbf{s}_2 + \mathbf{K}_2 \begin{pmatrix} \dot{\widetilde{x}}_1 \\ 0 \end{pmatrix}_{\mathbf{q}_1} + \mathbf{K}_2\mathbf{\Lambda} \begin{pmatrix} \widetilde{x}_1 \\ 0 \end{pmatrix}_{\mathbf{q}_1} \end{aligned} \tag{5.75}$$

Nevertheless, Theorems 5.4.1 and 5.4.2 are true with diagonal matrices, $\mathbf{K}_1$, $\mathbf{K}_2$ and $\mathbf{\Lambda}$, which can be verified by writing the closed-loop system as in (5.21):

$$\begin{aligned}
\mathbf{M}(\mathbf{q}_1)\dot{\mathbf{s}}_1 + \mathbf{C}(\mathbf{q}_1, \dot{\mathbf{q}}_1)\mathbf{s}_1 + (\mathbf{K}_1 + \mathbf{K}_2 \begin{bmatrix} 1 & 0 \\ 0 & 0 \end{bmatrix})\mathbf{s}_1 &= \mathbf{u}(t) \\
\mathbf{M}(\mathbf{q}_2)\dot{\mathbf{s}}_2 + \mathbf{C}(\mathbf{q}_2, \dot{\mathbf{q}}_2)\mathbf{s}_2 + (\mathbf{K}_1 + \mathbf{K}_2 \begin{bmatrix} 1 & 0 \\ 0 & 0 \end{bmatrix})\mathbf{s}_2 &= \mathbf{u}(t) \\
\mathbf{u}(t) &= \mathbf{K}_2 \begin{bmatrix} 1 & 0 \\ 0 & 0 \end{bmatrix} (\mathbf{s}_1 + \mathbf{s}_2)
\end{aligned} \tag{5.76}$$

It is straightforward to prove that Theorems 5.4.1 and 5.4.2 still hold. This is because

$$(\mathbf{K}_1 + \mathbf{K}_2 \begin{bmatrix} 1 & 0 \\ 0 & 0 \end{bmatrix}) \text{ and } (\mathbf{K}_1 - \mathbf{K}_2 \begin{bmatrix} 1 & 0 \\ 0 & 0 \end{bmatrix}) \tag{5.77}$$

are still uniformly positive definite, enabling exponential synchronization and exponential convergence to the desired trajectory, respectively. Hence, we did not break any assumptions in the proof of Theorem 5.4.2. Figure 5-14 shows exponential synchronization of two identical robots with the partial coupling law above. All simulation parameters are the same as in Figure 5-6.

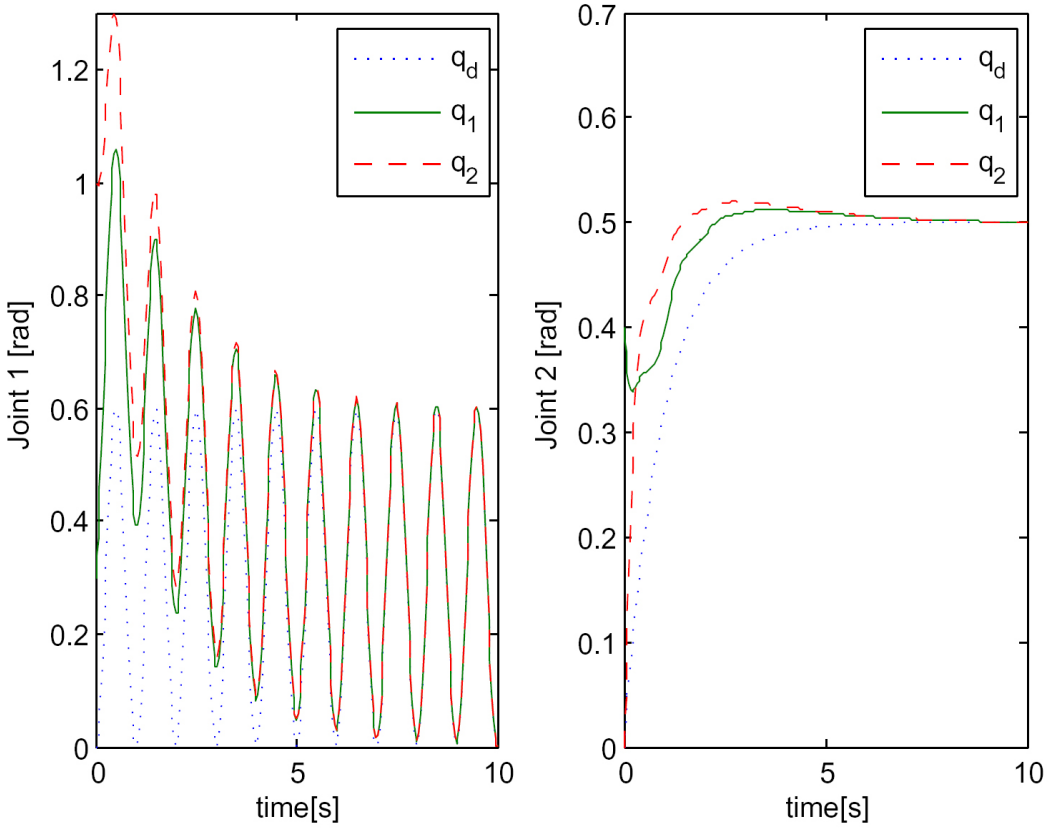

Figure 5-14: Synchronization of two identical robots with partial joint coupling

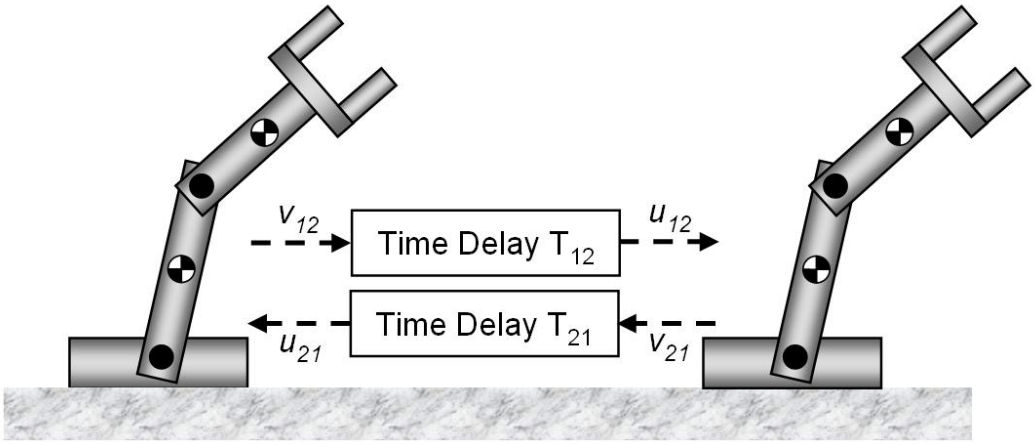

Figure 5-15: Synchronization of two identical robots with transmission delays

5.7 Effects of Transmission Delays and External Disturbances

Now let us discuss the robustness properties of the proposed synchronization framework.

5.7.1 Synchronization with Time Delays

Wang and Slotine [203] showed that contraction properties are conserved in time-delayed diffusion-like couplings. We show herein that the same principle can be applied to all the previous discussions in this chapter. In particular, the proposed synchronization coupling control law in (5.5) is proven to synchronize multiple robots as well as to track the common trajectory, regardless of time delays in the communication.

Figure 5-15 shows two two-link manipulators transmitting their state information to each other via time-delayed transmission channels. While T_{12} is a positive constant denoting the time delay in the communication from the first robot to the second robot, T_{21} denotes the delay from the second robot to the first robot. Similar to [203, 114], we can modify our original Lagrangian systems consisting of two identical robots in (5.21) as follows

$$\begin{aligned} \mathbf{M}(\mathbf{q}_1)\dot{\mathbf{s}}_1 + \mathbf{C}(\mathbf{q}_1, \dot{\mathbf{q}}_1)\mathbf{s}_1 + (\mathbf{K}_1 - \mathbf{K}_2)\mathbf{s}_1 + \mathbf{G}_{21}\tau_{21} = \mathbf{0} \\ \mathbf{M}(\mathbf{q}_2)\dot{\mathbf{s}}_2 + \mathbf{C}(\mathbf{q}_2, \dot{\mathbf{q}}_2)\mathbf{s}_2 + (\mathbf{K}_1 - \mathbf{K}_2)\mathbf{s}_2 + \mathbf{G}_{12}\tau_{12} = \mathbf{0} \end{aligned} \tag{5.78}$$

where $\mathbf{G}_{21}$ and $\mathbf{G}_{12}$ are constant matrices ($\mathbb{R}^{n\times n}$).

The communication between the two dynamics occurs by transmitting intermediate "wave" variables, defined as [203]

$$\begin{aligned} \mathbf{u}_{21} &= \mathbf{G}_{21}^T\mathbf{s}_1 + k_{21}\tau_{21} & \mathbf{v}_{12} &= \mathbf{G}_{21}^T\mathbf{s}_1 \\ \mathbf{u}_{12} &= \mathbf{G}_{12}^T\mathbf{s}_2 + k_{12}\tau_{12} & \mathbf{v}_{21} &= \mathbf{G}_{12}^T\mathbf{s}_2 \end{aligned} \tag{5.79}$$

where k_{21} and k_{12} are strictly positive constants. Time delays of T_{21} and T_{12} result in

$$\mathbf{u}_{12}(t) = \mathbf{v}_{12}(t - T_{12}) \qquad \mathbf{u}_{21}(t) = \mathbf{v}_{21}(t - T_{21}) \tag{5.80}$$

Notice that the original dynamics without any communication delays are contracting since $\mathbf{K}_1 -$

$\mathbf{K}_2 > 0$. Expanding (5.78), using the above relationships on the wave variables, yields

$$\begin{aligned}
&\mathbf{M}(\mathbf{q}_1)\dot{\mathbf{s}}_1 + \mathbf{C}(\mathbf{q}_1, \dot{\mathbf{q}}_1)\mathbf{s}_1 + (\mathbf{K}_1 - \mathbf{K}_2)\mathbf{s}_1 - \frac{1}{k_{21}}\mathbf{G}_{21}\left(\mathbf{G}_{12}^T\mathbf{s}_2(t - T_{21}) + \mathbf{G}_{21}^T\mathbf{s}_1(t)\right) = \mathbf{0} \\
&\mathbf{M}(\mathbf{q}_2)\dot{\mathbf{s}}_2 + \mathbf{C}(\mathbf{q}_2, \dot{\mathbf{q}}_2)\mathbf{s}_2 + (\mathbf{K}_1 - \mathbf{K}_2)\mathbf{s}_2 - \frac{1}{k_{12}}\mathbf{G}_{12}\left(\mathbf{G}_{21}^T\mathbf{s}_1(t - T_{12}) + \mathbf{G}_{12}^T\mathbf{s}_2(t)\right) = \mathbf{0}
\end{aligned} \tag{5.81}$$

We can verify that (5.81) becomes equivalent to the original two-robot dynamics in (5.21) by setting $k_{12} = k_{21} = 1$ and $\mathbf{G}_{12} = \mathbf{G}_{12} = \sqrt{\mathbf{K}_2}$. Note that $\sqrt{\mathbf{K}_2}$ is the Cholesky decomposition of the positive-definite symmetric matrix, $\mathbf{K}_2$.

The resultant equations reflecting the time-delayed transmissions become

$$\begin{aligned}
&\mathbf{M}(\mathbf{q}_1)\dot{\mathbf{s}}_1 + \mathbf{C}(\mathbf{q}_1, \dot{\mathbf{q}}_1)\mathbf{s}_1 + \mathbf{K}_1\mathbf{s}_1 - \mathbf{K}_2\mathbf{s}_2(t - T_{21}) = \mathbf{0} \\
&\mathbf{M}(\mathbf{q}_2)\dot{\mathbf{s}}_2 + \mathbf{C}(\mathbf{q}_2, \dot{\mathbf{q}}_2)\mathbf{s}_2 + \mathbf{K}_1\mathbf{s}_2 - \mathbf{K}_2\mathbf{s}_1(t - T_{12}) = \mathbf{0}
\end{aligned} \tag{5.82}$$

which can be shown to be *asymptotically* contracting using the following differential length similar to [203]:

$$V = \frac{1}{2}\delta\mathbf{s}_1^T\mathbf{M}(\mathbf{q}_1)\delta\mathbf{s}_1 + \frac{1}{2}\delta\mathbf{s}_2^T\mathbf{M}(\mathbf{q}_2)\delta\mathbf{s}_2 + \frac{1}{2}V_{1,2} \tag{5.83}$$

where

$$V_{1,2} = \int_{t-T_{12}}^{t} \delta\mathbf{v}_{12}^T\delta\mathbf{v}_{12}d\epsilon + \int_{t-T_{21}}^{t} \delta\mathbf{v}_{21}^T\delta\mathbf{v}_{21}d\epsilon - \int_{-T_{12}}^{0} \delta\mathbf{v}_{12}^T\delta\mathbf{v}_{12}d\epsilon - \int_{-T_{21}}^{0} \delta\mathbf{v}_{21}^T\delta\mathbf{v}_{21}d\epsilon$$

In conclusion, the robot network systems, individually contracting (exponentially converging) and interacting through time-delayed diffusion-like coupling in (5.81) are asymptotically contracting regardless of the values of the time delays. This in turn implies that individual robots still synchronize and follow the common trajectory asymptotically regardless of the time delays. We have exactly matched the analysis in [203] to allow the derivation of a time-delayed version of the proposed tracking control law in this chapter. This shows that the proposed control law and its closed-loop system in (5.10) possess some robustness properties with respect to time delays.

5.7.2 Effect of Bounded Disturbances

Due to exponential tracking convergence of the proposed scheme, the property of robustness to bounded deterministic disturbances can easily be determined. For example, consider the closed-loop system in (5.18), which is now subject to a vanishing perturbation [92] such that $\mathbf{g}(t, \mathbf{x} = \mathbf{0}) = \mathbf{0}$:

$$[\mathbf{M}]\dot{\mathbf{x}} + [\mathbf{C}]\mathbf{x} + [\mathbf{L}^p_{\mathbf{K}_1,-\mathbf{K}_2}]\mathbf{x} = \mathbf{g}(t, \mathbf{x}) \tag{5.84}$$

The perturbation term $\mathbf{g}(t, \mathbf{x})$ vanishes at the equilibrium manifold $\mathbf{x} = \mathbf{0}$. Let us further assume that it satisfies the linear growth bound such that

$$\|\mathbf{g}(t, \mathbf{x})\| \leq \gamma\|\mathbf{x}\|, \quad \forall t > 0. \tag{5.85}$$

where γ is a positive constant.
The squared-length analysis yields

$$\begin{aligned}
\frac{d}{dt}\left(\delta\mathbf{x}^T[\mathbf{M}]\delta\mathbf{x}\right) &= 2\delta\mathbf{x}^T[\mathbf{M}]\delta\dot{\mathbf{x}} + \delta\mathbf{x}^T[\dot{\mathbf{M}}]\delta\mathbf{x} \\
&= 2\delta\mathbf{x}^T\left(-[\mathbf{C}]\delta\mathbf{x} - [\mathbf{L}^p_{\mathbf{K}_1,-\mathbf{K}_2}]\delta\mathbf{x} + \delta\mathbf{g}(t, \mathbf{x})\right) + \delta\mathbf{x}^T[\dot{\mathbf{M}}]\delta\mathbf{x} \\
&\leq -2\delta\mathbf{x}^T[\mathbf{L}^p_{\mathbf{K}_1,-\mathbf{K}_2}]\delta\mathbf{x} + 2\gamma\delta\mathbf{x}^T\delta\mathbf{x}
\end{aligned} \tag{5.86}$$

where we used the skew-symmetric property of $[\dot{\mathbf{M}}] - 2[\mathbf{C}]$.

Hence, the closed-loop system in (5.84) is contracting in the presence of the bounded disturbance

if $\|[\mathbf{L}^p_{\mathbf{K}_1,-\mathbf{K}_2}]\| > \gamma$. This condition corresponds to $\|\mathbf{K}_1 - \mathbf{K}_2\| > \gamma$ for two-robot systems. As a result, the tracking gain also determines how robust the closed-loop system is with respect to a bounded disturbance. For a nonvanishing perturbation such that $\|\mathbf{g}(t,\mathbf{x})\| \leq \gamma\|\|\mathbf{x}\| + \delta$, the comparison method [92] can straightforwardly be developed to derive a bound on the solution. It should be emphasized that the exponential stability of the closed-loop system facilitates such a perturbation analysis, which highlights another benefit of contraction analysis. In contrast, the proof of robustness with asymptotic convergence is more involved [92].

5.8 Adaptive Synchronization

Consider the following adaptive control law, which has the same local coupling structure as the proposed control law in (5.5):

$$\tau_i = \mathbf{Y}_i\hat{\mathbf{a}}_i - \mathbf{K}_1\mathbf{s}_i + \mathbf{K}_2\mathbf{s}_{i-1} + \mathbf{K}_2\mathbf{s}_{i+1} = \hat{\mathbf{M}}_i\ddot{\mathbf{q}}_{ir} + \hat{\mathbf{C}}_i\dot{\mathbf{q}}_{ir} + \hat{\mathbf{g}}_i(\mathbf{q}_i) - \mathbf{K}_1\mathbf{s}_i + \mathbf{K}_2\mathbf{s}_{i-1} + \mathbf{K}_2\mathbf{s}_{i+1} \quad (5.87)$$

where $\mathbf{s}_i$ denotes the composite variable for the i-th robot such that $\mathbf{s}_i = \dot{\mathbf{q}}_i - \dot{\mathbf{q}}_{ir}$.

The parameter estimate $\hat{\mathbf{a}}_i$ for the i-th member is updated by the correlation integral:

$$\dot{\hat{\mathbf{a}}}_i = -\boldsymbol{\Gamma}\mathbf{Y}_i^T\mathbf{s}_i \quad (5.88)$$

where $\boldsymbol{\Gamma}$ is a symmetric positive definite matrix. Hence, the closed-loop system for a network consisting of two non-identical robots can be written as

$$\begin{bmatrix}\mathbf{M}_1(\mathbf{q}_1) & \mathbf{0}\\ \mathbf{0} & \boldsymbol{\Gamma}^{-1}\end{bmatrix}\begin{pmatrix}\dot{\mathbf{s}}_1\\ \dot{\tilde{\mathbf{a}}}_1\end{pmatrix} + \begin{bmatrix}\mathbf{C}_1(\mathbf{q}_1,\dot{\mathbf{q}}_1) + \mathbf{K}_1 + \mathbf{K}_2 & -\mathbf{Y}_1\\ \mathbf{Y}_1^T & \mathbf{0}\end{bmatrix}\begin{pmatrix}\mathbf{s}_1\\ \tilde{\mathbf{a}}_1\end{pmatrix} = \begin{pmatrix}\mathbf{u}(t)\\ \mathbf{0}\end{pmatrix} \quad (5.89)$$
$$\begin{bmatrix}\mathbf{M}_2(\mathbf{q}_2) & \mathbf{0}\\ \mathbf{0} & \boldsymbol{\Gamma}^{-1}\end{bmatrix}\begin{pmatrix}\dot{\mathbf{s}}_2\\ \dot{\tilde{\mathbf{a}}}_2\end{pmatrix} + \begin{bmatrix}\mathbf{C}_2(\mathbf{q}_2,\dot{\mathbf{q}}_2) + \mathbf{K}_1 + \mathbf{K}_2 & -\mathbf{Y}_2\\ \mathbf{Y}_2^T & \mathbf{0}\end{bmatrix}\begin{pmatrix}\mathbf{s}_2\\ \tilde{\mathbf{a}}_2\end{pmatrix} = \begin{pmatrix}\mathbf{u}(t)\\ \mathbf{0}\end{pmatrix}$$

where $\mathbf{u}(t) = \mathbf{K}_2(\mathbf{s}_1 + \mathbf{s}_2)$. Additionally, $\tilde{\mathbf{a}}$ denotes an error of the estimate such that $\tilde{\mathbf{a}} = \hat{\mathbf{a}} - \mathbf{a}$. Note that $\mathbf{a}$ is a constant vector of the true parameter values, resulting in $\dot{\tilde{\mathbf{a}}}_i = \dot{\hat{\mathbf{a}}}_i$.

Similar to Section 5.5.4, applying the spectral transformation using

$$\mathbf{V} = \begin{bmatrix}\frac{1}{\sqrt{2}}\mathbf{I} & \frac{1}{\sqrt{2}}\mathbf{I} & \mathbf{0} & \mathbf{0}\\ \frac{1}{\sqrt{2}}\mathbf{I} & -\frac{1}{\sqrt{2}}\mathbf{I} & \mathbf{0} & \mathbf{0}\\ \mathbf{0} & \mathbf{0} & \mathbf{I} & \mathbf{0}\\ \mathbf{0} & \mathbf{0} & \mathbf{0} & \mathbf{I}\end{bmatrix} \quad (5.90)$$

to the system, defined by the vector $\mathbf{x} = \begin{pmatrix}\mathbf{s}_1 & \mathbf{s}_2 & \mathbf{a}_1 & \mathbf{a}_2\end{pmatrix}^T$, leads to the following generalized Jacobian matrix

$$\mathbf{J} = -\begin{bmatrix}\mathbf{K}_1 - \mathbf{K}_2 & \mathbf{0} & -\frac{1}{\sqrt{2}}\mathbf{Y}_1 & -\frac{1}{\sqrt{2}}\mathbf{Y}_2\\ \mathbf{0} & \mathbf{K}_1 + \mathbf{K}_2 & -\frac{1}{\sqrt{2}}\mathbf{Y}_1 & \frac{1}{\sqrt{2}}\mathbf{Y}_2\\ \frac{1}{\sqrt{2}}\mathbf{Y}_1 & \frac{1}{\sqrt{2}}\mathbf{Y}_1 & \mathbf{0} & \mathbf{0}\\ \frac{1}{\sqrt{2}}\mathbf{Y}_2 & -\frac{1}{\sqrt{2}}\mathbf{Y}_2 & \mathbf{0} & \mathbf{0}\end{bmatrix} \quad (5.91)$$

whose symmetric part indicates the system is semi-contracting with $\mathbf{K}_1 - \mathbf{K}_2 > 0$ and $\mathbf{K}_1 + \mathbf{K}_2 > 0$. Using Barbalat's lemma (see Section 5.5, Case II), it is straightforward to show that $\mathbf{s}_1$ and $\mathbf{s}_2$ tend to each other asymptotically while the parameter estimates $\mathbf{a}_1$ and $\mathbf{a}_2$ synchronize as well. This result implies that the adaptive synchronization law in (5.87) not only synchronizes the states of multiple dynamics in the network, but also makes the estimated physical parameters tend to each other in the presence of model uncertainties. Due to the asymptotic convergence of the adaptive control law in (5.87), the convergence result is now asymptotic instead of exponential.

5.9 PD Synchronization of Robots

One may consider the following PD coupling control law for two identical robots from (5.1) with $p = 2$,

$$\begin{aligned} \tau_1 &= -\mathbf{K}_1(\dot{\mathbf{q}}_1 + \mathbf{\Lambda}\tilde{\mathbf{q}}_1) + \mathbf{K}_2(\dot{\mathbf{q}}_2 + \mathbf{\Lambda}\tilde{\mathbf{q}}_2) \\ \tau_2 &= -\mathbf{K}_1(\dot{\mathbf{q}}_2 + \mathbf{\Lambda}\tilde{\mathbf{q}}_2) + \mathbf{K}_2(\dot{\mathbf{q}}_1 + \mathbf{\Lambda}\tilde{\mathbf{q}}_1) \end{aligned} \tag{5.92}$$

where $\tilde{\mathbf{q}}_i = \mathbf{q}_i - \mathbf{q}_d$ and the bounded reference position $\mathbf{q}_d$ has zero velocity such that $\dot{\tilde{\mathbf{q}}}_i = \dot{\mathbf{q}}_i$. For simplicity, the gravity term in (5.1) is assumed to be zero or canceled by a feed-forward control law. Then, the closed-loop dynamics satisfy

$$\begin{aligned} \mathbf{M}(\mathbf{q}_1)\ddot{\mathbf{q}}_1 + \mathbf{C}(\mathbf{q}_1, \dot{\mathbf{q}}_1)\dot{\mathbf{q}}_1 + (\mathbf{K}_1 + \mathbf{K}_2)\dot{\mathbf{q}}_1 + (\mathbf{K}_1 + \mathbf{K}_2)\mathbf{\Lambda}\tilde{\mathbf{q}}_1 &= \mathbf{u}(t) \\ \mathbf{M}(\mathbf{q}_2)\ddot{\mathbf{q}}_2 + \mathbf{C}(\mathbf{q}_2, \dot{\mathbf{q}}_2)\dot{\mathbf{q}}_2 + (\mathbf{K}_1 + \mathbf{K}_2)\dot{\mathbf{q}}_2 + (\mathbf{K}_1 + \mathbf{K}_2)\mathbf{\Lambda}\tilde{\mathbf{q}}_2 &= \mathbf{u}(t) \\ \mathbf{u}(t) = \mathbf{K}_2(\dot{\mathbf{q}}_1 + \dot{\mathbf{q}}_2) + \mathbf{K}_2\mathbf{\Lambda}(\tilde{\mathbf{q}}_1 + \tilde{\mathbf{q}}_2) & \end{aligned} \tag{5.93}$$

where $\mathbf{u}(t)$ is the common excitation input.

Similar to Section 5.5.3, we can perform a spectral decomposition:

$$\begin{aligned} &\left(\mathbf{V}^T[\mathbf{M}]\mathbf{V}\right)\mathbf{V}^T\ddot{\mathbf{x}} + \left(\mathbf{V}^T[\mathbf{C}]\mathbf{V}\right)\mathbf{V}^T\dot{\mathbf{x}} \\ &\quad + \left(\mathbf{V}^T[\mathbf{L}^p_{\mathbf{K}_1,-\mathbf{K}_2}]\mathbf{V}\right)\mathbf{V}^T\dot{\mathbf{x}} + \left(\mathbf{V}^T[\mathbf{L}^p_{\mathbf{K}_1\mathbf{\Lambda},-\mathbf{K}_2\mathbf{\Lambda}}]\mathbf{V}\right)\mathbf{V}^T\tilde{\mathbf{x}} = \mathbf{0} \end{aligned} \tag{5.94}$$

which can be represented as

$$\begin{aligned} &\begin{bmatrix} \frac{\mathbf{M}_1+\mathbf{M}_2}{2} & \frac{\mathbf{M}_1-\mathbf{M}_2}{2} \\ \frac{\mathbf{M}_1-\mathbf{M}_2}{2} & \frac{\mathbf{M}_1+\mathbf{M}_2}{2} \end{bmatrix}\begin{pmatrix} \ddot{\mathbf{q}}_p \\ \ddot{\mathbf{q}}_m \end{pmatrix} + \begin{bmatrix} \frac{\mathbf{C}_1+\mathbf{C}_2}{2} & \frac{\mathbf{C}_1-\mathbf{C}_2}{2} \\ \frac{\mathbf{C}_1-\mathbf{C}_2}{2} & \frac{\mathbf{C}_1+\mathbf{C}_2}{2} \end{bmatrix}\begin{pmatrix} \dot{\mathbf{q}}_p \\ \dot{\mathbf{q}}_m \end{pmatrix} \\ &\quad + \begin{bmatrix} \mathbf{K}_1 - \mathbf{K}_2 & 0 \\ 0 & \mathbf{K}_1 + \mathbf{K}_2 \end{bmatrix}\begin{pmatrix} \dot{\mathbf{q}}_p \\ \dot{\mathbf{q}}_m \end{pmatrix} + \begin{bmatrix} (\mathbf{K}_1 - \mathbf{K}_2)\mathbf{\Lambda} & 0 \\ 0 & (\mathbf{K}_1 + \mathbf{K}_2)\mathbf{\Lambda} \end{bmatrix}\begin{pmatrix} \tilde{\mathbf{q}}_p \\ \mathbf{q}_m \end{pmatrix} = \begin{pmatrix} \mathbf{0} \\ \mathbf{0} \end{pmatrix} \end{aligned} \tag{5.95}$$

where

$$\begin{aligned} \mathbf{M}_1 = \mathbf{M}(\mathbf{q}_1), \quad \mathbf{M}_2 = \mathbf{M}(\mathbf{q}_2), \quad \mathbf{C}_1 = \mathbf{C}(\mathbf{q}_1, \dot{\mathbf{q}}_1), \quad \mathbf{C}_2 = \mathbf{C}(\mathbf{q}_2, \dot{\mathbf{q}}_2) \\ \mathbf{V}^T\mathbf{x} = \begin{pmatrix} \mathbf{q}_p \\ \mathbf{q}_m \end{pmatrix} = \frac{1}{\sqrt{2}}\begin{pmatrix} \mathbf{q}_1 + \mathbf{q}_2 \\ \mathbf{q}_1 - \mathbf{q}_2 \end{pmatrix}, \quad \tilde{\mathbf{q}}_p = \frac{1}{\sqrt{2}}(\tilde{\mathbf{q}}_1 + \tilde{\mathbf{q}}_2). \end{aligned} \tag{5.96}$$

Using the following Lyapunov function, it is straightforward to show that this PD coupling control law drives the system to the desired rest state $\mathbf{q}_d$ globally and asymptotically while tending to the synchronized flow-invariant manifold, $\mathcal{M}_q$ in (5.27).

$$V = \frac{1}{2}\begin{pmatrix} \dot{\mathbf{q}}_p \\ \dot{\mathbf{q}}_m \end{pmatrix}^T \begin{bmatrix} \frac{\mathbf{M}_1+\mathbf{M}_2}{2} & \frac{\mathbf{M}_1-\mathbf{M}_2}{2} \\ \frac{\mathbf{M}_1-\mathbf{M}_2}{2} & \frac{\mathbf{M}_1+\mathbf{M}_2}{2} \end{bmatrix}\begin{pmatrix} \dot{\mathbf{q}}_p \\ \dot{\mathbf{q}}_m \end{pmatrix} + \frac{1}{2}\begin{pmatrix} \tilde{\mathbf{q}}_p \\ \mathbf{q}_m \end{pmatrix}^T \begin{bmatrix} (\mathbf{K}_1 - \mathbf{K}_2)\mathbf{\Lambda} & 0 \\ 0 & (\mathbf{K}_1 + \mathbf{K}_2)\mathbf{\Lambda} \end{bmatrix}\begin{pmatrix} \tilde{\mathbf{q}}_p \\ \mathbf{q}_m \end{pmatrix} \tag{5.97}$$

The rate of V can be computed as

$$\frac{dV}{dt} = -\begin{pmatrix} \dot{\mathbf{q}}_p \\ \dot{\mathbf{q}}_m \end{pmatrix}^T \begin{bmatrix} \mathbf{K}_1 - \mathbf{K}_2 & 0 \\ 0 & \mathbf{K}_1 + \mathbf{K}_2 \end{bmatrix}\begin{pmatrix} \dot{\mathbf{q}}_p \\ \dot{\mathbf{q}}_m \end{pmatrix} \leq 0 \tag{5.98}$$

which implies that $\dot{V}$ is negative semi-definite with $\mathbf{K}_1 + \mathbf{K}_2 > 0$ and $\mathbf{K}_1 - \mathbf{K}_2 > 0$.

By invoking LaSalle's invariant set theorem in Chapter 2, we can conclude that $\dot{\mathbf{q}}_p$, $\tilde{\mathbf{q}}_p$, $\dot{\mathbf{q}}_m$, and $\mathbf{q}_m$ tend to zero with global and asymptotic convergence. This implies that $\mathbf{q}_1$ and $\mathbf{q}_2$ will follow $\mathbf{q}_d$ while $\mathbf{q}_1$ and $\mathbf{q}_2$ synchronize asymptotically.

Theorem 5.9.1 ***PD Synchronization of Two Identical Robots***
Two identical robots synchronize asymptotically and globally with the PD coupling law in (5.92) if $\exists$

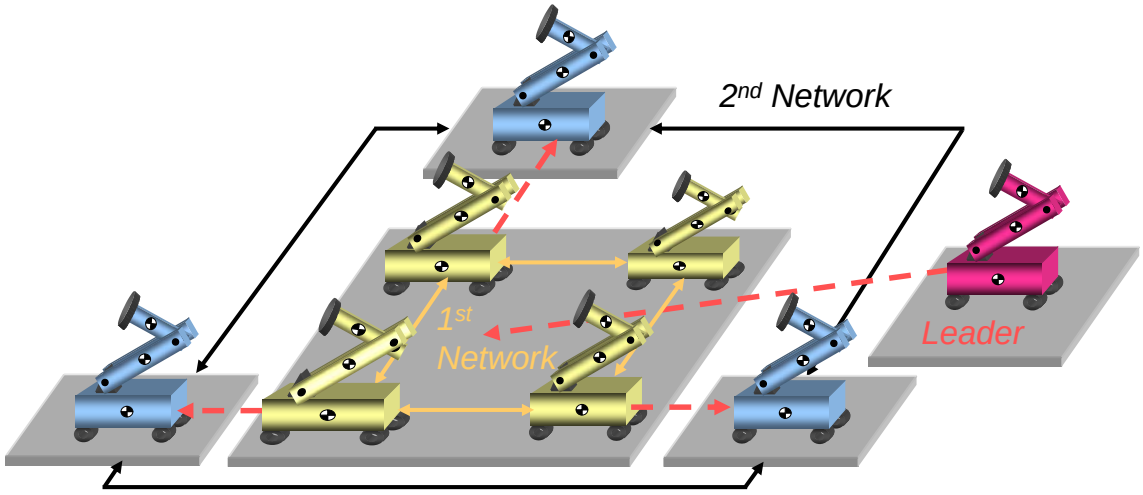

Figure 5-16: Concurrent synchronization between two different groups. The desired trajectory inputs are denoted by the dashed-lines whereas the solid lines indicate mutual diffusive couplings. The independent leader sends the same desired trajectory input to the first network group.

$\mathbf{K}_2 > 0$ *such that*

$$\mathbf{K}_1 + \mathbf{K}_2 > 0 \qquad \mathbf{\Lambda} > 0$$

In addition, $\mathbf{K}_1 - \mathbf{K}_2 > 0$ *is required for asymptotic stability of the PD control.*

5.9.1 Velocity Coupling, $\mathbf{\Lambda} = 0$

Note that if $\mathbf{\Lambda} = 0$, the PD coupling control law in (5.92) reduces to

$$\begin{aligned} \tau_1 &= -\mathbf{K}_1\dot{\mathbf{q}}_1 + \mathbf{K}_2\dot{\mathbf{q}}_2 \\ \tau_2 &= -\mathbf{K}_1\dot{\mathbf{q}}_2 + \mathbf{K}_2\dot{\mathbf{q}}_1 \end{aligned} \tag{5.99}$$

This velocity coupling control can also be derived from the exponential tracking control law in (5.5) by setting $\mathbf{q}_d = 0, \dot{\mathbf{q}}_d = 0$ and $\mathbf{\Lambda} = 0$. Therefore, the proof of Theorem 5.9.1 with $\mathbf{\Lambda} = 0$ is the same as Section 5.5.3 whereas the convergence rate is now exponential compared to the asymptotic convergence of the PD control. On the other hand, we can find that positions do not synchronize *in the absence of the gravity term* even though the velocities synchronize exponentially fast.

5.10 Concurrent Synchronization

In [152], *concurrent synchronization* is defined as a regime where the ensemble of dynamical elements is divided into multiple groups of fully synchronized elements, but elements from different groups are not necessarily synchronized and can exhibit entirely different dynamics. Mathematically, it can be shown that such a regime corresponds to a flow invariant linear subspace of the global state space.

In the context of the synchronization of multiple Lagrangian dynamics, discussed in this chapter, we are interested in the concurrent synchronization of different aggregates of multiple identical or nonidentical dynamics. As discussed in the previous sections, we pay particular attention to the fact that there exist two different time scales of the proposed synchronization tracking control law. In the case of a two-robot network, one rate is associated with the trajectory tracking $(\mathbf{K}_1 - 2\mathbf{K}_2)$ while the other represents the convergence rate of the synchronization $(\mathbf{K}_1 + \mathbf{K}_2)$. This in turn implies that there are two different inputs to the system, namely, the desired common trajectory $\mathbf{q}_d(t)$ and the diffusive couplings with the adjacent members.

Accordingly, we exploit a desired trajectory $\mathbf{q}_d(t)$ to create multiple combinations of different dynamics groups. For instance, Figure 5-16 represents the concurrent synchronization of two different dynamical networks. The first network, consisting of four different robots, has the diffusive coupling structure proposed by the tracking control law in (5.5). The independent leader sends a desired trajectory command $\mathbf{q}_d$ to the first network. With an appropriate selection of gains, each dynamics in the first network synchronize while exponentially following the leader. Therefore, the proposed scheme can be interpreted in the context of the leader-follower problem ([86, 108, 204]).

The second network consists of three non-identical dynamics, also different from those of the first group. Each element receives a different desired trajectory input from the adjacent element of the first network. However, once the first network is synchronized, the second network also ends up receiving the same desired trajectory to follow while they interact to synchronize exponentially fast. Accordingly, we can achieve concurrent synchronization between two different network groups. This can be extended to arbitrarily large groups of synchronized dynamics by appropriately assigning the desired trajectory inputs and the diffusive couplings. Note that the number of agents in one layer can be different from that of another layer as seen in Figure 5-16.

5.11 Conclusions

This chapter has presented the new synchronization tracking control law that can be directly applied to cooperative control of multi-agent systems and oscillation synchronization in robotic manipulation and locomotion. The proposed decentralized control law, which requires only local coupling feedback for global exponential convergence, eliminates both the all-to-all coupling and the feedback of the acceleration terms, thereby reducing communication burdens and complexity. Furthermore, in contrast with prior work which used simple single or double integrator models, the proposed method permits highly nonlinear systems. Providing exact nonlinear stability results constitutes one of the main contributions of this chapter; global and exponential stability of the closed-loop system has been derived by using contraction theory. Contraction analysis, overcoming a local result of Lypunov's indirect method, yields global results based on differential stability analysis. It has been emphasized that there exist two different time-scales in the closed-loop systems: the faster convergence rate represents the transient boundary layer dynamics of synchronization while the slower rate determines how fast the synchronized systems track the common reference trajectory. Exponential synchronization with a faster convergence rate enables reduction of multiple dynamics into a simpler form thereby simplifying the stability analysis. As opposed to the stable tracking case, where non-identical dynamics are permitted, the synchronization that leads to instability requires identical dynamics. It should be noted that the tracking convergence rate also determines the robustness of the closed-loop system with respect to a bounded disturbance.

Simulation results show the effectiveness of the proposed control strategy. The proposed bidirectional coupling has also been generalized to permit partial-joint coupling and uni-directional coupling. Further extensions to PD coupling, time-delayed communications, adaptive synchronization, and concurrent synchronization exemplify the benefit of the differential stability analysis based on contraction theory. For future work, we are interested in extending the proposed method to dynamical networks on unbalanced or open graphs. Since this chapter is based on the assumption of fully actuated dynamics, it would be useful to consider multi-agent systems consisting of underactuated mechanical systems.

Chapter 6

Nonlinear Control of Underactuated Tethered Systems

6.1 Chapter Objective

The previous chapters were based on the assumption that the spinning tethered system is fully actuated (both F and u are available). Motivated by the controllability analysis in Chapter 3, which indicates that both array resizing and spin-up are fully controllable by the reaction wheels (u) and the tether motor, the aim of the present chapter is to introduce some new nonlinear control techniques for spinning tethered arrays without thrusters ($F = 0$). To our knowledge, this work reports the first propellant-free underactuated control results for tethered formation flying spacecraft. This chapter also fulfills the potential of the proposed strategy by providing a new momentum dumping method without torque-generating thrusters; the compound pendulum mode and array spin rate are stabilized using only the linear thruster and translational actuator on the tether during the operation of momentum dumping.

Such a tethered system without thrusters is *underactuated* since it has fewer inputs than configuration variables. In contrast with linear systems, in which an underactuated control law can be synthesized easily, designing a nonlinear controller for nonlinear underactuated systems poses a challenge, mainly due to the lack of full state feedback linearizability. The outline of this chapter is as follows: First, we briefly review the key aspects of underactuated mechanical systems in Section 6.2. We exploit gain-scheduling LQR control (Section 6.3), partial feedback linearization (Section 6.4), feedback linearization via momentum decoupling (Section 6.5), and backstepping (Section 6.6). Simulation results presented in Section 6.8 support our conclusion that the nonlinear approach is much more efficient in the tracking problem than the linear LQR control. Last, Section 6.9 presents a new momentum dumping strategy. We shall consider only the case of the fixed tether length, focusing on the spin-up attitude control problem on the assumption that the tether length is controllable separately.

6.2 Fundamentals of Underactuated Systems

We have proven in Chapter 4 that a fully decentralized control law designed from a single-tethered spacecraft can also stabilize arbitrarily large circular arrays of spacecraft, as well as a three inline configuration. Consequently, we first focus on control of an underactuated single-tethered system (see Figure 6-1(c)), and then discuss decentralization and decoupling in Section 6.7.

Underactuated mechanical systems are characterized by fewer actuators than degrees of freedom (DOF) or configuration variables, and encountered in a wide range of applications such as walking robots [194, 206], aerospace vehicles [67, 145], and nonholonomic systems [22]. Popular two-DOF examples include the acrobot (Figure 6-1(a)) and the pendubot (Figure 6-1(b)), where the control input is available only to one joint variable. In contrast, the single-tethered system shown in Figure

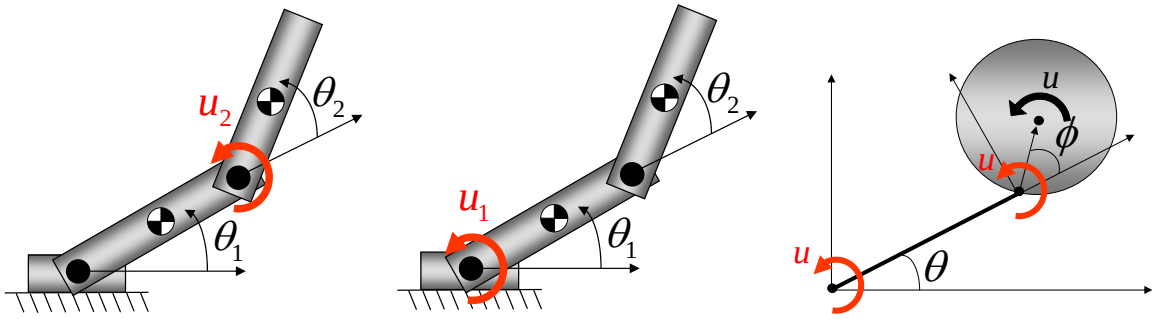

(a) Acrobot (b) Pendubot (c) Tethered-spacecraft without thrusters

Figure 6-1: Three representative cases of underactuated two-link mechanical systems

6-1(c) is underactuated via input coupling. This chapter also serves the purpose of proposing the single-tethered system as another underactuated control benchmark problem. We also attempt to make a connection between the single-tethered system, which is a fundamental building block for constructing multi-spacecraft arrays, and a two-link planar robot, which has been a representative example in nonlinear control theory.

Recalling (3.14), the equations of motion for the single-tethered system under the torque actuator only ($u \neq 0, F = 0$) becomes

$$\mathbf{M_1}(\phi) \begin{pmatrix} \ddot{\theta} \\ \ddot{\phi} \end{pmatrix} + \mathbf{C_1}(\phi, \dot{\theta}, \dot{\phi}) \begin{pmatrix} \dot{\theta} \\ \dot{\phi} \end{pmatrix} = \begin{pmatrix} \tau_\theta \\ \tau_\phi \end{pmatrix} = \begin{pmatrix} 1 \\ 1 \end{pmatrix} u \tag{6.1}$$

where $\mathbf{M_1}(\phi)$ and $\mathbf{C_1}(\phi, \dot{\theta}, \dot{\phi})$ are given in (3.14). Note that we can derive the above equation from the two-link robot manipulator dynamics, by assuming that the mass and moment of inertial of the first link are zero and gravity is absent.

Equation (6.1) clearly shows that the single input u enters both the configuration variables θ and ϕ, as opposed to the acrobot $\tau = \begin{pmatrix} 0 & u \end{pmatrix}^T$ and the pendubot $\tau = \begin{pmatrix} u & 0 \end{pmatrix}^T$. Even though all three cases in Figure 6-1 are derived from the two-link manipulator robot, there exists another fundamental difference. The effect of gravity is ignored in the tethered system (see the modeling assumptions in Chapter 3). In particular, underactuated mechanical systems such as the acrobot are in general not controllable in the absence of the gravity. However, the artificial gravity, induced by the centripetal force associated with array rotation, plays a crucial role in making the tethered system controllable and stable (see the discussion in Chapter 3).

Most prior work, which has been reviewed in Section 1.6.6, is restricted to a single-body dynamics problem. In this chapter, the decentralized control strategy from Chapter 4 is extended to the underactuated control of multi-vehicle tethered formation flying. To our knowledge, this work presents the first linear and nonlinear control results for underactuated tethered formation flight systems.

6.2.1 Challenges of Nonlinear Underactuated Systems

As mentioned earlier, an underactuated mechanical system is not, in principle, exactly input-state feedback linearizable. Its lack of feedback linearizability, along with its complex nonholonomic behavior, characterizes the difficult nonlinear control problem. It has been shown in [135] that the acrobot is not feedback linearizable with static state feedback and nonlinear coordinate transformation. In this section, we derive a similar result for the single tethered system given in (6.1) and Figure 6-1(c).

Theorem 6.2.1 *Input-State Linearization [178, 200]*

Given a nonlinear system, affine in the control input u,

$$\dot{\mathbf{x}} = \mathbf{f}(\mathbf{x}) + \mathbf{g}(\mathbf{x})u \tag{6.2}$$

The system is input-state linearizable in an open set U such that a nonlinear feedback control law $u = \alpha(\mathbf{x})v + \beta(\mathbf{x})$ and a diffeomorphism $\mathbf{z} = \phi(\mathbf{x})$, transform (6.2) to the resultant linear dynamics

$$\dot{\mathbf{z}} = \mathbf{A}\mathbf{z} + \mathbf{b}v \tag{6.3}$$

if and only if

1. *dim span$\{g, ad_f g, \cdots, ad_f^{n-1} g\}(\mathbf{x}) = n$, $\forall \mathbf{x} \in U$ in $\mathbb{R}^n$– i.e., the vector fields are linearly independent.*
2. *span$\{g, ad_f g, \cdots, ad_f^{n-2} g\}$ is an involutive distribution on U*

where $ad_f^i g$ is the iterated Lie bracket $[f, \cdots, [f, g] \cdots]$.

The first condition corresponds to a controllability test and agrees with the linear controllability analysis about the relative equilibria in Chapter 3. The more subtle second condition, derived by Frobenius' theorem, warrants further discussion. To meet the involutivity condition, the following vector fields

$$[g, ad_f g] \quad [g, ad_f^2 g] \quad [ad_f g, ad_f^2 g] \tag{6.4}$$

must lie in the distribution $\Delta = \text{span}\{g, ad_f g, ad_f^2 g\}$. It can be verified via Mathematica (see Appendix C.1) that the matrix constructed by one of the above vector fields and Δ has full rank of four. This in turn implies that they do not lie in the distribution Δ (all vectors are independent). As a result, similar to the acrobot, the underactuated single-tethered system fails the involutivity test, and hence is not input-state feedback linearizable.

Nevertheless, there might exist an output function to render input-output feedback linearizability. Finding such an output function is not trivial and the associated zero dynamics should be stable. This is one of the reasons that designing an efficient control law of a large class of underactuated systems is generally an open problem. In Section 6.5, we introduce a nonlinear diffeomorphism that permits model reduction and simple feedback linearization about the transformed state vector, inspired by the following normal forms [145].

6.2.2 Normal Forms for Underactuated Systems

Olfati-Saber [145] developed cascade normal forms for underactuated mechanical systems, based on the mechanical symmetry introduced in Chapter 2. Normal forms can be further classified into triangular normal forms and nontriangular forms. Both strict-feedback and strict-feedforward systems are called "triangular" by analogy with linear systems. In particular, a strict-feedback system permits a systematic nonlinear control design called backstepping.

Definition Strict feedback form
A nonlinear system in strict feedback form has the following triangular structure

$$\begin{aligned} \dot{z} &= f(z, \xi_1) \\ \dot{\xi}_1 &= \xi_2 \\ &\cdots \\ \dot{\xi}_m &= u \end{aligned} \tag{6.5}$$

Let us consider the dynamics similar to the acrobot such that the input is applied only to the shape variable q_2:

$$\begin{aligned} m_{11}(q_2)\ddot{q}_1 + m_{12}(q_2)\ddot{q}_2 + h_1(q_1, q_2, \dot{q}_1, \dot{q}_2) &= 0 \\ m_{21}(q_2)\ddot{q}_1 + m_{22}(q_2)\ddot{q}_2 + h_2(q_1, q_2, \dot{q}_1, \dot{q}_2) &= \tau \end{aligned} \tag{6.6}$$

where the dynamics are kinetic symmetric with respect to q_2 such that $m_{ij}(\mathbf{q}) = m_{ij}(q_2)$. Similar to the partial linearization, there exists an invertible change of control input $\tau = \alpha(\mathbf{q})u + \beta(\mathbf{q}, \dot{\mathbf{q}})$, which transforms the dynamics into

$$\begin{aligned} \dot{q}_1 &= p_1 \\ \dot{p}_1 &= -m_{11}^{-1}(q_2)h_1(q_1, q_2, p_1, p_2) - m_{11}^{-1}(q_2)m_{12}(q_2)u \\ \dot{q}_2 &= p_2 \\ \dot{p}_2 &= u \end{aligned} \tag{6.7}$$

Since the linearization was performed on the actuated variable q_2, such a change of control is called collocated partial feedback linearization. Ref. [145] introduces a diffeomorphism transforming the above equation into a strict-feedback form:

$$\begin{aligned} \dot{z}_1 &= m_{11}^{-1}(\xi_1)z_2 \\ \dot{z}_2 &= g(z_1, \xi_1) \\ \dot{\xi}_1 &= \xi_2 \\ \dot{\xi}_2 &= u \end{aligned} \tag{6.8}$$

where $g(\cdot, \cdot)$ is the gravity term. Unfortunately, the single-tethered system shown in Figure 6-1(c) does not permit the same strict-feedback form due to its input coupling and the lack of such a gravity function. Nevertheless, in Section 6.5, we show that the same transformation yields a useful coordinate transformation permitting feedback linearization and backstepping control design for the reduced variables z_1 and z_2.

We can also show that the pendubot in Figure 6-1(b) can be transformed into a cascade nonlinear system in nontriangular quadratic normal form by a similar transformation:

$$\begin{aligned} \dot{z}_1 &= m_{21}^{-1}(\xi_1)z_2 \\ \dot{z}_2 &= g(z_1, \xi_1) + (z_2, \xi_2)\pi(\xi_1)(z_2, \xi_2)^T \\ \dot{\xi}_1 &= \xi_2 \\ \dot{\xi}_2 &= u \end{aligned} \tag{6.9}$$

Stabilization of a nontriangular form, addressed in [145], is in general much more difficult than that of a triangular form. For example, backstepping or forwarding [145] is not applicable. Even though the single-tethered dynamics in Figure 6-1 can be transformed into a non-triangular form, such a method is not pursued in this dissertation due to the challenge associated with a nontriangular form. Instead, we apply feedback linearization and backstepping to the reduced system by using a transformation similar to (6.8), in addition to gain-scheduling linear control and partial feedback linearization.

6.3 Gain-Scheduled LQR Approach

The main focus of the present chapter is on nonlinear control of the underactuated tethered system. For comparison purposes, we introduce a gain-scheduling linear control technique in this section. Even though we embraced this linear control technique in the actual implementation in Chapter 7, for simplicity, this section argues that the linearization-based control would only provide a local stability result, as opposed to global convergence of the nonlinear control strategies in the subsequent sections.

Again, the controllability analysis in Chapter 3 states that the spinning underactuated tethered system is fully controllable around the relative equilibrium manifold ($\dot{\theta} = \omega$, $\phi = 0$, and $\dot{\phi} = 0$). This indicates that the configuration variable ϕ is not subject to a large angle rotation as seen in a swing-up maneuver of the acrbot [187], but rather has to be stabilized at the equilibrium $\phi = 0, \dot{\phi} = 0$

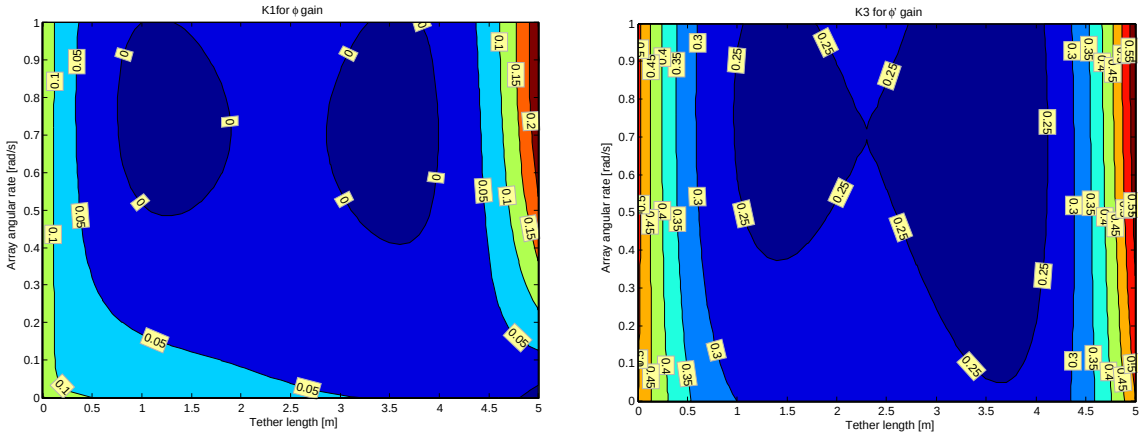

(a) K1 for ϕ (b) K3 for $\dot{\phi}$

Figure 6-2: LQR gains scheduled for a range of $\dot{\theta}$ and ℓ

at all times. Thanks to this requirement, we can expect that the linear LQR control can perform reasonably well around the equilibrium point.

Recalling that the linearized equations in (3.26) are fully controllable using only the torque input u, we can construct a linear feedback control law $u = K(\phi, \dot{\theta}, \dot{\phi})$, based upon the following linearized equations of motion:

$$\frac{d}{dt}\begin{pmatrix}\phi\\ \dot{\theta}\\ \dot{\phi}\end{pmatrix} = \begin{bmatrix} 0 & 0 & 1 \\ \frac{r\omega^2\left(I_r+mr\ell\right)}{\ell I_G} & 0 & 0 \\ -\frac{r\omega^2\left(I_r+m\ell(2r+\ell)\right)}{\ell I_G} & 0 & 0 \end{bmatrix}\begin{pmatrix}\phi\\ \dot{\theta}\\ \dot{\phi}\end{pmatrix} + \begin{pmatrix} 0 \\ -\frac{r}{I_G\ell} \\ \frac{r+\ell}{I_G\ell}\end{pmatrix} u \tag{6.10}$$

where we intentionally left out the state θ since it is merely a rigid body rotation mode.
We assume that all the states $(\phi, \dot{\theta}, \dot{\phi})$ are available by the Kalman filter, which is presented in Chapter 7.
Then, we can design a Linear Quadratic Regulator (LQR) controller, which minimizes the following cost function,

$$J = \int_0^\infty \left[x^T Q x + u^T R u\right] dt. \tag{6.11}$$

The LQR controller specifically addresses the issue of achieving a balance between good system response and minimizing the control effort required. The LQR control possesses very good stability margins (Phase Margin of $\pm$ 60 degrees and Gain Margin of infinity).

Since the A matrix in (6.10) is a function of $\dot{\theta}$ and the tether length ℓ, the optimal LQR gains are computed for a range of angular rates and tether lengths. A continuous function is then fit to these discrete gains. As a result, the gain-scheduled LQR gain is a continuous function of $\dot{\theta}$ and tether length ℓ, as depicted in Figure 6-2:

$$u = -K_1(\dot{\theta}, \ell)\phi - K_2(\dot{\theta} - \dot{\theta}_d) - K_3(\dot{\theta}, \ell)\dot{\phi} \tag{6.12}$$

where K_2 turns out to be independent of $\dot{\theta}$ and ℓ.

Such a gain-scheduled LQR controller has been successfully implemented in the SPHERES testbed (see Chapter 7). This gain-scheduling approach has been a popular subject of research as alternative form of nonlinear control, as indicated in a recent survey paper [165]. One merit of the linearization is that it permits the use of mature and well-established linear control techniques to address nonlinear problems. However, stability can be assured only locally and in a "slow-variation" setting [165]. In [124], an alternative method to gain-scheduling is presented for control of nonlinear

systems. In the subsequent sections, we present several nonlinear control techniques, yielding global stability results.

6.4 Partial Feedback Linearization

The present section describes a nonlinear control law obtained by applying partial feedback linearization. The stability of the zero dynamics is also treated using contraction analysis introduced in Section 2.5.

6.4.1 Collocated Linearization

The partial feedback linearization technique [187, 145] is applied to (3.11), which is obtained by canceling the input-coupling of (6.1):

$$\begin{bmatrix} m_{11}(\phi) & m_{12}(\phi) \\ m_{21}(\phi) & m_{22}(\phi) \end{bmatrix} \begin{pmatrix} \ddot{\theta} \\ \ddot{\phi} \end{pmatrix} + \begin{pmatrix} h_1(\phi, \dot{\theta}, \dot{\phi}) \\ h_2(\phi, \dot{\theta}) \end{pmatrix} = \begin{pmatrix} 0 \\ u \end{pmatrix} \tag{6.13}$$

where m_{ij} and h_i are defined in (3.11), and different from those defined in (3.14).

Even though the inertial matrix is no longer symmetric ($m_{12} \neq m_{21}$), Equation (6.13) has eliminated the input coupling, thereby facilitating collocated or noncollocated partial feedback linearization. Equation (6.13) is physically meaningful, since it can be directly derived by the Newton-Euler formulation, as seen in Section 3.3. Note that the first equation (unactuated part) of (6.13) corresponds to the second-order nonholonomic constraint. This system can be partially feedback linearized for ϕ.

Multiplying the first equation by $m_{11}^{-1}(\phi)$, and then inserting the resulting equation for $\ddot{\theta}$ into the second equation yield

$$\begin{aligned} \ddot{\theta} &= -m_{11}^{-1}(\phi) m_{12}(\phi) \ddot{\phi} - m_{11}^{-1}(\phi) h_1 \\ \ddot{\phi} &= v \\ u &= \alpha(\phi) v + \beta(\phi, \dot{\theta}, \dot{\phi}) \\ \alpha(\phi) &= m_{22} - m_{21}(\phi) m_{11}^{-1}(\phi) m_{12}(\phi) \\ \beta(\phi, \dot{\theta}, \dot{\phi}) &= h_2 - m_{21}(\phi) m_{11}^{-1}(\phi) h_1 \end{aligned} \tag{6.14}$$

where v is now a new control input to the linearized ϕ dynamics. In addition, $\alpha(\phi)$ and $\beta(\phi, \dot{\theta}, \dot{\phi})$ define an invertible change of control between u and v.

Since ϕ is the actuated variable, it is called collocated partial feedback linearization [187]. Then, we can design the following controller v to asymptotically stabilize ϕ dynamics:

$$\begin{aligned} v &= -D\dot{\phi} - K(\phi - e) \\ e &= \tan^{-1}(A(\dot{\theta}_d - \dot{\theta})) \end{aligned} \tag{6.15}$$

where D, K, and A are all positive constants and $\dot{\theta}_d$ denotes the desired angular rate of the tethered array. Also note that we chose such a definition of e, instead of $e = A(\dot{\theta}_d - \dot{\theta})$, to avoid saturation by accommodating a large value of $(\dot{\theta}_d - \dot{\theta})$.

Assuming $\dot{e}$ and $\ddot{e}$ are sufficiently close to zero, (6.15) makes ϕ tend to e asymptotically ($\phi \to e$):

$$\ddot{\phi} + D\dot{\phi} + K(\phi - e) = 0 \tag{6.16}$$

The rationale behind this choice of v is to balance between the tracking error $\dot{\theta}_d - \dot{\theta}$ and the compound pendulum mode ϕ by transferring energy between them, similar to [187].

6.4.2 Analysis of Zero-Dynamics

The zero dynamics are defined to be the internal dynamics of the system when the system output is kept at zero by the input [178]. By analogy with linear systems, a nonlinear system with stable zero dynamics corresponds to a minimum phase system. To investigate the zero dynamics of θ under this control input v in (6.15), the θ dynamics in (6.14) are expanded as:

$$\begin{aligned}\ddot{\theta} &= -m_{11}^{-1}(\phi)m_{12}(\phi)\ddot{\phi} - m_{11}^{-1}(\phi)h_1 \\ &= -m_{11}^{-1}(\phi)(m_{12}(\phi)v + h_1) \\ &= \frac{mr\sin\phi(\dot{\theta}+\dot{\phi})^2 + mr\cos\phi(D\dot{\phi} + K(\phi - e))}{m(\ell + r\cos\phi)}\end{aligned} \tag{6.17}$$

If $\phi \to e$ and $\dot{\phi} \to 0$, the zero dynamics of θ become

$$\ddot{\theta} = -\frac{r\dot{\theta}^2}{\ell + r\cos\left[\tan^{-1}(A(\dot{\theta} - \dot{\theta}_d))\right]}\sin[\tan^{-1}(A(\dot{\theta} - \dot{\theta}_d))] \tag{6.18}$$

If $\ell > r$, which is a reasonable assumption, then $m_{11} = m(\ell + r\cos e) > 0$. In addition, if a reference array angular rate is a constant step input ($\ddot{\theta}_d = 0, \dot{\theta}_d \neq 0$), (6.18) reduces to

$$\frac{d}{dt}(\dot{\theta} - \dot{\theta}_d) + L(t)\sin[\tan^{-1}(A(\dot{\theta} - \dot{\theta}_d))] = 0 \tag{6.19}$$

where

$$L(t) = \frac{r\dot{\theta}^2}{\ell + r\cos\left[\tan^{-1}(A(\dot{\theta} - \dot{\theta}_d))\right]} > 0 \tag{6.20}$$

for nonzero $\dot{\theta}$.

Let us prove exponential stability of (6.19) by applying the partial contraction theory (see Section 2.5). The virtual y-system

$$\dot{y} + L(t)\sin[\tan^{-1}(Ay)] = 0 \tag{6.21}$$

has two particular solutions, namely, $(\dot{\theta} - \dot{\theta}_d)$ and 0. This y-system is contracting (see Chapter 2) since its associated Jacobian

$$-L(t)\cos\left[\tan^{-1}(Ay)\right]\frac{1}{(Ay)^2 + 1}A \tag{6.22}$$

is negative definite since $L(t) > 0, A > 0$, and $-\frac{\pi}{2} < \tan^{-1}(\cdot) < \frac{\pi}{2}$. Hence, all solutions of y tend to each other, which implies $\dot{\theta}$ tends to $\dot{\theta}_d$ exponentially.

From (6.15) and (6.16), the convergence of $e \to 0$ also implies $\phi \to 0$, which concludes the stability analysis of the proposed underactuated control law in (6.15). Its corresponding u is then defined by the relation between u and v shown in (6.14).

6.5 Momentum Decoupling and Feedback Linearization of Reduced Models

Even though exact feedback linearization is not possible for the underactuated tethered system, as discussed in Section 6.2.1, we show herein that there exists a diffeomorphism such that feedback linearization is made possible with respect to the relative equilibria of a spinning tethered system.

We recall the dynamics of the underactuated single-tethered system with the fixed tether length

from (6.1):

$$\begin{aligned}\frac{d}{dt}\frac{\partial L}{\partial \dot{\theta}} - \frac{\partial L}{\partial \theta} &= m_{11}\ddot{\theta} + m_{12}\ddot{\phi} + c_{11}\dot{\theta} + c_{12}\dot{\phi} = u \\ \frac{d}{dt}\frac{\partial L}{\partial \dot{\phi}} - \frac{\partial L}{\partial \phi} &= m_{21}\ddot{\theta} + m_{22}\ddot{\phi} + c_{21}\dot{\theta} + c_{22}\dot{\phi} = u\end{aligned} \tag{6.23}$$

Following [145], consider the nonlinear diffeomorphism applying the change of coordinates such that

$$\begin{aligned}z_1 &= \theta + \gamma(\phi) \\ z_2 &= m_{11}(\phi)\dot{\theta} + m_{12}(\phi)\dot{\phi}\end{aligned} \tag{6.24}$$

where

$$\gamma = \int_0^{\phi} \frac{m_{12}(s)}{m_{11}(s)} ds = \int_0^{\phi} \frac{I_r + mr\ell\cos(s)}{I_r + m\ell^2 + 2mr\ell\cos(s)} ds. \tag{6.25}$$

As discussed in Section 2.2.3, the kinetic symmetry with respect to θ in the absence of a gravitational effect leads to symmetry in mechanics such that

$$\frac{\partial K}{\partial \theta} = \frac{\partial L}{\partial \theta} = 0 \tag{6.26}$$

since the corresponding Lagrangian L is independent of θ.

Note that z_2 is essentially the first generalized angular momentum (see Section 2.2.3) such that

$$z_2 = \frac{\partial L}{\partial \dot{\theta}}, \qquad \dot{z}_2 = \frac{d}{dt}\frac{\partial L}{\partial \dot{\theta}} = \frac{\partial L}{\partial \theta} + u = u \tag{6.27}$$

In addition,

$$\dot{z}_1 = \dot{\theta} + \frac{m_{12}(\phi)}{m_{11}(\phi)}\dot{\phi} = \frac{m_{11}(\phi)\dot{\theta} + m_{12}(\phi)\dot{\phi}}{m_{11}(\phi)} = \frac{z_2}{m_{11}(\phi)} \tag{6.28}$$

Incorporating Equations (6.28) and (6.27), we obtain the following equations of z_1 and z_2:

$$\begin{aligned}\dot{z}_1 &= m_{11}^{-1}(\phi) z_2 \\ \dot{z}_2 &= u\end{aligned} \tag{6.29}$$

where $m_{11}(\phi) = I_r + m\ell^2 + 2mr\ell\cos\phi$. Note that $m_{11}(\phi) > 0,\ \forall\phi$ since $I_r = I_G + mr^2$.

A closer examination of the definition of z_1 and z_2 given in (6.24) reveals that z_1 corresponds to the superposition of two angular variables, θ and ϕ, whereas z_2 is the generalized momentum conjugate to θ.

By differentiating $\dot{z}_1$,

$$\begin{aligned}\ddot{z}_1 &= \left[\frac{\partial m_{11}^{-1}(\phi)}{\partial \phi}\dot{\phi} z_2\right] + m_{11}^{-1}(\phi)\dot{z}_2 \\ &= \frac{2mr\ell\sin\phi}{(I_r + m\ell^2 + 2mr\ell\cos\phi)^2}\dot{\phi} z_2 + m_{11}^{-1}(\phi) u \\ &= v\end{aligned} \tag{6.30}$$

The following definition of the new control input v guarantees exponential convergence of z_1 to z_{1d}:

$$v = \ddot{z}_{1d} - D(\dot{z}_1 - \dot{z}_{1d}) - K(z_1 - z_{1d}) \tag{6.31}$$

where the control gains K and D are positive constants.

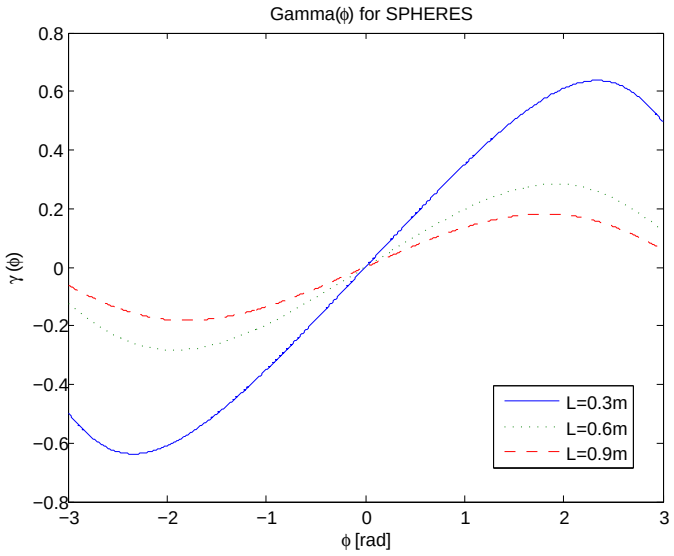

Figure 6-3: Plot of $\gamma(\phi)$ using ℓ=(0.3m, 0.6m, 0.9m) and the physical parameters Section 7.5.2

For $\phi_d = 0$ and $\dot{\phi}_d = 0$, the reference $\dot{z}_{1d}$ and $\ddot{z}_{1d}$ can be defined as

$$\dot{z}_{1d} = m_{11}^{-1}(\phi) z_{2d} = m_{11}^{-1}(\phi) \left(m_{11}(\phi)\dot{\theta}_d + m_{12}(\phi)\dot{\phi}_d \right) = \dot{\theta}_d, \quad \ddot{z}_{1d} = \ddot{\theta}_d \tag{6.32}$$

For the error $(z_1 - z_{1d})$, we are mainly concerned with the array angular rate $\dot{\theta}$ of the spinning tethered array rather than the angle θ. So we consider only the $\gamma(\phi)$ term from the definition of z_1 such that

$$z_1 - z_{1d} \approx \gamma(\phi) - \gamma(\phi_d) = \gamma(\phi) \tag{6.33}$$

where $\gamma(\phi)$ is analytically obtained from the integral in (6.24) using Mathematica:

$$\begin{aligned} \gamma(\phi) &= \int_0^{\phi} \frac{m_{12}(s)}{m_{11}(s)} ds = \int_0^{\phi} \frac{I_r + mr\ell\cos(s)}{I_r + m\ell^2 + 2mr\ell\cos(s)} ds \\ &= \frac{\phi}{2} + \frac{m\ell^2 - I_r}{\sqrt{-(m\ell^2 + I_r)^2 + 4m^2r^2\ell^2}} \tanh^{-1}\left(\frac{I_r + m\ell(\ell - 2r)}{\sqrt{-(m\ell^2 + I_r)^2 + 4m^2r^2\ell^2}} \tan\frac{\phi}{2} \right) \end{aligned} \tag{6.34}$$

Figure 6-3 plots the function $\gamma(\phi)$ in (6.34), which is a monotonic function of ϕ within a small range of the compound pendulum mode angle ϕ. From (6.30), the original torque input u can be computed:

$$u = m_{11}(\phi)v - \frac{2mr\ell\sin\phi}{m_{11}(\phi)}\dot{\phi}z_2 \tag{6.35}$$

where the new control input v is defined in (6.31).

As discussed in Section 6.2.1, the original nonlinear system in (6.1) is not fully feedback linearizable with respect to its states, $\theta, \dot{\theta}, \phi, \dot{\phi}$. Nonetheless, the nonlinear control law in (6.35) using feedback linearization is made possible with respect to the reduced variables, z_1 and z_2. The simulation results in Section 6.8 show that the control law in (6.35) is particularly efficient for tracking the desired trajectory of $\dot{\theta}_d$ while the desired ϕ_d and $\dot{\phi}_d$ are set to zero.

6.6 Tracking Control by Backstepping and Contraction Analysis

Feedback linearization often results in cancellations of useful nonlinearities. To the contrary, backstepping design is more flexible and does not force the designed system to appear linear. This implies that backstepping can avoid cancellations of useful nonlinearities and often allow for additional nonlinear terms in order to improve transient performance [100]. We present a backstepping nonlinear control design of the single tethered system, based upon the strict-feedback cascade normal form introduced in the previous section.

6.6.1 Review of Integrator Backstepping [100]

We augment a nonlinear system in (6.2) with an integrator

$$\begin{aligned} \dot{\mathbf{x}} &= \mathbf{f}(\mathbf{x}) + \mathbf{g}(\mathbf{x})\xi \\ \dot{\xi} &= u \end{aligned} \tag{6.36}$$

and suppose that the original dynamics in (6.2) has a stabilizing control function $u = \alpha(\mathbf{x})$ such that

$$\frac{\partial V(\mathbf{x})}{\partial \mathbf{x}}[\mathbf{f}(\mathbf{x}) + \mathbf{g}(\mathbf{x})\alpha(\mathbf{x})] \leq -W(\mathbf{x}) \leq 0 \tag{6.37}$$

where $W(\mathbf{x}) : \mathbb{R}^n \to \mathbb{R}$ is positive semidefinite. Then, via LaSalle-Yoshizawa theorem, $\lim_{t\to\infty} W(\mathbf{x}(t)) = 0$ is guaranteed. Furthermore, if $W(\mathbf{x})$ is negative definite, $\mathbf{x} = \mathbf{0}$ is the global asymptotic equilibrium of the original dynamics in (6.2).

Now we can design a stabilizing control $\dot{\xi} = u$ for the full system in (6.36) via backstepping. Based on [100], either of the following is true:

(1) if $W(\mathbf{x})$ is positive definite, then

$$V_a(\mathbf{x}, \xi) = V(\mathbf{x}) + \frac{1}{2}[\xi - \alpha(\mathbf{x})]^2 \tag{6.38}$$

is a Control Lyapunov Function (CLF) for the full system (6.36). In other words, there exists a feedback control $u = \alpha_a(\mathbf{x}, \xi)$ that renders $\mathbf{x} = \mathbf{0}, \xi = 0$ the globally asymptotically stable (GAS) equilibrium of (6.36).
One such control is

$$u = -c(\xi - \alpha(\mathbf{x})) + \frac{\partial \alpha(\mathbf{x})}{\partial \mathbf{x}}[\mathbf{f}(\mathbf{x}) + \mathbf{g}(\mathbf{x})\xi] - \frac{\partial V(\mathbf{x})}{\partial \mathbf{x}}\mathbf{g}(\mathbf{x}), \quad c > 0. \tag{6.39}$$

(2) If $W(\mathbf{x})$ is only positive semidefinite, then there exists a feedback control that renders $V_a \leq -W_a(\mathbf{x}, \xi) \leq 0$, such that $W_a(\mathbf{x}, \xi) > 0$ whenever $W(\mathbf{x}) > 0$ or $\xi \neq \alpha(\mathbf{x})$. This ensures global boundedness and convergence of $\begin{pmatrix} \mathbf{x}(t) & \xi(t) \end{pmatrix}^T$ to the largest invariant set M_a contained in the set, $W(\mathbf{x}) = 0, \xi = \alpha(\mathbf{x})$.

Significant design flexibility is allowed in the backstepping procedure by the choice of the stabilizing function $\alpha(\mathbf{x})$. In other words, a careful choice of $\alpha(\mathbf{x})$ avoids cancellations of useful nonlinearities, and allows for additional nonlinear terms to improve transient performance.

6.6.2 Nonlinear Control by Backstepping

Recalling the reduced dynamics of z_1 and z_2 from (6.29),

$$\begin{aligned} \dot{z}_1 &= m_{11}^{-1}(\phi) z_2 \\ \dot{z}_2 &= u \end{aligned} \tag{6.40}$$

where

$$z_1 = \theta + \int_0^{\phi} \frac{m_{12}(s)}{m_{11}(s)} ds$$
$$z_2 = m_{11}(\phi)\dot{\theta} + m_{12}(\phi)\dot{\phi} \tag{6.41}$$

The above strict-feedback system regards the variable ϕ as an exogenous variable, thereby allowing for backstepping. Let us define the stabilizing function $\alpha(z_1) = -c_1 z_1$, $c_1 > 0$ such that the dynamics

$$\dot{z}_1 = m_{11}^{-1}(\phi)\alpha \tag{6.42}$$

is asymptotically stable with $V = \frac{1}{2}{z_1}^2$. We define the error function e such that

$$e = z_2 - \alpha(z_1) = z_2 + c_1 z_1 \tag{6.43}$$

and its time derivative is

$$\dot{e} = \dot{z}_2 + c_1 \dot{z}_1 = u + c_1 m_{11}^{-1}(\phi)(e - c_1 z_1). \tag{6.44}$$

Suppose that a CLF for z_1 and z_2 is $V_a = \frac{1}{2}{z_1}^2 + \frac{1}{2}e^2$. Its time derivative should be bounded by the positive definite function $W(\mathbf{x})$ for asymptotic stability.

$$\begin{aligned}\dot{V}_a &= z_1\dot{z}_1 + e\dot{e} = z_1 m_{11}^{-1}(\phi)(e - c_1 z_1) + e[u + c_1 m_{11}^{-1}(\phi)(e - c_1 z_1)] \\ &= -c_1 m_{11}^{-1}(\phi){z_1}^2 + e[u + c_1 m_{11}^{-1}(\phi)e + (1 - {c_1}^2)m_{11}^{-1}(\phi)z_1]\end{aligned} \tag{6.45}$$

The following u renders $\dot{V}_a = -c_1 m_{11}^{-1}(\phi){z_1}^2 - c_2 e^2 < 0$ with $c_2 > 0$:

$$\begin{aligned}u &= -c_2 e - c_1 m_{11}^{-1}(\phi)e + ({c_1}^2 - 1)m_{11}^{-1}(\phi)z_1 \\ &= -[c_2 c_1 + m_{11}^{-1}(\phi)]z_1 - [c_2 + m_{11}^{-1}(\phi)c_1]z_2\end{aligned} \tag{6.46}$$

The closed-loop system in the (z_1, e) coordinates results in

$$\begin{pmatrix}\dot{z}_1 \\ \dot{e}\end{pmatrix} = \begin{bmatrix}-c_1 m_{11}^{-1}(\phi) & m_{11}^{-1}(\phi) \\ -m_{11}^{-1}(\phi) & -c_2\end{bmatrix}\begin{pmatrix}z_1 \\ e\end{pmatrix} \tag{6.47}$$

where c_1 and c_2 are positive constants.

The above equation shows an interesting property. The system matrix is uniformly (independent of time) negative definite due to the skew-symmetric off-diagonal terms and the positive $m_{11}(\phi)$ term. Possessing such a negative-definite system matrix is an important characteristic of backstepping design (see [100]). It is emphasized that a similar discussion automatically leads to contraction analysis introduced in Section 2.5. The resulting equation for (z_1, e) in (6.47) is contracting due to its uniformly negative definite Jacobian, hence $(0, 0)$ is an exponentially stable equilibrium of (z_1, e).

Since we are more interested in tracking control of the underactuated system, the following tracking control law is suggested based upon (6.46) and (6.47):

$$u = -[c_2 c_1 + m_{11}^{-1}(\phi)]z_1 - [c_2 + m_{11}^{-1}(\phi)c_1](z_2 - z_{2d}) + \dot{z}_{2d} \tag{6.48}$$

where $z_{2d} = m_{11}(\phi)\dot{\theta}_d$ and $\dot{z}_{2d} = m_{11}(\phi)\ddot{\theta}_d$ due to $\phi_d = 0, \dot{\phi}_d = 0$. Since we focus on the angular rate $\dot{\theta}$, z_{1d} is defined such that $z_1 - z_{1d} = z_1$ and $\dot{z}_{1d} = m_{11}^{-1}(\phi)z_{2d}$. Additionally, we set $e_d = z_{2d} + c_1 z_{1d}$ and $\dot{e}_d = \dot{z}_{2d} + c_1 \dot{z}_{1d}$. Then, the control law in (6.48) leads to the closed-loop system of the virtual variables y_1 and y_2, which has

$$\begin{pmatrix}y_1 \\ y_2\end{pmatrix} = \begin{pmatrix}z_1 - z_{1d} \\ e - e_d\end{pmatrix}, \quad \text{and} \quad \begin{pmatrix}y_1 \\ y_2\end{pmatrix} = \begin{pmatrix}0 \\ 0\end{pmatrix} \tag{6.49}$$

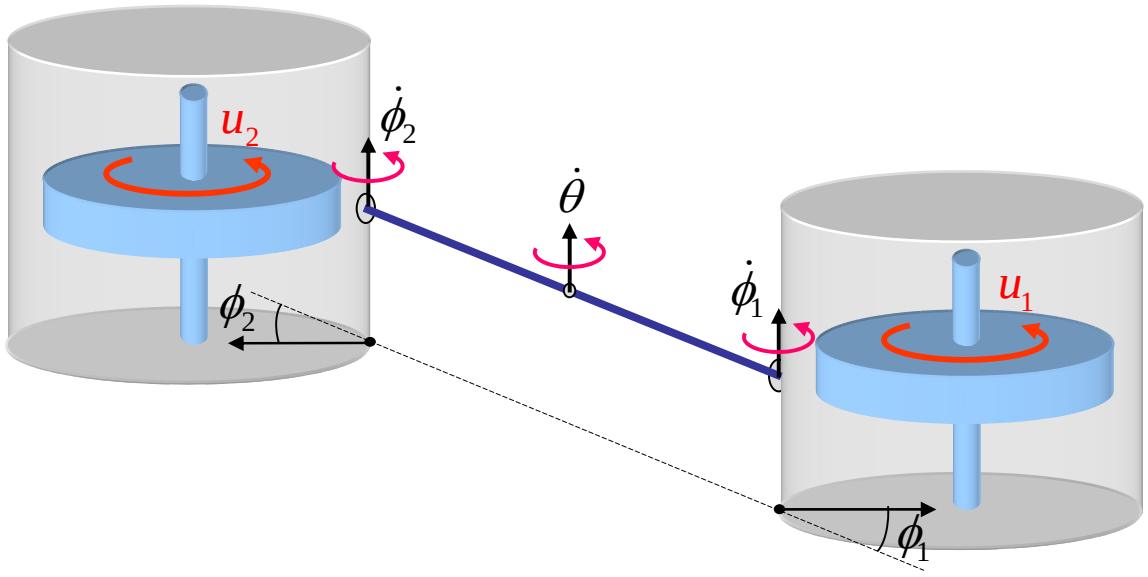

Figure 6-4: Two-spacecraft tethered system with a reaction wheel, depicted on the rotation plane. The ϕ_1 and ϕ_2 angles indicate the compound pendulum modes.

as particular solutions. Its virtual displacement equation results in

$$\begin{pmatrix} \delta\dot{y}_1 \\ \delta\dot{y}_2 \end{pmatrix} = \begin{bmatrix} -c_1 m_{11}^{-1}(\phi) & m_{11}^{-1}(\phi) \\ -m_{11}^{-1}(\phi) & -c_2 \end{bmatrix} \begin{pmatrix} \delta y_1 \\ \delta y_2 \end{pmatrix}. \tag{6.50}$$

This is contracting since the symmetric part of its Jacobian matrix

$$\begin{bmatrix} -c_1 m_{11}^{-1}(\phi) & 0 \\ 0 & -c_2 \end{bmatrix} \tag{6.51}$$

is uniformly negative definite (Theorem 2.5.1, Chapter 2). Hence all solutions of y_1 and y_2 tend to each other, resulting in $\dot{\theta} \to \dot{\theta}_d$ and $\phi, \dot{\phi} \to 0$ from the definition of z_1, z_2 and e. Furthermore, the contraction rate of z_1 is proportional to c_1 whereas c_2 independently determines the contraction rate of e. This indicates that we can properly tune the gains c_1 and c_2 for desired tracking performance of z_1 and z_2, respectively. In order to maintain the same convergence rate for z_2 over various tether lengths, we can set $c_2 \to c_2 m_{11}^{-1}(\phi)$.

6.7 Decentralized Control For Multi-Vehicle Systems

Following the model reduction technique introduced in Chapter 4, we show herein that a fully decentralized control law designed from the underactuated single-tethered system can stabilize a multi-vehicle tethered array. The decentralized controller will enable simple independent control of each satellite by eliminating the need for exchanging individual state information. This will significantly simplify both the control algorithm and hardware implementation, as well as eliminate any possibility of performance degradation due to noisy and delayed communications.

Consider a two-spacecraft array with only torque input (u_1, u_2), as illustrated in Figure 6-4:

$$\mathbf{M_2}(\phi_1, \phi_2) \begin{pmatrix} \ddot{\theta} \\ \ddot{\phi}_1 \\ \ddot{\phi}_2 \end{pmatrix} + \mathbf{C_2}(\phi_1, \phi_2, \dot{\theta}, \dot{\phi}_1, \dot{\phi}_2) \begin{pmatrix} \dot{\theta} \\ \dot{\phi}_1 \\ \dot{\phi}_2 \end{pmatrix} = \begin{pmatrix} u_1 + u_2 \\ u_1 \\ u_2 \end{pmatrix} \tag{6.52}$$

where $\mathbf{M_2}(\phi_1, \phi_2)$ and $\mathbf{C_2}(\phi_1, \phi_2, \dot{\theta}, \dot{\phi_1}, \dot{\phi_2})$ can also be derived by the parallel combination of the two independent single tethered dynamics (see Chapter 4).

In Chapter 4, it is shown that a linear decentralized control in (6.12)

$$\begin{aligned} u_1 &= -K_1\phi_1 - K_2(\dot{\theta} - \dot{\theta}_d) - K_3\dot{\phi}_1 \\ u_2 &= -K_1\phi_2 - K_2(\dot{\theta} - \dot{\theta}_d) - K_3\dot{\phi}_2 \end{aligned} \tag{6.53}$$

stabilizes the linearized tethered two-spacecraft dynamics of (6.52) if $rK_2 < (r+\ell)K_3,\ K_1 > 0,\ K_2 > 0$. Furthermore, it is proven that such a decentralized control synchronizes the compound pendulum oscillation, ϕ_1 and ϕ_2. Hence, we can expect that the decentralized nonlinear control techniques introduced in this section possess the same stability property for a multi-vehicle underactuated system if the behavior of the closed-loop systems is sufficiently close to the linearized dynamics. In the case of spinning tethered arrays, this is particularly true for a regulatory control in which a desired trajectory is time-invariant.

We can proceed to prove the stability of the nonlinear decentralized control law introduced in Section 6.5. The proof entails showing that such a decentralized control law can de facto synchronize the two compound pendulum mode angles– ϕ_1 and ϕ_2 for the two-spacecraft system. Recall that the second and third rows of (6.52) are the independent dynamics for ϕ_1 and ϕ_2, respectively:

$$\begin{aligned} (I_r + mr\ell\cos\phi_1)\ddot{\theta} + I_r\ddot{\phi_1} + mr\ell\dot{\theta}^2\sin\phi_1 = u_1 \\ (I_r + mr\ell\cos\phi_2)\ddot{\theta} + I_r\ddot{\phi_2} + mr\ell\dot{\theta}^2\sin\phi_2 = u_2 \end{aligned} \tag{6.54}$$

where the decentralized control law u_i, $i = 1, 2$ from (6.35) can be written as

$$u_i = m_{11}(\phi_i)[\ddot{\theta}_d - D(\dot{\theta} - \dot{\theta}_d)] - Dm_{12}(\phi_i)\dot{\phi}_i - Km_{11}(\phi_i)\gamma(\phi_i) - \frac{2mr\ell\sin\phi_i}{m_{11}(\phi_i)}\dot{\phi}_i z_2(\phi_i) \tag{6.55}$$

Since the ϕ angle is stabilized ($\phi \to 0$), assume that ϕ and $\dot{\phi}$ are sufficiently small such that $m_{11}(\phi) \approx m_{11}(0)$, $\cos\phi \approx 1$, and $\sin\phi\dot{\phi} \approx 0$. Then, the closed-loop dynamics in (6.54) can be simplified as

$$\begin{aligned} I_r\ddot{\phi_1} + Dm_{12}(\phi_1)\dot{\phi}_1 + Km_{11}(\phi_1)\gamma(\phi_1) + mr\ell\dot{\theta}^2\sin\phi_1 = g(t) \\ I_r\ddot{\phi_2} + Dm_{12}(\phi_2)\dot{\phi}_2 + Km_{11}(\phi_2)\gamma(\phi_2) + mr\ell\dot{\theta}^2\sin\phi_2 = g(t) \end{aligned} \tag{6.56}$$

where the common excitation input is defined as

$$g(t) = -(I_r + mr\ell)\ddot{\theta} + m_{11}(0)[\ddot{\theta}_d - D(\dot{\theta} - \dot{\theta}_d)] \tag{6.57}$$

Also, note that $m_{11}(\phi) > 0\ \forall\phi$ and $m_{12}(\phi) > 0$ for $|\phi| < \frac{\pi}{2}$.

Consider the virtual dynamics of y that has ϕ_1 and ϕ_2 as its particular solutions:

$$I_r\ddot{y} + Dm_{12}(y)\dot{y} + Km_{11}(y)\gamma(y) + mr\ell\dot{\theta}^2\sin y = g(t) \tag{6.58}$$

The above dynamics is contracting ($\delta y \to 0$) with $D > 0$ and $K > 0$ in the region $|\phi| < \frac{\pi}{2}$, indicating that any solutions of y converge to each other. This in turn implies that ϕ_1 tends to ϕ_2 exponentially fast. Once $\phi_1 \to \phi_2$, it is straightforward to show that the equation of motion for two-spacecraft in (6.52) reduces to the superposition of the reduced variables z_1 and z_2 for each spacecraft. As a result, a decentralized control law designed form the single-tethered dynamics not only stabilizes the coupled two-spacecraft dynamics, but also synchronizes the compound pendulum mode angles ϕ_1 and ϕ_2. Following the discussion in Chapter 4, the above result can be extended to a triangular configuration and a three-inline configuration. In particular, due to the hierarchical combination, the dynamics of a three-inline configuration reduce to those of the single-tethered system if the center spacecraft becomes exponentially stabilized. In other words, the above result shows that implementing an underactuated control law based on the single-tethered dynamics in Figure 6-1 ensures the stability of the rotation rate and the relative motions in an inline three-spacecraft array

(see the discussion in Chapter 4).

6.8 Simulation Results

In this section, we compare the tracking performance of the two nonlinear underactuated control laws, introduced in Sections 6.5 and 6.6, with that of the linear LQR control. In addition, we validate the effectiveness of a decentralized nonlinear underactuated control law for a two-spacecraft configuration as well as a three-spacecraft inline configuration, thereby further extending the theory in Chapter 4 to underactuated tethered systems.

6.8.1 Comparison with LQR Control

We illustrate that the nonlinear control approach is superior to the linear control in tracking a time-varying trajectory. For each simulation, the desired angular rate of the array $\dot{\theta}_d$ is given as

$$\begin{aligned} \dot{\theta}_d &= 0.25 + 0.02e^{-\tau t}(1 - \cos(2\pi f t)) \\ \ddot{\theta}_d &= 0.02e^{-\tau t}[2\pi f(\sin(2\pi f t)) - \tau(1 - \cos(2\pi f t))] \end{aligned} \tag{6.59}$$

where f=0.01, τ=0.02. The control law is also required to minimize the compound pendulum modes such that $\phi_d, \dot{\phi}_d = 0$ while trying to follow $\dot{\theta}_d$.

The initial conditions are defined as $\dot{\theta}_0$=0.25 rad/s, $\phi_0 = 0.1$ rad, and $\dot{\phi}_0 = -0.05$ rad/s. The physical parameters used in the simulations are selected from the actual values of the SPHERES testbed on the new air-bearing carriage described in Chapter 7. The radius of SPHERES, r is 0.15 m, the mass of SPHERES with the air-bearing carriage, m is 20.346 kg, and the moment of inertia I is 0.178 kgm^2. The tether length ℓ is either 0.5 m or 1 m.

Figure 6-5 shows the performance of the nonlinear tracking control using the feedback linearization of the reduced variables in (6.35). The gains are defined as $K = 1$ and $D = 2$. The nonlinear control is denoted by NLFL and compared with the LQR control. For the LQR control, the Q weighting matrix is diag($\begin{bmatrix}1 & 5 & 1\end{bmatrix}$) and the nominal angular rate of $\dot{\theta} = \omega$=0.25 rad/s are used. The simulation clearly indicates that the nonlinear control is superior to the LQR control in terms of tracking error. Both control approaches turn out to be equally efficient in minimizing the compound pendulum mode $(\phi, \dot{\phi})$. As the tether length ℓ increases from 0.5 m (Figure 6-5(a)) to 1.0 m (Figure 6-5(b)), the tracking performance for the LQR control degrades even though the change in the tether length was taken into account in computing the optimal LQR gains. This degradation in the performance of the LQR control has to do with the fact that the underactuated tethered system becomes less controllable as the tether length increases (see Chapter 3). In contrast, the nonlinear control achieves the same level of performance regardless of the tether length variation. In addition, cumbersome gain-scheduling is not required for the nonlinear control approach.

Likewise, Figure 6-6 represents the performance of the nonlinear tracking control law derived by the backstepping design approach in (6.48). The gains used for this simulation are $c_1 = 4$ and $c_2 = 2$. The figures clearly indicate that the nonlinear control approach using backstepping demonstrates more efficient tracking performance than the LQR control, whose performance deteriorates as the tether length increases.

6.8.2 Two-Spacecraft System

We simulate the proposed decentralized underactuated control law in (6.35) and (6.55) for the two-spacecraft tethered system shown in Figure 6-4. The desired trajectory $\dot{\theta}_d$ is defined as in the previous section. Since the total tether length in (6.52) is 2ℓ, ℓ=1 m is used. All other physical parameters of the SPHERES satellite remain the same as the previous section, including the control gains ($K = 1$ and $D = 2$). The initial conditions are defined as $\dot{\theta}(0)$=0.25 rad/s, $\dot{\psi}(0)$=0.25 rad/s, $\phi_1(0) = 0.1$ rad, $\dot{\phi}_1(0) = 0$ rad/s, $\phi_2(0) = -0.1$ rad, and $\dot{\phi}_2(0) = 0$ rad/s. As illustrated in Figure 6-7, the control law works efficiently to follow the trajectory $\dot{\theta}_d$ while minimizing the compound pendulum mode (ϕ_1 and ϕ_2). It should be stressed that the control law makes both the compound pendulum modes

angles synchronize exponentially (i.e., $\phi_1 \rightarrow \phi_2$) due to the discussion in Section 6.7. We can easily find why the state responses of the two-spacecraft system are similar to those of the single-tethered system in the previous section. Once the two individual spacecraft are synchronized, they behave as one unified closed-loop dynamics of the single-tethered system.

6.8.3 Three-Spacecraft Inline Configuration

Following the discussion in Section 6.7, we also investigate if the proposed method of designing a nonlinear underactuated control law from the decoupled single-tethered dynamics can be applied to the three inline configuration introduced in Chapters 3 and 4. Figure 6-8 shows a simulation result obtained by the same underactuated control law in (6.55) for the two outlying spacecraft in the linear three-spacecraft tethered array. For the center-spacecraft, a simple linear control law, $u_0 = -0.228(\dot{\psi} - \dot{\theta}_d)$, is used for a spin-up operation. The nonlinear control gains are $K = 0.5$ and $D = 2$ while the only nonzero initial conditions are given as $\dot{\psi} = 0$ and $\phi_1 = 0.05$ rad. During the spin-up maneuver of $\dot{\psi}$ from 0.25 to 0.27 rad/s, the compound pendulum modes ϕ_1 and ϕ_2 get excited due to the coupling motions of the underactuated dynamics. Eventually, the compound pendulum modes ϕ_1 and ϕ_2 oscillate *in sync* as they tend to zero (see the discussions in Chapter 4 and Section 6.7). In conclusion, the proposed underactuated control law, independently implemented in each spacecraft in a decentralized fashion, also ensures the stability of the closed loop system.

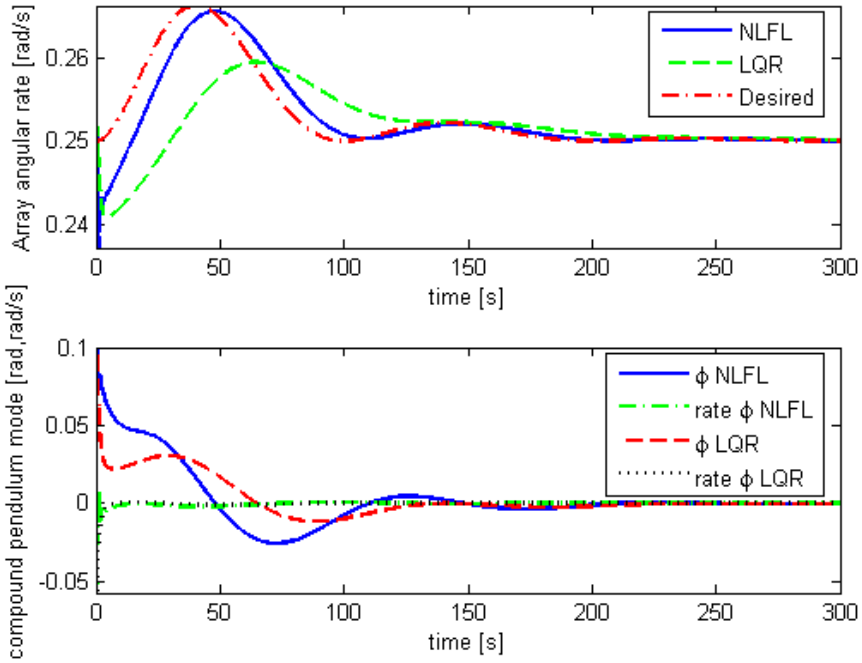

(a) tether length=0.5 m

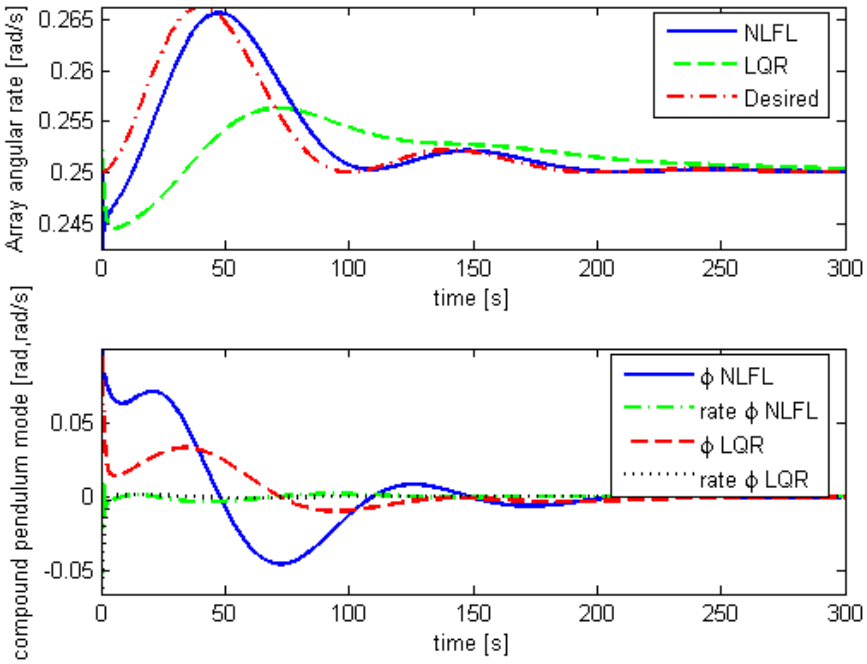

(b) tether length=1.0 m

Figure 6-5: Nonlinear tracking control using the feedback linearization of the reduced variable (NLFL) in Section 6.5 and the LQR control

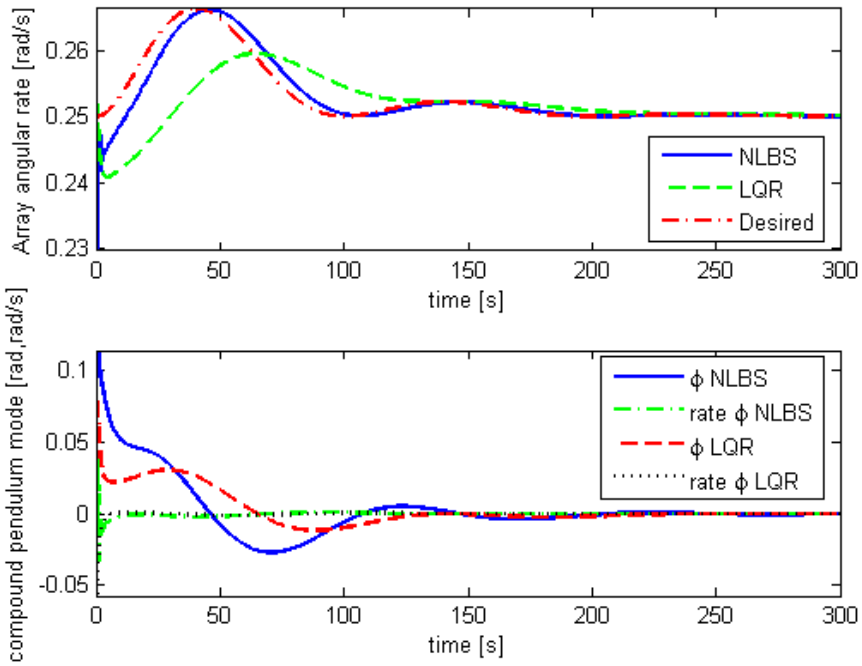

(a) tether length=0.5 m

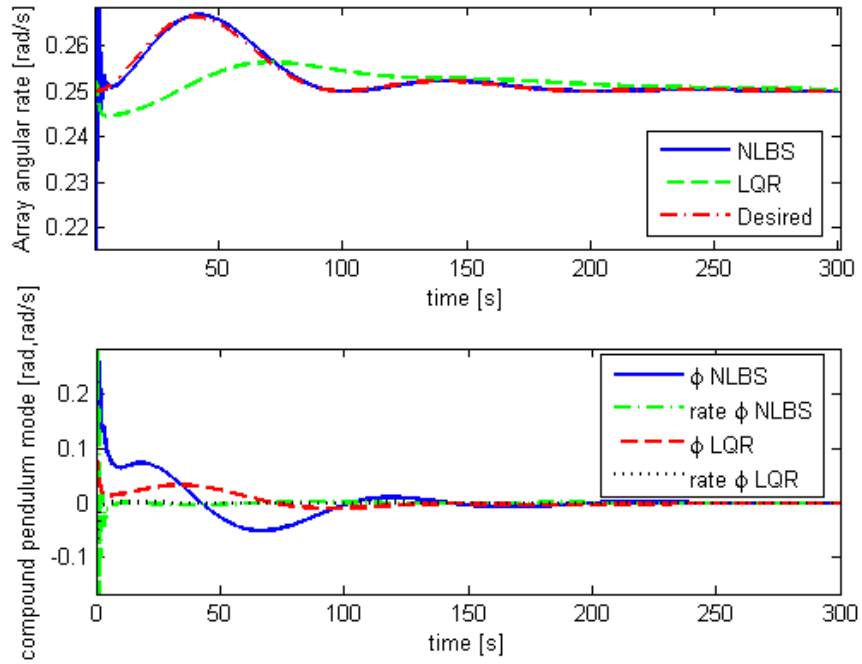

(b) tether length=1.0 m

Figure 6-6: Nonlinear tracking control using backstepping (NLBS) in Section 6.6 and the LQR control

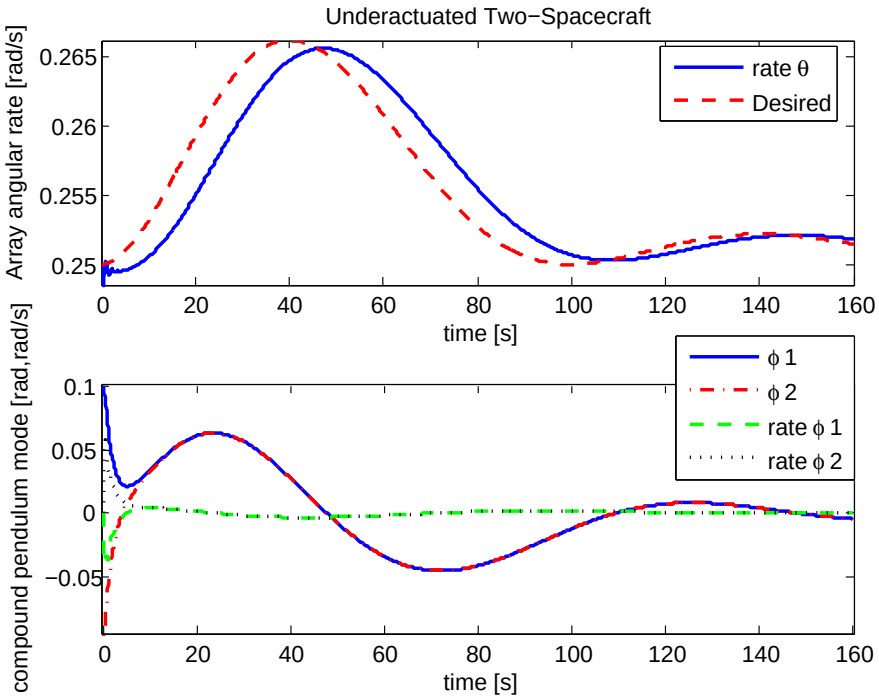

Figure 6-7: Simulation result of a decentralize control for Figure 6-4

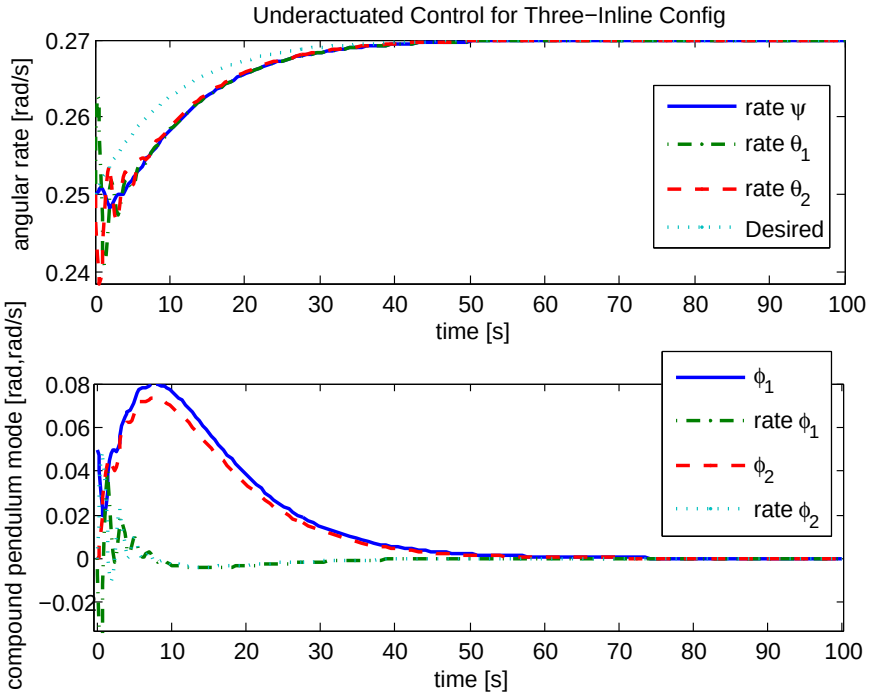

Figure 6-8: Simulation result of a decentralize control for a three-inline configuration

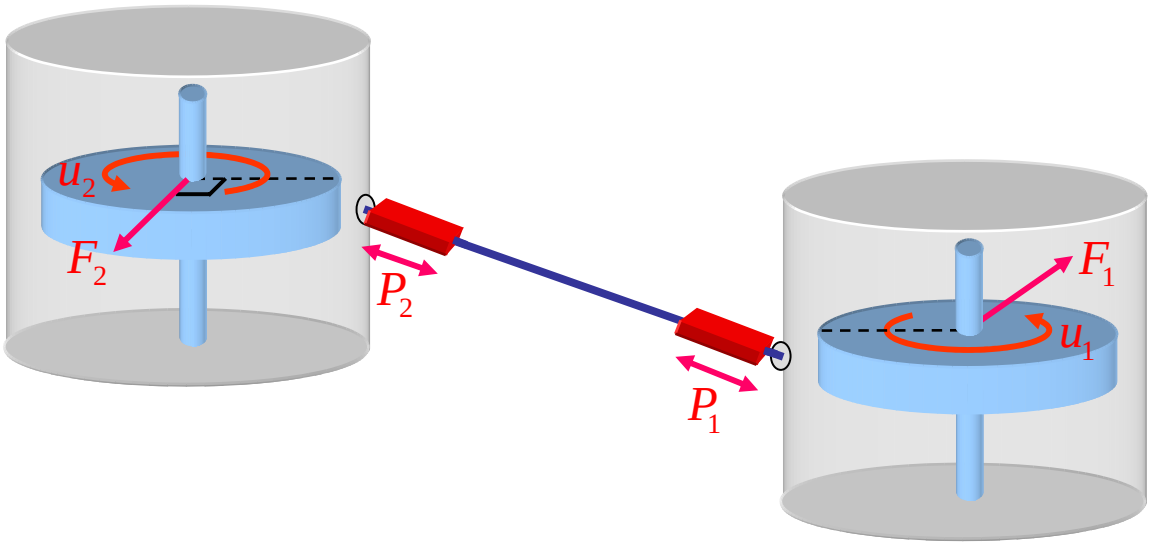

Figure 6-9: Two-spacecraft tethered system equipped with a high-bandwidth linear actuator on the tether (P), a reaction wheel (u), and a tangential thruster (F, not shown) in each spacecraft.

6.9 New Momentum Dumping Method for Saturated Wheels

If the linear velocity or angular velocity of each spacecraft is held constant, the increase of the tether length and external disturbance torque inevitably lead to the saturation of the wheel speed. For satellites in orbit, a pair of thrusters is conventionally used to dump the angular momentum of the saturated momentum wheel. This section focuses on the issue associated with managing the saturated angular momentum once a tethered array spun by reaction wheels reaches its maximum size. A new technique that can be used to extend the array beyond this size is proposed. The proposed method maintains the desired array spin-rate and zero compound pendulum mode during the momentum dumping operation. Maintaining the zero compound pendulum mode without diagonal thrusters poses a challenge since the reaction wheel, which directly controls the pendulum mode, is decelerated continuously in one direction.

Let us now assume that the tethered formation flight spacecraft shown in Figure 6-9 are equipped with only a reaction wheel (u), a tangential force thruster (F), and a high-bandwidth translational actuator on the tether (P) in each spacecraft. The direction of F is perpendicular to the line between the tether attachment point and the CM of the spacecraft. It is shown in Chapter 3 that a planar rotating array of tethered spacecraft can control all relevant degrees of freedom using only one reaction wheel (u) in each spacecraft. Due to the Coriolis force exerted on the spacecraft, a radial motion of the tether can exert torque with respect to the compound pendulum mode ϕ in Figure 6-9. Oscillatory motions of the tether from the force P can then be used as a means of controlling the pendulum mode. From (3.66), the dynamics of ϕ is coupled with $\dot{\ell}$ as

$$\ddot{\phi} + \frac{r\omega^2\big(I_r + m\ell(2r+\ell)\big)}{\ell I_G}\dot{\phi} = 2\frac{v}{\ell}\dot{\theta} + 2\frac{\omega}{\ell}\dot{\ell} - \frac{1}{m\ell}F + \frac{r+\ell}{I_G\ell}u \tag{6.60}$$

where v is the nominal tether speed, which is zero here.

Since $\dot{\ell}$ is mainly driven by the force P, we can control the compound pendulum mode ϕ by exerting the force P on the tether. Such an actuation method can be employed to dump the angular momentum stored on the reaction wheels. While constantly decelerating the wheel speed, the linear force P on the tether can be exerted in an oscillatory fashion to minimize the associated compound pendulum mode, while the linear thruster F maintains a constant array angular rate. In other words, it is straightforward to show that the system shown in Figure 6-9 is fully controllable by F

and P when u is not available (see Chapter 3). Hence, the momentum dumping method provides an alternative method for stabilizing the compound pendulum mode during momentum dumping operations.

A simulation of such a momentum dumping operation is presented in Figure 6-10. The torque from the reaction wheel (u) is set as $u = -0.01$ (Nm) such that the wheel speed can constantly be decelerated to zero. The tangential force thruster (F) and the translational actuator on the tether (P) exert the control forces in order to maintain the same angular rate $\dot{\theta}$ and zero compound pendulum mode ($\phi, \dot{\phi} = 0$):

$$\begin{aligned} F &= -10\phi - 10\dot{\phi} - 10(\dot{\theta} - \dot{\theta}_d) \\ u &= -0.01 \\ P &= -10\phi - 10\dot{\phi} - 10(\dot{\theta} - \dot{\theta}_d) - 40(\ell - \ell_d) - 40\dot{\ell} \end{aligned} \tag{6.61}$$

The top plot of Figure 6-10(a) shows the change in the angular momentum of the reaction wheel due to the constant deceleration $u = -0.01$ (Nm) while the control forces F and P effectively maintain the control states at the reference points (bottom plot). Figure 6-10(b) shows that the usage of the linear thruster (F) to maintain the array angular rate is relatively small. In contrast, large P is required to stabilize the compound pendulum mode in the absence of the RWA torque u. Small oscillations of both the control states and the tether length are acceptable since no interferometric observation is scheduled during the momentum dumping operation.

6.10 Conclusions

This chapter proposed a new approach for controlling the array spin rate and relative attitude without thrusters by exploiting the coupled dynamics. Such a tethered system without thrusters is underactuated since it has fewer inputs than configuration variables. This work reports the first propellant-free underactuated control results for tethered formation flying spacecraft. Such an underactuated control approach is particularly beneficial to stellar interferometers due to the increased mission life span and reduced optical contamination by exhaust from the thrusters. This chapter further illustrated the potential of the proposed underactuated strategy by providing a new momentum dumping method that does not use torque-generating thrusters.

In contrast with linear systems in which an underactuated control law can be synthesized easily, designing a nonlinear controller for nonlinear underactuated systems is a difficult control problem, mainly due to the lack of full state feedback linearizability. In this chapter, we derived several nonlinear control laws for spinning tethered systems: partial feedback linearization, feedback linearization via momentum decoupling, and backstepping. Our simulation results indicate that the nonlinear control methods are much more efficient in tracking time-varying trajectories than LQR control.

For future work, developing a robust nonlinear underactuated control method that deals with model uncertainties and sensor noise would be an interesting and challenging research topic. Even though the modeling on the two-dimensional rotational plane is justified by the decoupling presented in Chapter 3, it would also be useful to extend such an underactuated control strategy to three-dimensional attitude dynamics. In particular, precessing the array rotation might also be achievable using underactuated tethered systems.

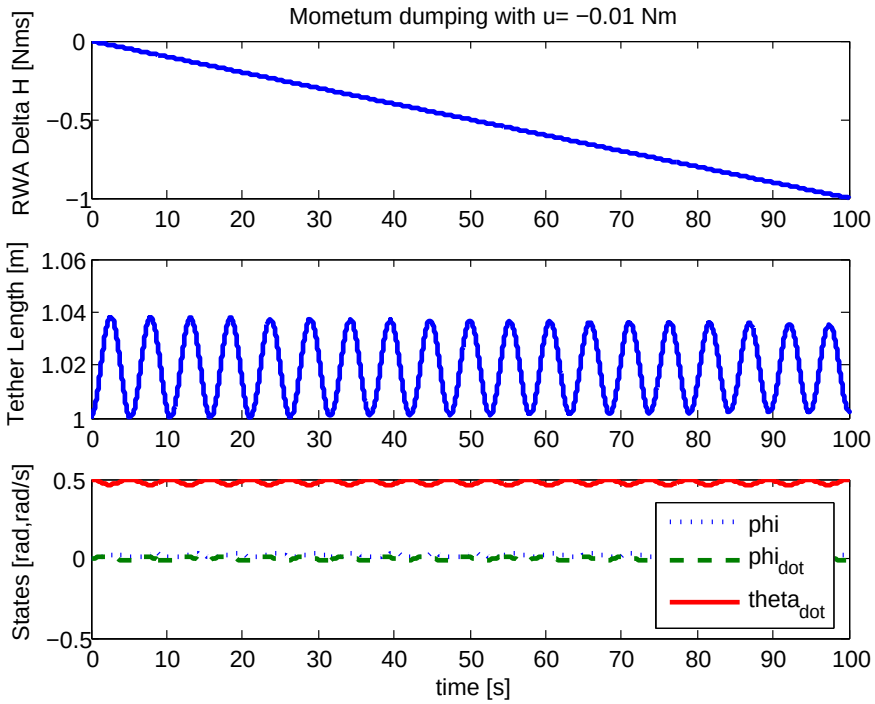

(a) Change in the RWA angular momentum and the control states

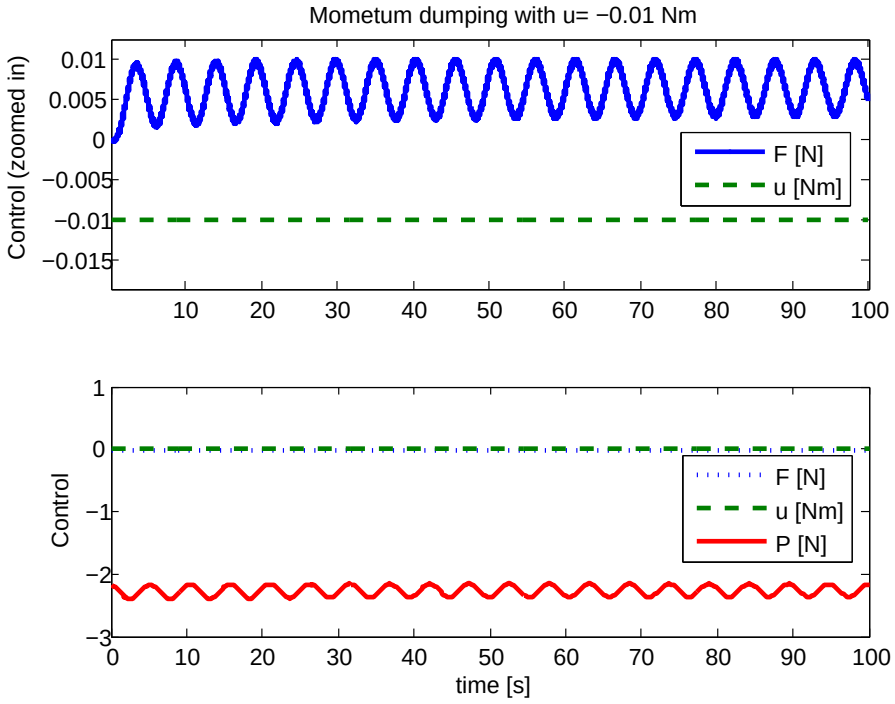

(b) Control

Figure 6-10: Momentum dumping operation with stabilization

Chapter 7

Testbed Development and Experimental Validation

7.1 Chapter Objective

This chapter describes the SPHERES tethered formation flying spacecraft testbed and its experimental validation of the proposed decentralized control strategy from the previous chapters. While a considerable portion of this chapter is devoted to the hardware and software modification of the existing SPHERES system, this chapter also focuses on multi-sensor data fusion with Kalman filtering, avionics design and motor controller design to support tethered formation flying experiments. It concludes with representative experimental results obtained at the NASA Marshall Space Flight Center (MSFC) flat floor facility on December, 2004 and September, 2006.

7.2 Tethered-SPHERES Testbed

The MIT Space Systems Laboratory (MIT-SSL) developed the multiple nano-satellite testbed called SPHERES (Synchronized Position Hold Engage and Reorient Experimental Satellites) to advance metrology, control, and autonomy technologies for use in formation flight and autonomous docking, rendezvous and reconfiguration algorithms (see Figure 7-1).

In order to support tethered formation flying experiments with the SPHERES testbed, a new suite of hardware has been designed and added. The aim of the present section is to describe such recent improvements to the SPHERES, including a new tether reel mechanism, a force-torque sensor to measure bearing angle, and an air-bearing carriage with a reaction wheel.

7.2.1 Overview of SPHERES Satellite

The SPHERES testbed was developed as part of the ongoing research initiatives of the MIT-SSL that utilize the space environment provided by the International Space Station (ISS) to validate dynamics and control algorithms of distributed spacecraft control, estimation, and autonomy. A good overview of SPHERES can also be found in [98] and [168]. At the time of writing, several SPHERES nano-satellites were launched to the ISS for control experiments in a three-dimensional environment. Motivated by the successful experimental results in this thesis, tethered formation flying experiments on ISS are currently being pursued. The micro-gravity facility in ISS provides six degrees-of-freedom (DOF) for each satellite to fully test control and estimation algorithms for NASA's future stellar interferometer missions such as TPF [11] and SPECS [107]. In the mean time, we verify our control algorithms in the 2-dimensional flat floor facilities at MIT and NASA MSFC. The three main operational environments of the SPHERES testbed are presented in Figure 7-1. The top two pictures show the zero-gravity 6 DOF environment on ISS (top left) and NASA's KC-135

(a) Formation flying experiments on ISS

(b) Formation flying experiments onboard KC-135 flight

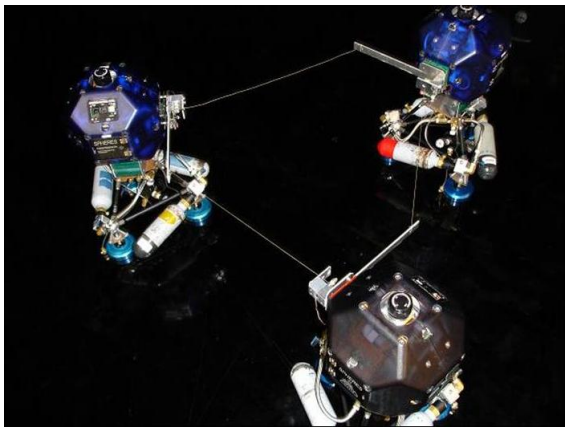

(c) Three triangular configuration on MSFC flat floor

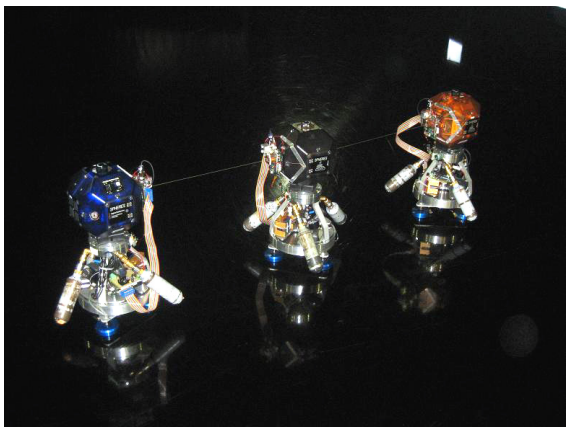

(d) Three inline configuration on MSFC flat floor

Figure 7-1: Three operational environments of SPHERES. ISS (a), KC 135 reduced-gravity flight (b), NASA MSFC flat floor (c,d)

reduced gravity aircraft (top right). The bottom pictures depict SPHERES sitting on the air-bearing carriages at the MSFC flat floor, which provides three DOF: yaw rotation and x,y translations.

The individual self-contained satellites have the ability to maneuver in up to six degrees of freedom (DOF) (three rotations and three translations), to communicate with each other and with the laptop control station, and to identify their position and attitude with respect to each other and to the experiment global reference frame. Figure 7-2(a) shows a SPHERES satellite. The diameter of a single SPHERES satellite is 0.25 m, and the mass of a SPHERES satellite, including a full gas tank, is 4.5 kg. The satellites are propelled by a cold-gas thruster system which uses carbon dioxide as propellant. The CO2 propellant is stored in liquid form at 860 psig; a regulator reduces the pressure to 35 psig. Twelve thrusters are positioned to provide full controllability in all six degrees of freedom, enabling both torque and translation control. Each thruster assembly, exerting a maximum of 0.12N of force, consists of a solenoid-actuated micro-valve with machined nozzles. The SPHERES satellite is capable of exerting 0.24 N of force and 0.012 Nm of torque using thrusters. The reaction wheel assembly (RWA) has been added to each air-bearing carriage to provide sufficient torque up to 0.207 Nm. These physical characteristics of a SPHERES satellite are summarized in Table 7.1.

The original SPHERES metrology system, using the ultrasound time-of-flight and rate gyroscopes, provides metrology information to the satellites in real-time. Since no global metrology system like GPS is actually available in deep space missions, the tethered SPHERES system utilizes a relative metrology system using the four ultrasound receivers (24 in total per each SPHERES satellite) on the line-of-sight face and the on-board beacon of the adjacent SPHERES satellite (see

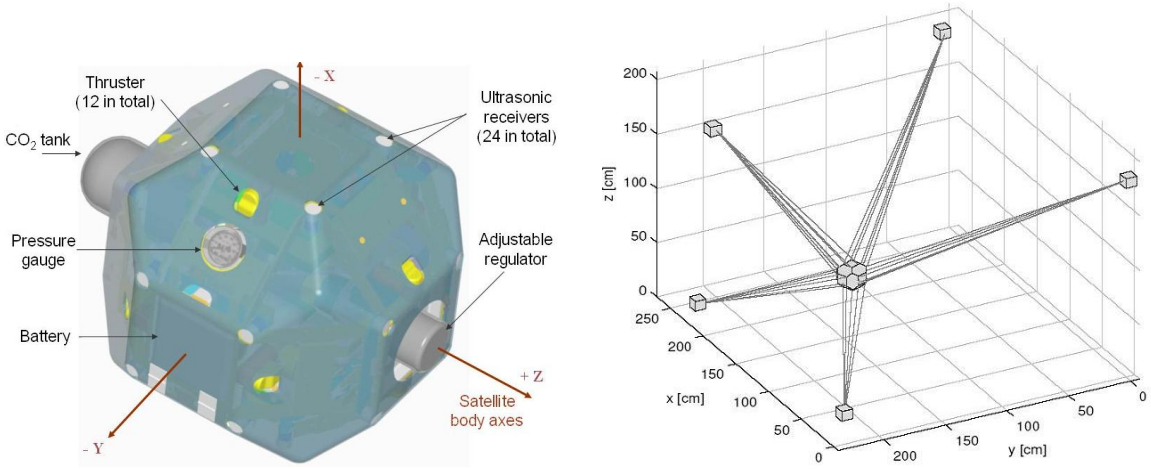

(a) Important external features of SPHERES

(b) A diagram of the global metrology system [80]

Figure 7-2: SPHERES nano-satellites

Figures 7-2 and 7-3). The relative metrology system is a pseudo-GPS ranging system that uses ultrasonic time-of-flight measurements from the target on-board beacon to the ultrasound (U/S) microphones distributed on the surface of each satellite. These time-of-flight measurements are converted to ranges and are then used to derive relative attitude and rate $(\phi, \dot{\phi})$ with respect to the reference frame using a series of Extended Kalman Filters (EKF). An additional Kalman filter, incorporating the gyroscope measurement, estimates all the states (compound pendulum mode and array rotation rate) needed for each satellite. A flow of measurement data is illustrated in Figure 7-3. Each estimation algorithm is decentralized in the sense that it uses the single-tethered dynamics in (3.18).

A Texas Instruments C6701 Digital Signal Processor provides the onboard computational capability. The ability of the C6701 to provide up to 1.0 GFLOPS allows for significant processing power to prevent it from being the limiting factor in the performance of the system. A FLASH memory size of 224 KB allows software re-configuration of the full operating system, making sure that multiple control algorithms are supported while the system is in the ISS or during the flat floor test.

The power system utilized onboard the ISS consists of packs of AA alkaline batteries while NiMH rechargeable packs are used on the ground facility. Each battery pack measures 12 volts and two battery packs provide each satellite with approximately two hours of operation; once a pack is consumed, it can be easily replaced. Each SPHERES satellite uses two separate frequency channels for communications, operating at 57.6 kbps each. One channel is used for satellite-to-satellite (STS)

Table 7.1: SPHERES Properties

Properties	**SPHERES Satellite**	**With RWA Air-Carriage**
Diameter	0.25 m	0.25 m
Mass	3.87 kg	15.856 kg
Number of CO_2 Tanks	1	4
Mass with Full Tanks	4.5 kg	20.346 kg
Moment of Inertia	0.0213 kgm^2	0.178 kgm^2
Max Linear Force Actuation	0.24 N	0.24 N
Max Torque Actuation	0.012 Nm (Thrusters)	0.207 Nm (RWA)
Power	15 W	30 W
Battery Life	1.5 Hr	1.5 Hr

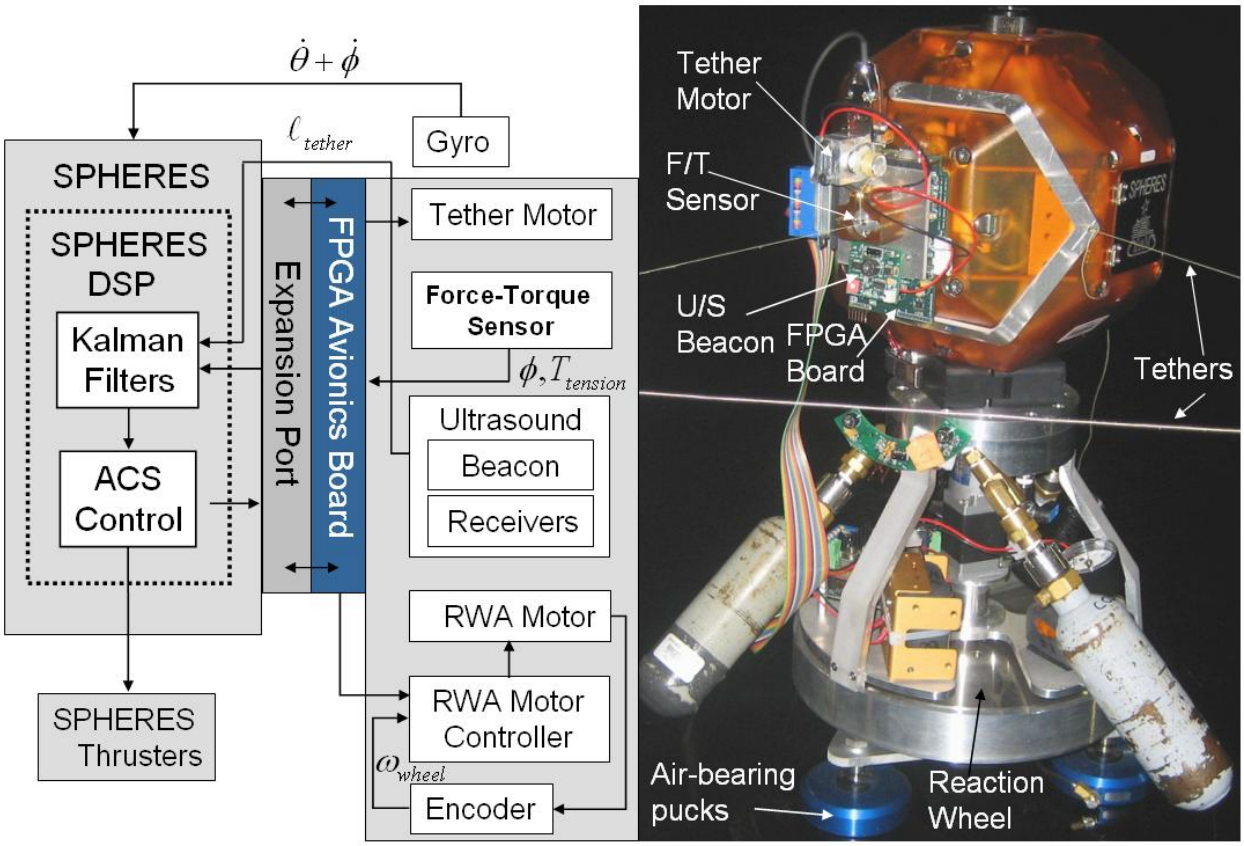

Figure 7-3: A SPHERES satellite on the new air-bearing carriage with a reaction wheel and its block diagram of signal and data transfer. A schematic of the FPGA board is expanded in Figure 7-8 and the motor control loop is detailed in Figure 7-11.

communications; the other channel enables satellite-to-laptop (STL) communications. Both channels are bi-directional; however, the communication hardware is half-duplex, meaning that only one unit can transmit at a time.

Each SPHERES satellite comes with an expansion port that provides a connectivity to the auxiliary hardware (see Figure 7-3). The expansion port interface provides the power ($\pm$ 5V, $\pm$ 15V and GND) and a series of data communication lines for data transfer (three analog inputs with a range of 5V, serial communication, etc). A tether deployment and retraction mechanism with tether force-torque sensors has been added to this expansion port to support the tethered formation tests, which is detailed in the subsequent sections.

7.2.2 Flight Quality Tether Reel with Force-Torque Sensor

The SPHERES satellite, with a prototype version of the tether reel with a force-torque sensor, is mounted on an air-bearing carriage equipped with a reaction wheel in Figure 7-3. Due to the increased overall weight of the system, we converted a single-puck system back to a three-puck system. The air-bearing carriages require 3 CO2 tanks, which allow for continuous operations of up to 30 minutes. The tether reel mechanism attaches to the SPHERES satellite via the expansion port, allowing for data and power transmission from the satellite. The prototype tether reel includes a motor and spool assembly to reel the tether in and out as well as a force/torque (F/T) sensor and ultrasound sensor to measure relative position and bearing of the neighboring satellite. A new flight tether reel is being developed for experiments in the ISS.

Figure 7-4 is a CAD rendering of the new ISS-flight tether reel developed by the MIT-SSL and

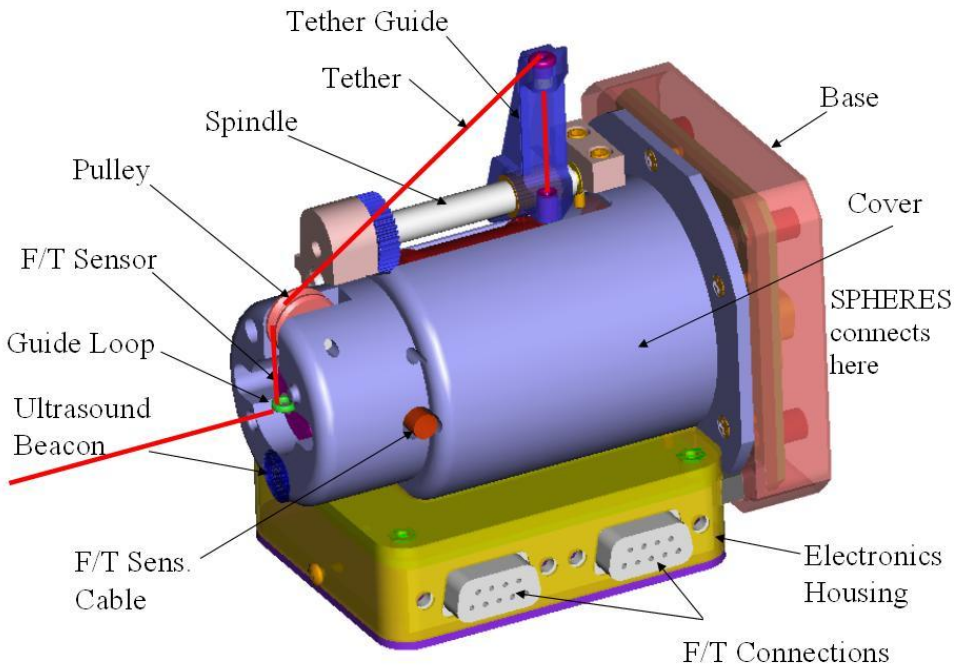

Figure 7-4: Space flight version of tether reel mechanism, courtesy: Payload Systems

Payload Systems Incorporated (PSI). The new version is designed to hold ten meters of tether. Some of the key design advantages of the new tether reel include an arm that moves along a shaft to ensure that the tether is evenly applied to the spool, as it reels in, and prevent loss of tension. This tether spindle and guide are depicted in Figure 7-5.

The spindle and tether guide maintain tension in the tether at all times. Rubber grommets provide friction so the the tether has to be pulled on to the spool and pulled off of the spool. The spindle is threaded to move the guide approximately one tether width per revolution of the spool.

Three different kinds of electronic sensor systems are embedded in the tether reel mechanism. First, a 6-DOF force-torque (F/T) sensor measures tether tension and bearing angles. Second, the ultrasound beacon emits ultrasonic signal to adjacent SPHERES for range and relative attitude measurements. Third, the new flight version of the tether reel will be equipped with a tether motor encoder to directly measure the tether length. Such a motor encoder is not present in the prototype version shown in Figure 7-3.

The previous generation of the tethered-SPHERES system could not measure tensile forces of the tether or slackness. One possible solution is to implement a strain gauge as in the case of another tethered spacecraft testbed [138]. One big drawback of such a system is that it only allows for force measurements in one direction. Consequently, a 6-DOF force-torque (F/T) sensor (commonly called as load cell) is selected for the SPHERES system. The selected load-cell, ATI Nano-17, can measure forces and torques in all three dimensions, and its compact size (diamter=0.669 in and height=0.571 in) allows it to fit into the small tether-reel (see Figure 7-6). It has a range up to 17 N for the z direction along the tether and 12N for the x and y directions. The resolution is 1/160 N.

A F/T sensor will be used to measure the bearing angle, ϕ that the tether makes with respect to the satellite in the horizontal plane. The new F/T sensor-based system simply compares two force outputs (F_x and F_y) to calculate the bearing angle ϕ– see Figure 7-13(b). The details of the metrology system are expanded in Section 7.4.5.

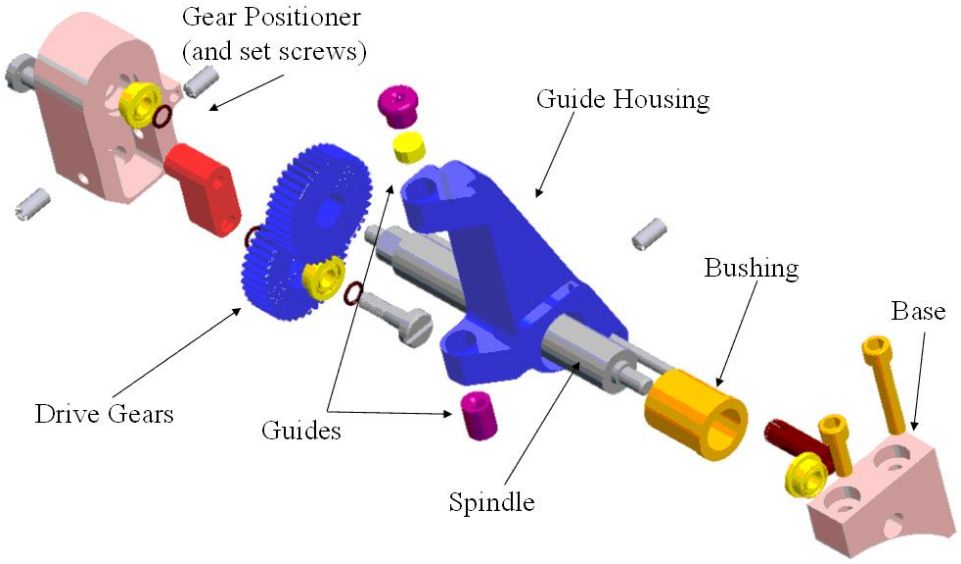

Figure 7-5: Exploded view of the tether guide, courtesy Payload Systems Incorporated.

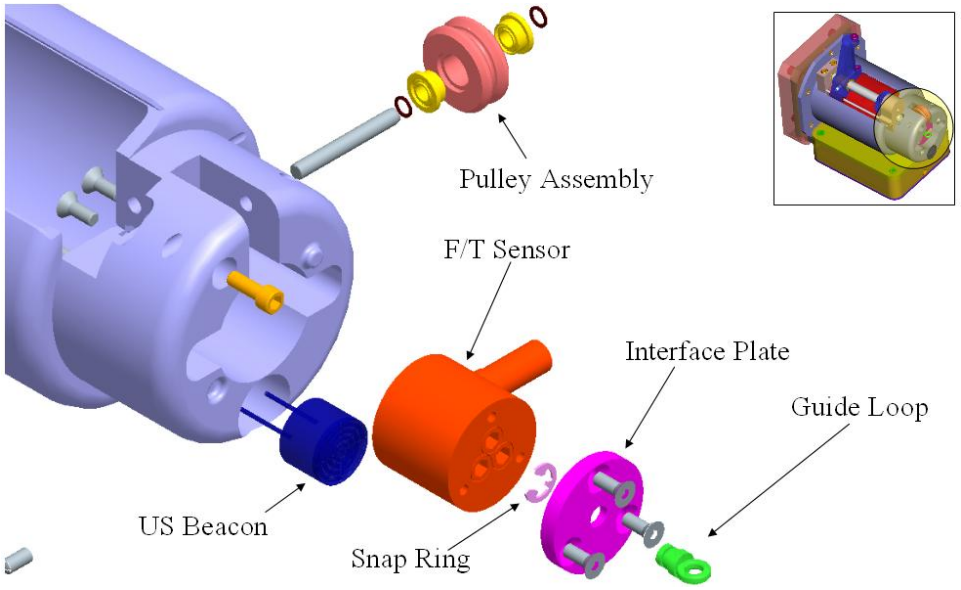

Figure 7-6: Exploded view of the reel head, courtesy Payload Systems Incorporated.

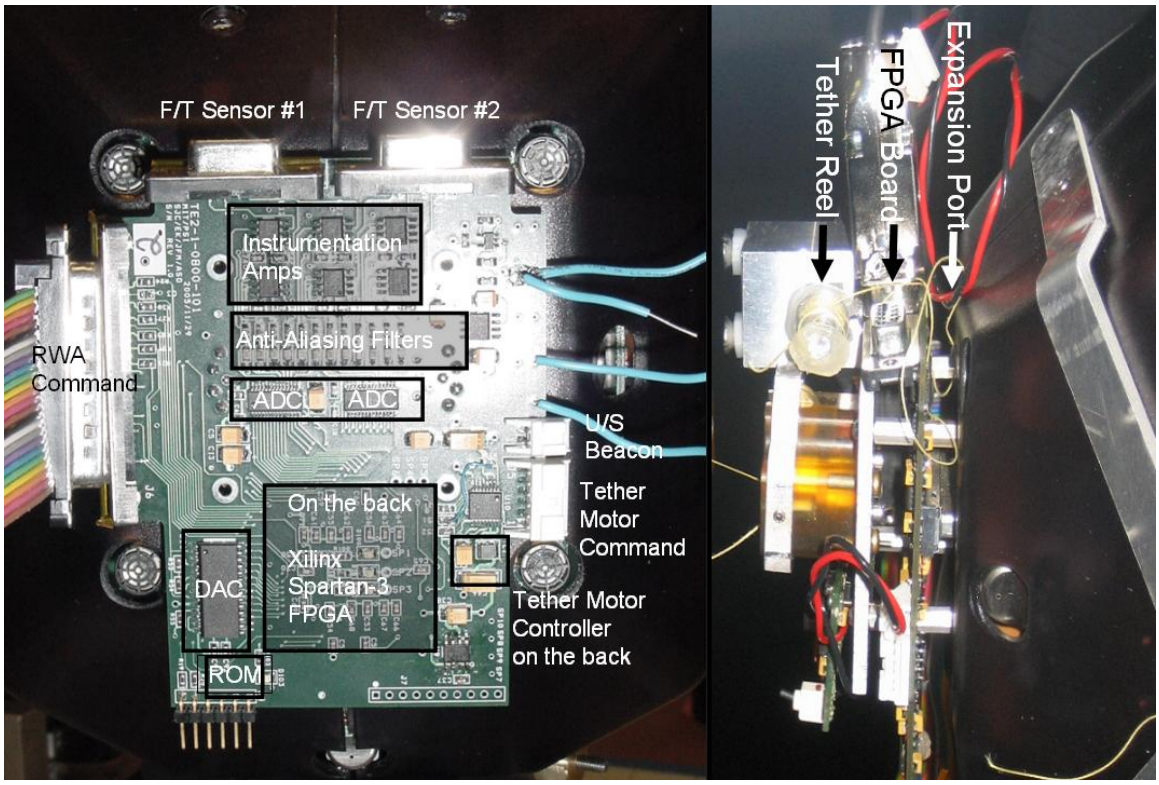

Figure 7-7: FPGA avionics board and its key components with a tether reel mechanism removed (left), A side view of the SPHERES Expansion port face (right). The FPGA board sits between the tether reel mechanism and the expansion port.

7.2.3 Tether Data Interface Module using FPGA

This section describes the functional details of the FPGA avionics board. As illustrated in Figure 7-7, the FPGA avionics board is sandwiched between the expansion port and the aluminum plate holding the tether reel mechanism. In essence, the FPGA avionics board is responsible for all sensor data and motor command transfers between the SPHERES satellite and its tether reel mechanism.

Figure 7-8 illustrates a flow of signals among different components of the FPGA. There are two F/T sensor connectors since the center SPHERES satellite, in a three-spacecraft inline configuration, has two tether attachment points. Table 7.2 lists the specifications of the selected FPGA IC chips. The raw voltage outputs (6 channels) from the F/T sensors are sent to the FPGA avionics board via a DB9 pin connector. The F/T sensor consists of six high-quality silicon strain gauges. An excitation voltage of +5V is supplied into the strain gauges while the low excitation voltage is tied to the ground (GND). In order to maximize the operating range of the F/T sensor, the raw F/T signals are amplified by a factor of 23.727. The anti-aliasing low-pass filters, with a cutoff-frequency at 29.693 Hz, were implemented to reduce high frequency noise sent to the 12-bit 12-channel DAC chip. The field programmable gate array (FPGA) then receives an array of converted digital signals from the F/T measurement and passes it to the SPHERES main memory via the SPHERES expansion port. The selected FPGA, Spartan-3 is a semiconductor device containing programmable logic components and programmable interconnects. The FPGA is also responsible for generating all sampling clock signals for both the DAC and ADC. The FPGA logic is programmed in VHDL programming language and uploaded to the FPGA Flash ROM (Xilinx XCF02S).

We decided to make extensive use of the serial port (RX and TX) on the SPHERES expansion port for the communications between the FPGA and the SPHERES main computer. This means

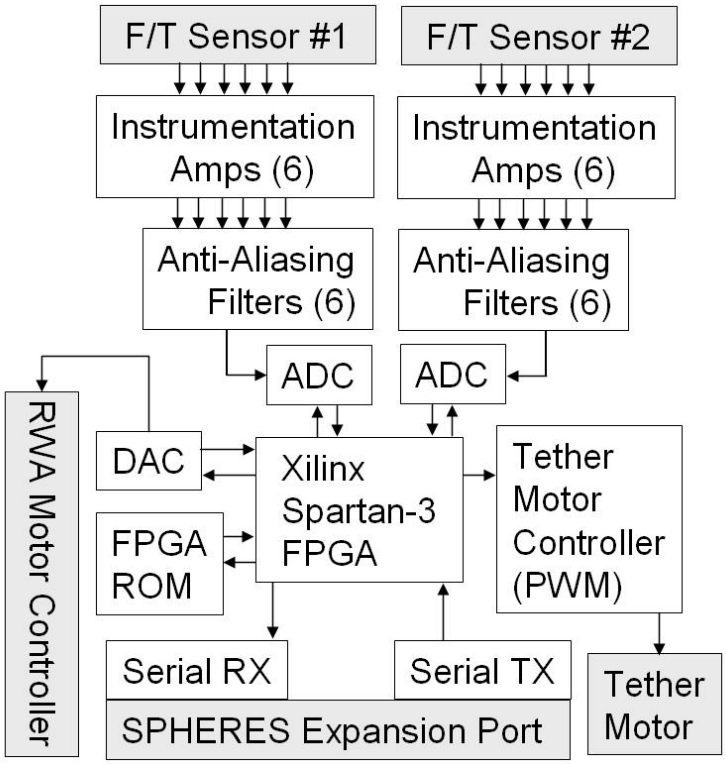

Figure 7-8: Schematic of FPGA avionics board showing a flow of signals between different components. The gray blocks indicate the external hardware connected to the FPGA board. The power lines from the expansion port are omitted. The RWA controller contains a DAC smoothing filter

Table 7.2: Key components of the FPGA board and F/T Sensor

Type	**Selection**	**Performance**
F/T Sensor	ATI Nano-17	max force 12-17 N, res. 1/160N
FPGA	Xilinx Spartan-3	200,000-gate, 12 18K-bit RAMs
Inst. Amp	Max4194	with R=2.2 kΩ, Gain =23.727
Anti-Aliasing Filter	R=5.36 kΩ, C=1.0 μF	cutoff freq=29.7 Hz
ADC (F/T input)	Max1294	12 bit, 6 channels, Input: 0-5V
DAC (RWA control)	BB DAC813	12 bit, Output: ±10V
Tether Motor Control	LB1836M	bipolar stepper-motor driver

that the speed command of the reaction wheel is transferred as a character string:

$$D[M][L][Dir][Spd]D[M][L][Dir][Spd]D[M][L][Dir][Spd]\ldots \tag{7.1}$$

where D denotes the start of one sample string, which includes: a 12-bit reaction wheel speed, divided into a 6-bit Most-Significant-Byte (MSB) string-[M] and a 6-bit Least-Significant-Byte (LSB)-[L] string; tether motor direction ([Dir]); and tether motor speed ([Spd]).

Then, the FPGA directly communicates with the 12-bit DAC to send a wheel speed command with a range of $\pm$10V to the motor controller (see Section 7.3). Note that this external motor controller contains a smoothing filter to reduce the high-frequency noise induced by the D/A conversion.

On the other hand, the signal-conditioned F/T measurements are sent to the SPHERES satellite as the following character string:

$$A[M]_1[L]_1[M]_2[L]_2[M]_3[L]_3[M]_4[L]_4[M]_5[L]_5[M]_6[L]_6B[M]_1[L]_1[M]_2[L]_2\ldots \tag{7.2}$$

where A and B indicate the start of the first and second F/T sensor, respectively while [M] and [L] denote the MSB and LSB bytes for each channel (6 channels per F/T sensor).

One string sample of the F/T measurement amounts to 26 Bytes, or 208 bits. This indicates that the serial communication with a baud rate of 115.2 kbps can reach a maximum sampling rate of 553 Hz.

The following 3×6 sensitivity matrix is provided by the F/T sensor manufacturer to compute the exact forces in the F/T sensor platform:

$$\begin{pmatrix} F_x \\ F_y \\ F_z \end{pmatrix} = \begin{bmatrix} -0.047 & -0.32 & 0.187 & 10.636 & 0.398 & -10.157 \\ -0.746 & -11.966 & -0.073 & 5.862 & -0.155 & 6.178 \\ 11.273 & 0.534 & 11.375 & 0.044 & 11.143 & 0.278 \end{bmatrix} \begin{pmatrix} Ch_1 \\ Ch_2 \\ Ch_3 \\ Ch_4 \\ Ch_5 \\ Ch_6 \end{pmatrix} \tag{7.3}$$

where $Ch_1, Ch_2, \ldots, Ch_6$ denote the 6 channel outputs from the Force-Torque sensor.

Once those forces are computed in the SPHERES main control loop, a series of EKFs estimate all relevant states by mixing the F/T output with high-bandwidth gyro measurement, as illustrated in Figure 7-3. We elaborate on the estimation techniques in Section 7.4.

One additional function of the FPGA is to generate 750-Hz Pulse-Width-Modulation (PWM) signals to run a tether motor attached to the FPGA board. The following summarizes some key FPGA codes handling all the functions described in this section.

- Britney_Tether.vhd: this main VHDL code defines the inputs and outputs, and calls the following subroutines.
- Clocker.vhd: generates multiple clock signals from the 50-MHz master clock, including sampling rates for ADC, DAC, and serial communications.
- ADController.vhd: provides data and interrupt codes for ADC interfacing.
- motor control.vhd: modulates the duty of 750Hz PWM to change the speed.
- uart_tx.vhd,uart_rx.vhd: handles the serial communication codes.

7.3 Reaction Wheel Air-Carriage

Figure 7-9 shows an air carriage with a reaction wheel embedded in its base. The reaction wheel is used to spin up the array of two or three satellites while the tether motor reels out the tether.

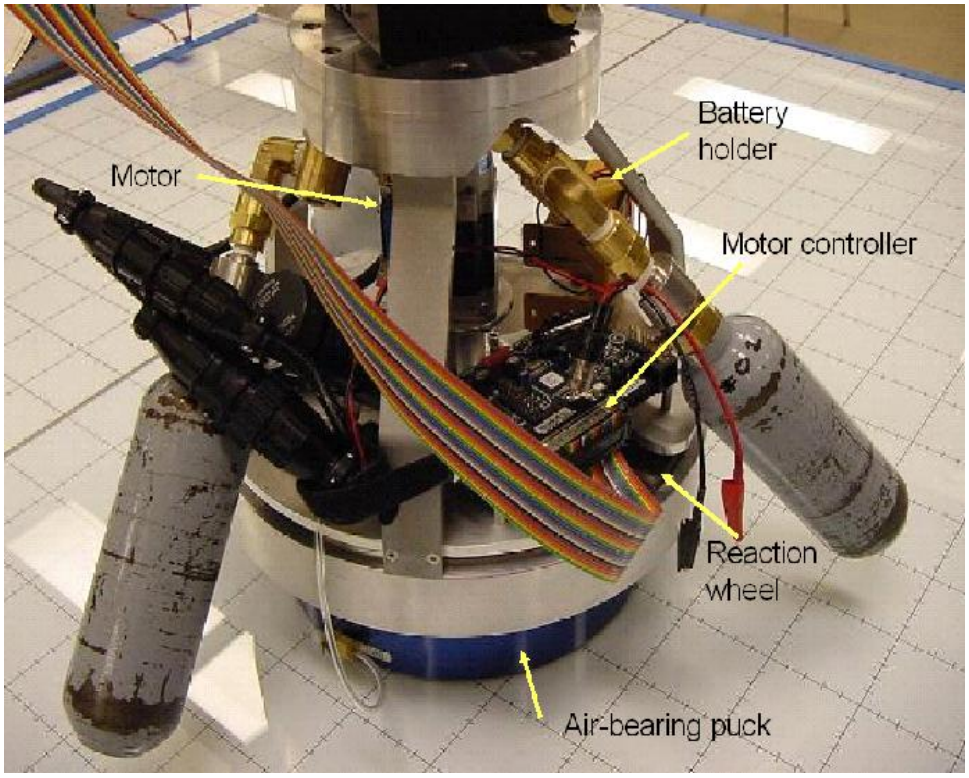

Figure 7-9: RWA motor controller and reaction wheel mounted on the air-carriage

7.3.1 Sizing the Wheel Using Observation Strategies from SPECS

Several decisions are not yet confirmed with respect to the NASA SPECS architecture, including the number of apertures and their configuration. Another open issue is the observation strategy. Given the basic goal of spiraling out and reaching some given level of UV plane coverage [42] (i.e. more UV filling with smaller gaps in the Modulation Transfer Function– MTF), there are several available strategies.

First, the array could rotate at constant angular momentum. In this case, an initial torque input starts the rotation, then the angular rate decreases as the array reels out. This strategy reduces thruster fuel consumption by exploiting the conservation of angular momentum. However, this would lead to extremely high values of uncontrolled array rotation when the collectors are reeled in (recall the instability in Chapter 3). A counterweight can be added to produce a more-slowly varying angular speed (e.g. Tetra-Star configuration [61]). A recent study [27] investigated the feasibility of constant angular momentum spinning tethered formations for space-based interferometry applications in an Earth trailing, heliocentric orbit.

Second, the array can be spun with constant thrust. This provides approximately constant angular rate [118]. It yields the most desirable UV plane coverage (see the more filled UV plane in Figure 7-10(a)), but the usage of propellant can be excessive. In this case, the ratio of the initial (H_i) and final angular momentum (H_i) is

$$\frac{H_o}{H_i} = \frac{m{\ell_o}^2\omega}{m{\ell_i}^2\omega} = \frac{{\ell_o}^2}{{\ell_i}^2} \tag{7.4}$$

where ℓ_i and ℓ_o denote the radius of the initial and final array, respectively.

Third, the array could rotate at constant linear velocity. This is useful for maintaining the same Signal to Noise Ratio (SNR) per baseline measurement since this mode ensures that the UV-point

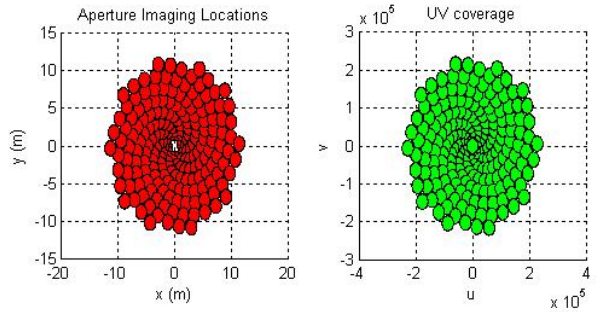

(a) constant angular rate mode

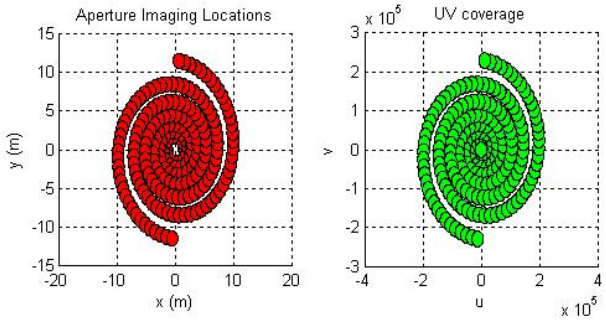

(b) constant linear velocity mode

Figure 7-10: Comparison of UV plots with the same initial velocities

blur is constant throughout the imaging process. The constant linear velocity mode is proposed by the MIT study as a good compromise between economical thrust usage of the constant angular momentum mode and more effective UV plane coverage of the constant angular rate mode. Figure 7-10 compares the UV plot of the constant linear velocity mode with that of the constant angular rate mode. The ratio of angular momentum, for the constant linear velocity mode, is calculated as

$$\frac{H_o}{H_i} = \frac{m\ell_o(\ell_o\omega_0)}{m\ell_i(\ell_i\omega_i)} = \frac{\ell_o}{\ell_i} \tag{7.5}$$

since $v{=}\ell_o\omega_o = \ell_i\omega_i{=}$constant.

Therefore, we can reduce the angular momentum that needs to be exchanged with the reaction wheel assembly by a factor of ℓ_o/ℓ_i by running in the constant linear velocity mode.

During the process of sizing the reaction wheel, various scenarios were considered to spin up the array to various baseline lengths on either a flat floor or in the International Space Station.

For example, the radius of the wheel is determined from the moment of inertia I_w and the maximum wheel speed ω_m:

$$\begin{aligned} I_w &= \frac{\rho\pi}{2}\left(r_{disk}^4 h_{disk} + (r_{cup}^4 - r_{disk}^4)h_{cup}\right) \\ H_w &= I_w\omega_m = H_o - H_i \end{aligned} \tag{7.6}$$

where ρ is the density of the wheel material, and r and h denote the radius and height of the cup (annulus disk) design.

In addition, the wheel angular momentum H_w is the difference between the initial momentum with

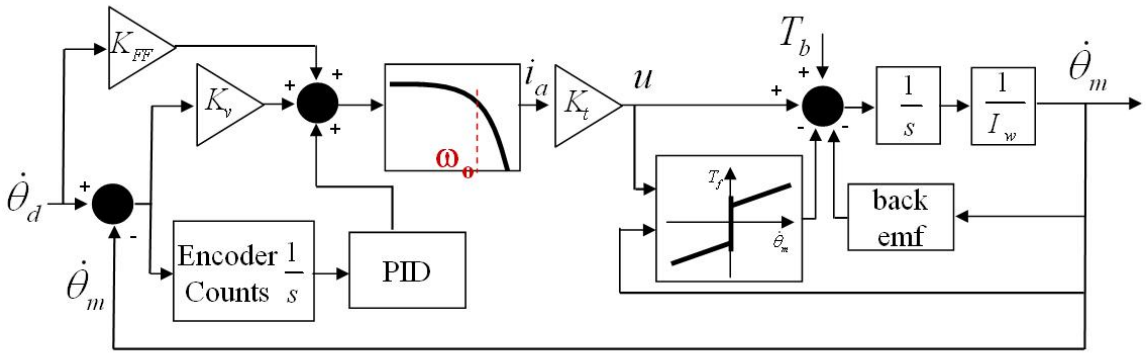

Figure 7-11: Schematic of the control loop of the RWA servo

$\ell = 0$ and the final momentum, operating at constant linear velocity such that

$$H_i = (I_G + mr^2)\omega$$
$$H_o = (I_G + m(r+\ell)^2)\frac{r\omega}{r+\ell} \tag{7.7}$$

The current momentum wheel has an angular momentum capacity of 15 Nms with the max torque rated at 0.318 Nm. The max speed is 3000 rpm.

7.3.2 Local Control of Reaction Wheel Motor

The main SPHERES code controls the reaction wheel speed, using an internal velocity control loop of the external motor controller. The PID gains and feed forward gains of this internal motor control loop have been carefully tuned to follow the desired velocity command from the SPHERES satellite. The desired torque from the selected attitude control law is integrated at 100 Hz in the main SPHERES control loop to output the desired wheel speed. The gains of the local motor controller were determined through both theoretical and empirical tests. The motor controllers are now configured using these settings such that the RWA motor responds robustly to the velocity command from the SPHERES DSP in the presence of friction and disturbance.

We performed the physical system identification of the motor dynamics as follows. The dynamics of the motor spinning at $\dot{\theta}_m$ is obtained as

$$I_w\ddot{\theta}_m + b\dot{\theta}_m = u = K_t i_a \tag{7.8}$$

where I_w denotes the combined inertia of the reaction wheel and motor rotor, b is the friction coefficient, i_a is the applied torque, and K_t denotes the motor torque constant. The location of the torque input u is shown in Figure 7-11.

The electrical loop is identified as:

$$L_a\frac{di_a}{dt} + R_a i_a = v_a - K_e\dot{\theta}_m \tag{7.9}$$

where $K_e\dot{\theta}_m$ is the back emf voltage expressed in terms of the wheel rotational velocity $\dot{\theta}_m$.

In reality, it is often possible to ignore the inductance L_a since the electric response is much faster than the rotor rotation [65]. In addition, we need to consider the existence of Coulomb friction and stiction for the case when $\dot{\theta}_m = 0$, along with the braking torque. By combining (7.8) and (7.9), with the additional external torque terms taken into account, the motor dynamics with the torque

Table 7.3: Physical and electrical parameters of the reaction wheel motor

Parameters	**Selection**
I_w (Wheel Inertia)	0.0473 kgm^2
K_t (Motor Torque Constant)	0.046 Nm/A
K_e (Back Emf Constant)	0.0048 V/rpm
R_a (Resistance of Armature Coil)	0.46 Ω
L_a (Inductance of Armature Coil)	0.64 mH
b (Velocity Friction Coefficient)	1.35 $\times 10^{-2}$ Nm/(rad/s)
μ_c (Coulomb Friction Torque)	0.0106 Nm

input $u = K_t i_a$ is obtained as

$$I_w \ddot{\theta}_m + \left(b + \frac{K_t K_e}{R_a} \right) \dot{\theta}_m = \frac{K_t}{R_a} v_a + T_c + T_b \tag{7.10}$$

where the Coulomb friction term T_c is

$$T_c = \begin{pmatrix} -\mu_c \text{sgn}(\dot{\theta}) & \|u\| > \mu_c \\ u & \|u\| \leq \mu_c \end{pmatrix}. \tag{7.11}$$

The braking torque is the result of the power electronics driving the motor coil. When the torque and the current command have opposite signs, the motor acts as a generator. Due to the back-emf, a significant voltage appears at the driving circuit port. This generated current must be dissipated to protect the motor circuitry. The braking torque is defined as [89]

$$T_b = \begin{pmatrix} -\text{sgn}(i_c) k_b \|\dot{\theta}\| & \text{if } (\dot{\theta} i_c) < 0 \\ 0 & \text{if } (\dot{\theta} i_c) \geq 0 \end{pmatrix} \tag{7.12}$$

where i_c is the internal reference current command.

Based upon this physical system identification of the motor servo loop in (7.10), the unknown parameters, such as the Coulomb friction μ_c and the velocity damping coefficient b, have been found by experiment. Most electrical parameters are given by the manufacturer. Table 7.3 lists all the parameters necessary to simulate the motor control loop.

Like most modern servo drives, we employed a modified PID control logic for controlling the torque and velocity of the reaction wheel. We selected a 24 VDC, 100 watt, brushless servo motor from Applied Motion Products (NEMA17 N0100-103A), whose torque capacity and maximum speed are rated as 0.318Nm and 3000rpm, respectively. The motor has a quadrature encoder that has a resolution of 8000 lines per revolution. The BLuDC4 servo controller from Applied Motion Products is responsible for all the data and power transfers among the motor, the encoder and the external 24-volt battery pack. The desired wheel velocity is sent at a frequency of 100Hz from the FPGA avionics board in Figure 7-8 into the analog input ($\pm$ 10V) port of the motor servo drive. This servo controller is equipped with the digital PID controller and low-pass filters. The PID loop compares the intended motor position to the actual motor position as reported by the encoder at a frequency of 4 kHz. The difference is called encoder count error, and the PID loop acts on this error in three ways: the Proportional term, the Integral term and the Derivative. The servo controller adds a number of extra gain terms to enable greater control authority. These gain terms are velocity feedback and feedforward, and acceleration feedback and feedforward. In particular, a direct feedback of the motor velocity is used to provide greater damping for the larger load of the reaction wheel. The final control torque input to the motor is given by

$$u = K_t \left[K_P U_n + K_I \sum_k U_k + K_D (U_n - U_{n-1}) + K_v (\dot{\theta}_{m,d} - \dot{\theta}_m) + K_{FF} \dot{\theta}_{m,d} \right] \tag{7.13}$$

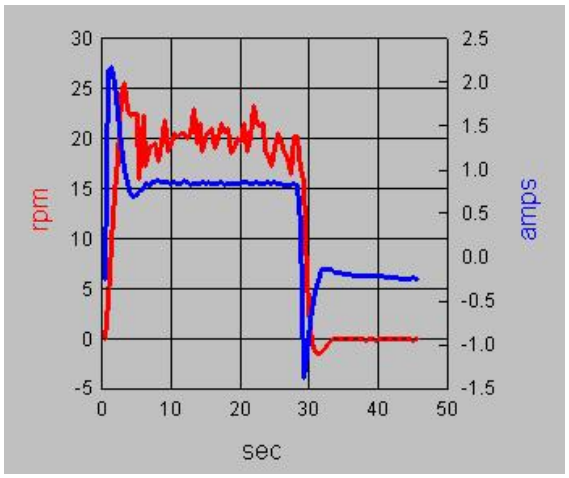

(a) Experimental result of a step velocity input. Wheel velocity (red) and internal motor current (blue).

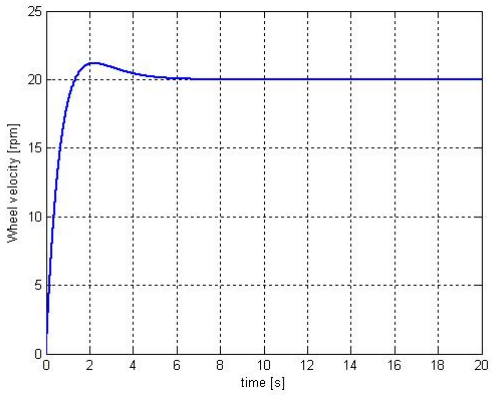

(b) Matlab-Simulink simulation with the same controller

Figure 7-12: Performance of the reaction wheel motor controller

while K_P, K_I, and K_D denote the proportional, integral and derivative gains for the encoder error counts and K_v is the velocity feedback. Also, U_n connotes an encoder output. In addition, K_{FF} is the feed-forward gain, and K_t denotes the torque constant of the motor in (7.8).
Note that there is a low pass filter attenuating the high-frequency noise of u, which results from the derivative control and velocity damping (see Figure 7-11).

Each control gain is carefully selected to meet the desired closed-loop characteristics. The final gains are $K_P = 800$, $K_I = 1$, $K_D = 2000$, $K_{FF} = 0$ and $K_v = 10000$ while the PID output filter has a cutoff frequency at 60Hz. Those gains yield a gain margin of 520 and phase margin of 85 degrees. Figure 7-12 compares the experimental data with the Simulink simulation when the wheel was instantaneously driven by a 20-rpm step command. Both the experimental data and the simulation achieve a rise time of around 1.5 seconds.

7.4 Relative Sensing and Decentralized Estimation

Any state feedback control algorithm requires that all states be strictly available for feedback. The role of the decentralized and relative estimator is to provide state estimates (tether length, and all the states including the bearing angle ϕ) independently of the satellites. Two different relative metrology systems in Figure 7-13 have been developed. We illustrate and compare those two metrology systems as well as the design of their Kalman filters in this section.

7.4.1 Rationale for Decentralized Relative Sensing

The effort to develop a robust and reliable metrology system for tethered formation flying SPHERES, concentrates on the following principal system requirement.

- ***The metrology system should be decentralized and relative***

Decentralized means that each measurement or estimation process should not involve an exchange of information with the adjacent satellites. Relative means that measured quantity is formulated with respect to the local frame of an individual SPHERES satellite.

The decentralized estimation, along with the decentralized controller, enables simple independent control of each satellite without the need for inter-satellite communications. This will significantly simplify both the control algorithm and hardware implementation. The decentralized scheme is realized by the decoupling technique discussed in Chapter 4.

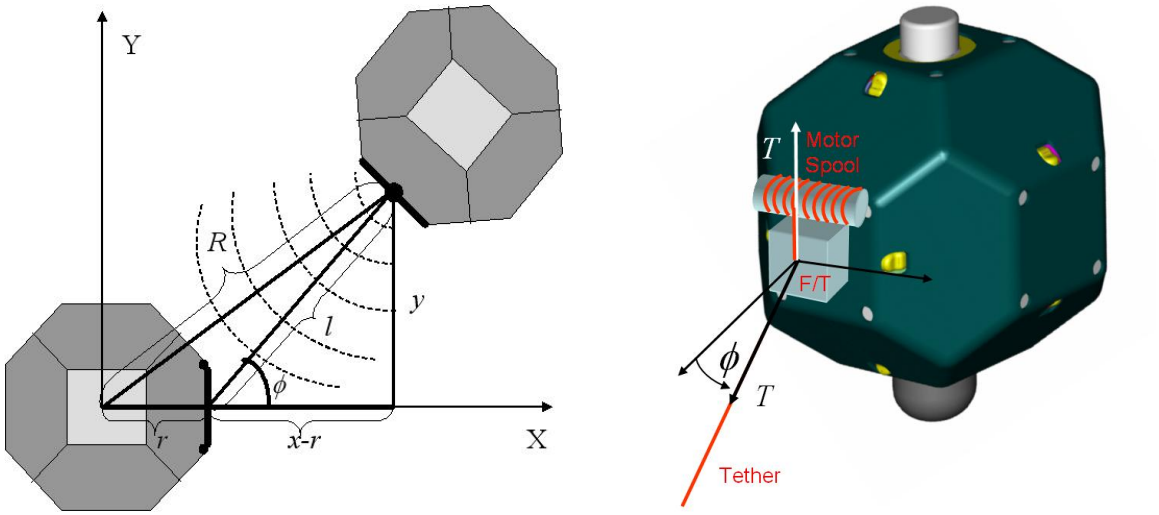

(a) Schematic of U/S system for measuring bearing angle (ϕ) and tether length (ℓ)

(b) Schematic of bearing angle measurement (ϕ) using Force-Torque (F/T) sensor outputs

Figure 7-13: Two different methods for measuring bearing angle

Table 7.4: Functional Requirements

Measured Variables	**Range**	**Resolution**	**Bandwidth**
Pendulum Mode Angle (ϕ)	120 deg	0.5 deg	100 Hz
tether length (l)	5 m	1 mm	100 Hz
tether tension (T)	10 N	0.0087 N	100 Hz

In deep space, absolute attitude might be available via star-trackers but the availability of absolute positions, like those provided by the Global Positioning System (GPS), is very limited. Note that all degrees of freedom defined in Chapter 3 are relative states (e.g. bearing angle, ϕ).

7.4.2 Functional Requirements

The functional requirements for a dynamic measurement system are mainly determined by resolution, range or field-of-view (FOV), and bandwidth. (see Table 7.4). For a pendulum mode angle (bearing angle) determination, a range of more than 120 degrees is desired. In addition, a resolution of 0.5 degrees is required and this is easily achievable using a 12 bit ADC. Other requirements are mainly driven by the maximum deployment size of the tethered array (5m) and physical parameters of the SPHERES testbed. Note that the tether length can also be accurately measured by reading the motor encoder output.

7.4.3 Previous Method using Ultrasonic Metrology System

This section describes the previous version of the relative state estimator based upon the SPHERES built-in ultrasound (U/S) metrology system. This approach had been used for the earlier experiments [43, 45], until this system was updated by adding a Force-Torque (F/T) sensor.

Each SPHERES satellite is equipped with an ultrasonic beacon located on its docking face. An additional on-board beacon is also mounted on the expansion port face where the tether mechanism package is attached (See Figure 7-3).

There are two extended Kalman filters combined in series to estimate relative states. The first extended Kalman filter estimates the x, y, z coordinates of the beacon on a second SPHERE in the

body frame of the first SPHERE, as depicted in Figure 7-13(a). The measurement process is similar to using the time delay between seeing the lightening and hearing the thunder clap to calculate how far you are away from a thunderstorm.

The estimation process occurs as follows. When the leader SPHERE requests a state update, it emits an infrared flash which is received by all the surrounding SPHERES. This is a time-synchronization step. All the SPHERES then start to listen for an U/S ping through their 24 U/S receivers located on the six faces. The beacons emit an US ping in sequence (20 milliseconds apart) to avoid interference. The pings are then received by each SPHERE and an array of time-of-flight data is sent to the computer. Since the range measurement is nonlinear, as seen in (7.14), an extended Kalman filter is employed to estimate the range in terms of x, y, and z coordinate values.

Once the U/S relative system estimates the location of the target beacon in its body-frame, the tether length ℓ and the bearing pendulum mode angle ϕ are computed from the geometry shown in Figure 7-13(a):

$$\begin{aligned} \ell &= \sqrt{(x-r)^2 + y^2 + z^2} \\ \phi &= \arcsin\left(y/\ell\right) \end{aligned} \tag{7.14}$$

The tether length is used in realtime for both the tether-motor control and the estimator. The direct ϕ measurement is used in the second Kalman filter, along with the high-frequency gyro measurement, to estimate $\dot{\theta}$ and $\dot{\phi}$. (see Figure 7-3).

The complementary extended Kalman filter makes use of the nonlinear equation developed in Chapter 3 in order to estimate ϕ, $\dot{\theta}$, and $\dot{\phi}$. It is formulated as follows.

Propagation
The estimated states are propagated over a time period Δt using the exact nonlinear equation of the singled-tethered system:

$$\begin{aligned} \frac{d}{dt}\begin{pmatrix} \hat{\phi} \\ \hat{\dot{\theta}} \\ \hat{\dot{\phi}} \end{pmatrix} = -\frac{1}{\ell I_{new}} \begin{bmatrix} -\ell I_{new}\hat{\dot{\phi}} \\ -r\sin\hat{\phi}[I_r(\hat{\dot{\theta}}+\hat{\dot{\phi}})^2 + mr\ell\hat{\dot{\theta}}^2\cos\hat{\phi}] \\ r\sin\hat{\phi}[I_r(\hat{\dot{\theta}}+\hat{\dot{\phi}})^2 + mr\ell\hat{\dot{\theta}}^2\cos\hat{\phi} + m\ell^2\hat{\dot{\theta}}^2 + mr\ell(\hat{\dot{\theta}}+\hat{\dot{\phi}})^2\cos\hat{\phi}] \end{bmatrix} \\ + \frac{1}{\ell I_{new}}\begin{pmatrix} 0 \\ -r\cos\hat{\phi} \\ \ell + r\cos\hat{\phi} \end{pmatrix} u \end{aligned} \tag{7.15}$$

where $I_r = I_G + mr^2$ and $I_{new} = I_G + mr^2(\sin\hat{\phi})^2$.

We also propagate the covariance matrix using

$$\dot{P} = A(\hat{x})P + PA(\hat{x})' + Q \tag{7.16}$$

where A is a linearized matrix from Eq. (6.10):

$$A(\hat{x}) = \begin{bmatrix} 0 & 0 & 1 \\ \frac{r\hat{\dot{\theta}}^2\left(I_G + mr(r+\ell)\right)}{\ell I_G} & 0 & 0 \\ -\frac{r\hat{\dot{\theta}}^2\left(I_G + m(r+\ell)^2\right)}{\ell I_G} & 0 & 0 \end{bmatrix} \tag{7.17}$$

In addition, P is the error covariance matrix and Q is the covariance matrix of the process noise.

Measurement Update

Table 7.5: Three approaches for measuring pendulum mode angle. AA filter denotes anti-aliasing filter.

Method	Range	Resolution	Bandwidth	directions
Requirement	120 deg	0.5 deg	100 Hz	three axes
U/S system	$<$ 51 deg	2-3 deg	10 Hz	three axes
Potentiometer	90 deg	by ADC	N/A	one axis
Force-Torque sensor	180 deg	0.1 deg	AA filter	three axes

The following standard Kalman filter equations are used for measurement update:

$$\begin{aligned} \hat{x}_k^+ &= \hat{x}_k^- + L_k(y_k - Cx_k^-) \\ L_k &= P_k^- C'[CP_k^- C' + R_k]^{-1} \\ P_k^+ &= (I - L_k C)P_k^-(I - L_k C)' + LR_k L' \end{aligned} \tag{7.18}$$

where L_k denotes the optimal Kalman gain and R_k is the discrete covariance matrix of the sensor noise ($v \sim N(0, R_k)$). It is noted that the Joseph form of the covariance measurement update is used to maintain the symmetric property. In addition, the measurement equation can be written as

$$y_k = \begin{bmatrix} \text{gyro measurement} \\ \phi \text{ from U/S beacon} \end{bmatrix} = C\hat{x}_k + v = \begin{bmatrix} 0 & 1 & 1 \\ 1 & 0 & 0 \end{bmatrix} \begin{pmatrix} \hat{\phi} \\ \hat{\dot{\theta}} \\ \hat{\dot{\phi}} \end{pmatrix} + v. \tag{7.19}$$

Note that the measurement updates can be divided into two measurement types: gyro update ($= \dot{\phi} + \dot{\theta}$) and ϕ update from the U/S system. We can easily verify that the system (C in (7.19) and A in (7.17)), is fully observable. Furthermore, the system is also fully observable only with the gyro measurements, if the rotational rate is not zero ($\hat{\dot{\theta}} \neq 0$). Let us define the gyro measurement by $C_1 = \begin{pmatrix} 0 & 1 & 1 \end{pmatrix}$. Then, the observability matrix

$$\begin{pmatrix} C_1 \\ C_1 A(\hat{x}) \\ C_1 A^2(\hat{x}) \end{pmatrix} \tag{7.20}$$

has a full rank of 3. Due to unreliable ultrasonic ϕ measurements, discussed in the next section, we often used only gyro measurements defined by $C_1 = \begin{pmatrix} 0 & 1 & 1 \end{pmatrix}$ in the Kalman filter formulation. The drawback of such an approach is that the estimator tends to diverge more frequently since it requires that $A(\hat{x})$ in (7.17) have a nonzero $\dot{\theta}$. Hence, a tethered array was initially spun up prior to turning on the estimator.

7.4.4 Problems with the Ultrasonic Measurement System

There are several reasons why a force-torque sensor is employed to measure the bearing angle, thereby replacing the ultrasound-based system.

1. The current U/S system theoretically has a three millimeter resolution in range. In reality, the best resolution it can achieve is one centimeter. This results in merely a few degrees of resolution in bearing angle for a 20 cm tether length.

2. The U/S system does not work well in close proximity due to the cone angle ($\pm$ 30 degrees) of U/S beacon. Experiments also reveal that measurements within 15 cm tend to be inaccurate.

3. The U/S system has a limitation in bandwidth. To avoid confusion, each SPHERES satellite needs to identify the signal from a specific beacon number, separated by a time gap of 20 ms.

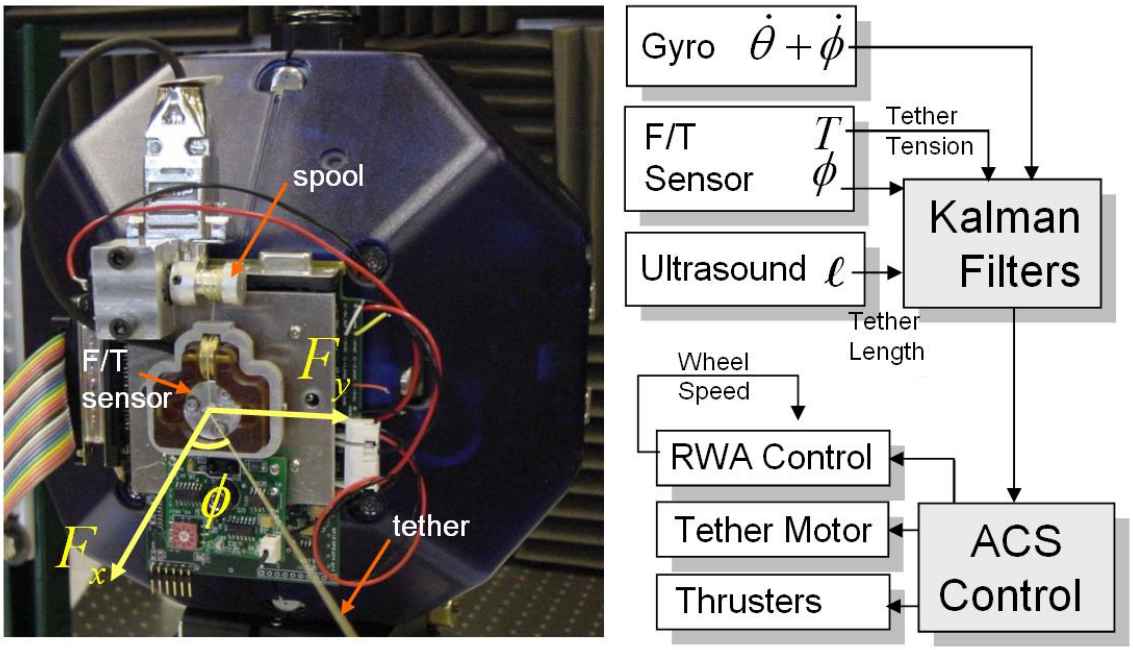

Figure 7-14: New bearing angle ϕ metrology system using a Force-Torque sensor (ϕ in the negative direction).

For a three-SPHERE array, we can only run this U/S metrology system at frequencies up to 10 Hz while avoiding the interference with thrusters.

Undesirable spikes also occur occasionally, affecting the performance of the measurement system. Those spikes are generated from the environmental noise and the reflectivity of the surrounding walls. Also note that neither tether tension nor slackness can be measured by the U/S system.

Table 7.5 compares three different methodologies for measuring the compound pendulum mode angle ϕ. A potentiometer, which was used in another tethered testbed [210], is also capable of measuring the bearing angle. However its measurement is limited to a two dimensional plane, and lacks a tension measurement.

In conclusion, the upgraded measurement system with a force-torque sensor should resolve all the issues identified in this section.

7.4.5 New Bearing Angle Measurement Method

The new bearing angle measurement system using a force-torque (F/T) sensor was devised to resolve all the issues identified in the previous section. A brief description of its estimator design is presented. As shown in Figure 7-14, the tether coming from the motor spool is bent 90 degrees on the horizontal plane, and goes toward the other adjacent SPHERES. Forces are exerted on the F/T sensor through a frictionless ring.

In order to show that this setup can also measure the out-of-plane angle (ϕ_z) in Figure 7-15(a), a general 3-dimensional case is considered first. From the free-body diagram of this setup (Figure 7-15), we can determine the tension and bearing angles using the following equations:

$$\begin{aligned} \Sigma_x \text{ (x forces on the F/T sensor)} &: F_x = T\cos\phi_z\cos\phi \\ \Sigma_y \text{ (y forces on the F/T sensor)} &: F_y = T\cos\phi_z\sin\phi \\ \Sigma_z \text{ (z forces on the F/T sensor)} &: F_z = T\sin\phi_z + T \end{aligned} \tag{7.21}$$

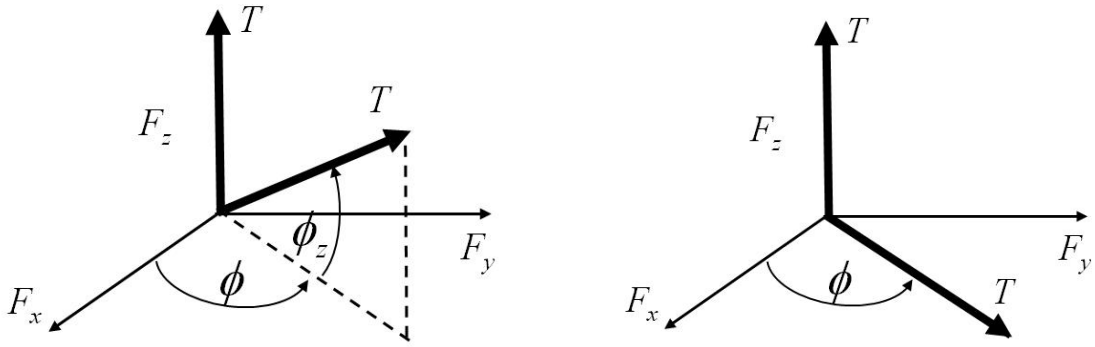

(a) 3-D setup

(b) 2-D setup

Figure 7-15: Forces on the F/T sensor of the tether reel, where the z axis indicates the vertical direction to the tether spool in Figure 7-14

where T denotes the tension in the tether.

Then, we can solve for T, ϕ (planar pendulum mode angle) and ϕ_z (vertical angle):

$$T = \frac{{F_x}^2 + {F_y}^2 + {F_z}^2}{2F_z}, \quad \phi = \tan^{-1}\frac{F_y}{F_x}, \quad \phi_z = \sin^{-1}\frac{{F_z}^2 - {F_x}^2 - {F_y}^2}{{F_x}^2 + {F_y}^2 + {F_z}^2} \tag{7.22}$$

where T is the tether tension, which remains the same at all locations in the tether for the case of inextensible and massless tethers. F_x, F_y and F_z denote force measurements of the F/T sensor in the x, y, z directions, respectively.

For the experiments on the flat floor facility, presented in this dissertation, only planar motions characterized by ϕ are considered, as illustrated in Figures 7-15(b) and 7-13. We use the relationship

$$\phi = \tan^{-1}\frac{F_y}{F_x} = \sin^{-1}\frac{F_y}{{F_x}^2 + {F_y}^2} \tag{7.23}$$

and the sensitivity matrix in (7.3) to compute ϕ from raw six channel F/T sensor outputs. Then, the ϕ measurement is incorporated in the Kalman filter to distinguish $\dot{\phi}$ from the combined angular rate $(\dot{\theta} + \dot{\phi})$ measured by the gyroscope. The algorithm formulation of the implemented Kalman filter is as follows.

Propagation
The estimator dynamics equation subject to the process noise ($w \sim N(0, Q)$) is given as:

$$\frac{d}{dt}\mathbf{x} = A_0\mathbf{x} + w \tag{7.24}$$

where the state vector $\mathbf{x}$ is defined as $\begin{pmatrix}\phi & \dot{\theta} & \dot{\phi}\end{pmatrix}^T$ and

$$A_0 = \begin{bmatrix}0 & 0 & 1\\ 0 & 0 & 0\\ 0 & 0 & 0\end{bmatrix} \tag{7.25}$$

The measurement equation incorporating both the gyro measurement and the ϕ angle measurement

from the F/T sensor results in

$$y = \begin{bmatrix} \text{gyro measurement} \\ \phi \text{ from F/T sensor} \end{bmatrix} = C\mathbf{x} + v = \begin{bmatrix} 0 & 1 & 1 \\ 1 & 0 & 0 \end{bmatrix} \begin{pmatrix} \phi \\ \dot{\theta} \\ \dot{\phi} \end{pmatrix} + v. \tag{7.26}$$

It is easily verified that the system is fully observable since

$$\begin{pmatrix} C \\ CA_0 \\ CA_0{}^2 \end{pmatrix} \rightarrow \begin{bmatrix} 0 & 1 & 1 \\ 1 & 0 & 0 \\ 0 & 0 & 1 \end{bmatrix} \tag{7.27}$$

has full rank.

The covariance matrix P is propagated by Euler integration:

$$\dot{P} = A_0 P + P A_0{}' + Q \tag{7.28}$$

where P is the error covariance matrix and Q is the covariance matrix of the process noise. Each update is performed whenever a new set of measurements is available. A F/T sensor measurement is updated at the rate of 30Hz while a new gyro measurement, filtered by a separate Kalman filter, is available at 20 Hz.

Measurement Update
The Kalman gain L_k and error covariance matrix P_k are updated at each measurement:

$$\begin{aligned} \hat{x}_k^+ &= \hat{x}_k^- + L_k(y_k - Cx_k^-) \\ L_k &= P_k^- C'[CP_k^- C' + R_k]^{-1} \\ P_k^+ &= (I - L_k C)P_k^-(I - L_k C)' + LR_k L' \end{aligned} \tag{7.29}$$

In order to achieve efficient performance of the Kalman filter, the noise parameters, $v \sim N(0, R)$ and $w \sim N(0, Q)$, must be properly estimated and tuned. By interpreting the frequency domain characteristics of the filter, we can find that the ratio Q/R largely determines a balance between the faster convergence of the estimator (larger Q/R), and less susceptibility to noise (smaller Q/R). The discrete covariance matrix of the sensor noise is found by $R_k = R/\Delta t$. For example, the noise covariance (R) of the gyroscope in continuous time is 0.0025 deg^2/s. By accounting for process noise w, the system can more readily deal with any deviations and ensure that the Kalman filter converges. We selected Q as diag$\begin{pmatrix} 0 & 0.01 & 0.04 \end{pmatrix}$ in order to sufficiently smooth out the noisy measurements, without compromising the filter performance. Future work in updating the current tethered-SPHERES testbed should be directed at tuning such parameters to improve the performance of the estimator. In the subsequent sections, we present experimental results that relied on the state estimator described in this section.

7.5 Experimental Results

The closed-loop experimental results are discussed in this section. We concentrate on examining the effectiveness of the decentralized control strategy introduced in Chapter 4 while validating the new relative metrology using a force-torque sensor.

7.5.1 Objective of Experimental Validation

As discussed in Section 1.2.6, many compelling reasons can be offered to articulate the importance of control experimentation. In the research and development cycle, control experiments can be used to improve the reliability, accuracy, repeatability and comprehensiveness of the dynamics modeling and controller. Furthermore, implementation issues and system-level integration of various subsystems

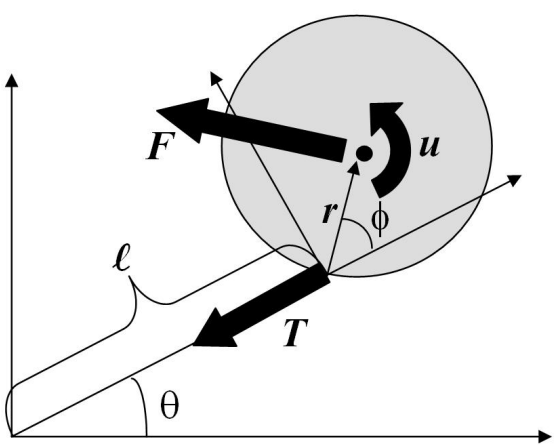

(a) Free-body diagram of a spinning singled-tethered SPHERES

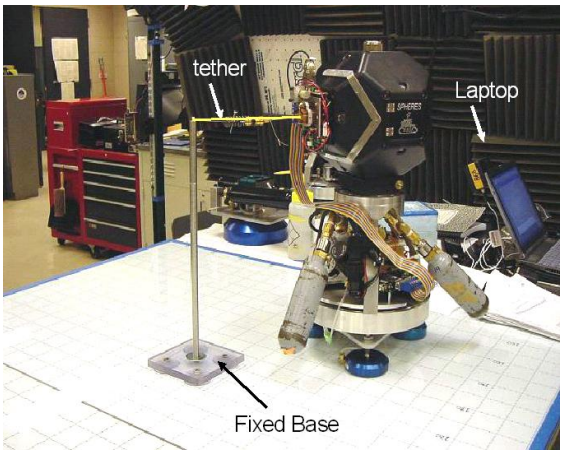

(b) Experimental setup

Figure 7-16: A spinning single-tethered SPHERES

can directly be addressed by developing an operational mode representative of real world spacecraft. More specifically, the aim of the control experiments for this dissertation can be stated as follows.

- to experimentally demonstrate the effectiveness of the decentralized nonlinear control framework introduced in Chapter 4 for spinning tethered formation flying arrays
- to investigate the feasibility and practicality of the proposed decentralized and relative estimator using a force-torque sensor and a gyroscope.

Even though we can still improve the overall performance by further tuning the control and estimator parameters, all tests described in this chapter show the effectiveness of the proposed decentralized strategy even in the presence of harsh disturbances (significant and irregular surface friction of the MSFC flat floor). Therefore, we can expect that the control techniques proposed in this dissertation will perform more efficiently in an ISS flight, which has a more realistic (zero-G) and much less dissipative environment.

7.5.2 Validation of Dynamics Modeling and Estimator

In this section, we briefly examine the accuracy of the nonlinear dynamics, and the efficiency of the proposed estimation strategy.

Dynamics Update With Physical Dissipation

A slightly modified form of the nonlinear equations of motion for the rotating single-tethered SPHERE in Figure 7-16 is presented:

$$\mathbf{M_1}(\phi)\begin{pmatrix}\ddot{\theta}\\ \ddot{\phi}\end{pmatrix} + \mathbf{C_1}(\phi,\dot{\theta},\dot{\phi})\begin{pmatrix}\dot{\theta}\\ \dot{\phi}\end{pmatrix} + \begin{bmatrix}k_1 & 0\\ 0 & k_2\end{bmatrix}\begin{pmatrix}\dot{\theta}\\ \dot{\phi}\end{pmatrix} = \begin{pmatrix}\tau_\theta\\ \tau_\phi\end{pmatrix} \tag{7.30}$$

where

$$\begin{aligned}
\mathbf{M_1}(\phi) &= \begin{bmatrix} I_r + m\ell^2 + 2mr\ell\cos\phi & I_r + mr\ell\cos\phi \\ I_r + mr\ell\cos\phi & I_r \end{bmatrix},\\
\mathbf{C_1}(\phi,\dot{\theta},\dot{\phi}) &= \begin{bmatrix} -mr\ell\sin\phi\dot{\phi} & -mr\ell\sin\phi(\dot{\theta}+\dot{\phi}) \\ +mr\ell\sin\phi\dot{\theta} & 0 \end{bmatrix}, \quad \begin{pmatrix}\tau_\theta\\ \tau_\phi\end{pmatrix} = \begin{bmatrix} r+\ell\cos\phi & 1 \\ r & 1 \end{bmatrix}\begin{pmatrix}F\\ u\end{pmatrix},\\
I_r &= I_G + mr^2
\end{aligned} \tag{7.31}$$

Note that we have added a viscous friction term with the diagonal matrix of k_1 and k_2, in order to account for the non-negligible friction between the flat floor and the air-bearing carriages. As shall be seen in the following discussion, the dynamics models such as (7.30), with the addition of the surface friction terms, correctly represent the real experimental setup.

Model Update

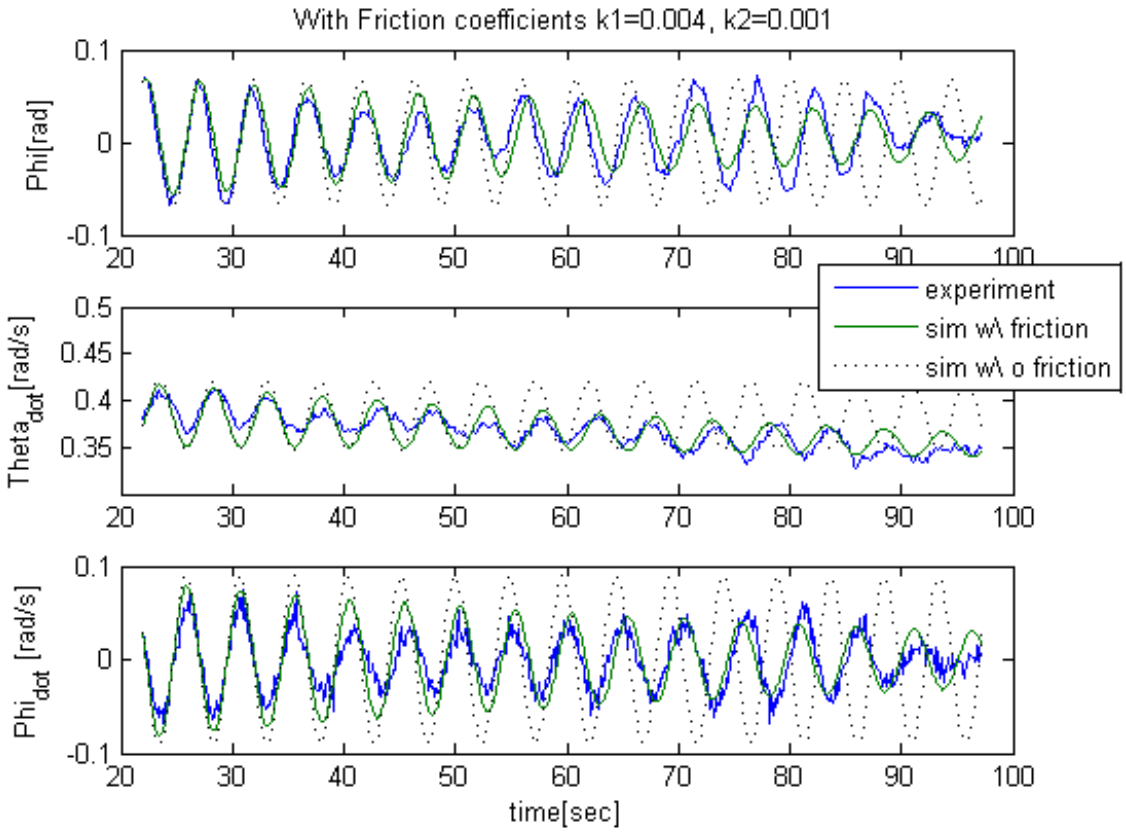

Figure 7-17: Free-rotation of single-tethered system. Experiment and Simulation

In order to evaluate the accuracy of dynamics modeling in this dissertation, the estimated system states are collected from a single SPHERES satellite, rotating freely ($F = 0, u = 0$) around a stationary post on the MIT glass table (see Figure 7-16(b)). It should be emphasized again that this single-tethered system becomes a basis model of the decentralized nonlinear control strategy for multi-vehicle tethered formation flying arrays, as described in Chapter 4.

Figure 7-17 compares the experimental data of a free rotation with the simulation prediction using Matlab-Simulink. The tether length (ℓ) used for the experiment is 0.25 m, and the overall mass (m) of the SPHERE satellite with the air-carriage is 20.35kg, as shown in Table 7.1. The radius of the SPHERE, r shown in Figure 7-16(a), needed to be amended since the tether attachment point is actually sticking off the SPHERES face by the depth of the tether reel, as shown in Figures 7-16(b) and 7-14. The correct r measures 0.15 m in length. The moment of inertia about CM, which was originally estimated by a three-string pendulum test and computation from the CAD model, was adjusted to account for the translation in the tether attachment point, resulting in I_G=0.178 kgm^2.

By setting up the same initial conditions for the system states, namely ϕ, $\dot{\theta}$ and $\dot{\phi}$, we can expect to see the simulation match the experimental data sufficiently well. This is not true in general,

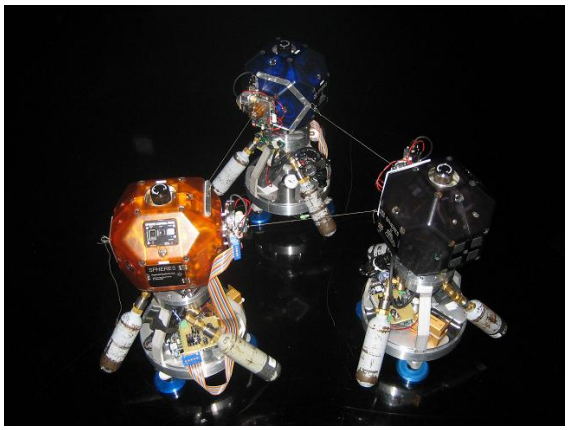

(a) Three triangular configuration

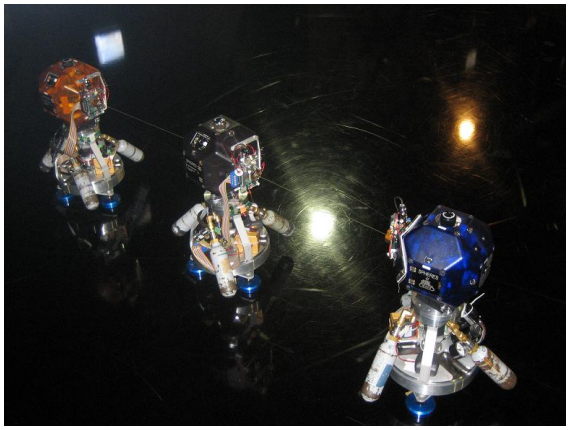

(b) Three-inline configuration

Figure 7-18: Test configurations at NASA MSFC, September 2006. The two-body formation is shown in Figure 7-22.

without physical dissipation taken into account. Due to the nature of the viscous friction of the airflow between the air-pucks and the flat floor, a simple velocity damping model is added as shown in (7.30). The friction coefficients k_1 and k_2 were carefully determined to match the experimental data by comparing the slopes of exponential decay. For this particular test, k_1 is found to be 0.004, and k_2 is 0.001. On the MSFC flat floor, k_1 and k_2 were once found to be 0.02 and 0.008, respectively. Even though these numbers depend to a large extent on the air pressure of the air-bearing pucks and the surface quality, the MSFC floor has friction coefficients larger than those of the MIT glass floor by a factor of five or more. The frequency obtained by (3.25) correctly predicted the actual oscillation frequency obtained from the gyro measurements. In essence, the simulation based upon the dynamics modeling matches the experimental data reasonably well, with the addition of the viscous friction model.

7.5.3 Overview of Control Experiments

We accomplished all necessary tests successfully at NASA MSFC during September 25-29, 2006, testing all configurations currently under investigation for SPECS (see Figure 7-18). Despite some hardware problems, we were able to successfully validate the effectiveness of our decentralized control and estimation algorithms.

One hardware problem that surfaced was critical. We discovered that the tether reel mechanism, when mounted on the expansion port, blocks transmission of the infrared (IR) signal from the master SPHERES satellite. This did not allow the master satellite to synchronize the ultrasound (US) metrology system. Therefore, no accurate measurement of the tether length ℓ was available. Note that no tether-motor encoder like the one in the new flight reel in Section 7.2.2, existed in the prototype version. However, we designed the two main attitude controllers as fault-tolerant systems with an intention to simulate sensor failures. As a result, we were able to demonstrate the efficacy of such a fault-tolerant control strategy under the circumstances with "actual" sensor failures: blocked IR signal and unavailability of ℓ. We also successfully performed all of our tests using this decentralization technique. In particular, we were able to increase the control bandwidth and reliability dramatically by eliminating the need for any inter-satellite communication.

The tested configurations included:

- Fully decentralized control and estimation for two-satellite, three-satellite-inline, and three-satellite-triangular (see Figure 7-19) configurations using both gain-scheduled LQR control (only using the reaction wheel) and nonlinear adaptive control, adapting to the model uncertainties like surface friction and tether length changes.

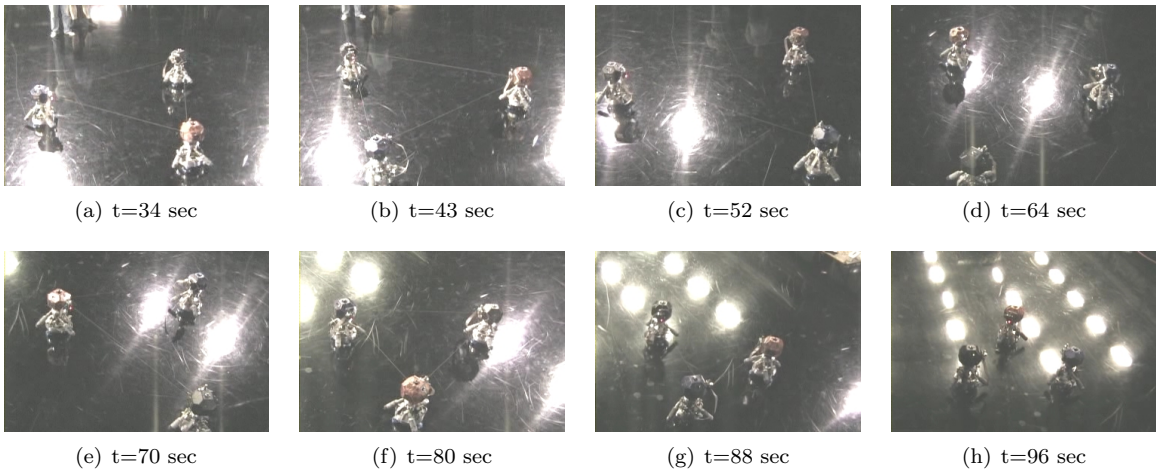

(a) t=34 sec (b) t=43 sec (c) t=52 sec (d) t=64 sec

(e) t=70 sec (f) t=80 sec (g) t=88 sec (h) t=96 sec

Figure 7-19: Control of three-triangular array

- Large diameter (4.6 m) three-satellite-inline with the nonlinear adaptive control.
- Two and three-SPHERE spin-up from zero initial conditions and deployment maneuvers starting completely docked.

To our knowledge, the experiments performed at NASA MSFC are the first experimental validation of tethered formation flight using

- Nonlinear/linear decentralized control and estimation.
- Control of a three-satellite-inline configuration.
- Development of a force sensor based attitude estimator.
- Reaction-wheel-only underactuated attitude control for all configurations.
- Decentralized fault-tolerant adaptive control under sensor failures.

In conclusion, the experimental results indicate that the proposed decentralized control strategy can be implemented in future tethered systems like SPECS, thereby reducing the complexity of hardware and software of the attitude control system significantly. We present some closed-loop experimental results in the subsequent sections.

7.5.4 Decentralized Gain-Scheduled LQR Control

Our approach to reduce the complexity of controlling multiple spacecraft connected by tethers is decentralization by oscillation synchronization. We successfully performed all of our tests using this decentralization technique. In this manner, we were able to dramatically increase the control bandwidth and reliability by eliminating the need for inter-satellite communications.

Figures 7-20 and 7-21 show the experimental data of a spin-up and deployment maneuver on the NASA MSFC flat floor, using two tethered SPHERES controlled using decentralized control laws. Still pictures from the video of the same test are presented in Figure 7-22. Such a maneuver emulates a possible mission scenario in which a completely docked, tethered-spacecraft array is deployed from a mother spacecraft. All the data was transmitted to the laptop computer at the frequency of 10 Hz in realtime via the wireless RF communication. It should also be noted that all the state estimates are delivered from the Kalman filter, which incorporates both the F/T sensor measurements and the angular rates from the gyroscope, described in Section 7.4.5. The controller implemented in this test was a decentralized gain-scheduled LQR controller running at 100 Hz. The scheduled LQR gain

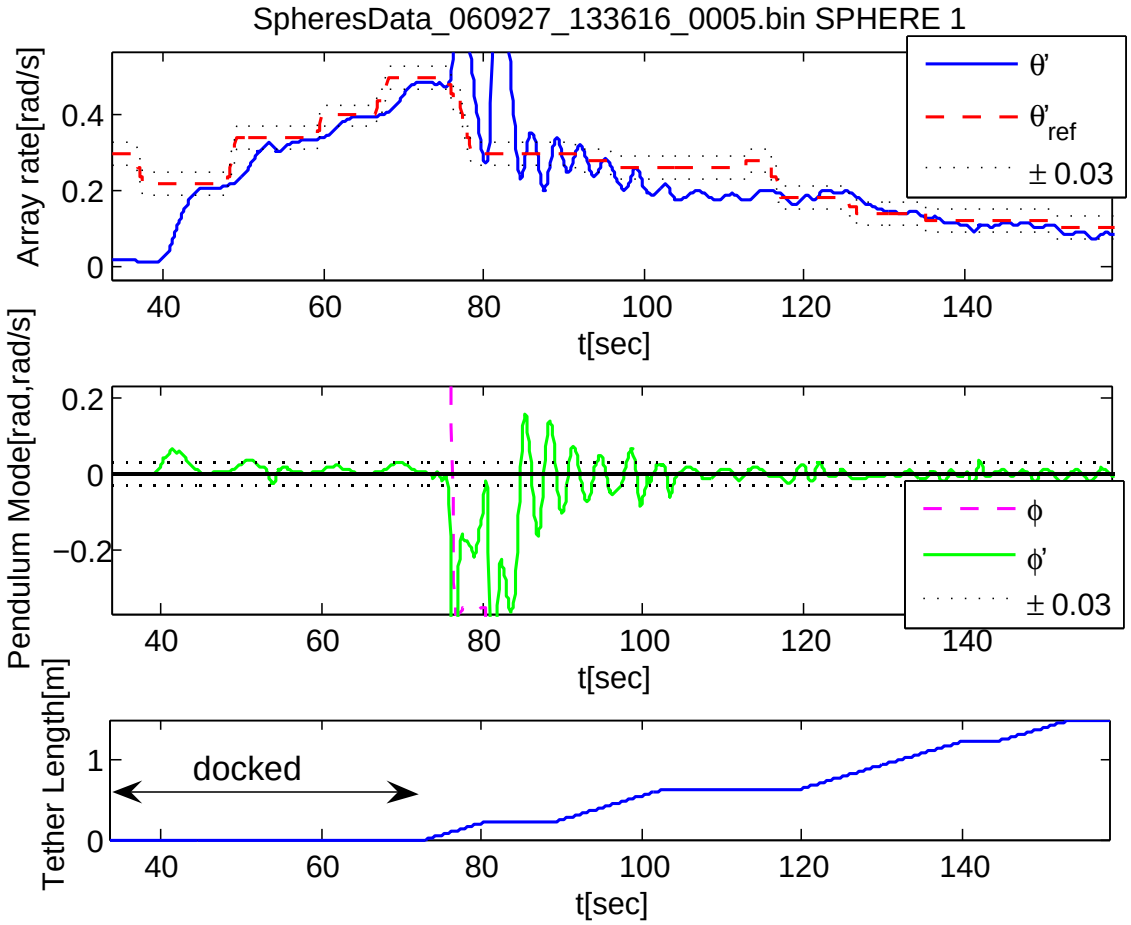

Figure 7-20: State estimates and commands from SPHERE #1 during spin-up and deployment of the two-satellite tethered formation using gain-scheduled LQR

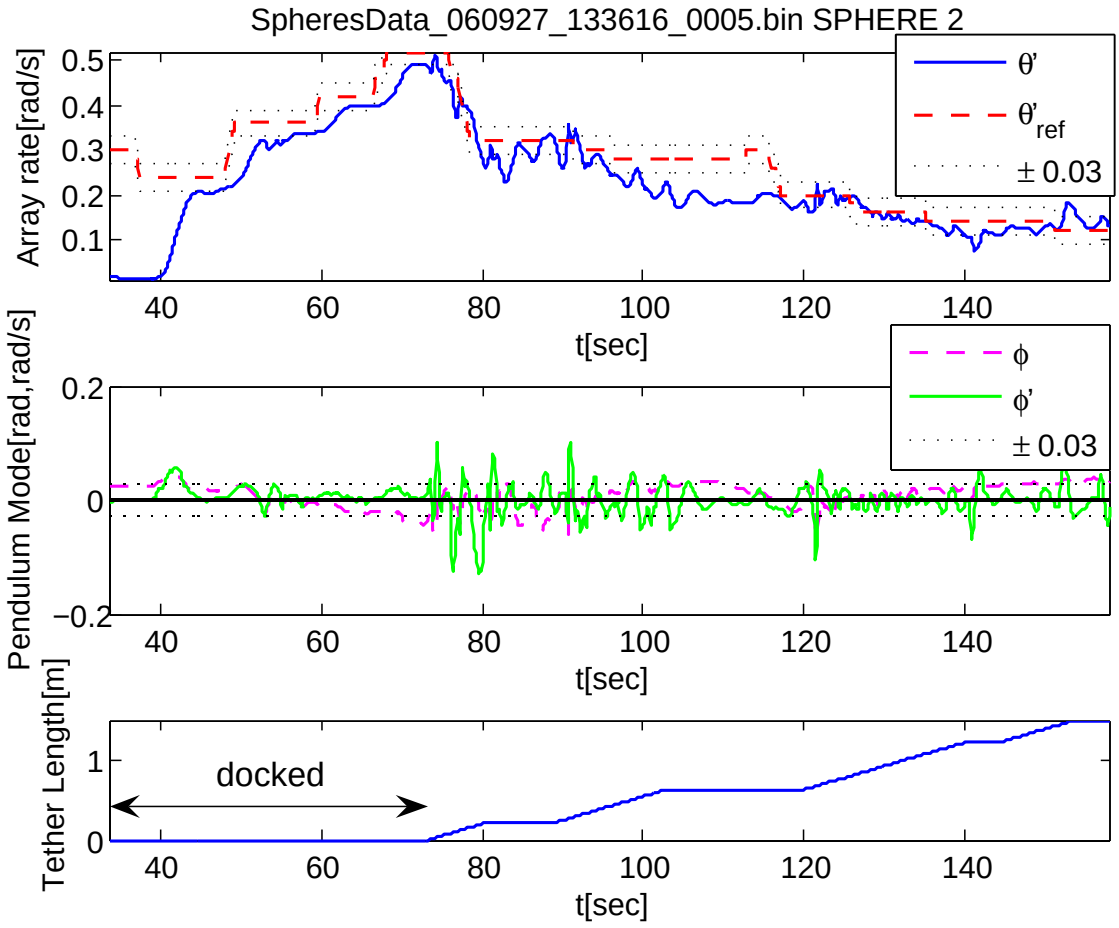

Figure 7-21: State estimates and commands from SPHERE #2 during spin-up and deployment of the two-satellite tethered formation using gain-scheduled LQR

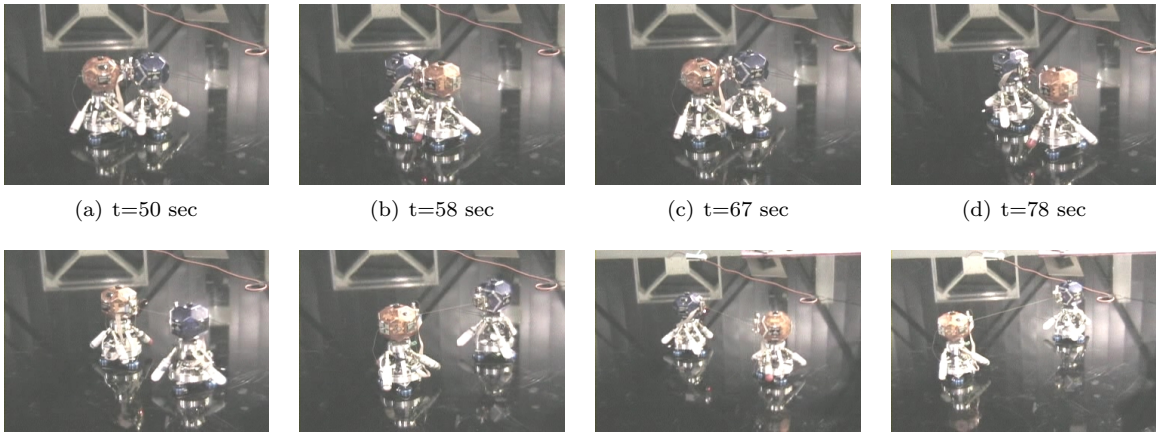

(a) t=50 sec (b) t=58 sec (c) t=67 sec (d) t=78 sec

(e) t=85 sec (f) t=95 sec (g) t=110 sec (h) t=130 sec

Figure 7-22: Two-SPHERES spin-up maneuver

is a continuous function of $\dot{\theta}$ but a discrete function of ℓ. This controller is significant in its own right, since it validates the feasibility of the minimal fuel control approach by controlling all the relevant degrees of freedom, including the array spin rate, using only the reaction wheels (see the underactuated control approaches in Chapter 6).

The top plot of Figures 7-20 and 7-21 shows the actual array angular rate ($\dot{\theta}$) as it is commanded to follow a desired trajectory ($\dot{\theta}_{ref}$). For SPHERE #1, the RMS of the error between $\dot{\theta}$ and $\dot{\theta}_{ref}$ after the initial spin-up (t≥44.8 sec) is 0.04 rad/s, ignoring the transient period (t=75-86 sec), which occurred due to the abrupt movement of the tether motor at 75 seconds. Such an undesirable response arises due to two problems: the initial stiction of the tether motor and the occasional tangling of the tether on the motor spool. These issues will be resolved in the new flight version described in Section 7.2.2. Nevertheless, the tracking error remained effectively well within ± 0.03 rad/s (1.7 deg/s) at the steady-state. During the period of t=100-112 sec, both the satellites were spinning on a particularly rough portion of the floor, thereby degrading the tracking performance.

While tracking the desired trajectory, the controller minimizes the compound pendulum motions ($\phi, \dot{\phi}$), shown in the middle plot of each figure. The ϕ and $\dot{\phi}$ before 75 sec should be discarded since the two SPHERES were docked, thereby preventing compound pendulum motion. The estimated tether length (ℓ) in the bottom plot indicates that the two SPHERES were completely docked when they started from rest ($\dot{\theta} = 0$) at 34 seconds. The estimated tether length was computed off-line from the On/Off time-history of the tether motor, since range measurements from the U/S system were not available in realtime due to the blocked IR transmission.

The RMS errors of the compound pendulum mode, ignoring the rough period (t=75-86 sec) are found to be smaller than 0.03 rad/s (1.7 deg/s). In particular, the bearing angle $\dot{\phi}$ for SPHERE #1 remained within ± 0.03 rad/s (1.7 deg/s) for 91% of the time span while the ϕ measurement failed for some unknown reason. The particular LQR controller implemented in this test had a zero ϕ gain, thereby minimizing the effect of such a sensor failure. For SPHERE #2, ϕ remained within the bound of ± 0.03 rad for 90% of time, while $\dot{\phi}$ remained within ± 0.03 rad/s for 91.3% of time. The experimental results of the decentralized LQR control are further analyzed in the next section.

7.5.5 Further Analyses

Even though the above results show the controller effectively tracking a desired trajectory under various conditions, the harsh surface friction and its irregularity depending on location, makes it difficult to identify the sources that degrade the control performance. As a result, the following control experimental results collected from the MIT glass table are presented for further analysis.

Figure 7-23 describes a single-SPHERE control experiment using the gain-scheduled LQR controller. The test starts with the SPHERE freely rotating around a stationary post (see Figure 7-16(b)). The control torque is turned on at t=85 sec. The figure shows a successful regulation of the angular rate $\dot{\theta}$ to the target rate of 0.3 rad/s, while minimizing the compound pendulum mode, ϕ and $\dot{\phi}$. More specifically, the RMS errors of ϕ and $\dot{\phi}$ at the steady state (t=100-180 sec.) are 0.0175 rad and 0.009 rad/s, respectively. We can also state that the $\dot{\phi}$ error remained within ± 0.015 rad/s for 91% of the time, which resulted in more than 25dB of attenuation of the compound pendulum oscillation. The tracking error between the target angular rate 0.3 rad/s and $\dot{\theta}$ has a RMS error of 0.0055 rad/s. In essence, the performance of the LQR control on the glass table is much more efficient, compared to the results obtained at the NASA MSFC flat floor shown in Figures 7-20 and 7-21. We can attribute this difference to the higher surface friction of the NASA MSFC flat floor.

7.5.6 Decentralized Nonlinear Control

A nonlinear control approach based on Input-State Feedback Linearization [178] is employed when the system is fully actuated (i.e. both thruster force F and torque u are available as control inputs). This computed torque controller is given as:

$$\tau_{\mathbf{1}} = \mathbf{M_1}(\mathbf{q})(\ddot{\mathbf{q}}_{\mathbf{d}} - 2\mathbf{\Lambda}\dot{\tilde{\mathbf{q}}} - \mathbf{\Lambda}^2\tilde{\mathbf{q}}) + \mathbf{C_1}(\mathbf{q}, \dot{\mathbf{q}})\dot{\mathbf{q}} \tag{7.32}$$

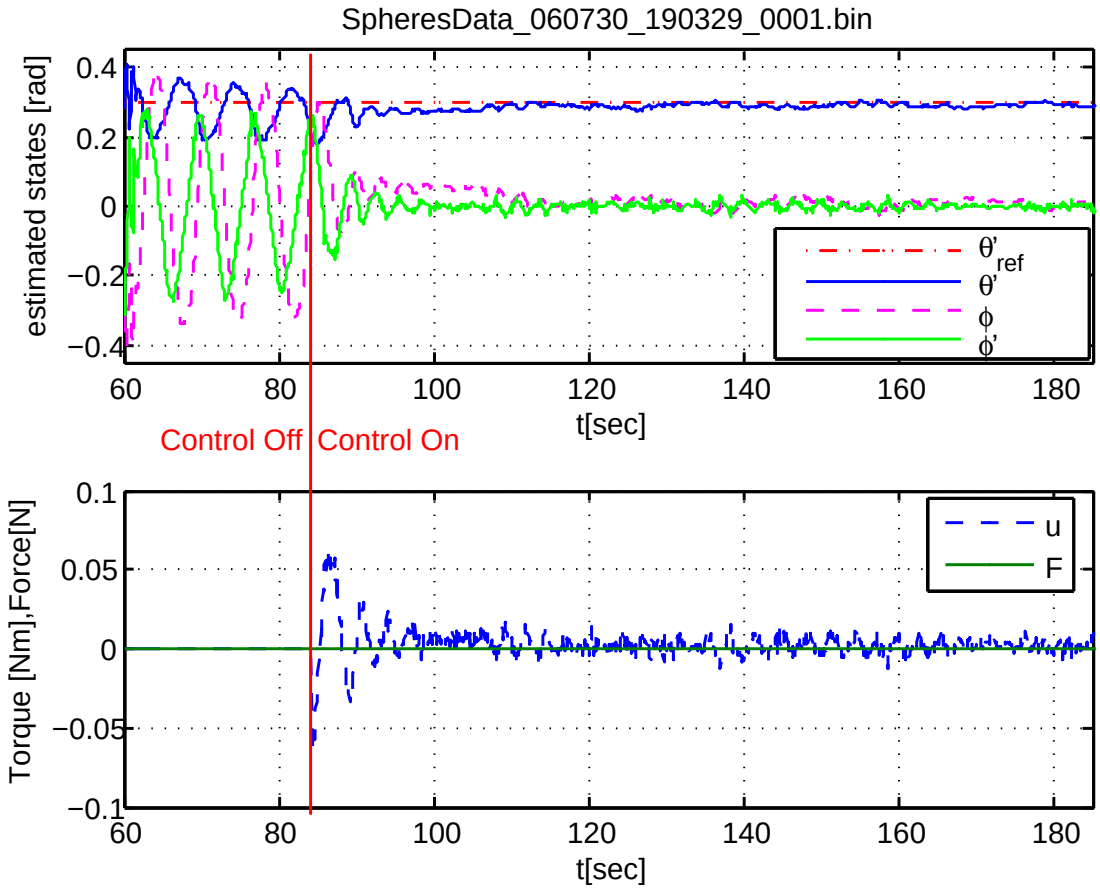

Figure 7-23: Gain-Scheduled LQR control on the MIT glass table

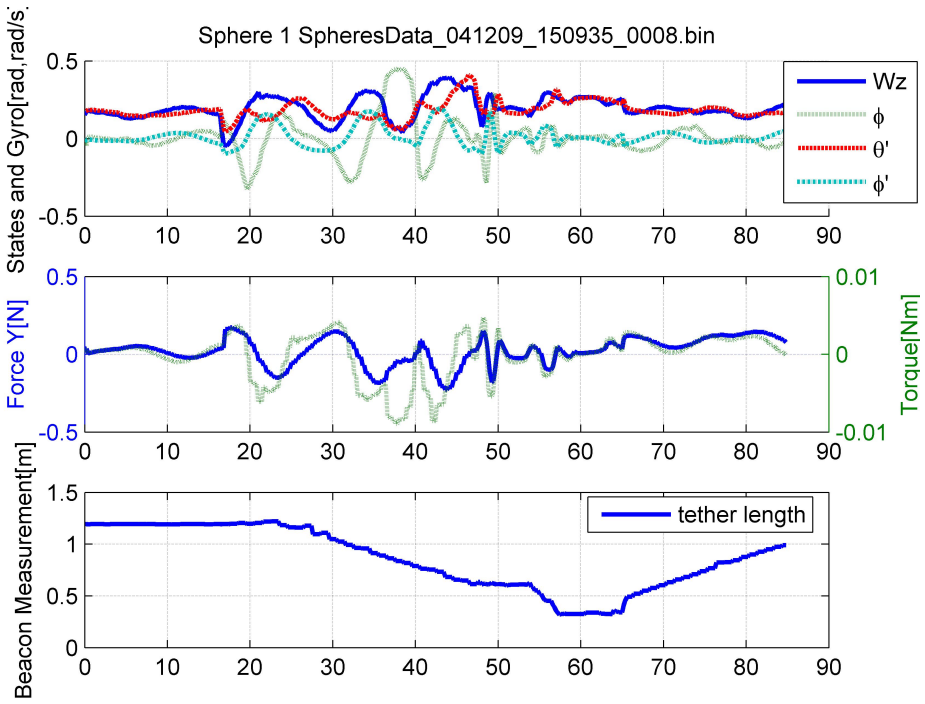

Figure 7-24: nonlinear controller with varying tether length in a two-body array, 1st SPHERES

which is equal to the controller in (4.12) with $\mathbf{K} = \mathbf{M_1}\mathbf{\Lambda}$ and $\dot{\mathbf{q}} \to \dot{\mathbf{q}}_\mathbf{r}$. Likewise, the controller for the second spacecraft can be similarly defined.

If the objective of the control is to spin up the interferometric array to the target angular rate ω, while minimizing the compound pendulum mode, the desired trajectory is defined as

$$\dot{\theta}_d = (\omega - \dot{\theta}_0)(1 - e^{-\tau t}) + \dot{\theta}_0, \quad \ddot{\theta}_d = (\omega - \dot{\theta}_0)\tau e^{-\tau t}, \tag{7.33}$$

$$\ddot{\phi}_d = 0, \quad \dot{\phi}_d = 0, \quad \phi_d = 0. \tag{7.34}$$

This will lead to an exponentially stable closed-loop set of dynamics, $\ddot{\tilde{\mathbf{q}}} + 2\mathbf{\Lambda}\dot{\tilde{\mathbf{q}}} + \mathbf{\Lambda}^2\tilde{\mathbf{q}} = 0$.

Figure 7-24 and 7-25 show the experimental data when this nonlinear controller is implemented on a two-body formation (see Figure 7-22). The lowest plot in both figures represents the tether length measured directly using the ultrasound ranging system. It is observed that the compound pendulum mode $(\phi, \dot{\phi})$ gets excited when the tether reels in, as predicted in Section 3.3.8. Note that the effect of varying the tether length, or the speed, $\dot{\ell}$ was not considered in the nonlinear model. So better performance is achievable by taking into account the motor speed $\dot{\ell}$.

Note that this nonlinear control result from a two-body formation was performed with the previous generation of the hardware. Therefore, neither the reaction wheel actuator nor the F/T-sensor estimator were available. With the addition of the reaction wheel, the overall weight of the system increased three-fold. During the experiments at NASA MSFC with the new hardware, finding the friction coefficients by offline analyses turned out to be cumbersome and time-consuming. More importantly, the friction coefficients significantly varied depending on location, air-carriage pressure and so on. Therefore, we focused on the nonlinear adaptive control, which not only adapts to the changes of physical parameters such as ℓ but also the friction coefficients.

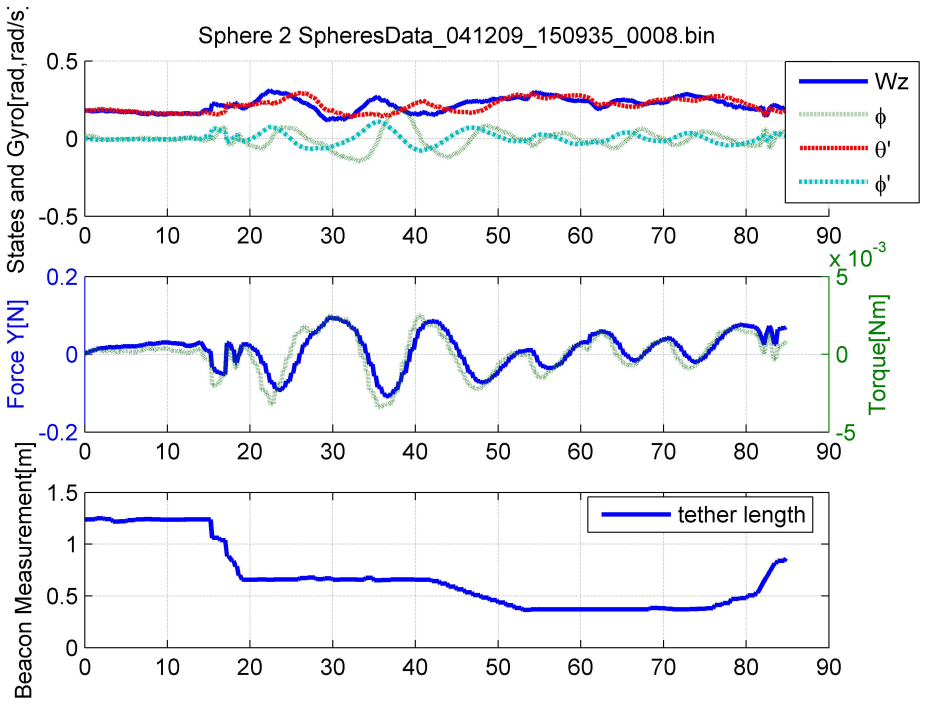

Figure 7-25: Nonlinear controller with varying tether length in a two-body array, 2nd SPHERES

7.5.7 Decentralized Nonlinear Adaptive Control

The nonlinear adaptive controller was designed such that it can overcome model uncertainties including: tether length change, floor surface friction, mass and inertia changes due to lack of precise modeling, and inherent mass change due to thruster firing. The proposed nonlinear adaptive controller was able to adjust its control output by adapting to the reasonably slow tether length changes. More importantly, through its online tuning, it was able to efficiently adapt to the rough and irregular surface of the NASA MSFC flat-floor. This controller used both thruster and reaction wheel control.

The nonlinear adaptive control adapted to all mass, inertial, and friction changes online and was particularly successful for the fully actuated control using both thrusters and reaction wheels. The friction of the floor did not have to be found a priori; for our 2004 MSFC experiments, finding the correct friction coefficients off-line was time-consuming but indispensable in achieving effective performance.

Recall the decentralized nonlinear adaptive controller for a circularly connected array:

$$\tau_i = \mathbf{Y}_i\hat{\mathbf{a}} - \mathbf{K}\mathbf{s}_i = \hat{\mathbf{M}}_\mathbf{1}\ddot{\mathbf{q}}_\mathbf{ir} + \hat{\mathbf{C}}_\mathbf{1}\dot{\mathbf{q}}_\mathbf{ir} - \mathbf{K}\mathbf{s}_i \tag{7.35}$$

where $\mathbf{s}$ denotes the composite variable $\mathbf{s}_i = \dot{\mathbf{q}}_i - \dot{\mathbf{q}}_{ir}$ with $\mathbf{q}_i = \begin{pmatrix}\theta & \phi_i\end{pmatrix}^T$.
In addition to three unknown physical parameters (I_G, m, and ℓ), the above adaptive control adapts to the slow changes of the surface friction coefficients, k_1 and k_2 from (7.30), in real-time. The unknown parameters are represented by a vector, $\mathbf{a}$ such that

$$\mathbf{a} = \begin{pmatrix} a_1 \\ a_2 \\ a_3 \\ a_4 \\ a_5 \end{pmatrix} = \begin{pmatrix} I_G + mr^2 + m\ell^2 \\ I_G + mr^2 \\ mr\ell \\ k_1 \\ k_2 \end{pmatrix} \tag{7.36}$$

We update the parameter estimates $\hat{\mathbf{a}}$, according to the following correlation integrals

$$\dot{\hat{a}}_i = -\mathbf{\Gamma} \mathbf{Y}_i^T \mathbf{s}_i \tag{7.37}$$

For each spacecraft, the new $\mathbf{Y}$ matrix is defined as

$$\mathbf{Y} = \begin{bmatrix} \ddot{\theta}_r & \ddot{\phi}_r & 2\cos\phi\ddot{\theta}_r + \cos\phi\ddot{\phi}_r - \sin\phi\dot{\phi}\dot{\theta}_r - \sin\phi(\dot{\phi}+\dot{\theta})\dot{\phi}_r & \dot{\theta}_r & 0 \\ 0 & \ddot{\theta}_r + \ddot{\phi} & \sin\phi\dot{\theta}\dot{\theta}_r & 0 & \dot{\phi}_r \end{bmatrix} \tag{7.38}$$

As discussed in Chapter 4, it is straightforward to show that the decentralized adaptive control law globally and asymptotically stabilizes the tethered spacecraft array. For example, Figure 7-26 shows an experimental result using this adaptive control law. At $t = 40$ sec, the controller is turned on, and the states asymptotically converge without any a-priori information about the physical parameters (ℓ, m, and I_G).

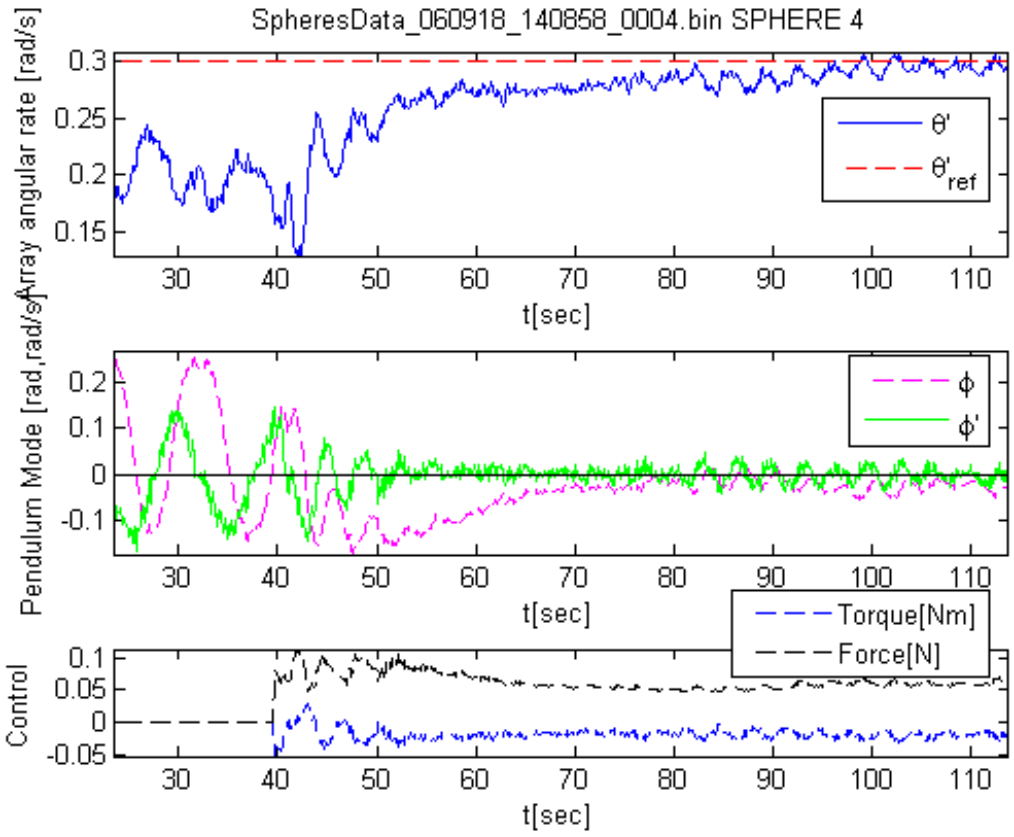

Figure 7-26: Experimental result using the adaptive control on the single-tethered system

7.6 Conclusions

This chapter has described the hardware development and experiments that were carried out to demonstrate the effectiveness of the proposed dynamics modeling, nonlinear decentralized control, and relative sensing. It should be noted that considerable effort has been concentrated on the development of the new tethered formation flying testbed using the SPHERES nano-satellites. The newly developed hardware includes a reaction-wheel air-carriage that provides substantially more torque than the thrusters of SPHERES. In particular, the new relative sensing mechanism using a 6DOF

force-torque sensor and gyroscope is devised and validated in the closed-loop control experiments. Our approach to control multiple spacecraft connected by tethers seeks a systematic way of reducing the complexity by oscillation synchronization. We successfully performed all of our tests using this decentralization technique. In this manner, we were able to dramatically increase the control bandwidth and reliability by eliminating the need for any inter-SPHERES communication. The tested configurations include two-satellite, three-satellite-inline and three-satellite-triangular arrays. While the reaction-wheel-only LQR control law validated the new method that enabled propellant-free attitude control, the decentralized nonlinear adaptive control could overcome model uncertainties such as tether length and surface friction changes. Video clips of the control experiments described in this chapter can be downloaded at *http://ssl.mit.edu/spheres/videos.html*.

Chapter 8

Conclusions and Recommendations

This chapter provides a brief summary of the thesis. The major contributions in the five areas are highlighted. Recommendations for further work are also made in the areas of control theory and hardware development.

8.1 Thesis Summary and Contributions

NASA's SPECS (Submillimeter Probe of the Evolution of Cosmic Structure) mission [77, 118, 61] is proposed as a tethered formation flight interferometer that detects submillimeter-wavelength light from the early universe. This dissertation identifies the inherent nonlinearity, complexity and cross-coupling of the multi-vehicle dynamics as several of the key technological gaps that need to be bridged for the success of the future tethered spacecraft missions like SPECS. To deal with such difficulties, this dissertation presents a new model reduction and decentralization strategy using synchronization. Additionally, we leverage the synchronization strategy for tethered formation flight for the benefit of other forms of dynamical networks such as multi-robot coordination and formation flying of aerospace vehicles.

Nonlinear Stability Analysis and Control by Contraction Theory

Chapter 2 illuminates some principal analysis tools and control strategies for highly nonlinear dynamics. The dynamics modeling using the Euler-Lagrangian formulation is preferred throughout the entire thesis due to its simplicity. For example, we show that the dynamics of a two-link manipulator robot can be reduced to the dynamics of a single-tethered spinning satellite. Also, the positive definite inertia matrix and symmetry of the nonlinear systems play a central role in our stability analysis and control synthesis. This dissertation uses contraction theory [176, 112, 202, 114], which uses a slightly different notion of stability- a system is stable in some region if initial conditions or temporary disturbances are somehow forgotten [112]. Lyapunov's linearization method indicates that the local stability of the nonlinear system can be analyzed using its differential approximation. What is new in contraction theory is that a differential stability analysis can be made exact, thereby yielding global and exponential convergence results in nonlinear systems. Dynamic combinations validated by contraction theory, such as hierarchical combinations, parallel combinations, and synchronized coupled oscillations, are explored to simplify the nonlinear dynamics of multiple dynamical systems.

Dynamic Modeling with Focus on the Compound Pendulum Mode and Spatial Decoupling

Chapter 3 introduces the dynamics equations of planar motion of the tethered formation flying spacecraft considered in the thesis. We pay particular attention to control of oscillations of the compound pendulum mode inherent in tethered formation flight satellites. Previously, the instability of the tether retrieval is usually discussed in the context of two point masses connected by a single

tether [101]. The representative work on tethered formation flight [55, 94, 26, 27, 132, 144] does not include this mode, by assuming that the spacecraft can be regarded as a point mass with a long tether. However, it is indispensable to examine this mode because of the instability occurring while retracting the tether for spinning arrays. The rationale behind the reduced dynamics modeling on the two-dimensional plane is that the symmetry of a spinning array can be exploited to decouple the rotational in-plane motions (aperture pupil plane) from the out-of-plane motions. In particular, the stability and controllability analyses, in conjunction with the compound pendulum modes of the tethered arrays, constitute the main contributions of Chapter 3. In addition, the dynamics modeling in Chapter 3 facilitates nonlinear spatial decoupling of multiple-spacecraft coupled arrays.

Decentralized Nonlinear Control by Oscillation Synchronization

In Chapter 4, we introduce a decentralized control technique by reducing the original dynamics to simpler stable closed-loop dynamics by exploiting oscillation synchronization. Contraction theory proves that a decentralized control law can be designed based on a single-tethered system in lieu of the coupled dynamics of multiple spacecraft, reducing the computation and communication burdens. Furthermore, the nonlinear stability of the combined system is global and exponential. The technique is extended to a three-spacecraft inline configuration and a triangular configuration, both of which are being studied for NASA's SPECS mission. The proposed decentralized control strategy is further extended to robust adaptive control to account for model uncertainties. Results of numerical simulations and experiments using the SPHERES testbed show the effectiveness of the proposed control strategy.

New Synchronization Tracking Control Law for Network Systems with Highly Nonlinear Dynamics

Chapter 5 proves global exponential convergence of the new synchronization tracking control law that can easily be applied to cooperative control of multi-agent systems and oscillation synchronization in robotic manipulation and locomotion. The proposed control law requires only local coupling feedback for global exponential convergence. By avoiding all-to-all coupling, communication burdens and complexity can be reduced. It should be emphasized that exponential stability of the synchronization of multiple robots is studied using contraction theory. Contraction analysis, overcoming a local result of Lypunov's indirect method, yields global results based on differential stability analysis. Exponential synchronization enables reduction of multiple dynamics into a simpler form thereby simplifying the stability analysis. Simulation results show the effectiveness of the proposed control strategy. The proposed bi-directional coupling is also generalized to permit partial-joint coupling and uni-directional coupling. Further extensions to PD coupling, time-delayed communications, adaptive synchronization and concurrent synchronization are also presented.

Exploiting Tether-Coupling to Derive Propellant-Free Attitude Control Strategies

Chapter 6 investigates the feasibility of controlling the array spin rate and relative attitude without thrusters. To our knowledge, this work reports the first propellant-free underactuated control results for tethered formation flying spacecraft. This chapter also fulfills the potential of the proposed strategy by providing a new momentum dumping method without torque-generating thrusters. Such a tethered system without thrusters is underactuated since it has fewer inputs than configuration variables. In contrast with linear systems, in which an underactuated control law can be synthesized easily, designing a nonlinear controller for nonlinear underactuated systems poses a challenge, mainly due to lack of full state feedback linearizability. We exploit gain-scheduling linear control, partial feedback linearization, feedback linearization via momentum decoupling, and backstepping. The simulation results indicate that the nonlinear control techniques demonstrate more efficient tracking performance than the LQR control, whose performance deteriorates as the tether length increases.

Experimental Validation of Tethered Formation Flight and Development of Relative Metrology System using Force-Torque Sensor

Chapter 7 describes the hardware development and experiments that were carried out to demonstrate the accuracy and effectiveness of the dynamics modeling, nonlinear decentralized control, and relative sensing that are introduced in this thesis. It should be emphasized that a great deal of effort has been concentrated on the development of the new tethered formation flying testbed using the SPHERES nano-satellites. The newly developed hardware includes a reaction-wheel air-carriage which provides substantially more torque than the thrusters of SPHERES. In particular, the new relative sensing mechanism, using a 6-DOF force-torque sensor and gyroscope, is devised and validated in the closed-loop control experiments. Our approach to control multiple spacecraft connected by tethers seeks a systematic way of reducing the complexity by oscillation synchronization. In particular, we validated experimentally that the decentralized linear and nonlinear control laws, designed from the single-tethered system, can also stabilize two-satellite, three-satellite-inline, and three-satellite triangular arrays. We successfully performed all of our tests using this decentralization technique. In this manner, we were able to dramatically increase the control bandwidth and reliability by eliminating the need for any inter-SPHERES communication.

Summary of Contributions

The five unique contributions of this dissertation are summarized below.

- Developed a decentralized nonlinear control technique by reducing the original dynamics into simpler stable dynamics by exploiting oscillation synchronization.
- Presented the dynamic models for the attitude dynamics of tethered formation flight, which focuses on the compound pendulum mode and spatial decoupling of multiple spacecraft.
- Exploited the coupled-dynamics to develop propellant-free attitude control laws. This work reports the first underactuated control results for tethered formation flight.
- Established a new synchronization framework for dynamic networks consisting of highly nonlinear dynamics. The proposed scheme is much simpler than earlier work in terms of both the computational load and the required signals while yielding global and exponential convergence.
- Developed the tethered satellite formation flight testbed for control experimentation. A new relative attitude metrology system that incorporates the gyro, force-torque sensor, and ultrasound ranging measurements has also been devised and validated experimentally.

8.2 Recommended Future Work

Recommendations for future work can be broken into two categories.

8.2.1 Further Theoretical Work

For the tethered formation flight problem, recommended future work mainly lies with the issue of increasing the fidelity of the dynamic models. The following work can be suggested:

- We can fully take into account the tether vibrations (transverse and longitudinal) in developing decentralized nonlinear control methodologies. Examining the effectiveness of the decentralized control laws under such tether vibrations would provide more conclusive results.
- The investigation of the influence of unmodeled disturbances, such as weak gravity variations at the L2 point can easily be performed. This dissertation provides a possible solution to a variety of disturbances and uncertainties. However, further modeling efforts are required to examine the efficiency of the robust adaptive control strategy that copes with parametric and non-parametric uncertainties.

- We can also extend the nonlinear underactuated control approach in Chapter 6 to variable-length tethers. In addition, since the attitude dynamic modeling has been confined to the 2D rotational plane, taking into account the three-dimensional attitude dynamics of tethered formation flight would pose a challenging underactuated control problem. In particular, the pointing and retargeting maneuver using the precession associated with the array rotation would provide an interesting research topic.

Additional theoretical work can be conducted in the following areas:

- Synchronization of underactuated mechanical systems:
  The synchronization framework in Chapter 5 is based upon the assumption that the nonlinear dynamical models are fully actuated. Hence, one immediate extension of the work is to develop a synchronization framework which can be applied to underactuated mechanical systems, which have fewer actuators than configuration variables.

- Even though robustness properties of nonlinear control with respect to bounded deterministic disturbances are well understood, examining the performance of nonlinear control in the presence of unbounded stochastic disturbances largely remains to be an open problem. In [58], stabilization of stochastic nonlinear systems is discussed. Similar work can be performed with focus on the attitude dynamics of tethered formation flight, which encompasses both the nonlinear rigid dynamics and the flexible vibration of the tether.

- The resulting closed-loop system with a negative-definite Jacobian matrix is one of the important aspects of backstepping design (see Chapter 6 and [100]). It should be noted that a similar discussion automatically leads to contraction analysis introduced in Section 2.5. Establishing a systematic connection between contraction analysis and backstepping is an interesting area of future work.

8.2.2 Suggested Improvements for Tethered SPHERES

- The significant and irregular surface friction of the MSFC flat floor was particularly problematic. Conducting additional experiments on a new MIT SSL flat floor is essential since the new facility will provide a larger operational area than the MIT glass table. Moreover, the surface friction will be significantly lower than that of the MSFC flat floor.

- During the experiment conducted for this dissertation, maintaining a constant tether speed was a difficult task due to the low reliability of the tether motor, and tangling of the tether on the spool. A new flight tether reel in Figure 7-4 is expected to solve such problems by using a high precision motor and a sophisticated reel mechanism. In addition, the encoder of the tether motor will be able to measure the tether length more accurately.

- The control techniques proposed in this dissertation are expected to perform more efficiently in the International Space Station (ISS), which has a more realistic (zero-G) yet much less dissipative environment. During the process of sizing the reaction wheel, various scenarios were considered to spin up the array to various baseline lengths either on a flat floor or in ISS. It was concluded for this dissertation work that the most logical way to progress with the reaction wheel design was to build and test a system that only functions on the flat floor. The follow-up work can be performed to equip the SPHERES testbed with a 3-DOF reaction wheel assembly for ISS flight experiments.

Appendix A

Analytical Solution of Torsional Vibrations of Tapered Tether

The analytical exact solutions for the natural frequencies and mode shapes of clamped-free torsional rods with linearly varying circular cross-sections are obtained and proven to agree with the numerical predictions by the finite element method. The difference between the natural frequencies of a uniform rod and a tapered rod is pronounced in the low modes but decreases as the mode number increases.

A.1 Introduction

Figure 1 shows a clamped circular shaft with the varying diameter, $D(x) = D_0(2 - a\frac{x}{L})$. If the tapering slope, a equals zero, the rod becomes a rod with the uniform diameter of $2D_0$. This brief note presents the analytical solutions for nonzero tapering slopes, obtained while the author took a graduate-level structural dynamics class at MIT. It is noted that the exact formulas for torsional shafts with varying cross-sections are not found in the well-known books [21, 153, 163]. Blevin [21] discusses only linearly tapered cantilever beams for bending with the numerical plots [120] without explicit formulation. Pilkey [153] also suggests to use the displacement method or transfer matrix procedure for torsional bars with variable section properties. The stress at any section is given with sufficient accuracy by the formulas for uniform bars [163], but the natural frequencies can become significantly different as will be shown here. More recently, Chen [38] shows that the natural vibration frequency of a torsion cylinder with varying cross section and an adhesive mass can be obtained from the zeros of a target function, which is found numerically from the governing ordinary differential equation. One objective of this appendix is to present an analytical solution to structural dynamics courses by complementing the existing formulas for uniform sections. It also provides an exact closed-form solution to verify approximate methods such as the Finite Element Method (FEM).

A.2 Solution By Numerical Method

The easiest approach is the displacement method based on the principle of complementary virtual work. Given a clamped end condition, the influence coefficients can be calculated from:

$$\text{Unit Torque, } T \text{ at } x_j = GJ(x)\frac{\partial\theta}{\partial x} = 1 \tag{A.1}$$

or

$$\frac{\partial\theta}{\partial x} = \frac{1}{GJ(x)} \tag{A.2}$$

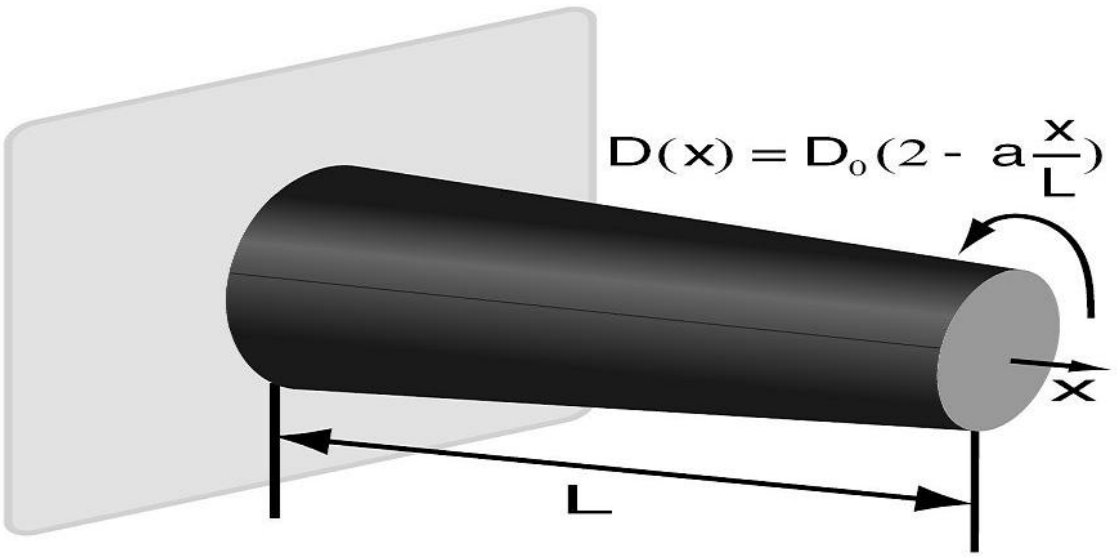

Figure A-1: Linearly Tapered Torsional Rod Clamped at One End

where G is the shear modulus of the elasticity with $J(x)$ denoting the polar mass moment of inertial per unit length.

By the geometry from Figure 1, $J(x)$ is calculated as follows:

$$J(x) = \frac{1}{32}\pi D(x)^4 = \frac{\pi {D_0}^4}{32}\left[2 - a\frac{x}{L}\right]^4 \tag{A.3}$$

where $0 < a < 2$ for nonnegative diameters.

Integrating Eq. (A.2) after inserting Eq. (A.3) yields:

$$\theta(x) = \int_0^x \frac{1}{G\frac{\pi}{32}\left[D_0(2 - a\frac{x}{L})\right]^4} dx + A \tag{A.4}$$

or in a form of the influential coefficients:

$$C_{ij} = \frac{32}{\pi G {D_0}^4}\int_0^{x_i} \frac{1}{\left(2 - a\frac{\xi}{L}\right)^4} d\xi + A \qquad \text{for } x_i \le x_j \tag{A.5}$$

where A is the constant of integration.

Solving the integral, Eq. (A.5) can be reduced to:

$$C_{ij} = \frac{32}{\pi G {D_0}^4}\left[\frac{-L}{24a} + \frac{L^4}{3a(2L - ax_i)^3}\right] \qquad \text{for } x_i \le x_j \tag{A.6}$$

Note that we removed A from Eq. (A.5) using the clamped boundary condition- $\theta(x_i = 0) = A = 0$.

If the rod is discretized into N equal lengths of Δx, the inertia can be lumped as follows:

$$I_i = \frac{1}{8} m_i {D_i}^2 = \frac{\pi \rho \Delta x {D_0}^4}{32}\left[2 - \frac{ax_i}{L}\right] \qquad i = 1, 2, \ldots, N-1 \tag{A.7}$$

From Eq. (A.6) and (A.7), the natural frequencies and their corresponding modal shapes can be determined as a conventional FEM problem.

A.3 Exact Analytical Solution

A.3.1 General Solution of Differential Equation

This section elaborates on an analytical method obtaining the transcendental equation of the natural frequencies and the corresponding mode shapes. The governing partial differential equation of a free torsional beam is given by:

$$\frac{\partial}{\partial x}\left[GJ(x)\frac{\partial\theta}{\partial x}(x,t)\right] = I_0(x)\frac{\partial^2\theta}{\partial t^2}(x,t) \tag{A.8}$$

where $I_0(x)$ is the polar mass moment of inertia per unit length with $J(x)$ denoting the polar moment of inertia of the cross section defined in Eq. (A.3).

By the geometry of the torsional rod in Figure 1, $I_0(x)$ can be obtained as:

$$I_0(x) = \frac{1}{2}m(x)\left(\frac{D(x)}{2}\right)^2 = \frac{\rho\pi {D_0}^4}{32}\left(2 - a\frac{x}{L}\right)^4 \tag{A.9}$$

where ρ is the density of the rod [kg/m^3] and $m(x)$ is the mass per unit length [kg/m^2].

Under the assumption of synchronous motions, the exact solution of Eq. (A.8) is separable in the spatial variable, x and time, t resulting in $\theta(x,t) = \Theta(x)T(t)$. Substituting $\frac{\partial^2\theta}{\partial t^2} = -\omega^2\Theta(x)T(t)$ and Eq. (A.3), (A.9) gives

$$\begin{aligned} G\frac{\pi {D_0}^4}{32}\left(2 - a\frac{x}{L}\right)^4\frac{d^2\Theta(x)}{dx^2} + G\frac{\pi {D_0}^4}{8}\left(-\frac{a}{L}\right)\left(2 - a\frac{x}{L}\right)^3\frac{d\Theta(x)}{dx} \\ = \frac{\rho\pi {D_0}^4}{32}\left(2 - a\frac{x}{L}\right)^4(-\omega^2\Theta(x)) \end{aligned} \tag{A.10}$$

or

$$GJ(x)\frac{d^2\Theta(x)}{dx^2} - GJ(x)\frac{4a}{2L - ax}\frac{d\Theta(x)}{dx} = \rho J(x)(-\omega^2\Theta(x)) \tag{A.11}$$

Since $J(x) \neq 0$, dividing Eq. (A.11) by $GJ(x)$ in Eq. (A.3) and yields

$$\frac{d^2\Theta}{dx^2} - \frac{4a}{2L - ax}\frac{d\Theta}{dx} + \frac{\rho\omega^2}{G}\Theta = 0 \tag{A.12}$$

In order to solve Eq. (A.12), the following new variables are introduced:

$$\beta^2 = \frac{\rho\omega^2}{G} \tag{A.13}$$

and

$$\bar{x} = \beta\left(2\frac{L}{a} - x\right) = \sqrt{\frac{\rho}{G}}\omega\left(2\frac{L}{a} - x\right) \tag{A.14}$$

which is always positive.

Equation (A.10) then becomes a more simplified form by inserting Eq. (A.13) and (A.14):

$$\beta^2\frac{d^2\Theta}{d\bar{x}^2} + 4\frac{\beta^2}{\bar{x}}\frac{d\Theta}{d\bar{x}} + \beta^2\Theta = 0 \tag{A.15}$$

$$\bar{x}\frac{d^2\Theta}{d\bar{x}^2} + 4\frac{\beta^2}{\bar{x}}\frac{d\Theta}{d\bar{x}} + \bar{x}\Theta = 0 \tag{A.16}$$

where the chain rule is applied to the first and second order differentiation as follows:

$$\begin{aligned} \frac{d\Theta}{x} &= \frac{d\Theta}{\bar{x}}\frac{d\bar{x}}{dx} = -\beta\frac{d\Theta}{\bar{x}}, \\ \frac{d^2\Theta}{x^2} &= \frac{d}{\bar{x}}\left(\frac{d\Theta}{dx}\right)\frac{d\bar{x}}{dx} = \beta^2\frac{d^2\Theta}{\bar{x}^2} \end{aligned} \tag{A.17}$$

It can be shown that $y = x^n J_n(x)$ is the particular solution of the following form of second-order differential equation for $x > 0$ [218]:

$$x\frac{d^2y}{dx^2} + (1-2n)\frac{dy}{dx} + xy = 0 \tag{A.18}$$

where $J_n(x)$ is a Bessel function of the first kind of order n.

Similarly, $y = x^{-n}J_n(x)$ satisfies the following equation for $x > 0$:

$$x\frac{d^2y}{dx^2} + (1+2n)\frac{dy}{dx} + xy = 0 \tag{A.19}$$

By comparing Eq. (A.18) and (A.19) with Eq. (A.16), we can set $n = -\frac{3}{2}$ and $n = \frac{3}{2}$ to obtain a solution of Eq. (A.16):

$$\Theta(x) = C_1\bar{x}^{-\frac{3}{2}}J_{-\frac{3}{2}}(\bar{x}) + C_2\bar{x}^{-\frac{3}{2}}J_{\frac{3}{2}}(\bar{x}) \tag{A.20}$$

or

$$\Theta(x) = \left[\beta_k\left(2\frac{L}{a} - x\right)\right]^{-\frac{3}{2}}\left[C_1 J_{-\frac{3}{2}}\big(\beta_k(2\frac{L}{a} - x)\big) + C_2 J_{\frac{3}{2}}\big(\beta_k(2\frac{L}{a} - x)\big)\right] \tag{A.21}$$

Note that $\bar{x}$ is always positive for $D(x) > 0$. We are now poised to apply the boundary conditions thereby reducing Eq. (A.20) to the eigenfunctions (mode shapes) of a particular system.

A.3.2 Eigenvalues by Boundary Value Problem

The coefficients C_1 and C_2 in Eq. (A.20) are then determined by the boundary conditions. A clamped end at $x = 0$ gives a rise to zero rotation at $x = 0$ and zero torque at the end, $x = L$:

$$\Theta(x=0) = \Theta(\bar{x} = 2\beta\frac{L}{a}) = 0 \tag{A.22}$$

$$\frac{d\Theta}{dx}(x=L) = -\beta\frac{d\Theta}{d\bar{x}}(\bar{x} = \beta(2/a-1)L) = 0 \Rightarrow \frac{d\Theta}{d\bar{x}}(\bar{x} = \beta(2/a-1)L) = 0 \tag{A.23}$$

The first boundary condition yields

$$C_1 J_{-\frac{3}{2}}(2\beta L) + C_2 J_{\frac{3}{2}}(2\beta L) = 0 \tag{A.24}$$

Evaluation of the second boundary condition from Eq. (A.23) involves differentiation of Bessel functions [218] as follows:

$$\begin{aligned} \frac{d}{dx}[x^v J_v(x)] = x^v J_{v-1}(x) &\Rightarrow \frac{d}{d\bar{x}}[\bar{x}^{-\frac{3}{2}}J_{-\frac{3}{2}}(\bar{x})] = \bar{x}^{-\frac{3}{2}}J_{-\frac{5}{2}}(\bar{x}) \\ \frac{d}{dx}[x^{-v} J_v(x)] = -x^{-v} J_{v+1}(x) &\Rightarrow \frac{d}{d\bar{x}}[\bar{x}^{-\frac{3}{2}}J_{-\frac{3}{2}}(\bar{x})] = -\bar{x}^{-\frac{3}{2}}J_{\frac{5}{2}}(\bar{x}) \end{aligned} \tag{A.25}$$

Accordingly, the second boundary condition yields

$$C_1 J_{-\frac{5}{2}}\big((\frac{2}{a}-1)\beta L\big) - C_2 J_{\frac{5}{2}}\big((\frac{2}{a}-1)\beta L\big) = 0 \tag{A.26}$$

Table A.1: Comparison of the natural frequencies

Natural Frequencies [Hz]	1st	2nd	3rd	4th	5th
Constant cross-section (a=0)	2580	7750	12920	18090	23260
FEM Method (a=1)	4160	8540	13400	18090	23420
Analytical Method (a=1)	4156	8542	13424	18455	23544

By combining Eq. (A.24) and (A.26), we can set up a matrix equation as the following:

$$\begin{bmatrix} J_{-\frac{3}{2}}(2\beta L) & J_{\frac{3}{2}}(2\beta L) \\ J_{-\frac{5}{2}}\big((\frac{2}{a}-1)\beta L\big) & -J_{\frac{5}{2}}\big((\frac{2}{a}-1)\beta L\big) \end{bmatrix} \begin{Bmatrix} C_1 \\ C_2 \end{Bmatrix} = \begin{Bmatrix} 0 \\ 0 \end{Bmatrix} \tag{A.27}$$

The determinant of the 2x2 matrix in Eq. (A.27) should be zero to obtain a nontrivial solution. It results in the transcendental equation of the natural frequencies of the torsional shaft as the following:

$$J_{-\frac{3}{2}}(2\beta L)J_{\frac{5}{2}}\big((\frac{2}{a}-1)\beta L\big) + J_{\frac{3}{2}}(2\beta L)J_{-\frac{5}{2}}\big((\frac{2}{a}-1)\beta L\big) = 0 \tag{A.28}$$

Its solutions are an infinite set of eigenvalues $\beta_k L$ and a numerical method is employed to find multiple eigenvalues satisfying Eq. (A.28). Thereafter, the natural frequencies can be obtained using Eq. (A.13):

$$\omega_k = \sqrt{\frac{G}{\rho}}\beta_k \qquad\qquad k = 1, 2, \ldots \tag{A.29}$$

The mode shapes or the eigenfunctions of the tapered torsional rod with a clamped end can be obtained by Eqn (A.24). By finding the relationship between C_1 and C_2,

$$C_2 = -\frac{J_{-\frac{3}{2}}(2\beta L)}{J_{\frac{3}{2}}(2\beta L)}C_1 \tag{A.30}$$

Inserting Eq. (A.30) into Eq. (A.2) leads to the following mode shape formula for the k-th mode:

$$\Theta_k(x) = C_k\left[\beta_k\left(2\frac{L}{a}-x\right)\right]^{-\frac{3}{2}}\left[J_{-\frac{3}{2}}\big(\beta_k(2\frac{L}{a}-x)\big) - \frac{J_{-\frac{3}{2}}(2\beta_k L)}{J_{\frac{3}{2}}(2\beta_k L)}J_{\frac{3}{2}}\big(\beta_k(2\frac{L}{a}-x)\big)\right] \tag{A.31}$$

where β_k is the k-th solution of the transcendental equation (A.28).

A.4 Numerical Validation and Conclusion

The first five natural freqencies for a linearly tapered aluminum rod with the tapering slope of $a = 1$ are compared with a constant cross-section, $a = 0$. We used the following properties: $D_0 = 1$ cm; $L = 30$ cm; Young's modulus, $E_{aluminum}$=70 GPa; the density, $\rho_{aluminum} = 2800$ kgm^{-3}; poisson ratio, $\nu_{aluminum} = 0.3$.

As shown in Table A.1, the natural frequencies obtained by Eq. (A.28) agree with those by the FEM. The first mode of a linearly varying torsional rod is higher than that of a uniform section. This is because little material was removed at the root area where most of the strain energy of the first mode is, while the inertia load was reduced towards the tip where most of the kinetic energy of the first mode is stored. This argument on the strain and kinetic energies becomes less true as the mode number is increased. This explains why the natural frequencies of the higher modes are closed to that of the rod with a uniform cross-section. The first four mode shapes from Eq. (A.31) plotted in Figure A-2 clearly exhibit a distinction from the simple sine function mode shapes-

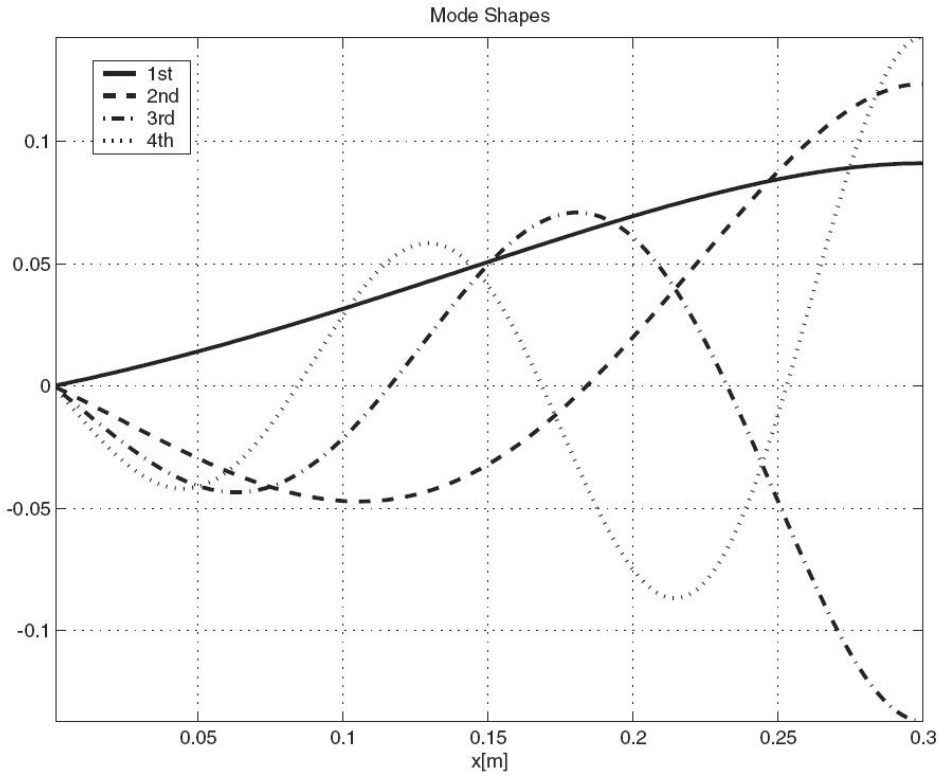

Figure A-2: First Four Mode Shapes of a=1

$sin\left(\frac{1}{2}(2k-1)\pi\frac{x}{L}\right)$ for a uniform section.

Appendix B

Orbital Dynamics of Tethered Array

We briefly review the orbital dynamics of a tethered spacecraft array in this section. Note that we later neglect the gravity term assuming that a tethered array operates in a weak gravity field. In order to obtain the equations of motion of the CM of multiple (n) spacecraft, we derive the kinetic energy K and potential energy V based on [132]:

$$K = \frac{1}{2}\dot{\mathbf{R}}_C \cdot \dot{\mathbf{R}}_C \sum_{i=1}^{n} m_i + \dot{\mathbf{R}}_C \cdot \sum_{i=1}^{n} m_i \dot{\mathbf{r}}_i + \frac{1}{2}\sum_{i=1}^{n} m_i \dot{\mathbf{r}}_i \cdot \dot{\mathbf{r}}_i \tag{B.1}$$

where the $\dot{\mathbf{R}}_C$ is the position vector of the array center of mass C with respect to the center of the Earth, while $\mathbf{r}_i$ is the position vector of the i-th spacecraft to C.

Since $\dot{\mathbf{r}}_i$ is defined from the array center C:

$$\sum_{i=1}^{n} m_i x_i = 0, \quad \sum_{i=1}^{n} m_i y_i = 0 \tag{B.2}$$

where the x-axis is aligned with the local vertical, the y-axis is in the direction of orbital motion, while the z-axis is along the orbit normal. Since the motion is confined to the plane of the center of mass, the z coordinates of the individual spacecraft are always zero.

Then, K is simplified using $\dot{\mathbf{r}}_i = (\dot{x}_i - \Omega y_i)\mathbf{i} + (\dot{y}_i + \Omega x_i)\mathbf{j}$:

$$K = \frac{1}{2}m\Omega^2 {R_c}^2 + \frac{1}{2}\sum_{i=1}^{n} m_i \left((\dot{x}_i^2 + \dot{y}_i^2) + 2(x_i\dot{y}_i - \dot{x}_i y_i) + \Omega^2(x_i^2 + y_i^2)\right) \tag{B.3}$$

where $R_c = \|\dot{\mathbf{R}}_C\|$ and Ω is the orbital angular velocity.

The potential energy of the system is obtained as

$$V = -\sum_{i=1}^{n} \frac{GM_e m_i}{\|\dot{\mathbf{R}}_C + r_i\|} \tag{B.4}$$

which can be rewritten by expanding the equation in a binomial series and exploiting (B.2) as

$$V = -\frac{GM_e m}{R_c} + \frac{GM_e m}{2{R_c}^3}\sum_{i=1}^{n} m_i(x_i^2 + y_i^2 - 3x_i^2) \tag{B.5}$$

Hence, the equations of motion can be developed using the Euler-Lagrangian equations. Note that the position vectors are subject to two types of constraint equations: the x and y constraint

equations in (B.2) and the constraints from the fixed tether length. We exploit such constraint equations to derive relative equations of motion in Section 3.5.

Appendix C

Mathematica Codes

C.1 Involutivity Test for Section 6.2.1

$M = \{\{a1 + 2 * a3 * Cos[x2], a2 + a3 * Cos[x2]\}, \{a2 + a3 * Cos[x2], a2\}\}$
$\{\{a1 + 2a3Cos[x2], a2 + a3Cos[x2]\}, \{a2 + a3Cos[x2], a2\}\}$
$B = \{-2 * a3 * Sin[x2] * x3 * x4 - a3 * Sin[x2] * x4\text{^}2, a3 * Sin[x2] * x3\text{^}2\}$
$\{-2a3x3x4Sin[x2] - a3x4^2Sin[x2], a3x3^2Sin[x2]\}$
invMB = Simplify[Inverse[M].B]
$\{\frac{a3(a2(x3+x4)^2+a3x3^2Cos[x2])Sin[x2]}{a2(-a1+a2)+a3^2Cos[x2]^2},$
$-\frac{2a3(a1x3^2+a2x4(2x3+x4)+a3(2x3^2+2x3x4+x4^2)Cos[x2])Sin[x2]}{-2a1a2+2a2^2+a3^2+a3^2Cos[2x2]}\}$
$x = \{x1, x2, x3, x4\}$
$\{x1, x2, x3, x4\}$
$f = \{x3, x4, -Part[invMB, 1], -Part[invMB, 2]\}$; MatrixForm[$f$]

$$\begin{pmatrix} x3 \\ x4 \\ -\frac{a3(a2(x3+x4)^2+a3x3^2Cos[x2])Sin[x2]}{a2(-a1+a2)+a3^2Cos[x2]^2} \\ \frac{2a3(a1x3^2+a2x4(2x3+x4)+a3(2x3^2+2x3x4+x4^2)Cos[x2])Sin[x2]}{-2a1a2+2a2^2+a3^2+a3^2Cos[2x2]} \end{pmatrix}$$

invG = Simplify[Inverse[M].$\{1, 1\}$]
$\{\frac{a3Cos[x2]}{a2(-a1+a2)+a3^2Cos[x2]^2}, \frac{-a1+a2-a3Cos[x2]}{a2(-a1+a2)+a3^2Cos[x2]^2}\}$
$g = \{0, 0, Part[invG, 1], Part[invG, 2]\}$; MatrixForm[$g$]

$$\begin{pmatrix} 0 \\ 0 \\ \frac{a3Cos[x2]}{a2(-a1+a2)+a3^2Cos[x2]^2} \\ \frac{-a1+a2-a3Cos[x2]}{a2(-a1+a2)+a3^2Cos[x2]^2} \end{pmatrix}$$

LieBracket[f_List, g_List, x_List]:=
Module[$\{i\}$, Transpose[Table[$D[g, x[[i]]], \{i, Length[x]\}]$]].$f$ −
Transpose[Table[$D[f, x[[i]]], \{i, Length[x]\}]$]].$g$]
adfg = LieBracket[f, g, x];
adf2g = LieBracket[f, adfg, x];
d1 = LieBracket[g, adfg, x];
d2 = LieBracket[g, adf2g, x];
d3 = LieBracket[adfg, adf2g, x];
Delta = AppendColumns[$\{g\}$, {adfg}, {adf2g}]; MatrixForm[Delta];
MatrixRank[AppendColumns[{d1}, $\{g\}$, {adfg}, {adf2g}]]
4
MatrixRank[AppendColumns[{d2}, $\{g\}$, {adfg}, {adf2g}]]
4

MatrixRank[AppendColumns[{d3}, {g}, {adfg}, {adf2g}]]
4

C.2 Controllability Test

C.2.1 Controllability Test for a Single Tethered Spacecraft

A={{0, 0, 0, 1, 0, 0}, {0, 0, 0, 0, 1, 0}, {0, 0, 0, 0, 0, 1},
{0, $\frac{r(\text{Ig}+mr(l+r))\omega^2}{\text{Ig}l}$, 0, $-\frac{2v}{l}$, 0, $-\frac{2\omega}{l}$}, {0, $-\frac{r(\text{Ig}+m(l+r)^2)\omega^2}{\text{Ig}l}$, 0, $\frac{2v}{l}$, 0, $\frac{2\omega}{l}$}, {0, 0, 0, $2(l+r)\omega$, $2r\omega$, 0}}
A//MatrixForm

$$\begin{bmatrix} 0 & 0 & 0 & 1 & 0 & 0 \\ 0 & 0 & 0 & 0 & 1 & 0 \\ 0 & 0 & 0 & 0 & 0 & 1 \\ 0 & \frac{r(\text{Ig}+mr(l+r))\omega^2}{\text{Ig}l} & 0 & -\frac{2v}{l} & 0 & -\frac{2\omega}{l} \\ 0 & -\frac{r(\text{Ig}+m(l+r)^2)\omega^2}{\text{Ig}l} & 0 & \frac{2v}{l} & 0 & \frac{2\omega}{l} \\ 0 & 0 & 0 & 2(l+r)\omega & 2r\omega & 0 \end{bmatrix}$$

B = Table[0, {6}, {2}];
B[[Range[4, 6], Range[1, 2]]] = MG
{{$-\frac{r}{2\text{Ig}l}$, $-\frac{r}{2\text{Ig}l}$}, {$\frac{1}{2}(\frac{l+r}{\text{Ig}l}+\frac{1}{\text{Ig}+mr^2})$, $\frac{r(\text{Ig}+mr(l+r))}{2\text{Ig}l(\text{Ig}+mr^2)}$}, {$\frac{r(\text{Ig}+mr(l+r))}{2\text{Ig}l(\text{Ig}+mr^2)}$, $\frac{1}{2}(\frac{l+r}{\text{Ig}l}+\frac{1}{\text{Ig}+mr^2})$}}
B//MatrixForm

$$\begin{bmatrix} 0 & 0 \\ 0 & 0 \\ 0 & 0 \\ -\frac{r}{2\text{Ig}l} & -\frac{r}{2\text{Ig}l} \\ \frac{1}{2}(\frac{l+r}{\text{Ig}l}+\frac{1}{\text{Ig}+mr^2}) & \frac{r(\text{Ig}+mr(l+r))}{2\text{Ig}l(\text{Ig}+mr^2)} \\ \frac{r(\text{Ig}+mr(l+r))}{2\text{Ig}l(\text{Ig}+mr^2)} & \frac{1}{2}(\frac{l+r}{\text{Ig}l}+\frac{1}{\text{Ig}+mr^2}) \end{bmatrix}$$

$$B = \begin{bmatrix} 0 & 0 \\ 0 & 0 \\ 0 & 0 \\ -\frac{r}{\text{Ig}l} & 0 \\ \frac{l+r}{\text{Ig}l} & 0 \\ 0 & \frac{1}{m} \end{bmatrix}$$

{{0, 0}, {0, 0}, {0, 0}, {$-\frac{r}{\text{Ig}l}$, 0}, {$\frac{l+r}{\text{Ig}l}$, 0}, {0, $\frac{1}{m}$}}
MatrixRank[A] 4
Con = {{0, 0, 0, 0, 0, 0}, {0, 0, 0, 0, 0, 0}, {0, 0, 0, 0, 0, 0}, {0, 0, 0, 0, 0, 0}, {0, 0, 0, 0, 0, 0}, {0, 0, 0, 0, 0, 0}}
{{0, 0, 0, 0, 0, 0}, {0, 0, 0, 0, 0, 0}, {0, 0, 0, 0, 0, 0}, {0, 0, 0, 0, 0, 0}, {0, 0, 0, 0, 0, 0}, {0, 0, 0, 0, 0, 0}}

Con[[Range[1, 6], Range[1, 2]]] = B
{{0, 0}, {0, 0}, {0, 0}, {$-\frac{r}{\text{Ig}l}$, 0}, {$\frac{l+r}{\text{Ig}l}$, 0}, {0, $\frac{1}{m}$}}
Con[[Range[1, 6], Range[3, 4]]] = Simplify[$A.B$]
{{$-\frac{r}{\text{Ig}l}$, 0}, {$\frac{l+r}{\text{Ig}l}$, 0}, {0, $\frac{1}{m}$}, {$\frac{2rv}{\text{Ig}l^2}$, $-\frac{2\omega}{lm}$}, {$-\frac{2rv}{\text{Ig}l^2}$, $\frac{2\omega}{lm}$}, {0, 0}}
Con[[Range[1, 6], Range[5, 6]]] = Simplify[$A.A.B$];
Con//MatrixForm

$$\begin{bmatrix} 0 & 0 & -\frac{r}{\text{Ig}l} & 0 & \frac{2rv}{\text{Ig}l^2} & -\frac{2\omega}{lm} \\ 0 & 0 & \frac{l+r}{\text{Ig}l} & 0 & -\frac{2rv}{\text{Ig}l^2} & \frac{2\omega}{lm} \\ 0 & 0 & 0 & \frac{1}{m} & 0 & 0 \\ -\frac{r}{\text{Ig}l} & 0 & \frac{2rv}{\text{Ig}l^2} & -\frac{2\omega}{lm} & \frac{r(lmr(l+r)^2\omega^2+\text{Ig}(-4v^2+l(l+r)\omega^2))}{\text{Ig}^2l^3} & \frac{4v\omega}{l^2m} \\ \frac{l+r}{\text{Ig}l} & 0 & -\frac{2rv}{\text{Ig}l^2} & \frac{2\omega}{lm} & -\frac{r(lm(l+r)^3\omega^2+\text{Ig}(-4v^2+l(l+r)\omega^2))}{\text{Ig}^2l^3} & -\frac{4v\omega}{l^2m} \\ 0 & \frac{1}{m} & 0 & 0 & \frac{4rv\omega}{\text{Ig}l} & -\frac{4\omega^2}{m} \end{bmatrix}$$

MatrixRank[Con]

C.2.2 Controllability Test for a Two-Spacecraft Array

$$M = \begin{bmatrix} 2\text{Ig} + 2m(l+r)^2 & \text{Ig} + mr(l+r) & \text{Ig} + mr(l+r) \\ \text{Ig} + mr(l+r) & \text{Ig} + mr^2 & 0 \\ \text{Ig} + mr(l+r) & 0 & \text{Ig} + mr^2 \end{bmatrix}$$

$\{\{2\text{Ig}+2m(l+r)^2, \text{Ig}+mr(l+r), \text{Ig}+mr(l+r)\}, \{\text{Ig}+mr(l+r), \text{Ig}+mr^2, 0\}, \{\text{Ig}+mr(l+r), 0, \text{Ig}+mr^2\}\}$

$$K = \begin{bmatrix} 0 & 0 & 0 \\ 0 & mrl\omega^2 & 0 \\ 0 & 0 & mrl\omega^2 \end{bmatrix}$$

$\{\{0,0,0\}, \{0, lmr\omega^2, 0\}, \{0, 0, lmr\omega^2\}\}$

$$B = \begin{bmatrix} 1 & 1 \\ 1 & 0 \\ 0 & 1 \end{bmatrix})$$

$\{\{1,1\}, \{1,0\}, \{0,1\}\}$

MK = FullSimplify[−Inverse[M].K];

MK//MatrixForm

$$\begin{pmatrix} 0 & \frac{r(\text{Ig}+mr(l+r))\omega^2}{2\text{Ig}l} & \frac{r(\text{Ig}+mr(l+r))\omega^2}{2\text{Ig}l} \\ 0 & -\frac{r(\text{Ig}^2+m^2r^2(l+r)^2+2\text{Ig}m(l^2+lr+r^2))\omega^2}{2\text{Ig}l(\text{Ig}+mr^2)} & -\frac{r(\text{Ig}+mr(l+r))^2\omega^2}{2\text{Ig}l(\text{Ig}+mr^2)} \\ 0 & -\frac{r(\text{Ig}+mr(l+r))^2\omega^2}{2\text{Ig}l(\text{Ig}+mr^2)} & -\frac{r(\text{Ig}^2+m^2r^2(l+r)^2+2\text{Ig}m(l^2+lr+r^2))\omega^2}{2\text{Ig}l(\text{Ig}+mr^2)} \end{pmatrix}$$

MG = FullSimplify[Inverse[M].B];

MG//MatrixForm

$$\begin{bmatrix} -\frac{r}{2\text{Ig}l} & -\frac{r}{2\text{Ig}l} \\ \frac{1}{2}(\frac{l+r}{\text{Ig}l} + \frac{1}{\text{Ig}+mr^2}) & \frac{r(\text{Ig}+mr(l+r))}{2\text{Ig}l(\text{Ig}+mr^2)} \\ \frac{r(\text{Ig}+mr(l+r))}{2\text{Ig}l(\text{Ig}+mr^2)} & \frac{1}{2}(\frac{l+r}{\text{Ig}l} + \frac{1}{\text{Ig}+mr^2}) \end{bmatrix}$$

A = Table[0, {6}, {6}];

$\{\{0,0,0,0,0,0\}, \{0,0,0,0,0,0\}, \{0,0,0,0,0,0\}, \{0,0,0,0,0,0\}, \{0,0,0,0,0,0\}, \{0,0,0,0,0,0\}\}$

A[[Range[1, 3], Range[4, 6]]] = IdentityMatrix[3];

A[[Range[4, 6], Range[1, 3]]] = MK;

A//MatrixForm

$$\begin{bmatrix} 0 & 0 & 0 & 1 & 0 & 0 \\ 0 & 0 & 0 & 0 & 1 & 0 \\ 0 & 0 & 0 & 0 & 0 & 1 \\ 0 & \frac{r(\text{Ig}+mr(l+r))\omega^2}{2\text{Ig}l} & \frac{r(\text{Ig}+mr(l+r))\omega^2}{2\text{Ig}l} & 0 & 0 & 0 \\ 0 & -\frac{r(\text{Ig}^2+m^2r^2(l+r)^2+2\text{Ig}m(l^2+lr+r^2))\omega^2}{2\text{Ig}l(\text{Ig}+mr^2)} & -\frac{r(\text{Ig}+mr(l+r))^2\omega^2}{2\text{Ig}l(\text{Ig}+mr^2)} & 0 & 0 & 0 \\ 0 & -\frac{r(\text{Ig}+mr(l+r))^2\omega^2}{2\text{Ig}l(\text{Ig}+mr^2)} & -\frac{r(\text{Ig}^2+m^2r^2(l+r)^2+2\text{Ig}m(l^2+lr+r^2))\omega^2}{2\text{Ig}l(\text{Ig}+mr^2)} & 0 & 0 & 0 \end{bmatrix}$$

B = Table[0, {6}, {2}];

B[[Range[4, 6], Range[1, 2]]] = MG

$\{\{-\frac{r}{2\text{Ig}l}, -\frac{r}{2\text{Ig}l}\}, \{\frac{1}{2}(\frac{l+r}{\text{Ig}l} + \frac{1}{\text{Ig}+mr^2}), \frac{r(\text{Ig}+mr(l+r))}{2\text{Ig}l(\text{Ig}+mr^2)}\}, \{\frac{r(\text{Ig}+mr(l+r))}{2\text{Ig}l(\text{Ig}+mr^2)}, \frac{1}{2}(\frac{l+r}{\text{Ig}l} + \frac{1}{\text{Ig}+mr^2})\}\}$

B//MatrixForm

$$\begin{bmatrix} 0 & 0 \\ 0 & 0 \\ 0 & 0 \\ -\frac{r}{2\text{Ig}l} & -\frac{r}{2\text{Ig}l} \\ \frac{1}{2}(\frac{l+r}{\text{Ig}l} + \frac{1}{\text{Ig}+mr^2}) & \frac{r(\text{Ig}+mr(l+r))}{2\text{Ig}l(\text{Ig}+mr^2)} \\ \frac{r(\text{Ig}+mr(l+r))}{2\text{Ig}l(\text{Ig}+mr^2)} & \frac{1}{2}(\frac{l+r}{\text{Ig}l} + \frac{1}{\text{Ig}+mr^2}) \end{bmatrix}$$

Con[[Range[1, 6], Range[1, 2]]] = Simplify[B]

$\{\{0,0\}, \{0,0\}, \{0,0\}, \{-\frac{r}{2\text{Ig}l}, -\frac{r}{2\text{Ig}l}\}, \{\frac{1}{2}(\frac{l+r}{\text{Ig}l}+\frac{1}{\text{Ig}+mr^2}), \frac{r(\text{Ig}+mr(l+r))}{2\text{Ig}l(\text{Ig}+mr^2)}\}, \{\frac{r(\text{Ig}+mr(l+r))}{2\text{Ig}l(\text{Ig}+mr^2)}, \frac{1}{2}(\frac{l+r}{\text{Ig}l}+\frac{1}{\text{Ig}+mr^2})\}\}$

Con[[Range[1, 6], Range[3, 4]]] = Simplify[$A.B$]

$\{\{-\frac{r}{2\mathrm{Ig}l}, -\frac{r}{2\mathrm{Ig}l}\}, \{\frac{1}{2}(\frac{l+r}{\mathrm{Ig}l} + \frac{1}{\mathrm{Ig}+mr^2}), \frac{r(\mathrm{Ig}+mr(l+r))}{2\mathrm{Ig}l(\mathrm{Ig}+mr^2)}\}, \{\frac{r(\mathrm{Ig}+mr(l+r))}{2\mathrm{Ig}l(\mathrm{Ig}+mr^2)}, \frac{1}{2}(\frac{l+r}{\mathrm{Ig}l} + \frac{1}{\mathrm{Ig}+mr^2})\}, \{0, 0\}, \{0, 0\}, \{0, 0\}\}$

Con[[Range[1, 6], Range[5, 6]]] = Simplify[$A.A.B$]

$\{\{0, 0\}, \{0, 0\}, \{0, 0\}, \{\frac{r(l+r)(\mathrm{Ig}+mr(l+r))\omega^2}{2\mathrm{Ig}^2l^2}, \frac{r(l+r)(\mathrm{Ig}+mr(l+r))\omega^2}{2\mathrm{Ig}^2l^2}\},$

$\{-\frac{r(\mathrm{Ig}^3(l+r)+m^3r^4(l+r)^3+\mathrm{Ig}^2m(2l^3+3l^2r+5lr^2+3r^3)+\mathrm{Ig}m^2r^2(2l^3+6l^2r+7lr^2+3r^3))\omega^2}{2\mathrm{Ig}^2l^2(\mathrm{Ig}+mr^2)^2},$

$-\frac{r(\mathrm{Ig}^3(l+r)+m^3r^4(l+r)^3+\mathrm{Ig}^2mr(3l^2+5lr+3r^2)+\mathrm{Ig}m^2r^2(2l^3+6l^2r+7lr^2+3r^3))\omega^2}{2\mathrm{Ig}^2l^2(\mathrm{Ig}+mr^2)^2}\},$

$\{-\frac{r(\mathrm{Ig}^3(l+r)+m^3r^4(l+r)^3+\mathrm{Ig}^2mr(3l^2+5lr+3r^2)+\mathrm{Ig}m^2r^2(2l^3+6l^2r+7lr^2+3r^3))\omega^2}{2\mathrm{Ig}^2l^2(\mathrm{Ig}+mr^2)^2},$

$-\frac{r(\mathrm{Ig}^3(l+r)+m^3r^4(l+r)^3+\mathrm{Ig}^2m(2l^3+3l^2r+5lr^2+3r^3)+\mathrm{Ig}m^2r^2(2l^3+6l^2r+7lr^2+3r^3))\omega^2}{2\mathrm{Ig}^2l^2(\mathrm{Ig}+mr^2)^2}\}\}$

Con[[Range[1, 6], Range[7, 8]]] = Simplify[$A.A.A.B$];

Con[[Range[1, 6], Range[9, 10]]] = Simplify[$A.A.A.A.B$];

Con[[Range[1, 6], Range[11, 12]]] = Simplify[$A.A.A.A.A.B$];

MatrixRank[Con]

6

C.3 Diagonalization Transformation in Chapter 4

$$M = \begin{bmatrix} 2\mathrm{Ig} + 2m(l+r)^2 & \mathrm{Ig} + mr(l+r) & \mathrm{Ig} + mr(l+r) \\ \mathrm{Ig} + mr(l+r) & \mathrm{Ig} + mr^2 & 0 \\ \mathrm{Ig} + mr(l+r) & 0 & \mathrm{Ig} + mr^2 \end{bmatrix}$$

$\{\{2\mathrm{Ig}+2m(l+r)^2, \mathrm{Ig}+mr(l+r), \mathrm{Ig}+mr(l+r)\}, \{\mathrm{Ig}+mr(l+r), \mathrm{Ig}+mr^2, 0\}, \{\mathrm{Ig}+mr(l+r), 0, \mathrm{Ig}+mr^2\}\}$

$$K = \begin{bmatrix} 0 & 0 & 0 \\ 0 & mrl\omega^2 & 0 \\ 0 & 0 & mrl\omega^2 \end{bmatrix}$$

$\{\{0, 0, 0\}, \{0, lmr\omega^2, 0\}, \{0, 0, lmr\omega^2\}\}$

$$B = \begin{bmatrix} 1 & 1 \\ 1 & 0 \\ 0 & 1 \end{bmatrix}$$

$\{\{1, 1\}, \{1, 0\}, \{0, 1\}\}$

FullSimplify[Inverse[M].K//MatrixForm]

$$\begin{bmatrix} 0 & -\frac{r(\mathrm{Ig}+mr(l+r))\omega^2}{2\mathrm{Ig}l} & -\frac{r(\mathrm{Ig}+mr(l+r))\omega^2}{2\mathrm{Ig}l} \\ 0 & \frac{r(\mathrm{Ig}^2+m^2r^2(l+r)^2+2\mathrm{Ig}m(l^2+lr+r^2))\omega^2}{2\mathrm{Ig}l(\mathrm{Ig}+mr^2)} & \frac{r(\mathrm{Ig}+mr(l+r))^2\omega^2}{2\mathrm{Ig}l(\mathrm{Ig}+mr^2)} \\ 0 & \frac{r(\mathrm{Ig}+mr(l+r))^2\omega^2}{2\mathrm{Ig}l(\mathrm{Ig}+mr^2)} & \frac{r(\mathrm{Ig}^2+m^2r^2(l+r)^2+2\mathrm{Ig}m(l^2+lr+r^2))\omega^2}{2\mathrm{Ig}l(\mathrm{Ig}+mr^2)} \end{bmatrix}$$

FullSimplify[Eigenvalues[Inverse[M].K]]

$\{0, \frac{lmr\omega^2}{\mathrm{Ig}+mr^2}, \frac{r(\mathrm{Ig}+m(l+r)^2)\omega^2}{\mathrm{Ig}l}\}$

$\{\mathrm{V1}, \mathrm{V2}, \mathrm{V3}\}$ = Eigenvectors[Inverse[M].K]

$\{\{1, 0, 0\}, \{0, -1, 1\}, \{-\frac{\mathrm{Ig}+lmr+mr^2}{\mathrm{Ig}+l^2m+2lmr+mr^2}, 1, 1\}\}$

V1 = V1/Sqrt[V1.M.V1]; V2 = V2/Sqrt[(V2.M.V2)]; V3 = V3/Sqrt[V3.M.V3];

V1 = FullSimplify[V1]; V2 = FullSimplify[V2]; V3 = FullSimplify[V3];

V = Transpose[{V1, V2, V3}]; V//MatrixForm

$$\begin{bmatrix} \frac{1}{\sqrt{2\mathrm{Ig}+2m(l+r)^2}} & 0 & -\frac{(\mathrm{Ig}+mr(l+r))\sqrt{\frac{\mathrm{Ig}l^2m}{\mathrm{Ig}+m(l+r)^2}}}{\sqrt{2}\mathrm{Ig}l^2m} \\ 0 & -\frac{1}{\sqrt{2\mathrm{Ig}+2mr^2}} & \frac{1}{\sqrt{2}\sqrt{\frac{\mathrm{Ig}l^2m}{\mathrm{Ig}+m(l+r)^2}}} \\ 0 & \frac{1}{\sqrt{2\mathrm{Ig}+2mr^2}} & \frac{1}{\sqrt{2}\sqrt{\frac{\mathrm{Ig}l^2m}{\mathrm{Ig}+m(l+r)^2}}} \end{bmatrix}$$

Simplify[Transpose[V].M.V]

$\{\{1, 0, 0\}, \{0, 1, 0\}, \{0, 0, 1\}\}$

Simplify[Transpose[V].K.V]

$\{\{0, 0, 0\}, \{0, \frac{lmr\omega^2}{\mathrm{Ig}+mr^2}, 0\}, \{0, 0, \frac{r(\mathrm{Ig}+m(l+r)^2)\omega^2}{\mathrm{Ig}l}\}\}$

$$P=\begin{bmatrix} 0 & \text{K1} & \text{K1} \\ 0 & \text{K1} & 0 \\ 0 & 0 & \text{K1} \end{bmatrix};Q=\begin{bmatrix} 2*\text{K2} & \text{K3} & \text{K3} \\ \text{K2} & \text{K3} & 0 \\ \text{K2} & 0 & \text{K3} \end{bmatrix};$$

$$\{\frac{1}{\sqrt{2\text{Ig}+2m(l+r)^2}},0,0\}$$

VQV = FullSimplify[Transpose[V].Q.V]; VQV//MatrixForm

$$\begin{bmatrix} \frac{\text{K2}}{\text{Ig}+m(l+r)^2} & 0 & \frac{\text{Ig}(-\text{K2}+\text{K3})+m(l+r)(-\text{K2}r+\text{K3}(l+r))}{\sqrt{\frac{\text{Ig}l^2m}{\text{Ig}+m(l+r)^2}}(\text{Ig}+m(l+r)^2)^{3/2}} \\ 0 & \frac{\text{K3}}{\text{Ig}+mr^2} & 0 \\ \frac{\text{K2}lm(l+r)}{\sqrt{\frac{\text{Ig}l^2m}{\text{Ig}+m(l+r)^2}}(\text{Ig}+m(l+r)^2)^{3/2}} & 0 & \frac{(l+r)(\text{Ig}(-\text{K2}+\text{K3})+m(l+r)(-\text{K2}r+\text{K3}(l+r)))}{\text{Ig}l(\text{Ig}+m(l+r)^2)} \end{bmatrix}$$

$$\begin{bmatrix} \frac{\text{K2}}{\text{Ig}+m(l+r)^2} & 0 & \frac{\text{Ig}(-\text{K2}+\text{K3})+m(l+r)(-\text{K2}r+\text{K3}(l+r))}{\sqrt{\frac{\text{Ig}l^2m}{\text{Ig}+m(l+r)^2}}(\text{Ig}+m(l+r)^2)^{3/2}} \\ 0 & \frac{\text{K3}}{\text{Ig}+mr^2} & 0 \\ \frac{\text{K2}lm(l+r)}{\sqrt{\frac{\text{Ig}l^2m}{\text{Ig}+m(l+r)^2}}(\text{Ig}+m(l+r)^2)^{3/2}} & 0 & \frac{(l+r)(\text{Ig}(-\text{K2}+\text{K3})+m(l+r)(-\text{K2}r+\text{K3}(l+r)))}{\text{Ig}l(\text{Ig}+m(l+r)^2)} \end{bmatrix}$$

qs = Simplify[(VQV[[3, 1]] + VQV[[1, 3]])/2]

$$\frac{\text{Ig}(-\text{K2}+\text{K3})+m(l+r)(\text{K2}(l-r)+\text{K3}(l+r))}{2\sqrt{\frac{\text{Ig}l^2m}{\text{Ig}+m(l+r)^2}}(\text{Ig}+m(l+r)^2)^{3/2}}$$

FullSimplify[qs^2 − VQV[[1, 1]] ∗ VQV[[3, 3]]]

$$\frac{(\text{K2}-\text{K3})^2}{4\text{Ig}l^2m}$$

$$\{\{\frac{\text{K2}}{\text{Ig}+m(l+r)^2},0,\frac{\text{Ig}(-\text{K2}+\text{K3})+m(l+r)(-\text{K2}r+\text{K3}(l+r))}{\sqrt{\frac{\text{Ig}l^2m}{\text{Ig}+m(l+r)^2}}(\text{Ig}+m(l+r)^2)^{3/2}}\},$$
$$\{0,\frac{\text{K3}}{\text{Ig}+mr^2},0\},\{\frac{\text{K2}lm(l+r)}{\sqrt{\frac{\text{Ig}l^2m}{\text{Ig}+m(l+r)^2}}(\text{Ig}+m(l+r)^2)^{3/2}},0,\frac{(l+r)(\text{Ig}(-\text{K2}+\text{K3})+m(l+r)(-\text{K2}r+\text{K3}(l+r)))}{\text{Ig}l(\text{Ig}+m(l+r)^2)}\}\}[3,3]$$

G = FullSimplify[Transpose[V].P.V]; G//MatrixForm

$$\begin{bmatrix} 0 & 0 & \frac{\text{K1}}{\sqrt{\frac{\text{Ig}l^2m}{\text{Ig}+m(l+r)^2}}\sqrt{\text{Ig}+m(l+r)^2}} \\ 0 & \frac{\text{K1}}{\text{Ig}+mr^2} & 0 \\ 0 & 0 & \frac{\text{K1}(l+r)}{\text{Ig}l} \end{bmatrix}$$

Transpose[G].G

$$\{\{0,0,0\},\{0,\frac{\text{K1}^2}{(\text{Ig}+mr^2)^2},0\},\{0,0,\frac{\text{K1}^2}{\text{Ig}l^2m}+\frac{\text{K1}^2(l+r)^2}{\text{Ig}^2l^2}\}\}$$

Simplify[Inverse[$\begin{pmatrix} \frac{1}{\sqrt{2\text{Ig}+2m(l+r)^2}} & 0 & -\frac{(\text{Ig}+mr(l+r))\sqrt{\frac{\text{Ig}l^2m}{\text{Ig}+m(l+r)^2}}}{\sqrt{2}\text{Ig}l^2m} \\ 0 & -\frac{1}{\sqrt{2\text{Ig}+2mr^2}} & \frac{1}{\sqrt{2}\sqrt{\frac{\text{Ig}l^2m}{\text{Ig}+m(l+r)^2}}} \\ 0 & \frac{1}{\sqrt{2\text{Ig}+2mr^2}} & \frac{1}{\sqrt{2}\sqrt{\frac{\text{Ig}l^2m}{\text{Ig}+m(l+r)^2}}} \end{pmatrix}$]]//MatrixForm

$$\begin{bmatrix} \sqrt{2\text{Ig}+2m(l+r)^2} & \frac{\text{Ig}+mr(l+r)}{\sqrt{2}\sqrt{\text{Ig}+m(l+r)^2}} & \frac{\text{Ig}+mr(l+r)}{\sqrt{2}\sqrt{\text{Ig}+m(l+r)^2}} \\ 0 & -\frac{1}{2}\sqrt{2\text{Ig}+2mr^2} & \frac{\sqrt{\text{Ig}+mr^2}}{\sqrt{2}} \\ 0 & \frac{\sqrt{\frac{\text{Ig}l^2m}{\text{Ig}+m(l+r)^2}}}{\sqrt{2}} & \frac{\sqrt{\frac{\text{Ig}l^2m}{\text{Ig}+m(l+r)^2}}}{\sqrt{2}} \end{bmatrix}$$

Bibliography

[1] Abraham, R., Marsden, J.E., and Ratiu, T., *Manifolds, Tensor, Analysis, and Applications*, 2nd Ed., Springer-Verlag, New York, 1988.

[2] Ahsun, Umair, "Dynamics and Control of Electromagnetic Satellite Formations," Ph.D. dissertation, Department of Aeronautics and Astronautics, MIT, June 2007.

[3] Ambrose, R.O., Aldridge, H., Askew, R.S., Burridge, R., Bluethman, W., Diftler, M.A., Lovchik, C., Magruder, D. and Rehnmark, F., "ROBONAUT: NASA's Space Humanoid", IEEE Intelligent Systems Journal, August 2000.

[4] Anderson, R., and Spong, M.W., "Bilateral Control of Teleoperators," IEEE Trans. Aut. Contr., 34(5), 494- 501, 1989.

[5] Apostolos Argyris, et al., "Chaos-based Communications at High Bit Rates Using Commercial Fibre-optic Links," Nature 438, 343-346, November 2005.

[6] Apostolos Argyris, et al., "Spectral Synchronization in Chaotic Optical Communication Systems," IEEE Journal of Quantum Electronics, VOL. 41, NO. 6, June 2005.

[7] Atkeson, C. G., Moore, A. W., and Schaal, S., "Locally Weighted Learning for Control," Artificial Intelligence Review, 11, 1997.

[8] Bamieh, B., Paganini, F., and Dahle, M.A., "Distributed Control of Spatially Invariant Systems," IEEE Transactions on Automatic Control, Vol. 47, No. 7., 2002.

[9] Bay, J. S., and Hemami, H., "Modeling of a Neural Pattern Generator with Coupled Nonlinear Oscillators," IEEE Transactions on Biomedical Engineering, April 1987.

[10] Bedrossian, N.S., "Linearizing Coordinate Transformations and Riemann Curvature," Proc. of the 31st Conference on Decision and Control, Tucson, AZ, 1992.

[11] Beichman, C.A., Woolf, N.J., and Lindensmith, C.A., "The Terrestrial Planet Finder (TPF): A NASA Origins Program to Search for Habitable Planets," JPL Publication 99-3, 1999.

[12] Beichman, C.A., et al., *Summary Report on Architecture Studies for the TPF*, JPL Publication 02-011, June 2002.

[13] Belanger, G.M., et al., "Decentralized Control of Satellite Clusters Under Limited Communication," AIAA 2004-5023, AIAA GNC Conference, Providence, RI, 2004.

[14] Beletsky and Levin, *Dynamics of Space Tether Systems*, American Astronautical Society Publication Vol. 83.

[15] Bernelli-Zazzera, F., "Active Control of Tether Satellites Via Boom Rotation: A Proof of Concept Experiment," Advances in the Astronautical Sciences, Vol. 108, Pt. 2, 2001, pp. 1225-1240.

[16] Berthoz, A., *The Brain's Sense of Movement*, Translated by Giselle Weiss, Harvard university press, Cambridge, MA, 2000.

[17] Bennett, M., Schatz, M.F., Rockwood, H., and Wiesenfeld, K., "Huygens's clocks," in Proc. (A) of the Royal Society, 2001.

[18] Bergamaschi, S., and Bonon, F., "Coupling of Tether Lateral Vibration and Subsatellite Attitude Motion," J. Guidance, Control, and Dynamics, Vol. 15, No, 5.

[19] Bernstein, N., "The Coordination and Regulation of Movements," Perseus, 1967. Review 18:442-445.

[20] Bizzi E., Giszter S.F., Loeb E., Mussa-Ivaldi F.A., and Saltiel P., "Modular organization of motor behavior in the frog's spinal cord," Trends in Neurosciences. Review 18:442-445, 1995.

[21] Blevins, R. D., *Formulas for Natural Frequency and Mode Shape*, Robert E. Kieger Publishing Company, New York, 1979.

[22] Bloch, A.M, Baillieul, J., Crouch, P., and Marsden, J., *Nonholonomic Mechanics and Control*, Springer-Verlag, New York, 2003.

[23] Bloch, A. M., Chang, D.E., Leonard, N.E., and Marsden, J.E., "Potential and Kinetic shaping for Control of Underactuated Mechanical Systems," Proc. Amer. Control Conf., pp. 3913-3917, 2000.

[24] Bloch, A.M., Krishnaprasad, P.S., Marsden, J.E., and Sanchez De Alvarez, G., "Stabilization of Rigid Body Dynamics by Internal and External Torques," Automatica, vol. 28, no. 4, pp. 745-756, 1992.

[25] Bogdanov, A., "Optimal Control of a Double Inverted Pendulum on a Cart," Technical report No. CSE-04-006, CSE Dept., OGI School of Science & Engineering, OHSU, December 2004.

[26] Bombardelli, C., Lorenzini, E.C., Quadrelli, M.B., "Retargeting Dynamics of a Linear Tethered Interferometer," AIAA J. of Guidance, Control and Dynamics, Vol. 27, No.6, Nov-Dec 2004.

[27] Bombardelli, C., Lorenzini, E.C., Quadrelli, M.B., "Formation Pointing Dynamics of Tether-Connected Architecture for Space Interferometry," Journal of the Astronautical Sciences, Vol. 52, No. 4, pp. 475-493,October-December 2004.

[28] Bondhus, A.K. and Pettersen, K.Y., "Control of Ship Replenishment by Output Feedback Synchronization," Proc. OCEANS 2005 Americas MTS/IEEE Conference, Washington, D.C, 2005.

[29] Bryson Jr, A.E., and Ho, Y-C. *Applied Optimal Control*, Hemisphere Publishing Corporation, 1975.

[30] Brooks, R., *Cambrian Intelligence*, M.I.T. Press, 1999.

[31] Brown, S.C., Passino, K.M., "Intelligent Control for an Acrobot," Journal of Intelligent and Robotic Systems, Vol. 18, pp. 209-248, 1997.

[32] Brown, R.G., and Hwang, P.Y.C, *Introduction to Random Signals and Applied Kalman Filtering*, 3rd ed., John Wiley & Sons, Inc., 1997.

[33] Bullo, F., Lewis, A.D., and Lynch, A.D., "Controllable Kinematic Reductions for Mechanical Systems: Concepts, Computational Tools, and Examples," 2002 International Symposium on Mathematical Theory of Networks and Systems, August 2002.

[34] Bullo, F., and Lynch, A.D., "Kinematic Controllability for Decoupled Trajectory Planning in Underactuated Mechanical Systems," IEEE Transactions on Robotics and Automation, 17(4):402-412, August 2001.

[35] Bullo, F., and Lewis, A.D., *Geometric Control of Mechanical Systems- Modeling Analysis, and Design for Simple Mechanical Control Systems*, Texts in Applied Mathematics, Springer-Verlag, 2004.

[36] Burdick, J., "Global kinematics for manipulator planning and control," Proc. SPIE Vol. 1196, p. 57-68, Intelligent Control and Adaptive Systems, 1990.

[37] Chang, D.E., and Marsden, J.E., "Reduction of Controlled Lagrangian and Hamiltonian Systems with Symmetry," SIAM J. Control OPTIM., Vol. 43, No. 1, pp. 277 - 300.

[38] Chen, Y. Z., "Torsional Free Vibration of a Cylinder with Varying Cross-Section and Adhesive Masses," J. Sound and Vibration, 2001, 243(3), pp. 503-512.

[39] Cho and N. H. McClamroch, "Feedback Control of Triaxial Attitude Control Testbed Actuated by Two Proof Mass Devices," Proceedings of 41st IEEE Conference on Decision and Control, 2002, 498-503.

[40] Chopra, N., and Spong, M.W., "On Synchronization of Networked Passive Systems with Applications to Bilateral Teleoperation," Society of Instrumentation and Control Engineering of Japan Annual Conference, Okayama, Japan, August 8-10, 2005.

[41] Chung, F., *Spectral Graph Theory*, Number 92 in CBMS Regional Conference Series in Mathematics, American Mathematical Society, 1997.

[42] Chung, S.-J., Miller, D.W., deWeck, O.L., "ARGOS Testbed: Study of Multidisciplinary Challenges of Future Spaceborne Interferometric Arrays," SPIE Optical Engineering, Vol. 43, No. 9, pp. 2156-2167, September 2004.

[43] Chung, S.-J., Kong, E., and Miller, D.W., "Dynamics and Control of Tethered Formation Flight Spacecraft Using the SPHERES Testbed," Proceedings of AIAA Guidance, Navigation and Control Conference, AIAA 2005-6089, San Francisco, August 2005.

[44] Chung, S.-J., Adams, D., Saenz-Otero, A., Kong, E., Miller, D.W., Leisawitz, D., Lorenzini, E., and Sell, S., "SPHERES Tethered Formation Flight Testbed: Advancements in Enabling NASA's SPECS Mission," Proceedings of Astronomical Telescopes and Instrumentation 2006 Conference, SPIE Paper No. 6268-11, May 2006.

[45] Chung, S.-J., Slotine, J.-J.E., and Miller, D.W., "Nonlinear Model Reduction and Decentralized Control of Tethered Formation Flight," Journal of Guidance, Control, and Dynamics, Vol. 30, No. 2, 2007.

[46] Clarke, D.W., Mohtadi, C., and Tuffs, P.C., "Generalized Predictive Control - Part 1: The Basic Algorithm," *Automatica*, Volume 23, pp. 137-148, 1987.

[47] Clarke, D.W., Mohtadi, C., and Tuffs, P.C., "Generalized Predictive Control - Part 2: The Basic Algorithm," *Automatica*, Volume 23, pp. 149-163, 1987.

[48] Collins, J.J., and Stewart, I.N., "Coupled Nonlinear Oscillators and the Symmetries of Animal Gaits," Nonlinear Science, 3:349-392, 1993.

[49] Cosmo, M., and Lorenzini, E.M., *Tethers in Space Handbook*, Cambridge, Massachusetts, 3rd ed., 1997, prepared for NASA/MSFC by Smithonian Astrophysical Observatory.

[50] Craig, J.J., *Introduction to Robtics, Mechanics and Control*, 2nd ed., Addison Wesley, 1989.

[51] Craig, J.J., *Adaptive Control of Mechanical Manipulators*, Addison-Wesley, Reading, MA, 1988.

[52] Crassidis, J.L., and Junkins, J.L., *Optimal Estimation of Dynamic Systems*, CRC Press, Boca Raton, FL, 2004.

[53] Crouch, P.E., "Spacecraft Attitude Control and Stabilization: Applications of Geometric Control Theory to Rigid Body Models," IEEE Transactions on Automatic Control, Vol. 29, No. 4, April 1984.

[54] DAvella, A., Saltiel, P., Bizzi, E., "Combinations of Muscle Synergies in the Construction of a Natural Motor Behavior," Nature Neuroscience, 2003.

[55] DeCou, A.B., "Tether Static Shape for Rotating Multimass, Multitether, Spacecraft for Triangle Michelson Interferometer," Journal of Guidance, Control and Dynamics, Vol. 2, No. 2, March 1989, pp. 273-275.

[56] Demidovich, B.P., "Dissipativity of a Nonlinear System of Differential Equations," *ser. matematika mehanika, part I* **N.6***, pp. 19–27; part II* **N.1***, pp.3–8* Vestnik Moscow State University, 1962.

[57] Deng, H., and Krstić, M., "Output-Feedback Stochastic Nonlinear Stabilization," *IEEE Transactions on Automatic Control*, Vol. 44, No. 2, February 1999.

[58] Deng, H., and Krstić, M., and Williams, R.J., "Stabilization of stochastic nonlinear systems driven by noise of unknown covariance," *IEEE Transactions on Automatic Control*, 46(8):1237-1253, 2001.

[59] Doya, K., Kimura, H., and Kawato, M., "Neural Mechanisms of Learning and Control," *IEEE Control Systems Magazine*, Vol. 21, August 2001.

[60] Egeland, O. and Godhavn, J.-M., "Passivity-based adaptive attitude control of a rigid spacecraft," IEEE Transactions on Automatic Control, Volume 39, Issue 4, Pp. 842 - 846, April 1994.

[61] Farley, R.E., and Quinn, D. A., "Tethered Formation Configurations: Meeting The Scientific Objectives of Large Aperture And Interferometric Science," AIAA 2001-4770.

[62] Fierro, R., Song, P., Das, A., and Kumar, V., "Cooperative Control of Robot Formations," in Cooperative Control and Optimization: Series on Applied Optimization, Kluwer Academic Press, 79-93, 2002.

[63] Fowler, J. M., and D'Andrea, R., "A Formation Flight Experiment," IEEE Control Systems Magazine, October 2003.

[64] Gelb. A, *Applied Optimal Estimation*, M.I.T. Press, 1974.

[65] Franklin, G.F., Powell, J.D., and Emami-Naeini, A., *Feedback Control of Dynamical Systems*, Addison Wesley, 3rd ed., 1995.

[66] Franklin, G.F., Workman, M.L., and Powell, J.D., *Digital Control of Dynamic Systems*, Addison Wesley, 3rd ed., 1997.

[67] Frazzoli, Emilio, "Robust Hybrid Control for Autonomous Vehicle Motion Planning," Ph.D. Thesis, Department of Aeronautics and Astronautics, MIT, May 2001.

[68] Fujii, H.A., Watanabe T., and Trivailo, P.M., "Wave-Absorbing Control of Transverse Vibration of Tethered System," Journal of Astronautical Sciences, Vol 51, No.3, pp 249-259, 2004.

[69] Fujii, H.A., Watanabe, T., Taira, W., and Trivailo, P.M., "An Analysis of Vibration and Wave-Absorbing Control of Tether Systems," AIAA Guidance, Navigation, and Control Conference, Montreal, Canada, 2001, AIAA01-37340.

[70] Golubitsky, M., and Stewart, I., "Synchrony versus Symmetry in Coupled Cells," Equadiff 2003: Proceedings of the International Conference on Differential Equations, 2003.

[71] Goswami, A., Thuilot, B., and Espiau, B., "A study of the passive gait of a compass-like biped robot: symmetry and chaos," International Journal of Robotics Research, Vol. 17, No. 12, 1998.

[72] Grocott, S.C.O., *Comparison of Control Techniques for Robust Performance on Uncertain Structural Systems*, Master of Science Thesis, MIT, 1994.

[73] Grossberg, S., "The Complementary Brain: a Unifying View of Brain Specialization and Modularity," Trends in Cognitive Sciences, 2000.

[74] Gurfil, P., Idan, M., and Kasdin, N.J., "Adaptive Neural Control of Deep-Space Formation Flying", Journal of Guidance, Control and Dynamics, Vol. 26, No. 3, May-June 2003.

[75] Gwaltney, D. A., and Greene, M. E., "Ground-Based Implementation and Verification of Control Laws for Tethered Satellites," Journal of Guidance, Control, and Dynamics, Vol. 15, No. 1, 1992, pp. 271-273.

[76] Haley, P. and Soloway, D. "Generalized Predictive Control for Active Flutter Suppression," *IEEE Control Systems Magazine*, Volume: 17, Issue:4,Aug 1997.

[77] Harwit, M. "Kilometer-Baseline Far-Infrared/Submillimeter Interferometer Vision Mission: Final Report," Interferometer Vision Mission Team. May, 2005.

[78] Hartmann, P., *Ordinary differential equations John Wiley & Sons, New York*, 1964.

[79] Hernandez-Garduno, A., Lawson, J.K., and Marsden, J.E., "Relative Equilibria For The Generalized Rigid Body," Journal of Geometry and Physics 53, pp. 259-274, 2005.

[80] Hilstad, M., *Multi-Vehicle Testbed and Interface Framework for the Development and Verification of Separated Spacecraft Control Algorithms*, Master of Science thesis, MIT, 2002.

[81] Hokayem, P.F, and Spong, M.W., "Bilateral Teleoperation: An Historical Survey," Automatica, submitted, 2004. .

[82] Horn, R.A., and Johnson, C.R., *Matrix Analysis*, Cambridge University Press, 1985.

[83] Hyland, D.C., and Scharf, D.P., "Adaptive Neural Control for MACE II," AIAA Paper Number 99-4588.

[84] Ihle, I.-A. F., Jouffroy, J, and Fossen, T.I., "Formation Control of Marine Surface Craft using Lagrange Multipliers," IEEE CDC-ECC 2005, Seville, Spain, 2005.

[85] Ijspeert, A. J., et al., "Simulation and Robotics Studies of Salamander Locmotion: Applying Neurobiological Principles to the Control of Locomotion in Robotics," Neuroinformatics. 3(3):171-95, 2005.

[86] Jadbabaie, A., Lin, J., and Morse, A. S., "Coordination of Groups of Mobile Autonomous Agents Using Nearest Neighbor Rules," IEEE Transactions on Automatic Control, May 2003.

[87] Jadbabaie, A., "Receding Horizon Control of Nonlinear Systems: A Control Lyapunov Function Approach," Ph.D. Thesis, Caltech, 2000.

[88] Johnson, E.N. and Calise, A.J., "Limited Authority Adaptive Flight Control for Reusable Launch Vehicles," Journal of Guidance, Control, and Dynamics, Vol. 26, No. 6, November-December 2003.

[89] Jung, D., and Tsiotras, P., "A 3-DOF Expreimental Test-Bed for Integrated Attitude Dynamics and Control Research," AIAA Guidance, Navigation and Control Conference, 2003, Austin, Texas.

[90] Kaltantzis, S., Modi, V.J., Pradhan, S., and Misra, A.K, "Order-N Formulation and Dynamics of Multibody Tethered Systems," Journal of Guidance, Control, and Dynamics, Vol. 21, No. 2, March-April 1998.

[91] Kandel, E.R., Schwartz, J.H., and Jessel, T.M., *Principles of Neural Science*. 4th ed.McGraw-Hill, 2000.

[92] Khalil, H.K., *Nonlinear Systems*, 3rd Ed.,Prentice Hall, Upper Saddle River, NJ, 2002.

[93] Khatib, O., Yokoi, K., Chang, K., Ruspini, D., Holmberg, R., Casal, A., "Vehicle/Arm Coordination and Multiple Mobile Manipulator Decentralized Cooperation," Proc. of IEEE/RSJ Int. Conf. Intelligent Robots and Systems, IROS'96, Osaka, Japan, 1996, pp. 546-553.

[94] Kim, M., and Hall, C. D., "Control of a Rotating Variable-Length Tethered System," J. of Guidance, Control and Dynamics, Vol.27, No.5, Sep-Oct 2004.

[95] Kline-Schoder, R., and Powell, J. D., "Recent Laboratory Results of the KITE Attitude Dynamics Simulator," Proceedings of 2nd International Conference on Tethers in Space, edited by L. Gnerriero and I. Bekey,Washington, DC, 1987, pp. 61-66.

[96] Kojima, H., et al., "Nonlinear Control of Librational Motion of Tethered Satellites in Elliptic Orbits," J of Guidance, Control and Dynamics, Vol.27, No. 2, March-April 2004.

[97] Kokubun, K., et al., "Deployment,Retrieval Control of Tethered Subsatellite Under Effect of Tether Elasticity," J. of Guidance, Control and Dynamics, Vol.19,No.1, January-February 1996.

[98] Kong, M. C., et al., "SPHERES as a Formation Flight Algorithm Development and Validation Testbed: Current Progress and Beyond," 2nd International Symposium on Formation Flying Missions and Technologies, Washington, DC.,September 14-16, 2004.

[99] Krishnaprasad, P. S., and Tsakiris, D., "Oscillations, SE(2)-Snakes and Motion Control: A Study of the Roller Racer, " Dynamics and Stability of Systems, 2001.

[100] Krstic, K., Kanellakopoulos, I., and Kokotovic, P., *Nonlinear and Adaptive Control Design*, John Wiley and Sons, 1995.

[101] Kumar, K.D, "Review of Dynamics and Control of Nonelectrodynamic Tethered Satellite Systems," Journal of Spacecraft and Rockets, Vol. 43, No. 4, July-August 2006.

[102] Kumar, K. D. and Yasaka, Y., "Rotating Formation Flying of Three Satellites Using Tethers," J. Spacecraft and Rockets, Vol. 41, No. 6, Nov-Dec 2004.

[103] Liu, K.-C. A. , "Stochastic Performance Analysis and Staged Control System Designs for Space Based Interferometers," Ph.D. thesis, MIT, 2003.

[104] Lee, D. and Li, P.Y., "Formation and Maneuver Control of Multiple Spacecraft ," Proceedings of the 2003 American Control Conference, Vol.1, pp. 278 - 283, June 2003.

[105] Lee, D. and Spong, M.W., "Passive Bilateral Teleoperation with Constant Time-Delay," Transactions on Robotics, vol. 22, no. 2, pp. 269-281, April 2006.

[106] Lee, D. and Spong, M.W., "Stable Flocking of Multiple Inertial Agents on Balanced Graph," Proceedings of the 2006 American Control Conference, June 2006.

[107] Leisawitz, D., et al., "Scientific Motivation and Technology Requirements for the SPIRIT and SPECS Far-infrared/Submillimeter Space Interferometers," Proceedings SPIE 4013, 2000, p. 36.

[108] Leonard, N.E., and Fiorelli, E., "Virtual Leaders, Artificial Potentials and Coordinated Control of Groups," 40th IEEE Conference on Decision and Control, 2001.

[109] Lewis, D.C., "Metric properties of differential equations," *American Journal of Mathematics,* **71**, pp. 294–312, 1949.

[110] Liberzon, D. and Morse, A.S., "Basic Problems in Stability and Design of Switched Systems," IEEE Control Systems Magazine, October 1999.

[111] Lin, Z., Broucke, M., and Francis, B., "Local Control Strategies for Groups of Mobile Autonomous Agents. IEEE Trans. on Automatic Control, 2004.

[112] Lohmiller, W., and Slotine, J.J.E., "On Contraction Analysis for Nonlinear Systems," Automatica, 34(6), 1998.

[113] Lohmiller, W., and Slotine, J.J. E., "Nonlinear Process Control Using Contraction Theory," A.I.Ch.E. Journal, March 2000.

[114] Lohmiller, W., and Slotine, J.J. E., "Control System Design for Mechanical Systems Using Contraction Theory," IEEE Transactions on Automatic Control, Vol. 45, No. 5, May 2000.

[115] Lohmiller, W., and Slotine, J.J.E., "Contraction Analysis of Nonlinear Distributed Systems," International Journal of Control, 78(9), 2005.

[116] Lohmiller, W., and Slotine, J.J.E., "High-Order Nonlinear Contraction Analysis," MIT NSL Report, NSL-050901, September 2005.

[117] Lorenz, E.N., "Deterministic Non-periodic Flow," J. Atmos. Sci. 20 (1963) 130-141.

[118] Lorenzini, E., Bombardelli, C., Cosmo, M., Harwit, M., Leisawitz, D., Farley, R., Rinehart, S., Quinn, D., and Miller, D., "Far-Infrared/Submillimeter Astronomical Interferometry with Spaceborne Tether Formations," Astrophys Space Sci., 302:225-239, 2006.

[119] Lynch, K. M., Shiroma, N., Arai, H., and Tanie, K., "Collision-free trajectory planning for a 3-DOF robot with a passive joint," International Journal of Robotics Research, 19(12):1171-1184, December 2000.

[120] Mabie, H. H., and Rogers, C. B., 1972, "Transverse Vibrations of Double-Tapered Cantilever Beams," J. Acoust. Soc. Am. 51, pp. 1771-1774.

[121] Marsden, J. E., Tromba, A. J., and Weinstein, A., *Basic Multivariable Calculus*, Springer-Verlag, New York, 1993.

[122] Masterson, R.A., Miller, D.W., and Grogan, R.A., "Development And Validation of Reaction Wheel Disturbance Models: Empirical Model," Journal of Sound and Vibration (2002) 249(3), 575-598.

[123] Mather, J.C et al., "The Submillimeter Frontier: A Space Science Imperative," Astrophysics 1998, astro-ph/9812454.

[124] McConley, M.W., Appleby, B.D., Dahleh, M.A., and Feron, E., " Computationally Efficient Lyapunov-Based Scheduling Procedure for Control of Nonlinear Systems with Stability Guarantees," IEEE Trans. Aut. Control, Jan 2000.

[125] Megretski, A., *6.243 Dynamics of Nonlinear Systems*, MIT Lecture Notes, available at http://ocw.mit.edu.

[126] Mesbahi, M., and Hadaegh, F.Y., "Formation Flying of Multiple Spacecraft via Graphs, Matrix Inequalities, and Switching," AIAA Journal of Guidance, Control, and Dynamics, (24) 2: 369-377, 2001.

[127] Miller, D.W. and Mallory, J.W., "Control Testbeds and Flight Demonstrations: Transitioning Theory to Application," Proceedings of the American Control Conference, Philadelphia, PA, June 1998.

[128] Miller, D.W., and von Flotow, A.H., "A Traveling Wave Approach to Power Flow in Structural Networks," Journal of Sound and Vibration, 128(1), 145-162, 1989.

[129] Miller, D.W., Hall, S.R., and von Flotow, A.H., "Optimal Control of Power Flow at Structural Junctions," Journal of Sound and Vibration, 140(3), 475-497, 1990.

[130] Miller, D.W., and Hall, S.R., "Experimental Results Using Active Control of Traveling Wave Power Flow," AIAA Journal of Guidance, Control, and Dynamics, Vol. 14, No. 2, March-April 1991, pp. 350-359.

[131] Miller, D.W., and Grocott, S.C., "Robust control of the Multiple Mirror Telescope adaptive secondary mirror," Optical Engineering 38(08), p. 1276-1287.

[132] Misra, A. K., "Equilibrium Configurations of Tethered Three-Body Systems And Their Stability," Paper AAS 01-191.

[133] Misra, A.K., and Modi,V.J., "A Survey on the Dynamics and Control of Tethered Satellite Systems," Advances in the Astronautical Sciences,Vol. 62, 1986, pp. 667-719.

[134] Murray, R.M., "Nonlinear Control of Mechanical Systems: A Lagrangian Perspective," Annual Reviews in Control, v21, pp 31-45, 1997.

[135] Murray, R.M. and Hauser, J., "A Case Study in Approximate Linearization: The Acrobot Example," University of California, Berkeley Technical Report No. UCB/ERL M91/46, 1991.

[136] Murray, R.M., Rathinam, M., and Sluis, W., "Differential Flatness of Mechanical Control Systems: A Catalog of Prototype Systems," 1995 ASME Int'l Eng Congress and Expo, San Francisco, CA, 1995.

[137] Murray, R.M., Li, Z., and Sastry, S., *A Mathematical Introduction to Robotic Manipulation*, CRC Press, Boca Raton, FL, 1994.

[138] Nakaya, K, et al., "Formation Deployment Control for Spinning Tethered Formation Flying - Simulations and Ground Experiments," AIAA GNC Conference, August 2004, AIAA 2004-4896.

[139] Nakaya, K, and Matunaga, Saburo, "On Attitude Maneuver of Spinning Tethered Formation Flying Based on Virtual Structure Method," AIAA GNC, August 2005, San Francisco, CA, AIAA 2005-6088.

[140] Narendra, K.S. and Mukhopadhyay, S., "Intelligent Control Using Neural Networks," *IEEE Control Systems Magazine*, Vol.12, Issue:2, April 1992.

[141] Narendra, K.S., "Neural Networks for Control: Theory and Practice," *Proceedings of the IEEE*, Vol. 84, Issue:10, Oct. 1996.

[142] Narendra, K.S. and N. Ol Oleng, "Exact Output Tracking in Decentralized Adaptive Control Systems," *IEEE Transactions on Automatic Control*, Vol.47, No. 2, February 2002.

[143] Niemeyer, G., and Slotine J.J.E., "Telemanipulation with Time Delays," International Journal of Robotics Research, 23(9), 2004.

[144] Quadrelli, M. B., "Modeling and Dynamics Analysis of Tethered Formations for Space Interferometry," Paper AAS 01-231.

[145] Olfati-Saber, R., "Nonlinear Control of Underactuated Mechanical Systems with Application to Robotics and Aerospace Vehicles," Ph.D. thesis, Department of EECS, MIT, February 2001.

[146] Olfati-Saber, R., and Murray, R.M., "Consensus Problems in Networks of Agents with Switching Topology and Time-Delays," in the special issue of the IEEE Transactions On Automatic Control on Networked Control Systems, VOL. 49, NO. 9, Sept. 2004.

[147] Ögren, P., Egerstedt, M. and Hu, X., "A Control Lyapunov Function Approach to Multiagent Coordination," *IEEE Transactions on Robotics and Automation*, Vol. 18, No. 5, October 2002.

[148] Ögren, P., Fiorelli, E., and Leonard, N.E., "Cooperative Control of Mobile Sensor Networks: Adaptive Gradient Climbing in a Distributed Environment," IEEE Trans. on Automatic Control, 49(8):1292.1302, 2004.

[149] Passino, K. M., "Bridging the Gap between Conventional and Intelligent Control," *IEEE Control Systems Magazine*, Vol. 13 , Issue: 3, June 1993.

[150] Parlitz, U., Kocarev, L., Stojanovski, T., and Preckel, H., "Encoding Messages Using Chaotic Synchronization," Phys. Rev. E, vol. 53, no. 5, pp. 4351-4361, 1996.

[151] Pecora, L.M., and Carroll, T.L., "Synchronisation in chaotic systems, Phys. Rev. Letter," 64, 821-824, 1990.

[152] Pham, Q.-C., and Slotine, J.J. E., "Stable Concurrent Synchronization in Dynamic System Networks," Neural Networks, 20(1), 2007.

[153] Pilkey, W. D., 1994, *Formulas for Stress, Strain and Structural Matrices*, John Wiley & Sons, Inc., New York,

[154] Pitti, A., Lungarella, M. and Kuniyoshi,Y. "Synchronization: Adaptive Mechanism Linking Internal and External Dynamics," Proc. of the 5th Int. Workshop on Epigenetic Robotics, 2006.

[155] Pogromsky, A. Santoboni, G, and Nijmeijer H., "Partial synchronization: from symmetry towards stability, " Physica D, 172, 65-87, 2002.

[156] Quinn, D. A., and Folta, D. C., "A Tethered Formation Flying Concept for the SPECS Mission," Proceedings of the 23rd Rocky Mountain Guidance and Control Conference, Vol. 104, Univelt, San Diego, CA, 2000, pp. 183-196.

[157] Ramamoorthy, S. and Kuipers, B., "Qualitative Hybrid Control of Dynamic Bipedal Walking," 2006 Robotics: Science and Systems Conference, August 16-19, 2006, Philadelphia, Pennsylvania.

[158] Rantzer, Anders, "A dual to Lyapunov's stability theorem," Systems and Control Letters, 42:3, pp. 161–168, 2001.

[159] Rathinam, M. and Murray, R.M., "Configuration Flatness of Lagrangian Systems Underactuated by One Control," SIAM Journal on Control and Optimization, 1996.

[160] Sedwick, R.J, et al., "Propellantless Spin-up of Tethered or Electromagnetically Coupled Sparse Apertures," Proceedings of SPIE, Vol. 4849, Highly Innovative Space Telescope Concepts, December 2002, pp. 193-204.

[161] Reyhanoglu, M., van der Schaft, A., McClamroch, N. H., and Kolmanovsky, I., "Dynamics and Control of a Class of Underactuated Mechanical Systems," IEEE Transactions on Automatic Control, 44(9):1663-1671, 1999.

[162] Richards, A.G., "Robust Constrained Model Predictive Control," MIT, Ph.D. Thesis, December 2004

[163] Roark, R. J., and Young, W. C., 1975, *Formulas for Stress and Strain*, McGraw-Hill Book Company, New York.

[164] Rodriguez-Angeles, A., and Nijmeijer, H., "Mutual Synchronization of Robots via Estimated Sate Feedback: A Cooperative Approach," IEEE Transactions on Control Systems Technology, Vol. 12, No. 4, 2004.

[165] Rugh, W.J., and Shamma, J.S., "Research on Gain Scheduling," Automatica, 36, 1401-1425, 2000.

[166] Rui, C., Kolmanovsky, I.V., McClamroch, N.H., "Nonlinear Attitude and Shape Control of Spacecraft with Articulated Appendages and Reaction Wheels," IEEE Transactions on Automatic Control, Vol. 45, No. 8, 2000.

[167] Saeed, S. I., "Optimal Control of Tethered Artificial Gravity Spacecraft," Ph.D. thesis, Stanfrod University, March 1997.

[168] Saenz-Otero, Alvar, "Design Principles for the Development of Space Technology Maturation Laboratories Aboard the International Space Station," Ph.D. Thesis, Department of Aeronautics and Astronautics, MIT, June 2005.

[169] Sanner, R. M. and Slotine, J-J E., "Gaussian Networks for Direct Adaptive Control," *IEEE Transactions on Neural Networks*, Vol. 3., No. 6, November 1992.

[170] Sanner, R. M. and Slotine, J-J E., "Structurally Dynamic Wavelet Networks for the Adaptive Control of Uncertain Robotic Systems," Proc. of the 34th Conference on Decision and Control, New Orleans, LA, December 1995.

[171] Sanyal, A. K., Shen, J., and McClamroch, N.H., "Control of a Dumbbell Spacecraft using Attitude and Shape Control Inputs Only," Proceedings of American Control Conference, Boston, 2004.

[172] Sastry, S. S., *Nonlinear Systems: Analysis, Stability, and Control*, Springer-Verlag, 1999.

[173] Shan, J., and Liu, H.-T., "Close-Formation Flight Control with Motion Synchronization," Journal of Guidance, Control, and Dynamics, Vol. 28, No. 6, 2005.

[174] Shen, J., Sanyal, A.K., Chaturvedi, N.A., Bernstein, D., ans McClamroch, H., "Dynamics and Control of a 3D Pendulum," 43rd IEEE Conference on Decision and Control December 14-17, 2004 Atlantis, Paradise Island, Bahamas.

[175] Sinopoli, B., Sharp, C., Schaffert, S., Schenato, L., and Sastry, S., "Distributed control applications within sensor networks," IEEE Proceedings Special Issue on Distributed Sensor Networks, November 2003.

[176] Slotine, J.-J.E., "Modular Stability Tools for Distributed Computation and Control," Int. J. Adaptive Control and Signal Processing, 17(6), 2003.

[177] Slotine, J.J.E. and Benedetto, M.D.D., "Hamiltonian Adaptive Control of Spacecraft," IEEE Transactions on Automatic Control, Vol. 35, No. 7, July 1990, pp. 848-852.

[178] Slotine, J.-J.E., and Li, W., *Applied Nonlinear Control*, Prentice Hall,. New Jersey, 1991.

[179] Slotine, J.-J.E., and Li, W., "On the Adaptive Control of Robot Manipulators," Int. J. Robotics Research, Vol.6, No. 3, pp. 49-59, Fall 1987.

[180] Slotine, J.-J.E., and Lohmiller, W., "Modularity, Evolution, and the Binding Problem: A View from Stability Theory," Neural Networks, 14(2), 2001.

[181] Slotine, J.-J.E., Wang, W., and El Rifai, K., "Synchronization in Networks of Nonlinearly Coupled Continuous and Hybrid Oscillators," Sixteenth International Symposium on Mathematical Theory of Networks and Systems (MTNS 2004), July 2004.

[182] Smith, R. S., and Hadaegh, F. Y., "Control of Deep-Space Formation-Flying Spacecraft; Relative Sensing and Switched Information," AIAA J. GCD, Vol. 28, No. 1 Jan-Feb 2005.

[183] Soloway, D. and Haley, P. J., "Neural Generalized Predictive Control-A Newton-Raphson Implementation," *Proc. of the 1995 IEEE International Symposium on Intelligent Control*, Dearborn, MI, September 1996.

[184] Sontag, E.D., "A Lyapunov-like Characterizatoin of Asymptotic Controllability," SIAM Journal on Control and Optimization, 1983.

[185] Sontag, E.D., "A Universal Construction of Arstein's Theorem on Nonlinear Stabiliation," System and Control Letters, 1989.

[186] Spong, M.W., "Remarks on Robot Dynamics: Canonical Transformations and Riemannian Geometry," Proc. of the 1992 IEEE International Conference on Robotics and Automation, Nice, France, 1992.

[187] Spong, M.W., "Swing Up Control Problem For the Acrobot," IEEE Control Systems Magazine, Feb., 1995.

[188] Spong, M.W. and Vidyasagar, M., *Robot Dynamics and Control*, John Wiley & Sons, 1989.

[189] Spong, M.W., and Bhatia,G., "Further Results on Control of the Compass Gait Biped," Proc. of the 2003 IEEE/RSJ, Int'l Conference on Intelligent Robots and Systems, Las Vegas, Nevada, October 2003.

[190] Strang, G., *Introduction to Applied Mathematics*, Wellesley-Cambridge Press, Wellesey, MA, 1986.

[191] Strogatz, S., *Sync: The Emerging Science of Spontaneous Order*, New York: Hyperion, 2003.

[192] Subbarao, K. and Junkins, J. L., "Structured Model Reference Adaptive Control for a Class of Nonlinear Systems," Journal of Guidance, Control and Dynamics, Vol. 26, No. 4, July-August 2003.

[193] Nair, S., and Leonard, N.E., "Stable Synchronization of Mechanical System Networks," Submitted to SIAM Journal of Control and Optimization.

[194] Tedrake, R. L., "Applied Optimal Control for Dynamically Stable Legged Locomotion," Ph.D. thesis, Massachusetts Institute of Technology, 2004.

[195] Tillerson, M., Breger, L., and How, J.P., "Distrbuted Coordination and Control of Formation Flying Spacecraft," Proceedings of the American Control Conference, Vol. 2, IEEE, 2003, pp. 1740-1745.

[196] Tragesser, S.G., "Formation Flying with Tethered Spacecraft," AIAA/AAS Astrodynamics Specialist Conference, August 2000, A00-39828.

[197] Tsiotras, P., Corless, M., and Longuski, J.M, "A Novel Approach to the Attitude Control of Axi-Symmetric Spacecraft," Automatica, Vol. 31, No. 8, pp. 1099-1112, 1995.

[198] Tsiotras, P., and Luo, J., "Reduced-Effort Control Laws for Underactuated Rigid Spacecraft," AIAA Journal of Guidance, Control, and Dynamics, Vol. 20, No. 6, pp. 1089–1095, 1997.

[199] Tsiotras, P. and Luo, J., "Control of Underactuated Spacecraft with Bounded Inputs," Automatica, Vol. 36, No. 8, pp. 1153-1169, 2000.

[200] Vidyasagar, M., *Nonlinear Systems Analysis*, 2nd ed., SIAM Classics in Mathematics, SIAM, Philadelphia, 1993.

[201] Wang, P.K.C., Hadaegh, F.Y., and Lau, K., "Synchronized Formation Rotation and Attitude Control of Multiple Free-Flying Spacecraft," Journal of Guidance, Control, and Dynamics, Vol. 22, No. 1, 1999.

[202] Wang, W., and Slotine, J.J.E., "On Partial Contraction Analysis for Coupled Nonlinear Oscillators," Biological Cybernetics, 92(1). 2004.

[203] Wang, W., and Slotine, J.J.E., "Contraction Analysis of Time-Delayed Communications Using Simplified Wave Variables," IEEE Trans. Aut. Control, 51(5), 2006.

[204] Wang, W., and Slotine, J.J.E., "A Theoretical Study of Different Leader Roles in Networks," IEEE Transactions on Automatic Control, 51(7), 2006.

[205] Wang, W., Yi, J., Zhao, D., and Liu, D., "Design of a Stable Sliding-Mode Controller for a Class of Second-Order Underactuated Systems," IEE Proc.-Control Theory Appl., Vol. 151, No. 6, November 2004.

[206] Westervelt, E.R., Buche, G., and Grizzle, J. W., "Experimental Validation of a Framework for the Design of Controllers that Induce Stable Walking in Planar Bipeds," The International Journal of Robotics Research, Vol. 23, No. 6, 559-582 (2004)

[207] Wiesel, W.E., *Spaceflight Dynamics*, 2nd ed., McGraw Hill, 1997.

[208] Wie, Bong, *Space Vehicle Dynamics and Control*, AIAA, Reston, Virginia, 1998.

[209] Williams, P., Watanabe, W., Blanksby, C., Trivailo, P., and Fujii, H.A., "Libration Control of Flexible Tethers Using Electromagnetic Forces and Movable Attachment," AIAA Journal of Guidance, Control and Dynamics, Vol. 27, No. 5, 2004.

[210] Wilson, J.M., "Control of a Tethered Artificial Gravity Spacecraft," Ph.D. thesis, Stanford University, 1990.

[211] Wong, B. and Misra, A.K, "Dynamics of Lagrangian Point Multi-Tethered Satellite Systems," Journal of the Astronautical Sciences, Vol. 53, No. 3, 2005, pp. 221-250.

[212] Woolsey, C., Reddy, C.K., Bloch, A.M., Chang, D.E., Leonard, N.E., and Marsden, J.E., "Controlled Lagrangian systems with gyroscopic forcing and dissipation," European Journal of Control (Special Issue on Lagrangian and Hamiltonian Methods for Nonlinear Control) 10(5), pp. 478-496, December 2004.

[213] Yu, S., "Dynamic Model and Control of Mass-Distributed Tether Satellite System," J. Spacecraft and Rockets, Vol.39 No.2, March-April 2002.

[214] Zhang, M., and Tarn, T.-J., "A Hybrid Switching Control Strategy for Nonlinear and Underactuated Mechanical Systems," IEEE Trans. on Automatic Control, Vol. 48, No. 10, October 2003.

[215] Zhong, W. and Rock, H., "Energy and Passivity Based Control of the Double Inverted Pendulum on a Cart," Proc. of the 2001 IEEE International Conf. on Control Applications, Mexico, 2001.

[216] Zhou, K., Doyle, J.C., and Glover, K., *Robust and Optimal Control*, Prentice-Hall, 1996.

[217] Zhou, K, and Doyle, J.C., *Essentials of Robust Control*, Prentice Hall, 1998.

[218] Zill, D. G., and Cullen, M. R., 1992, *Advanced Engineering Mathematics*, PWS Publishing Company, Boston, pp. 307-316.